

**The development of integrated high-resolution geophysical,
photogrammetric and GPS surveying applied to landslides
in the South Wales Coalfield**

Alessia Taboga



A thesis presented for the degree of Doctor of Philosophy

Cardiff University, 2011

School of Earth and Ocean Sciences
Cardiff University
Main Building
Park Place
Cardiff CF10 3AT
United Kingdom

UMI Number: U585580

All rights reserved

INFORMATION TO ALL USERS

The quality of this reproduction is dependent upon the quality of the copy submitted.

In the unlikely event that the author did not send a complete manuscript and there are missing pages, these will be noted. Also, if material had to be removed, a note will indicate the deletion.



UMI U585580

Published by ProQuest LLC 2013. Copyright in the Dissertation held by the Author.
Microform Edition © ProQuest LLC.

All rights reserved. This work is protected against
unauthorized copying under Title 17, United States Code.



ProQuest LLC
789 East Eisenhower Parkway
P.O. Box 1346
Ann Arbor, MI 48106-1346

ABSTRACT

The aim of this research is to develop an integrated and cost-effective site investigation approach for slow moving landslides or potentially unstable slopes found within the South Wales Coalfield, an area of complex geology and hydrogeology. The research was based on the use and assessment of a wide range of surface geophysical techniques, supported by GPS and Digital Photogrammetry surveying, and the joint interpretation of the results which such techniques provide.

The South Wales Coalfield has one of the highest concentrations of urban landslides in the UK due to its layered Carboniferous geology, Quaternary / Holocene geomorphology, coal mining history and relatively high rainfall. Mynydd yr Eglwys landslide (Ystrad, Rhondda Cynon Taff) was selected as the field study site because it can be considered representative of the active landslides found within the area. In autumn 1998, following an exceptional heavy rainfall period, a new compound deep-seated failure developed in a previously mined hillslope. This deep-seated failure then caused the reactivation of ancient periglacial debris slides downslope creating a serious risk to the modern housing estate located close to the toe.

Electromagnetic (GEM-2), self potential, electrical resistivity tomography, seismic refraction tomography, MASW and induced polarization geophysical data were all acquired on the landslide. This combination of techniques provided information on lithology, faulting, degree of rock fracturing/weathering, thickness of displaced material, spatial distribution of areas with high water/clay content and the direction of groundwater flow. The repetition of a few ERT and SP profiles showed the applicability of geophysical monitoring in detecting changes in groundwater content and defining preferential groundwater pathways within the hillslope.

Digital Photogrammetry from Helium balloon can provide a 3D landslide topographic model with 10cm-level accuracy. Topcon HiPer Pro GPS+ instrument can be used in RTK mode to monitor movement with 12mm and 15mm horizontal and vertical precision respectively.

ACKNOWLEDGEMENTS

Firstly, I would like to thank my university supervisors Dr. Peter Brabham and Professor Charles Harris, for their support, their advice and their help during data acquisition on the slopes of the Rhondda Valley.

This research was funded by an EPSRC CASE studentship, with Terradat (UK) Ltd as industrial partner. Therefore my thanks go to Terradat directors Nick Russill and Dr Rob McDonald for investing in my research and for their help and advice both in the office and on site (acquisition of photogrammetry and seismic data). I am also grateful to Dr. J. Thomas for advice on data processing, and to Christian Bird, Mike Bottomley, Angharad Matthews and Anthony Butcher for their help with fieldwork.

I would also like to thank Howard J. Siddle and Malcolm Turner from the Halcrow office in Cardiff for providing information on landslides and for sharing with me some of their expert opinions. Moreover, D. P. Jones provided RCTCBC EDM movement monitoring information, while Katie Edwards and Chris Turler (from Amgen Cymru/Rhondda Ltd) provided some of the rainfall data which I used for this project.

I am also grateful to: Leighton Davies (from Topcon), for his technical support with GPS instrument, and Andrew Wiltshire and Alun Rogers (Cardiff University) for helping me with the numerous software I had to install and use on my PC.

My project was very demanding in terms of fieldwork and it would not have been possible without all the people who helped me carrying equipment and acquiring data on the hillslopes of the Rhondda Valley. Dr Peter Brabham and Dr. Andrew Gray spent most of these days with me and I cannot just thank them enough for this. Over the years, Andrew has really become like a brother. Dr. Neil Ross, Dr Martina Luetschg, Dr. Sarah Ling and Leon Jones came also on site with me. Dave James and Owain Davies came in the field with me in summer 2008 as part of their undergraduate projects.

For their support, I would like to thank also my friends Jaynie Evans, Cristina Neagu, Carla Barnaba, Sereņa Covasso, Ana Maia, David Gamboa, Julia Becker, Mohamad N. Isah, Mark Harwood, and many other people I was lucky to meet during my years in Cardiff. For their moral support, I am grateful also to Dr. Tim Jones, Dr. Sergio Lourenco, Dr. Giovanna Della Porta, Dr. Jenny Pike and the members of Cardiff University security staff.

Finally, but most importantly, I am very grateful to my family, my mum Rosalina and my sister Rossella, who have always been so supportive of my choices and have always been there for me. My dad Ermes unfortunately died during the years of this project. To paraphrase what the poet Domenico Zannier said about him, my dad was 'a teacher at school and in life'. He believed in the beauty of knowledge and in the importance of using it to improve the conditions of the people around him. He set an important example for me and my sister and all the people of my village in Italy. Life has not been the same since his death and it will never be. I would like to remember also my aunty Elvira and my grandparents, in particular my grandfather Arduino, a very wise man.

TABLE OF CONTENTS

Declaration and statements	i
Abstract	ii
Acknowledgements	iii
Table of contents	iv
List of figures	viii
List of tables	xxii

Chapter 1 Introduction	1
1.1 Research overview.....	1
1.2 Introduction to landslides	6
1.2.1 Definition and classification of landslides.....	6
1.2.2 Landslide terminology	10
1.2.3 Basic principles of landsliding	15
1.2.4 Landslide causes	18
1.2.5 Slope stability assessments	19
1.3 Global Positioning Systems for the monitoring of surface displacements...	22
1.4 Digital Photogrammetry	24
1.5 The use of geophysics on landslides.....	25
1.5.1 Seismic methods (refraction, reflection and surface waves)	27
1.5.2 Electrical resistivity methods.....	29
1.5.3 Electromagnetic induction methods	31
1.5.4 Electrical Self Potential	32
1.5.5 Induced polarization	33
1.5.6 Other geophysical methods	33
1.6 Landslides in the South Wales Coalfield.....	36
1.6.1 Geology, structure and geomorphological history	36
1.6.2 Mining	42
1.6.3 Other human activities.....	48
1.6.4 Hydrology and hydrogeology	49
1.6.5 Engineering geology and types of failure.....	53
1.7 The site: Mynydd yr Eglwys landslide	57

1.8	Aims and objectives.....	59
1.9	Thesis outline.....	64
Chapter 2	Research Methods.....	65
2.1	Introduction	65
2.2	Light Detection and Ranging (LIDAR).....	66
2.2.1	Background.....	66
2.2.2	LIDAR data used in this project	71
2.3	Digital photogrammetry	74
2.3.1	Basic principles.....	74
2.3.2	Precision, accuracy and internal reliability.....	79
2.3.3	Digital photogrammetry at Mynydd Yr Eglwys landslide	79
2.4	Global Positioning System (GPS)	105
2.4.1	Basic Principles	105
2.4.2	GLONASS.....	113
2.4.3	GPS theoretical precision in landslide monitoring	114
2.4.4	The use of Global Positioning Systems for the monitoring of surface movements at Mynydd Yr Eglwys landslide.....	115
2.4.5	The use of GPS receivers for surveying position and topography at Mynydd yr Eglwys	133
2.5	Electromagnetic induction or ground conductivity mapping with reference to the Geophex GEM-2 instrument.....	136
2.5.1	Background to electromagnetic induction methods	136
2.5.2	The broadband multi-frequency instrument Geophex GEM-2.....	140
2.5.3	Limitations of EMI methods.....	146
2.5.4	Data acquisition at Mynydd yr Eglwys landslide	147
2.5.5	Data processing and visualisation.....	148
2.6	Self-potential (SP)	149
2.6.1	Background.....	149
2.6.2	SP Limitations	151
2.6.3	Data acquisition at Mynydd yr Eglwys landslide.....	151
2.6.4	SP data processing	154
2.7	Seismic refraction tomography.....	154
2.7.1	Background.....	154

2.8	Multichannel analysis of surface waves (MASW)	165
2.8.1	Background.....	165
2.8.2	Limitations of MASW method	168
2.8.3	Seismic refraction tomography and MASW data acquisition at Mynydd yr Eglwys landslide	169
2.8.4	Data processing.....	170
2.9	Electrical resistivity tomography (ERT).....	172
2.9.1	Background.....	172
2.9.2	Limitations.....	177
2.9.3	ERT data acquisition at Mynydd yr Eglwys landslide	178
2.9.4	ERT data processing.....	181
2.10	Induced Polarization (IP).....	182
2.10.1	Data acquisition and processing	185
2.11	Monitoring of groundwater pressures at Mynydd Yr Eglwys landslide	191
2.12	Rainfall Data.....	197
2.13	Summary and technical discussion.....	198
Chapter 3	Mynydd yr Eglwys Landslide.....	217
3.1	Introduction	217
3.2	Site location and general site description	218
3.3	Historical land use	222
3.4	Geology	228
3.4.1	Solid geology.....	228
3.4.2	Superficial deposits.....	230
3.4.3	Structure.....	231
3.5	Mining	239
3.6	Geomorphology	244
3.7	Hydrology and hydrogeology	251
3.7.1	Results from continuous monitoring of ground water levels	255
3.8	Landslide failure mechanisms and potential surfaces of rupture	268
3.9	Causes of new deep-seated failure.....	272
3.10	Remediation works.....	275
3.11	Landslide kinematics	276

3.11.1	Landslide movements determined by EDM measurements (by RCTCBC).....	276
3.11.2	Landslide movements determined by GPS observations	279
3.11.3	Photo sequence of Mynydd yr Eglwys Landslide	291
3.12	Summary.....	296
Chapter 4 Geophysical characterisation of Mynydd yr Eglwys Landslide.....		301
4.1	Introduction	301
4.2	Results and interpretation of electromagnetic data acquired with Geophex GEM-2 instrument.....	301
4.3	Results and interpretation of the Self Potential mapping data.....	308
4.4	Results and interpretation of seismic refraction tomography and MASW data.....	315
4.5	Results and interpretation of ERT profiles	323
4.6	Results and interpretation of IP data.....	329
4.7	Discussion.....	332
4.7.1	Joint interpretation of geophysical results leading to conceptual model of the landslide.....	332
4.7.2	Effectiveness of geophysical methods.....	336
Chapter 5 Results of geophysical monitoring at Mynydd yr Eglwys Landslide.....		339
5.1	Introduction	339
5.2	Results and interpretation of monitoring measurements along ERT 1L	340
5.2.1	Monitoring along ERT line X (also with SP profiles).....	345
5.3	Summary and discussion	349
Chapter 5 Conclusions		350
References.....		355
Website references.....		371
Appendix A Classification of slope movements by Hutchinson (1988)		A-1
Appendix B Classification of landslides of flow type by Hungr et al. (2001).....		B-1

Appendix C Literature review of published papers on the application of geophysics to landslide research.....	C-1
Appendix D Generical legend for historical maps.....	D-1
Appendix E Electrical Resistivity Tomography lines acquired at Mynydd yr Eglwys landslide.....	E-1

List of figures

Figures – Chapter 1

Figure 1.1 World and regional distribution of natural disasters by type for the years 1991 to 2005 (modified from figure produced by ISDR [WWW 1.2], source of data OFDA/CRED International Disaster Database EM-DAT.....	2
Figure 1.2 Fatalities and cost of damages caused by landslides during the period 1903-2004 for each continent (Nadim et al., 2006).....	3
Figure 1.3 Landslide distribution in Great Britain as recorded in the National database (Lee et al., 2000).....	4
Figure 1.4 Schematic diagram illustrating the types of movements described by Varnes (1978) (produced by BGS [WWW 1.4]).....	9
Figure 1.5 Schematic diagrams for the landslides classified by Hutchinson as confined failures, rotational slips and compound slides (Hutchinson, 1988).....	10
Figure 1.6 Landslide features shown on the block diagram of an idealised landslide (Varnes, 1978).	11
Figure 1.7 Diagram illustrating the landslide features described in the Multilingual Landslide Glossary (after WP/WLI, 1993 and Cooper, 2007).....	11
Figure 1.8 Diagram illustrating the states of activity of landslides (after WP/WLI, 1993; in Cooper, 2007).....	13
Figure 1.9 - Diagram illustrating styles of activity (after WP/WLI, 1993; in Cooper, 2007).....	14
Figure 1.10 Landslide velocities and possible consequences (after Cruden and Varnes, 1996).....	15
Figure 1.11 Block diagram of forces acting on a mass of soil/rock resting on a surface of rupture	16

Figure 1.12 Planar (a), wedge (b), toppling (c) and rotational (d) failures in rock. The type of failure is influenced by the geometry of the discontinuities (modified from Tanzini, 2001 and references therein)	20
Figure 1.13 Geology, Structure and landslide distribution in the South Wales Coalfield (modified from Bentley and Siddle, 1996 and Edina Digimap). The map underlines the location of the landslides mentioned in the text and of other well known failures which have been studied by other researchers.....	37
Figure 1.14 Generalised stratigraphy for the Central South Wales Coalfield (Brabham, 2004).....	39
Figure 1.15 Influence of deep coal mining on slope stability (modified from Halcrow, 1998).....	46
Figure 1.16 Influence of shallow coal mining on a hillslope (modified from Halcrow, 1998).....	47
Figure 1.17 Influence of human activities on slope stability (modified from Halcrow, 1989).....	49
Figure 1.18 Running 9-year average of rainfall at Treherbert rain gauge and significant landslide events in the Rhondda Valleys (Siddle and Bentley, 2000).....	50
Figure 1.19 Hydrogeology and landslides in the South Wales Coalfield (modified from Daughton et al., 1977 and Conway et al., 1980).....	52
Figure 1.20 Evolution of a typical deep-seated landslide in the South Wales Coalfield (Halcrow, 1998).....	56
Figure 1.21 Location of Mynydd yr Eglwys landslide at Ystrad, in the upper reaches of the Rhondda Fawr valley. Digital terrain model derived from Environmental Agency LIDAR data.....	59
Figure 1.22 Schematic diagram of a deep-seated landslide which has reactivated periglacial debris slides downslope, showing the targets of interest and the geophysical methods which can potentially detect them.....	63

Figures – Chapter 2

Figure 2.1 Main components of a LIDAR system: ranging unit (comprising of laser transmitter and receiver), mechanical scanner, and control, monitoring and recording units, positioning and orientation systems (dGPS and IMU). Other sensors (i.e. digital cameras) may be integrated to the system. While the airplane moves forward, the laser beam is scanned across the direction of flight. Airborne dGPS, GPS ground station

and IMU provide positioning and corrections for pitch, roll and yaw (or heading) of the aircraft (top image from website [WWW 2.1], bottom diagram from Wehr and Lohr, 1999)	67
Figure 2.2 Transmitted and received signal for a full-waveform LIDAR system with small (A) and large footprint (B) in a wooded area (from Mallet and Bretar, 2009) ..	69
Figure 2.3 Flow-chart of typical processing of LIDAR data (Wehr and Lohr, 1999).	71
Figure 2.4 The three datasets supplied by UK Environmental Agency for the area comprising Mynydd Yr Eglwys landslide (Tile D00046021): (A) unfiltered digital surface model, (B) filtered digital surface model or digital terrain model and (C) the applied filter mask.	73
Figure 2.5 Diagram showing the relationship between the terms in the collinearity equations (from Lillesand et al., 2004).....	76
Figure 2.6 Top: a view of the targets (ground control points) spread on the terrain at Mynydd yr Eglwys landslide from the top of the main scarp (photo by P. J. Brabham). Bottom: one of the vertical photographs taken from the camera mounted on the helium balloon (photo by N. Russill). In this photograph, each target is represented by a number of white pixels that ranges approximately between 100 and 150 (or the targets have a diameter of approximately 10-13 pixels).....	82
Figure 2.7 Camera set up (A) and image acquisition (B and C) at Mynydd yr Eglwys landslide. The camera was mounted on a helium balloon and then towed across the slope while taking photographs every 15 seconds (photos by P. J. Brabham).....	83
Figure 2.8 Topcon's PI-3000v3 orientation screen: measurement of ground control points and pass points before bundle adjustment	86
Figure 2.9 Topcon's PI-3000 stereo screen: closed polyline and breakline drawn on a rectified stereo-pair for successive automatic surface measurements	87
Figure 2.10 3D views of Mynydd yr Eglwys landslide with photo-texturing in Topcon's PI-3000v3 software	89
Figure 2.11 3D views of Mynydd yr Eglwys landslide without photo-texturing in Topcon's PI-3000v3 software. The final result was a collage of seven separate TINs (with reduced overlap).....	90
Figure 2.12 View of the four TINs used successively to assess the internal reliability of the method. TIN A and TIN C are the same as in Figure 2.11, while TIN B and TIN D are wider as they were created for an increased area of overlap with the adjacent TINs	91

Figure 2.13 3D view of Mynydd yr Eglwys landslide with contours overlaid on photo-texturing. Contour spacing is 2.5 m and 10 m for yellow and red lines respectively .	91
Figure 2.14 Ortho-photograph of Mynydd yr Eglwys landslide with 0.10 m/pixel resolution generated in Topcon's PI-3000v3 and then geo-referenced in Surfer 8 (Golden Software)	92
Figure 2.15 Post map of points contained in file allTINs.csv	93
Figure 2.16 Surface plot of the digital elevation model obtained gridding file allTINs.csv (top). Perspective view of Mynydd Yr Eglwys landslide obtained overlaying the orthophotograph on the digital elevation model (bottom).....	94
Figure 2.17 Surface plot of photogrammetric DEM showing the locations of: the TIN points exported from the photogrammetry software (blue dots), the photogrammetry ground control points (yellow crosses) and the GPS check-points (profile and monitoring movement markers as red and magenta circles respectively).....	96
Figure 2.18 Graph showing the distribution of height errors for the check-points along the GPS profile	98
Figure 2.19 Classified post map highlighting the range of height errors at check-point locations. The highest errors are located in the southern part of the profile and at movement marker CU 7	98
Figure 2.20 Post map of TIN A and TIN B. The heights in the overlapping area were compared to assess internal reliability.....	100
Figure 2.21 Post map of TIN C and TIN D. The heights in the overlapping area were compared to assess internal reliability.....	100
Figure 2.22 Image map showing the height differences between TIN A and TIN B in their overlapping area	103
Figure 2.23 Image map showing the height differences between TIN C and TIN D in their overlapping area	104
Figure 2.24 Classed post map of height differences between TIN A and TIN B in their overlapping area. The map highlights the location of the points characterised by highest variation	104
Figure 2.25 Classed post map of height differences between TIN C and TIN D in their overlapping area. The map highlights the location of the points characterised by highest variation	105
Figure 2.26 Determination of 3D receiver coordinates from measurement of pseudoranges with code ranging method (modified from Gili et al., 2000).....	109

Figure 2.27 Measurement of antenna positions with carrier phase method (modified from Gili et al., 2000)	109
Figure 2.28 Installation of anchor-marker at GPS base station (photos by the author)	117
Figure 2.29 Installation of a ground grip marker with raised head at one of the movement monitoring locations. Steel bars of another ground grip marker and of two econo-markers are shown on the grass (photos by the author).....	117
Figure 2.30 Topcon HiPer Pro GPS+ base antenna set up with tripod (plus tribrach) at the movement monitoring base station on Mynydd Yr Eglwys slope (photo by the author).....	121
Figure 2.31 GPS movement monitoring at markers CU5 (left) and CU13 (right) at Mynydd Yr Eglwys landslide. The rover antenna is set up on a tripod (plus tribrach)	121
Figure 2.32 GPS movement monitoring at surveyor reference points SB81 (left) and SB85 (right) along Meadow Walk. The two locations are not ideal for GPS monitoring because the receiver is close to obstacles (edge and buildings) that partly obscure the sky visibility and can cause multipath effects.....	122
Figure 2.33 Occupation view for GPS base station of 14 November 2008 at Mynydd Yr Eglwys landslide from Topcon Tools software. It is a time-scale chart of the GPS and GLONASS satellites in view during the data logging.....	125
Figure 2.34 Map view from Topcon Tools software showing stations and observation vectors after adjustment for Mynydd yr Eglwys base of 14 November 2008. One of the 10 closest stations (MACH) was not downloaded from Ordinance Survey web site because it was reported as not being healthy.....	125
Figure 2.35 Apparent movement in Eastings and Northings of “fixed” points during the monitoring period. The dimensions of the boxes are the same: 0.20 m in Eastings and 0.25 m in Northings. As expected, the scattering in coordinates is minimum for CU1	128
Figure 2.36 Graph showing the variation in elevation at “fixed” point CU 1 during the different GPS campaigns in comparison with its mean value (180.018 m)	129
Figure 2.37 Instruments used during the project for surveying topography and/or position: (A) Topcon EDM GTS-3B20 and Trimble dGPS Backpack, (B) Topcon HiPer Pro GPS+ and (C) Trimble Pathfinder ProXT GPS (photos by P.J. Brabham)	135

Figure 2.38 Schematic diagram illustrating the principle of electromagnetic induction methods (modified from Sharma, 1997).....	136
Figure 2.39 Vector diagram illustrating the amplitude and phase relationships between primary (P), secondary (S) and resultant (R) electromagnetic fields (Kearey et al., 2002).....	137
Figure 2.40 Conductivity (or resistivity) values for geological materials found in sedimentary environments (Table provided by Terradat UK Ltd, modified from Knight and Endres, 2005 and reference therein)	139
Figure 2.41 Conductivity (or resistivity) values for geological materials found in igneous or metamorphic environments (Table provided by Terradat UK Ltd, modified from Knight and Endres, 2005 and reference therein)	139
Figure 2.42 GEM-2 instrument used in horizontal coplanar configuration for the acquisition of EMI data at Mynydd yr Eglwys Landslide (photo P. J. Brabham).....	140
Figure 2.43 Schematic diagram illustrating geometrical and frequency sounding with EMI methods (from Won at [WWW 2.10])	142
Figure 2.44 Diagram illustrating the relationship between instrument frequency, ground conductivity and skin depth. For example, in an area of igneous rocks, if the source sweeps between 100 Hz and 100 KHz, the skin depth is 40-1500 m (from Won, 1980).....	144
Figure 2.45 Schematic diagram illustrating non-polarizing electrodes used for SP measurements	149
Figure 2.46 Self-potential equipment used for the surveys at Mynydd yr Eglwys landslide.....	152
Figure 2.47 Seismic velocity tables compiled and provided by Terradat UK Ltd	157
Figure 2.48 Diagram illustrating travel-time curves for direct, reflected and critically refracted waves (modified from Sharma, 1977).....	162
Figure 2.49 Schematic diagram for seismic tomography (see text) (from manual of SeisImager/2D, OYO Corporation).....	163
Figure 2.50 Illustration summarising the principles of MASW methodology (from Park et al., 2007).....	167
Figure 2.51 Acquisition of seismic refraction data along Line D at Mynydd yr Eglwys landslide (photos P. J. Brabham).....	170
Figure 2.52 Schematic diagram of a generic electrode configuration.....	173
Figure 2.53 Schematic diagram illustrating Wenner, Wenner-Schlumberger and	

Dipole-Dipole electrode configurations	174
Figure 2.54 Acquisition of multi-electrode data and their arrangement to obtain a pseudo-section (modified from RES2DINV software manual)	176
Figure 2.55 Graph (a) shows the decrease in bulk resistivity associated to an increase in saturation from 10 to 100% and for three different values of effective porosity (3%, 10% and 30%). Graph (b) shows the decrease in resistivity in terms of percent changes. The diagrams were obtained by Suzuki and Higashi (2001) applying Archi's law and considering the percentage change in resistivity equal to $\Delta\rho=[\log_{10}\rho-\log_{10}\rho_0]/\log_{10}\rho_0$ for $m=1.5$ and $n=2.0$	177
Figure 2.56 Acquisition of ERT data at Mynydd yr Eglwys Landslide (photo c by N. Ross)	179
Figure 2.57 Schematic diagrams illustrating determination of apparent polarizability and apparent chargeability (Parasnis, 1997).....	183
Figure 2.58 Membrane (left) and electrode polarization (right; modified from Telford et al., 1990)	185
Figure 2.59 IP non-polarizing electrodes built for this project, using gardening pots, copper wire, copper sulphate and jelly. The jelly was not completely set and sponges were put in side the pots, at their base, to insure contact of the jelly with the ground, but without emptying the pot.....	186
Figure 2.60 Chargeability sections for IP Test Line A, acquired with copper rods and jelly pots in Dipole-Dipole configuration and with jelly pots in Wenner-Schlumberger electrode configuration.....	189
Figure 2.61 Chargeability sections for IP line Y, acquired with copper rods and tent pegs, in both Dipole-Dipole and Wenner-Schlumberger electrode configurations...	190
Figure 2.62 Schematic diagram showing installation of Divers inside a borehole and the values necessary to correct the water level readings to a reference point (modified from instrument manual)	194
Figure 2.63 Data download from Mini-Diver installed in borehole 3 at Mynydd yr Eglwys landslide.....	195
Figure 2.64 Data download from CTD-Diver installed in borehole 11 at Mynydd yr Eglwys landslide (photo by A. Gray)	196

Figures – Chapter 3

Figure 3.1 View of Mynydd yr Eglwys Landslide from Nant y Gwyddon landfill site on the opposite side of the valley (photo P. J. Brabham)	219
Figure 3.2 Terrain model of Mynydd yr Eglwys Landslide obtained by overlaying 2000 air photography (Getmapping website [WWW3.1]) onto LIDAR data (Environmental Agency UK).....	220
Figure 3.3 Slope angle map for part of Mynydd yr Eglwys hillslope, derived from LIDAR data	220
Figure 3.4 Topography across the Rhondda Fawr from Mynydd yr Eglwys to Mynydd y Gelli (top) and in the area of Mynydd yr Eglwys Landslide only (bottom). The images were obtained from EA LIDAR data using Surfer 8.....	221
Figure 3.5 Part of the 1875 Ordnance Survey Map 6" to 1 Mile coloured	224
Figure 3.6 Reproduced from 1900 (top) and 1919 (bottom) Ordnance Survey Maps, (©Crown copyright 2009. An Ordnance Survey/EDINA supplied service; [WWW 3.2]). The red box shows the approximate location of the main scarp visible today. See Appendix D for legend	225
Figure 3.7 Geo-referenced air photography of 1948 (RAF: Welsh Assembly Government archive)	226
Figure 3.8 Reproduced from 1962 Ordnance Survey Map, 1:2500 (with 1:25000 OSM in transparency) (©Crown Copyright/database right 2009. An Ordnance Survey/EDINA supplied service; [WWW 3.2]). The red box shows the approximate location of the main scarp. See Appendix D for legend.....	226
Figure 3.9 Air photography of 5 May 1993 (Ordnance Survey) and air photography of 2000 (Bottom; Getmapping [WWW 3.1]). The two photographs show Mynydd yr Eglwys slope before (top) and after (bottom) the new deep-seated landslide event .	227
Figure 3.10 1948 air photography (top) and geological map (bottom) overlaid on LIDAR DTM data. The geological map is reproduced from Glamorgan Sheet XVIII S.W., published in 1960, from an original geological survey by W. Gibson in 1896, resurveyed by W. B. Evans in 1953 and A. W. Woodland in 1946. Red circles and red arrows indicate mine shafts and mine adits respectively.....	232
Figure 3.11 Solid geology map digitized from Halcrow report on Pentre Landslide (Halcrow, 1979) and overlaid on LIDAR data (top). Zoom on the area of Mynydd yr Eglwys Landslide showing the location of boreholes driven into the ground in 2003 by C.J. Associates (bottom).....	233

Figure 3.12 Geological plan for Mynydd yr Eglwys landslide reproduced from Halcrow report (1999) (the geological cross section is shown in Figure 3.13).....	234
Figure 3.13 Geological section of Mynydd yr Eglwys Landslide reproduced from Halcrow report (1999) (location of section and legend are shown in Figure 3.12)...	235
Figure 3.14 Cross section of Mynydd yr Eglwys Landslide (along resistivity line 1) showing lithology, water levels and potential surface of failure. The figure was compiled using information provided in the reports of C. J. Associates (2003) and Earth Science Partnership (2004)	236
Figure 3.15 Outcrop of No 3 Rhondda Seam. The strata above it, in the area of mine adit L5, have collapsed	237
Figure 3.16 Blocks of argillaceous shale with iron staining can be found in the northern part of the central debris slides	237
Figure 3.17 View of the minor scarp immediately downslope of boreholes 3, 3A, 4 and 4A. As evident from borehole logs and outcrops at cracks and scarps, landslide superficial deposits are characterised in this area by gravel of mudstone/siltstone and highly weathered argillaceous rocks.....	238
Figure 3.18 Abandonment mine plan of No 3 Rhondda Seam (Coal Authority) overlaid onto LIDAR data and 1948 air photograph.....	240
Figure 3.19 Abandonment mine plan of Tormynydd Seam (Coal Authority) overlaid onto LIDAR data and the 1948 air photograph	241
Figure 3.20 - 1927 Gordon's map of the South Wales coalfield (mineral takings) ..	243
Figure 3.21 Geomorphological map of the area of Mynydd yr Eglwys Landslide investigated for this project, based on walk over surveys and GPS surveying carried out at the end of March and beginning of April 2007	247
Figure 3.22 Orthophotograph of the northern central part of Mynydd yr Eglwys Landslide obtained from processing of digital photogrammetry. Annotations highlight some of the landforms described in the text	248
Figure 3.23 Perspective view of the northern central part of Mynydd yr Eglwys Landslide from Topcon's PI-3000v3 photogrammetry software. Annotations highlight some of the landform described in the text.....	249
Figure 3.24 View of the western part of the main scarp showing the outcrop of No 3 Rhondda Seam with clear evidence of seepage from its base	249
Figure 3.25 View of one of the fissures above the main scarp (left; photo by N. Ross) and of the shear zone that crosses debris slide B from the area North of borehole 5	

towards the minor scarp (right; photo by P. J. Brabham).....	250
Figure 3.26 View of ridges with upslope facing scarps located at the base of the main scarp. The southern ridge, immediately upslope of boreholes 4 and 4A, consists of a detached block of strata tilted downslope (photo by P. J. Brabham)	250
Figure 3.27 Monthly rainfall for the years 2005-2008 and for January-May 2009. A best estimate was obtained from the records of rain gauges and weather stations close to the site (as explained in section 2.12). Estimate may still suffer from errors due to gaps and uncertainties in the data provided. For the period June-October 2008 data from Treherbert rain gauge are shown in addition to the estimate based mainly on Blaencwm rain gauge because probably more reliable (see section 2.12)	251
Figure 3.28 Mean monthly effective rainfall and mean monthly total rainfall for the years 1997-2006 for the 40 by 40 km square 155. Data were supplied by the Meteorological Office MORECS for a phd project on Nant y Gwyddon landfill site located on the opposite valley side (Ling, 2007).....	252
Figure 3.29 Log of borehole 6, located above the main scarp of the landslide. The figure shows the depth at which the Diver was installed and the minimum and maximum water levels measured by the logger between the 30 th of May 2008 and the 20 th of May 2009. The elevation of the ground level is the one measured with the dual-frequency Topcon HiPer Pro GPS+ for the project.....	256
Figure 3.30 Log of borehole 3, located in the area of the ancient deep-seated landslide blocks. The figure shows the depth at which the Diver was installed and the minimum and maximum water levels measured by the logger between the 30 th of May 2008 and the 20 th of May 2009. During the years of the project the depth of the borehole was found to be much reduced with respect to the original, possibly because of damage caused by ground movements. The elevation of the ground level is the one measured with the dual-frequency Topcon HiPer Pro GPS+ for the project.....	257
Figure 3.31 Log of borehole 11, located South of the wet area at the toe of debris slide C. The figure shows the depth at which the CTD Diver was installed and the minimum and maximum water levels measured by the logger between the 27 th of August 2008 and the 20 th of May 2009. The elevation of the ground level is the one measured with the dual-frequency Topcon HiPer Pro GPS+ for the project	258
Figure 3.32 Daily rainfall and water levels recorded at borehole 3 during all the monitoring period. The maximum value of water level was recorded on the 5 th of September 2008, following a wet period. There appears to be a clear correspondence	

between heavy rainfall events and picks in the water level values	260
Figure 3.33 Daily rainfall and water levels recorded at borehole 6 during all the monitoring period. The maximum value of water level was recorded on the 6th of July 2008, following a wet period. There appears to be a clear correspondence between heavy rainfall events and picks in the water level values.....	260
Figure 3.34 Daily rainfall and water levels recorded at borehole 11 during all the monitoring period. The relationship between water levels and rainfall is not clear from the graph	261
Figure 3.35 Daily rainfall and water level at borehole 3 for the period 1 st of June to 31 st of August 2008. Picks in water level are evident in correspondence of the intensive rainfall of 5th and 9 July and the wet period of 5-19 August	261
Figure 3.36 Daily rainfall and water level at borehole 3 for the period from 1 st of September to 30 th of November 2008. The highest water level in borehole 3 for the entire logging period was recorded on the 5 th of September 2008. Other picks are evident in the graph, such as the one following the intensive rainfall of 4 th October 2008	262
Figure 3.37 Daily rainfall and water level at borehole 6 for the same period of Figure 3.36. While in borehole 3 the response to the heavy rainfall of 4 th October 2008 seems to start on the same day and carry on the following, in borehole 6 water level appears to rise over the two days following the rainfall event	262
Figure 3.38 Contrary to what noticed in boreholes 3 and 6, water level at borehole 11 does not have an immediate and simple response to the rainfall (see for example rainfall of the 4 th of October).....	263
Figure 3.39 Daily rainfall and water level at borehole 3 for the period 1 st of December 2008 to 28 th of February 2009. The rise in water levels is again clearly evident in correspondence of heavy rainfall events. After the rainfall of the 13 th of December the weather was relatively dry for the following 29 days. During this time the water level continues to decrease asymptotically. However, it decreases mainly during the first 6 days.....	264
Figure 3.40 Daily rainfall and water level at borehole 6 for the same period	264
Figure 3.41 Daily rainfall and water level at borehole 11 for the same period. During this period there seems to be a correspondence between rainfall and water level increase also in this borehole.....	265
Figure 3.42 Cross-correlogram for water level in borehole 3 and rainfall provided by	

A. Gray. The correlation coefficient is above the upper limit of confidence for lags of 0, 1 and 4 days.	267
Figure 3.43 Cross-correlogram for water level in borehole 6 and rainfall provided by A. Gray. The correlation coefficient is above the upper limit of confidence for lags of 3 and 4 days.	267
Figure 3.44 Cross-correlogram for water level in borehole 11 and rainfall provided by A. Gray. There are no positive correlation coefficients above the upper limit of confidence.....	268
Figure 3.45 Instalment of drainage in the area between the toe of debris slide B and the ditch (photos by the author).....	275
Figure 3.46 Drainage after completion of works (photo by the author).....	276
Figure 3.47 Location of GPS movement markers (installed and surveyed for this project) and approximate location (in December 2007) of six of the markers surveyed with EDM on behalf of the Rhondda Cynon Taff County Borough Council (D.P. Jones, personal communication). CU1, SB81 and SB85 are control points, whereas CU15 and CU16 were surveyed only once (not monitored)	278
Figure 3.48 Cumulative inclined movement for markers P3, P6, P7, P17, P18 and P60 surveyed with EDM instrument by surveyors on behalf of Rhondda Cynon Taff County Borough Council. The results of their movement were provided by Halcrow (Cardiff office). Marker locations were shown in Figure 3.47.....	279
Figure 3.49 Change in Eastings and Northings coordinates for markers CU2-CU14 during all the GPS monitoring campaigns. For ease of comparison, all the boxes have the same dimensions: 0.50 m in Eastings and 1.4 m in Northings.....	284
Figure 3.50 Vertical movement versus horizontal movement for markers CU3-CU14. For ease of comparison, all the boxes have the same dimensions. The approximate value of the inclination of the vector of movement (in degrees) is indicated in red .	285
Figure 3.51 Total horizontal displacement vectors obtained with GPS surveying over the period 27 November 2007 (or 11 December 2007) and 16 December 2008. Markers CU2 and CU4 were stolen after April 2008.....	286
Figure 3.52 Cumulative horizontal (top) and vertical (bottom) movement for markers CU3-CU14 over the monitoring period (27 November 2007 – 16 December 2008). The two graphs have a different vertical scale	287
Figure 3.53 Cumulative inclined movement for markers CU3-CU14 (top), water level measured at Borehole 3 (centre – available only from 30 May 2008) and	

daily/cumulative rainfall for the period of GPS monitoring.....	288
Figure 3.54 Comparison between EDM results for P3 and GPS results for marker CU13. EDM surveys were carried out on behalf of RCTCBC and values of cumulative inclined movement were provided by Halcrow (Cardiff office).	289
Figure 3.55 Comparison between EDM results for P6 and GPS results for marker CU12. EDM surveys were carried out on behalf of RCTCBC and values of cumulative inclined movement were provided by Halcrow (Cardiff office)	290
Figure 3.56 Comparison between EDM results for P18 and GPS results for marker CU10. EDM surveys were carried out on behalf of RCTCBC and values of cumulative inclined movement were provided by Halcrow (Cardiff office)	290
Figure 3.57 Comparison between EDM results for P60 and GPS results for marker CU6. EDM surveys were carried out on behalf of RCTCBC and values of cumulative inclined movement were provided by Halcrow (Cardiff office)	291
Figure 3.58 Photograph of Mynydd yr Eglwys Landslide taken in October 1999 by P. J. Brabham	292
Figure 3.59 Photograph of Mynydd yr Eglwys Landslide taken in January 2000 by P.J. Brabham.....	292
Figure 3.60 Photograph of Mynydd yr Eglwys Landslide taken in September 2000 by P.J. Brabham.....	293
Figure 3.61 Photograph of Mynydd yr Eglwys Landslide taken in November 2000 by P.J. Brabham.....	293
Figure 3.62 Photograph of Mynydd yr Eglwys Landslide taken in June 2002 by P.J. Brabham.....	294
Figure 3.63 Photograph of Mynydd yr Eglwys Landslide taken in August 2002 by P.J. Brabham.....	294
Figure 3.64 Photograph of Mynydd yr Eglwys Landslide taken in March 2003 by P.J. Brabham.....	295
Figure 3.65 Photograph of Mynydd yr Eglwys Landslide taken in September 2004 by P.J. Brabham.....	295
Figure 3.66 Photograph of Mynydd yr Eglwys Landslide taken in May 2009 by P.J. Brabham.....	296

Figures – Chapter 4

Figure 4.1 Location of lines acquired with the instrument GEM-2 (Geophex) at

Mynydd yr Eglwys Landslide.....	305
Figure 4.2 Maps of apparent electrical conductivity at 47025, 30025 and 15025 Hz produced from GEM-2 data acquired at Mynydd yr Eglwys Landslide	306
Figure 4.3 Map of apparent magnetic susceptibility at 15025 Hz produced from GEM-2 data acquired at Mynydd yr Eglwys landslide.....	307
Figure 4.4 Self potential map derived from data acquired in December 2006 (on the 15 th for the area of the main scarp and on the 19 th and 21 st for the central area). Location of SP stations is indicated with a white circle	310
Figure 4.5 Self Potential map derived from data acquired in December 2006 draped onto a 3D LIDAR surface.....	311
Figure 4.6 Self Potential map derived from data acquired in March 2007. Data in the central and toe areas were acquired on the 8 th and 12 th of March. Data along the three crossing profiles at 195480N, 195490N and 195550N were acquired on the 14 th of March. Location of SP stations is indicated with a white circle.....	312
Figure 4.7 Self Potential map of data acquired in March 2007 draped onto a 3D LIDAR surface	313
Figure 4.8 Self Potential measurements along the three cross profiles acquired on the 14 th of March along 195480 N, 195490 N and 195500 N	314
Figure 4.9 Daily rainfall (best estimate) for the period 25 th November to 25 th December 2006. SP surveys were carried out on the 15 th , 19 th and 21 st of December	314
Figure 4.10 Daily rainfall for the period 17 th February to 17 th March 2007. SP surveys were carried out on the 8 th , 12 th and 14 th of March.....	315
Figure 4.11 Location of seismic refraction tomography and MASW lines acquired at Mynydd yr Eglwys Landslide.....	319
Figure 4.12 Seismic refraction tomography lines, Mynydd yr Eglwys landslide	320
Figure 4.13 MASW line A processed by M. Bottomley (2008); H:V exaggeration 1:2. The figure has been here modified only by plotting Borehole 4 using the same legend of Figure 4.12. The blue circle indicates an anomaly possibly due to processing, whereas red lines indicate boundaries of velocity contrast identified by M. Bottomley in its processing of seismic refraction data.....	321
Figure 4.14 MASW line B processed by M. Bottomley (2008); H:V exaggeration 1:2. For Bottomley, red line indicates a seismic refraction boundary	321
Figure 4.15 MASW line E processed by M. Bottomley (2008); H:V exaggeration 1:2.	

The figure has been here modified only by plotting Boreholes 7 and 7A using the same legend of Figure 4.12. Red lines indicate boundaries of velocity contrast identified by M. Bottomley in its processing of seismic refraction data.....	322
Figure 4.16 Location of ERT profiles acquired at Mynydd yr Eglwys landslide	326
Figure 4.17 ERT lines 1L, 1s and X	327
Figure 4.18 ERT lines 8L, 9L and 4L.....	328
Figure 4.19 Location of IP tomography profiles acquired at Mynydd yr Eglwys landslide.....	330
Figure 4.20 IP lines 13top, IP Test line A and IP line Y	331
Figure 4.21 Conceptual model of Mynydd yr Eglwys landslide obtained from joint interpretation of all geophysical techniques employed on site.....	335

Figures – Chapter 5

Figure 5.1 Location of ERT and SP monitoring profiles acquired at Mynydd yr Eglwys landslide.....	342
Figure 5.2 Repeated ERT line 1L shown as resistivity colour contour plots and daily rainfall.....	343
Figure 5.3 Monitoring results for Line 1L (shown as plots of resistivity differences calculated from reference profile of 26 January 2006) and rainfall	344
Figure 5.4 Results of ERT monitoring line X presented as resistivity contour colour plots and results of two SP profiles acquired along the same line (in purple along 297755E and in blue along 297760E)	347
Figure 5.5 Monitoring results for Line X (shown as plots of resistivity differences from reference profile of 2 June 2008), rainfall and water levels recorded by Diver in borehole 3.....	348

List of tables

Tables – Chapter 1

Table 1.1 Classification of slope movements proposed by Varnes (1978)	7
Table 1.2 Definition of landslide features according to WP/WLI (1993) (in Cruden and Varnes, 1996; Dikau et al., 1996; Cooper, 2007). Numbers refer to Figure 1.7. .	12

Table 1.3 Definition of states of activity of landslides (WP/WLI, 1993 as reported in Dikau et al., 1996). Numbers refer to Figure 1.8.....	13
Table 1.4 Definitions of styles of landslide activity (WP/WLI, 1993; reported in Dikau et al., 1996). Numbers refer to Figure 1.9.....	14
Table 1.5 Geophysical methods and their potential applications for investigation and monitoring of landslides	35
Table 1.6 Deep-seated landslides which have occurred in the South Wales Coalfield since mining commenced (modified from Jones and Siddle, 2000).....	46

Tables – Chapter 2

Table 2.1 Calibration parameters of camera Ricoh GR Digital II used for the acquisition of images at Mynydd yr Eglwys landslide as determined by Topcon's PI-calib software.....	80
Table 2.2 Overall result list (above), stereo camera conditions and ground resolution information (below) determined by bundle adjustment	85
Table 2.3 Camera external orientation parameters computed by bundle adjustment for the images kept in the project as they provided good stereo-pairs	85
Table 2.4 Summary of statistic analysis of height errors (difference between height of DEM and height of GPS) for the check-points along the GPS profile.....	97
Table 2.5 Differences between heights extracted from the DEM and heights measured with GPS at movement marker locations	99
Table 2.6 Distribution of height differences between the TINs in their overlapping areas	102
Table 2.7 Summary of statistic analyses for the values of differences in heights between overlapping areas of TINs.....	102
Table 2.8 Survey accuracy of Topcon HiPer Pro GPS+ instrument defined when observing a minimum of 6 GPS satellites with 15 degrees angle cut-off, according to manufacturer specifications (Topcon, 2006)	116
Table 2.9 Summary of GPS monitoring campaigns at Mynydd yr Eglwys landslide	120
Table 2.10 Summary of GPS post-processing results for the base station.....	127
Table 2.11 Summary of statistical analysis of coordinates of “fixed” points SB81, SB85 and CU1 considering all monitoring campaigns	128
Table 2.12 Summary of standard deviations for redundant observations	130
Table 2.13 Summary of differences between coordinates of re-occupied points and	

their previous coordinates.....	132
Table 2.14 Summary of seismic acquisition parameters	169
Table 2.15 Summary of ERT profiles acquired at Mynydd yr Eglwys.....	180
Table 2.16 Summary of ERT profiles acquired with permanent electrodes	181
Table 2.17 Materials that can cause effect on IP measurements (Zonge et al., 2005)	185
Table 2.18 IP tomography profiles acquired at Mynydd yr Eglwys landslide.....	187
Table 2.19 Technical specifications for the Mini-Divers (20 m water range) and the CTD-Diver (30 m water range) used to monitor water levels at Mynydd yr Eglwys landslide (Instruments manuals).....	193
Table 2.20 Details on weather stations or rain gauges used for the determination of daily rainfall.....	198

Tables – Chapter 3

Table 3.1 Summary of relevant changes that occurred on site or in the surrounding area from 1875 to 1962.....	222
Table 3.2 Summary of dip and dip direction of strata provided by Earth Science Partnership (2004)	231
Table 3.3 Severity of rainfall events for the rain gauge at Parc Colliery for the period October 1998 to February 1999 from Halcrow report (1999). Values of rainfall where reported also as reduced by 17% (adjusted) because the readings at RCTCBC rain gauge were found to be 17% higher than the ones at Treherbert rain gauge	253
Table 3.4 Summary of the range of values of water levels (AOD) recorded by the Divers during the period of water level monitoring	258
Table 3.5 Results of correlations carried out by A. Gray with SPSS v 16 statistical analysis software.....	266
Table 3.6 Materials with potentially low shear horizons or with observed slip planes within according to Earth Science Partnership (2004)	271
Table 3.7 Depths of some of the boreholes at Mynydd yr Eglwys measured with a dip- metre by a member of the crew during field work	272
Table 3.8 Summary of the possible preparatory factors that may have contributed to the initiation of the compound deep-seated landslide in 1998-99 at Mynydd yr Eglwys identified and discussed by Halcrow (1999)	273

Table 3.9 Summary of EDM monitoring results for the period May 1999-May 2000 (modified from Halcrow, 2000).....	277
Table 3.10 Summary description of GPS marker locations in reference to the geomorphological elements identified in Figure 3.21 and described in section 3.6 .	280
Table 3.11 Horizontal (H), vertical (V) and inclined (I) movement for each marker in relation to its coordinates from the previous survey.....	281

Tables – Chapter 4

Table 4.1 Approximate depths of investigation for each of the GEM-2 frequencies over a range of material conductivities (calculated from equation 2.16)	304
---	-----

Chapter 1 Introduction

1.1 Research overview

Over the last few decades the number of reported worldwide natural disasters, including landslides, has increased. Natural disasters have caused fewer fatalities, but have affected more people and resulted in greater estimated costs for remediation (Source of information: OFDA/CRED International Disaster Database EM-DAT [WWW 1.1]).

The worldwide increase in number of landslide events seems especially related to deforestation and various other human activities such as: poor urban planning, poor land-use management, an ever increasing population (which has pushed urban development further into hazardous terrains) and possibly more frequent severe weather events associated with climate change (Nadim et al., 2006; [WWW 1.1]).

According to the international disaster database EM-DAT, landslides account only for the 5% of natural disasters worldwide (Figure 1.1) and are generally considered less important than other natural hazards in terms of loss of lives, ranking only seven in the list for causes of death as a result of natural disasters (after drought, storms, floods, earthquakes and volcanoes; Nadim et al., 2006). However, this is probably an underestimation, due to the fact that fatalities are recorded in the database under the first trigger (i.e. earthquake, flood) even if they were caused by the associated landslides (Nadim et al., 2006). It may also be that some events have simply not been reported, or do not satisfy the database entry requirements (a minimum of 10 or more people reported killed, 100 or more others affected, a declaration of state of emergency and/or a call for international assistance).

366 major landslide events were reported worldwide from 1980 to 2008. They killed 20,008 people (an average of 690 per year), affected 7,031,523 others (average of 242,466 per year) and caused an estimated US\$ 6,059,838,000 of economic damage (data and statistics elaborated by [WWW 1.3] using EM-DAT information).

The continents most affected by landslides in terms of fatalities are the Americas, followed by Asia and Europe, while Europe suffers from the greatest economic damages (Figure 1.2). In terms of loss of lives, moderate to high landslide hazard hotspots are located in: NW Canada, USA, Central America, NW South America, Caucasus region, Alborz and Zagros mountain ranges in Iran, Turkey, Tajikistan, Kyrgyzstan, Himalayan belt, Taiwan, Philippines, Indonesia, New Guinea, New Zealand, Italy and Japan (Nadim et al., 2006).

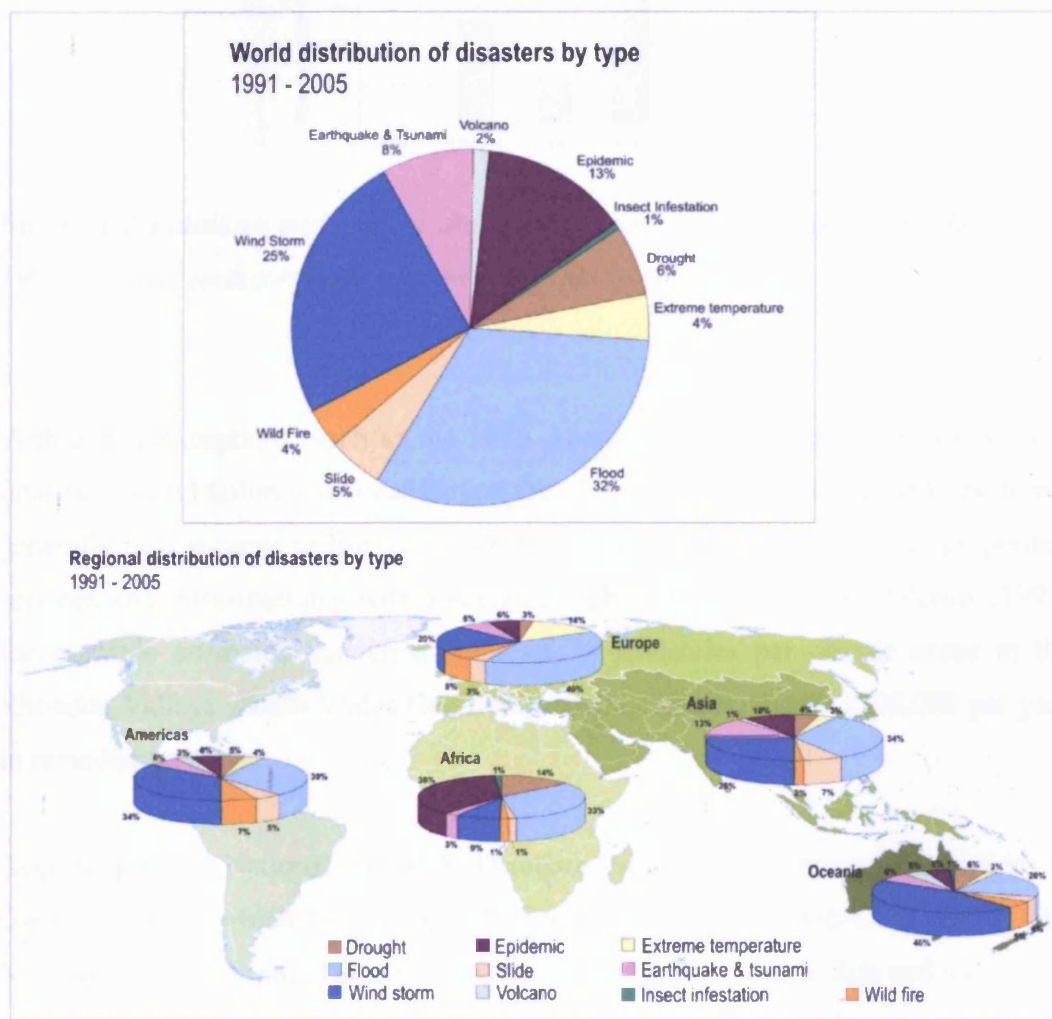


Figure 1.1 World and regional distribution of natural disasters by type for the years 1991 to 2005 (modified from figure produced by ISDR [WWW 1.2], source of data OFDA/CRED International Disaster Database EM-DAT)

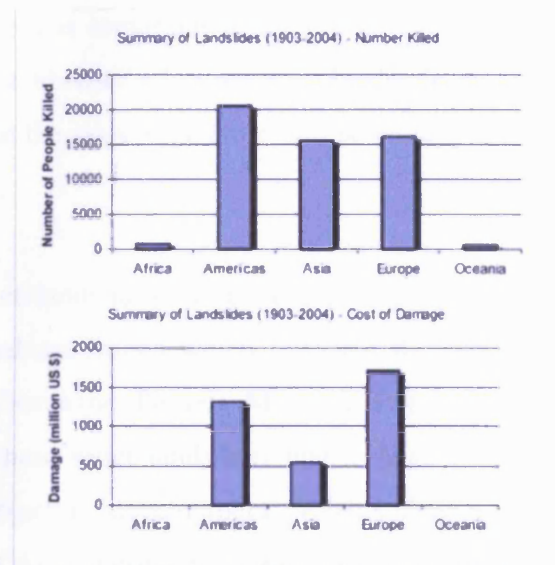


Figure 1.2 Fatalities and cost of damages caused by landslides during the period 1903-2004 for each continent (Nadim et al., 2006)

With a few exceptions, such as the 1996 Aberfan tip failure in South Wales, (144 fatalities), rapid failures in Great Britain are very rare and therefore landslides do not generally pose a threat to life. However, they can cause severe damage to properties, services and infrastructures with associated high remediation costs. Halcrow (1993) for example estimated that an average of 15 landslides per decade occur in the Rhondda Valleys (South Wales Coalfield), costing approximately £300,000 per year in remediation costs.

According to the National Landslide Database there are 8835 recorded landslides in Great Britain, of which 1302 are costal (Geomorphological Services Ltd, 1987). The National database is based on a review of available and accessible data and not on any systematic surveys. Therefore the database lacks consistency and it is probably an underestimation of the actual distribution of landslides in Great Britain. Although to a first approximation, the database reveals that slope stability is widespread across the UK and that the inland reported landslides are concentrated mostly in the regions of the: South Wales Coalfield, Scottish Highlands, North Yorkshire Moors, Pennines, East Midland Plateau, Ironbridge Gorge, Vale of Clwyd, Peak District, Cotswolds,

and the hill slopes around Bath, Exmoor, East Devon Plateau, Weald and the London Basin (Geomorphological Services Ltd, 1987; Department of the Environment, 1996). It is important to underline that as the National database was simply a census, the absence of a reported landslide at a particular site does not necessarily mean that the slope is stable or not potentially unstable (Department of the Environment, 1996).

The majority of inland landslides are relict, usually dormant failures, which originated during the periglacial conditions which followed the end of last glaciation, around 13,000 years ago (Devensian Period). Most recent inland events are associated with the reactivation of these relict landslides due to heavy rainfall or human activities, such as new infrastructure development projects (Halcrow, 1993; Jones and Lee, 1994; Department of the Environment, 1996; Lee et al., 2000).



Figure 1.3 Landslide distribution in Great Britain as recorded in the National database (Lee et al., 2000)

The South Wales Coalfield has one of the highest concentrations of landslides in Great Britain (6.72 per 100 km²; Geomorphological Services Ltd, 1987). In the ‘South Wales Coalfield landslip survey’ published in 1980 (Conway et al., 1980), 579 landslides were identified and mapped. However, this number is an underestimation. For example, in their systematic and detailed survey of the Rhondda Valleys, Halcrow (1993) identified 152 landslides, while BGS only 110. Some of the landslides were probably not recognised by BGS or were below the minimum selected mapping threshold (10 m in diameter; Forster et al., 2000).

The high density of landslides in the South Wales Coalfield landslides is due to many inter-related factors, such as geology, structure, geomorphological history, hydrology, hydrogeology and human activities. Between the 1860s and the 1960s, several significant landslides caused damage to infrastructures, resulting in injuries and fatalities. This period coincided in South Wales with the century of intensive coal mining activities and associated rapid urban development (Bentley and Siddle, 1996; Siddle and Bentley, 2000). The most important landslide disaster was the Aberfan tip failure (October 1966), which raised global hazard awareness, research interest in landslide geotechnics and the hazards and risks of uncontrolled spoil tipping and slope instability in general.

After Aberfan disaster, there has been a significant reduction in landslides which coincides with the demise of the South Wales coal industry. However, more recently, two significant deep-seated landslides have occurred in the Rhondda Fawr Valley: Blaencwm (1989) and Mynydd yr Eglwys (1998). These two landslide events coincided with peaks in winter rainfall, raising concerns with the possibility that a higher incidence of extreme rainfall events, possibly associated with climate change, will likely increase the frequency of slope failures in the future.

For this PhD research project, Mynydd yr Eglwys landslide has been studied and monitored using a wide range of geophysical and surveying techniques including:

- electrical resistivity tomography;

- electrical induced polarization;
- electrical self potential;
- electromagnetic ground conductivity mapping;
- seismic surveying (P-wave refraction tomography and multichannel analysis of surface waves, MASW);
- digital photogrammetry from a helium balloon;
- GPS positional surveying.

The primary aim of this thesis is to develop an integrated and cost-effective site investigation approach for slow moving landslides or potentially unstable slopes found within the South Wales Coalfield, or in other areas of complex geology and hydrogeology. The research is based on the use and assessment of the numerous geophysical and surveying techniques listed above and the joint interpretation of the results which they provide.

A general introduction to landslides and a literature review on the use of GPS, digital photogrammetry and geophysical techniques on landslides is provided in the next sections, which are followed by a description of landslides in the South Wales Coalfield. The chapter concludes with a more detailed description of the aims of the project.

1.2 Introduction to landslides

1.2.1 Definition and classification of landslides

A landslide is defined by Cruden (1991) as “the movement of a mass of rock, debris or earth down a slope”. Several classifications of landslides have been proposed over the past 50 years. The most widely known and adopted systems are the ones of Varnes (1978), Cruden and Varnes (1996) and Hutchinson (1988). The classifications of Varnes (1978) and Cruden and Varnes (1996) are based on the definition of the type of movement and the type of material involved in the movement, as described before displacement (Table 1.1; Figure 1.4). Five types of movement can be recognised

(Cruden and Varnes, 1996):

1. Fall: “starts with the detachment of soil or rock from a steep slope along a surface on which little or no shear displacement takes place. The material then descends mainly through the air by falling, bouncing or rolling”;
2. Topple: “is the forward rotation out of the slope of a mass of soil or rock about a point or axis below the centre of gravity of the displaced mass”;
3. Slide: “is a downslope movement of soil or rock mass occurring dominantly on surfaces of rupture or on relatively thin zones of intense shear strain”;
4. Spread: “is an extension of a cohesive soil or rock mass combined with a general subsidence of the fractured mass of cohesive material into softer underlying material. The surface of rupture is not a surface of intense shear. Spreads may result from liquefaction or flow (and extrusion) of the softer material”;
5. Flow: “is a spatially continuous movement in which surfaces of shear are short-lived, closely spaced, and usually not preserved. The distribution of velocities in the displacing mass resembles that in a viscous liquid”.

Table 1.1 Classification of slope movements proposed by Varnes (1978)

TYPE OF MOVEMENT			TYPE OF MATERIAL		
			Bedrock	Engineering Soils	
				Predominantly coarse	Predominantly fine
FALLS			Rock fall	Debris fall	Earth fall
TOPPLES			Rock topple	Debris topple	Earth topple
SLIDES	ROTATIONAL	Few units	Rock slump	Debris slump	Earth slump
	TRANSLATIONAL		Rock block slide	Debris block slide	Earth block slide
			Many units	Rock slide	Debris slide
	LATERAL SPREADS			Rock spread	Debris spread
FLOWS			Rock flow (deep creep)	Debris flow (soil creep)	Earth flow
COMPLEX			Combination of two or more principal types of movement		

The term ‘complex landslide’ was included in the classification of Varnes (1978) to indicate a combination of two or more major types of movements within one landslide, whereas in Cruden and Varnes (1996) and in the Multilingual Landslide

Glossary (WP/WLI, 1993) ‘complex’ describes a style of landslide activity in which two or more types of movement occur in a time sequence (see section 1.2.2.3).

Slides can be further sub-divided according to the shape of the surface of rupture into rotational or translational slides, with curved or approximately planar shear surfaces respectively (Varnes, 1978; Cruden and Varnes, 1996). In accordance with Hutchinson (1988), Cruden and Varnes (1996) also consider a third an intermediate type of slide called ‘compound’, which is particularly common in the South Wales Coalfield. A compound slide is characterised by a non-circular surface of rupture, which is steep at the rear scarp and flattens downslope. Due to the shape of the surface of rupture, movement occurs only after development of internal displacements and shears within the displaced material with the possible formation of obsequent (up-hill facing) scarps and grabens (Hutchinson, 1988; Cruden and Varnes, 1996; Figure 1.5).

Earth materials are divided into rock (or bedrock) and engineering soils, which are further subdivided into debris and earth. They are defined as:

1. Rock (Bedrock): “hard or firm mass that was intact and in its natural place before the initiation of movement” (Cruden and Varnes, 1996 in accordance with Shroder, 1971 and Varnes, 1978);
2. Engineering soils: “any loose, unconsolidated, or poorly cemented aggregate of solid particles, generally of natural mineral, rock, or inorganic composition and either transported or residual, together with any interstitial gas or liquid” (Varnes, 1978). They can be further divided into:
 - a) Debris: “material in which 20 to 80 percent of the fragments are greater than 2 mm (0.08 in) in size and the remainder of the fragments less than 2 mm” (Varnes, 1978 in accordance with Shroder, 1971).
 - b) Earth: “material in which about 80 percent or more of the fragments are smaller than 2 mm; it includes a range of materials from nonplastic sand to highly plastic clay” (Varnes, 1978 citing Shroder, 1971).

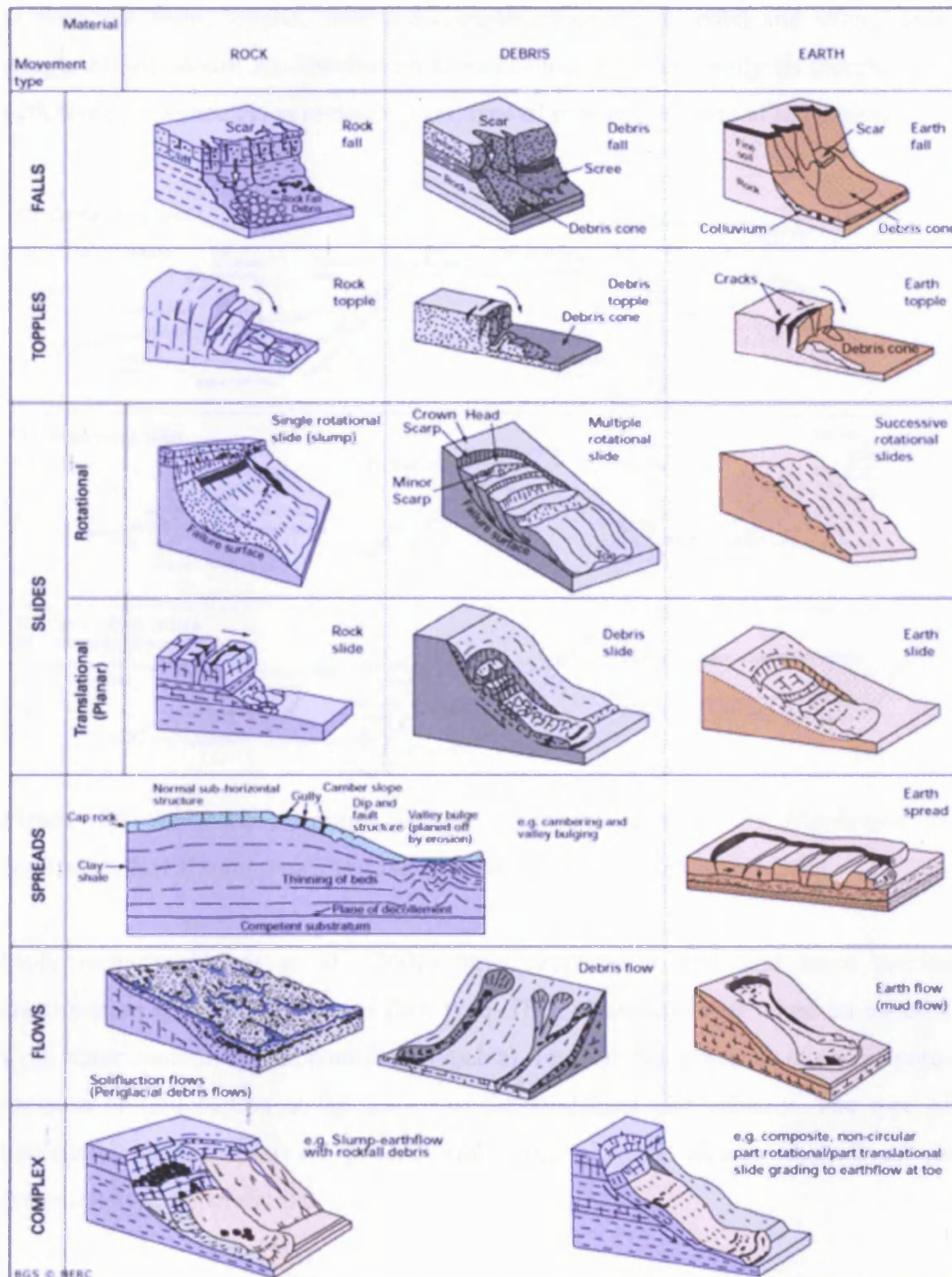


Figure 1.4 Schematic diagram illustrating the types of movements described by Varnes (1978) (produced by BGS [WWW 1.4])

The classification of Hutchinson (1988) is also still widely used and it is more comprehensive than other schemes. Sub-aerial movements are divided in eight categories (rebound, creep, sagging of mountain slopes, landslides, debris movements

of flow-like form, topples, falls and complex slope movements) and several sub-categories (Appendix A). Hutchinson classification is based mainly on morphology, with some relevance given to mechanism, type of material and rate of movement.

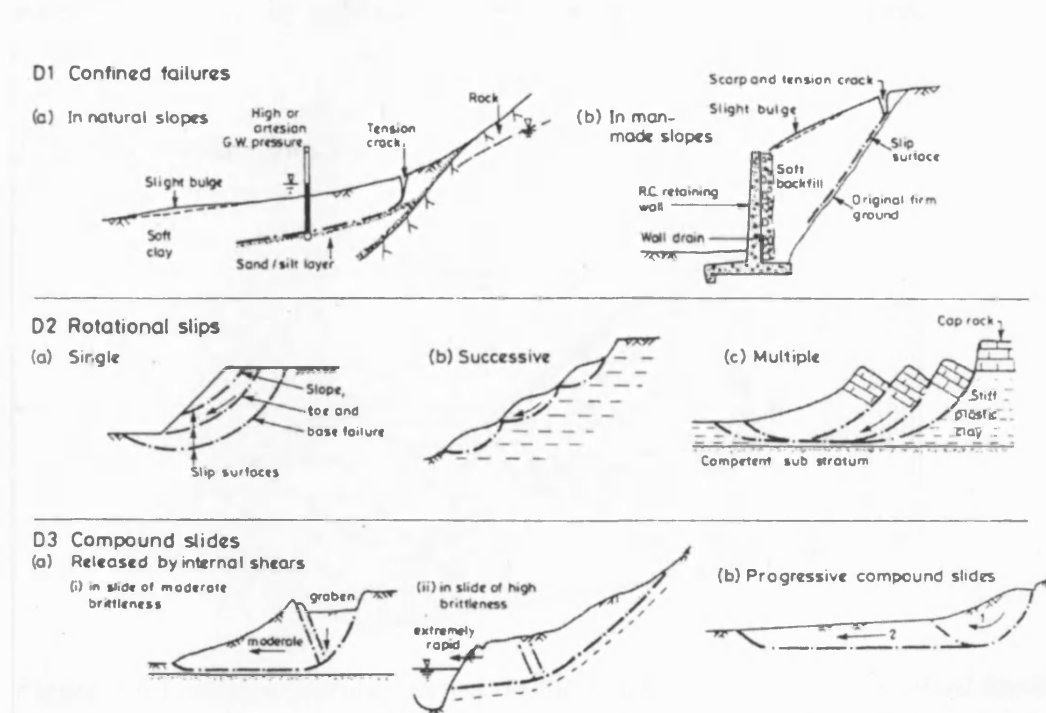


Figure 1.5 Schematic diagrams for the landslides classified by Hutchinson as confined failures, rotational slips and compound slides (Hutchinson, 1988)

More recently, Hungr et al. (2001) have proposed a new and more precise classification for the landslides of flow type. Their classification is based on material type, water content, special conditions (such as, for example, presence of excess pore-pressure or liquefaction at the source of the landslide) and velocity. The type of material is defined by its genetic and morphological aspects instead of its granulometry (Appendix B).

1.2.2 Landslide terminology

The Working Party on the World Landslide Inventory (WP/WLI), created for the International decade for Natural Disasters Reduction (1990-2000) by the International Geotechnical Societies and UNESCO, produced a Multilingual Landslide Glossary (WP/WLI, 1993), promoting the use of standard terminology for the description of

landslides (for features, dimensions, types, states/distribution/styles of activity and velocity). Thorough discussion of the terminology can be found in Cruden and Varnes (1996). This terminology was adopted throughout the thesis and the one for features, states/styles of activity and velocity is reported in the following sections.

1.2.2.1 Landslide features

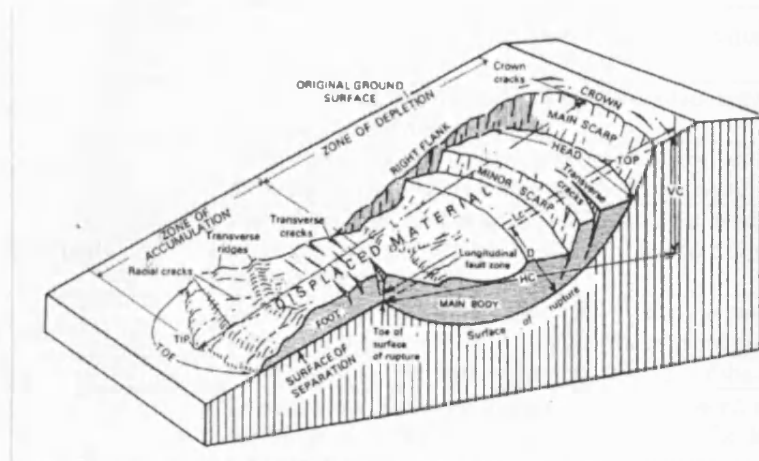


Figure 1.6 Landslide features shown on the block diagram of an idealised landslide (Varnes, 1978).

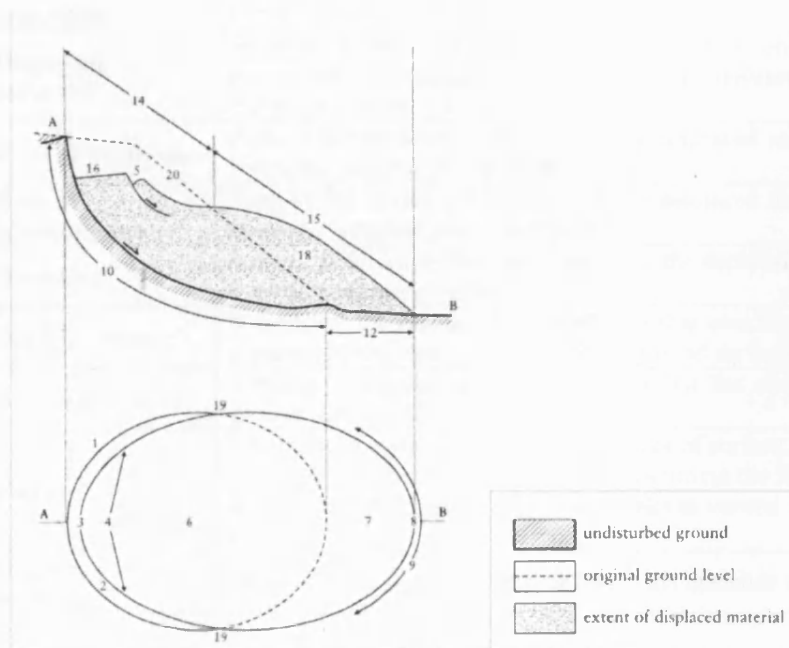


Figure 1.7 Diagram illustrating the landslide features described in the Multilingual Landslide Glossary (after WP/WLI, 1993 and Cooper, 2007)

Table 1.2 Definition of landslide features according to WP/WLI (1993) (in Cruden and Varnes, 1996; Dikau et al., 1996; Cooper, 2007). Numbers refer to Figure 1.7.

Number	Name	Definition
1	Crown	Practically undisplaced material still in place and adjacent to the highest parts of the main scarp (2)
2	Main scarp	Steep surface on the undisturbed ground at upper edge of the landslide, caused by movement of the displaced material (13) away from the undisturbed ground. It is the visible part of the surface of rupture (10)
3	Top	Highest point of contact between the displaced material (13) and the main scarp (2)
4	Head	Upper parts of the landslide along the contact between the displaced material and the main scarp (2)
5	Minor scarp	Steep surface on the displaced material of the landslide produced by differential movements within the displaced material
6	Main body	Part of the displaced material (13) of the landslide that overlies the surface of rupture (10) between the main scarp (2) and the toe of the surface of rupture (11)
7	Foot	Portion of the landslide that has moved beyond the toe of the surface of rupture (11) and overlies the original ground surface (20)
8	Tip	Point of the toe (9) farthest from the top (3) of the landslide
9	Toe	Lower, usually curved margin of the displaced material (13) of a landslide; it is the most distant margin of the landslide from the main scarp (2)
10	Surface of rupture	Surface that forms (or that has formed) the lower boundary of the displaced material (13) below the original ground surface (20)
11	Toe of surface of rupture	Intersection (usually buried) between the lower part of the surface of rupture (10) of a landslide and the original ground surface (20)
12	Surface of separation	Part of the original ground surface (20) now overlain by the foot (7) of the landslide
13	Displaced material	Material displaced from its original position on the slope by movement in the landslide; it forms both the depleted mass (17) and the accumulation (18)
14	Zone of depletion	Area of the landslide within which the displaced material (13) lies below the original ground surface (20)
15	Zone of accumulation	Area of the landslide within which the displaced material (13) lies above the original ground surface (20)
16	Depletion	Volume bounded by the main scarp (2), the depleted mass (17), and the original ground surface (20)
17	Depleted mass	Volume of the displaced material (13) that overlies the surface of rupture (10) but underlies the original ground surface (20)
18	Accumulation	Volume of the displaced material (13) that lies above the original ground surface (20)
19	Flank	Undisplaced material adjacent to the sides of surface of rupture (10). Compass directions are preferable in describing the flanks, but if left and right are used, they refer to the flanks as viewed from the crown (1)
20	Original ground surface	Surface of the slope that existed before the landslide took place

1.2.2.2 States of activity of landslides

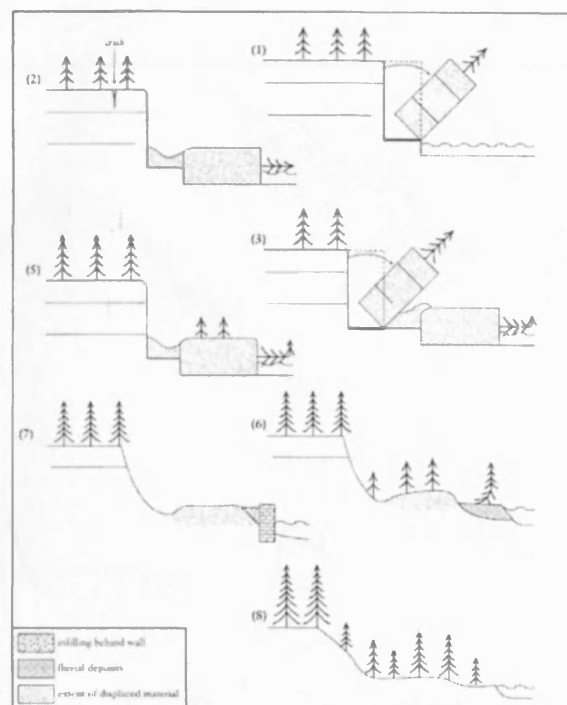


Figure 1.8 Diagram illustrating the states of activity of landslides (after WP/WLI, 1993; in Cooper, 2007)

Table 1.3 Definition of states of activity of landslides (WP/WLI, 1993 as reported in Dikau et al., 1996). Numbers refer to Figure 1.8.

Example	State	Definition
1	Active	is currently moving; example shows that erosion at the toe of the slope causes a block to topple
2	Suspended	has moved within the last 12 months but is not active (1) at present; example shows local cracking in the crown of the topple
3	Reactivated	is an active (1) landslide which has been inactive (4); example shows that another block topples, disturbing the previously displaced material
4	Inactive	Has not moved within the last 12 months and can be divided in states (5)-(8)
5	Dormant	Is an inactive (4) landslide which can be reactivated (3) by its original causes or by other causes, example shows that the displaced mass begins to regain tree cover, scarps are modified by weathering
6	Abandoned	Is an inactive (4) landslide which is no longer affected by its original causes; example shows that fluvial deposition has protected the toe of the slope, the scarp begins to regain its tree cover
7	Stabilised	Is an inactive (4) landslide which has been protected from its original causes by remedial measures; example shows that a wall protects the toe of the slope
8	Relict	Is an inactive (4) landslide which developed under climatic or geomorphological conditions considerably different from those at present; example shows that uniform tree cover has been established

1.2.2.3 Styles of landslide activity

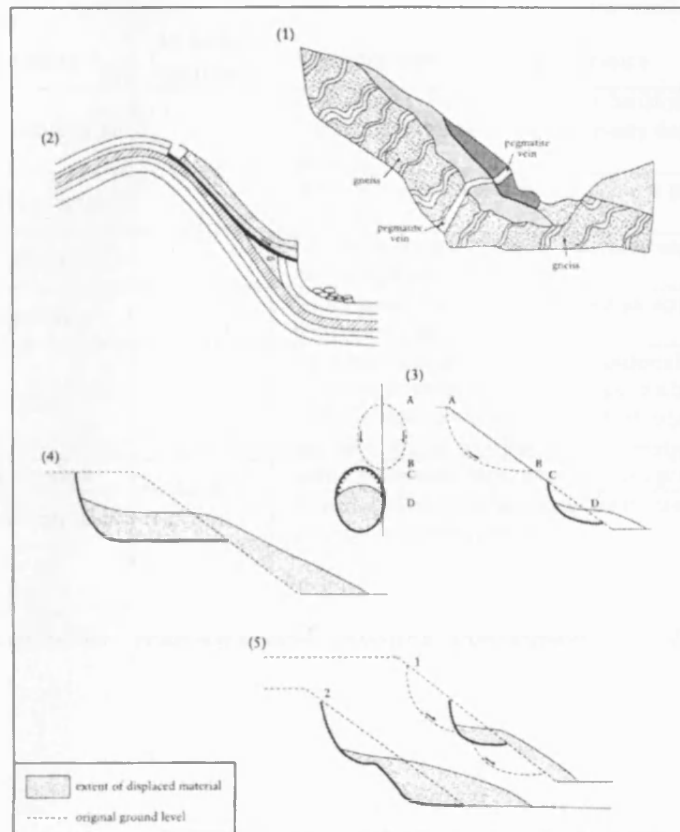


Figure 1.9 - Diagram illustrating styles of activity (after WP/WLI, 1993; in Cooper, 2007)

Table 1.4 Definitions of styles of landslide activity (WP/WLI, 1993; reported in Dikau et al., 1996). Numbers refer to Figure 1.9

Example	Style	Description
1	Complex	Landslide exhibits at least two types of movement (falling, toppling, sliding, spreading and flowing) in sequence; example shows gneiss and migmatites toppled with valley incision. Alluvial deposits fill in the valley bottom. After weathering weakened the toppled material, some of the displaced mass slid
2	Composite	Landslide exhibits at least two types of movement simultaneously in different parts of the displacing mass; example shows that limestones have slid on the underlying shales causing toppling below the toe of the slide rupture surface
3	Successive	Landslide is the same type as nearby, earlier landslide, but does not share displaced material or a rupture of surface with it; example shows that the later slide, AB, is the same type as slide DC, but does not share displaced material or a rupture surface with it
4	Single	Landslide is a single movement of displaced material
5	Multiple	Landslide shows repeated development of the same type of movement

1.2.2.4 Velocity classes

Velocity class	Description	Velocity (mm/sec)	Probable destructive significance
7	Extremely rapid		Catastrophe of major violence; buildings destroyed by impact of displaced material; many deaths; escape unlikely
6	Very rapid	5×10^1	Some lives lost; velocity too great to permit all persons to escape
5	Rapid	5×10^1	Escape evacuation possible; structures, possessions, and equipment destroyed
4	Moderate	5×10^1	Some temporary and insensitive structures can be temporarily maintained
3	Slow		Remedial construction can be undertaken during movement; insensitive structures can be maintained with frequent maintenance work if total movement is not large during a particular acceleration phase
2	Very slow	5×10^1	Some permanent structures undamaged by movement
1	Extremely slow	5×10^1	Imperceptible without instruments; construction possible with precautions

Figure 1.10 Landslide velocities and possible consequences (after Cruden and Varnes, 1996)

1.2.3 Basic principles of landsliding

Landslides occur when the disturbing or shearing stresses acting along a potential surface of rupture exceed the available resisting stresses or shear strength of the soil or rock.

Figure 1.11 shows the forces acting on a single mass of soil or rock resting on a plane inclined at an angle β to the horizontal. This plane could be a discontinuity, a bedding plane or simply a suspected potential surface of rupture in a soil/rock slope. If other external sources are excluded, the main force acting on the soil/rock mass is the weight W , which can be resolved in its two components, one parallel ($T=W\sin\beta$) and one perpendicular ($N=W\cos\beta$) to the plane. The main destabilising force is therefore the component of the weight acting down the plane, which in terms of stresses (i.e. force per unit area) can be defined as the destabilising or shear stress (τ_s):

$$\tau_s = \frac{W}{A} \sin \beta \quad \text{Eq. 1.1}$$

where A is the area of the shear plane on which the weight operates.

The component of the weight acting perpendicular to the plane generates pressure between the grains and therefore friction at the base of the mass of soil/rock. The total resisting stress (r), which opposes to sliding, depends on both the cohesion and the frictional strength of the material:

$$r = c + \left(\frac{W}{A} \cos \beta \right) \tan \phi = c + n \tan \phi \quad \text{Eq. 1.2}$$

where c is the cohesion, n is the normal stress and ϕ is the angle of internal friction or angle of shearing resistance of the material. The cohesion is an inherent property of the material, due to the attractions between particles, and it is independent of normal stress. The angle of internal friction describes how the friction caused by normal stress contributes to the strength of the material.

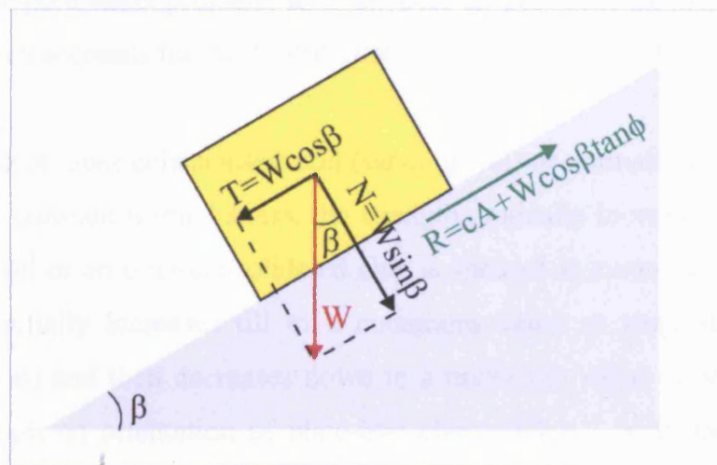


Figure 1.11 Block diagram of forces acting on a mass of soil/rock resting on a surface of rupture

When the pores of the soil or broken rock are filled with water, the pore water reduces the contacts between the grains and supports part of the normal pressure. Therefore, the principle of effective stress is introduced.

For a saturated soil, the maximum shear strength or the shearing resistance of the material (τ_f) can be described by the equation of Mohr-Coulomb as:

$$\tau_f = c' + (n - u) \tan \phi' = c' + n' \tan \phi' \quad \text{Eq. 1.3}$$

where n' is the effective stress supported by the grain structure, n is the total normal stress, u is the pore water pressure, c' and ϕ' are the cohesion and the angle of internal friction determined using effective stress.

The pore water pressure depends on the height of the water table. As for most hard rocks and many sandy/gravelly soils the water does not alter significantly the values of c' and ϕ' , it is evident from equation 1.3 that an increase in water table (i.e. due to rainfall) causes a decrease in intergranular friction and therefore in the effective stress and the shear strength of the material.

For partially saturated soils, the shear strength is given by (Fredlund et al., 1978):

$$\tau_f = c' + (n - u_w) \tan \phi' + (u_w - u_a) \tan \phi'' \quad \text{Eq. 1.4}$$

where u_w is the pore water pressure, u_a is the pore air pressure and ϕ'' is the property of the soil which accounts for the contribution of $(u_w - u_a)$ on strength.

When a sample of loose cohesionless soil (sand, gravel) or normally-consolidated clay is sheared at a constant normal stress, the strength gradually increases. When a dense cohesionless soil or an over-consolidated clay is sheared at a constant normal stress, the strength initially increases till to a maximum value or peak strength (due to dilation, friction) and then decreases down to a minimum value or residual strength (due for example to orientation of plate-like clay particles), with the formation of shearing surfaces.

In nature, sliding has been observed to occur in soils along a single slip surface of only millimetres thickness (i.e. along a particular weak horizon such as a bedding plane) or along shear zones (i.e. when shearing affects a thick bed of uniform material). A change of soil fabric occurs in these shear surfaces/zones, but can also occur in the material above the slip surface/zone, due to distortions in the displaced material. Peak strength will be mobilised in a first-time landslide, but not everywhere at the same time, with the development of a progressive failure within the slope. If shear zones/planes exist already on site, as for example in the case of relict landslides,

than the shear strength will be at/near the residual value and will be more easily mobilised. These and other basic concepts of soil and rock mechanics can be found in many textbooks (i.e. Brunsden and Prior, 1984; Anderson and Richards, 1987; Bromhead, 1992; Tanzini, 2001).

1.2.4 Landslide causes

The causes of landsliding can fall under the following three categories: factors that contribute to increased shear stresses acting on the potential surface of rupture; factors that contribute to low shear strength of the soil/rock and factors that contribute to reduce shear strength of soil/rock (Varnes, 1978; Cruden and Varnes, 1996).

Factors that contribute to increased shear stresses include (Varnes, 1978; Cruden and Varnes, 1996):

- Removal of lateral or underlying slope support (due for example to: erosion by streams, rivers, waves and glaciers; weathering; previous landsliding; subsidence or faulting; human activities such as quarrying, cutting, mining, removal of retaining walls and alteration of water levels in artificial lakes or reservoirs);
- Imposition of surcharges/loads (such as: weight of water from rain, springs or leaking services; seepage pressures; weight of snow or accumulated sediments; human constructions such as fills, waste piles and buildings);
- Transitory earth stresses (mainly due to earthquakes, but also volcanic or anthropogenic explosions, failures in adjacent slopes, vibrations caused by human activities);
- Uplift or regional tilting (due for example to tectonic forces, volcanic pressures or melting of extensive ice sheets);
- Increased lateral pressure (due for example to presence or freezing of water in cracks and swelling pressures of clays).

Factors that contribute to low shear strength include (Varnes, 1978; Cruden and Varnes, 1996):

- Composition and texture of materials (weak or potentially weak materials, materials with loose fabrics or textures);
- Mass structure and slope geometry (weakening due to discontinuities; presence of massive beds over weak/plastic ones; alternation of permeable

sands/sandstones and impermeable weak clays/shales; strata inclined towards a free face);

Factors that contribute to reduced shear strength include (Varnes, 1978; Cruden and Varnes, 1996):

- Changes due to weathering and other physiochemical reactions (such as: fissuring; hydration or base exchange in clays; removal of cement solutions; physical disintegration of granular rocks);
- Changes in intergranular forces due to water content and water pressure in pores and fractures;
- Changes in structure (fissuring and fracturing caused by human activities);
- Other causes, such as weakening due to creep or to action of trees or burrowing animals.

A thorough discussion of landslide causes can be found in Crozier (1986). According to this author, slopes can be in one of three states: stable, unstable / marginally stable (they will fail sometime in the future), and actively unstable (movement is already occurring). With reference to these three states, the causes leading to failure can be grouped into:

- preparatory factors, which cause a stable slope to become susceptible to failure (marginally stable), but without initiating movement;
- triggering factors, which initiate movement, causing a marginally stable slope to become actively unstable;
- controlling (or perpetuating) factors, which are responsible for the type, the duration and the rate of movement of an actively unstable slope.

It is important to underline that a landslide can rarely be attributed to a single cause (Varnes, 1978).

1.2.5 Slope stability assessments

Slope stability assessments commonly use a traditional deterministic limit equilibrium approach, based on the calculation of a factor of safety for the most critical surface of rupture. The factor of safety is defined as the ratio between the resisting forces (and/or their moments) and the destabilising forces (and/or their moments) and it is theoretically equal to 1 when the slope is at the verge of failure, is less than 1 when

the slope is unstable and more than 1 when the slope is stable. After considering the likely shape of the surface of rupture, one of the several existing methods based on force and/or momentum equilibrium equations is selected. The slope above the surface of rupture is generally divided in slices. The number of unknowns is higher than the number of equations and therefore in each method some assumptions are made to obtain a solution (they are discussed and compared for example in: Graham, 1984; Nash, 1987; Duncan, 1996 and Tanzini, 2001).

For a rock slope, stability depends mainly on the geometry and the properties of discontinuities: their characteristics (planarity and smoothness of surface), their orientation with respect to the horizontal and to the rock face, their openness with presence of infill/water and their interactions with other discontinuities. Before carrying out calculations of factor of safety, the structure of the slope must be analysed with stereographic plots to see if movement is kinematically possible. Then, limit equilibrium methods can be applied for the calculation of safety. Four types of rock failures are generally recognised: planar, wedge, toppling and rotational failures.

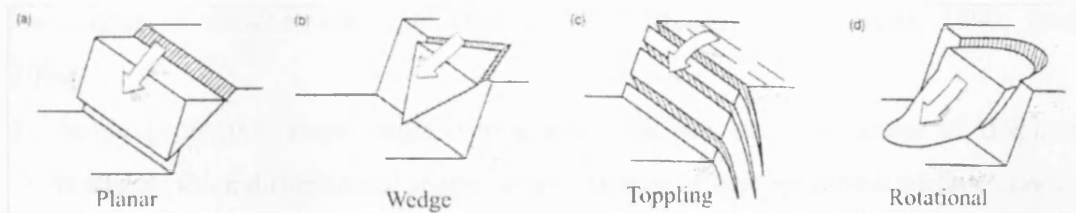


Figure 1.12 Planar (a), wedge (b), toppling (c) and rotational (d) failures in rock. The type of failure is influenced by the geometry of the discontinuities (modified from Tanzini, 2001 and references therein)

The traditional methods of limit equilibrium evaluation do not take into consideration the relationship between stresses and deformations, which is they do not provide information on rates/distribution of displacements and therefore do not allow the prediction or the modelling of landslide movements. On the contrary, finite element methods, in which the slope is divided into a mesh of elements with particular stress-strain behaviour, can provide information on progressive failure and rate of displacements. Moreover, they can model more complex slope conditions and

changes in loads and geometry in time. Discussion and examples of applications of finite element methods can be found in Duncan (1996) Griffiths and Lane (1999). More recently, François et al. (2007) and Ferrari and Laloui (2011) have described the use of a 2D and 3D finite element mesh for the hydro-mechanical modelling of large landslides characterised by slow movements primarily caused by variations in water pressure. Firstly, advanced 3D hydrogeological finite element modelling is used to calculate the values of water pressures at any point and time within the slope. Then, these calculated water pressures are used as inputs for 2D and 3D geo-mechanical modelling. Numerical simulations are carried out to calculate variations of stresses and displacements in space and time. The calculated displacements are then calibrated against the measured ones. The final valid model provides a useful platform to analyse the physical behaviour of the slope, in particular it allows evaluating the effects of variation of different parameters, establishing critical water levels and predicting rates and distribution of displacements in response to different conditions induced for example by climate change or remedial works.

Slope stability assessments of unstable or potentially unstable slopes require the knowledge of (Bogoslovsky and Ogilvy, 1977; McCann and Forster, 1990; Hack, 2000):

1. Slope geometry: slope angle, topography, surface area, thickness of displaced material, three dimensional shape on any surface of rupture (shear surface/zone);
2. Slope geology;
3. Slope structure: location and geometry of faults / fractures, dip of strata and bedding planes ;
4. Geotechnical and mechanical proprieties of slope materials;
5. Hydrogeology: height of the groundwater table, distribution of moisture content above the water table, temporal and seasonal variations in the groundwater table;
6. Ground movement: quantification and characterisation of ground displacements in both time and space.

The investigation of an unstable (or potentially unstable) slope starts with a detailed desk study of all available information (i.e. published literature, existing geotechnical reports, topographic maps, geological maps, remote sensing, air photographs, digital terrain data and satellite imagery). After the desk study, site reconnaissance (walk-

over surveys), topographic and engineering geomorphological mapping are carried out. The ground is normally invasively investigated using trial pits, trenches, boreholes (or rarely with expensive adits and shafts). All exposures and boreholes are logged and samples taken for geotechnical analysis. The hydrogeology of the slope is investigated by monitoring groundwater levels with piezometers and also by carrying out dye tracing and pumping tests. Identification and classification of slope materials and the determination of their engineering properties is carried out using *in situ* tests (i.e. vane shear, *in situ* shear box, dynamic and static cone penetrometer, *in situ* shear test) and laboratory tests on samples (i.e. shear box, triaxial apparatus, shear ring). Displacements are monitored with ground surveying (i.e. with EDM, GPS), photogrammetry or other instruments such as inclinometers and extensimeters. A thorough description of all these conventional methods and instruments are available in all slope stability textbooks (i.e. Bromhead, 1992; Cornforth, 2005; Tanzini, 2001).

1.3 Global Positioning Systems for the monitoring of surface displacements

Global Positioning Systems (GPS) are increasingly being used for surveying on landslides in Great Britain (HSMO, 1996), but they are still not used in common practice, perhaps because considered too expensive and require a high level of technical competence in their use. Mynydd yr Eglwys landslide for example is monitored by professional surveyors on behalf of the Rhondda Cynon Taff Borough County Council (RCTCBC) using a conventional EDM (Electronic Distance Measurement instrument). GPS systems allow the operator to navigate and obtain three-dimensional positions everywhere on the Earth's surface, by receiving and processing communication signals broadcast by satellites in a 20,200 km high orbit .

Typically, the precision quoted for the conventional EDM monitoring of landslide surface displacements is of the order of a centimetre in accuracy and precision (Gili et al., 2000). In recent years, several authors (Gili et al., 2000; Rizzo, 2002; Coe et al., 2003; Mora et al., 2003; Brückl et al., 2006; Demoulin, 2006; Peyret et al., 2008) have demonstrated that dual-frequency GPS systems can be used for this purpose at sub-

centimetre accuracy and precision.

When compared with traditional EDM surveying methods, GPS monitoring has several advantages (Gili et al., 2000; Malet et al., 2002; Brückl et al., 2006):

- a) The technique does not require line of sight surveying;
- b) The technique can be used in poor weather conditions;
- c) The technique provides high accuracy over large survey areas which can be covered in relatively short survey time;
- d) The cost of instruments is reducing constantly and is now similar to a high quality surveying total station.

However, to obtain maximum GPS accuracy and precision there must be good satellite coverage and geometry and measurements can be negatively affected by nearby obstacles (multipath issues). Moreover, a high level of technical competence by the operator is required.

When compared with data obtained using other instruments (i.e. inclinometers, extensometers and traditional geodetic techniques), GPS displacement measurements have all shown good agreement (comparisons are reported in Gili et al., 2000; Malet et al., 2002; Coe et al., 2003; Squarzoni et al., 2005). These displacement measurements have often been compared with rainfall and pore water pressures for a better understanding of landslide dynamics (examples can be found in Malet et al., 2002; Coe et al., 2003; Demoulin, 2006; Peyret et al., 2008; Baldi et al., 2008).

GPS has been also used for continuous monitoring by Malet et al. (2002), Mora et al. (2003), Peyret et al. (2008) and Baldi et al. (2008). Continuous GPS monitoring could be very useful to establish the threshold of pore water pressures necessary for initiate or accelerate ground movement and as a possible early warning system (Malet et al., 2002). However, such continuous monitoring techniques are very expensive and may be suited to remote Alpine research projects, but not practically applicable on landslides that are subject to urban vandalism such as the one considered in this project.

More technical details on the GPS surveying techniques used in this research project are provided in Chapter 2.

1.4 Digital Photogrammetry

Lillesand et al. (2004) define photogrammetry as the “science and technology of obtaining spatial measurements and other geometrically reliable derived products from photographs”. In digital photogrammetry, such measurements and products are derived from digital or digitized historical film-based imagery (Konecny, 2003).

Since the 1970s-1980s, analytical photogrammetry has substituted analogue photogrammetry and has been widely used to produce digital elevation models (DEMs) and to evaluate surficial ground movements. If the camera parameters are known, or if the software used for photogrammetry has self-calibration options, high resolution DEMs and ortho-rectified photos can be obtained from quality historical aerial photographs taken in different epochs. Displacement vectors and DEMs of height difference can be calculated to determine changes of volume (Oka, 1998; Brückl et al., 2006; Wangenstein et al., 2006; Walstra et al., 2007; Baldi et al., 2008). When compared with GPS and geodetic techniques, photogrammetry has the advantage of not requiring physical site access (a very important health and safety consideration in landslides). It can provide high spatial resolution DEMs over large areas and information on long-term landslide kinematics (Casson et al., 2003; Mora et al., 2003; Chen et al., 2006; Baldi et al., 2008; Dewitte et al., 2008).

Unfortunately analytical photogrammetry has historically relied on the use of expensive and complex stereo-plotters that need experienced operators (Chandler, 2001). Modern digital photogrammetry potentially offers several advantages over older traditional methods (Chandler, 1999; Baily et al., 2003):

- Automatic generation of DEMs by image matching techniques;
- Production of DEMs of consistent precision because based on regular grids;
- Production of high-density DEMs due to an increase in ground sampling rates (sampling rates are 100 times those of manual photogrammetric methods and

1000 times those of modern ground surveying techniques);

- The possibility to modify DEM resolution according to the user's needs, without significant changes in costs;
- Availability of relatively inexpensive software packages that run on UNIX machines or high specification PCs;
- Availability of user-friendly software packages that can be used potentially by inexperienced photogrammetrists (although according to Baily et al. (2003) a high level of expertise is still required to avoid simple pitfall errors);
- Availability of software packages that can create additional products (i.e. fly-throughs, animations, ortho-photographs) and provide additional image analysis tools;
- Improvement in overall accuracy and processing time when compared to analytical photogrammetry, if the area under investigation is extensive and requires dense data coverage.

Digital imagery can be obtained by scanning conventional large format analogue photographs or directly using high-resolution digital cameras. Traditionally analogue film is generally preferred option for aerial applications however advances in professional digital imagery have now virtually replaced film. Photogrammetric high-quality scanners are too expensive for occasional users (Chandler, 2001 and references therein; Baily et al., 2003). To date, digital cameras have not been used for aerial applications because they do not provide the necessary high resolution required to be cost-efficient (Chandler, 1999; 2001 and references therein). However, digital camera technology is constantly changing and inexpensive cameras can provide sufficient resolution for close-range applications.

1.5 The use of geophysics on landslides

The practical application of terrestrial applied geophysical techniques to landslide characterisation is fairly recent: the first technical articles on this subject were published in the 1960s and 1970s (Cadman and Goodman, 1967; Denness et al., 1975; Bogoslovsky and Ogilvy, 1977; Müller, 1977; Novosad et al., 1977; Yamaguchi, 1977). The restricted use of geophysics to landslide research was mainly due to the logistical difficulties of transporting the heavy analogue equipment and batteries over

areas of difficult landslide terrain. These pioneering articles concentrated predominantly on techniques such as geoaoustic, vertical electrical sounding, electrical profiling/mapping, seismic refraction and self potential mapping. The use of electromagnetic techniques was first introduced in the 1990s, with the research of McCann and Forster (1990) and Caris and Van Asch (1991). The recent development of highly portable, digital geophysical equipment has lead to increased applications of geophysical surveying for landslide research. Over the past decade, improvements in digital technology and data analysis has allowed the application of two and three-dimensional imaging techniques to landslide research (e.g. 2D/3D electrical resistivity tomography : Bichler et al., 2004; Lebourg et al., 2005; Friedel et al., 2006; self-potential tomography in: Lapenna et al., 2003; Perrone et al., 2004; Colangelo et al., 2006; 2D/3D seismic refraction tomography in: Meric et al., 2005; Godio et al., 2006; Heincke et al., 2006). Authors have also explored the use of four-dimensional imaging using electrical resistivity and self potential tomography repeated in time (e.g. Suzuki and Higashi, 2001; Jomard et al., 2007; Colangelo et al., 2006). Also other techniques have recently been applied to landslide characterisation, such as ground penetrating radar (Bruno and Marillier, 2000; Cardarelli et al, 2003; Bichler et al., 2004; Heincke et al., 2005), high-resolution seismic reflection (Bruno and Marillier, 2000; Ferrucci et al., 2000; Brückl and Paroditis, 2001) and spectral analysis of surface waves (Israil and Pachauri, 2003; Godio et al., 2006).

Traditional methods for the investigation of landslides (i.e. boreholes, trial pits, *in situ* and laboratory tests) usually provide accurate and quantitative site information at precise locations. However, they are logistically expensive, intrusive and provide only single-location information at a particular time, requiring uncertain interpolations and extrapolations between a number of locations. Moreover, boreholes often suffer from several practical difficulties, including restricted access to critical locations and eventual disruption due to the ground movement. Samples have limited size and may not reflect the strong spatial variability of parameters and the presence of discontinuities. By contrast, geophysical techniques can provide a non-invasive (therefore environmental-friendly) high-resolution means of investigating the subsurface along continuous profiles, providing wet and dry parameters of soils/rocks *in situ* over large ground volumes (Bogoslovsky and Ogilvy, 1977; McCann and Forster, 1990).

A brief introduction to geophysical methods with an explanation of the principles behind their applicability for the characterisation and monitoring of landslides is reported in the next sections. More details on the principles of the geophysical techniques selected for the project are provided in Chapter 2 and in references therein.

1.5.1 Seismic methods (refraction, reflection and surface waves)

Near-surface seismic refraction is based on the measurement of the times required for elastic waves (compressional or shear) to travel from a source to motion sensors (geophones) deployed on the ground after being refracted at boundaries of contrasting seismic velocity. These travel times provide information on the layer velocities and the depth to refracting boundaries. In general, compressional (P-wave) seismic velocities depend on lithology, degree of compaction/litification, density, porosity, pore structure, fracturing/weathering degree, saturation degree and properties of the pore fluids. Shear or (S-) waves do not propagate through fluids and will be only slightly affected by the presence of water due to the consequent slight increase in density (Israil and Pachauri, 2003).

The physical properties of landslide materials may be very similar to those of the underlying undisturbed geology. However, landslide materials usually undergo changes in physical structure and texture that result in changes in their bulk properties and therefore in their P and S wave velocities (Bruno and Marillier, 2000). Variations in seismic velocity in the displaced material can result from changes in: materials' shear or bulk modulus caused by ground movements (extension/compression), degrees of fracturing/weathering, porosity and presence of interstitial groundwater. As a consequence, displaced materials are often characterised by seismic velocities lower than the ones for bedrock geology and by higher coefficients of attenuation (Bogoslovsky and Ogilvy, 1977; Caris and van Asch, 1991). Moreover, Bogoslovsky and Ogilvy (1977) showed that areas characterised by different values of velocities may develop across the displaced material due to different degrees of compaction and deformation within the slope.

Seismic velocities may also provide information on the mechanical and geotechnical parameters of the materials composing the slope. If the velocities of both P and S-waves are known, a seismically derived Young's modulus and Poisson's ratio can be determined. Furthermore, seismic velocities measured in the field can be compared to the ones measured in laboratory to assess the quality of rock (RQD).

Seismic refraction has indeed been widely employed on landslides to define their internal structure (i.e. depth and geometry of shear surfaces/zones and bedrock, thickness of displaced material), the mechanical properties of soils and rocks composing the slopes and the fracturing degree of rock masses. Examples are reported in: Bogoslovsky and Ogilvy (1977), Müller (1977), McCann and Forster (1990), Caris and van Asch (1991), Giraud et al. (1995), Frasheri et al. (1998), Mauritsch et al. (2000), Cardarelli et al. (2003), Israil and Pachauri (2003), Bichler et al. (2004), Meric et al. (2005), Brückl and Brückl (2006), Godio et al. (2006), Heincke et al. (2006).

The fundamental requirement for the seismic refraction to work is that the velocity must increase with depth. Moreover, thin layers with poor velocity contrasts (hidden layers) or gradational changes in velocity are often very difficult to detect (i.e. slip surface in homogeneous material; Bogoslovsky and Ogilvy, 1977).

The seismic reflection technique is not affected by velocity inversions and can potentially provide information on slope structure in areas of complex geometry. The technique is based on the measurement of two-way travel times of waves reflected by boundaries of contrasting acoustic impedance (product of density and velocity). However, the practical use of seismic reflection on landslides is very limited. This is due to the fact that it is technically difficult and expensive to obtain shallow high frequency reflection data at terrestrial sites, particularly in areas of varying topographic relief (Brabham et al., 2005). The examples of seismic reflection data reported in the literature (Bruno and Marillier, 2000; Ferrucci et al., 2000) provide information on slope structure at depth but are characterised by lack of signal at near surface, the depth of interest in terms of displaced material and surface of rupture.

Stiffness is an important parameter in slope stability analysis as it can be related to shear strength (Hack, 2000). Shear (S) waves are more sensitive to changes in normal stiffness than compressional (P) waves, but they are more difficult to generate by using impulsive and explosive sources and therefore are less commonly used. As a consequence, the possibility of determine S-wave velocities through the measurement of surface waves, which are very easy to produce and detect, has generated a lot of interest over the last few years. The surface wave technique is robust and has the additional advantage of not suffering from the problem of hidden layers. In the method of spectral analysis of surface waves (SASW), surface waves are detected by a pair of receivers and the recorded signals are processed to produce a profile of shear wave velocity in depth (details can be found in Israil and Pachauri, 2003). Examples of the use of SASW on landslides are reported in Israil and Pachauri (2003) and Godio et al. (2006).

During the 1990s, the Kansas Geological Survey developed a new method of multichannel analysis of surface waves (MASW), which provides 2D profiles of S-wave velocity through multi-channel recording of surface waves. The simultaneous use of more than two geophones reduces acquisition time and improves data quality compared to SASW technique (Park et al., 1999; Miller et al., 1999; 2000). MASW method is badly affected by lateral changes in elastic properties and by severe topography. Therefore its applicability on landslides is not certain. For this project, MASW data were acquired at Mynydd yr Eglwys landslide as part of a Leeds University M.Sc. thesis (Bottomley, 2008) simultaneously with seismic refraction (P-) wave data.

1.5.2 Electrical resistivity methods

Electrical resistivity techniques are based on the in-situ field measurement of contrasts in the electrical resistivity of Earth materials. In electrical sounding, profiling and mapping, data acquisition involves the injection of current into the ground (using a 12V battery) via a couple of electrodes and the measurement of voltage through another couple of electrodes. In electrical resistivity tomography (or ERT) instead an array of electrodes is deployed, which work alternatively as current or potential electrodes. Hundreds of readings are taken along a profile which are used

to obtain a 2D section or a 3D distribution of resistivity within the slope. Detectable contrasts in electrical resistivity are observed when there are changes in: lithology (i.e. clay content), degree of fracturing, porosity, permeability, water content and water conductivity.

Previous landslide research has shown that the contrast in resistivity between the displaced material and the stable material is mainly due to differences in water content and/or fracturing degree. Furthermore, Bogoslovsky and Ogilvy (1977) and Müller (1977) underlined that shear surfaces/zones are generally characterised by mechanical disturbance, altered mineralogical composition, increased water and/or clay content, and increased water salinity: all factors which lead to a decrease in resistivity.

Electrical resistivity methods have been deployed on landslides to determine the lateral limits and the thickness of the displaced material, to define the internal structure and the geology of the slope (in particular the depth to and the geometry of the shear surface/zone) and mainly to investigate the groundwater distribution and the moisture content of the different layers composing the slope (Bogoslovsky and Ogilvy, 1977; Caris and van Asch, 1991; Frasheri et al., 1998; Lapenna et al., 2003; Perrone et al., 2004; Meric et al., 2005; Lebourg et al., 2005; Sass et al., 2008). In addition, laboratory experiments and field applications have shown that the repetition of resistivity surveys in time can provide information about groundwater distribution and flow and their changes in time (electrical resistivity mapping in: Denness, 1975; Bogoslovsky and Ogilvy, 1977; Yamaguchi, 1977; electrical resistivity tomography in: Suzuki & Higashi, 2001; Lebourg et al., 2005; Friedel et al., 2006; Jomard et al., 2007).

For example, Suzuki and Higashi (2001) were able to draw a conceptual cross section model of groundwater flow for a weathered rock slope in Japan by evaluating the changes in resistivity in a repeated profile and by comparing these changes to rainfall and pressure head. Jomard et al. (2007) carried out a controlled water injection on part of the deep-seated La Capière landslide in the French Alps. This injection was coupled with hydrological studies (natural and artificial tracings), time-lapse resistivity tomography and geodetic monitoring using a tacheometer. This

combination of studies led to delineation and quantification of two different water flows (shallow and deep) within the slope, but no surface displacements were detected, meaning that the relatively rapid shallow water flow along the slip surface did not cause the increase in pore water pressure necessary for detectable displacements to occur.

Many ERT profiles were acquired on Mynydd yr Eglwys landslide as part of this project. A sub-set of lines were also repeated in time and the resistivity changes were compared with local rainfall, borehole water levels and GPS monitoring data.

1.5.3 Electromagnetic induction methods

The electrical conductivity of the subsurface (inverse of resistivity) can be measured using electromagnetic low frequency ground conductivity instruments. These instruments have the advantage of not requiring direct contact with the ground, being consequently less time-consuming and invasive than electrical resistivity techniques to deploy. A primary electromagnetic field is generated by a transmitter coil and propagates through the ground inducing eddy currents in conductive materials. These eddy currents generate a secondary electromagnetic field which is detected by a receiver coil and it is compared with the primary field to determine the conductivity of the materials in the subsurface.

Fixed frequency EM-31 and EM-34 ground conductivity metres have been used on landslides mainly to investigate the water distribution within the slope (McCann and Forster, 1990; Caris and van Asch, 1991) and to delineate the lateral limits of the displaced material (Caris and van Asch, 1991; Bruno and Marillier, 2000; Meric et al., 2005). The electromagnetic profiles acquired by Caris and van Ash (1991) and by Bruno and Marillier (2000) showed higher values of conductivity on displaced materials. The authors interpreted these high values as due to wetter conditions or to an increase in the clay content respectively. The profiles acquired by Meric et al. (2005) instead were characterised by lower values of conductivity across the displaced mass. These low values were attributed to a high fracturing degree.

In electromagnetic induction methods, the variation of conductivity with depth can be determined either by changing the coil spacing of fixed frequency instruments (if possible, as for EM-34) or by using a multi-frequency instrument with fixed coil spacing (Won et al., 1996; Witten et al., 1997; Won, 2003). In 1995 Geophex developed a highly portable, broadband multi-frequency electromagnetic instrument (GEM-2), which could offer the possibility of rapidly mapping 3D conductivity changes over large areas and at different depths. Its use on landslides has not been reported in the literature and it was tested on Mynydd yr Eglwys landslide as part of this project.

1.5.4 Electrical Self Potential

The self potential method is based on the measurement of natural electrical voltage potentials measured between two points on the ground. These potentials can be generated by electrochemical or mechanical processes in the subsurface.

Electrical self potential (SP) variations measured on landslides have been associated with moving groundwater (or streaming potentials). Negative voltage anomalies correlate with the downward movement of groundwater and positive anomalies to upward flow. By repeating the surveys, the SP method can also be used to investigate the variations of groundwater flow with time. Moreover, SP anomalies have been used to delineate the landside lateral limits as the measurements become generally strongly positive when crossing onto the displaced material. Examples on the applications of SP profiling/mapping can be found in: Bruno and Marillier (2000), Lapenna et al. (2003), Perrone et al. (2004), Meric et al. (2005) and Colangelo et al. (2006). Lapenna et al. (2003) and Perrone et al. (2004) acquired also SP tomography profiles, which provide 2D sections of the charge occurrence probability factor (COP) function. Strong horizontal changes in COP seemed to correlate well with the lateral limits of the landslides.

Bogoslovsky and Ogilvy (1977) underlined that the patterns and signs of SP anomalies can be influenced also by lithology (i.e. a positive anomaly can be due to flowing water but also to high clay content) and therefore results must be compared with other techniques.

Self potential profiling and mapping was carried out at Mynydd yr Eglwys and a few SP profiles were repeated again as part of a longer-term monitoring project.

1.5.5 Induced polarization

Induced polarization (IP) is an electrical technique that measures the electrical capacitance effects of ground materials, i.e. the ability of a material to store electrical charge. If current is injected through the ground, polarization may occur in areas with clay or metallic grains. Therefore when the current is switched off, electrical potential does not drop immediately to zero, but decays in time. IP could in theory help by resolving the geophysical ambiguity between clay-rich and wet silica-rich areas. Both these lithologies found on landslides are characterised by low electrical resistivity values. Many modern resistivity instruments have the capability of simultaneously measuring resistivity and IP, however this procedure can increase the surveying time by at least three fold. To date, the IP method has hardly ever been used in any landslide research studies (Marescot et al., 2008).

Marescot et al. (2008) used the IP technique in combination with resistivity measurements in order to distinguish areas of high water content from faults/fracture zones rich in clay or areas of localised graphite enrichment in the bedrock.

A few IP profiles were acquired at Mynydd yr Eglwys as part of this project and practical comparative trials were undertaken using a variety of types of electrodes.

As resistivity (or conductivity), chargeability and self potential contrasts can be due to several different factors, all these methods require borehole calibration or integration with other techniques for a more reliable interpretation of the results.

1.5.6 Other geophysical methods

Compared to electrical resistivity and seismic methods, ground penetrating radar (GPR) has the potential to provide the high resolution at shallow depth necessary to detect very thin slip zones (Sass et al., 2008). The method is based on the measurement of the travel times of electromagnetic waves reflected at boundaries of

contrasting dielectric constant. GPR can define the exact depths of boundaries that appear as sharp contrasts, instead of smoothed zones as in ERT inversions (Sass et al., 2008). However, GPR surveys have proven unsuccessful on landslides due to the common presence of clay and boulders. Clay causes rapid radar signal attenuation and boulders act as diffraction sources (Bruno and Marillier, 2000; Friedel et al., 2006; Sass et al., 2008). Moreover, the acquisition and processing of GPR data in areas of rugged landslide topography involves complex topographic corrections (Heincke et al., 2005). Only a few successful examples of GPR on landslides have been reported in the literature and involve mainly surveys on rock masses (Cardarelli et al., 2003; Heincke et al., 2005; Spillman et al., 2007).

When a landslide is actively moving, rocks and soils will transmit transient audio-frequency waves. By adapting available earthquake monitoring technology, these landslide micro-seismic events can be used to predict sliding surfaces and remotely record landslide activity. This is the only geophysical method which would provide a real-time warning of an impending failure. Such telemetric systems are very expensive to deploy and monitor, but examples of their use are reported by Cadman and Goodman (1967), Müller (1977), Novosad et al. (1977), Rouse et al., (1991), Frasheri et al. (1998).

Despite these research advances, geophysical methods are still not routinely used on active and relict landslides, especially in the UK. The reasons for this, often cited by engineers, are that geophysics provides information on physical parameters not strictly correlated to the geotechnical and mechanical properties required by engineers. Geophysicists may also have a tendency to overestimate the capabilities of particular techniques and to not properly explain to engineers the limitations of physical penetration depth and resolution of any geophysical technique (Jongmans and Garambois, 2007).

A summary of the applicability of the methods is reported in Table 1.5, whereas a summary of the literature review is provided in Appendix C. Reviews on the application of geophysics to landslide research can be found also in Bogoslovsky and Ogilvy (1977), Müller (1977), McCann and Forster (1990), Hack (2000) and Jongmans and Garambois (2007).

Table 1.5 Geophysical methods and their potential applications for investigation and monitoring of landslides

Geophysical method	Potential application on landslides
Electrical resistivity tomography (ERT)	Delineation of landslide lateral limits Determination of slipping material thickness Determination of depth and geometry of slip surfaces/zones Determination of changes in lithology (i.e. clay) and/or water content Monitoring of changes in ground water table and moisture content with time/rainfall
Induced polarization (IP)	Distinction between areas of water saturated silica-rich sediments and areas with predominantly clay.
Self potential (SP)	Delineation of landslide lateral limits Determination of direction of groundwater flow Monitoring of changes in groundwater regime with time/rainfall
Electromagnetics (low frequency) (EM)	Delineation of landslide lateral limits Identification of changes in water/clay content within the slope
Ground penetrating radar (GPR)	Determination of near surface structures Determination of location and geometry of fracture and fault systems in rockslides/rockfalls <i>(Very limited success on landslides due to common presence of wet and clay-rich materials, vegetations and surface fractures)</i>
High-resolution seismic reflection	Determination of internal structure and geometry of the slope at depth <i>(limited applications)</i>
Seismic refraction (P & S waves)	Determination of internal structure (i.e. depth and geometry of slip surface and bedrock) Determination of rock quality and rock fracturing degree Determination of seismic Young's modulus and Poisson's ration (engineering properties)
Surface waves analysis	Determination of degree of compaction
Microseismic monitoring	Determination of landslide activity with possibility of issuing a prompt warning; Determination of slip surface location

1.6 Landslides in the South Wales Coalfield

Conway et al. (1980) identified 579 landslide sites in the South Wales Coalfield. The landslides are mainly concentrated in the Ebbw, Sirhowy and Rhymney valleys of the north-eastern coalfield and in the Rhondda, Ogwr, Garw and Llynfi valleys of the central coalfield (Conway et al., 1980; Forster et al., 2000). These high density and uneven distribution of landslides are a reflection of several inter-related factors which will be briefly discussed in the following sections: geology, structure, geomorphology, mining and other human activities, hydrology, hydrogeology and engineering properties of the materials.

1.6.1 Geology, structure and geomorphological history

The South Wales Coalfield is an east-west trending asymmetric synclinal basin, which extends from the coastal area of Kidwelly in the west to Pontypool in the east, covering approximately 2700 km², and which is characterised by sedimentary rocks of Upper Carboniferous (Westphalian) age known locally as the Coal Measures. The Coal Basin is underlain and surrounded around the edge by the older rocks of Millstone Grit, Carboniferous Limestone and Upper Old Red Sandstone. The geological contact between Coal Measures and Millstone Grit is considered to be the boundary of the Coalfield (Figure 1.13; Conway et al., 1980).

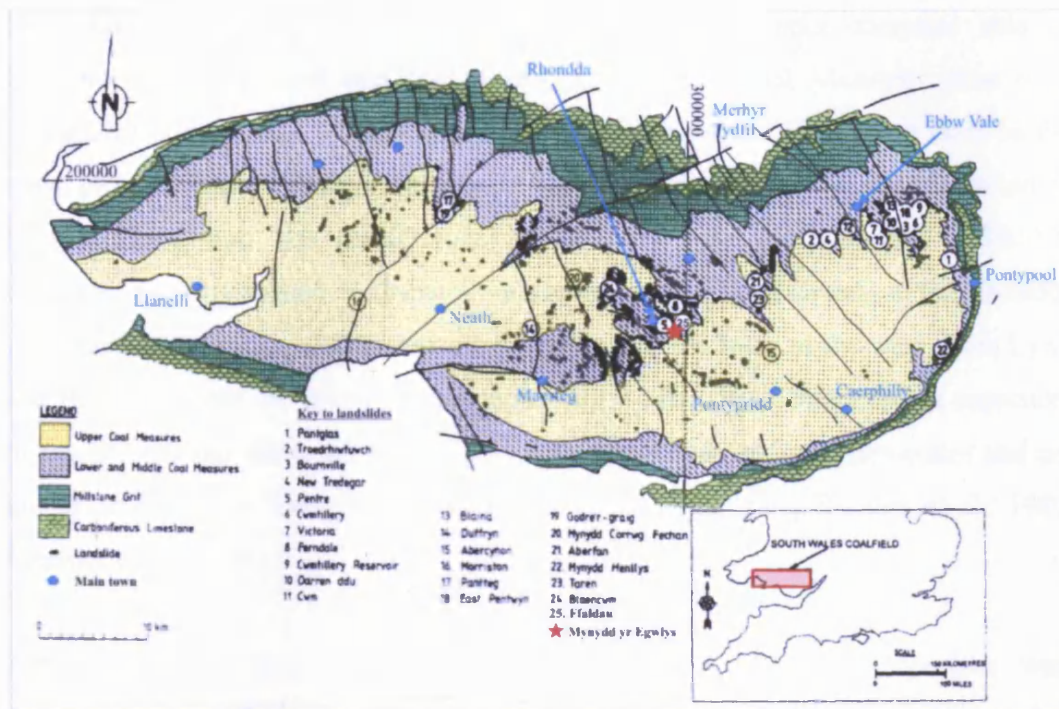


Figure 1.13 Geology, Structure and landslide distribution in the South Wales Coalfield (modified from Bentley and Siddle, 1996 and Edina Digimap). The map underlines the location of the landslides mentioned in the text and of other well known failures which have been studied by other researchers.

The Coal Measures, which were deposited in a tropical costal-deltaic environment, are characterised by cyclic sedimentation (cyclothems). They have been historically divided into Lower, Middle and Upper Coal Measures on the basis of three widespread marine bands (Figure 1.14; Woodland and Evans, 1964).

The Lower and Middle Coal Measures outcrop along the edges of the Coalfield and in the lower part of the valley slopes found in the centre of the coalfield. They are mainly argillaceous and contain the majority of the productive coal seams and ironstones. The cyclic sequences consist predominantly of mudstones and siltstones capped by seatearths and coal seams, although also thin sandstone bands are present (Woodland and Evans, 1964; Conway et al., 1980).

The Upper Coal Measures consist predominantly of poorly sorted, fluvial, sub-graywacke sandstones (or Pennant Sandstone) which form the high central plateau of

the Coalfield. Although sandstones dominate, the sequences comprise also of mudstone, siltstones and thin coal seams. The Upper Coal Measures have been divided into Llynfi, Rhondda, Brithdir, Hughes, Swansea and Grovesend Beds on the basis of coal seams which are persistent across the coalfield. The sedimentation of Pennant Sandstone was diachronous in the basin and proceeded in a SW-NE direction. As a consequence, Pennant Sandstone can be found already in the Rhondda beds in the western area, whereas only from the Brithdir beds in the west. Both Llynfi and Rhondda Beds are mainly argillaceous in the east. Here they contain sequences of mudstones and siltstones intercalated with sandstones and conglomerates and are known as 'Red' or 'Deri Beds' (Woodland and Evans, 1964; Bentley et al., 1980; Conway et al., 1980).

After their deposition, during the Variscan orogeny, the Coal Measures were deformed and uplifted. The South Wales Coalfield generally has the structure of an east-west trending asymmetric syncline, with a steeper southern limb and with thinning of the sedimentary succession towards east. Several folds, numerous normal faults and thrusts are super-imposed onto this synclinal structure. The major folds are the Pontypridd-Maesteg Anticline and the Llantwit-Caerphilly, Pengam, Gowerton and Llanelli Synclines. The faults trend predominantly NW-SE (Hercinyan trend), although some other major faults, such as the Neath and Swansea Valley Disturbances, follow a Caledonian NE-SW trend (Conway et al., 1980; Donnelly, 2005). These major faults are generally not single isolated discontinuities, but are broad zones of fracturing, which may extend over tens of metres, and usually have a clay-gauge infill which can be saturated or not (Donnelly, 2005).

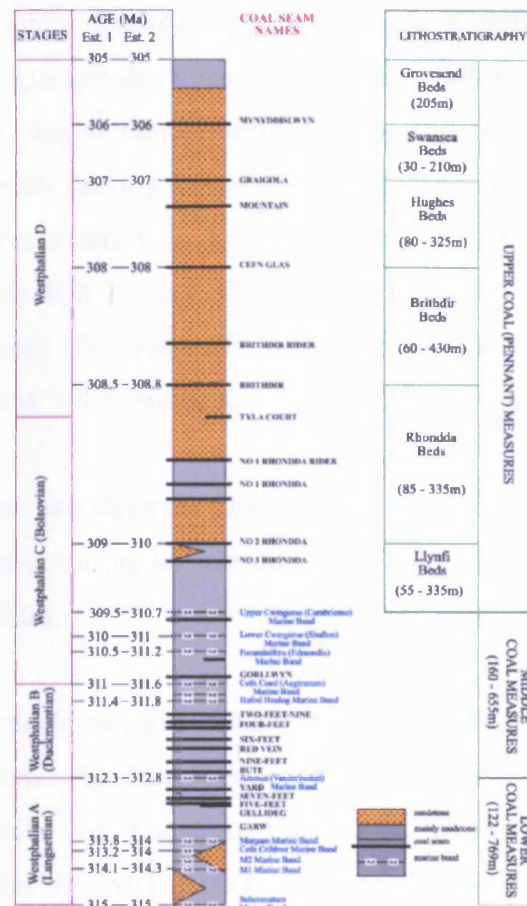


Figure 1.14 Generalised stratigraphy for the Central South Wales Coalfield (Brabham, 2004)

Tertiary uplift resulted in the formation of several erosional surfaces or plateaux, which were subsequently dissected by southerly to south-westerly draining rivers. The river systems may have been super-imposed on the Coal Measure structure due to the possible erosion of Mesozoic-Tertiary sediments on which they originally developed and therefore show little geomorphological relationship with exposed geology and structure (Conway et al., 1980; Bentley and Siddle, 1996).

During the Quaternary period, temperatures oscillated many times between glacial and interglacial conditions in the South Wales Coalfield. However, it is the last glaciation (the Devensian) and the rapid warming and the periglacial conditions which followed that had a great impact on the geomorphology and the superficial deposits which characterise the area as seen today. The ice left the central coalfield around 10,000 years ago. In the Dimlington Stadial of the Devensian (approximately 26,000-

13,000 years BP), major icefields approached the Coalfield from the Brecon Beacons and smaller glaciers developed in coalfield valleys. Glaciers eroded the valley sides and then, due to rapid warming at the end of the Dimlington Stadial, retreated relatively rapidly leaving the valleys over-deepened and with over-steepened sides. After, there was a return to cold conditions in the Loch Lomond Stadial (approximately 10,800-10,000 years BP) followed by a final rapid warming in the Flandrian (approximately 1000 years BP; Woodland and Evans, 1964; Conway et al., 1980; Wright and Harris, 1980; Siddle and Bentley, 2000; Wright, 2000).

Glacial sediments, such as lodgement tills (Boulder Clay) and melt out tills (Sand and Gravels), were deposited during the Devensian period and can now be found in the valley floors and hillsides.

With the melting ice, thick, wet and unstable moraine material would have resulted in very unstable conditions. The Periglacial conditions and over-steepened valley sides promoted the initiation of numerous landslides and other downslope mass movements. Landslides involved the formation of shear surfaces/zones which now remain as relic features in the landscape as they have become stabilised. Frost weathering and solifluction originated drift deposits ('Head'), which consist mainly of gravel of sandstones/mudstones and can be found almost everywhere in the Coalfield in the upper and top parts of the valley slopes (Woodland and Evans, 1964; Conway et al., 1980; Wright and Harris, 1980).

Till sediments were left in potentially unstable positions on over-steepened valley sides and may have undergone mudflow/gelifluction. Therefore, although still mapped as Boulder Clay, the tills now found in the lower parts of the valley sides and eventually spread on the valley floors have been reworked, that is they are not *in situ* (Wright and Harris, 1980; Wright, 2000).

Apart from the glacial and periglacial deposits described above, superfcials also include alluvium, forming the valley bottoms, and hill peat.

In the highest areas of the Central and Eastern Coalfield plateau, the Pennant Sandstone is characterised by the presence of narrow and relatively fresh fissures

(dilated joints) clearly caused by coal mining activities but also by the presence of exceptionally wide and long fault grabens, fault scarps, topographic scarps, trenches and gulls, which trend parallel or obliquely to the valley crests. A graben can be more than 4 km long, 300 m wide and up to 6 m deep, while the fault scarps can be 1-4 m high and up to 5 km long. These are features typical of lateral spreading, involving extension of the jointed/faulted strong Pennant Sandstone caprock on the more deformable argillaceous sequences underneath, which cannot be explained by mining subsidence alone. They were probably originated by valley de-glaciation and gravitational stress relief following the Devensian ice retreat. Lateral spreading, tilting, rotation and fault reactivation in the Pennant Sandstone may have occurred in periglacial conditions, during cambering, valley bulging, landsliding and other forms of mass wasting, although mining subsidence can have later contributed to the acceleration/reactivation of movements. Interestingly NW-SE trending graben and fault scarps can be found near or at the intersection of the scarps of some of the major first-time deep-seated rotational or compound landslides that have occurred in the last 150 years (i.e. New Tredegar, East Pentwyn, Bournville and Daren Ddu landslides in Ebbw Fach Valley and Blaencwm landslide in the Rhondda Fawr Valley). These features are probably characterised by a high fracturing degree and by joint dilation and provide preferential groundwater flow pathways. These factors reduce the rock strength and introduce water within the slope and therefore increase the susceptibility to failure (Donnelly et al., 2000; Donnelly, 2005).

In terms of present landscape, the Neath and the Cynon-Taff valleys divide the dissected plateaux in three parts: the Western, the Central and the Eastern Coalfield Plateau. Of these, the Central and Eastern Plateaux are characterised by higher topographic relief (up to 600 m - at Craig y Llyn), narrower valleys (up to 300 m deep), steeper valley sides and by caprocks of strong and well jointed Pennant Sandstone overlying weaker argillaceous sequences (Conway et al., 1980; Siddle et al., 2000b). All these factors contribute to make these slopes more susceptible to failure.

1.6.2 Mining

The South Wales Coalfield is one of the most extensively mined areas in the World. The long history of ironstone and coal mining has defined the region, its urbanization and has modified the landscape of the area with significant effects on slope stability.

In the north-eastern coalfield, ironstone was worked at least from the middle of the 16th century. Initially it was dug by hand and successively extracted from pits and horizontal tunnels driven into the valley sides (adits). Coal was mined on small scale certainly from the 13th century and probably also before, in Roman times (Conway et al., 1980). Large scale mining in pre-industrial times was concentrated in the areas of Llanelli and Neath, and then, in industrial times, spread from the north-east outcrop of Aberdare-Blaenavon across the coalfield (Statham, 2004). From the 17th century until 1850, coal was mined mainly in the south west for copper smelting, iron manufacture and house use. From 1850 until 1913, the demand for Welsh steam coal increased dramatically, leading to a very significant growth in the number of collieries and in population in the central South Wales Coalfield. The 1920s economic depression and the loss of many foreign markets after World War I, caused a rapid decline in the demand for coal. After WWII, the coal export trade had died away, then there was a gradual decline after nationalisation in 1947, until the last deep mine, Tower Colliery closed in 2009 (Brabham, 2005).

Since records began (around 1850), more than 1,300 coal-mining operations have been mapped within the coalfield, extracting an estimated total of 3 billion tons of coal. Vertical sequences of as many as 13 exploitable coal seams have been mined in some coalfield areas. The distribution of coal mines across the Coalfield was not uniform. It was determined by a combination of topography, stratigraphy, geological structure, coal quality, transport and technological developments. Coal mining was very limited in the area north-west of the Neath Disturbance due to structural complexities, whereas it was very significant in the central and north-eastern parts of the coalfield. The highest density of coal mines was in the Rhondda valleys, where an estimated half a billion tons of coal were extracted over 160 years (Statham, 2004; Brabham, 2005).

Coal was initially extracted from bell pits and horizontal tunnels driven into the valley sides (adits or drifts) and then from deep shafts. From the early 1800s, underground mining was carried out by the 'pillar and stall' method of extraction, while from the early 1900s mainly by the mechanised longwall method (Donnelly, 2005). In the 'pillar and stall' method, drifts (stalls) were driven into the coal seam, while areas of unworked coal (pillars) of similar or narrower width were left between them to support the roof, with partial coal extraction (60-70%). These relatively low extraction rates were however improved by the middle of the 19th century for example by halving of the pillars or their removal during retreat. In the longwall method, parallel drifts were driven into the seam and the coal between them was worked in slices, providing support only to the face. After the slice was mined, support was withdrawn and moved forward in the direction of the advancing coal face, leaving the unsupported area to collapse behind (Statham, 2004). Nowadays, these methods of coal extraction can be seen in the underground tours and exhibitions at Big Pit National Coal Museum (Blaenafon, Ebbw Vale).

Coal mine workings can cause local and regional subsidence, with lowering and tilting of the ground surface. Using the longwall mining method, the ground collapses and subsides over a wide area almost immediately (within a few months; Statham, 2004). On the contrary, subsidence above 'pillar and stall' mine workings can affect small areas if the strata above collapse into a mine void (crownholes), or wide areas if some of the coal pillars deteriorate or collapse. Moreover, subsidence can vary considerably and randomly in time, depending on many factors, such as depth of workings, seam thickness, geological stability, groundwater levels and possible infilling at the time of mining (backstowing) (Statham, 2004).

A mining subsidence trough can develop when several coal seams are mined at depth up to a common inter-colliery boundary. As a consequence, the ground may tilt towards the subsidence trough, rendering the slope more susceptible to failure, as probably happened for the deep-seated Ffaldau landslide, in the Rhondda Fach Valley (Halcrow, 1998; Siddle, 2000).

Apart from lowering and tilting of the ground surface, regional mining subsidence can have other effects which influence slope stability, such as the alteration of stress and

strain patterns within the slope, the modification of hydrogeology and the reactivation of normal faults.

While a coal seam is mined, the strata above and in front of the advancing face within the 'angle of draw' are subjected to tensile strains, whereas the strata immediately behind to compressive strains. Therefore, while underground mining proceeds, strata experience different phases of tension/compression, with widening of joints and development of new fissures. These fractures and fissures have a strong effect on the hydrogeology of the Coal Measures, as they increase the transmissibility and storage capacity of sandstones while they may render ineffective argillaceous aquicludes (see next section; Bentley et al., 1980).

Tracer experiments at Aberfan showed also that groundwater can move faster within the sandstone caprock along the tension corridors created by mining subsidence and that the boundaries between compressional and tensional zones can indeed function as hydraulic discontinuities (Mather, 2000).

Mining subsidence can also cause fault reactivation. Since 1876, at least 45 cases of mining-induced fault reactivations have been reported in the South Wales Coalfield. The reactivation of mainly NW-SE trending principal faults has generated topographic scarps on the ground surface, sometimes associated with fissures and compressional features, causing damage to buildings, services and utilities in urban and industrial areas. Fault movements have also promoted first-time failures of natural slopes and the reactivation of relict (periglacial) landslides. As previously mentioned, the fault scarps and the associated fissures found on the upland Pennant Sandstone plateaux have magnitude and extension significantly greater than the features found in other mining areas in the United Kingdom. These faults were probably reactivated during valley deglaciation and mining subsidence has only later intensified their movements. It is difficult to differentiate between features induced by mining subsidence and features due to valley de-glaciation alone. Faults may reactivate also many years after ceasing of mining subsidence probably because of groundwater level rise induced by water discharge or mine-water rebound following the switch off of mine pumps (Donnelly, 2005).

Also shallow workings can influence slope stability. For example they may offer preferential groundwater paths or they may affect the distribution and magnitude of fractures, displacements and stresses/strains within a hillslope.

It has been noted that an unusual relatively high number of major first-time deep-seated landslides have occurred in the South Wales Coalfield in the last 150 years compared to only 44 deep-seated landslides of periglacial origin mapped by Conway et al. (1980). This observation lead to the study of the influence of mining on hillslope stability in the South Wales Coalfield, and on deep-seated failures in particular, carried out by Halcrow and the Department of Mining Engineering of Nottingham University (Halcrow, 1998; Jones and Siddle, 2000). Physical and numerical modelling showed that shallow workings carried out on steep hillslopes in a shallow seam with pillars of unworked coal left at the outcrop and deeper in the hillside have a strong influence on slope stability, especially if the pillars trend parallel to the valley side. Results showed that after coal extraction: high-angle vertical fractures can reach the surface (joint opening) in the area above the deeper pillar; compressive stresses concentrate in the areas above the pillars, while tensional stresses develop between them (with potential bed separation); the compressive stresses are concentrated in the small areas of the pillar floors (punching of the pillar into the floor) with development of lateral displacements in the rocks below the seam. Furthermore, a high number of continuous fractures develop above and below the deeper pillar consistent with the fractures observed on site and with the formation of potential deep-seated slip zones.

Table 1.6 Deep-seated landslides which have occurred in the South Wales Coalfield since mining commenced (modified from Jones and Siddle, 2000)

Date	Site	Impact
First time slides		
1893	Bournville	None but eventually threatened road
1905	New Tredegar	Damage to road, colliery and railway
1916	Ffaldau	Disruption of railway at toe
(1915-46)	Bournville	Farm abandoned
1930	New Tredegar	Severe damage to railway and colliery, both closed
1930s	Duffryn Ropeway	40 houses progressively affected
1954	East Pentwyn	12 houses abandoned
1989*	Blaencwm	Placed houses at risk from flooding
1999*	Mynydd yr Eglwys	Placed houses at risk
Reactivation +/- first time elements		
1860-61	Pantglas	Trapped miners
c1866/c1903	Troedrihiwfuwch	Affected school, houses, bridge. Village abandoned
c1880	Daren Ddu	Disrupted road bridge, services: all replaced
(1897-1915)/1930s	Maesycod	None
1911/1913	Cwmtillery	Two (?) houses, farm and church damaged

Bracked dates indicate the time interval in which the failure occurred

*Failures occurred after the research carried out by Halcrow and Nottingham University

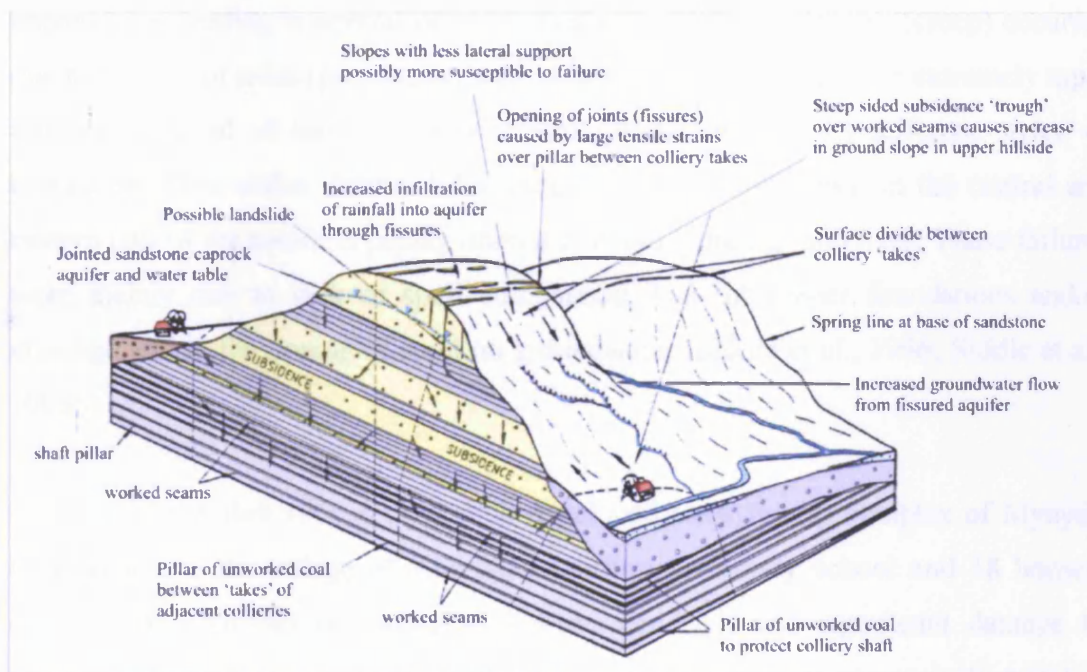


Figure 1.15 Influence of deep coal mining on slope stability (modified from Halcrow, 1998)

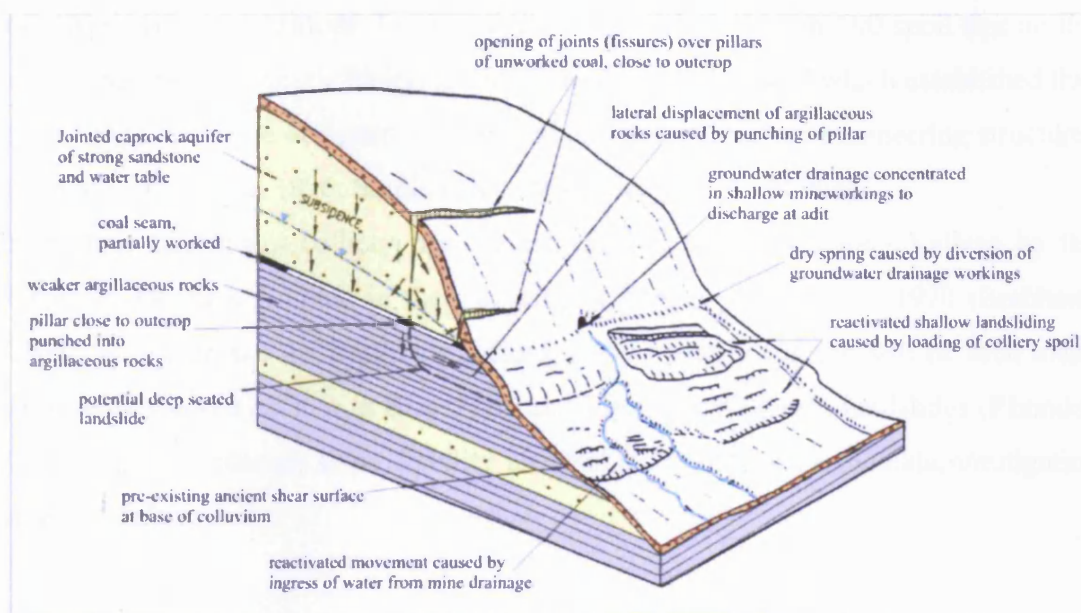


Figure 1.16 Influence of shallow coal mining on a hillslope (modified from Halcrow, 1998)

Before the Aberfan disaster in 1966, tipping of coal spoil on the valley sides/tops was uncontrolled leading to several cases of instability. Slow movements (creep) occurred due to loading of relict (periglacial) slip surfaces. Rapid, very rapid or extremely rapid failures occurred at least in 23 occasions (at 16 sites), with different styles of movement (flow slides, debris slides, outbursts and debris flows) in the central and eastern part of the coalfield posing often a threat to buildings and lives. These failures were mainly due to lack of spoil compaction, lack of proper foundations and/or drainage and to the tipping of spoil on groundwater (Siddle et al., 1996; Siddle et al., 2000b).

On the 21st October 1966 a flow slide developed from the tip complex of Mynydd Merthyr above the village of Aberfan engulfing a primary school and 18 houses, causing 144 fatalities (of which 116 were children) and significant damage to property. Groundwater trapped in the Pennant Sandstone was successively released due to the removal of spoil by the flow slide and gave origin to a mud flow which flooded the village and damaged further houses (Mather, 2000; Penman, 2000).

The dramatic consequences of the Aberfan tip failure promoted many investigations

and research and raised awareness on the potential risks of uncontrolled spoil tipping on valley sides and hilltops. In 1970 there were still more than 500 spoil tips on the valley sides/tops of South Wales. In 1971 a law was introduced which established that spoil heaps had to be designed, constructed and maintained as engineering structures (Bentley and Siddle, 1996; Siddle et al., 1996; Siddle et al., 2000b).

Forty-four significant colliery tips were identified in the Rhondda Valleys by the Rhondda Borough Council in their development plan published in 1970 (Brabham, 2005). Although not the triggering factors, some waste heaps can still be seen today on unstable slopes such as at Blaencwm and Mynydd yr Eglwys landslides (Rhondda Fawr valley) rendering slope stability analyses and landslide remediation/mitigation more complex.

1.6.3 Other human activities

Apart from mining and waste tipping, other human activities can affect slope stability. There are many examples in which the excavation of road cutting or the building of new houses and road/railway embankments lead to the reactivation of periglacial relict slip surfaces (Halcrow, 1993; Siddle and Bentley, 2000).

The South Wales valleys were once carpeted in deep forest, but by the 1960s were largely devoid of trees. Deforestation in South Wales started as far back as the Bronze age, but it was enhanced from the 16th century onwards due to the use of charcoal for iron manufacture and wood later for pit props. The removal of forest has lead to an increase in rain infiltration and rapid surface run-off events. However, the Forestry Commission has started a process of re-forestation of the valley slopes, which can be seen for example in coniferous trees in the Rhondda Fawr valley and on the remediated Coad Maendy landslides.

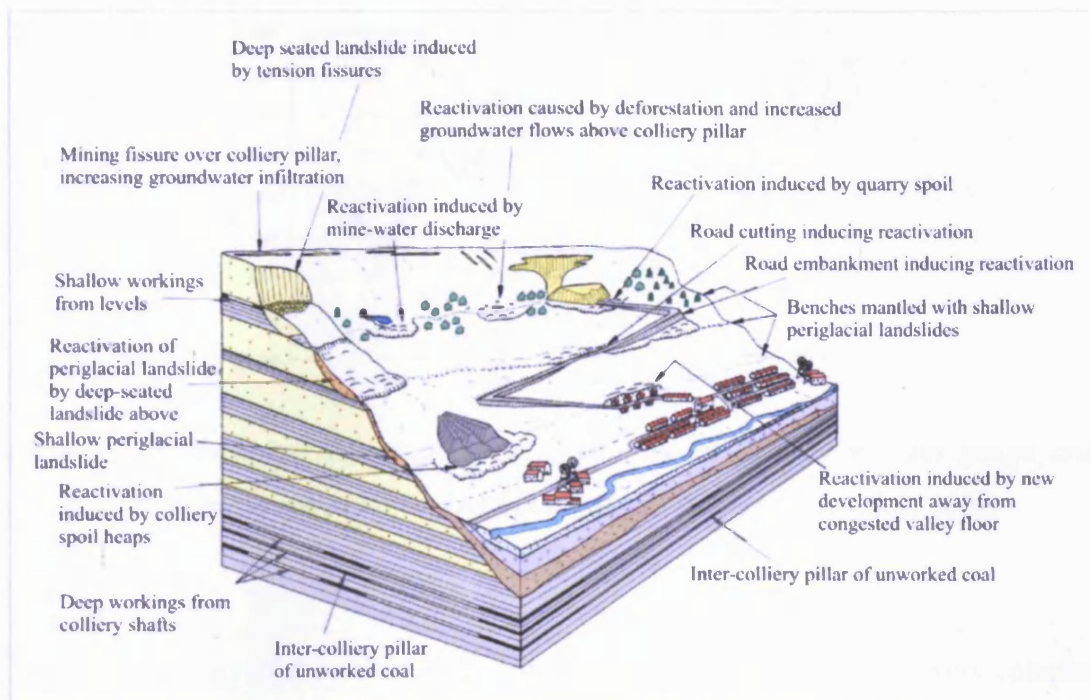


Figure 1.17 Influence of human activities on slope stability (modified from Halcrow, 1989)

1.6.4 Hydrology and hydrogeology

The South Wales Coalfield is characterised by wet weather throughout the year and has a high annual rainfall when compared to the rest of the United Kingdom (*UK Met Office*). The annual rainfall is particularly high (>2400mm/year) in the central part of the coalfield (Siddle et al., 2000b).

In terms of climate change, the analysis of long-term rain gauges showed that there is a cyclical behaviour super-imposed onto a trend of generally increasing rainfall and that both major recent first-time deep-seated landslides in the Rhondda Valleys, Blaencwm and Mynydd yr Eglwys, have occurred at peaks in average winter rainfall (Figure 1.18; Siddle and Bentley, 2000).

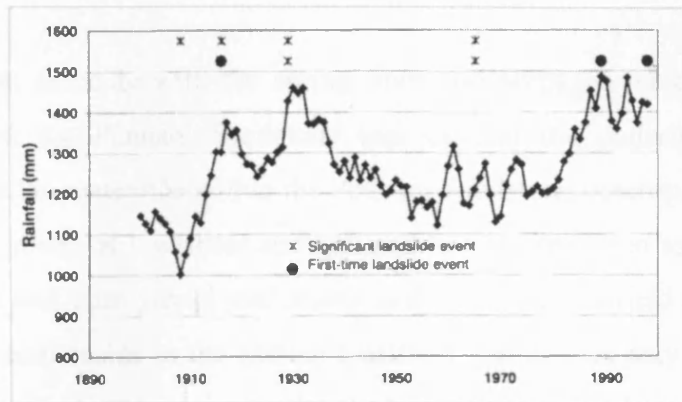


Figure 1.18 Running 9-year average of rainfall at Treherbert rain gauge and significant landslide events in the Rhondda Valleys (Siddle and Bentley, 2000)

The hydrogeology of the valley slopes in the South Wales Coalfield is very complex due to cyclic alternations of permeable and impermeable layers, secondary permeabilities induced by glacial and mining subsidence and water path modifications caused by mine workings.

Due to its high proportion of clay matrix, fresh Pennant Sandstone exhibits low primary porosity and permeability. However, the numerous discontinuities (joints, fissures and faults) result in a significant secondary permeability. Therefore Pennant Sandstone acts as an aquifer, capable of storing and transmitting large amounts of water. On the contrary, the mainly argillaceous sequences (coal, seatearths, mudstones and siltstones) are poorly jointed and have low porosity and permeability and as a consequence generally act as aquicludes.

Rainwater falling on outcropping Pennant Sandstone percolates through joints and fissures until it reaches an impermeable layer, such as a seatearth or a mudstone/siltstone. Then the water moves laterally along the bedding above this impermeable horizon, giving rise to springs and seepages or entering superficial deposits on the valley slopes (Bentley et al., 1980; Conway et al., 1980).

Minor sandstone units within the Lower and Middle Coal Measures can act as confined aquifers, with artesian water pressures (Conway et al., 1980; Forster et al., 2000).

Landslides often coincide with the spring lines and seepages which develop at the contact between the Pennant Sandstone caprock and the underlying argillaceous sequences, or at the seatearths within the Pennant Sandstone outcrop. These seatearths are indeed also zones of low shear strength and failures are often associated with the No. 2 Rhondda and Tormynydd coal seams in the central Coalfield and with Brithdir and Cefn Glas coal seams in the eastern Coalfield. Landslides may occur also at the spring lines and seepages associated with the base of minor sandstone units within the Lower and Middle Coal Measures (Conway et al., 1980; Forster et al., 2000).

As described in the previous section, mining activities have strongly modified the hydrological regime of the South Wales Coalfield. Mining subsidence has caused the dilation of joints and faults and the creation of new fissures which have increased the permeability of sandstones and rendered some of the argillaceous aquicludes ineffective. Furthermore, mining subsidence may have induced zones of tensile and compressive strains within the Pennant caprock leading to the formation of preferential groundwater corridors or hydraulic boundaries as below the spoil tips at Aberfan. Shallow mine workings may provide preferential water paths and drainage adits may issue water on a hillslope promoting instability of superficial material. Moreover, water levels may rebound following mine pumps switch off.

As previously mentioned, preferential groundwater flow is probably increased along the remarkable features of lateral spreading (i.e. graben, fault scarps, dilated joint systems) found on the Pennant Sandstone plateaux in the central and eastern areas of the coalfield and in particular at/near the scarp of major recent deep-seated landslides. Following intense or prolonged rainfall periods, large volumes of groundwater can flow rapidly through these features towards the valley sides promoting slope instability. At ground surface, springs and seeps are common along the fault lines and waterlogged ground or ponds are often found on the downthrow side of the faults, close to their walls (Donnelly et al., 2000; Donnelly, 2005).

Periglacial Head and glacial till deposits found on the valley sides exhibit highly variable permeabilities, with tills being generally less permeable than head. If superfcials are permeable and they overly a spring line, water may move downslope

through the sediments and emerge at a point on the slope lower than expected. On the contrary, if superficial sediments are impermeable, they can promote surface run-off and restrict infiltration. Moreover, a sufficiently thick till can prevent the release of water from underlying jointed/fissured sandstones. This leads to water pressure build up and to the release of water from the uphill boundary of the till promoting instability of the superficial deposits (Conway et al., 1980; Forster et al., 2000). It has been indeed noted that there is an association between landslide distribution and the upslope margin of the till. This could be explained also by the fact that till deposits represent a topographical bench of lower slope angle which has stopped the downward movement of material displaced from the base of the Pennant Sandstone and, if permeable, improving its under drainage (Forster et al., 2000).

Glacial deposits that have experienced sorting during periglacial conditions may be found rearranged in layers characterised by different permeabilities (Wright and Harris, 1980).

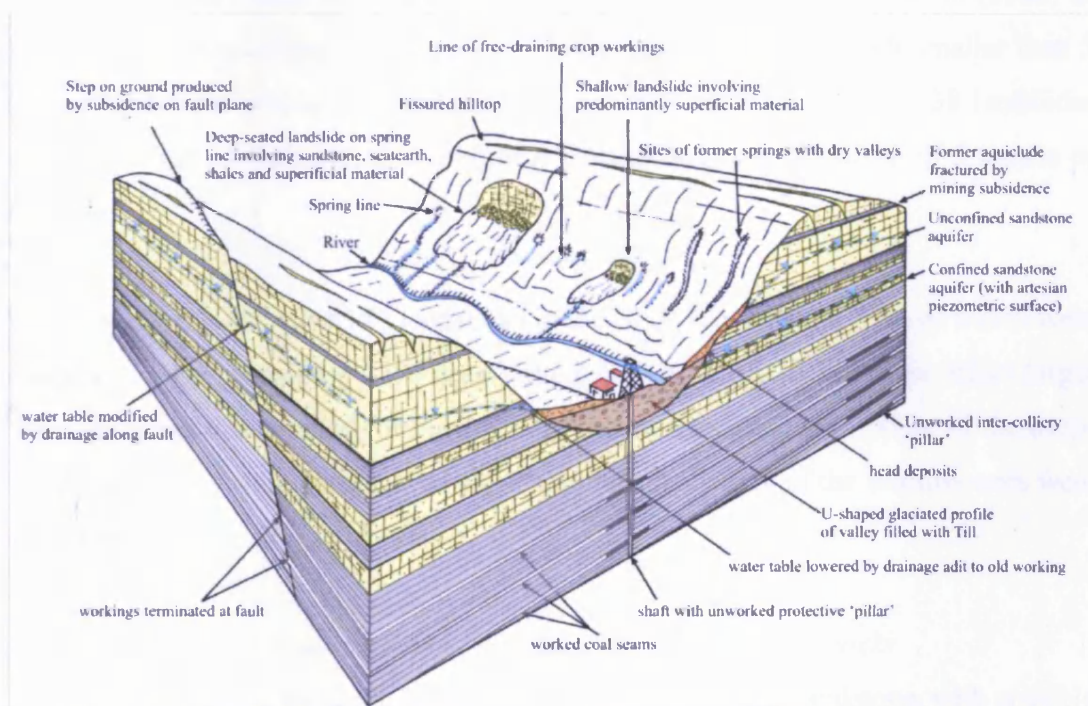


Figure 1.19 Hydrogeology and landslides in the South Wales Coalfield (modified from Daughton et al., 1977 and Conway et al., 1980)

1.6.5 Engineering geology and types of failure

Of the 579 landslides identified in the 'South Wales Coalfield landslip survey' by Conway et al. (1980) approximately 75% were considered complex. However, a major mode of failure was generally recognised and was classified as: fall, rotational, translational, flow or founder (deep-seated failure controlled by a nearly vertical fault running behind and parallel to a steep valley side). In terms of major movements, landslides were mainly translational (43%), followed by flow (21%) and rotational (13%), while founder failures were quite rare (less than 1%; Forster et al., 2000). The remaining landslides were characterised by multiple major components. In reality, many of the landslides defined by Conway et al. (1980) as flows would be now described as shallow translational movements of soil/rock debris (Bentley and Siddle, 1996).

In terms of depth, most of the landslides were classified by Conway et al. (1980) as shallow (93%), involving weathered or superficial materials to depth smaller than 5 metres, and were considered to occur predominately in head deposits. 38 landslides were classified as deep-seated, therefore involving bedrock to a depth of 5 metres or more.

Halcrow (1993) identified 152 landslides in the Rhondda Valleys, 87% of which were shallow and the remaining 13% deep-seated. However, these last ones affect larger areas and indeed accounted for the 54% of the total landslide area. Most of the deep-seated landslides were dormant, whereas approximately half of the shallow ones were classified as active or recently active.

Failures in Pennant Sandstone and argillaceous Coal Measures rocks

Rock falls may occur on natural or artificial cliffs of Pennant Sandstone, with possible bouncing and rolling of rocks downhill which can pose a threat to people and properties (Halcrow, 1993).

The strong Pennant Sandstone caprock is characterised by predominantly vertical or nearly vertical joints of at least two orthogonal sets, one of which trends parallel to the

main faults. Blocks of sandstone can separate from the cliff along joints, fissures and faults and move on bedding or joint planes. Planar, wedge or toppling rock failures may occur depending on the geometry and characteristics of the discontinuities, their relationship with the rock face and water conditions (Figure 1.12; Conway et al., 1980). Toppling of sandstone within a deep-seated landslide is quite rare and can be seen for example in the Rhondda Fawr on the main scarp of Blaencwm landslide (Siddle, 2000b).

As discontinuities are mainly sub-vertical, the Pennant Sandstone caprock can accommodate only the nearly vertical upper portion of the surface of rupture of a deep-seated rotational or compound landslide. The curved portion of the surface of rupture must develop in a more randomly and densely fractured sequence, such as the predominantly argillaceous Rhondda Beds of the north-east Coalfield (Bentley et al., 1980; Conway et al., 1980).

Groundwater conditions, mining influences and geotechnical characteristics /heterogeneities within the slope sequences are all factors that need to be taken into account as preparatory or triggering factors.

During their research on the influence of mining on slope stability, Halcrow (1998) considered five first-time 'recent' deep-seated landslides (seven events) which occurred between 1893 and 1954: East Pentwyn, New Tredegar, Ffaldau, Bournville and Troedrhiwfuch. They noticed how all these landslides were characterised by the following common factors:

- they occurred at the base of a Pennant Sandstone caprock, where this overlies a thick argillaceous sequence (such as the 'Red Beds');
- The strata dip was at a low angle (obliquely) towards the face of the slope, apart from the landslide at Treodrhiwfuch ;
- Faults or other features cropped near/at the rear scarp;
- The geometry of the surface of rupture was influenced by the presence of joints parallel to the valley crest or discontinuities/faults perpendicular to the direction of the dip of strata;
- Before failure the slope was at an angle of 28-32 degrees;
- Heavy rainfall could have been the triggering factor but the variety of

antecedent rainfall conditions for the landslide events suggested more complicated failure processes.

Before the main failure episode, deep-seated landslides normally show some signs of instability with relatively slow movements. Displacements increase, becoming eventually rapid, during the main episode. Then displacements usually carry on, at an extremely slow to moderate rate, for a long period after the main failure, showing a relationship with rainfall (Halcrow, 1993).

Figure 1.20 shows the typical stages of evolution of a deep-seated landslide in the South Wales Coalfield (Halcrow, 1998). The surface of rupture is usually non-circular. It is steep at the rear scarp, where develops on the fissures/joints of the Pennant Sandstone, and flattens at the sole, where it tends to follow the dip of weak strata, such as seatearths or shales (Conway et al., 1980; Halcrow, 1998). The deep-seated failure in the upper valley side may cause the reactivation of relict (periglacial) shallow slides down slope. These may remain active for decades or be reactivated by successive episodes of deep-seated failure and eventually affect property downhill (Halcrow, 1993; 1998).

Deep-seated landslides generally involve large areas causing damages to properties, but likely these can be usually evacuated on time preventing fatalities or injuries (Halcrow, 1993).

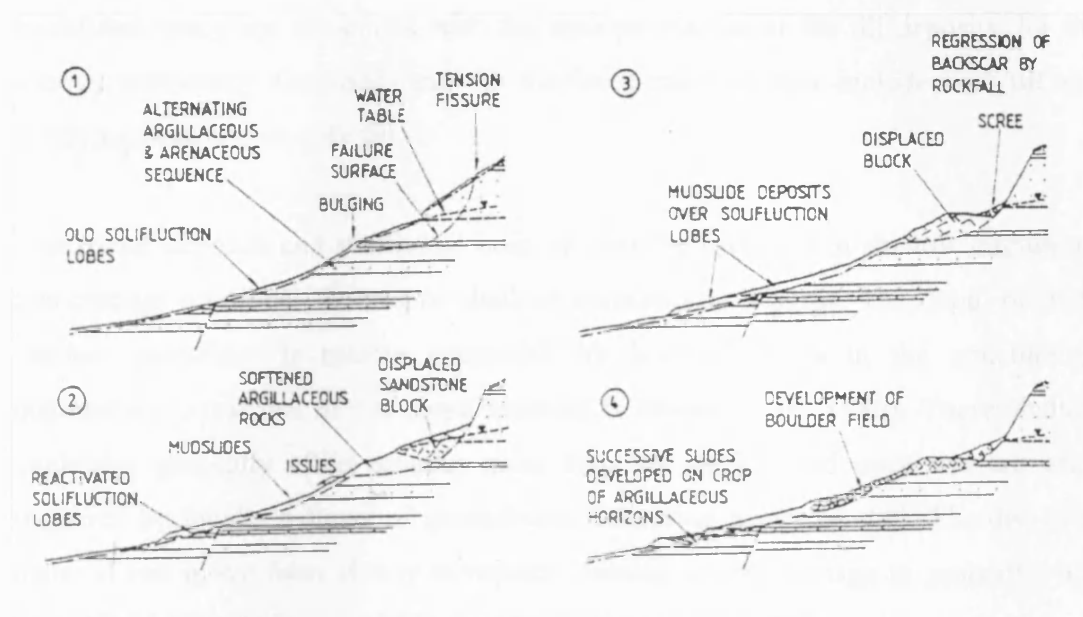


Figure 1.20 Evolution of a typical deep-seated landslide in the South Wales Coalfield (Halcrow, 1998)

Coal Measures shales tend to soften and easily break down into gravel-size material by weathering. This material can be involved in shallow circular and non-circular rotational failures or shallow translational failures. Within the Coal Measures sequences there are several potential planes of weakness which may facilitate/promote failure: seatearths, which have the lowest shear strength in the sequences and are characterised by often slickensided shear zones; pre-existing shear surfaces, which are widespread in the sequences and are at or near residual strength; and structural discontinuities (bedding planes, joints, fissures and faults) which may also promote rock weathering (Conway et al., 1980).

Most of the shallow landslides in the South Wales Coalfield occur in head deposits. These materials tend to be relatively weak when compared with tills and commonly contain pre-existing shear surfaces. The limiting equilibrium angle for head deposits is 17 degrees which is very close to the average angle of the valley slopes. Therefore, they are easily mobilised by water issuing from the base of the sandstone caprock or other locations on the valley sides (Conway et al., 1980).

Till deposits are characterised by a wide range of lithologies, shear strengths and permeabilities (Conway et al., 1980). When considering the distribution of shallow

landslides, many are associated with the upslope margin of the till deposits, for the reasons previously discussed, and the displaced material may include both till and overlying head and or only till.

Superficial deposits and weathered bedrock may be involved in shallow circular or non-circular rotational failures or shallow translational failures. The depth of these shallow landslides is mainly controlled by heterogeneities in the structure or engineering properties of the slope material (Conway et al., 1980). These shallow landslides generally affect smaller areas than the deep-seated ones and are often triggered by localised flows of groundwater following heavy rainfall. The displaced material can move from slowly to rapidly, causing severe damage to properties and possibly injuries (Halcrow, 1993).

Flows can occur in superficial deposits and weathered debris when there is a rapid localised and significant release of surface water or groundwater (Conway et al., 1980; Halcrow, 1993). They are often found at the foot of deep-seated and shallow slides. Due to their rapid to very rapid movement, flows cause severe damage to properties and may cause injuries and fatalities (Conway et al., 1980; Halcrow, 1993).

1.7 The site: Mynydd yr Eglwys landslide

The study site at Mynydd yr Eglwys landslide is located on the hillside above the village of Ystrad, in the Rhondda Fawr Valley (National Grid References SS 977956; Figures 1.13 and 1.21). In 1998-99 a new compound deep-seated landslide developed on the escarpment of the Mynydd yr Eglwys ('Church Mountain'). A bedrock failure on the south-facing slope reactivated ancient periglacial debris slides, which advanced down the slope towards a modern housing estate. The precise date of failure is not known. However, analyses of rainfall data carried out by Halcrow (1999; 2000) suggest that the new failure was triggered by the exceptionally heavy rainfall of autumn 1998. The causes of failure have yet to be defined as several preparatory factors, typical of the South Wales Coalfield and discussed in the previous sections, may have contributed to render this slope more susceptible to failure.

The slope is composed of Middle Coal Measures overlain by Llynfi Beds of the Upper Coal Measures. The Llynfi Beds comprise developments of sandstone, such as the Llynfi Rock, forming the escarpment in which the new deep-seated failure developed. Two coal seams (No 3 Rhondda and Tormynydd), which were mined from horizontal levels until 1906, outcrop on the hillside. The slope was undermined by deep workings up to the 1940s, with consequent subsidence and opening of fissures now visible in the crown area. Generally the strata dip at a low angle, obliquely out of the hillslope. The NW-SE trending Cymmer Fault, which downthrows strata to the SW, crosses the mid part of the slope and it is believed that this could act as a barrier or as a preferential path for groundwater flow. Several perched water tables may be present due to the alternation of argillaceous and arenaceous sequences and the low permeability glacial till found on the lower part of the slope creates the potential for artesian groundwater pressures (see Chapter 3; Halcrow, 1999; 2000).

The landslide is still active and displacements appear to be greater in the central ancient debris slides, which are advancing at relatively slow rates towards the housing estate located near their toe. Two horizontal deep drains were installed between the debris toe and the houses in summer 2008.

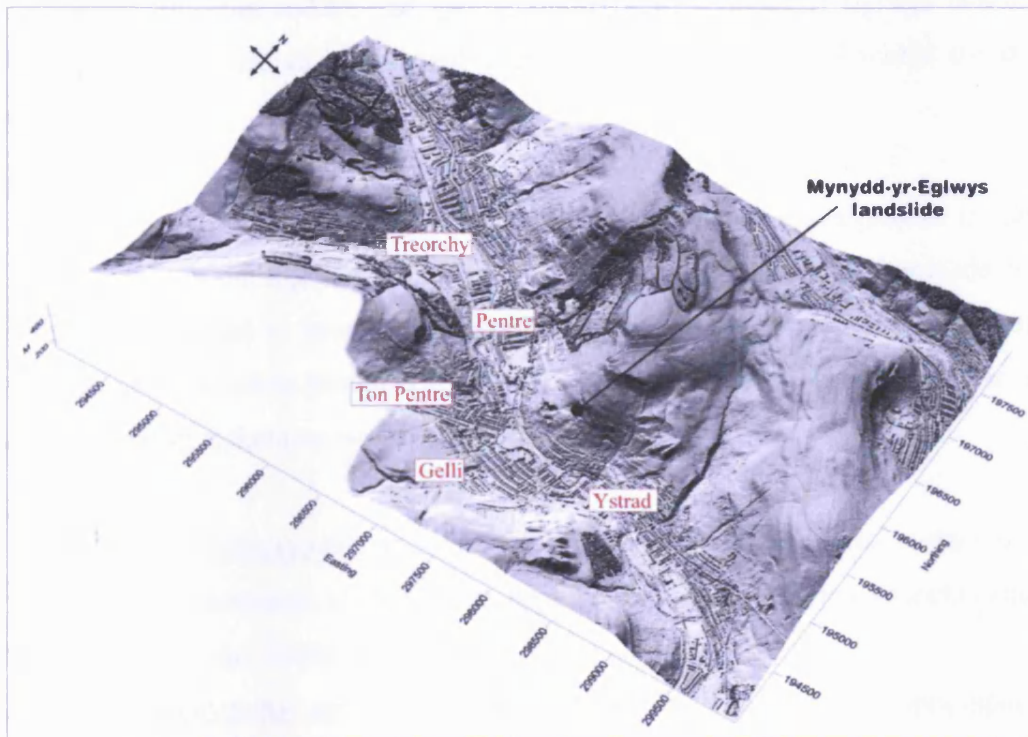


Figure 1.21 Location of Mynydd yr Eglwys landslide at Ystrad, in the upper reaches of the Rhondda Fawr valley. Digital terrain model derived from Environmental Agency LIDAR data

1.8 Aims and objectives

The primary aim of this project is to develop an integrated and cost-effective site investigation approach to active landslides, utilising surface geophysical techniques, supported by GPS and Digital Photogrammetric surveying. The secondary aims are to characterise and monitor slow moving landslides or potentially unstable slopes found in the urban areas of the South Wales Coalfield, which are characterised by complex geology and hydrogeology. It should be emphasised that the research solutions had to be logistically practical, economically cost-effective and also practically applicable in areas prone to urban vandalism.

The aims were achieved by testing several geophysical techniques (ERT, SP, IP, Electromagnetics, seismic refraction tomography and MASW), GPS

surveying/monitoring and Digital Photogrammetry at Mynydd yr Eglwys landslide, which can be considered representative of active landslides found within the study area.

At the beginning of the project it was realised that a detailed topographic model is essential to carry out high resolution geophysical studies on an active landslide. Such terrain models could be constructed using the commercially available LIDAR data at a 2m ground resolution provided by the UK Environmental Agency. However, two other surveying techniques were also tested on site:

1. Digital Photogrammetry: to provide a higher resolution digital surface model (at cm resolution); to evaluate its applicability for the movement monitoring of slow-moving landslides;
2. GPS surveying and monitoring: to provide location and topography of geomorphological features and geophysical profiles/grids to mm accuracy; to establish high precision ground movement rates and spatial distribution of surface displacements.

After a detailed surface model of the landslide was constructed, the subsurface could be investigated by a variety of geophysical techniques. Each selected geophysical technique was tested separately against its specific physical property targets as established from the study of published literature (Figure 1.22):

1. Electrical resistivity tomography: to determine lateral limits and thickness of displaced material, depth/shape of surface of rupture, lithology (i.e. arenaceous/argillaceous sequences, clay), fault zone, moisture content and water table;
2. Self Potential: to determine the lateral limits of displaced material and direction of groundwater flow;
3. Induced Polarization: to discriminate between sub-surface zones rich in clay and areas rich in water, as they will both appear as low resistivity zones in ERT profiles;
4. Electromagnetics (Geophex Gem-2): to determine lateral limits of displaced material and variation in clay/moisture content across the slope and at various

depths;

5. Seismic refraction tomography (P waves): to determine depth/shape of surface of rupture, depth to bedrock, rock fracturing degree and geotechnical parameters;
6. Multichannel Analysis of Surface Waves (MASW): to determine compaction degree and velocity of S waves for calculation of engineering properties.

The results provided by each technique were then compared with each other and integrated together at interpretation level to produce a primary conceptual model of the site.

Once a geophysical conceptual model of the landslide had been developed, the final stage was to monitor temporal changes within the landslide by repeated surveys. Therefore, a few ERT and SP profiles were repeated in time with the purpose of:

1. Investigating changes in the groundwater table, in moisture content and in possible water pathways;
2. Determine the relationship between such changes and the amount of rainfall and their effect on surface displacements (by comparison with GPS monitoring results and information on rainfall, borehole water levels and EDM surface displacements provided by the Halcrow Office in Cardiff);
3. Develop a refined conceptual model of the site and propose future long-term monitoring strategies.

The main causes for landslides in the United Kingdom and worldwide are the result of badly designed development projects and very heavy rainfall events, which could both potentially increase due to increasing population growth and climate change respectively.

Slope stability standard procedures for the investigation and management of unstable or potentially unstable ground prior to development hardly mention or consider the use of geophysics as part of the investigation process (Department of the environment, 1996). It was anticipated that research outcomes would support the applicability and cost-effectiveness of the use of a combination of geophysical methods on both unstable and potentially unstable ground and would provide a firm

basis for recommendations on geophysical best practice.

The UK-wide network on Climate Impact Forecasting For Slopes (CLIFFS) underlined the importance of understanding the relationship between variations in pore water pressures and rainfall. Knowledge of the effect of such groundwater variations on displacement is still very limited in complex geological environments and improving this knowledge is fundamental for a successful forecast of the effects of climate change (changes in amounts of effective rainfall; Dijkstra and Dixon, 2010). The results of this research project were expected to provide recommendations for the use of a combination of geophysical and surveying techniques aimed at understanding the relationship between water level variations (with development of preferential water pathways), rainfall and displacements. Furthermore, the more sophisticated hydrological or hydro-mechanical models (Malet et al., 2005) which are able to include simulated forecasted scenarios, rely on the input of very detailed spatial and temporal information (i.e. rate of displacements, materials, water levels). Results of this research were expected to demonstrate the advantages of using a combination of geophysical/surveying techniques in providing such information.

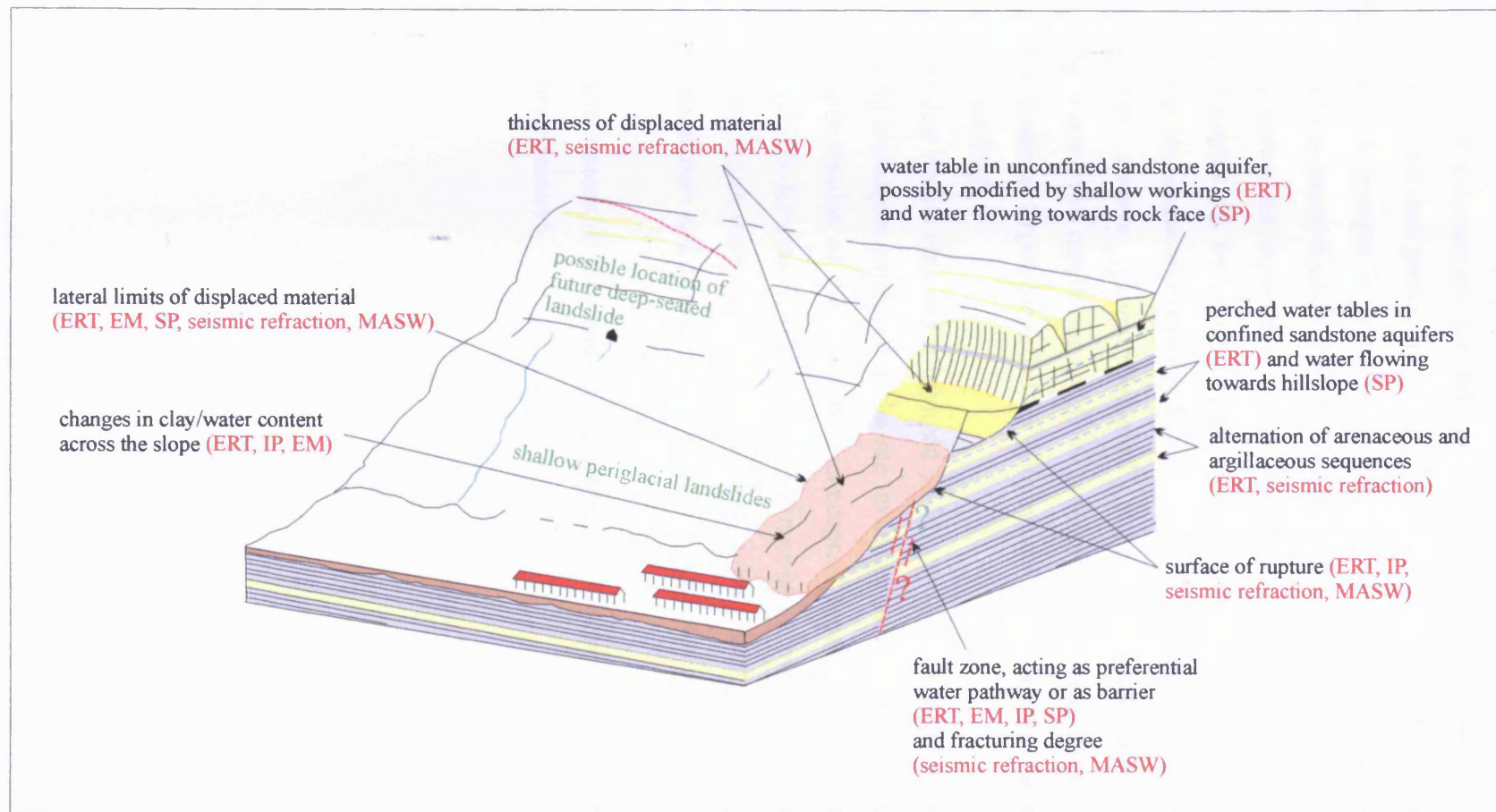


Figure 1.22 Schematic diagram of a deep-seated landslide which has reactivated periglacial debris slides downslope, showing the targets of interest and the geophysical methods which can potentially detect them

1.9 Thesis outline

Following this introductory chapter, a detailed explanation of theoretical background, data acquisition and data processing of all the surveying and geophysical techniques used during this research is given in Chapter 2. The chapter concludes with a summary and a technical discussion of the methods employed.

Chapter 3 describes the Mynydd yr Eglwys landslide site, focusing on its geology, mining, geomorphology, hydrology and hydrogeology, landslide failure mechanisms, landslide possible causes and landslide kinematics. The chapter also includes results of walk-over surveys, geomorphological mapping, digital photogrammetry processing, water levels monitoring and GPS movement monitoring carried out by the author. The potential targets identified for geophysical investigations and monitoring are also summarised.

The geophysical results obtained at Mynydd yr Eglwys (MYE) landslide for each of the surveying techniques employed in the site investigations are shown in Chapter 4. From the interpretation of these results, a conceptual model of the landslide was developed and it is discussed in terms of effectiveness of the methods in detecting the specific targets, which were introduced in the aims of this research project.

Chapter 5 summarises and discusses the results of geophysical monitoring at Mynydd yr Eglwys.

The main conclusions of this study are presented in Chapter 6, with remarks and topics for future research.

Chapter 2 Research Methods

2.1 Introduction

This chapter describes theoretical background, data acquisition and data processing of all the surveying and geophysical techniques employed during this research project for the investigation and monitoring of Mynydd yr Eglwys landslide:

- Airborne LIDAR (data provided by UK Environmental Agency);
- Digital Photogrammetry;
- Global Positioning Systems (GPS);
- Electromagnetic Induction (with instrument GEM-2);
- Self Potential (SP);
- Seismic refraction tomography;
- Multichannel analysis of surface waves (MASW);
- Electrical resistivity tomography (ERT);
- Induced Polarization (IP);

Information on borehole monitoring of groundwater pressures and on rainfall datasets used for geophysical data calibration is also provided.

Acquisition and processing of digital photogrammetry and GPS monitoring data are described more in detail because results were assessed in terms of their accuracy and precision.

The chapter concludes with a summary and a technical discussion of the methods, in terms of optimal field procedures, data quality, data resolution, limitations and predicted commercial costs of using the techniques. These considerations are based on the experience gained by the author during data acquisition and processing throughout the project.

2.2 Light Detection and Ranging (LIDAR)

2.2.1 Background

LIDAR (LIght Detection And Ranging) is an active remote sensing technique which provides distance (range) measurements from a laser scanner to the ground or objects above ground level (i.e. top of trees and buildings). Data is provided in the form of three-dimensional point clouds (Baltsavias, 1999a; Baltsavias, 1999b; Wehr and Lohr, 1999; Mallet and Bretar, 2009). The acronym LADAR (LAser Detection and Ranging) is also in use (Wehr and Lohr, 1999).

An airborne laser scanner system consists of (Baltsavias, 1999b; Wehr and Lohr, 1999; Challis, 2006; Mallet and Bretar, 2009): a laser range finder (including laser, transmitting and receiving optics), a mechanical scanner, a storage media, and control, monitoring and recording units. The three-dimensional coordinates of the measured points are obtained directly during data acquisition via a position and orientation system (POS) comprising of an airborne dGPS with GPS ground reference station/s in the area under investigation and an inertial measurement unit (IMU) that corrects for pitch, roll and yaw (or heading) of the aircraft. Other optional sensors, such as video and digital cameras, can be integrated to the system (Figure 2.1).

While the aircraft (airplane or helicopter) moves forward, a beam of laser energy is projected to the ground surface and scanned across the flight direction in a specific pattern (Figure 2.1). The transmitted signal is reflected back by the ground surface (or by the object above it) and returns back to the system receiver.

The scan pattern on the ground depends on the type of scanner, on the direction and speed of flight and on the terrain topography (Wehr and Lohr, 1999). Several types of uni- or bi-directional scanners are in use, for example oscillating mirrors, rotating polygons and nutating mirrors (Palmer scan). They produce patterns of parallel lines, zigzag-shaped lines, meandering bidirectional parallel lines or elliptical scans

(Baltsavias, 1999a; Wehr and Lohr, 1999).

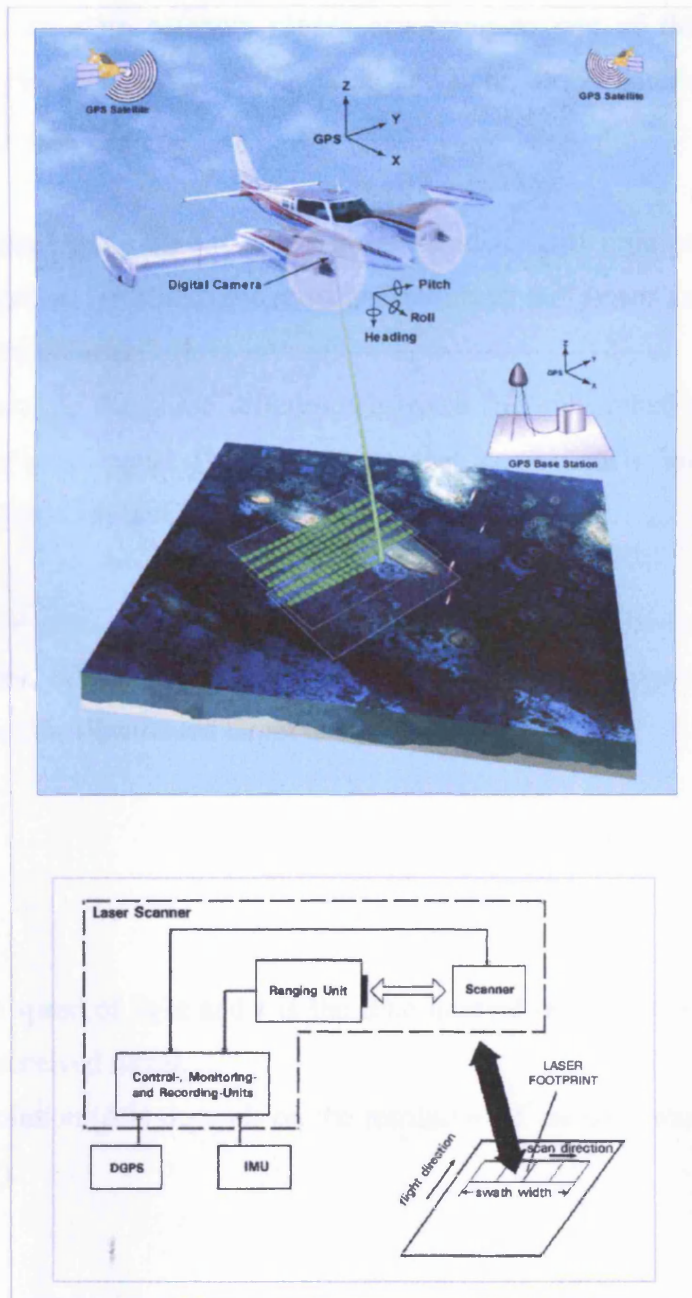


Figure 2.1 Main components of a LIDAR system: ranging unit (comprising of laser transmitter and receiver), mechanical scanner, and control, monitoring and recording units, positioning and orientation systems (dGPS and IMU). Other sensors (i.e. digital cameras) may be integrated to the system. While the airplane moves forward, the laser beam is scanned across the direction of flight. Airborne dGPS, GPS ground station and IMU provide positioning and corrections for pitch, roll and yaw (or heading) of the aircraft (top image from website [WWW 2.1], bottom diagram from Wehr and Lohr, 1999)

Airborne laser scanners compute ranges according to one of the following two physical principles (Baltsavias, 1999a; Wehr and Lohr, 1999; Thiel and Wehr, 2004; Mallet and Bretar, 2009):

- 1- by measuring the time required for an emitted short light pulse to reach the earth surface (or object above it) and return to the sensor as a backscattered signal (pulse lasers);
- 2- by measuring the phase difference between the transmitted and the received backscattered signal (laser scanners that continuously emit light, called continuous wave or CW systems).

Commercial airborne laser scanners are usually pulse systems (Wehr and Lohr, 1999; Thiel and Wehr, 2004). For pulse lasers, the distance (or range, R) between the ranging unit and the illuminated target is equal to:

$$R = c \frac{t}{2} \quad \text{Eq. 2.1}$$

where c is the speed of light and t is the time interval between the emitted and the backscattered received signal.

The range resolution (ΔR) depends on the resolution of the time measurement of the instrument (Δt):

$$\Delta R = c \frac{\Delta t}{2} \quad \text{Eq. 2.2}$$

The maximum unambiguous range for pulse systems is limited by the maximum time interval that can be measured by the time counter and by the pulse rate. Ranging accuracy is proportional to the rise time of the pulse and inversely proportional to the square root of the signal-to-noise ratio.

All the basic relations and formulas for pulse and CW airborne laser scanners,

comprising the ones mentioned above, can be found in Baltsavias (1999a), Wehr and Lohr (1999), Mallet and Bretar (2009).

The first airborne/satellite laser scanners, designed in the 1970s, were used to acquire data along one-dimension profiles and were able to record only one backscattered echo (Mallet and Bretar, 2009). Modern systems can record several (up to five) backscattered echoes for a single emitted pulse (multi-echo or multipulse systems). Typically, the first and the last pulse echoes are recorded. As LIDAR signal can partly penetrate through canopy, in this way the top of the trees and the ground surface underneath can be both determined simultaneously (Baltsavias, 1999b; 1999c; Wehr and Lohr, 1999; Mallet and Bretar, 2009). Moreover, since 2004 some airborne laser scanners that can record the complete backscattered waveform (full-wave LIDAR systems) have become commercially available (Mallet and Bretar, 2009). They are used mainly for the study of forested areas (Figure 2.2). Some systems can record also information on the intensity of the backscattered signal which is related to the laser wavelength and the reflectivity of the target (Wehr and Lohr, 1999).

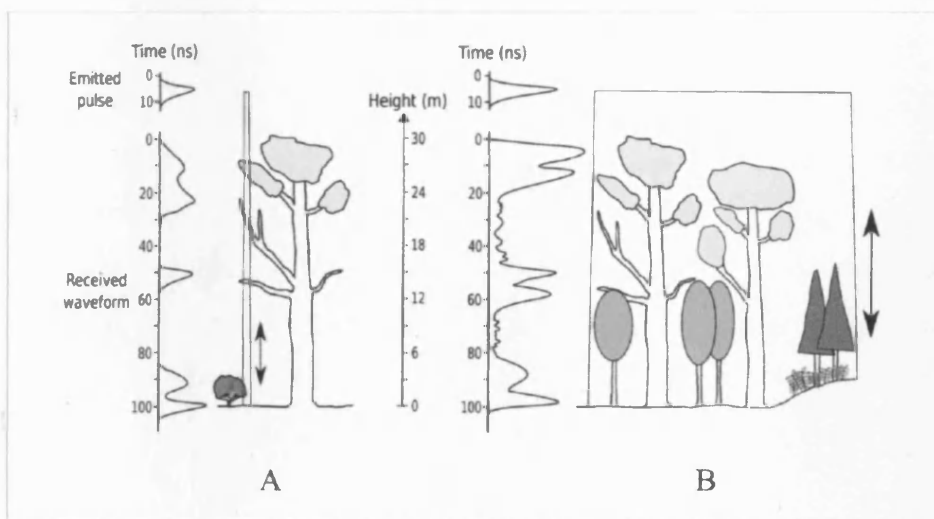


Figure 2.2 Transmitted and received signal for a full-waveform LIDAR system with small (A) and large footprint (B) in a wooded area (from Mallet and Bretar, 2009)

The density of points depends on the aircraft altitude, the aircraft velocity and on the laser system used (Wehr and Lohr, 1999). For some specific applications, point

density can reach more than 100 pts/m², but generally does not exceed 25 pts/m² (Mallet and Bretar, 2009). Technical parameters of commercially available airborne laser scanners are discussed for example in Baltsavias (1999b) and Mallet and Bretar (2009).

After acquisition, LIDAR data are processed with the aim of producing digital surface models (DSM) and digital terrain models (DTM, ground surface without objects above it). All the information from the positioning and orientation system (POS) are combined with measured ranges and scan angles, system calibration data and mounting parameters in order to compute three-dimensional points in WGS84 coordinate system. Firstly, a coordinate transformation is applied to convert positions and elevations in the wanted local coordinate system. Secondly, the cloud of points, distributed according to the scan pattern of the instrument used, is sorted and filtered to separate points on the ground surface from points related to objects above surface (i.e. buildings and trees). Data are successively interpolated and thinned out (Figure 2.3; Wehr and Lohr, 1999).

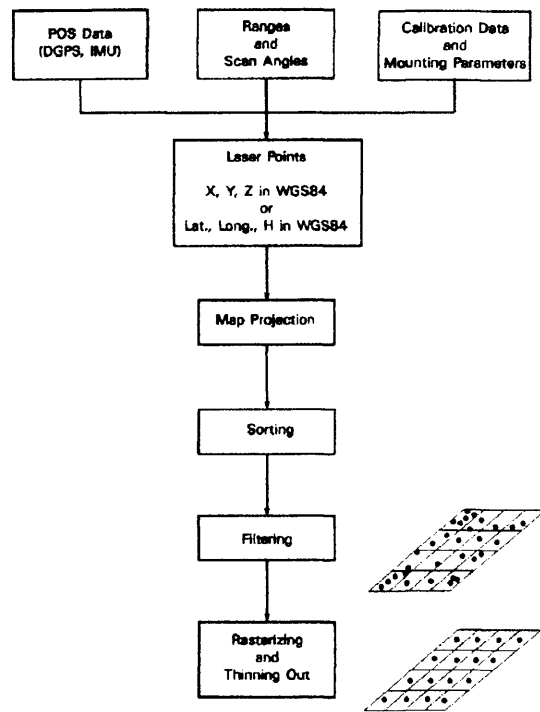


Figure 2.3 Flow-chart of typical processing of LIDAR data (Wehr and Lohr, 1999)

Defining quality and accuracy of the 3D coordinates provided by LIDAR is complicated, because they are affected by several factors, such as: laser system (i.e. accuracy of range, GPS and IMU), data characteristics (i.e. point density, flight altitude and scan angle), target characteristics (i.e. type of terrain/object, topography, density of canopy) and data processing (i.e. accuracy of coordinates transformation, errors in data interpolation and filtering) (Huising and Pereira, 1998; Baltsavias 1999a; Ahokas et al., 2003). Moreover, system firms do not normally provide detailed information on the conditions for which the system accuracy was established (Baltsavias, 1999b).

2.2.2 LIDAR data used in this project

The LIDAR data used in this project were supplied by the UK Environmental Agency and were originally acquired for UK flood defence and management purposes. The data comprising the area of Mynydd yr Eglwys landslide (Tile D00046021) were captured in April/May 2005 from a flying height of approximately 800 m, using an

Optech ALTM2033 LIDAR (Mike Plant of Geomatics Group, personal communication). This instrument is a discrete return system, which operates at 1047 nm (near infrared) and is capable to record both first and last signal returns for each pulse. It is typically used to collect 0.5 points/m², scanning perpendicularly to the direction of flight and resulting in a zig zag pattern of data points (Brown et al., 2003 in Challis, 2006; Watt et al., 2003).

The vertical accuracy of this survey was ± 8.1 cm RMSE. The horizontal accuracy of the data points, defined as 1/2000 of flying height for the Optech ALTM 2033, was approximately ± 40 cm, although it was subsequently reduced by 2 m gridding (pers.com. Mike Plant EA Geomatics Group).

Editing, filtering and processing of data were carried out by the Environmental Agency (Geomatics group section). Coordinates of measured data points were converted from WGS84 to British National Grid Eastings and Northings and elevation over OSGB36 datum. Cloud data were sorted, filtered and re-sampled in regular grids of 2 m cell and supplied as xyz files in 2 km square tiles. Information on last echo signal return and signal intensity were not provided. The resulting digital terrain models (DTMs) were generated using Arcview3.3, Terrascan and in-house filtering programs and algorithms (pers.com. Mike Plant). According to Challis (2006) and references therein, the Environmental Agency eliminates landscape clutter from the digital surface models (DSMs) using a 3 x 3 m cell variance filter with a threshold limit of 66.6° slope gradient. DTMs are then obtained removing the filtered data from the dataset and filling in the gaps by interpolation of elevation data.

For the tile comprising Mynydd yr Eglwys landslide, the Environmental Agency supplied all these three products: DSM, DTM and the applied filter mask (Figure 2.4).

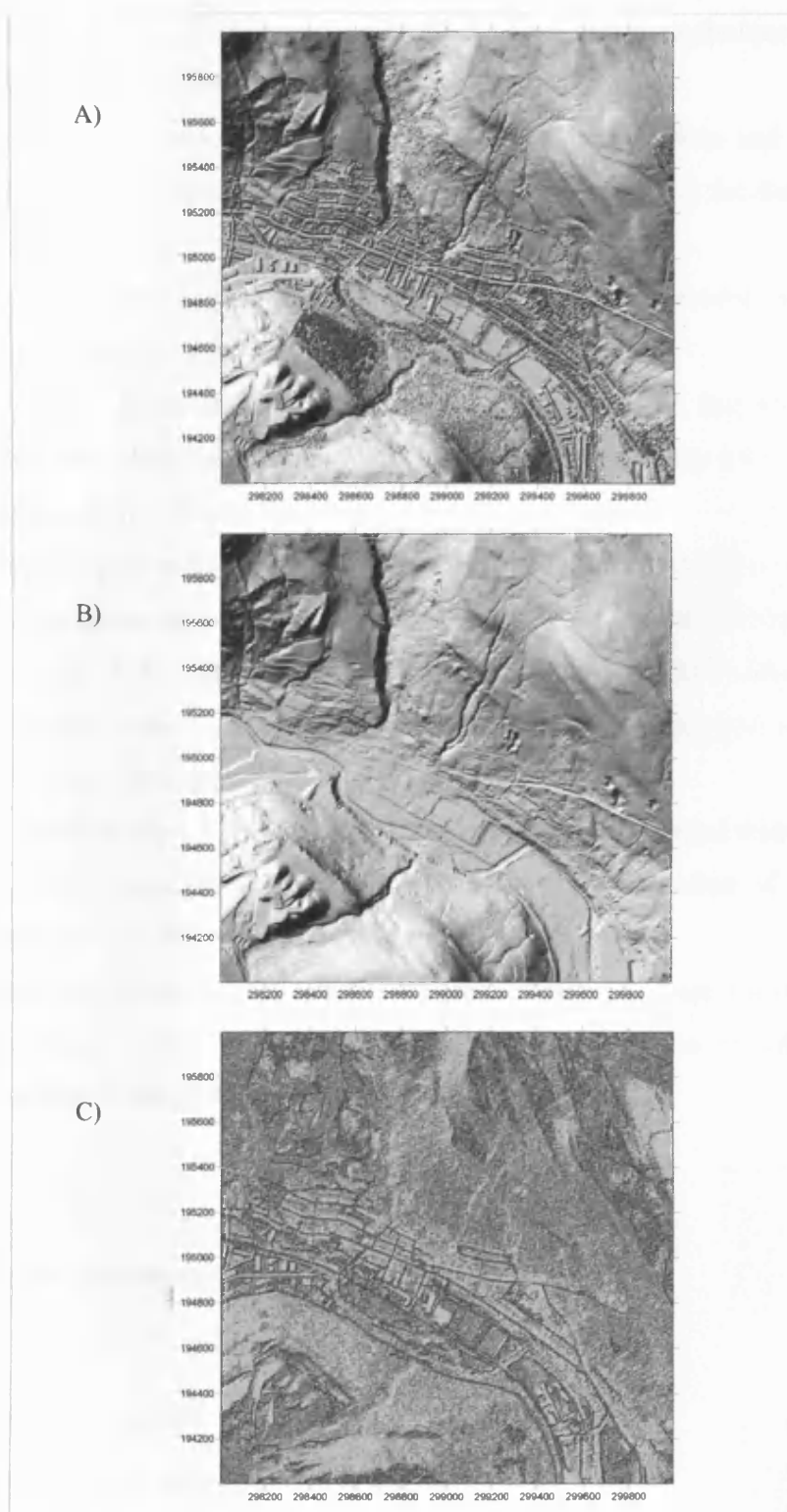


Figure 2.4 The three datasets supplied by UK Environmental Agency for the area comprising Mynydd Yr Eglwys landslide (Tile D00046021): (A) unfiltered digital surface model, (B) filtered digital surface model or digital terrain model and (C) the applied filter mask.

For this project, these LIDAR data were gridded using Kriging technique and plotted or analysed in Surfer 8 to obtain:

1. Terrain model: LIDAR data were firstly plotted as a surface and then an air photograph from Getmapping [WWW 2.2] was overlain on it for the desk study (Chapter 3);
2. Analyses of slope angles: LIDAR DTM data were re-gridded using terrain modelling functions in Surfer for the desk study (Chapter 3) ;
3. Geological 3D plots: geological information were digitized and geo-referenced from BGS and Halcrow geology maps and then overlain onto the LIDAR DTM for the desk study (Chapter 3);
4. Geomorphological maps: LIDAR data were plotted as surface and as shaded relief maps with various directions of illumination. Some land forms and features could be recognised and mapped directly by interpretation of LIDAR data. Moreover, LIDAR shaded relief plots were used as base maps during geomorphological walk-over surveys (Chapter 3);
5. Survey location maps: LIDAR data plotted as surface and shaded relief maps were used as base maps for the plotting and planning of location of geophysical profiles/grids and GPS monitoring;
6. Basemaps for SP and GEM results: SP and GEM data were overlain on both LIDAR shaded relief and surface plots to improve data visualization and interpretation (Chapter 4).

2.3 Digital photogrammetry

2.3.1 Basic principles

Fundamental to digital photogrammetry are:

1. The use of the collinearity equations for the mathematical treatment of the relationship between three-dimensional object coordinates and two-dimensional image coordinates;
2. The use of image matching techniques for identifying and measuring conjugate points in overlapping photographs;

3. The automatic generation of digital elevation models and orthophotographs.

Collinearity equations

“Collinearity is the condition in which the exposure station of any photograph, any object point in the ground coordinate system and its photographic image all lie in a straight line. This condition holds irrespective of the angular tilt of the photograph” (Lillesand et al., 2004; Figure 2.5). This principle is described mathematically by the following collinearity equations (Lillesand et al., 2004):

$$x_p = -f \left[\frac{m_{11}(X_p - X_L) + m_{12}(Y_p - Y_L) + m_{13}(Z_p - Z_L)}{m_{31}(X_p - X_L) + m_{32}(Y_p - Y_L) + m_{33}(Z_p - Z_L)} \right] \quad \text{Eq. 2.3}$$

$$y_p = -f \left[\frac{m_{21}(X_p - X_L) + m_{22}(Y_p - Y_L) + m_{23}(Z_p - Z_L)}{m_{31}(X_p - X_L) + m_{32}(Y_p - Y_L) + m_{33}(Z_p - Z_L)} \right] \quad \text{Eq. 2.4}$$

where x_p and y_p are the image coordinates of any point P, f is the focal length, X_p , Y_p and Z_p are the ground coordinates of point P, X_L , Y_L and Z_L are the ground coordinates of the exposure station L, $m_{11} \dots m_{33}$ are the coefficients of a rotation matrix defined by the angles ω , ϕ and κ and that transforms the ground coordinate system to the image coordinate system.

The collinearity equations are non linear and to be solved are linearized with Taylor's series.

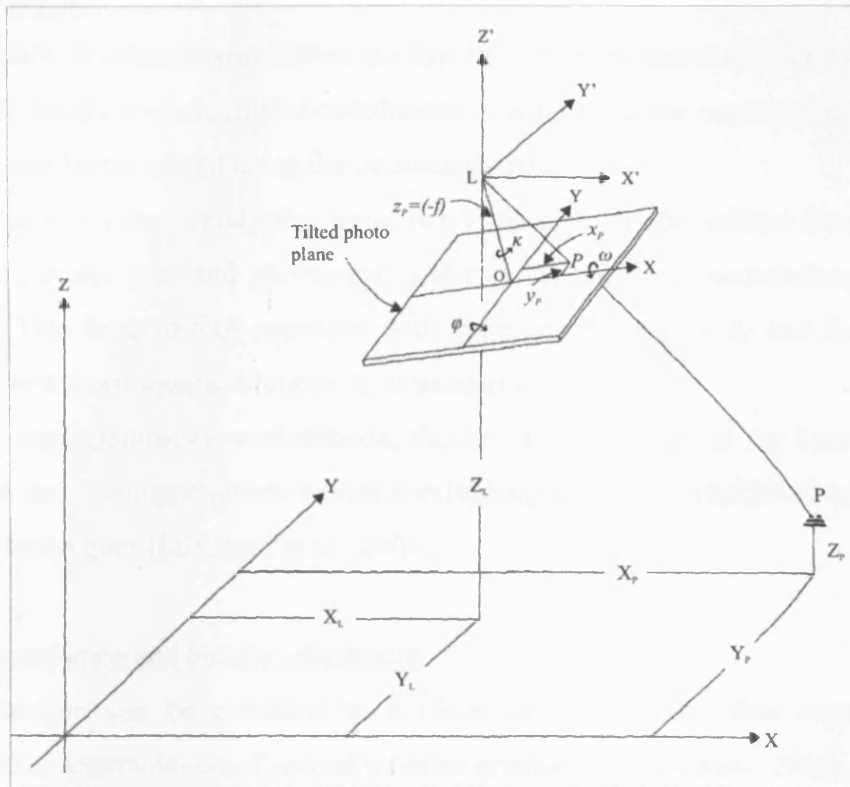


Figure 2.5 Diagram showing the relationship between the terms in the collinearity equations (from Lillesand et al., 2004)

Space resection

The coordinates of the exposure station (X_L , Y_L and Z_L) and the angles of camera orientation (ω , φ and κ) define the exterior orientation of a photograph and are also called exterior orientation parameters (Lillesand et al., 2004). If these parameters are not known, they can be determined through a process called space resection by measuring at least three ground control points identifiable in the images (Konecny, 2003; Lillesand et al., 2004).

Two collinearity equations can be written for each of the three ground control points, leading to a total of six equations that can be solved simultaneously for the six unknowns (X_L , Y_L , Z_L , ω , φ and κ). If more than three ground control points are measured, more than six equations are available and a least square solution is adopted (Lillesand et al., 2004).

Space intersection

If the exterior orientation parameters are known (i.e. from direct GPS measurements and IMUs) the three-dimensional coordinates of a point in the overlapping area of a stereopair can be computed using the collinearity equations.

For each point in the overlapping area, two equations can be written for its image coordinates in the left-hand photograph and two for its image coordinates in right-hand one. This leads to four equations with three unknowns (X_P , Y_P and Z_P) that can be solved with least square solutions (Lillesand et al., 2004).

In digital photogrammetry workstations, this process is usually at the base of DEM generation and conjugate points within overlapping areas are established with image matching techniques (Lillesand et al., 2004).

Aerial triangulation and bundle adjustment

Space resection can be extended to a block of photographs thus requiring the simultaneous determination of several exterior orientations (Konecny, 2003; Lillesand et al., 2004).

Software packages generally use an algorithm called bundle adjustment that is based on least squares. This algorithm provides the best estimate for the exterior orientation parameters of all the images and for the coordinates of pass points (Chandler, 1999; Lillesand et al., 2004). At least three ground control points are required, but the use of more than three is recommended (Chandler, 1999).

If provided by the software, the self-calibration version of the bundle adjustment can compute also camera parameters (Chandler, 1999).

Image matching

There are three main known image matching techniques (Schenk, 1997):

1. Area-based matching. The entities matched are grey levels in image patches and similarity is measured by correlation or least-squares techniques;
2. Feature-based matching. The entities matched are edges or interest points and similarity is evaluated by a cost function;
3. Symbolic matching. The matching entities are symbolical descriptions and similarity is evaluated by a cost function.

In the case of area-based matching, a reference window of a limited number of pixels (with associated grey levels) on the left hand image is compared with a window of the

same size in the right hand image. The window in the right hand image is moved across within a defined search area, pixel by pixel, and correlation coefficients can be calculated for each position. The highest correlation coefficients are associated with the best image matching result thus determining the position of the conjugate point (Konecny, 2003; Lillesand et al., 2004). Instead of using correlation, image matching can be carried out with least-squares techniques. In this case, the position of the conjugate point is at the minimum of the square sum of the gray level differences between the matrix in the left-hand image and the geometrically transformed matrix in the right-hand window (Konecny, 2003).

Image matching procedures are highly dependent upon the quality of the digital images in terms of sharpness, contrast etc. (Chandler, 1999).

Generation of digital elevation models (DEMs)

Digital elevation models are generated automatically applying image matching techniques and space intersection to the overlapping areas of stereopairs (Lillesand et al., 2004). It is important to underline that the DEMs obtained automatically represent the visible surface and not necessarily the ground surface. If objects above the ground (i.e. tree canopy or buildings) are present and only the ground surface level is wanted, the height of the objects needs to be subtracted from the model (Chandler, 1999). DEMs can be generated using regular raster grids, triangular or planar faces irregular networks, iso-contour and breaklines networks (Paroditis and Polidori, 2002). As the distribution of samples is often sparse, regular grids are not the best option and irregular networks should be preferred (Paroditis and Polidori, 2002).

Generation of orthophotographs

Any point of an orthophotograph (x_p, y_p) can be computed from the collinearity equations if the external orientation parameters ($X_L, Y_L, Z_L, \omega, \varphi$ and κ) and the coordinates of the point on the ground (X_p, Y_p, Z_p) are known (Lillesand et al., 2004). The exterior orientation parameters are known from available instrumentation (GPS and IMUs) or as a result of aerial triangulation, while X_p, Y_p, Z_p are determined by the DEM. As a consequence, the quality of the orthophotograph depends upon the quality of these two datasets (Kasser and Palidori, 2002).

2.3.2 Precision, accuracy and internal reliability

According to Chandler (1999) and references therein, the quality of digital photogrammetry data can be assessed in terms of three factors:

1. Precision: which depends on the precision of image measurements, and scale and geometry of images and can be evaluated from the results of bundle adjustment;
2. Accuracy: which depends on the knowledge of camera parameters and the accuracy of ground control points and is normally estimated by comparing photogrammetry-derived heights with accepted heights (i.e. from GPS surveys) at a number of check point locations;
3. Internal reliability: which is estimated by comparing the elevation provided by adjacent DEMs in overlapping areas.

The quality of the automatically generated DEM depends also on: the resolution and quality of the images, the terrain characteristics, the grid density of the DEM, the algorithm and strategy parameters selected for automatic data extraction (Gooch et al., 1999; Baily et al., 2003; Smith et al., 1997).

2.3.3 Digital photogrammetry at Mynydd Yr Eglwys landslide

2.3.3.1 Data acquisition and processing

At Mynydd Yr Eglwys (MYE) landslide, images were acquired using a digital camera mounted on a helium balloon on the 20th of February 2008. Data were successively processed using Topcon's PI-3000v3 software, running on a Windows XP Workstation. This program can be used to generate very accurate 3D models of landscapes and objects from stereo photographs taken in theory with any fixed focal length digital camera, providing that camera lens calibration parameters are known. The software has been used successfully in several fields, such as archaeology, geology and geotechnics, land surveying and topography, quarrying, accident and crime scene investigation. A few case studies are reported on the TerraDat Geomatics web site [WWW 2.3]. The English version of the technical manual of the software is

quite poor, however one-day-training and tutorial material were provided by Terradat UK Ltd. A more useful review of the software is provided by Masinton (2008) [WWW 2.4].

Acquisition and processing of the digital photogrammetry data involved several stages that are summarised in the following paragraphs. Some details are here reported as reference for future users due to the poor quality of the software manual.

- **Stage 1: Camera Calibration.** A Ricoh GR Digital II fixed focal length camera (10 MPixels) was selected for the acquisition of air photographs at MYE landslide. Camera parameters were obtained through Topcon's PI-calib software (part of the same package of Topcon's PI-3000 software) by following easy instructions. Firstly, a calibration sheet with a defined pattern of dots was photographed from five different directions keeping the camera focus at infinity, using an aperture as small as possible. Secondly, the five images were imported in the calibration software and measurements were made. Camera calibration parameters were then computed automatically by the software and stored in a file to be used during data processing (Table 2.1).

Table 2.1 Calibration parameters of camera Ricoh GR Digital II used for the acquisition of images at Mynydd yr Eglwys landslide as determined by Topcon's PI-calib software.

Camera Parameters	Value
Focal length of lenses (f)	5.899725 mm
Radial distortion of lenses: K_1	0.001678713
Radial distortion of lenses: K_2	-3.33346e-005
Tangential distortion of lenses: P_1	5.792469e-005
Tangential distortion of lenses: P_2	0.0003373058
Location of principal point of camera sensor: X_p	3.639317 mm
Location of principal point of camera sensor: Y_p	2.609994 mm

- **Stage 2: Data acquisition.** Firstly, 35 targets (white paper dishes with a marked letter on them) were distributed on the landslide area characterised by the main scarp and the hummocky terrain (Figure 2.6). Secondly, the fixed focal length Ricoh GR Digital II camera, set at infinite focus, was mounted on a helium balloon and towed across the area of interest along parallel lines of flight (Figure 2.7). The camera was set to automatically capture an image every 15 seconds. The positions of the ground targets (control points) were surveyed with the Topcon HiPer Pro GPS+ in RTK mode. The GPS base station was set up on a tripod at a known location and the rover antenna was mounted on a 2 m pole with optical plummet and used to survey the centre of the targets. The rover antenna was set to record only fixed positions with a precision of 0.015 m and 0.030 m in horizontal and vertical plane respectively. A close-up photograph of each target and its surrounding area was taken using another digital camera as a record to help identify the targets observed on the air images.



Figure 2.6 Top: a view of the targets (ground control points) spread on the terrain at Mynydd yr Eglwys landslide from the top of the main scarp (photo by P. J. Brabham). Bottom: one of the vertical photographs taken from the camera mounted on the helium balloon (photo by N. Russill). In this photograph, each target is represented by a number of white pixels that ranges approximately between 100 and 150 (or the targets have a diameter of approximately 10-13 pixels)

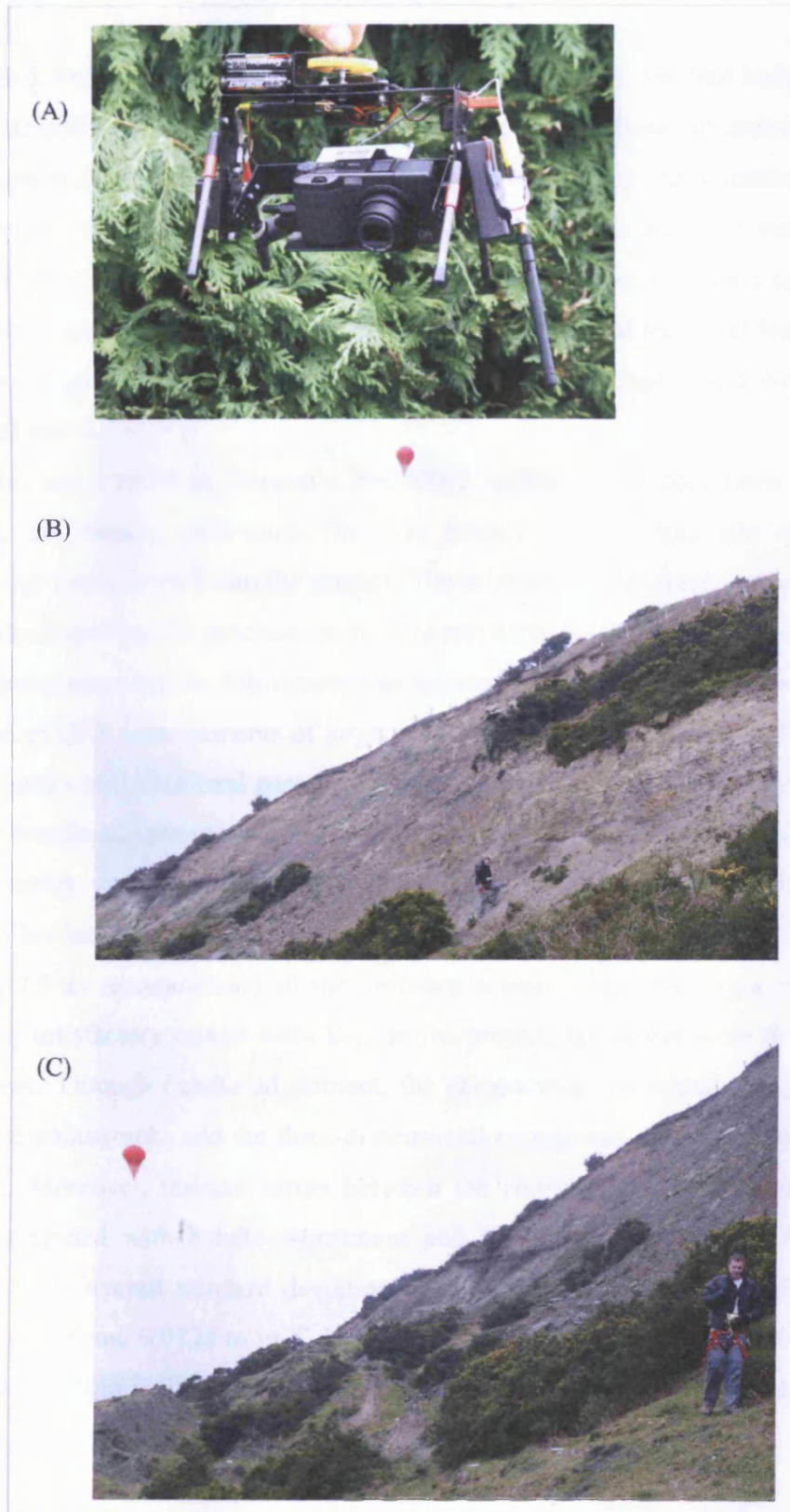


Figure 2.7 Camera set up (A) and image acquisition (B and C) at Mynydd yr Eglwys landslide. The camera was mounted on a helium balloon and then towed across the slope while taking photographs every 15 seconds (photos by P. J. Brabham)

- **Stage 3. Data processing.** The digital camera took over a hundred images but the best 22 air photographs of the landslide were selected for photogrammetric analysis. The images were printed and spread out on a table to simplify identification of useful stereo-pairs. Unfortunately, the letters marked on the targets were not visible in the photographs. Therefore, as the targets were all the same size and same colour, they could not be immediately recognized. By using a GPS map of the target locations and the close up photos, all the targets in each printed photograph could with time be identified and marked up.

A project was created in Topcon's PI-3000v3 software and data were processed. Initially, the camera calibration file was loaded and the xyz file with target coordinates was imported into the project. The selected images were imported (image registration) and then the potential pairs were registered as stereo-pairs. Moving to the orientation screen, bundle adjustment was selected as the orientation method and the precision of GPS measurements of target locations was specified. The visible ground control points and additional pass points were measured for each stereo-pair (Figure 2.8) and bundle adjustment was computed. Results of bundle adjustment, presented in form of tables, were checked for being successful, that is to be judged "OK", to have a Y-parallax less than 1 pixel, and to have a base/height ratio approximately between 0.3 and 0.5 as recommended in the software manual. Only the eight stereo-pairs providing satisfactory results were kept in the project, the others were deleted from the dataset. Through bundle adjustment, the camera external orientation parameters for all the photographs and the three-dimensional coordinates of the pass points were obtained. Moreover, residual errors between the coordinates of the ground control points computed with bundle adjustment and the ones surveyed with GPS were provided. The overall standard deviation of the residual errors was 0.0060 m in X, 0.0063 m in Y and 0.0128 m in Z. Maximum residuals were -0.0142 m in X, 0.0148 in Y and 0.0289 m in Z. Some of the results are summarised in Tables 2.2 and 2.3.

Table 2.2 Overall result list (above), stereo camera conditions and ground resolution information (below) determined by bundle adjustment

Pair Name	Result list		
	Judge	Y-Parallax (pixels)	Image coordinates (pixels)
4b R0010938 - 1b R0010928	Ok	0.45 ok	0.44 ok
1b R0010928 - R0010924	Ok	0.37 ok	0.44 ok
2a R0010894 - 2b R0010898	Ok	0.37 ok	0.26 ok
3c R0010825 - 3d R0010818	Ok	0.64 ok	0.55 ok
3d R0010818 - 3e R0010807	Ok	0.61 ok	0.54 ok
1b R0010928 - 1c R0010917	Ok	0.49 ok	0.46 ok
5b R0010732r - 5c R0010737r	Ok	0.73 ok	0.38 ok
R0010721r - 5b R0010732r	Ok	0.52 ok	0.38 ok

Pair Name	Stereo camera conditions			Ground resolution	
	B: Base Length (m)	H: Height (m)	B/H ratio	Plane Resolution (m)*	Depth Resolution (m)**
4b R0010938 - 1b R0010928	39.2292	74.9949	0.52	0.0254	0.0486
1b R0010928 - R0010924	22.7245	74.9426	0.30	0.0254	0.0838
2a R0010894 - 2b R0010898	17.0631	60.9510	0.28	0.0207	0.0738
3c R0010825 - 3d R0010818	26.8516	61.8512	0.43	0.0210	0.0483
3d R0010818 - 3e R0010807	39.2641	70.0251	0.56	0.0237	0.0423
1b R0010928 - 1c R0010917	34.9804	76.7979	0.46	0.0260	0.0572
5b R0010732r - 5c R0010737r	28.4237	80.8781	0.35	0.0274	0.0780
R0010721r - 5b R0010732r	38.0420	76.1512	0.50	0.0258	0.0517

* Plane resolution is defined as $\Delta XY = \frac{H}{f} dp$ where dp is the image resolution

** Depth resolution is defined as $\Delta Z = \frac{H}{B} \Delta XY$ (Topcon's PI-3000 manual)

Table 2.3 Camera external orientation parameters computed by bundle adjustment for the images kept in the project as they provided good stereo-pairs

Image name	X _L (m)	Y _L (m)	Z _L (m)	Omega (deg)	Phi (deg)	Kappa (deg)
1b R0010928	297763.3628	195600.3994	345.5563	-2.825	-9.008	-2.477
1c R0010917	297786.8753	195575.7555	337.5896	-2.485	-4.681	8.715
2a R0010894	297746.6499	195550.4022	313.7246	-1.254	-13.050	12.636
2b R0010898	297757.4840	195559.9657	322.8085	-1.446	-7.950	11.424
3c R0010825	297782.3397	195541.8404	311.0174	-4.467	-20.638	13.282
3d R0010818	297808.9274	195545.1107	312.8631	-0.161	-21.676	9.864
3e R0010807	297842.6169	195563.8144	320.4034	1.348	-20.638	12.390
4b R0010938	297724.3985	195602.7902	349.4293	-2.555	-4.693	0.403
R0010924	297781.5252	195587.8486	340.1706	-2.171	-12.562	3.821
5b R0010732r	297751.6806	195477.0584	306.2974	3.295	-6.601	113.833
5c R0010737r	297759.8732	195449.8689	305.0647	4.603	-7.081	132.906
R0010721r	297750.9303	195515.0803	305.4244	1.940	1.209	118.676

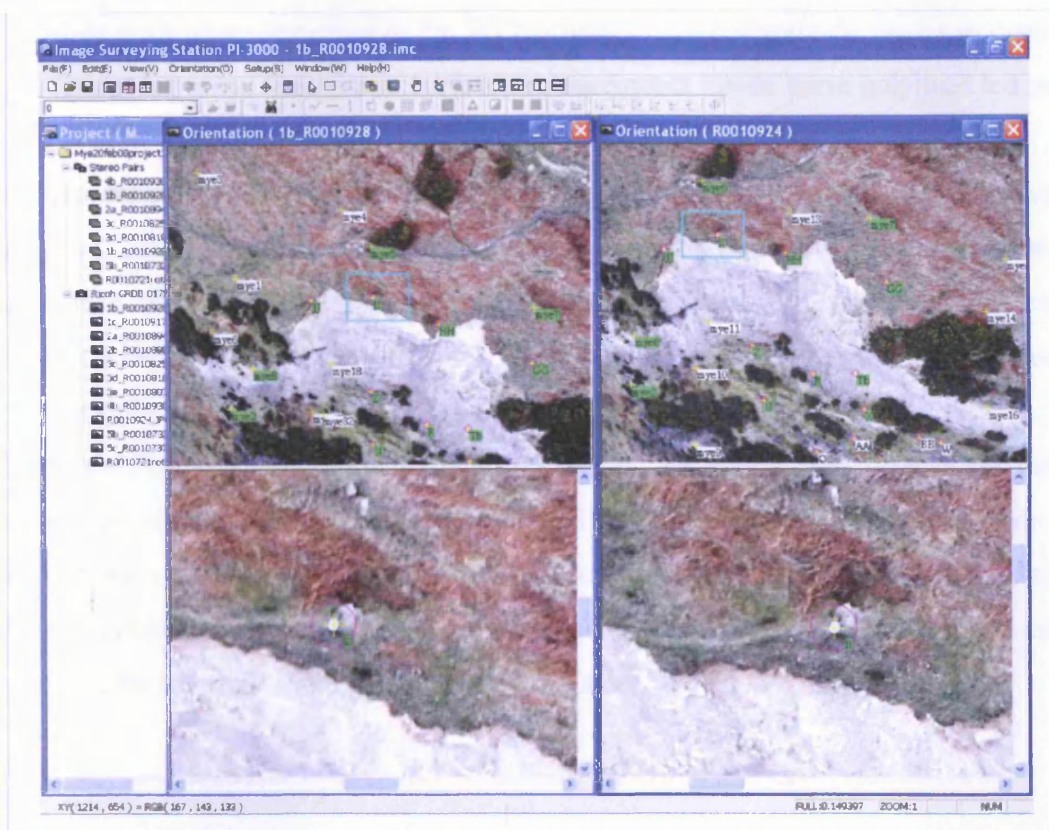


Figure 2.8 Topcon's PI-3000v3 orientation screen: measurement of ground control points and pass points before bundle adjustment

The eight pairs of photographs providing good photogrammetric computation results were transformed automatically to true stereo-pairs in a few minutes by simply moving to the stereo-screen. Here, closed polylines and breaklines were drawn on the left-hand images while refining their positions on the right-hand images (Figure 2.9). The closed polylines were successively selected for automatic surface measurements (created as triangular irregular networks - TINs) with a mesh of 0.25 m. In Topcon's PI-3000v3 there is no option for selecting different surface extraction methods or detailed strategy parameters. Only the following choices could be made for the automatic creation of the TINs:

- TINs were set to fit breaklines when present in the area (but not the outlines);
- A median filtering was applied (the other available option is a mean filtering);
- The texture mapping was applied and selected according to the image considered the best for each stereo-pair.

Initially, a polyline for each stereo-pair was drawn keeping overlapping areas with adjacent stereo-pairs to a minimum, because it was noted that the visualisation of the

landslide with photo-texturing in the 3D platform of the software decreases in quality in overlapping areas. Automatic surface measurements inside these polylines led to a total of eight TINs.

An attempt to merge the eight TINs (averaging values in the overlapping areas) was made as this option is available in the photogrammetry software, but the result was not satisfactory. This processing step was very time-consuming (it ran on PC for more than two days), it created a lot of unwanted interpolated data between the different TINs and finally no image texture option was applicable to the resulting surface.

A second different polyline was drawn on two of the stereo-pairs (one in the main scarp area and one in the hummocky area of the landslide) to maximise the areas of overlap with their adjacent stereo-pair. Surface measurements were made also inside these polylines to create TINs with increased overlap that could be successively used to assess the internal reliability of the method (as explained in section 2.3.3.2).

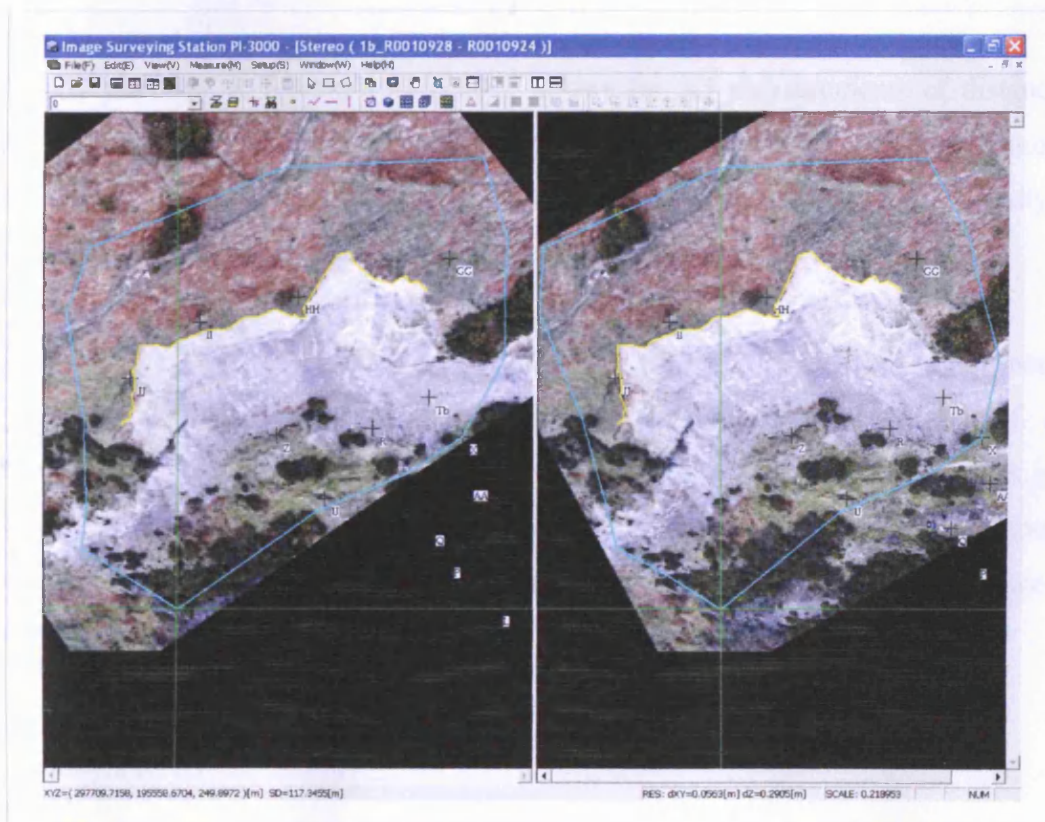


Figure 2.9 Topcon's PI-3000 stereo screen: closed polyline and breakline drawn on a rectified stereo-pair for successive automatic surface measurements

- **Stage 4: Data visualisation and output/export.** The measured surfaces (TINs) were visualised in the 3D platform of the software with or without photo-texturing (Figures 2.10 and 2.11). Here it was possible to select which meshes, polylines and breaklines to visualise and to rotate the resulting image. In Figures 2.10 and 2.11, seven of the eight surfaces with minimum overlap are shown. The TIN obtained from one of the stereo-pairs (photo pair 1b_R0010928 and 1c_R0010917) was not further considered because it represents a small area of the landslide already imaged by another stereo-pair. These seven TINs and the ground control points were exported as one file (*allTINs.csv*) containing a total of 239700 points.

In addition, two of these TINs and two other TINs, created with a maximum area of overlap with the previous adjacent ones, were exported as four separated files to be used for the assessment of the internal reliability of the method (see section 2.3.3.2). The four TINs (shown in Figure 2.12) will be referred in the future as TIN A, TIN B, TIN C and TIN D.

The 3D platform of Topcon's PI-3000v3 allows for 3D measurements of distances and cross-sections and for the creation of contours (Figure 2.13) and animations useful for subsequent talks and presentations. The 3D platform was used to analyse the geomorphological landforms of Mynydd yr Eglwys landslide.

Moreover, the TINs shown in Figure 2.11 together with the images chosen for photo-texturing in Figure 2.10 were selected for the automatic generation of an orthophotograph with ground resolution of 0.10 m/pixel (in .jpg format). With the .jpg file, the photogrammetry software generates a .txt file containing information about the coordinates of the corners of the ortho-image. These coordinates were used to geo-reference the orthophotograph in Surfer 8 (Golden software; Figure 2.14).

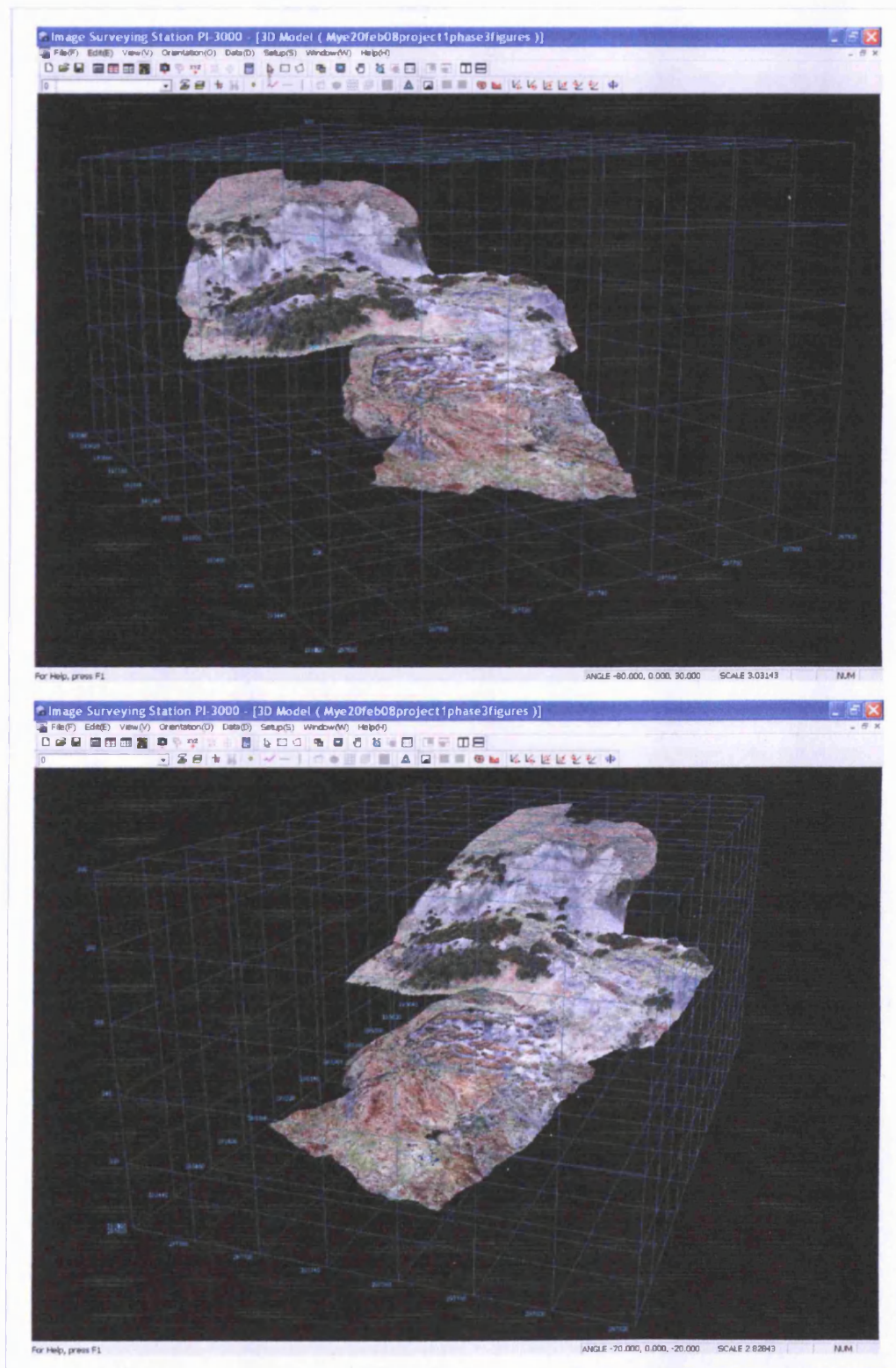


Figure 2.10 3D views of Mynydd yr Eglwys landslide with photo-texturing in Topcon's PI-3000v3 software

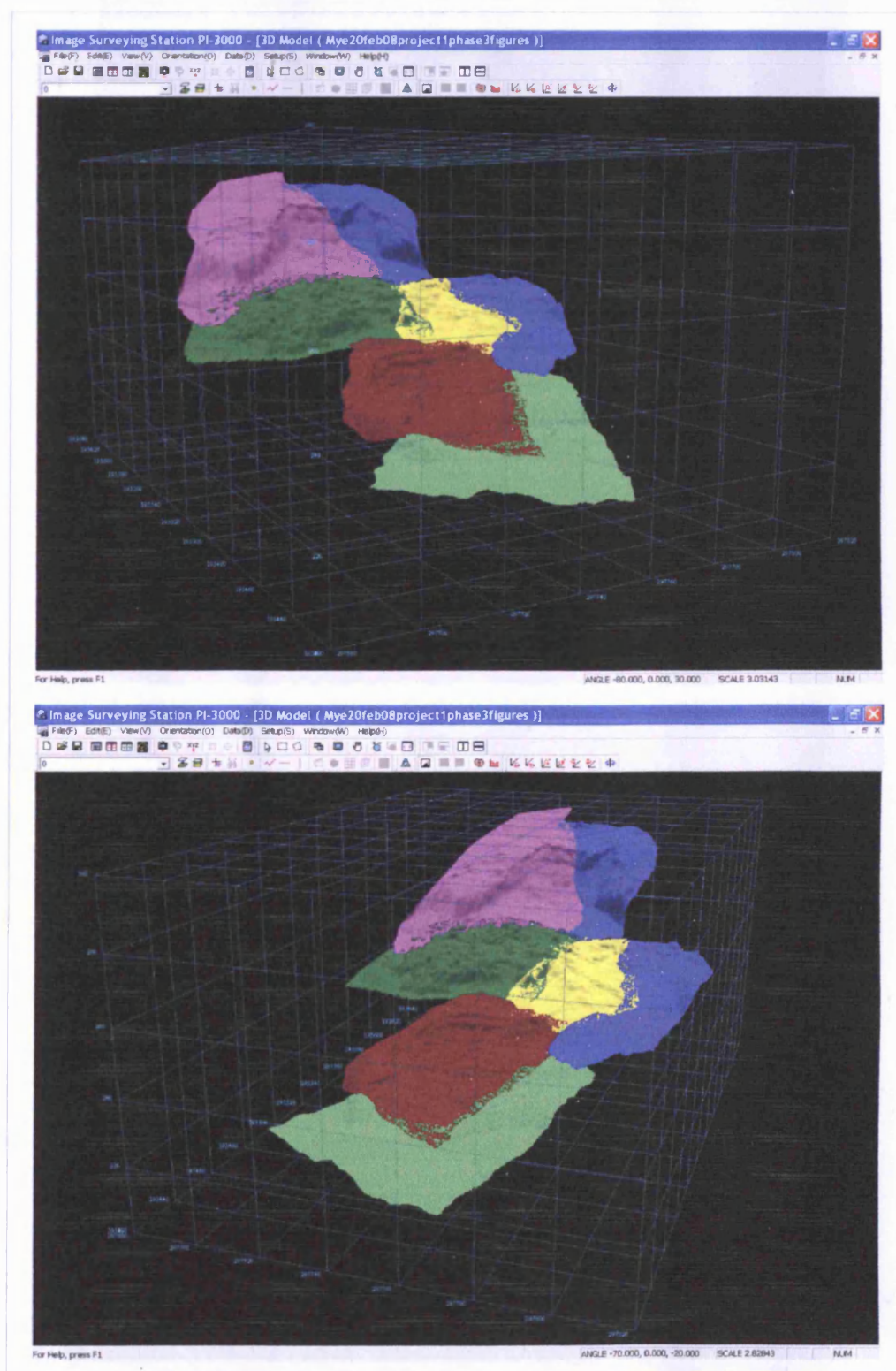


Figure 2.11 3D views of Mynydd yr Eglwys landslide without photo-texturing in Topcon's PI-3000v3 software. The final result was a collage of seven separate TINs (with reduced overlap)

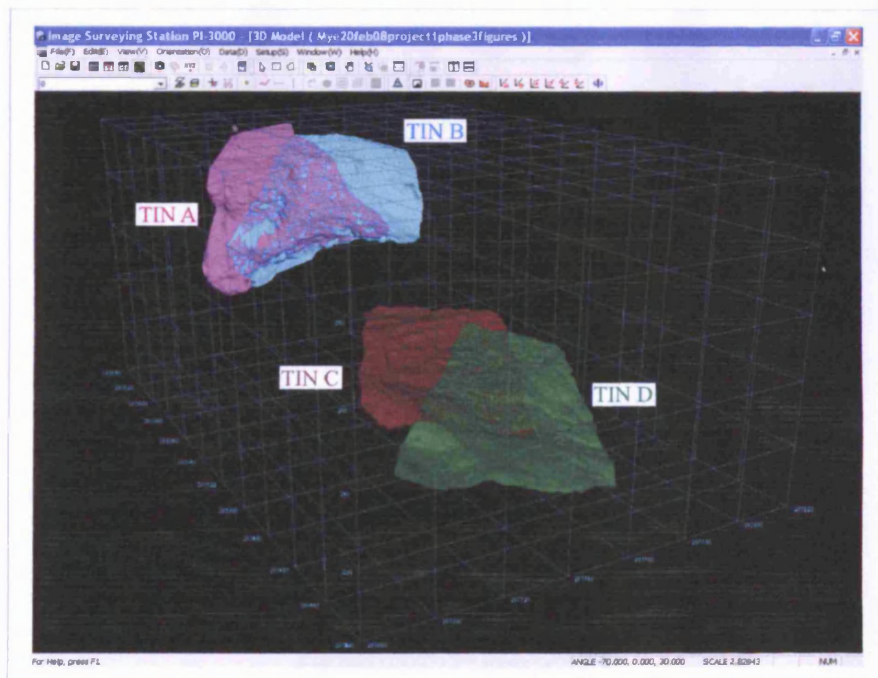


Figure 2.12 View of the four TINs used successively to assess the internal reliability of the method. TIN A and TIN C are the same as in Figure 2.11, while TIN B and TIN D are wider as they were created for an increased area of overlap with the adjacent TINs

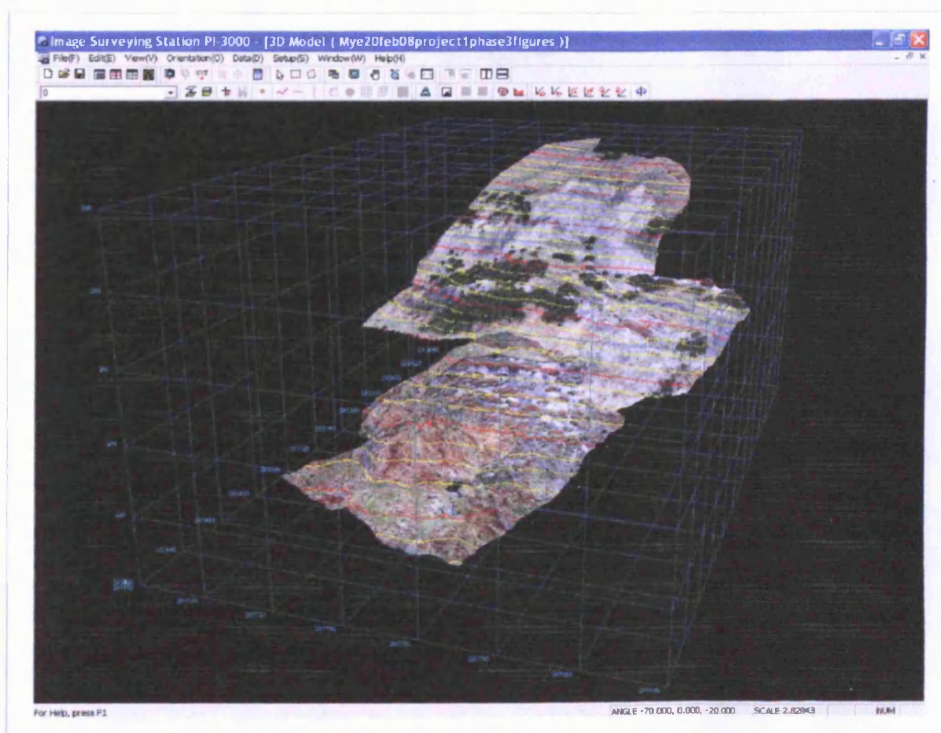


Figure 2.13 3D view of Mynydd yr Eglwys landslide with contours overlaid on photo-texturing. Contour spacing is 2.5 m and 10 m for yellow and red lines respectively

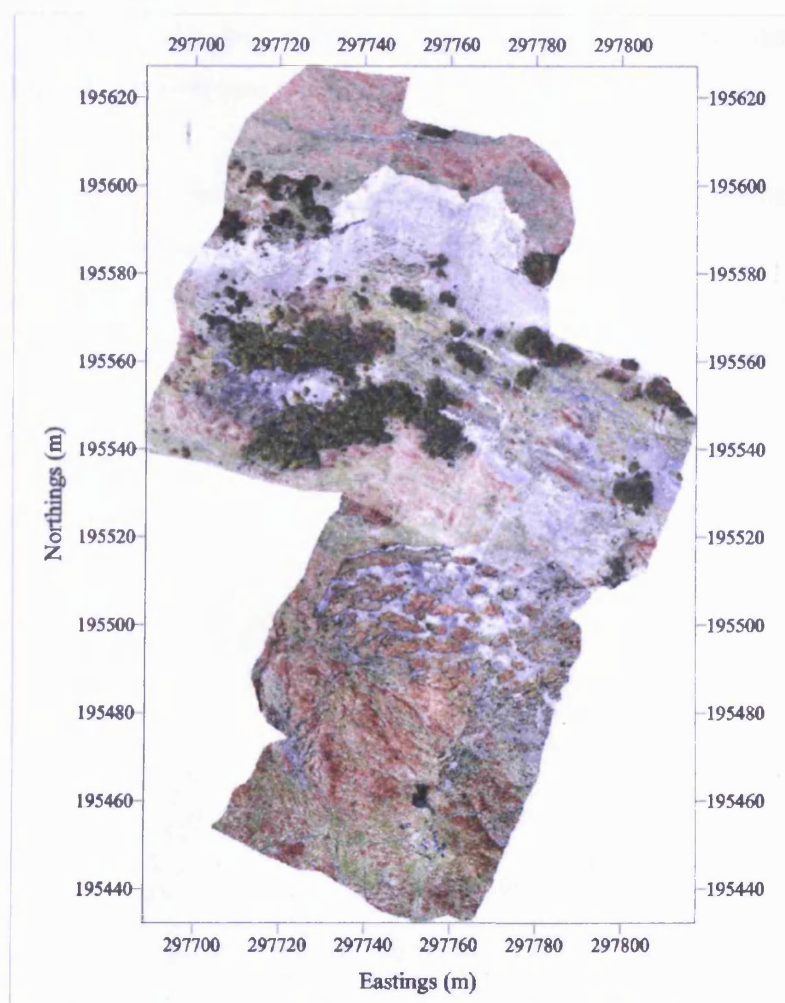


Figure 2.14 Ortho-photograph of Mynydd yr Eglwys landslide with 0.10 m/pixel resolution generated in Topcon's PI-3000v3 and then geo-referenced in Surfer 8 (Golden Software)

Unfortunately, Topcon's PI-3000v3 software does not allow exporting TINs with photo-texturing in any format. As a consequence, for a realistic 3D image of the landslide outside PI-3000 platform, the orthophotograph of Mynydd yr Eglwys landslide was overlaid on the digital elevation model in Surfer 8 (Golden Software). Figure 2.15 shows a post map of the 239700 points exported from the photogrammetry software. Firstly, these points were gridded using a kriging technique at 0.25 m spacing and a search radius of 4 m. Secondly, the resulting grid was blanked to its real extents to exclude the areas of interpolation outside the boundaries of the TINs. Finally, the grid was plotted as a surface to produce a DEM and the geo-referenced orthophotograph was overlaid on it (Figure 2.16). The resulting

perspective view could be annotated to highlight specific landforms for geomorphological purposes (see Chapter 3).

The resulting digital elevation model was not edited to remove vegetation/objects above ground level. However, comparing Figures 2.16 and 2.17 it is evident that small isolated bushes and the student group standing around the area of the pond (GR 297755, 195440) have been filtered out by the photogrammetry software during the creation of the TINs.

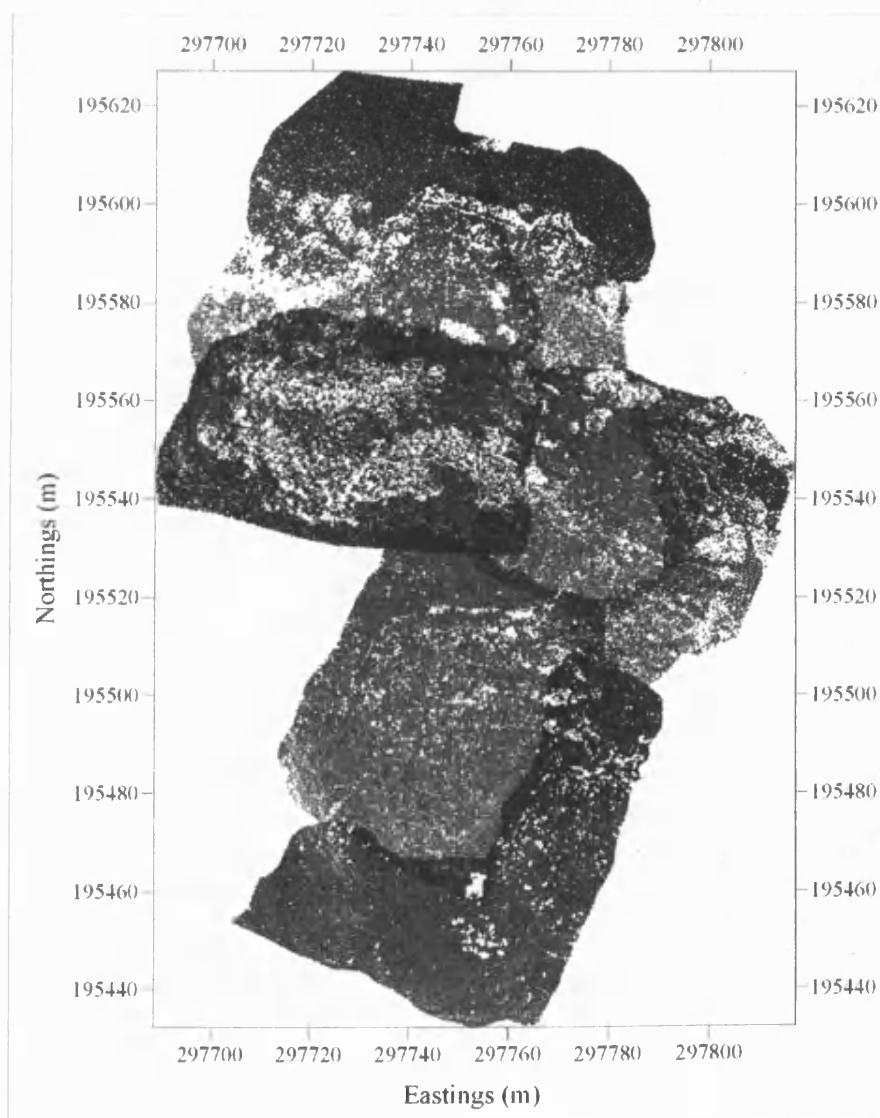


Figure 2.15 Post map of points contained in file allTINs.csv

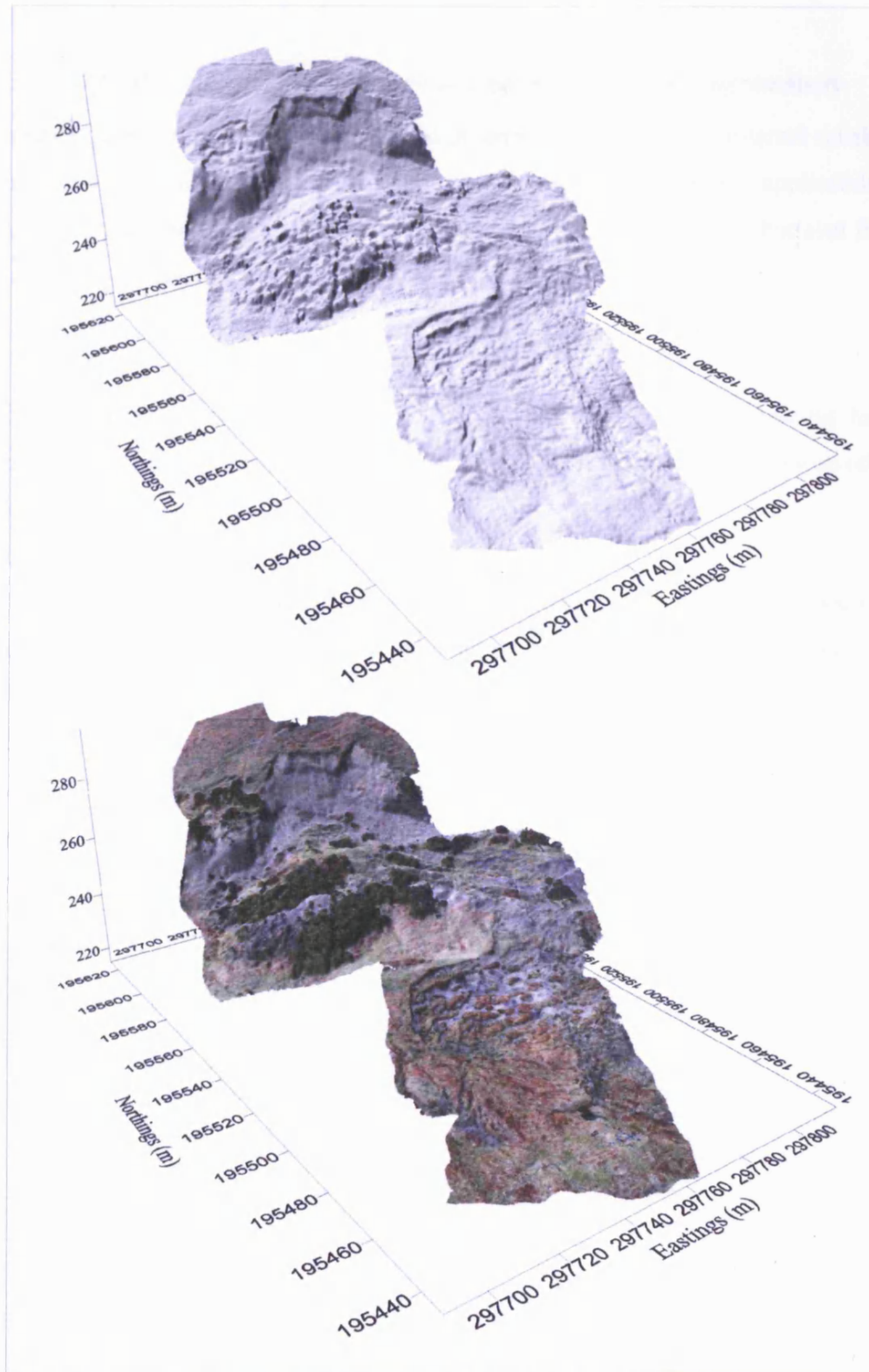


Figure 2.16 Surface plot of the digital elevation model obtained gridding file *allTINs.csv* (top). Perspective view of Mynydd Yr Eglwys landslide obtained overlaying the orthophotograph on the digital elevation model (bottom)

2.3.3.2 Quality assessment of DEM generated from digital photogrammetry

The digital elevation model was analysed in terms of accuracy and internal reliability. The aim of the quality assessment was to provide indications on the applicability of the method not only for the reconstruction and analysis of landforms but also for the monitoring of landslide movement.

Accuracy

The accuracy of the photogrammetric DEM was assessed by comparing heights extracted from the DEM with heights measured with GPS at specific locations (check-points).

A dual-frequency Topcon HiPer Pro GPS+ instrument was used in RTK mode on the 13th of February 2008 for a landslide movement monitoring campaign and on the 19th of February 2008 for surveying the electrodes of a resistivity/IP profile (details on GPS surveying are reported in section 2.4). Six movement monitoring markers and 62 electrodes (at 2 m spacing) were located in the area of the DEM (Figure 2.17) and their GPS coordinates were used as check-points for accuracy assessment. Photogrammetry targets and check-points were referred to the same coordinate system (same GPS base station with same assigned coordinates).

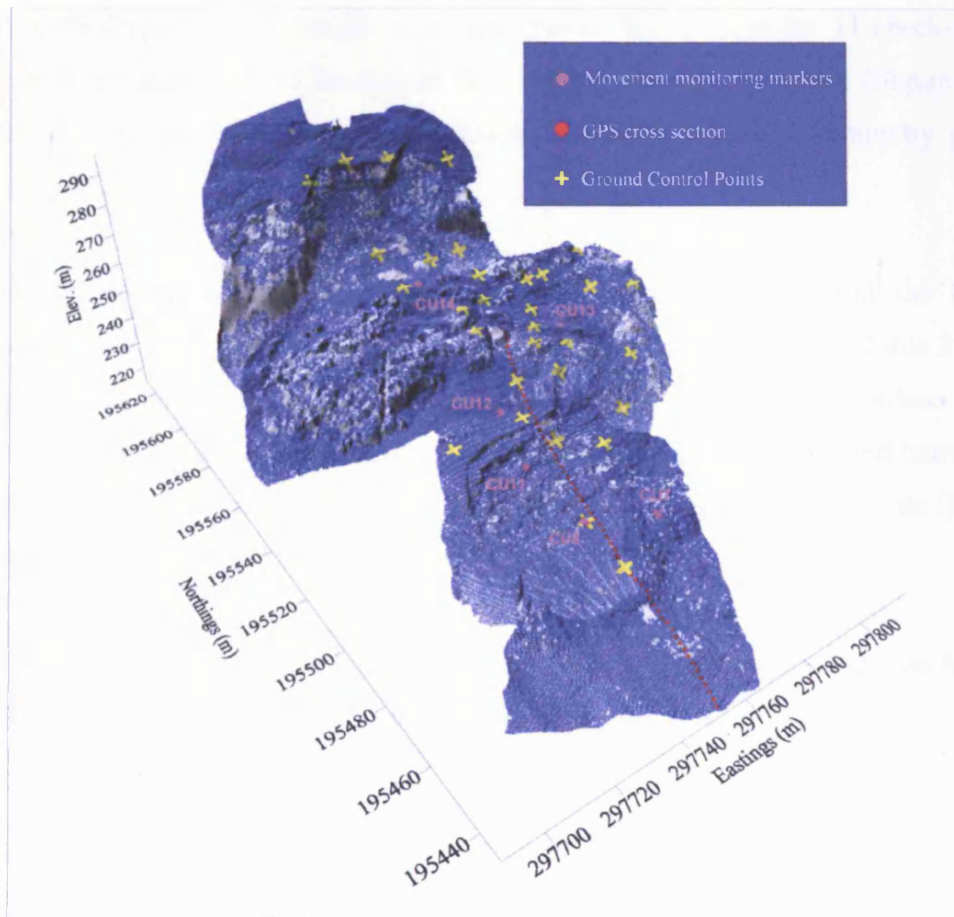


Figure 2.17 Surface plot of photogrammetric DEM showing the locations of: the TIN points exported from the photogrammetry software (blue dots), the photogrammetry ground control points (yellow crosses) and the GPS check-points (profile and monitoring movement markers as red and magenta circles respectively)

The elevations at check-point locations were extracted from the photogrammetric DEM by slicing the DEM in Surfer 8 (Golden Software) along GPS coordinates. Then the differences between the heights extracted from the DEM and the ones surveyed with GPS were calculated. Finally, the resulting values were analysed statistically and a classified post map was created in Surfer 8 (Golden Software) to help visualise the spatial distribution of the height errors.

The height differences for the 62 check-points along the GPS profile range between -0.095 and 0.503 m, with an overall mean of 0.103 m and a standard deviation of 0.140 m (Table 2.4). The majority of the values (40 out of 62) are between -0.10 and 0.10 m and the heights extracted from the DEM are generally higher than the ones surveyed

with GPS (Figure 2.18). Height errors are greater than 0.20 m for 11 check-points. These check-points are all located at the southern end of the profile (Figure 2.19), where the ground is not particularly rough, but far from photogrammetry ground control points.

The differences between the heights extracted from the DEM and the heights measured with GPS at the movement markers locations are reported in Table 2.5. The height error is high for marker CU7 (-0.409 m), while for the other markers ranges between -0.093 and 0.113 m. Marker CU7 is located in a very active and hummocky area of the landslide and is far from photogrammetry ground control points (Figures 2.17 and 2.19).

Table 2.4 Summary of statistic analysis of height errors (difference between height of DEM and height of GPS) for the check-points along the GPS profile

Number of values	62
Minimum value (m)	-0.095
Maximum value (m)	0.503
Mean (m)	0.103
Standard deviation of the mean (m)	0.018
95% confidence interval of the mean (m)	0.036
Standard Deviation (m)	0.140

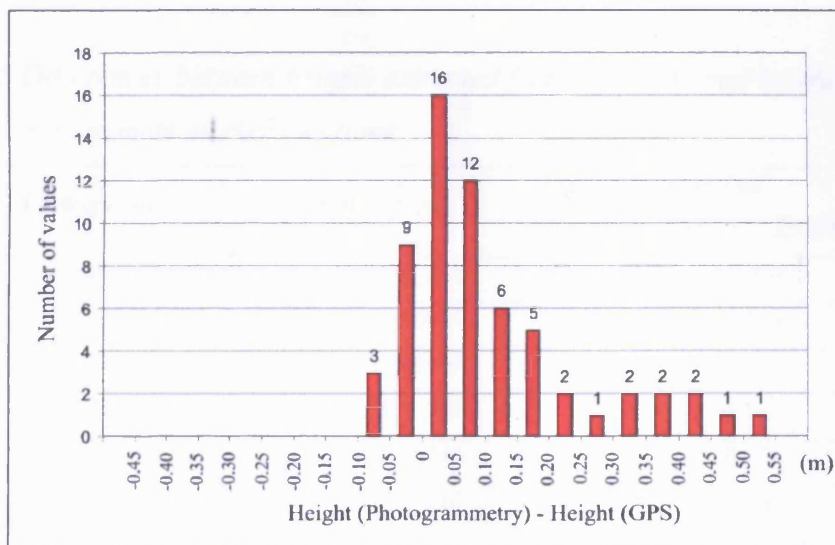


Figure 2.18 Graph showing the distribution of height errors for the check-points along the GPS profile

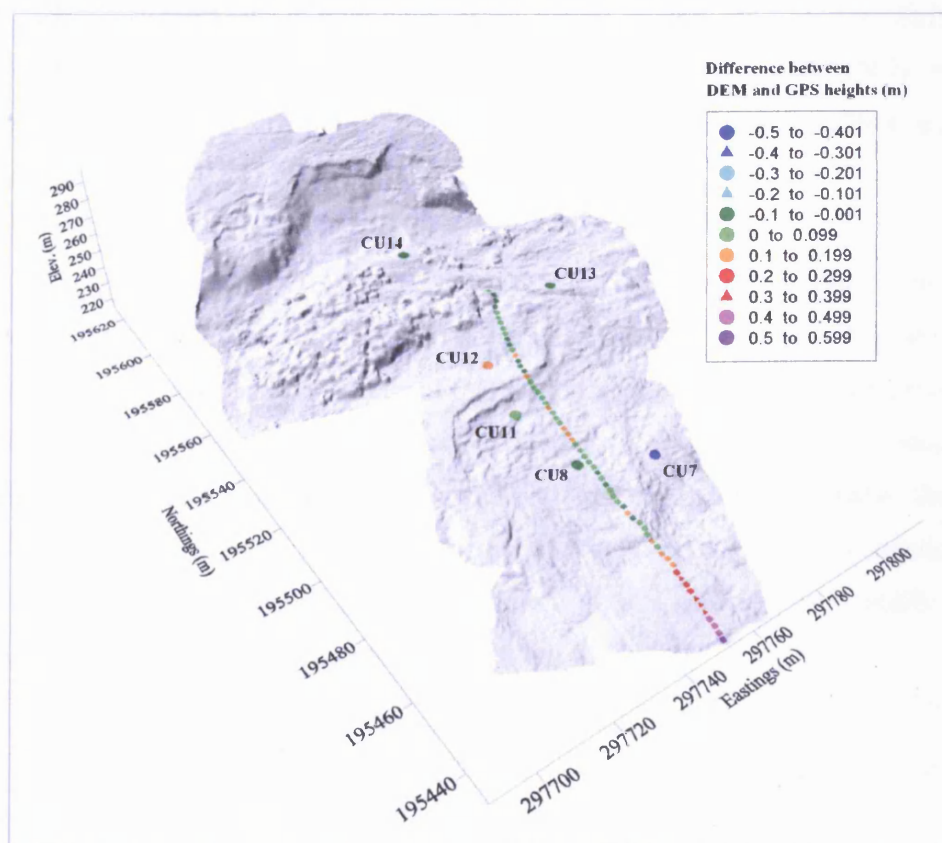


Figure 2.19 Classified post map highlighting the range of height errors at check-point locations. The highest errors are located in the southern part of the profile and at movement marker CU 7

Table 2.5 Differences between heights extracted from the DEM and heights measured with GPS at movement marker locations

Marker	Eastings (m)	Northings (m)	Height difference (m) [Z(Photogrammetry) - Z(GPS)]
CU 7	297773.262	195481.216	-0.409
CU 8	297754.726	195488.634	-0.034
CU 11	297750.367	195508.998	0.075
CU 12	297753.667	195525.721	0.113
CU 13	297784.541	195539.430	-0.038
CU 14	297754.569	195567.940	-0.093

Internal reliability

The internal reliability of the DEM was assessed by comparing the heights obtained from different TINs in overlapping areas using Surfer 8 (Golden Software). Overlapping areas between two TINs in the back scarp (TIN A and TIN B; Figures 2.12 and 2.20) and two TINs in the hummocky area of the landslide (TIN C and TIN D; Figures 2.12 and 2.21) were considered.

Firstly, the .cvs files of TIN A, TIN B, TIN C and TIN D exported from the photogrammetry software were gridded separately using a kriging technique with a spacing of 0.25 m and a search radius of 0.50 m to the edges of an area comprising the TIN itself and the adjacent one. Secondly, two grids of difference, TIN A minus TIN B and TIN C minus TIN D, were created and plotted as image maps. Finally, the grids of difference were converted to ASCII format and only the values in the overlapping areas were retained. The values of height differences were analysed statistically and in terms of spatial distribution using classed post maps.

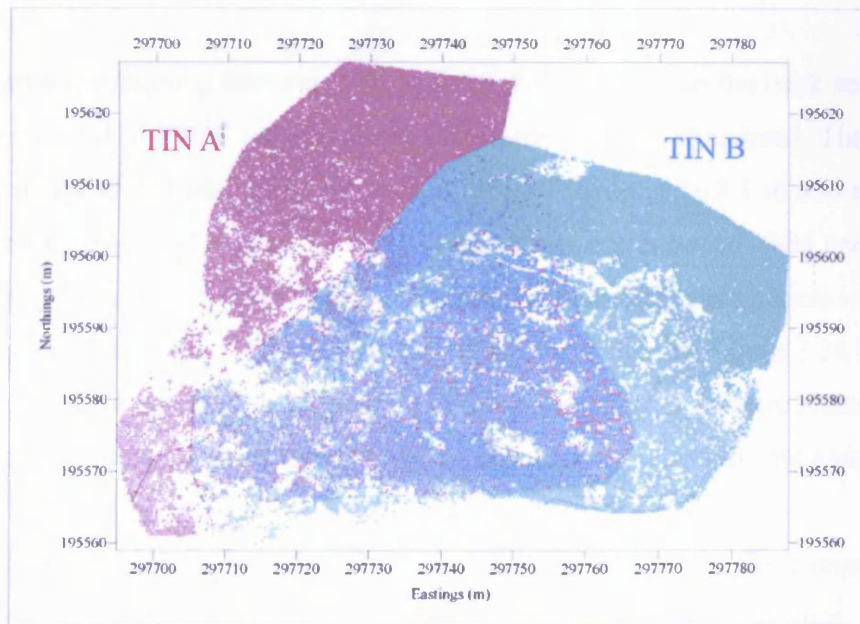


Figure 2.20 Post map of TIN A and TIN B. The heights in the overlapping area were compared to assess internal reliability

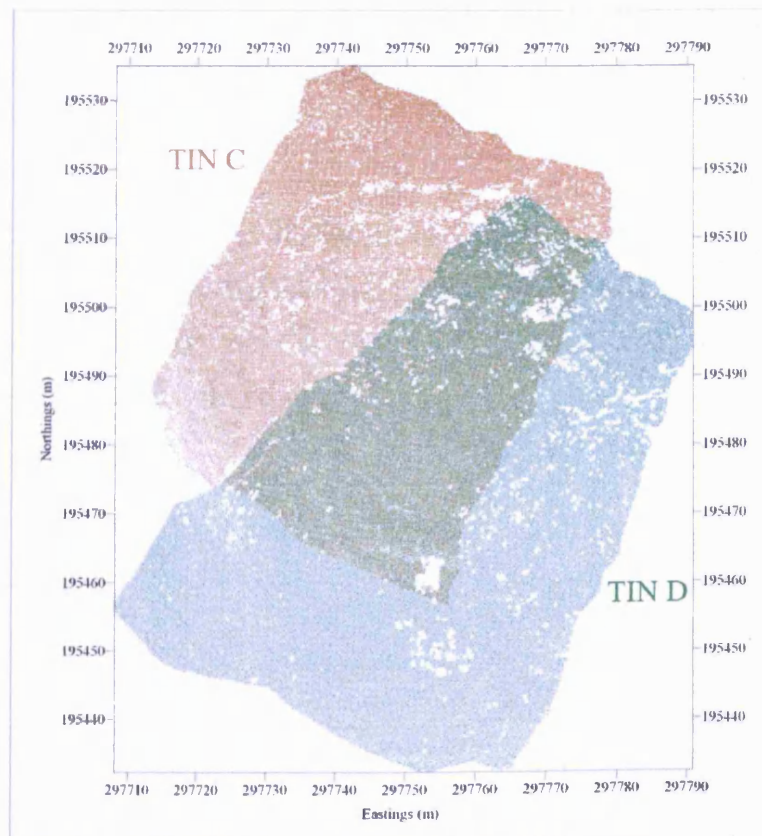


Figure 2.21 Post map of TIN C and TIN D. The heights in the overlapping area were compared to assess internal reliability

For the area overlapping between TIN A and TIN B, located in the back scarp of the landslide, a total of 17567 values of height differences were calculated. These values range between -0.279 and 0.685 m, with an overall mean of 0.001 m and a standard deviation of 0.024 m (Table 2.7). 98.1% of the values are between -0.05 and 0.049 m (Table 2.6). The distribution of height differences in the overlapping areas is shown in the image map in Figure 2.22, whereas the classed post map in Figure 2.24 highlights the location of the points with major high differences. These points are located mainly in the break of slope on top of the main scarp and in areas closed to data gaps.

For the area overlapping between TIN C and TIN D, located in the hummocky and nowadays more active part of the landslide, a total of 17912 values of height differences were calculated. These values range between -0.078 and 0.424 m, with an overall mean of 0.001 m and a standard deviation of 0.010 m (Table 2.7). 99.5% of the values are between -0.05 and 0.049 m (Table 2.6). The distribution of height differences is shown in the image map in Figure 2.23, whereas the classed post map in Figure 2.25 highlights the location of the few points with more than ± 0.05 m height difference.

Comparing the values reported in the tables (Table 2.6 and 2.7) and the figures (Figure 2.22-2.25), it is clear that internal reliability of TIN A and B is worse than that of TIN C and D. This is probably due to the terrain characteristics. The slope in the area of TIN A and TIN B is much steeper.

Table 2.6 Distribution of height differences between the TINs in their overlapping areas

Classes of height difference (m)	TIN A – TIN B		TIN C – TIN D	
	n. of values	%	n. of values	%
-0.3 to -0.251	1	0.0	0	0.0
-0.25 to -0.201	3	0.0	0	0.0
-0.2 to -0.151	3	0.0	0	0.0
-0.15 to -0.101	14	0.1	0	0.0
-0.1 to -0.051	73	0.5	4	0.0
-0.05 to -0.001	6959	43.8	6967	43.0
0 to 0.049	8640	54.3	9141	56.5
0.05 to 0.099	94	0.6	64	0.4
0.1 to 0.599	37	0.2	12	0.1
0.15 to 0.199	29	0.2	3	0.0
0.2 to 0.249	10	0.1	0	0.0
0.25 to 0.299	9	0.1	0	0.0
0.3 to 0.349	7	0.0	0	0.0
0.35 to 0.399	7	0.0	0	0.0
0.4 to 0.449	5	0.0	1	0.0
0.45 to 0.499	5	0.0	0	0.0
0.5 to 0.549	1	0.0	0	0.0
0.55 to 0.599	0	0.0	0	0.0
0.6 to 0.649	1	0.0	0	0.0

Table 2.7 Summary of statistic analyses for the values of differences in heights between overlapping areas of TINs

	Z (TIN A) – Z (TIN B)	Z (TIN C) – Z (TIN D)
Number of values	17567	17912
Minimum value (m)	-0.279	-0.078
Maximum value (m)	0.685	0.424
Mean (m)	0.001	0.001
Standard error of the mean (m)	0.000	0.000
95% confidence interval of mean (m)	0.000	0.000
Standard deviation (m)	0.024	0.010

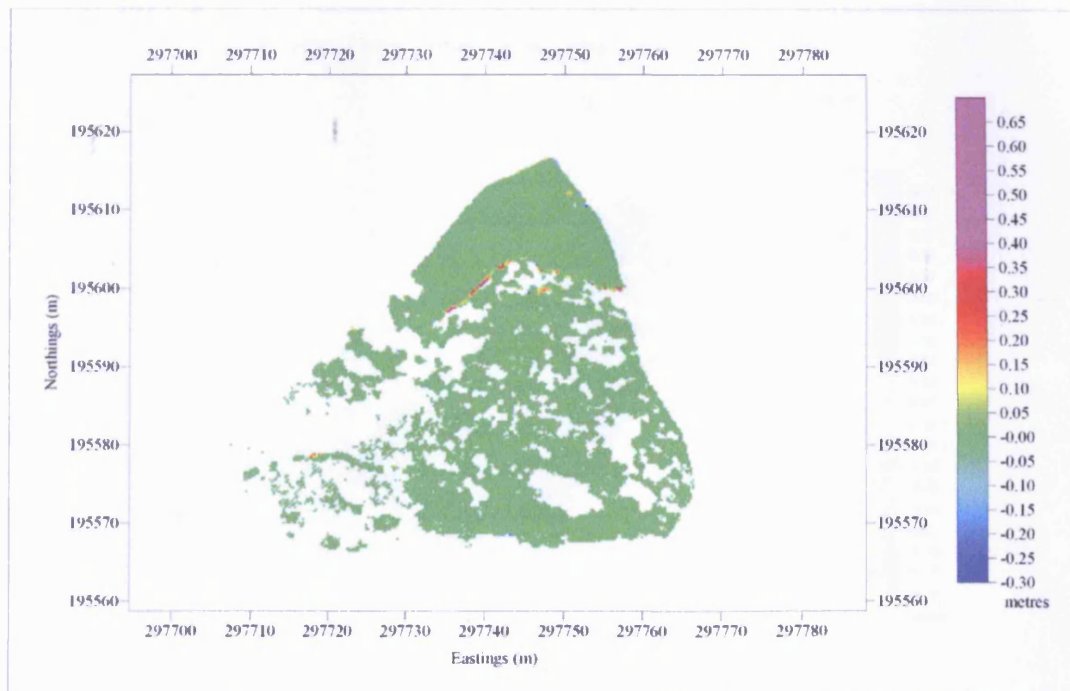


Figure 2.22 Image map showing the height differences between TIN A and TIN B in their overlapping area

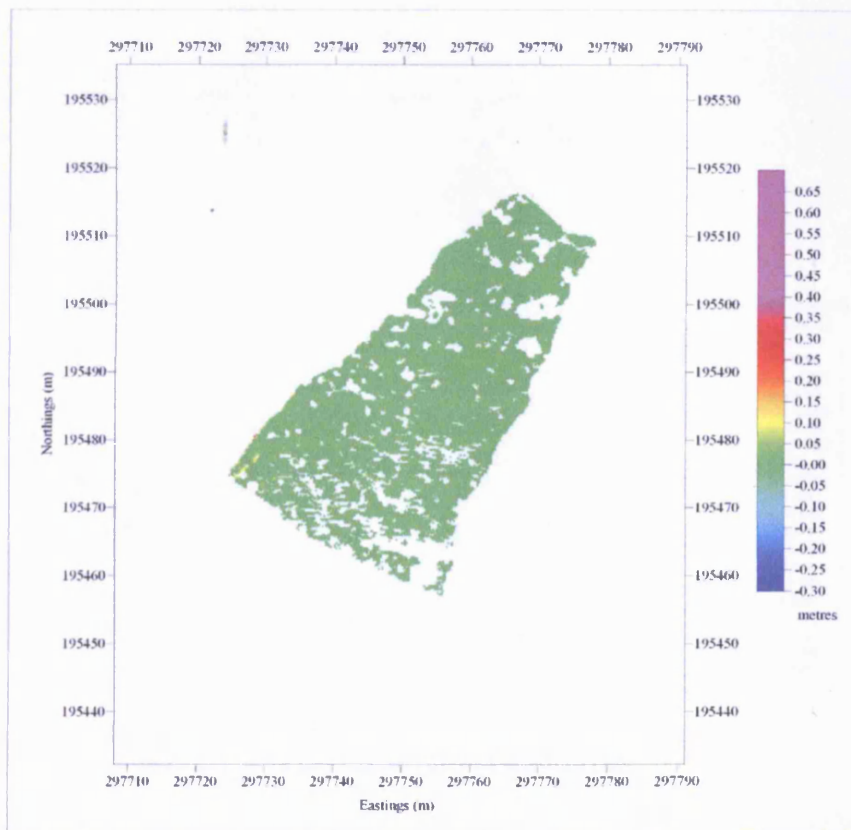


Figure 2.23 Image map showing the height differences between TIN C and TIN D in their overlapping area

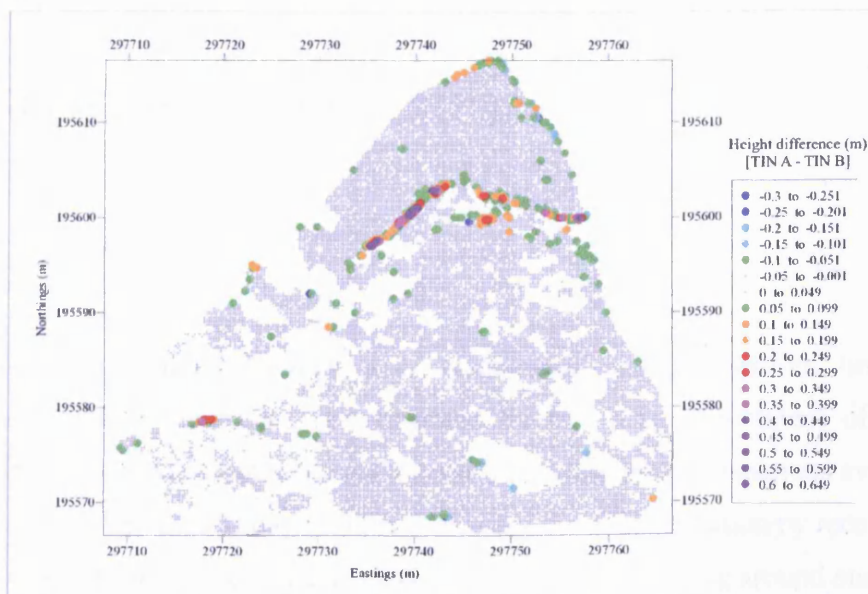


Figure 2.24 Classed post map of height differences between TIN A and TIN B in their overlapping area. The map highlights the location of the points characterised by highest variation

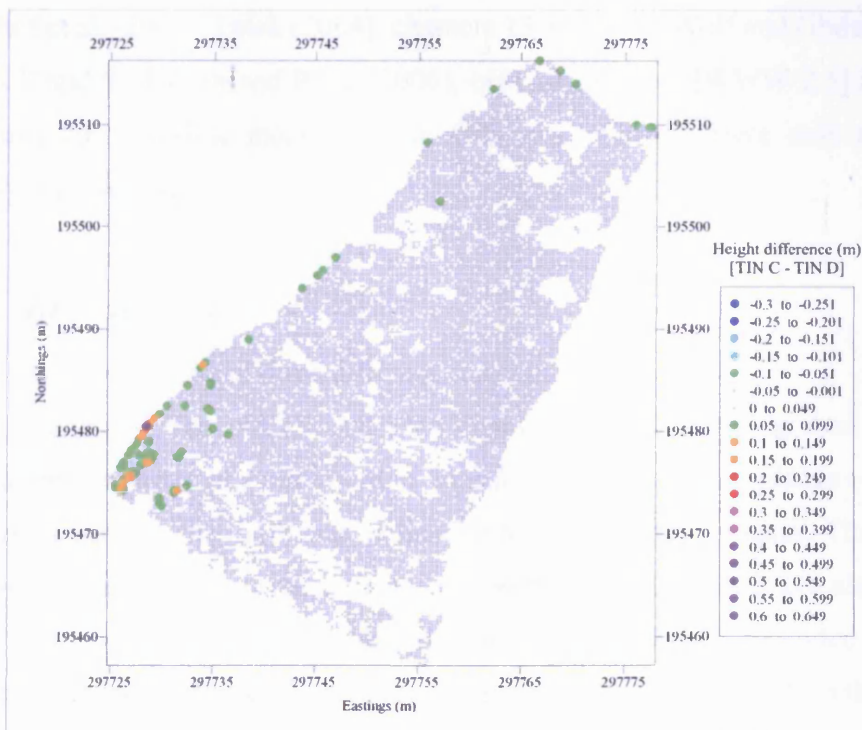


Figure 2.25 Classed post map of height differences between TIN C and TIN D in their overlapping area. The map highlights the location of the points characterised by highest variation

2.4 Global Positioning System (GPS)

2.4.1 Basic Principles

The Global Positioning System is a space-based radionavigation, timing and positioning system, developed and operated by the U.S. Department of Defense (DoD). It allows a user to navigate and obtain three-dimensional positions everywhere on the Earth, at any time of day/night and in every weather condition by receiving and processing electromagnetic signals broadcast by satellites orbiting around our planet. GPS coordinate system is based on the World Geodetic System 1984 (WGS-84) and reference time is UTC (USNO).

The principles of GPS system and GPS surveying are discussed in detail in Hofmann-Wellenhof et al. (2001), Leick (2004), chapters 13 and 14 of Wolf and Ghilani (2002), chapters 7 and 8 of Uren and Price (2006), official websites [WWW 2.5] and, more specifically for landslide monitoring, in Gili et al. (2000). Here only a relevant summary is presented.

2.4.1.1 GPS Segments

The GPS system consists of three different segments or sectors:

- 1- Space segment. The NAVSTAR (NAVigation Satellite Timing And Ranging) constellation comprises of a minimum of 24 satellites orbiting on 6 planes (4 satellites for plane) centred on the Earth and inclined at 55° to the Earth equator. The satellites move around the Earth at a mean altitude of approximately 20200 km along nearly circular orbits with a period of 12 sidereal hours. Each satellite is provided by one or more atomic clocks and broadcast continuously electromagnetic signals in the L-band.
- 2- Control segment. It consists of a master control station (located at Colorado Springs, USA), five monitor (or tracking) stations and three ground control stations. The tracking stations monitor the satellites at all time and send information relative to their orbits and clocks to the master control station where near-future predicted satellite orbital positions and clock parameters can be calculated. The results are sent to the antennas at the three ground control stations to be uploaded to the satellites and then broadcast to the user.
- 3- User segment. It is the equipment owned by the user (military or civilian), consisting of one or more receivers. The receivers are characterised by the observables (i.e. code pseudoranges and/or carrier phases) and the codes (i.e. C/A-code, P-code and/or Y-code) measured, by the number of satellites they can simultaneously track (number of channels) and by the surveying methods they can be used for.

2.4.1.2 GPS Signal

Each satellite broadcast electromagnetic signals on two carrier frequencies, L1 (1575.42 MHz) and L2 (1227.60 MHz), corresponding to wavelengths of approximately 0.19 and 0.24 m respectively.

A navigation code and a pseudo-random noise are modulated onto these carrier waves.

The navigation code is uploaded onto the satellites by the ground control stations with the aim of helping the user to determine satellite positions. It is a data message including information about clock correction, satellite orbital positions (ephemerides), atmospheric correction, almanac (approximate information on orbits and clock corrections for all satellites) and satellite health.

The pseudo-random noise (PRN) is a unique sequence of binary values broadcast by each satellite to be used by the receiver to calculate time and distance to the satellites. Two PRN codes are sent by each satellite:

- The Coarse/Acquisition (or C/A) code, designated as the Standard Positioning Service (SPS) and available to civilian users. Each satellite broadcast a unique C/A code, modulated only on the L1 carrier and with an effective wavelength of approximately 300 m.
- The Precise (or P) code, designated as the Precise Positioning System (PPS) and available only to U.S. military and authorised users. It is modulated on both L1 and L2 carriers and has an effective wavelength of approximately 30 m. It is usually encrypted and changed to a secret Y code by the DoD for military purposes (process known as anti-spoofing). There is only one P code and each satellite broadcast a different portion of the code, repeated every 7 days.

BlockIIR-M satellites broadcast also a new military M-code on L1 and L2 and a new L2 civilian signal (L2CS). The future satellites of BlockIIF will broadcast an additional L5 civil signal [WWW 2.5].

2.4.1.3 GPS observables

The position of the user receiver is obtained by the determination of distances (ranges) to the satellites. These distances can be computed with code ranging or carrier phase measuring methods or a combination of both. In both methods, satellite and receiver clocks are used. As computations are affected by the satellite and receiver clock biases, the term pseudorange is usually preferred to range. Moreover, four equations and, as a consequence, at least four satellites are necessary to solve for the four unknowns (the three dimensional receiver coordinates and the clock error).

According to the Topcon user manual (Topcon, 2006), a fifth satellite is necessary to provide fault tolerance.

The code ranging method is based on the measurement of the time required by the C/A code broadcast by the satellite to reach the receiver. This time is called propagation delay. When the receiver locks onto a satellite, it generates a replica of the satellite C/A code and the two codes are compared through autocorrelation. The shift in time applied to the receiver code to have a maximum correlation equals the propagation delay. This time is then multiplied by the speed of light (signal velocity) to compute the distance between the satellite and the receiver (Figure 2.26).

GPS receivers relying on code ranging method are not expensive (i.e. hand-held and mapping grade receivers). However, as P-code is not accessible to civilian users, these instruments have low accuracy (10-20 m at 95% probability level) and are as a consequence not suitable for high-precision surveying such as for landslide movement monitoring.

In contrast, the more expensive receivers based on carrier phase method can achieve millimetre accuracies being suitable for high-precision surveying. These receivers compute the phase shift between the satellite carrier waves L1 and L2 and similar signals produced by the receivers themselves. However, the integer number of wavelengths present between the receiver and the satellites is difficult to determine (ambiguity resolution) and the solution of complicated algorithms is required (single, double and triple differencing). Integer wavelength number and phase shift are after used to calculate distances to satellites (Figure 2.27).

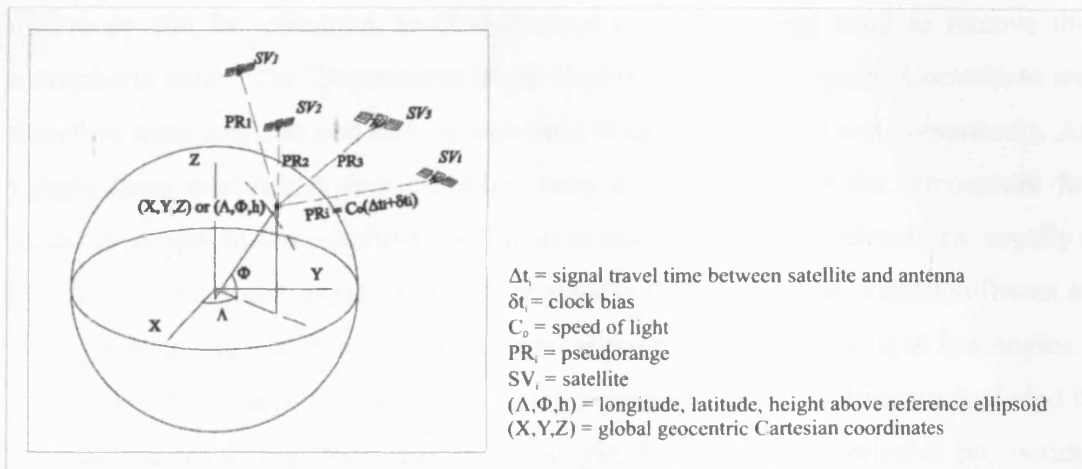


Figure 2.26 Determination of 3D receiver coordinates from measurement of pseudoranges with code ranging method (modified from Gili et al., 2000)

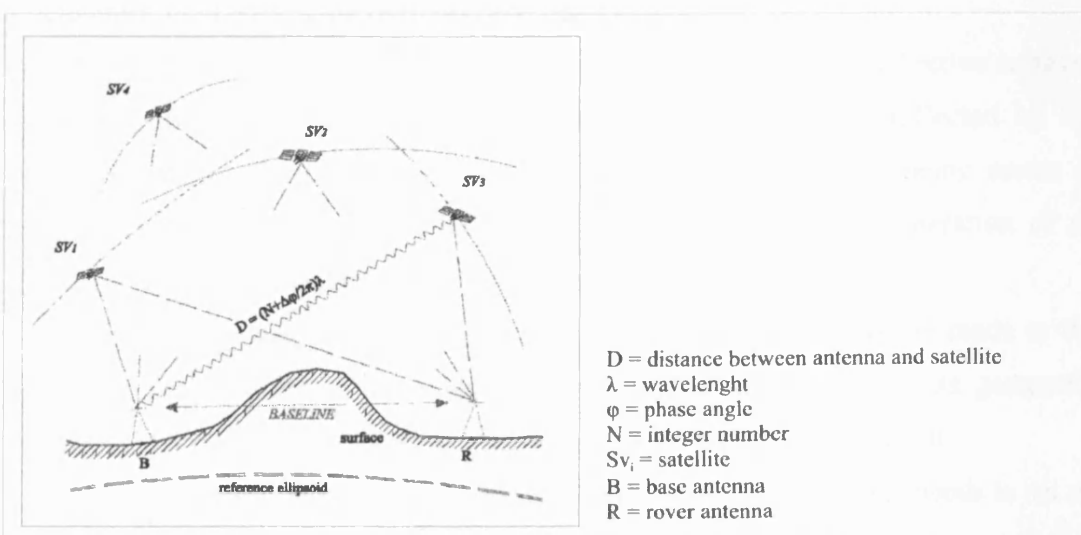


Figure 2.27 Measurement of antenna positions with carrier phase method (modified from Gili et al., 2000)

2.4.1.4 Theoretical or a priori errors in GPS surveying

The precision or accuracy of GPS results depend on several factors:

1. Ionospheric and tropospheric delays. GPS signals are refracted and delayed when propagating through the atmosphere. The Ionosphere acts as a dispersive medium and, as a consequence, L1 and L2 waves arrive at the receiver at different times. This time

difference can be measured by dual-frequency receivers and used to remove the ionospheric delay. The Troposphere is not dispersive for GPS signals. Corrections are therefore more difficult and rely on available models of dry and wet components. As signals from satellites at low elevation have to travel through the atmosphere for longer distances and troposphere is difficult to model at such low elevations, usually a threshold angle (mask angle) of 10-15 degrees is included in the control software of the receiver to exclude from position computations the signals arriving at low angles.

2. Clock errors. Satellite clock errors can be corrected using coefficients included in the satellite navigation messages or by single differencing in relative positioning techniques. Receiver clock errors can be corrected considering distances to at least four satellites or by double differencing in relative positioning techniques.

3. Satellite ephemerides or orbital errors. Satellite orbits are updated by the control segment every 2 hours; however predicted positions will always be affected by fluctuations in gravity, solar radiation and other anomalies.

4. Multipath. When the receiver antenna is close to obstacles and reflective surfaces (such as buildings, fences, vehicles, water), GPS signals can be reflected by the obstacles and then reach the receiver from additional paths, introducing errors in position computation. The term imaging is used to describe the generation of an image of the real antenna by a reflecting obstacle.

5. Antenna phase centre offset and variation. Signal measurements are made to the electronic phase centre of the antenna that is usually different from its geometric centre. This offset must be taken into consideration as well as its variation.

6. Antenna centring and antenna height measurement errors. The user needs to set up the antenna above the centre of the surveying point and measure the antenna height above it. Practical errors occur during these field measurements.

7. Number and geometry of satellites visible at the time of observation. This concept is normally expressed in terms of DOP (Dilution of Precision) factors, with low values indicating good geometry. The actual precision of the measurement is obtained multiplying the DOP factor for the precision of the GPS instrument used.

Position accuracy increases significantly when using differential or relative positioning techniques, based on two or more receivers instead of a single one. For small size sites (for example up to 20 Km), both receivers (base and rover) record very similar systematic errors (i.e. orbital errors, clock biases, atmospheric delays)

that can, as a consequence, be eliminated.

Discrepancies in GPS results have been attributed also to the use of different algorithms or software packages for data processing (Ashkenanzi and Yau, 1986 in Gili et al., 2000).

2.4.1.5 Differential and relative GPS

1. Differential GPS (dGPS). Two (or more) receivers are employed. One receiver is kept at a fixed known location (base station) while the other (rover) is moved at the unknown positions. The two receivers must track simultaneously at least four common satellites. The difference between calculated and known coordinates or between observed pseudoranges and calculated ranges at the base station is used to compute corrections that are transmitted to the rover antenna and applied to obtain positions that are more accurate when compared with the ones determined with a single receiver. The term differential GPS is usually applied to code ranging measuring instruments and accuracies of 0.5-5 m can be achieved. However, sub-centimetre accuracies have been reported for dGPS surveying with carrier phase dual frequency instruments.

Instead of establishing a local base station, the user may use only one receiver and rely on data corrections transmitted by existing ground-based network of beacons (Ground Base Augmentation Systems) or by satellites belonging to Satellite-Based Augmentation Systems (i.e. the European EGNOS and the American WASS). For the United Kingdom, the General Lighthouse Authority (GLA) provides a free public service of corrections transmitted by 14 ground-based reference stations for maritime use [WWW 2.6].

Relative Positioning. Normally, for higher accuracies, the carrier phase method is used. Two receivers are used to measure phase signals broadcast from common satellites simultaneously at both locations. In contrast with differential positioning, simultaneous measurements at both receivers are directly combined. The vector (baseline) between the base (or reference) antenna and the rover antenna is determined (Figure 2.27) and then added to the base position to obtain the rover

position. Providing that the base and rover antennas are collecting data at the same time and rate (epoch), single, double and triple differencing calculations can be applied to remove most of the systematic errors from the baseline vector.

In relative positioning, there are several surveying methods available: static, rapid or fast static, pseudokinematic, kinematic and real time kinematic (or RTK). They vary for the length of time required for each observation (session) and the level of accuracy provided. The real time kinematic (or RTK) method is the most productive. The base receiver remains fixed, while the rover moves to unknown locations. The base continuously transmits data to the rover, for example via a radio link, and corrected coordinates can be instantaneously computed on site. Therefore, contrary to the other methods, data post-processing is not required.

The Ordnance Survey has installed throughout Great Britain a network of more than 100 active permanent GPS stations that record dual-frequency data 24 hours a day at 30 second epoch rate [WWW 2.7]. Since October/November 2008, the stations hardware has been updated and the new stations have GNSS (GPS and GLONASS) receivers and antennas. The coordinates of the active stations are available from the Ordnance Survey website [WWW 2.7]. Moreover, from the same website, data from the active stations in RINEX (Receiver Independent Exchange) format can be downloaded (for free if within 30 days from the day of the survey) and be used by users to post-process their own GPS datasets.

The datum of the Ordnance Survey network is ETRS89 (European Terrestrial Reference System 1989, that coincided with WGS-84 in 1989.0). ETRS89 GPS positions can be converted to OSGB36 National Grid and ODN (Ordnance Datum Newlyn) coordinates using National Grid Transformation OSTN02 and National Geoid Model OSGM02 [WWW 2.7].

2.4.2 GLONASS

The Global Navigation Satellite System (GLONASS) is the Russian equivalent to the American GPS system and is operated by the Russian Military Space Forces (MSF).

As with the American GPS, the Russian system is also composed of 3 segments:

- 1- The space segment consists of 24 satellites orbiting on 3 planes (8 satellites per plane) inclined at 64.8° to the Earth equator. The satellites move along circular orbits at 19100 km of altitude with a period of approximately 11 hours and 15 minutes.
- 2- The control segment comprises a System Control Centre and the network of Command and Tracking Stations spread throughout the Russian territory.
- 3- The user segment consists of the equipment owned by the user.

The GLONASS coordinate system is the PZ-90 and the time is the National Reference of Coordinate Universal Time UTC(SU).

In contrast with the GPS system, GLONASS uses a technique called Frequency Division Multiple Access (FDMA): every satellite transmits navigation signals on two satellite-specific carrier frequencies in the L1 (approximately 1.6 GHz) and L2 (approximately 1.2 GHz) sub-bands. A standard accuracy signal is broadcast for civil users in L1 by GLONASS satellites and in L1 and L2 by GLONASS-M satellites, while the high accuracy signal is available to authorised users only.

Three binary signals are modulated onto the carrier frequencies:

- PR ranging code, with period of 1 millisecond;
- Navigation message, with information about the satellite transmitting the signal and about all the other satellites;
- 100 Hz auxiliary meander sequence.

GLONASS constellation status, almanac, PDOP values and service of real-time monitoring are provided by the Russian Space Agency Information-Analytical Centre [WWW 2.8]. From the same web site, an Interface Control Document providing details on GLONASS can be downloaded.

Receivers measuring signals from both GPS and GLONASS satellites must lock to at least five satellites instead of four to account for the time scale differences of the two systems. A sixth satellite is necessary to provide fault tolerance (Topcon, 2006).

2.4.3 GPS theoretical precision in landslide monitoring

The theoretical precision achievable in landslide monitoring using relative positioning techniques is discussed in Gili et al. (2000) and here the main results are briefly reported.

The position at the rover antenna is given by:

$$X_{rover} = X_{base} + \Delta X_{baseline} \quad Eq. 2.5$$

and the error in measuring the length of the baseline, $e(\Delta X_{baseline})$, is defined by manufacturer specifications. Considering the human errors in setting up the antennas at base and rover locations, $e(baset-up)$ and $e(rover-set-up)$, and the error in base coordinates, $e(X_{base})$, the total error at rover location is:

$$e(X_{rover}) = e(X_{base}) + e(baset-up) + e(\Delta X_{baseline}) + e(rover-set-up) \quad Eq. 2.6$$

The ground surface movement at the rover location at time t (M_{rover}^t) is given by the difference in position for this location between two successive measurements:

$$M_{rover}^t = (X_{rover})^t - (X_{rover})^0 = (X_{base} + \Delta X_{baseline})^t - (X_{base} + \Delta X_{baseline})^0 \quad Eq. 2.7$$

and if the coordinates at the base are constant:

$$M_{rover}^t = (\Delta X_{baseline})^t - (\Delta X_{baseline})^0 \quad Eq. 2.8$$

From this equation, it is clear that any error in base coordinates will have no influence on movement monitoring providing that the base is in a position not affected by ground movement. Therefore, the remaining errors, considered random and independent are:

$$e(M_{rover}) = e(basetup)' + e(\Delta X_{baseline})' + e(roversetup)' - [e(basetup)^0 + e(\Delta X_{baseline})^0 + e(roversetup)^0]$$

Eq. 2.9

The errors in setting up base and rover antenna depend on the method used. If the antenna is set up directly over a rock outcrop or a cylinder of concrete, the error is approximately 1 mm, while using a tripod with optical plummet the error is 1-3 mm. If only a telescopic pole or rod is used for the rover antenna, the precision decreases and errors can increase to 15 mm (Gili et al., 2000).

2.4.4 The use of Global Positioning Systems for the monitoring of surface movements at Mynydd Yr Eglwys landslide

2.4.4.1 Data acquisition

A dual-frequency Topcon HiPer Pro GPS+ instrument was used in RTK surveying mode for the monitoring of surface movements at Mynydd Yr Eglwys landslide. This 20-channel instrument is capable of tracking both GPS and GLONASS satellites, receiving and processing both L1 and L2 signals and measuring code and carrier phases. It is characterised by high survey accuracy (Table 2.8) being suitable for the high precision professional surveyor. The system includes features such as multipath mitigation, co-op tracking and Receiver Autonomous Integrity Monitoring (RAIM), that detects and removes faulty GPS and GLONASS from position computation (Topcon, 2006).

The instrument comprises of two very physically similar receivers, one functions as Base Station and the other as Rover Station. In RTK mode, data are transmitted from

the Base to the Rover antenna via radio link. Topcon's TopSURV software, installed on a handset PC (Topcon's data collector FC-100), allows interfacing with the receivers during the survey. The handset can be connected to the receivers via cable or via wireless Bluetooth.

Table 2.8 Survey accuracy of Topcon HiPer Pro GPS+ instrument defined when observing a minimum of 6 GPS satellites with 15 degrees angle cut-off, according to manufacturer specifications (Topcon, 2006)

Survey Mode	Survey Accuracy (for L1 + L2)
Static and Fast Static	H: 3mm + 0.5 ppm (x baseline length) V: 5 mm + 0.5 ppm (x baseline length)
Kinematic and RTK	H: 10 mm + 1.0 ppm (x baseline length) V: 15 mm + 1.0 ppm (x baseline length)
dGPS	< 1 m

Base and rover receiver were initially configured according to RTK survey mode by Topcon's Cardiff technician L. Davies who also provided the necessary training for GPS data acquisition and processing.

On the 20th of November 2007, seventeen markers were installed on the slope at Mynydd Yr Eglwys at locations selected on the basis of landslide geomorphological map, site constraints and sky visibility. A ground anchor marker was deployed at the GPS base station. The base station was installed at a location considered not to be affected by any landslide movement and visible by the survey crew on the landslide area (Figure 2.28). A selection of 0.30, 0.50 and 0.60 m steel bars were also installed on the landslide at 15 movement monitoring locations (markers CU2 to CU16; Figure 2.29).

The addition of a few control points outside the landslide movement area was advisable in order to evaluate the quality of GPS monitoring results. The RCTCBC monitoring network is surveyed with an EDM from two locations (SB81 and SB85) along Meadow Walk marked on the tarmac with surveyor nails. These two "fixed"

reference points were also included in the GPS campaigns. However, it was anticipated that their locations would not be ideal for GPS surveying as the two points are close to obstacles (buildings, edges, cars) that obscure part of the sky and/or can cause multipath effects (Figure 2.32). Moreover, one of the two points (SB85) is on a parking space at times occupied by a car and could not always be monitored. For these reasons, an additional surveyor nail (marker CU1) was installed on the kerb along Meadow Walk at a location with clearer sky visibility away from houses.



Figure 2.28 Installation of anchor-marker at GPS base station (photos by the author)



Figure 2.29 Installation of a ground grip marker with raised head at one of the movement monitoring locations. Steel bars of another ground grip marker and of two econo-markers are shown on the grass (photos by the author)

From November 2007 to December 2008, nine GPS movement monitoring campaigns were carried out following similar field work procedures. A summary of the movement monitoring campaigns is provided in Table 2.9.

Firstly, the Base antenna was set up using a tripod (plus tribrach) with optical plummet over the base anchor marker (Figure 2.30). The antenna was turned on and left to initialise for a few minutes. Base antenna height was measured with a tape measure from the centre of the marker on the ground to the slant height measure mark

on the HiPer Pro Minter (receiver's minimum interface) and entered in TopSURV software as slant height. The antenna was then either left to find its coordinates (auto-position) for a few minutes or it was assigned the coordinates obtained from a previous survey. From this moment the base receiver began to collect static observations data and transmitting its location and observations to the Rover antenna. When the Base receiver was left to auto-position, data were recorded for post-processing, generally at least for four hours.

GPS data were sampled at 1 second intervals. The elevation mask was 10 degrees for positioning and, as for default, only 5 degrees for the logging file (but increased to 15 degrees in the post-processing software).

Secondly, the Rover antenna was set up using a tripod (plus tribrach) with optical plummet over a movement marker (Figures 2.31 and 2.32). Antenna height was measured with the same procedure adopted for the Base antenna and the value was entered in TopSURV. Without moving the tripod, the same measurement was carried out only once at each marker in November and December 2007, but 3 or 6 times during the other campaigns for quality purposes. Moreover, 1 to 3 movement markers were re-occupied during each campaign (except in December 2008) to help evaluating GPS practical errors (Table 2.9).

The Rover receiver sampling rate was 1 second and mask angle was 10 degrees. The receiver was set to record only fixed positions and to accept the position coordinates when achieving a precision of 0.002 m in both horizontal and vertical directions. As a consequence, the time of observation varied, ranging approximately from 26 seconds to more than 4 minutes. GPS baselines ranged between approximately 120 m (distance vector between Base and CU11) and 288 m (distance vector between Base and SB81). Data were stored in the data collector FC-100.

The Ordnance Survey's National Grid Transformation OSTN02 and National Geoid Model OSGM02 have been integrated into Topcon's TopSURV software and base and markers coordinates were shown on site in terms of National Grid Eastings, Northings and ODN elevation (all in metres).

Only one day was allowed for each GPS campaign. Due to safety reasons and reduced

markers visibility, the field work was carried out only during hours of daylight. Except for campaign of December 2007, the markers on top of the slope (CU15 and CU16) were excluded from the movement monitoring network as it was taking too much time to reach these locations. After gaining experience with the field work, all the other markers (accounting also for 6 measurements for marker and re-occupation of 1 to 3 points of the network) could be surveyed in one day. Unfortunately, two markers (CU2 and CU4) were vandalised sometime after 26 April 2008.

Table 2.9 Summary of GPS movement monitoring campaigns at Mynydd yr Eglwys landslide.

Date of campaign	Days elapsed since previous campaign	Logging at GPS Base?	Logging duration	Base name	Surveyed markers (in order of acquisition)	Number of measurements at each marker	Re-occupied markers (with number of measurements)
27/11/07	Not applicable	Yes	5h17m02s	Base 3	CU1, SB85, SB81, CU3, CU4, CU2, CU6, CU5, CU7, CU10, CU9	1	CU1 (1)
11/12/07	14	No	-	-	CU12, CU13, CU14, CU15, CU16, CU1, SB81, CU2, CU4, CU7, CU9, CU8, CU11	1	CU12, CU13 and CU14 (1)
13/02/08	64	No	-	-	CU12, CU13, CU14, CU11, CU7, CU9, CU10, CU8, CU6, CU5, CU3, CU2, CU4, SB81, CU1	6	CU11, CU6 and CU1 (6)
26/04/08	73	Yes	7h23m24s	Base 3B	CU12, CU14, CU13, CU11, CU8, CU7, CU9, CU10, CU5, CU6, CU3, CU4, CU2, SB81, SB85, CU1	6	CU11 and CU5 (6), CU1 (1)
24/06/08	59	Yes	8h32m44s	Base 3C	CU12, CU13, CU14, CU11, CU8, CU7, CU9, CU10, CU5, CU6, CU3, SB81, SB85, CU1	6	CU8 and CU5 (6)
15/08/08	52	No*	-	-	CU12, CU13, CU14, CU11, CU8, CU7, CU9, CU10, CU5, CU6, CU3, CU1, SB85, SB81	6	CU8 and CU5 (6)
03/10/08	49	Yes	6h37m19s	Base 3D	CU12, CU13, CU14, CU11, CU8, CU7, CU9, CU10, CU6, CU5, CU3, SB81, SB85, CU1	6	CU9, CU5 and SB81 (6)
14/11/08	42	Yes	5h27m00s	Base 3E	CU12, CU13, CU14, CU11, CU8, CU7, CU9, CU10, CU5, CU6, CU3, SB81, SB85	6	CU9 (6)
16/12/08	32	Yes	3h19m14s	Base 3F	CU12, CU13, CU14, CU11, CU8, CU7, CU9, CU10, CU5, CU6, CU3, SB81, SB85, CU1	3	-

*data at base station were logged, but the antenna memory became full after only 2 hours and 41 minutes of recording and as a consequence the file was not taken into consideration for post-processing. Memory availability of base antenna can be checked only connecting the antenna to a computer with Topcon's software PCDU and no sign of lack of memory is provided on site. After this occasion, attention was paid to the size of memory available on the base antenna before going in the field.



Figure 2.30 Topcon HiPer Pro GPS+ base antenna set up with tripod (plus tribrach) at the movement monitoring base station on Mynydd Yr Eglwys slope (photo by the author)



Figure 2.31 GPS movement monitoring at markers CU5 (left) and CU13 (right) at Mynydd Yr Eglwys landslide. The rover antenna is set up on a tripod (plus tribrach)



Figure 2.32 GPS movement monitoring at surveyor reference points SB81 (left) and SB85 (right) along Meadow Walk. The two locations are not ideal for GPS monitoring because the receiver is close to obstacles (edge and buildings) that partly obscure the sky visibility and can cause multipath effects

2.4.4.2 Data post-processing

The data stored inside the data collector FC-100 were exported from Topcon's TopSURV software and transferred to a desktop PC through PC-card. These files showed only point names, point grid coordinates (in National Grid Eastings, Northings and ODN elevation) and point codes. To recover more information about the accepted measurements (i.e. start/end time of observation, observation duration, horizontal and vertical precision, number of GPS and GLONASS satellites in view at time of observation, and values of PDOP, VDOP and HDOP) it was necessary to navigate to TopSURV jobs inside the handset with the software Microsoft ActiveSync and then open the jobs with TopconLink v7.1 (Topcon) software.

The data logged inside the Base antenna were downloaded to a desktop PC connecting the receiver to the PC and using the interfacing software PC-CDU (Topcon). The same software allows to check and to change receiver configurations, to check receiver free memory space and to delete permanently logged files.

The files logged at the Base were post-processed and adjusted against the Ordnance

Survey Network stations with the software Topcon Tools (Topcon). For coherent processing of all movement monitoring data, all the base station files have been re-processed in May 2009 with the new version of the software (Topcon Tools version 7.1) and all GPS RTK datasets have been corrected according to such results, while during field work a previous version of the software was used.

Projection OSTN02 and geoid OSGM02 are included in the software and were selected as coordinate system for all the post-processing projects. As a consequence, coordinates for GPS Base station and OS Network stations are calculated in National Grid Eastings, Northings and ODN elevation (all in metres).

Three datasets were necessary and needed to be imported in the software in order to process the GPS Base files:

1. Coordinates of the fixed OS Network stations (published coordinates of the OS Network stations to which the network has to be finally adjusted to). In version 7.1 of the software, the OS Network coordinates are extracted automatically from the RINEX files. In previous versions of the software, the coordinates had to be imported from files available on the Ordnance Survey GPS website [WWW 2.7] and provided by Topcon [WWW 2.9].
2. File of GPS Base receiver (raw data previously downloaded in Topcon's PC-CDU software). Information on antenna type, antenna height and height measurement method used during field work had to be added to the file in Topcon Tools.
3. RINEX data from active stations of the OS Network. GPS (and GLONASS) data recorded by the 10 stations closest to Base location during a period of time including the time of logging at the Base on the landslide (i.e. at least from one hour before starting to one hour after ending the Base logging) were downloaded for free from the Ordnance Survey GPS website [WWW 2.7] the day after field work. If not healthy, the stations were excluded from the download. When importing the RINEX file in Topcon Tools, the software automatically recognised the antenna information related to the OS stations with the exception of the new updated antennas. These had to be entered manually.

For the post-processing, an elevation mask of 15 degrees and a system comprising of both GPS and GLONASS were selected.

The selection of the processing mode is automatic in Topcon Tools and depends on the length of the vectors. As all the vectors in the projects were between 30 and 40 km, a Wide Lane solution type was adopted and solution was always fixed (all ambiguities were fixed to integers). The broadcast ephemerides were used for the processing.

Before running an adjustment, several tests were performed on the network according to the quality control criteria selected in the job configuration:

- 1) Checking vector coordinates. The difference between the coordinates of baseline end points and baseline coordinates had to be less than 1000 m;
- 2) Analysis of repeated observations. The coordinates of vectors between 2 or more observations with common start/end names were averaged and the averaged value substituted the repeated observations. The test failed if the differences in values were more than 0.02 m in horizontal and 0.05 m in vertical plane;
- 3) Analysis for identical points. The coordinate differences between all points in the job were computed. The test failed if precision was worse than 0.02 m in horizontal and 0.05 m in vertical plane;
- 4) Analysis of vertical and horizontal control points. Control points were checked to have both horizontal and vertical coordinates;
- 5) Analysis of consistency of control (control tie analysis). The coordinates of the control points were compared with the ones computed using GPS observations. The test failed if precision was worse than 0.02 m and 0.05 m horizontally and vertically respectively.

The confidence level for the adjustment was set to 95%. The observations that had failed the tests were automatically rejected from the network adjustment. Rejected observations appeared highlighted in red in the map view (Figure 2.34), in the GPS observation tabular view and in reports of adjustment results.

At the end of the adjustment, the new corrected coordinates for the Base receiver were provided, together with information about standard deviations in Eastings, Northings and elevation. The same shift (difference between corrected and raw coordinates of GPS base) was applied to the entire RTK dataset in Excel (Microsoft).

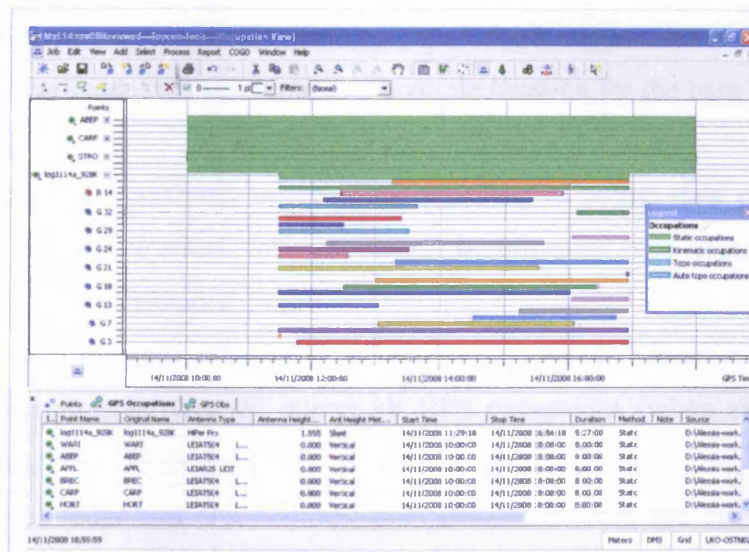


Figure 2.33 Occupation view for GPS base station of 14 November 2008 at Mynydd Yr Eglwys landslide from Topcon Tools software. It is a time-scale chart of the GPS and GLONASS satellites in view during the data logging

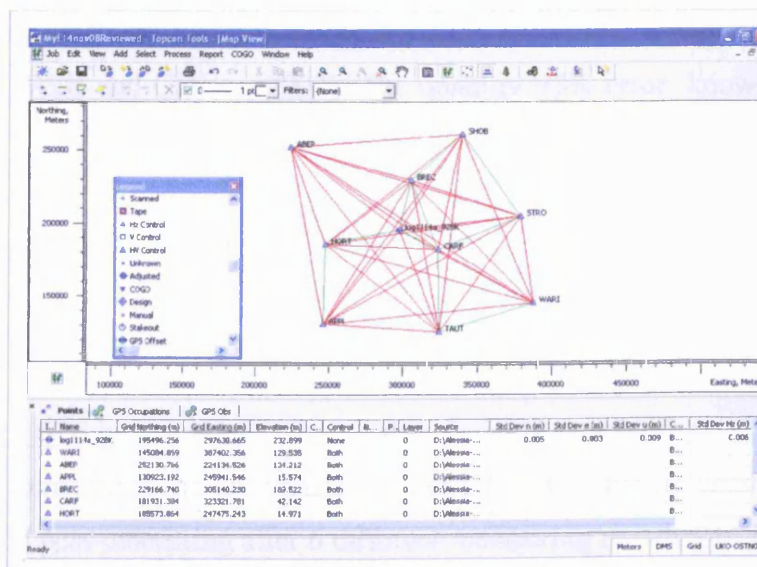


Figure 2.34 Map view from Topcon Tools software showing stations and observation vectors after adjustment for Mynydd yr Eglwys base of 14 November 2008. One of the 10 closest stations (MACH) was not downloaded from Ordnance Survey web site because it was reported as not being healthy

2.4.4.3 Data quality assessment

Firstly, post-processed coordinates obtained from the 6 logged files at GPS Base were compared to evaluate if the assumption of a stable location for the base was correct.

Secondly, data were analysed in terms of precision to assess data quality and the applicability of the method for movement monitoring. The practical precision achieved on site was evaluated from:

1. Analysis of apparent movement of points in “stable” locations: comparison between measurements obtained during all GPS campaigns (when available) at the “fixed” points SB81, SB85 and CU1;
2. Analysis of redundant observations: comparison between the 3-6 measurements taken at each marker without moving the tripod during the same GPS campaign;
3. Analysis of re-occupied points.

As the GPS measurements were carried out always with the same equipment and the same procedure, the arithmetic mean of redundant observations was considered to be the most probable value for the marker coordinates. Precision was estimated in terms of dispersion (range of values), standard deviation (σ) and 95% confidence level (E_{95} , 95% error) (Wolf and Ghilani, 2002). The quantity 95% error, known also as two-sigma error, is defined as:

$$E_{95} = \pm 1.9599\sigma \quad \text{Eq. 2.10}$$

Evaluation of GPS base

Table 2.10 summarises the coordinates of the GPS base station obtained from data recording and post-processing after 6 different monitoring campaigns. Due to the low standard deviation (0.005 m in Eastings, 0.003 m in Northings and 0.016 m in elevation) and the scattering of values, the assumption of a stable location for the base was judged to be correct. Therefore, the mean coordinates were considered to be the most precise and accurate value for the base and were used to shift all the subsequent GPS monitoring datasets.

Table 2.10 Summary of GPS post-processing results for the base station

Date	Base name	Coordinates after post-processing			Standard deviation for each Base			
		Eastings (m)	Northings (m)	Elev (m)	e(m)	n(m)	u(m)	Hz(m)
27 Nov 07	Base 3	297630.660	195496.265	232.879	0.003	0.005	0.010	0.006
26 Apr 08	Base 3B	297630.650	195496.260	232.904	0.004	0.004	0.010	0.006
24 Jun 08	Base 3C	297630.657	195496.258	232.906	0.003	0.005	0.009	0.006
03 Oct 08	Base 3D	297630.660	195496.261	232.928	0.003	0.005	0.010	0.006
14 Nov 08	Base 3E	297630.665	195496.256	232.899	0.003	0.005	0.009	0.006
16 Dec 08	Base 3F	297630.656	195496.260	232.897	0.004	0.006	0.009	0.007

Mean		297630.658	195496.260	232.902				
Standard deviation		0.005	0.003	0.016				
E ₉₅		0.010	0.006	0.031				

Analysis of apparent movement of “fixed” points

The results of statistical analysis carried out on the coordinates of “fixed” points SB81, SB85 and CU1 considering all GPS campaigns are reported in Table 2.11. In addition, Figure 2.35 shows the apparent movement in Eastings and Northings of these three markers during the monitoring period.

As underlined in section 2.4.4.1 and in Figure 2.32, the location of SB81 and SB85 is not ideal for GPS monitoring due to the limited sky visibility and the possible presence of multipath effect. Moreover, SB81 is the farthest marker from the GPS base of the entire monitoring network. As a consequence, the results on precision at SB81 (0.0030 m in Eastings, 0.0063 m in Northings and 0.0143 m in elevation) can be considered the worse obtained on site and associated also with the worse case scenario. In fact, the standard deviation for CU1, located in an area with better sky visibility, is lower, being 0.0022 m in Eastings, 0.0025 m in Northings and 0.0077 m in elevation.

These values are below the errors provided by instrument specifications (Table 2.8).

Table 2.11 Summary of statistical analysis of coordinates of “fixed” points SB81, SB85 and CU1 considering all monitoring campaigns

		Range		Mean	Standard deviation	E ₉₅
		Min	Max			
SB81	Eastings (m)	297819.609	297819.617	297819.613	0.0030	0.0060
	Northings (m)	195286.052	195286.071	195286.059	0.0063	0.0124
	Elevation (m)	176.267	176.309	176.287	0.0143	0.0281
SB85	Eastings (m)	297717.749	297717.763	297717.758	0.0048	0.0094
	Northings (m)	195292.835	195292.851	195292.843	0.0050	0.0098
	Elevation (m)	180.419	180.448	180.430	0.0103	0.0201
CU1	Eastings (m)	297681.773	297681.779	297681.776	0.0022	0.0043
	Northings (m)	195306.181	195306.187	195306.185	0.0025	0.0049
	Elevation (m)	182.007	182.030	182.018	0.0077	0.0151

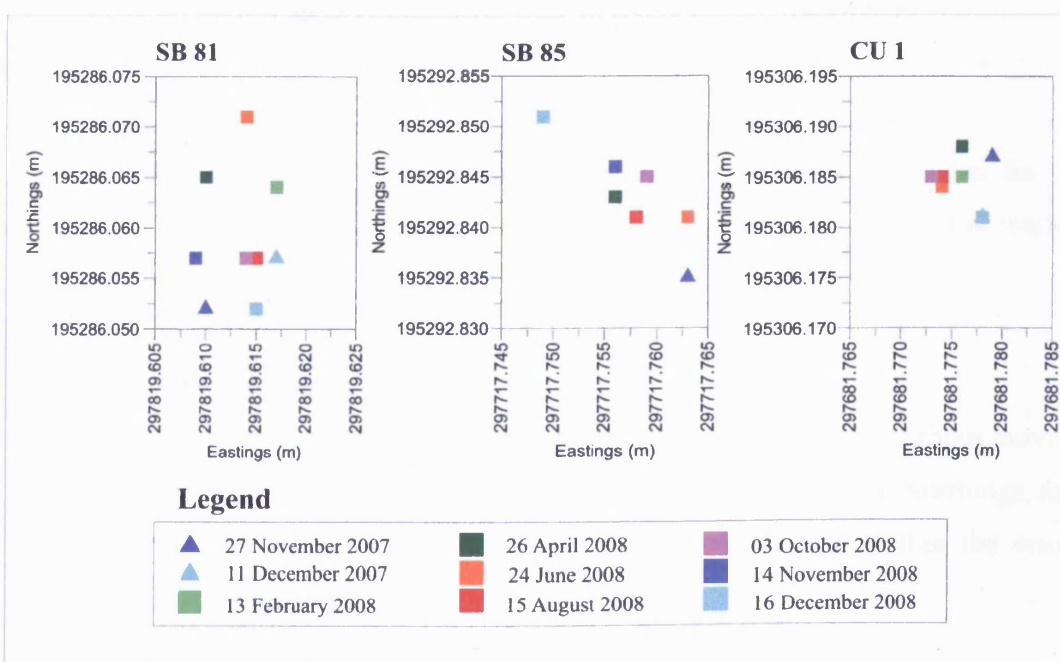


Figure 2.35 Apparent movement in Eastings and Northings of “fixed” points during the monitoring period. The dimensions of the boxes are the same: 0.20 m in Eastings and 0.25 m in Northings. As expected, the scattering in coordinates is minimum for CU1

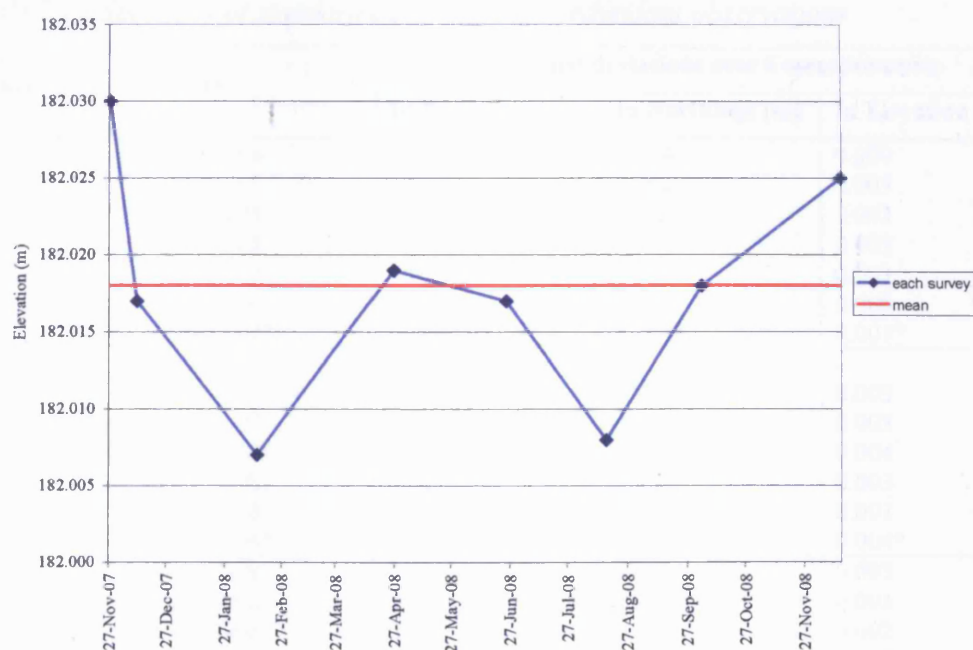


Figure 2.36 Graph showing the variation in elevation at “fixed” point CU1 during the different GPS campaigns in comparison with its mean value (180.018 m)

As expected from instrument specifications, the standard deviation is higher for the elevation. Figure 2.36 shows a graph of the apparent change in elevation at marker CU1 in comparison with its mean value.

Analysis of redundant observations

Standard deviations of measurements carried out on the same marker without moving the tripod range between: 0 and 0.006 m in Eastings, 0 and 0.005 m in Northings, and 0.001 and 0.015 m in elevation (Table 2.12). These values are within the errors provided by the instrument specifications (Table 2.8).

Table 2.12 Summary of standard deviations for redundant observations

Marker	Date	Standard deviations over 6 measurements		
		In Eastings (m)	In Northings (m)	In Elevation (m)
SB81	13/02/08	0.001	0.004	0.009
	26/04/08	0.001	0.002	0.005
	24/06/08	0.001	0.002	0.003
	15/08/08	0.002	0.001	0.005
	03/10/08	0.002	0.001	0.003
	14/11/08	0.003	0.002	0.005
	16/12/08*	0.002*	0.004*	0.007*
SB85	13/02/08	-	-	-
	26/04/08	0.002	0.002	0.003
	24/06/08	0.001	0.003	0.003
	15/08/08	0.001	0.002	0.004
	03/10/08	0.001	0.002	0.003
	14/11/08	0.002	0.002	0.003
	16/12/08*	0.001*	0.002*	0.004*
CU1	13/02/08	0.001	0.002	0.003
	26/04/08	0.003	0.002	0.003
	24/06/08	0.001	0.002	0.002
	15/08/08	0.002	0.004	0.005
	03/10/08	0.001	0.003	0.001
	14/11/08	-	-	-
	16/12/08*	0.002*	0.001*	0.003*
CU2	13/02/08	0.002	0.003	0.005
	26/04/08	0.001	0.003	0.006
CU3	13/02/08	0.002	0.003	0.006
	26/04/08	0.002	0.003	0.003
	24/06/08	0.006	0.005	0.015
	15/08/08	0.001	0.005	0.003
	03/10/08	0.001	0.002	0.004
	14/11/08	0.001	0.001	0.001
	16/12/08*	0.001*	0.001*	0.001*
CU4	13/02/08	0.001	0.005	0.008
	26/04/08	0.002	0.001	0.007
CU5	13/02/08	0.003	0.002	0.004
	26/04/08	0.001	0.008	0.005
	24/06/08	0.001	0.004	0.004
	15/08/08	0.001	0.001	0.002
	03/10/08	0.001	0.001	0.002
	14/11/08	0.002	0.003	0.004
	16/12/08*	0.002*	0.002*	0.001*
CU6	13/02/08	0.001	0.003	0.004
	26/04/08	0.002	0.002	0.004
	24/06/08	0.001	0.001	0.001
	15/08/08	0.002	0.002	0.003
	03/10/08	0.001	0.002	0.002
	14/11/08	0.001	0.002	0.001
	16/12/08*	0.000*	0.003*	0.002*
CU7	13/02/08	0.001	0.002	0.003
	26/04/08	0.002	0.002	0.005
	24/06/08	0.001	0.004	0.002
	15/08/08	0.001	0.002	0.003
	03/10/08	0.001	0.003	0.005
	14/11/08	0.001	0.001	0.001
	16/12/08*	0.000*	0.001*	0.001*

(continue into next page)

Marker	Date	Standard deviations over 6 measurements		
		In Eastings (m)	In Northings (m)	In Elevation (m)
CU8	13/02/08	0.001	0.001	0.004
	26/04/08	0.002	0.001	0.003
	24/06/08	0.000	0.001	0.003
	15/08/08	0.001	0.001	0.003
	03/10/08	0.001	0.002	0.005
	14/11/08	0.002	0.003	0.004
	16/12/08*	0.001*	0.002*	0.001*
CU9	13/02/08	0.001	0.001	0.001
	26/04/08	0.004	0.002	0.010
	24/06/08	0.001	0.005	0.006
	15/08/08	0.002	0.003	0.006
	03/10/08	0.002	0.002	0.005
	14/11/08	0.001	0.002	0.002
	16/12/08*	0.001*	0.001*	0.002*
CU10	13/02/08	0.001	0.002	0.002
	26/04/08	0.003	0.001	0.004
	24/06/08	0.003	0.003	0.008
	15/08/08	0.002	0.002	0.002
	03/10/08	0.002	0.002	0.004
	14/11/08	0.001	0.001	0.003
	16/12/08*	0.002*	0.003*	0.005*
CU11	13/02/08	0.002	0.002	0.003
	26/04/08	0.002	0.004	0.008
	24/06/08	0.001	0.002	0.001
	15/08/08	0.003	0.002	0.009
	03/10/08	0.001	0.001	0.002
	14/11/08	0.002	0.004	0.004
	16/12/08*	0.000*	0.001*	0.002*
CU12	13/02/08	0.002	0.004	0.004
	26/04/08	0.001	0.002	0.002
	24/06/08	0.002	0.003	0.004
	15/08/08	0.001	0.001	0.003
	03/10/08	0.002	0.004	0.006
	14/11/08	0.001	0.001	0.006
	16/12/08*	0.001*	0.003*	0.002*
CU13	13/02/08	0.002	0.001	0.004
	26/04/08	0.001**	0.002**	0.004**
	24/06/08	0.001	0.002	0.003
	15/08/08	0.002	0.001	0.001
	03/10/08	0.001	0.002	0.002
	14/11/08	0.002	0.001	0.007
	16/12/08*	0.001*	0.000*	0.005*
CU14	13/02/08	0.001	0.002	0.004
	26/04/08	0.001	0.001	0.004
	24/06/08	0.001	0.001	0.004
	15/08/08	0.002	0.002	0.002
	03/10/08	0.001	0.004	0.007
	14/11/08	0.001	0.003	0.002
	16/12/08*	0.001*	0.001*	0.003*

*only three measurements

**only one measurement

Analysis of re-occupied points

As explained previously, some markers were re-occupied during the GPS campaigns to consider the influence of re-setting the antenna on the marker and of a change in satellite geometry. The differences between coordinates of re-occupied points and coordinates from the previous occupation are reported in Table 2.13. The differences range between: -0.005 and 0.010 m in Eastings, -0.007 and 0.004 m in Northings, and -0.011 and 0.011 m in elevation.

Table 2.13 Summary of differences between coordinates of re-occupied points and their previous coordinates

Date	Re-occupied Marker	Coordinate differences (Re-occupied minus Previous occupation)		
		In Eastings (m)	In Northings (m)	In Elevation (m)
27/11/07	CU1	0.001	-0.004	0.011
11/12/07	CU12	0.007	0.000	0.008
	CU13	-0.005	-0.004	-0.002
	CU14	-0.002	0.001	0.007
13/02/08	CU1	-0.001	0.001	0.004
	CU6	0.002	0.000	-0.008
	CU11	0.004	-0.002	-0.001
26/04/08	CU1	0.003	-0.004	0.000
	CU5	0.000	0.004	-0.003
	CU11	-0.001	0.004	0.006
24/06/08	CU5	0.010	-0.007	0.002
	CU8	0.007	-0.003	-0.001
15/08/08	CU5	0.001	0.003	-0.008
	CU8	0.000	0.004	-0.011
03/10/08	SB81	0.002	-0.003	-0.002
	CU5	-0.001	0.002	0.005
	CU9	-0.001	-0.002	0.001
14/11/08	CU9	-0.002	0.002	0.001
16/12/08	none	not applicable	not applicable	not applicable

To conclude and summarise these analyses, the highest standard deviation for redundant observations (without moving the tripod) is 0.006 m in Eastings, 0.005 m in Northings and 0.015 m in elevation, in accordance with instruments specifications for RTK surveying. The apparent movement of “fixed” point SB81 (considered worse scenario in terms of location) is of the same order. The difficulties in setting up the tripod exactly on the same point seem to have added only 2-3 millimetres to possible errors in Eastings and Northings.

According to Halcrow (2000), the limit of movement detection for the EDM surveying carried out at Mynydd yr Eglwys is approximately 0.050 m. This value is significantly less accurate than the precision achieved using the GPS.

2.4.4.4 Data analysis

GPS surface displacements were analysed in terms of cumulative horizontal, cumulative vertical and cumulative inclined (or total) movement for all “moving” markers. The aim of this analysis was to obtain the rates of movement at each marker and to identify differences in activity within the landslide area. Moreover, displacements were compared with rainfall and pore water pressures in order to investigate the relationship between movement and rainfall. The results are reported in Chapter 3.

GPS movement monitoring results were compared with the measurements carried out with an electronic distance meter (EDM) by surveyors for the Rhondda Cynon Taff County Borough Council (RCTCBC). Unfortunately, movement markers and dates of monitoring campaigns do not coincide. However, a comparison was attempted between GPS markers CU6, CU10, CU12, CU13 and EDM (RCTCBC) markers P60, P18, P6 and P3 respectively.

2.4.5 The use of GPS receivers for surveying position and topography at Mynydd yr Eglwys

The same instrument, Topcon’s HiPer Pro GPS+, was used in RTK mode for most of the surveying carried out during this project (Figure 2.37B). The procedure of data acquisition was similar to the one for surface movement monitoring previously described. However, due to the less accuracy required, there were some differences:

1. GPS data at base location were recorded for post-processing only once. During following surveys, the obtained post-processed coordinates were assigned to the base antenna;
2. The rover antenna was mounted on a 2 m pole with optical plummet (not a tripod plus tribrach);
3. The rover antenna was set to average measurements of three epochs, reaching a precision of at least 0.015 m and 0.03 m in horizontal and vertical plane respectively.

With these settings, the rover antenna was moved to unknown and wanted locations

to:

- Survey position and elevation of electrodes and geophones;
- Set up SP grids and profiles;
- Survey position and elevation of SP stations;
- Set up GEM2 grid;
- Survey position and elevation of photogrammetry targets;
- Survey position of land forms and wet areas for geomorphological mapping.

For correct processing of SP and GEM2 data, centimetric accuracy of topography was not necessary. However, horizontal location was still important in order to plot such data correctly on a LIDAR digital elevation model and digital basemap. As the use of an EDM was not advisable due to the size and the complex topography of the area under investigation, other two kinds of GPS receivers were employed: a Trimble backpack dGPS and a Trimble GPS Pathfinder ProXT.

A Trimble GPS Pathfinder ProXT receiver was used during the electromagnetic GEM-2 surveys to record the position of every data point (Figure 2.37C). This is a lightweight, plastic, single-frequency GPS/SBAS receiver with 12 channels, measuring L1 code and carrier and provided with multipath rejection technology. It is accessorised with an external patch antenna that is housed in the pocket of a baseball cap. Trimble's TerraSync software installed on a handset PC was used to interface with the receiver during the survey. When EGNOS signal is available, the system can provide sub-metre accuracy. If the EGNOS signal is not reliable during a GEM2 survey the area of interest can be divided in 50 x 50 m grids set up with the more accurate Topcon's HiPer Pro GPS+ instrument.

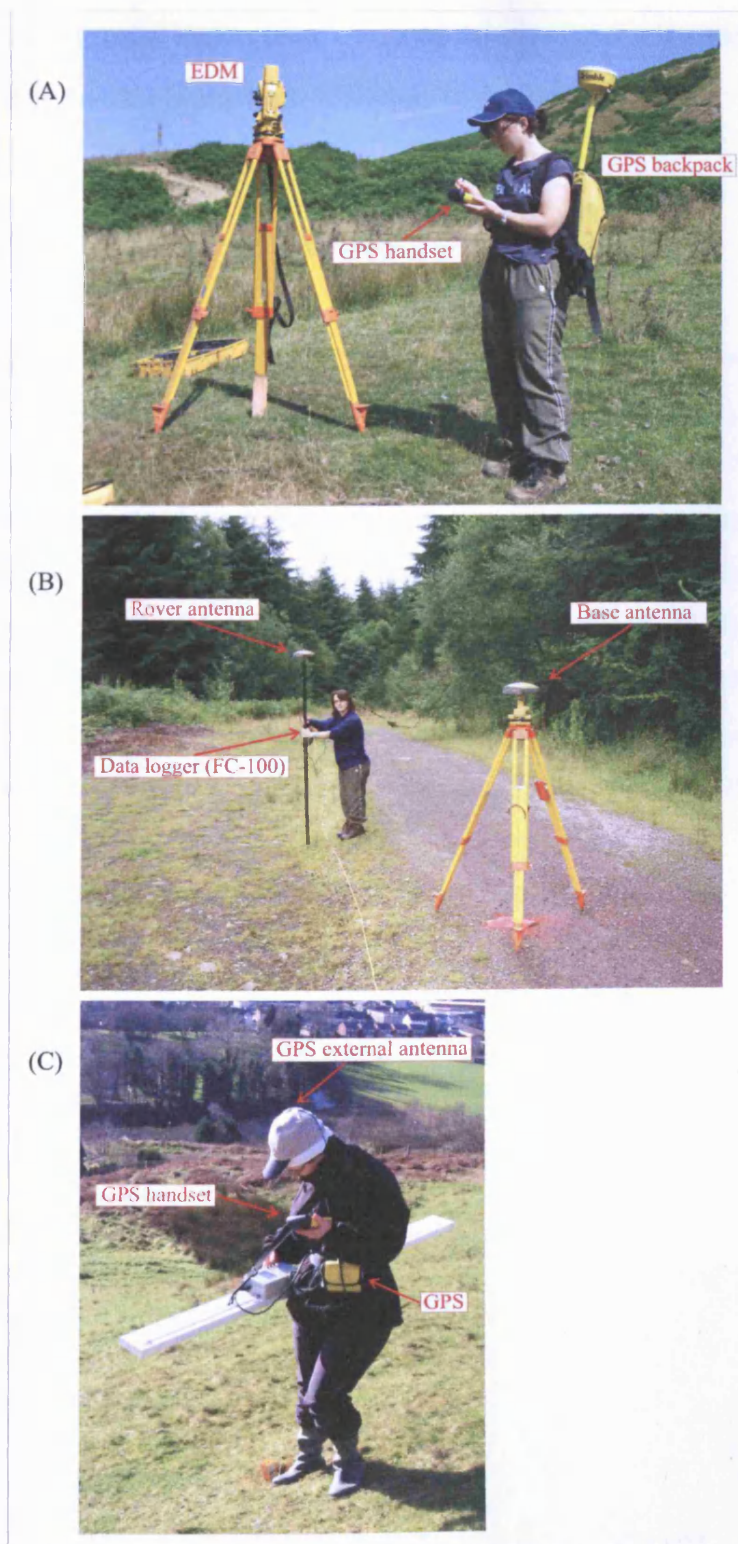


Figure 2.37 Instruments used during the project for surveying topography and/or position: (A) Topcon EDM GTS-3B20 and Trimble dGPS Backpack, (B) Topcon HiPer Pro GPS+ and (C) Trimble Pathfinder ProXT GPS (photos by P.J. Brabham)

2.5 Electromagnetic induction or ground conductivity mapping with reference to the Geophex GEM-2 instrument.

2.5.1 Background to electromagnetic induction methods

A transmitter coil with an alternating current placed above the ground generates a primary electromagnetic field that propagates both above and below the ground surface. According to EM induction laws, the time-varying magnetic field generated by the alternating current of the transmitter induces eddy currents in any conductor in the subsurface, which in turn generate a secondary time-varying magnetic field. A receiver coil placed above the surface can detect the resultant of the primary and secondary magnetic fields. The differences in phase and intensity between received and transmitted fields can provide information on the electrical properties, geometry and location of the conductor (Figure 2.38; McNeill, 1980b; Sharma, 1997; Kearey et al., 2002;).

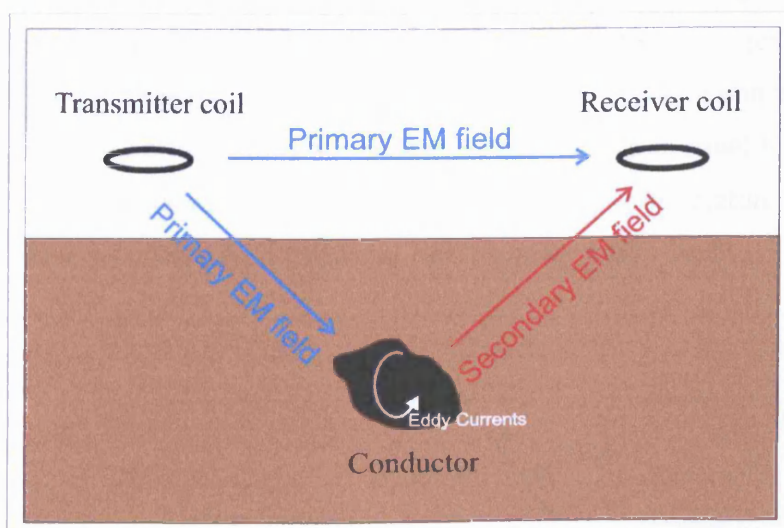


Figure 2.38 Schematic diagram illustrating the principle of electromagnetic induction methods (modified from Sharma, 1997)

In-phase and quadrature readings

The primary electromagnetic field generated by the transmitter travels through the air maintaining its original phase and with only a very limited decrease in amplitude due to geometrical spreading. The alternating voltage induced in the conductor in the ground has the same frequency as the primary field but has a phase lag of $\pi/2$. The properties of the conductor cause an additional phase lag Φ equal to:

$$\Phi = \tan^{-1}\left(\frac{2\pi fL}{r}\right) \quad \text{Eq. 2.11}$$

where f is the frequency of the electromagnetic field, L and r are the inductance and the resistance of the conductor respectively. Therefore, the secondary field has a $\pi/2 + \Phi$ phase lag behind the primary field. For very good conductors the phase of the secondary field is almost π behind the primary field (as r tend to 0 and Φ to $\pi/2$), whereas for very poor conductors is $\pi/2$ behind the primary field (as r tend to ∞ and Φ to 0).

The relationship between primary (P), secondary (S) and resultant (R) fields measured by the receiver can be illustrated through a vector diagram (Figure 2.39). The horizontal projection of the secondary field (on the primary field) is equal to $S\sin\Phi$, is at π phase from the primary and is known as the in-phase or real component of the secondary field. The vertical projection of the secondary field is equal to $S\cos\Phi$, is at $\pi/2$ phase from the primary and is known as the out-of-phase, quadrature or imaginary component of the secondary field (Sharma, 1997; Kearey et al., 2002).

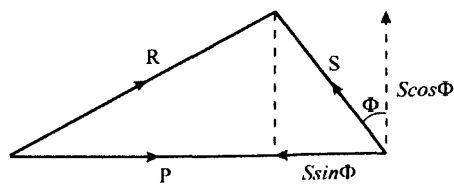


Figure 2.39 Vector diagram illustrating the amplitude and phase relationships between primary (P), secondary (S) and resultant (R) electromagnetic fields (Kearey et al., 2002)

Applications and usual targets

Electromagnetic induction (EMI) instruments have been widely used for site characterisation in environmental and engineering studies as they offer a rapid and cost-effective means to map electrical conductivity variations. Compared to conventional galvanic resistivity techniques, the electromagnetic induction method does not require contact with the ground.

The differences in electrical conductivity mapped using EMI instruments can be associated with changes in rock/soil type, fracturing degree, porosity, clay content, water saturation degree, and electrical properties of water/fluid in the soil (i.e. contaminants such as dissolved salts or acid mine drainage; McNeill, 1990; Fitterman and Labson, 2005). Typical values of conductivity (or resistivity) for geological materials found in sedimentary or igneous/metamorphic environments are reported in Figures 2.40 and 2.41. Moreover, as metals can cause strong EM anomalies, EMI methods have been often used to locate buried metallic containers/pipes or unexploded ordnance (UXO).

In general, a wide range of electromagnetic methods and instruments are available to the geophysicist. Descriptions of several instruments and methods together with detailed EM mathematical background can be found in many geophysical text books and articles, such as McNeill (1980), Sharma (1997), Kearey et al. (2002), Fitterman and Labson (2005) and references therein. The following section focuses on the instrument GEM-2 (Geophex), which was used for this project.

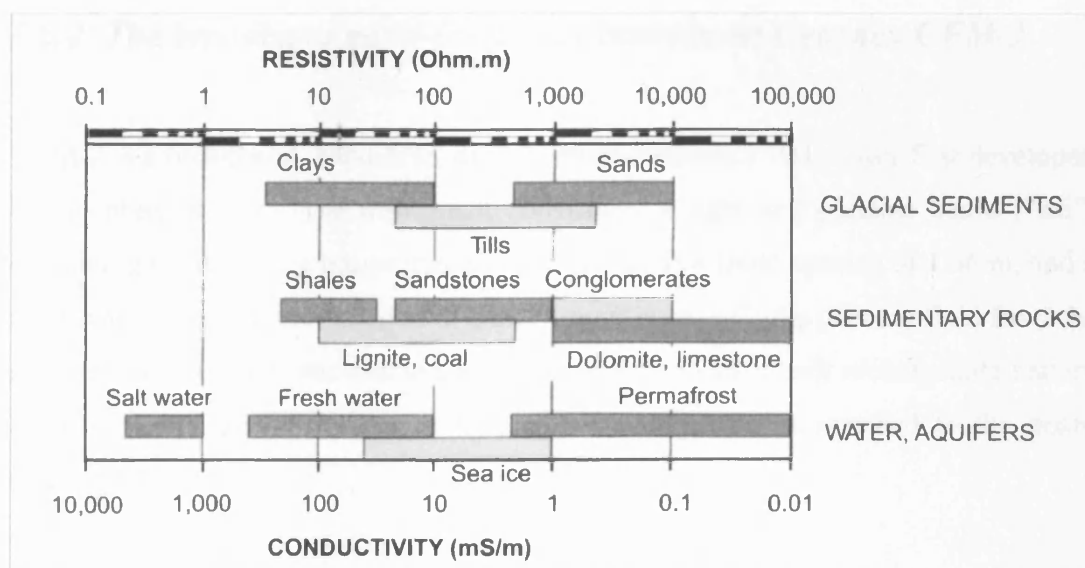


Figure 2.40 Conductivity (or resistivity) values for geological materials found in sedimentary environments (Table provided by Terradat UK Ltd, modified from Knight and Endres, 2005 and reference therein)

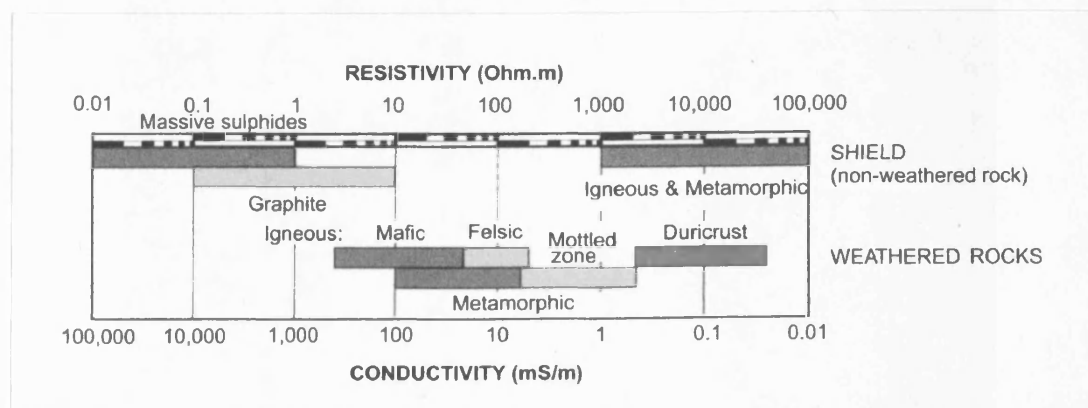


Figure 2.41 Conductivity (or resistivity) values for geological materials found in igneous or metamorphic environments (Table provided by Terradat UK Ltd, modified from Knight and Endres, 2005 and reference therein)

2.5.2 The broadband multi-frequency instrument Geophex GEM-2

GEM-2 is a broadband, hand-held, digital, multi-frequency EM sensor first developed by Geophex in 1995. The instrument consists of a light and portable board (“ski”) containing three coils: a transmitter and a receiver, at a fixed spacing of 1.66 m, and a third coil, which has the function of cancelling (“bucking”) the primary field from the receiver coil. A small removable control console with an inbuilt rechargeable battery used to power the instrument with inbuilt memory card is attached to the board (Figure 2.42).



Figure 2.42 GEM-2 instrument used in horizontal coplanar configuration for the acquisition of EMI data at Mynydd yr Eglwys Landslide (photo P. J. Brabham)

The instrument owned by Cardiff University can operate in a frequency range between 330 Hz and 47970 Hz and with up to 15 simultaneous frequencies. However, as the transmitter energy is shared between any selected frequencies, usually up to 3-5 frequencies are normally recommended for a survey (GEM-2 Manual).

The frequencies selected by the operator are converted into a digital “bit-stream”,

which is used to construct a transmitter waveform for the survey, with a technique called pulse-modulation. In the UK a base period of $1/25^{\text{th}}$ of a second for the bit-stream must be selected to minimise noise from the power supply operating at 50 Hz (Won et al., 1996).

The EM signal is digitally recorded by both bucking and receiver coils. These time-series are successively convolved with sets of sine and cosine series to obtain the values of in-phase and quadrature in part-per-million, which are the raw data values stored by the instrument (ppm; Won et al., 1996):

$$\text{ppm} = 10^6 \frac{\text{secondary magnetic field at receiver coil}}{\text{primary magnetic field at receiver coil}} \quad \text{Eq. 2.12}$$

These values expressed in ppm are sensor specific but they can be converted to values of apparent conductivity (values of conductivity for a ground below the sensor assumed to be a homogeneous and isotropic half-space) using an instrument calibration factor. Used in a horizontal coplanar configuration, the secondary field normalized against the primary at the receiver coil (or mutual coupling ratio, Q) is (Won et al., 1996):

$$Q = \frac{H_s}{H_p} - 1 = -r^3 \int_0^\infty \lambda^2 R(\lambda) J_0(\lambda r) e^{-2\lambda h} d\lambda \quad \text{Eq. 2.13}$$

where R is the kernel function for a uniform half-space:

$$R(\lambda) = \frac{\lambda - \sqrt{\lambda^2 + i2\pi f \mu \sigma}}{\lambda + \sqrt{\lambda^2 + i2\pi f \mu \sigma}} \quad \text{Eq. 2.14}$$

H_s and H_p are the secondary and primary field at the receiver coil, r is the coil spacing, h is the height of the sensor above the ground, J_0 is the zeroth-order Bessel function, f is the transmitter frequency (in Hz), μ is the magnetic permeability and σ is the earth conductivity.

Equations 2.12 and 2.13 differ only for a factor of 10^6 . Therefore, knowing coil separation, instrument height and operating frequency, the observed ppm values can be converted to apparent conductivity (Won et al., 1996). Huang and Won (2000) provide more details on this process of conversion to apparent conductivity.

Advantages of frequency sounding and definition of skin depth

In general, the depth of a target can be determined in two ways with EMI methods (Figure 2.43; Won et al., 1996; Witten et al., 1997; Won, 2003):

- By geometrical sounding: using an instrument operating at a fixed frequency and taking measurements using different coil separations;
- By frequency or broadband sounding: using an instrument with a fixed coil separation but taking measurements over a range of different frequencies (e.g. GEM-2).

The instruments relying on geometrical sounding (e.g. Geonics EM34-3) have the disadvantage of requiring multiple operators and suffering from the difficulty of maintaining an accurate coil separation. By contrast, the GEM-2 instrument is extremely portable, lightweight (4 kg) and can be operated by one person, rendering it an attractive solution in areas of rugged landslide terrain.

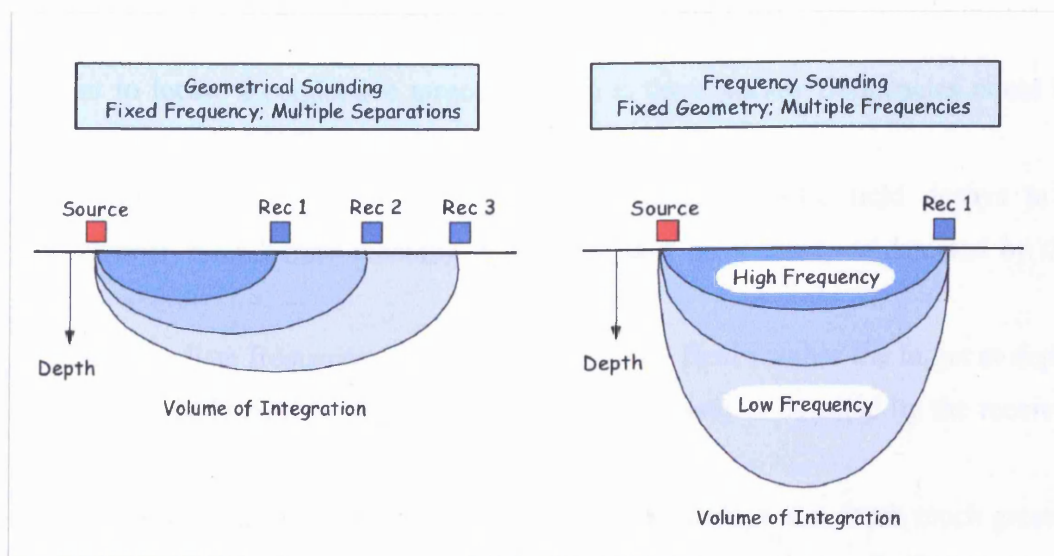


Figure 2.43 Schematic diagram illustrating geometrical and frequency sounding with EMI methods (from Won at [WWW 2.10])

While propagating through the ground, the amplitude of electromagnetic waves decreases exponentially with depth (Kearey et al., 2002). For a homogeneous medium, the depth at which the amplitude of a plane wave is reduced to $1/e$ (or to 37%) of its original value is called the skin depth (δ) and is equal to (Sharma, 1997; Huang, 2005):

$$\delta = \sqrt{\frac{2}{\sigma\mu\omega}} \quad \text{Eq. 2.15}$$

where σ and μ are the conductivity and the magnetic permeability of the medium respectively and ω is the angular frequency of the plane wave. The value of skin depth can be calculated also as $503.8/\sqrt{(\sigma f)}$, with conductivity in S/m and frequency in Hz (Kearey et al, 2002).

From equation 2.15 it is evident that skin depth depends on the frequency of the source and on the conductivity of the ground. Figure 2.44 shows a simple diagram that can be used for a rapid evaluation of skin depth (Won, 1980). More in particular, the skin depth is inversely proportional to frequency, meaning that in a conductive earth low frequencies travel deeper into the ground than high frequencies, leading to the possibility of using broadband instruments for depth sounding (Won, 1980; Won et al., 1996).

In order to locate a conductive target at depth z , three survey frequencies could be used (Witten et al., 1997):

- a high frequency, for which the primary electromagnetic field decays to a negligible value before reaching depth z so that no anomaly is detected by the receiver coil;
- an intermediate frequency, for which the primary field reaches the target at depth z causing eddy currents so that a measurable anomaly is detected by the receiver coil;
- a very low frequency, for which the primary field decays at a depth much greater than z , so that only a weak anomaly is detected by the receiver coil. The weakness of this anomaly is due to the fact that the receiver measures a response that is a

depth-integrated function of the conductivity inversely weighted for the depth and the target occupies only a small portion of such depth.

Theoretical studies conducted by Won (1980) showed that, for a target in a conductive half-space, peak amplitude of response occurs at the frequency with the corresponding skin depth slightly greater than the depth of the target.

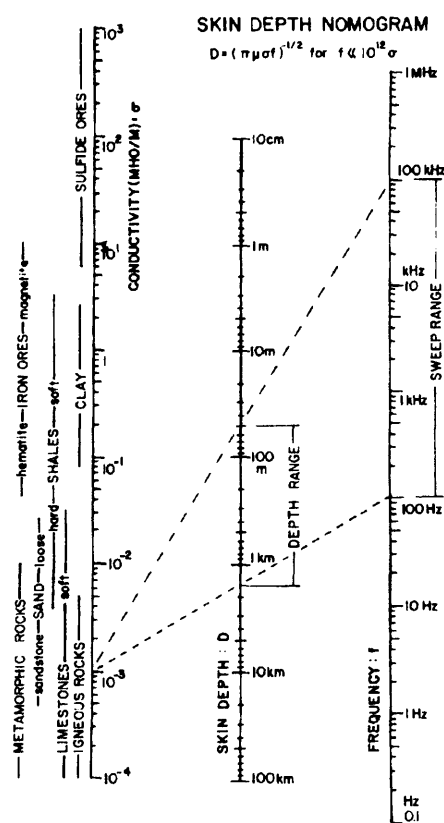


Figure 2.44 Diagram illustrating the relationship between instrument frequency, ground conductivity and skin depth. For example, in an area of igneous rocks, if the source sweeps between 100 Hz and 100 KHz, the skin depth is 40-1500 m (from Won, 1980)

Investigation depth

Investigation depth is defined as the maximum practical depth for which a given target in a given host material can be detected by a sensor (Huang, 2005). Although skin depth is often considered by authors a synonymous with the investigation depth,

the two terms are actually different. Investigation depth is empirical and depends on many factors, such as type of sensor, data processing and interpretation methods, properties of target and host material, and site noise (Huang, 2005).

Mathematical empirical equations for the determination of investigation depth for the GEM-2 instrument at a specific detection threshold have been proposed and discussed by Huang (2005). For the simplified case of a half-space below a single layer, the approximate investigation depth (DI) is:

$$DI \approx \sqrt{\delta_1} \varphi(T) \Psi(r) \quad \text{Eq. 2.16}$$

where:

$$\varphi(T) = 3.10 - 0.61 \ln(T) \quad \text{Eq. 2.17}$$

$$\Psi(r) = 0.84 + 0.10r - 0.0015r^2 \quad \text{Eq. 2.18}$$

δ_1 is the skin depth of the upper layer, T is the detection threshold (in percentage) and r is the coil spacing (equal to 1.66 m for GEM-2).

The concept of cumulative conductance can be applied for the detection of a half-space at a depth z below multiple layers. The multiple layers above the half-space can be substituted by an equivalent single layer of effective conductivity σ_e up to a depth z and the equation for two layers (eq. 2.16) can therefore be applied.

The cumulative conductance of the multiple layers down to depth z is given by (Huang, 2005):

$$S(z) = \int_0^z \sigma(z) dz \quad \text{Eq. 2.19}$$

where $\sigma(z)$ is conductivity as a function of depth, and the effective conductivity σ_e is equal to:

$$\sigma_e(z) = \frac{S(z)}{z} \quad \text{Eq. 2.20}$$

Imaging algorithms and inversion techniques applied to layered earth models for broadband data acquired with the GEM-2 instrument are still under research (i.e. in Witten et al., 1997; Huang, 2005). Generally GEM-2 data (as in-phase and quadrature ppm or apparent conductivity and magnetic susceptibility) are plotted as a series of coloured contour maps, one for each frequency used. It can be observed that targets at particular depths are only evident for particular frequency bands. The target depth is qualitatively estimated by visual comparison of the different plots. Technical explanations on the reasons behind the reliability of the instrument GEM-2 for depth sounding regardless of its small coil separation are discussed in Won, 2003 (perhaps as an answer to criticism from McNeill, 1996 of Geonics).

Examples on the use of GEM-2 to locate abandoned wells, buried pipes, trenches of waste disposal, underground structures and archaeological features can be found in the literature (Won et al., 1996; Witten et al., 1997; Witten et al., 2003; Gochioco and Ruev, 2006) and on the Geophex web site [WWW 2.10]. Moreover, Won and Huang (2004) have shown that at sufficiently low frequencies (within the resistive limit) the instrument can function as an “active magnetometer”, because it responds only to magnetic susceptibility, but only for shallow investigations and with the advantage of producing reduced-to-pole anomalies when compared to a conventional proton magnetometer.

2.5.3 Limitations of EMI methods

Near surface metallic objects located just below the instrument (e.g. buried services) can cause strong anomalies, which mask the signature of the investigated target.

2.5.4 Data acquisition at Mynydd yr Eglwys landslide

Ground conductivity data were acquired at MYE Landslide using a GEM-2 (Geopex) instrument, in horizontal coplanar coil configuration mode (Figures 2.42), along lines of approximately 2-3 m spacing and at a sampling rate of 120 ms. Prior of going on site, the instrument was configured to operate at five frequencies: 47025 Hz, 30025 Hz, 15025 Hz, 5125 Hz and 975 Hz. Ground positioning was achieved by connecting the GEM-2 instrument to a Trimble Pathfinder ProXT GPS (Figure 2.37C; see section 2.4.5 for GPS details).

The area of investigation was divided in three grids:

- Grid 1. The survey was carried out on the 24th of January 2008, in the central and toe areas of the landslide (approximately between 297700 and 297800 m in Eastings and between 195350 and 195450 m in Northings). Data were acquired in alternating directions along lines oriented W-E along the land contours to minimise topographic effects. Due to the lack of availability of the EGNOS satellite for the Trimble Pathfinder ProXT GPS, positioning was imprecise. Therefore a grid of pegs 50 x 50 m was set up using the Topcon HiPer Pro GPS+. The line spacing between the GEM-2 lines was approximately 3 m;
- Grid 2. This survey was carried out on the 25th of January 2008 as a continuation of the previous grid northwards. This grid extends from Eastings 297700 - 297800 m and Northings 195450 to 195550 over the most active part of the landslide;
- Grid 3. It was acquired on the 12th of May 2009 in the NW area of the site, between Eastings 297560 - 297670 and Northings 195460 - 195550. Data were acquired over parallel SW-NE lines at 2 m spacing. The orientation of the lines was selected to run perpendicular to the major fault zone. As the satellite EGNOS signal was available by this time, it was not necessary to set up rigid positioning grid with the Topcon HiPer Pro GPS+ and the surveying procedure became very rapid.

According to the GEM-2 instrument manual, the instrument is calibrated, it does not require nulling on site and readings do not drift in time. Nevertheless, during surveys

Grid 1 and 2, the author returned to a fixed location multiple times to check for any obvious instrument drift.

At the end of each survey day, data were downloaded to PC using WinGEMv3 software. After inputting the instrument's height above the ground the quadrature and in-phase values were automatically converted to values of apparent conductivity and magnetic susceptibility. Datasets were successively exported and conversion of GPS coordinates from latitude/longitude to UK National Grid was performed using the Grid InQuest v6.0 software (Quest Geo Solutions Ltd).

2.5.5 Data processing and visualisation

Grid 1 and Grid 2 datasets were affected by many GPS positional errors. The size of the positional errors was not easy to assess due a lack of ground control points. A positional error of less than 2m was deemed acceptable and large positional jumps were edited out manually using Microsoft Excel and Geosoft Oasis Montaj v6.3.

When the GEM-2 was left to collect data at the same location over a few minutes, standard deviations between 0.061 and 0.574 were found in the values of ground conductivity (mS/m) for the three highest frequencies (47025 Hz, 30025 Hz and 15025 Hz). The standard deviation was slightly higher (0.031 to 1.059) for 5125 Hz. The time drift of the average value of ground conductivity measured at the base station was of the same order of standard deviation.

Apparent ground conductivity and magnetic susceptibility values at each frequency were gridded using a kriging method at a grid spacing of 0.75 m and a search radius of 5 m using Surfer 8 software. The grids were successively contoured and overlaid onto the geomorphological base map of the site to highlight changes in ground conductivity and/or magnetic susceptibility across the site and their possible correlation with geomorphological features. The plots produced from different frequencies were visually compared to qualitatively evaluate the variation of apparent ground conductivity and magnetic susceptibility with depth. Results are reported in

Chapter 4.

2.6 Self-potential (SP)

2.6.1 Background

The self-potential method is a passive potential field technique based on the measurement of the spontaneous or natural voltage potential between two points on the ground. Voltage measurements are usually carried out with non-polarizing electrodes. These consist of porous pot with a metal immersed in a saturated solution of a salt of the metal (e.g. copper in copper sulphate). The solution leaks out of the porous pot making electrical contact with the ground (Figure 2.45).

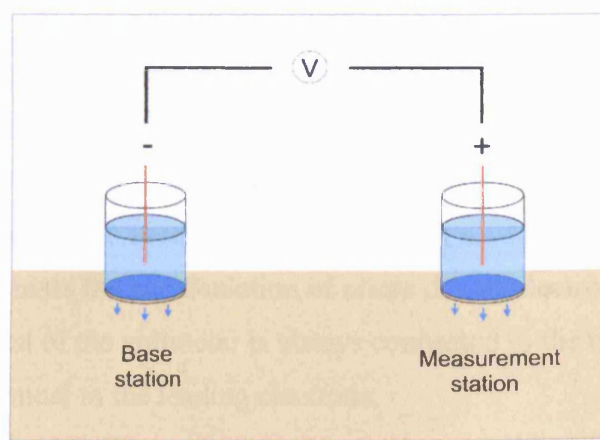


Figure 2.45 Schematic diagram illustrating non-polarizing electrodes used for SP measurements

Origin of natural potential

The origins of spontaneous potentials are not completely understood. However, the main sources quoted are (Sharma, 1997; Telford et al., 1990):

- Electrofiltration or streaming potential: voltage is generated along the flow path by the flow of a fluid through a capillary or porous medium. It is probably caused

by electrokinetic coupling between the fluid ions and the walls of the capillary;

- Thermoelectrical potential: it is generated by the presence of a temperature gradient through the rocks typical in hydrothermal areas;
- Electrochemical or static potential: it is a combination of two effects. One is caused by the difference in mobilities of ions between solutions of different concentration (liquid-junction or diffusion potential). The other can be observed when two identical metal electrodes are immersed in solutions of different concentration (Shale or Nernst potential);
- Mineralization potential: it is observed in areas of sulphide ore-deposits and its origin is not well understood. One of the best known SP models requires the mineral body to bisect the water table (Sato and Mooney, 1960).

Survey configurations

SP measurements are carried out using two non-polarizing electrodes connected by an insulated wire to a high-impedance voltmeter. Without taking into consideration multi-electrode systems, there are two possible survey configurations (Corwin, 1990; Sharma, 1997):

- Gradient (or dipole, leapfrog or fixed-electrode) configuration: two SP electrodes (kept at a constant distance) are connected by a short length of wire. After the measurement of potential at the first reading station, the first electrode is then leapfrogged over to the second electrode to form a second reading station. This technique minimises the accumulation of errors due to electrode polarization. The negative terminal of the voltmeter is always connected to the trailing electrode and the positive terminal to the leading electrode;
- Fixed base (or total field) configuration: one electrode (the base electrode) is kept at a fixed location, while the other (roving or measuring electrode) connected by a long wire on a reel, is constantly moved on to measuring stations. The negative terminal of the voltmeter is always connected to the base electrode.

The fixed base configuration has the practical disadvantage of using a very long wire on site. However, the technique provides high quality SP data, because it is less prone to cumulative errors. It is also more flexible on site in terms of station positioning or reoccupation, and in case of the necessity of additional reading to investigate an anomalous area. Therefore it should be preferred to the gradient configurations, unless

in case of very difficult terrain and site conditions. The spacing between stations should be chosen according to the expected anomaly wavelength, which depends on configuration, size and depth of the target (Corwin, 1990).

The amplitude of anomalies generated by targets of environmental and/or engineering interest may be very small. A useful discussion on recommended SP equipment, good data acquisition procedures and forms of data quality control is reported in Corwin (1990). His suggestions were taken into consideration to improve the surveying procedures of this project.

Applications

Self-potential is a cheap and simple reconnaissance method that has been used in mineral exploration to locate sulphide ore-bodies and in geothermal exploration to locate areas of hydrothermal fluids (Sato and Mooney, 1960; Corwin and Hoover, 1979; Corry, 1985). For environmental and engineering applications the SP method has mainly been used for the study of water leakage from dams and reservoirs (Ogilvy et al., 1969; Bogoslovsky and Ogilvy, 1970; 1970b) and the investigation of groundwater movement (Bogoslovsky and Ogilvy, 1972; Corwin, 1990 and references within).

2.6.2 SP Limitations

SP anomalies applied to environmental and engineering applications are typically small and care must be taken to minimise/recognise unwanted effects due to electrode polarization, drift and background electrical noise.

2.6.3 Data acquisition at Mynydd yr Eglwys landslide

Self-potential data were acquired at MYE landslide using two non-polarizing electrodes, consisting of two ceramic pots containing a copper mesh immersed in a saturated solution of copper sulphate (Figure 2.46). Measurements were carried out using a high impedance voltmeter and with a fixed-base electrode configuration.

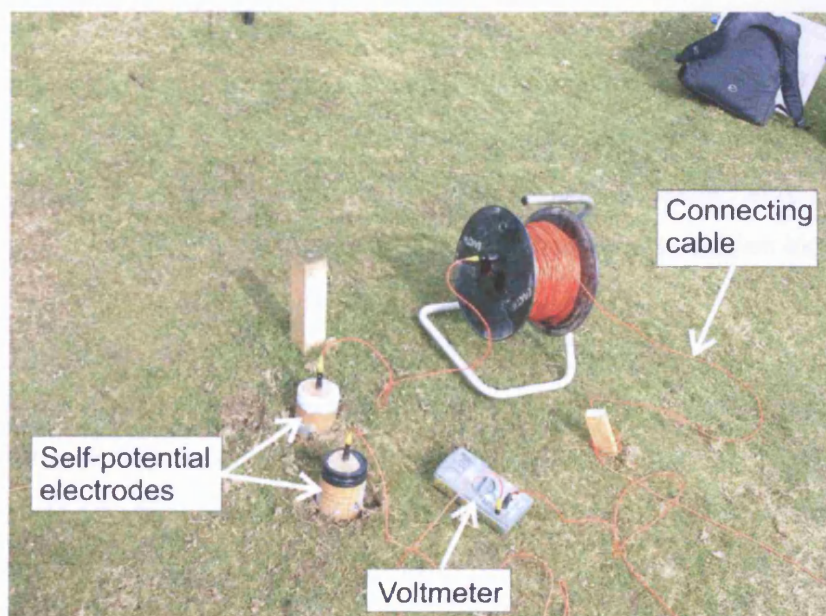


Figure 2.46 Self-potential equipment used for the surveys at Mynydd yr Eglwys landslide

Self-potential mapping surveys were carried out in December 2006 and March 2007, while SP monitoring of two small grids was carried out in 2008. The following paragraphs provide details of these SP surveys.

Mapping of December 2006

- Northern grid. SP data were acquired on an irregular grid with approximately 5-10 m station spacing in the area of the landslide comprised between the main and the secondary scarp, on the 15th of December. The base electrode was dug in at the base of the main landslide scarp. The location of measurement points was surveyed with the Trimble backpack GPS;
- Central grid. SP data were acquired with the same procedure in the more active area of the landslide on the 19th and 21st of December.

Mapping of March 2007

- Southern (or toe) grid. SP data were acquired over a 20 by 20 m station spacing on the 8th of March. The location of the base electrode was moved closer to GR

297701,195425. The grid was set up with Topcon HiPer Pro GPS+, which was also used to record the station locations. The grid was infilled on the 12th of March at a higher 10 m x 10 m resolution.

- Three cross profiles were collected along Northings 195480, 195490 and 195550 at a station spacing of 10 m. The location of the base electrode was the same as above (approximately at GR 297701,195425). The profiles were set up with Topcon HiPer Pro GPS+, which was also used to record the station locations.

SP monitoring

- In summer 2008 a water drainage system was installed at the landslide toe. A small SP grid with a station spacing of 5 m was acquired before (30/06/08) and after (31/10/08) the completion of the drainage system. The base location was the same as in March 2007. The grid was set up with Topcon HiPer Pro GPS+, which was also used to record the station locations and relocate them during the repeated survey.
- A small SP grid employing a 5 m station spacing was acquired on the 15th of July 2008 and repeated on the 06th December 2008 over the central and more active area of the landslide, where resistivity monitoring using permanent electrodes was also carried out. The base location was the same as in March 2007. The grid was set up with Topcon HiPer Pro GPS+, which was also used to record the station locations and relocate them during the repeated survey.

As anomalies were expected to be low, great care was taken during data acquisition to avoid or be able to recognise sources of measurement errors and to improve data reproducibility, according to recommendations reported in Corwin (1990):

- Initial and final electrode polarization was checked measuring the voltage between base and roving electrode while they were immersed in a bath of electrolyte (copper sulphate solution) before and after each survey;
- The porous junction of the measuring electrode was cleaned from soil between measurements to reduce electrochemical drift;
- Contact resistance was very rapidly measured after each SP measurement to check for integrity of the connecting wire;
- Electrode holes were dug to a few centimetres of depth to improve reading consistency and such holes were covered if the station had to be successively

reoccupied to avoid changes in moisture content and/or temperature due to air exposure;

- Readings at base location and at a few other stations were repeated within each survey to check for time drifts;
- Notes were taken regarding soil moisture variations to be able to distinguish between positive anomalies due to wet soil condition and upward movement of water.

The major problem encountered on site was the handling of a very long wire in an area of severe topography and, during summer, dense and high vegetation. The wire had to be very carefully deployed and retrieved to avoid tangles and breakages.

2.6.4 SP data processing

SP datasets were corrected for voltage drift at the base station to which a 0 mV was assigned. SP values (in mV) were gridded using the kriging method in Surfer 8 (Golden Software) and then plotted as contour maps in mV increments. The plots were successively overlain onto the landslide geomorphological base map and onto the 3D LIDAR terrain model. Analysis of data was only qualitative and based on the observation of changes of voltage across the slope with reference to landside features. SP monitoring data were considered as separate profiles and data were plotted as line graphs using Microsoft Excel. The results of SP mapping and monitoring are reported in Chapter 4 and 5 respectively.

2.7 Seismic refraction tomography

2.7.1 Background

For near-surface seismic refraction surveying, elastic (or seismic) waves are generated at or just below the earth surface using controlled sources. Both compressional (P)

and shear (S) waves can be used. Sources include small explosives, buffalo guns, sledgehammers struck against metal plate or weight drops. The elastic waves propagate through the ground away from the source. The waves may be critically refracted along boundaries of contrasting elastic properties and then return back to the surface. The travel times of the waves in milliseconds are measured at a variety of distances away from the source by surface motion detectors (geophones). These traveltimes data are plotted on a time versus distance graph. Analysis of these data using standard algorithms results in a measurement of layer velocities and an estimated depth to a refracting interface.

The refraction method has been widely employed in engineering and environmental applications to map shallow layers, to identify the water table, to determine depth to bedrock and estimate the geotechnical properties of rocks. The basic principles of the refraction method are discussed in detail in several books and articles, such as Brabham (1986), Lankston (1990), Carrara et al. (1992), Sharma (1997), Kearey et al. (2002), Knight and Endres (2005), Pelton (2005 and 2005b).

2.7.1.1 Seismic waves and their velocities

There are two types of seismic waves: body waves, which propagate through the internal volume of a material (P and S waves), and surface waves, which propagate along the boundary of a solid.

Body waves

There are two types of body waves:

- 1) Compressional, longitudinal or P- (primary) waves, in which the particles oscillate about a fixed point in the direction of wave propagation, involving compression and dilatation of the material;
- 2) Shear, transverse or S- (secondary) waves, in which the particles oscillate about a fixed point in a plane (horizontal, S_H or vertical, S_V) perpendicular to the direction of wave propagation.

They are both non dispersive.

The velocities of P- and S-waves (V_p and V_s respectively) depend on the density and the relevant elastic moduli of the material through which they propagate. For an

homogeneous and isotropic material, they are given by the following equations:

$$V_p = \sqrt{\left(\frac{K + 4\mu/3}{\gamma} \right)} \quad \text{Eq. 2.21}$$

$$V_s = \sqrt{\frac{\mu}{\gamma}} \quad \text{Eq. 2.22}$$

where γ is the density, K is the bulk modulus and μ is the shear (or rigidity) modulus of the medium. The bulk modulus describes the relationship between changes in volume and hydrostatic pressure, while the shear modulus the relationship between variations in shape and pure shear stress.

From equations 2.21 and 2.22, it can be seen that V_p is always greater than V_s in the same medium. As fluids and gaseous media lack of rigidity or shear strength ($\mu=0$), S-waves do not propagate through these media. Typical values of P- and S-wave velocities for several common near-surface materials are reported in Figure 2.47.

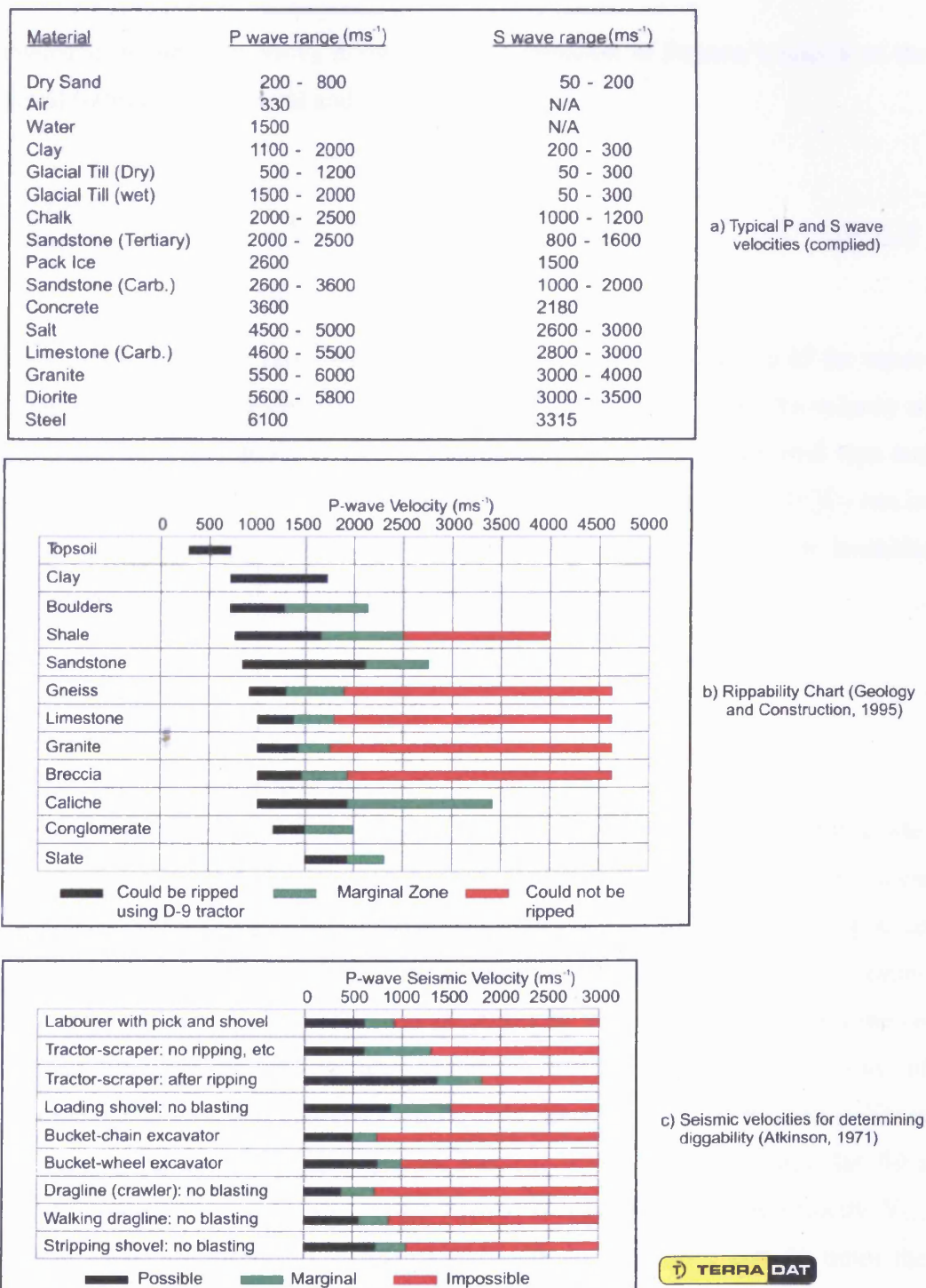


Figure 2.47 Seismic velocity tables compiled and provided by Terradat UK Ltd

In general, elastic wave velocities are affected by: lithology (mineral composition and clay content), degree of compaction and litification, density, porosity and pore structure, degree of fracturing, degree of saturation and properties of pore fluids.

Knowledge of the ratio V_P/V_S allows the determination of Poisson's ratio ν of the material (ratio between lateral and longitudinal strain):

$$\nu = \frac{1}{2} \frac{(V_P/V_S)^2 - 2}{(V_P/V_S)^2 - 1} \quad \text{Eq. 2.23}$$

Poisson's ratio generally varies between 0.05 for very hard rocks and 0.45 for water-bearing unconsolidated materials. From an engineering point of view, the velocity of P-waves can be related to the degree of fracturing/jointing of a known rock type and empirical relationships between velocities and rock quality designation (RQD) can be found. V_S measurements can be more useful than V_P measurements for landslide characterisation because they can be related to shear strength.

Surface waves

There are two types of surface waves:

1) Rayleigh waves, in which the particles move in a counterclockwise (retrograde) elliptical direction and in a vertical plane containing the direction of wave propagation. These waves propagate only in solids and along a free surface (such as the earth-air interface) or at the boundary between two different media. They originate from interference between P- and S_V -waves (Xia et al., 1999). In a solid homogeneous half-space, Rayleigh waves are non dispersive and propagate at a velocity of approximately $0.9194V_S$, if Poisson's ratio is 0.25 (Sheriff and Geldart, 1982 in Xia et al., 1999). By contrast, in layered materials they can be dispersive. In particular, for a layer of velocity V_{S1} overlying a solid homogeneous half-space of velocity V_{S2} , Rayleigh waves are dispersive if their wavelength is between 1 and 30 times the thickness of the first layer (Stokoe et al., 1994 in Xia et al., 1999). For example, if the Rayleigh wave wavelength is smaller than the thickness of the first layer, its velocity is approximately $0.9194V_{S1}$, whereas if the Rayleigh wave wavelength is more than 30 times the thickness of the first layer, its velocity is approximately $0.9194V_{S2}$ (Stokoe et al., 1994 in Xia et al., 1999). In general, for a given mode, longer wavelengths penetrate deeper into the ground, have greater phase velocities and are

more influenced by the elastic properties of deeper layers (Babuska and Cara, 1991 in Xia et al., 1999). The dispersion property of ground roll forms the base of MASW method (see section 2.8);

2) Love waves, in which the particles move parallel to the free surface of the material and perpendicularly to the direction of wave propagation. These waves propagate only in non-uniform media, when the upper layer has a shear velocity lower than the underlying one. They are dispersive. Their velocity is intermediate between the shear velocity of the upper layer and that of the deeper layers.

2.7.1.2 Attenuation

While propagating away from the source, the amplitude of the seismic waves decreases due to geometrical spreading of the energy and due to losses caused by the frictional movement of the particles. Higher-frequency waves attenuate more rapidly in terms of time and distance when compared to lower frequency waves.

2.7.1.3 Reflection, refraction and diffraction

A P- or S-wave incident on a plane boundary between two homogeneous and isotropic elastic media characterised by different velocity (or acoustic impedance) is partly reflected back and partly transmitted (refracted) below the interface. The relationship between the angles of incidence, refraction and reflection is governed by Snell's Law. For example, for a P-wave incident on an interface between a medium of velocity V_1 overlying a medium of velocity V_2 , the relationship between the angle of incidence i and the angle of refraction r is:

$$\frac{\sin i}{\sin r} = \frac{V_1}{V_2} \quad \text{Eq. 2.24}$$

while the angle of reflection equals the angle of incidence.

When $V_2 > V_1$ the angle of refraction is greater than the angle of incidence ($r > i$). The refracted angle equals 90° for a particular angle of incidence called the critical angle

(i_c) :

$$\sin i_c = \frac{V_1}{V_2} \quad \text{Eq. 2.25}$$

Therefore for $i=i_c$ a critically refracted wave travels along the interface between the two media with the higher velocity V_2 causing the generation of secondary waves (head waves) that travel with velocity V_1 in the first layer and re-emerge at the surface at the same angle i_c (see Figure 2.48).

If an incident seismic wave strikes an interface with a sharp break, such as a fault, or a structure/object with curvature radius smaller than the seismic wavelength, such as a boulder, the energy is scattered (diffraction).

2.7.1.4 Determination of velocities and depth of layers

Layer geometry and topography on landslides are generally complex. The simplified case of a planar interface between two homogeneous and isotropic materials is here briefly reported as fundamental to understand the basic principles of seismic refraction surveying and data interpretation.

Two-layer case with planar interface

Figure 2.48 shows a schematic diagram of a single horizontal interface at depth h_1 separating a surficial layer of velocity V_1 from an underlying layer of higher velocity V_2 ($V_2 > V_1$). Elastic energy is realised at the source S in all directions and the wave that strikes the interface at the critical angle i_c is refracted critically.

The first wave to arrive at the geophones close to the source is the direct wave travelling in the surficial layer with velocity V_1 . The travel time of these first arrivals is:

$$T_d = \frac{x}{V_1} \quad \text{Eq. 2.26}$$

where x is the distance between the source and the geophone. After a certain distance, called critical distance (x_c), also the critically refracted wave starts to be recorded at the geophones on the surface. Beyond a certain distance, called cross-over distance (x_{co}), the critically refracted waves arrive at the geophones before the directed waves and are so the first arrivals to be recorded. The travel time of the critically refracted waves is:

$$T_r = \frac{x}{V_2} + \frac{2h_1 \sqrt{(V_2^2 - V_1^2)}}{V_2 V_1} \quad \text{Eq. 2.27}$$

Identifying and plotting the first arrivals on a graph of travel-time versus distance from the source allows the identification of the two straight lines T_d and T_r that have a slope of $1/V_1$ and $1/V_2$ respectively. T_r passes through the time-distance origin, whereas, as evident from equation 2.27, the straight line representing the critically refracted arrivals intercepts the time axis ($x=0$) at a time called intercept time (T_i) equal to:

$$T_i = 2h_1 \frac{\sqrt{(V_2^2 - V_1^2)}}{V_2 V_1} \quad \text{Eq. 2.28}$$

Therefore, the depth of the refractor h_1 can be calculated from equation 2.28 by measuring V_1 , V_2 and intercept time T_i from the travel-time curves:

$$h_1 = \frac{T_i}{2} \frac{V_1 V_2}{\sqrt{V_2^2 - V_1^2}} \quad \text{Eq. 2.29}$$

The depth h_1 can be determined also considering that at the cross-over distance (x_{co}) the direct wave and the refracted wave arrive simultaneously ($T_d=T_r$). Therefore, from equations 2.26 and 2.27 follows that:

$$h_1 = \frac{x_{co}}{2} \sqrt{\frac{V_2 - V_1}{V_2 + V_1}} \quad \text{Eq. 2.30}$$

Re-arranging equation 2.30, it can be seen that the cross-over distance is always greater than $2h_1$.

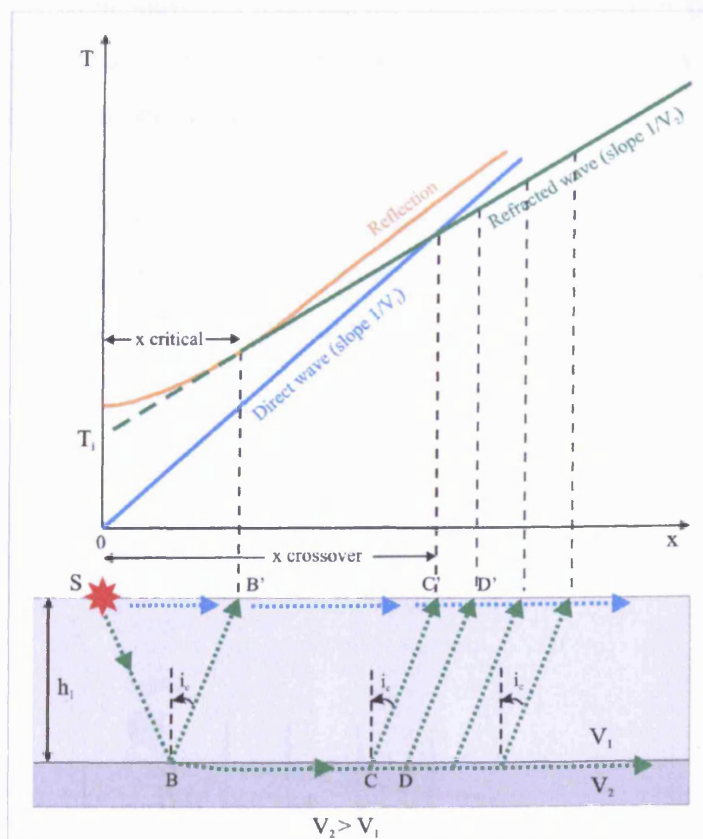


Figure 2.48 Diagram illustrating travel-time curves for direct, reflected and critically refracted waves (modified from Sharma, 1977)

Case of irregular interfaces: Seismic tomography

Applying the seismic refraction technique to landslides requires the use of more sophisticated interpretation techniques in order to resolve complex velocity distributions and to make measurements of the depth to the refractor below each geophone. Among the most commonly applied interpretation techniques are: the plus-minus method (Hagerdoon, 1959) and the generalized reciprocal method (Palmer,

1980). For this landslide project, refraction data were analysed by tomographic inversion.

Tomography starts with an initial velocity model composed of cells of constant velocity. Ray tracing, based on Huygens principle, is applied to simulate ray propagation through the model, which is changed iteratively in order to minimise the difference between observed and calculated travel-times (SeisImager/2D manual, OYO Corporation). Calculations have the aim to find the minimum time required for each ray to travel from source to receiver for each source-receiver pair in the dataset (SeisImager/2D manual, OYO Corporation). The mathematics is complex and is based on the non-linear least squares method.

Considering a velocity model defined by cells of slowness (inverse of velocity) s_j and ray paths l_{ij} (Figure 2.49), travel-times can be expressed in discrete form as (SeisImager/2D manual, OYO Corporation):

$$t_i = \sum_{j=1}^N s_j l_{ij} \quad \text{Eq. 2.31}$$

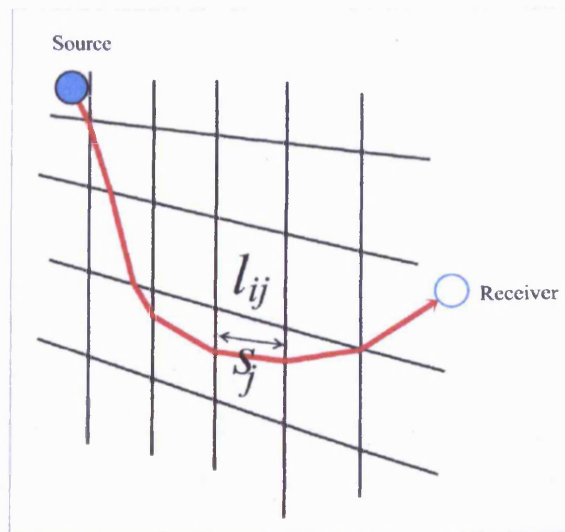


Figure 2.49 Schematic diagram for seismic tomography (see text) (from manual of SeisImager/2D, OYO Corporation)

If N is the number of cells through which the ray goes through and M the number of travel-times, equation 2.31 can be written as:

$$\begin{aligned} t_1 &= l_{11}s_1 + l_{12}s_2 + \dots + l_{1N}s_N \\ t_2 &= l_{21}s_1 + l_{22}s_2 + \dots + l_{2N}s_N \\ &\dots \\ t_M &= l_{M1}s_1 + l_{M2}s_2 + \dots + l_{MN}s_N \end{aligned} \quad \text{Eq. 2.32}$$

or in matrix format as:

$$LS = \begin{bmatrix} l_{11} & l_{12} & \dots & l_{1N} \\ l_{21} & l_{22} & \dots & l_{2N} \\ \dots & & & \\ l_{M1} & l_{M2} & \dots & l_{MN} \end{bmatrix} \begin{bmatrix} s_1 \\ s_2 \\ \dots \\ s_N \end{bmatrix} = \begin{bmatrix} t_1 \\ t_2 \\ \dots \\ t_M \end{bmatrix} = T \quad \text{Eq. 2.33}$$

where matrixes L and S describe respectively the length of the ray passing through each cell and the velocity model. L is a Jacobian matrix and generally $M > N$. Therefore, equation 2.31 can be solved with least square method with the aim to minimise the error $e = LS - T$, leading to the necessity to solve the equation:

$$L^T LS = L^T T \quad \text{Eq. 2.34}$$

which allows determination of S and so the velocity model (SeisImager/2D manual, OYO Corporation).

However, in order to define the ray paths l_{ij} and the matrix L , a velocity model is required (L is a function of S). Consequently, a non-linear least squares method and an iterative procedure are necessary. From an initial velocity model S_0 , an initial Jacobian matrix L_0 and the initial theoretical travel-times T_o^c can be calculated. The difference between the theoretical and the observed travel-times is used to calculate a correction and then apply it to the initial velocity model. This process is iterated till the travel-time residuals are considered to be acceptable (SeisImager/2D manual, OYO Corporation).

Mathematical examples of the procedure are provided in SeisImager/2D manual, (OYO Corporation).

2.7.1.5 Limitations of seismic refraction method

For the condition of critically refraction to occur an increase in velocity with depth is required. A layer can be detected only if its thickness and its velocity contrast are great enough to produce critically refracted waves that reach the surface as first arrivals.

2.8 Multichannel analysis of surface waves (MASW)

2.8.1 Background

The multichannel analysis of surface waves (or MASW) method exploits the dispersion property of the planar fundamental-mode Rayleigh wave to obtain 1D (in depth) and 2D (in depth and surface distance) profiles of shear velocity. The technique is fairly recent as it was developed at the Kansas Geological Survey during the '90s and was introduced in the journal *Geophysics* by Park et al. in 1999. The method has been applied to map bedrock surface, to identify possible areas of fractures or erosional channels within bedrock, to locate subsidence-prone areas and to locate pits and trenches (Miller et al., 1999; 2000). Moreover, as it provides V_s can be used for the estimation of material strength and dynamic shear modulus.

In the active MASW method, surface waves are generated by an impulsive source (i.e. sledge-hammer or weight drop) or a swept source and the receiver array is linear. The investigation depth is generally 10-30 m (Park et al., 1999; 2007). In the passive MASW method, surface waves can be generated by local traffic (passive roadside) or by natural activities (passive remote). In the first case the receiver spread is linear, in the second has a symmetric shape (i.e. circle or cross) and the investigation depth can reach a few hundred of metres (Park et al., 2007).

The MASW technique comprises of three main steps: acquisition of multichannel field records, extraction of dispersion curves (one from each record) and inversion of each dispersion curve to obtain 1D V_s profiles (one profile for each curve). Successively, all the 1D V_s profiles can be plotted in correspondence of the middle point of the relative recording spread to obtain a 2D profile (Figure 2.50; Park et al., 2007).

Step 1: acquisition

When using an impulsive compressional source, planar fundamental-mode Rayleigh waves are generated together with many other waves: air wave, body waves (directed, reflected and refracted), higher-mode surface waves, non-planar near source surface waves, surface waves backscattered by horizontal discontinuities (i.e. building foundations) and non source-generated waves or ambient cultural noise (Figure 2.50; Park et al., 1999; 2007). All these waves are recorded on site and can be identified in a multichannel record (Figure 2.50; Park et al., 2007). Among all the waves generated, the Rayleigh ones have the strongest energy.

Step 2: extraction of dispersion curves

The multichannel record is successively decomposed into swept frequency plots of time (t) versus source offset (x). The measurement of the slope (dx/dt) of each frequency component allows the calculation of the phase velocities of the waves and identification of un-wanted signals (Park et al., 1999; 2007). Dispersion curves, which are normally plots of phase velocity versus frequency, can be obtained through a automated wave-field transformation method [WWW 2.11]

Step 3: inversion of dispersion curves

When considering a layered earth model, the phase velocity of Rayleigh waves is a function of S- and P-wave velocities, density and layer thickness. However, for frequencies above 5 Hz, the phase velocity of Rayleigh waves is influenced mainly by V_s . Therefore, an inversion procedure can be applied to the dispersion curves to obtain V_s profiles (Xia et al., 1999).

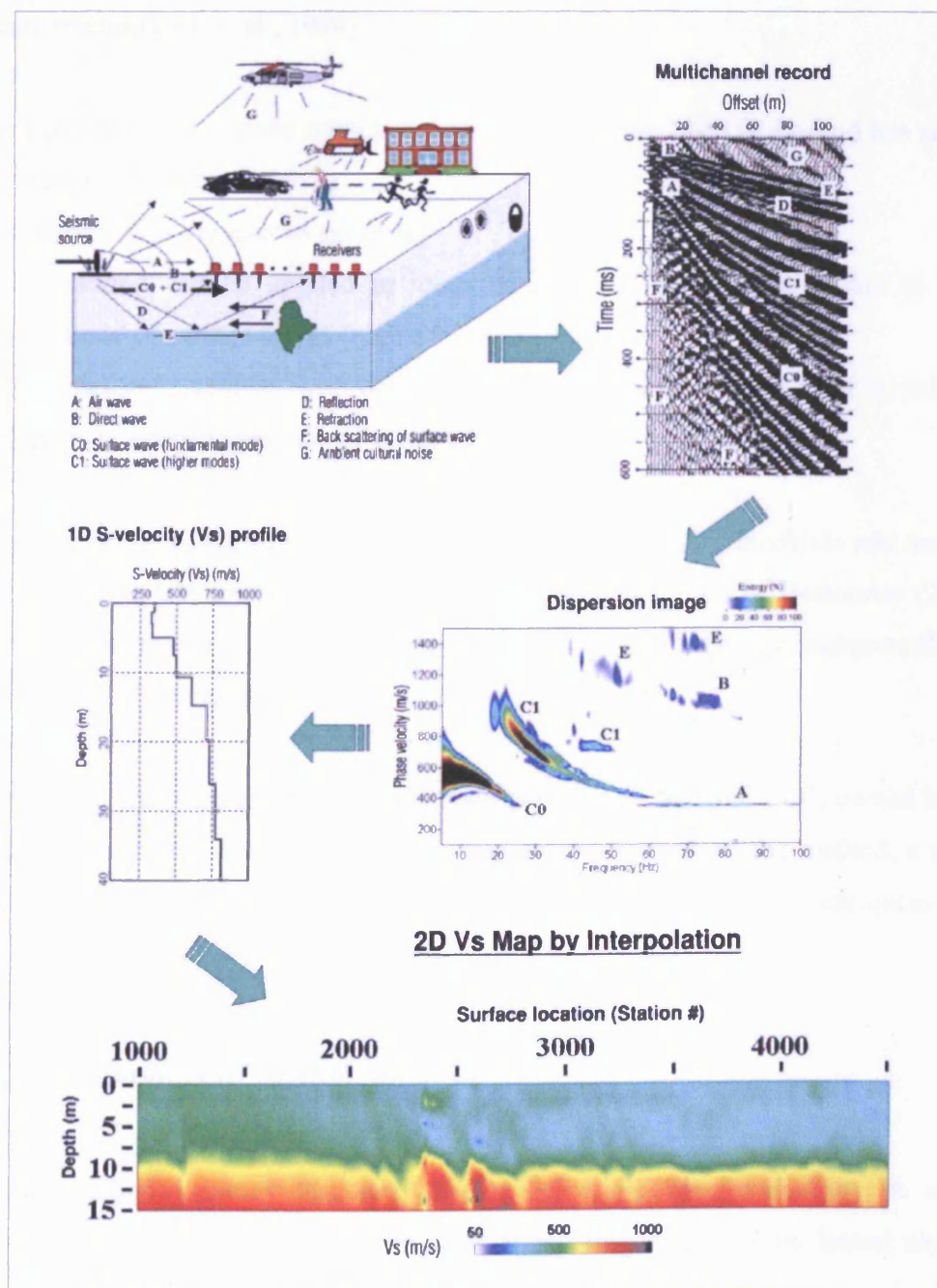


Figure 2.50 Illustration summarising the principles of MASW methodology (from Park et al., 2007)

When compared to surface waves methods based on the use of a single pair of receivers (spectral analysis of surface waves or SASW technique), multichannel recording offers the advantage of easy identification and elimination of un-wanted signals during extraction and analysis of dispersion curves. Moreover, multichannel acquisition is less time-consuming and improves data quality due to the redundancy of

measurements (Park et al., 1999).

When compared to seismic refraction and reflection, the MASW method has several advantages (Miller et al., 1999):

- surface waves are easy to generate;
- the method can be applied in areas of elevated cultural noise due to high-amplitude of surface waves (high S/N ratio);
- an increase in velocity with depth and/or the presence of a contrast in velocity, density or acoustic impedance is not required.

The applicability of the MASW method on Mynydd yr Eglwys landslide and on other sites across the UK was the subject of the master dissertation of Bottomley (2008). Therefore, the reader is referred to this for details on methodology background, data acquisition and processing.

Furthermore, the website [WWW 2.11] operated by Park Seismic LLC, owned by one of the inventors of the method, provides a good explanation of the method, a useful table with the latest recommended acquisition parameters and a list of references.

2.8.2 Limitations of MASW method

MASW method assumes that near-surface materials have variations in elastic properties that can be modelled with vertical layering and have no lateral changes (Park et al.; 1999).

Surface waves are best generated if the ground is flat within at least the length of a geophone spread. The technique is severely affected by a surface relief greater than 10% of the geophone spread [WWW 2.11].

Lateral changes in elastic properties and severe topography are expected on landslides. Therefore, care during MASW data acquisition should be taken in order to minimise these adverse conditions. However, site conditions could still be too severe for the method to be successful.

2.8.3 Seismic refraction tomography and MASW data acquisition at Mynydd yr Eglwys landslide

Seismic data were acquired along five profiles across the slope of Mynydd yr Eglwys landslide using a high-precision 48-channel GEODE seismic system and 10-Hz vertical geophones. The geophone spacing was 1 m and a 10-kg sledgehammer struck against a metal plate was used as a source. The surveys were performed by forward and reverse intra-spread and off-ends shots.

All profiles were deployed close to boreholes for data calibration. Furthermore, areas of relatively flat ground had to be selected as a requirement for MASW technique.

Line D was acquired only for seismic refraction on the 24th October 2006. Shots were deployed every 6 geophones and at off-ends of 10, 20 and 30 m and data were recorded after 5 stacks. Topography was surveyed with an EDM.

The other profiles (lines A, C, B and E) were carried out on the 14th of May and on the 14th of June 2008 for both seismic refraction and MASW. Therefore, shots were deployed (with usually only 1 to 3 stacks) at every geophone and at every metre from the start/end profile to 10 m off-end of the geophone spread. Additional far off-ends shots were deployed, with more stacks, for seismic refraction processing only. Surveying of the profiles was carried out with the Topcon HiPer Pro GPS.

Line B was acquired also with a 0.5 m spacing only for an assessment of the influence of geophone spacing on the quality of MASW results for Bottomley's project.

Table 2.14 Summary of seismic acquisition parameters

Line length	47 m
Geophone spacing	1 m (also 0.5 m for line B)
Source	Sledgehammer and plate
Geophone frequency	10 Hz
Sample interval	0.125 ms
Recording length	1 s



Figure 2.51 Acquisition of seismic refraction data along Line D at Mynydd yr Eglwys landslide (photos P. J. Brabham)

2.8.4 Data processing

Seismic refraction data were processed with PICKWIN and PLOTREFA software (modules of SeisImager/2D, of OYO Corporation).

PICKWIN was used to assign shot geometry and to determine first-arrival times. Identification of first-arrival times was often difficult for the traces close to the shot points, due to strong interference with air wave. Furthermore, very often the quality of the signal was poor for the farthest traces of the shots for lines A, B, C and E. Back-counting was applied when possible. These problems were probably due to the type of source (hammer-plate), the presence of pit at surface, site conditions (heterogeneity and high fracturing degree of the material) and the limited number of stacks selected for MASW.

PLOTREFA was used to analyse and invert the travel-time curves. Firstly, some quality checks were carried out on the travel-time curves:

- If a single travel-time appeared to be wrong it was checked again in PICKWIN and successively deleted or moved to a new position;

- Travel-time curves were shifted vertically across the screen to check for parallelism along sectors associated to the same refractor;
- The error between reciprocal times was calculated and checked to be low on the basis that the total travel-time measured between source and receiver in forward and reverse shots should be the same for the principle of reciprocity.

Successively, elevation data were imported in the software and an initial model for tomography inversion was generated. Tomography inversions were carried out and evaluated by comparison between theoretical and observed travel-time values with an iterative procedure.

Velocity lines were drawn on the travel-time curves to establish the values of apparent velocity for different sectors of the curves, and to evaluate the number of layers for each section. Such values were taken into consideration as input parameters when converting the contour velocity models into a layer model.

Attempts to convert the tomography inversion results into layers were made. However, contour models were judged to be more appropriate, due to the geology of the site.

Although line D was acquired with more stacks than the others and data quality seemed higher during picking of first arrivals, the line was characterised by the highest error during checking of reciprocal times and after inversion. Differences of reciprocal times when picking seemed real and were probably due to seismic waves travelling along different paths when shooting in forward and reverse direction in this area due to the relatively severe topographic effects and a complex geological model. There was a severe fall in topography between the last geophone and the reverse off-ends and the line may also cross a fault zone. Furthermore, the presence of very wet and fast material at shallow depth at the two farthest reverse off-ends caused travel-times from these two shots to be shorter than an intermediate off-end. Unfortunately, it was difficult to change the simple contour model of the software to match the real site conditions, leading to a higher error of inversion (RMSE approximately equal to 2.5), when compared to the other refraction lines.

MASW data were processed by Bottomley (2008) as part of his master dissertation, using the software SurfSeis 2.05 (Kansas Geological Survey).

2.9 Electrical resistivity tomography (ERT)

2.9.1 Background

For the acquisition of electrical resistivity tomography data, several electrodes are driven into the ground at a regular spacing and are after connected via multi-core cables to a central control unit. Apparent resistivity values are recorded for a combination of pairs of current and potential electrodes selected by the operator to produce a pseudo-section below the survey profile. The pseudo-section of apparent resistivity values can after be inverted to obtain a true resistivity section.

Low-frequency alternating current is injected into the ground through a pair of electrodes (C_1 and C_2) and potential difference is measured between another pair of electrodes (P_1 and P_2 ; Figure 2.52). The instrument measures the ratio (impedance, Z) between the current introduced into the ground (I) and the measured voltage (V). Impedance is a complex quantity with an amplitude or real part, and a phase or imaginary part. The amplitude is related to the bulk resistance of the ground (investigated by the ERT method), while the phase is associated to the chargeability or energy storage capacity of the ground (investigated by the IP method; Zonge et al., 2005). Resistivity is a measure of the bulk resistance, normalized for length and cross-sectional area and is measured in Ohm.m.

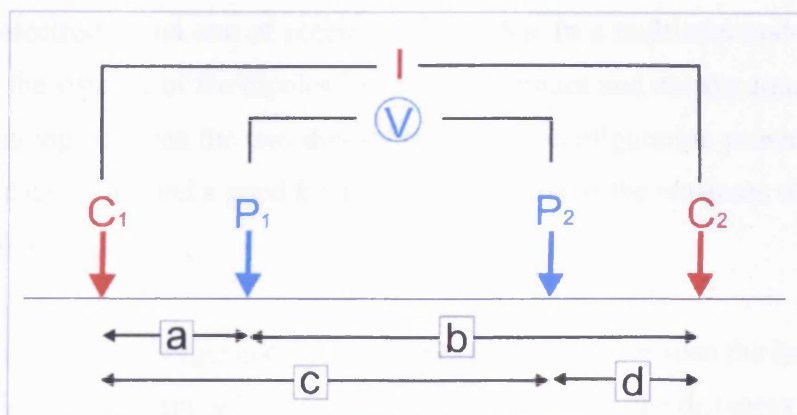


Figure 2.52 Schematic diagram of a generic electrode configuration

For a generic electrode array (Figure 2.52), the value of apparent resistivity (ρ_a), which is the value of resistivity for a ground assumed to be homogenous and isotropic, is equal to:

$$\rho_a = 2\pi \frac{V}{I} \frac{1}{\left(\frac{1}{a} - \frac{1}{b} - \frac{1}{c} + \frac{1}{d} \right)} \quad \text{Eq. 2.35}$$

The quantities a , b , c and d depend on the geometry of the electrode array.

Electrode arrays

Figure 2.53 shows three of the most widely used electrode arrays: Wenner, Wenner-Schlumberger and Dipole-Dipole.

In the Wenner configuration four electrodes are uniformly spread at a constant spacing (a), with potential electrodes positioned between the current ones. For a multi-electrode acquisition, greater depths are investigated by increasing the electrode spacing. The number of readings is quite limited. This array is recommended for the investigation of vertical layered changes but has a low resolution in terms of lateral changes (Hack, 2000; George, 2006).

In the Dipole-Dipole configuration data are acquired from two separate dipoles, one

of current electrodes and one of potential electrodes. In a multi-electrode acquisition procedure, the spacing of the dipoles (a) is kept constant and always equal or smaller than the spacing between the two dipoles (na). This configuration provides a greater number of data points and a good lateral resolution, but at the expenses of penetration depth (George, 2006).

In the Wenner-Schlumberger configuration the spacing (a) between the inner potential electrodes is kept constant, while increasing logarithmically the distances between the current and the potential electrodes (na), with an improvement in data resolution (George, 2006).

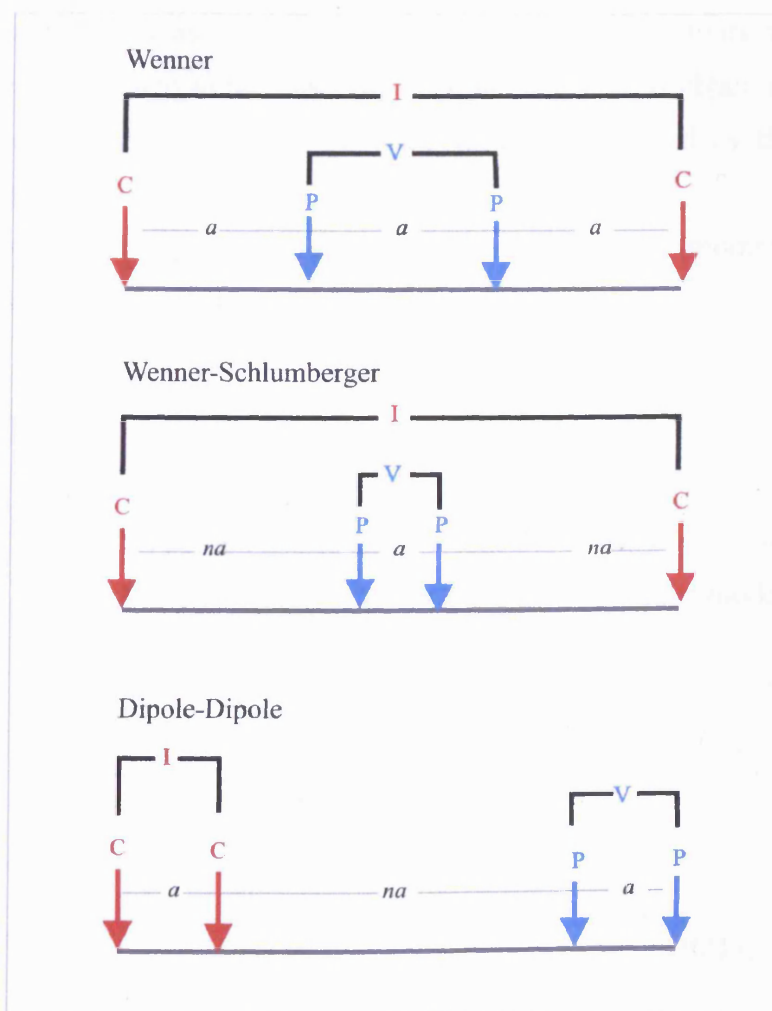


Figure 2.53 Schematic diagram illustrating Wenner, Wenner-Schlumberger and Dipole-Dipole electrode configurations

During multi-electrode acquisition, data are measured according to the selected array configuration for different values of current-potential electrode spacings (n) (Figure 2.54). The measured values are then plotted according to the value of n and the horizontal position of the centre of the operating electrodes to obtain a pseudo-section (Figure 2.54). The term “pseudo” is adopted to underline that the values are measurements of apparent and not true resistivity and are plotted in a location that is only conventional.

In order to obtain a true resistivity section, measurements need to be inverted. For example, in the software RES2DINV (Geotomo Software) used for this project, the measurements of the pseudo-section are used to build a 2D model block of resistivity values. The model is iteratively inverted to obtain apparent resistivity measurements, which are then compared to the observed data and adjusted to obtain a best fit. The difference between theoretical and observed value is described by the root-mean-squared error (RMS).

The inversion routine applied by the software is based on the smoothness-constrain least-squares method and therefore on the equation:

$$(J^T J + uF)d = J^T g \quad \text{Eq. 2.36}$$

where $F = f_x f_x^T + f_z f_z^T$, f_x is the horizontal flatness filter, f_z is the vertical flatness filter, J is the matrix of partial derivatives, u is the damping factor, d is the model perturbation vector and g is the discrepancy vector.

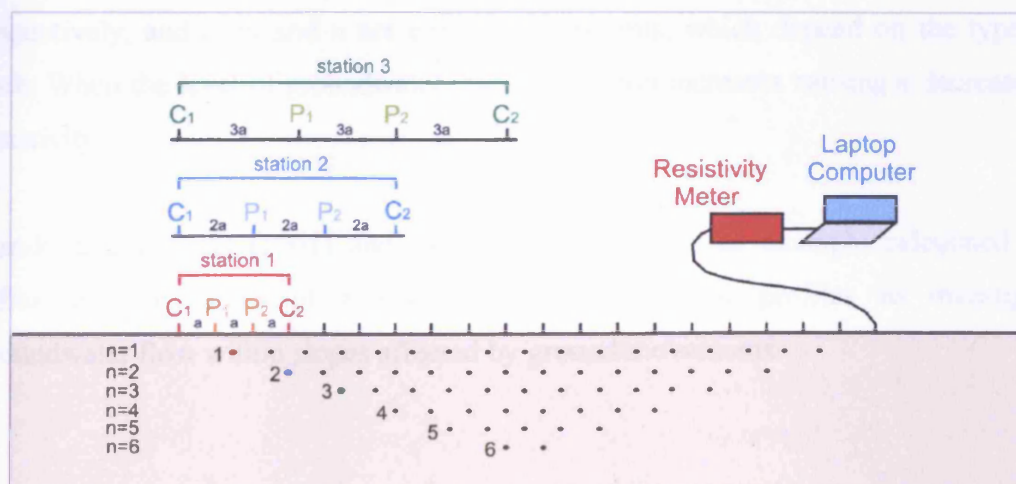


Figure 2.54 Acquisition of multi-electrode data and their arrangement to obtain a pseudo-section (modified from RES2DINV software manual)

Method applications and resistivity values

As already explained for the EMI method, variations in resistivity (or conductivity) can be related to changes in water/fluid content, water/fluid conductivity, porosity, permeability, fracturing degree and lithology (i.e. clay content). Unfortunately, as shown in Figures 2.40 and 2.41 the same lithology can have a wide range of resistivity values and there are significant overlaps between different lithologies. Therefore resistivity alone is not a good indicator of lithology. There are numerous examples in the literature of applications of resistivity methods to map these changes in resistivity for environmental and engineering studies.

Due to the strong influence of porosity and degree of water saturation on resistivity values, ERT has been applied also for the monitoring of groundwater flow at different hydrogeological stages (i.e after heavy rainfall).

For the vadose zone, the relationship between the resistivity of a layer (ρ_R) and the resistivity of the pore water (ρ_W) is described by Archie's law (Suzuki and Higashi, 2001):

$$\rho_R = a\phi^{-m}S^{-n}\rho_W \quad \text{Eq. 2.37}$$

where ϕ and S are the effective porosity and the saturation of the medium

respectively, and a , m and n are empirical constants, which depend on the type of rock. When the level of groundwater rises, saturation increases causing a decrease in resistivity.

Suzuki and Higashi (2001) and Jomard et al. (2007) for example calculated the differences in values of resistivity between repeated profiles to investigate groundwater flow within slopes affected by ground movements.

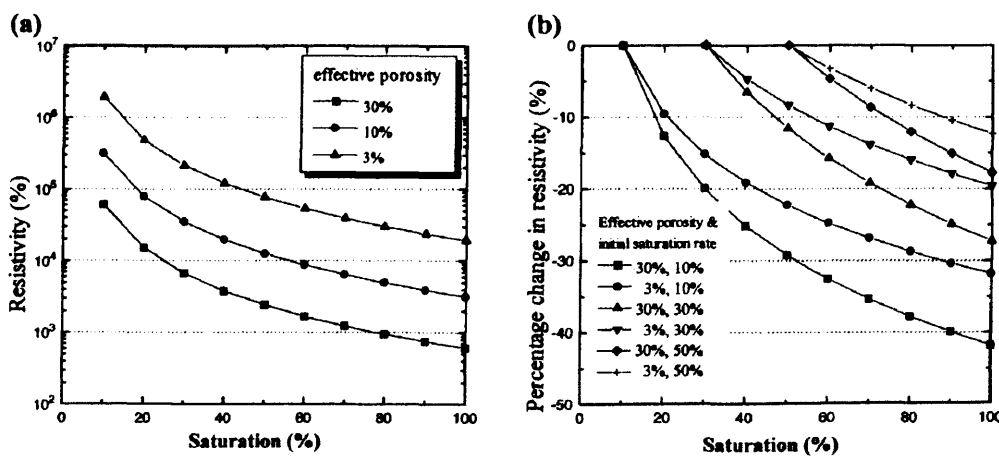


Figure 2.55 Graph (a) shows the decrease in bulk resistivity associated to an increase in saturation from 10 to 100% and for three different values of effective porosity (3%, 10% and 30%). Graph (b) shows the decrease in resistivity in terms of percent changes. The diagrams were obtained by Suzuki and Higashi (2001) applying Archie's law and considering the percentage change in resistivity equal to $\Delta\rho = [\log_{10}\rho - \log_{10}\rho_0] / \log_{10}\rho_0$ for $m=1.5$ and $n=2.0$

2.9.2 Limitations

Measurements are negatively affected by a poor contact with the ground and by the presence of metal features and services.

Depth of penetration depends on the maximum value of electrode spacing, causing possible site constraints.

Greater depths are achieved at the expenses of resolution, which is determined by the

minimum electrode spacing.

2.9.3 ERT data acquisition at Mynydd yr Eglwys landslide

Several ERT profiles were acquired at Mynydd yr Eglwys Landslide from the 26th January 2006 till 10 December 2008. All the profiles were acquired using a 72-channel IRIS SYSCAL resistivity system, a maximum of 72 electrodes and a minimum electrode spacing of 2 or 5 m (Figure 2.56). The profiles were generally acquired using Wenner-Schlumberger electrode array and stainless steel electrodes. Copper rods and dipole-dipole array were used when profiles were acquired also for IP measurements.

Some of the lines were repeated in time for monitoring purposes. The lines were generally marked with wooden pegs to facilitate correct electrode repositioning. However, to improve precision, permanent electrodes (steel tent pegs) were driven almost completely into the ground for monitoring lines X, Y and Z.

Care was taken to check for a good and relatively uniform contact of the electrodes with ground ($< 3\text{--}4$ kohm). Due to stony and dry condition of the ground in some areas of the landslide, water was used to try to lower the value of resistance. Salty water was not used to not compromise reading comparisons.

The lines were deployed across and along the slope according to site constraints and close to boreholes for data calibration. Only one line (line 14s) was deployed in SW-NE direction in order to be perpendicular to the Cymmer Fault.

Surveying of the lines was carried out initially with an EDM and after always with Topcon HiPer Pro GPS+.

Tables 2.15 and 2.16 provide a summary of all the lines acquired on site. As a convention the letters “L” and “s” in the name of the lines indicate Large (5 m) and small (2 m) minimum electrode spacing respectively.

At the end of each field work day, data were downloaded and quality checked with

the software Prosys (IRIS Instruments).

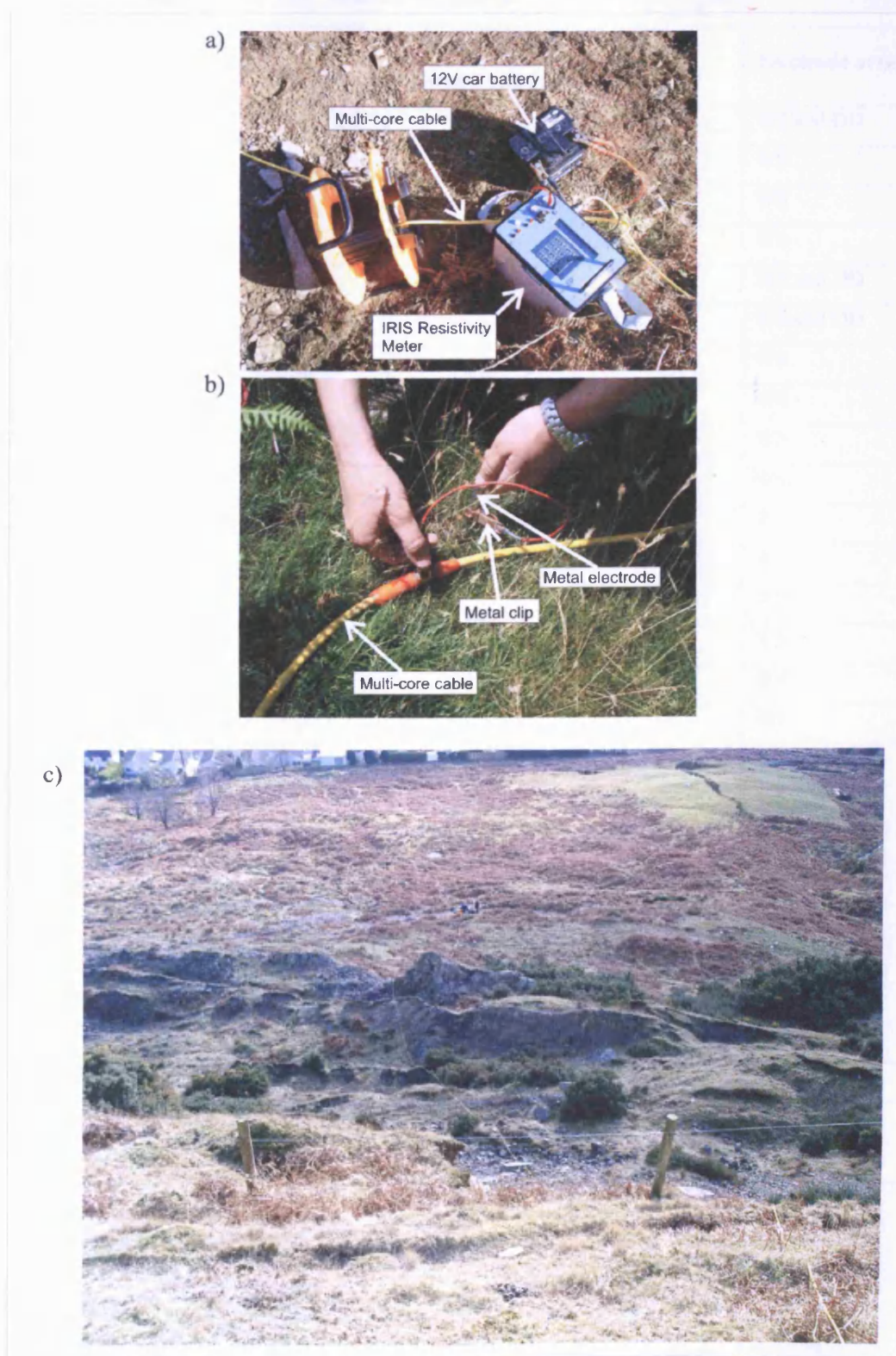


Figure 2.56 Acquisition of ERT data at Mynydd yr Eglwys Landslide (photo c by N. Ross)

Table 2.15 Summary of ERT profiles acquired at Mynydd yr Eglwys

Line	Electrode Spacing (m)	Length (m along ground)	Date	Electrode array*
1L	5	355	26 Jan 06	WS and DD
			17 Jul 06	WS
			13 Dec 06	WS
			20 Feb 07	WS
			03 May 07	WS and DD
			01 Feb 08	WS and DD
1s	2	142	19 Jul 06	WS
			20 Dec 06	WS
2s (test line)	5	175	26 Jan 06	WS
3L	5	265	05 May 06	WS
4L	5	295	18 Jul 06	WS
5s	2	142	19 Jul 06	WS
			20 Dec 06	WS
			26 Jun 08	WS
			24 Oct 08	WS
6L	5	250	13 Dec 06	WS
6s	2	142	20 Jul 06	WS
7L	5	235	14 Dec 06	WS
7s	2	142	25 Jul 06	WS
			20 Dec 06	WS
8L	5	265	18 Dec 06	WS
8s	2	142	18 Dec 06	WS
9L	5	265	20 Mar 07	WS
9s	2	142	28 May 08	WS
10s	2	70	20 Feb 08	WS and DD
13s	2	142	26 Jun 08	WS
			24 Oct 08	WS
14s	2	142	28 Nov 08	WS and DD

* WS= Wenner-Schlumberger and DD= Dipole-Dipole

Table 2.16 Summary of ERT profiles acquired with permanent electrodes

Line	Electrode Spacing (m)	Length (m along ground)	Date	Electrode array*
X	2	142	2 Jun 08	WS
			13 Jun 08	WS
			14 Jul 08	WS
			17 Jul 08	WS
			22 Aug 08	WS
			27 Aug 08	WS
			10 Dec 08	WS
Y	2	106	02 Jun 08	WS
			14 Jul 08	WS
Z	2	142	13 Jun 08	WS
			14 Jul 08	WS

* WS= Wenner-Schlumberger and DD=Dipole-Dipole

2.9.4 ERT data processing

ERT data were firstly analysed with the software Prosys (Iris Instruments). Data with a standard deviation greater than 3 and data with negative values of resistivity were deleted from the datasets. Furthermore, topography was assigned to each electrode.

The profiles were successively inverted into resistivity profiles with the program RES2DINV (Geotomo Software), choosing a refined model with a cell equal to half electrode spacing.

The values of resistivity were then exported and gridded in Surfer 7 (Golden Software).

To quantify and evaluate the resistivity changes in time between repeated profiles, each resistivity monitoring profile was firstly exported from RES2DINV in xyz format. Secondly the resistivity differences between the analysed profile and the reference profile were calculated in Excell (Microsoft) for each cell (X, Y) in common. For a profile acquired at time $t1$, the resistivity difference in relation to the

reference profile acquired at time t_0 , could be described as:

$$(X, Y, \Delta\rho) = (X, Y, \rho_{t_1}) - (X, Y, \rho_{t_0}) \quad \text{Eq. 2.38}$$

The differences in resistivity were gridded afterwards in surfer to obtain contour plots representing increase/decrease in resistivity when compared to the reference profile.

Calibration experiments carried out by Rahman Yaccup (Cardiff University) as part of his PhD project have revealed that the IRIS resistivity meter used for the field work of this project reads values 1.85 times higher than a calibrated reference solution. This information was provided only at the end of this project, therefore the value of the colour scale of the ERT profiles here presented have been simply divided by this value. The correction was instead applied to the values of resistivity of the monitoring profiles before calculating the value of resistivity differences. All resistivity data collected throughout this project have an internal consistency as the same IRIS instrument was used.

2.10 Induced Polarization (IP)

Induced polarization surveys can be carried out with the same system used for ERT data acquisition, although the use of non-polarizing electrodes is generally recommended. The instrument must be able to provide an additional parameter which describes the chargeability or the energy storage capacity of the ground (Zonge et al., 2005).

IP measurements can be carried out in time or in frequency domain:

Measurements in time

If the injection of current into the ground is interrupted, the voltage measured between two electrodes may not drop immediately to zero, but decays in time. The decay of voltage can be measured at one or more different times after current cut off to

determine IP effect, expressed in terms of apparent polarizability or apparent chargeability (Figure 2.57; Parasnis, 1997).

If the current is cut off and a decay in voltage (ΔV_t) is measured at the time t , apparent polarizability is defined as the ratio between ΔV_t (expressed in mV) and the value of the voltage just before current cut off, V_0^T (expressed in V):

$$(P_t^T)_a = \frac{\Delta V_t}{V_0^T} \quad \text{Eq. 2.39}$$

Apparent chargeability is instead the normalized time integral of the area below the decay curve between two times t_1 and t_2 , after the current has been cut off:

$$(M_{t_1, t_2}^T)_a = \frac{1}{V} \int_{t_1}^{t_2} \Delta V_{IP} dt \quad \text{Eq. 2.40}$$

and is measured in milliseconds (ms).

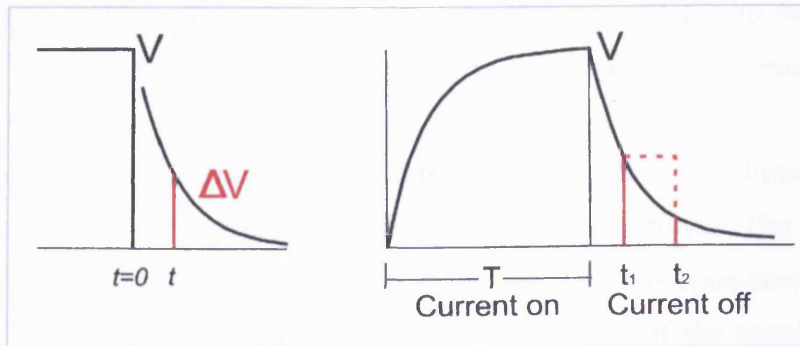


Figure 2.57 Schematic diagrams illustrating determination of apparent polarizability and apparent chargeability (Parasnis, 1997)

Measurements in frequency

In frequency domain, the instrument measures the value of apparent resistivity at two different frequencies, f and F . The IP value can then be expressed in terms of apparent frequency effect as (Parasnis, 1997):

$$(FE_{F,f})_a = \frac{\rho_a(f) - \rho_a(F)}{\rho_a(f)} \quad \text{Eq. 2.41}$$

or as metal factor:

$$(M_{F,f})_a = \frac{\rho_a(f) - \rho_a(F)}{\rho_a(f)\rho_a(F)} \quad \text{Eq. 2.42}$$

Moreover, IP effect can be determined from the phase difference between the voltage measured at electrodes P_1 and P_2 and the current injected into the ground.

Origin of IP effects

IP effects can be caused by two mechanisms (Telford et al., 1990; Parasnis, 1997; Zonge et al., 2005):

- Membrane polarization (Figure 2.58, left). Rock minerals, mostly clays, have a negative charge at the contact with the pore fluid and as a consequence they attract positive ions. When a current is applied, a preferential distribution of ions in the electrolyte develops as negative ions cannot pass through the zone of positive ions accumulation. When the current is switched off the ions move to return to their original position of equilibrium producing a residual current and therefore a decay of voltage in time;
- Electrode polarization (Figure 2.58, right). Metallic grains distributed within the rocks can act as metal electrodes immersed in an electrolyte. The presence of charges of opposite sign at the surface of the metal causes extra-accumulation of ions in the area of the electrolyte close to the surface of the metal. When the current is turned off, the charges return slowly to their original position of equilibrium, characterised by only a thin layer of negative ions fixed to the surface of the metal.

As both membrane and electrode polarization are surface effects, the values of IP will be greater for clay and particles diffused into the rock.

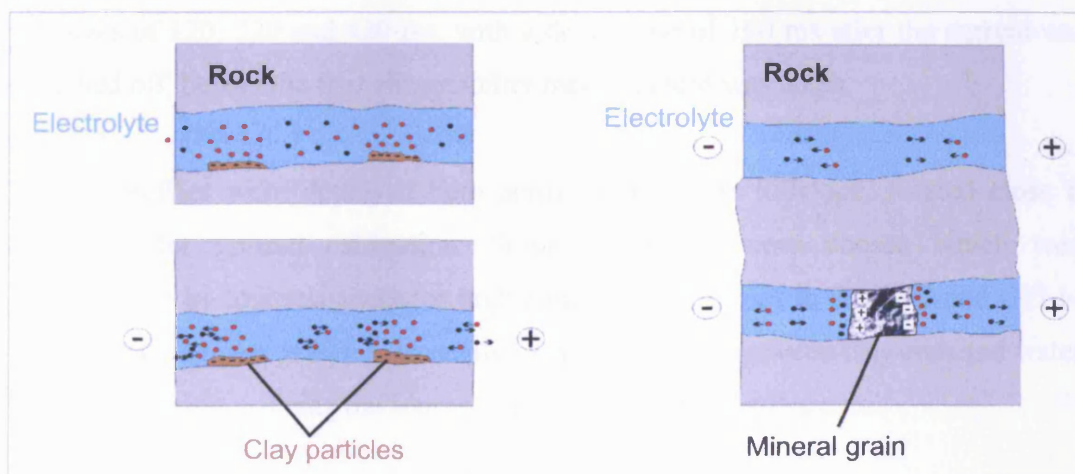


Figure 2.58 Membrane (left) and electrode polarization (right; modified from Telford et al., 1990)

The IP method has been widely used in mineral exploration. More recently it has been applied to environmental studies to map for example landfills and contaminated plumes (Zonge et al., 2005). Some of the materials that can cause IP anomalies and can as a consequence be investigated using this technique are listed in Table 2.17.

Table 2.17 Materials that can cause effect on IP measurements (Zonge et al., 2005)

Layered silicates, clays, alteration products (i.e. montmorillonite, illite, kaolinite, chlorite)
Metallic luster minerals (i.e. pyrite, chalcopyrite, pyrrhotite, galena and graphite)
Organic materials, green waste and anoxic carbon-rich deposits
Municipal waste (due to metallic debris, green waste, etc.)
Other minerals (ilmenite, hematite, etc.)

2.10.1 Data acquisition and processing

Seven Induced Polarization (IP) tomographic profiles were acquired at Mynydd yr Eglwys landslide between February and November 2008 (Table 2.18). All profiles were acquired with the same IRIS SYSCAL instrument as employed for the ERT surveys. Measurements were carried out in the time domain and provided IP data as the apparent chargeability of the ground (in mV/V). The current injection time was 1000 ms and the voltage decay curve was approximated from the three preset IP time

windows of 120, 220 and 420 ms, with a delay time of 160 ms after the current was switched off, before the first chargeability measurement was taken.

The IP profiles were deployed both across and up the hillslope, located close to boreholes for ground calibration. Survey locations were chosen which were characterised by low resistivity (or high conductivity) values in the ERT and GEM-2 results, with the aim of trying to resolve any ambiguity between clay-rich and water-bearing materials as being the source of such conductivity anomalies.

Non-polarizing electrodes are recommended for IP surveys rather than steel electrodes. 36 plastic gardening pots containing a jelly mix of saturated copper sulphate solution with a copper wire immersed into it and holes in their base to make ground contact were constructed for this project (Figure 2.59). These Copper Sulphate jelly electrodes were used for the acquisition of IP data with both Dipole-Dipole and Wenner-Schlumberger electrode configuration along test line A. The same survey line was also acquired using conventional copper rod electrodes, in order to compare data collected with both electrode types and array configurations.



Figure 2.59 IP non-polarizing electrodes built for this project, using gardening pots, copper wire, copper sulphate and jelly. The jelly was not completely set and sponges were put inside the pots, at their base, to insure contact of the jelly with the ground, but without emptying the pot

In June 2008 tent pegs were also installed and used for the monitoring of three ERT profiles. An IP test was carried out along line Y to obtain chargeability measurements but also to compare data collected using copper rods and tent pegs in both Wenner-Schlumberger and Dipole-Dipole electrode configurations. All the remaining IP

profiles were acquired using Dipole-Dipole electrode configuration and, with the exception of IP line X, also with copper rods.

Ground contact resistances were generally good and relatively uniform for all the electrode types employed (< 2-3 k ohm). If any individual electrode displayed very high contact resistances, water was then used to lower the values of the contact resistance.

Topographic surveying of the lines was carried out with the Topcon HiPer Pro GPS+.

Table 2.18 IP tomography profiles acquired at Mynydd yr Eglwys landslide

Line name	Electrode Spacing (m)	Length (m along ground)	Date (in 2008)	Type of Electrodes	Array configuration*
IP test A (along ERT 1L)	2	70	08 February	Jelly pots	DD
				Jelly pots	WS
				Copper rods	DD
				Copper rods	WS
IP 1 central (along ERT 1L)	2	142	19 February	Copper rods	DD
IP X	2	142	17 July and 27 August	Tent pegs	DD
IP Y (first 36 electrodes of ERT Y)	2	70	18 July	Copper rods	DD
				Copper rods	WS
				Tent pegs	DD
				Tent pegs	WS
IP 10	2	70	20 February	Copper rods	DD
IP 13s (last 36 electrodes of ERT 13s)	2	70	24 October	Copper rods	DD
IP 14s	2	106	28 November	Copper rods	DD

* WS= Wenner-Schlumberger and DD=Dipole-Dipole

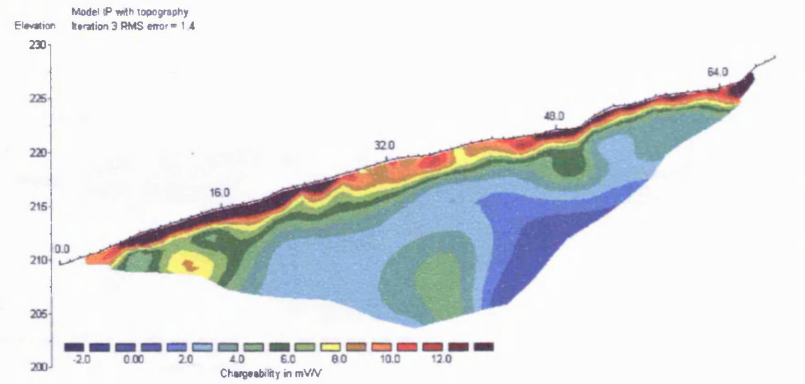
At the end of each field day, data were downloaded and quality checked with the software Prosys (IRIS Instruments). The data files contained information on both resistivity and chargeability. Data with a standard deviation greater than 3 and data with negative values of resistivity were deleted from the datasets, as well as data with isolated noisy chargeability values. Furthermore, topographic data were assigned to each electrode point.

The IP lines were successively inverted into true chargeability profiles with the

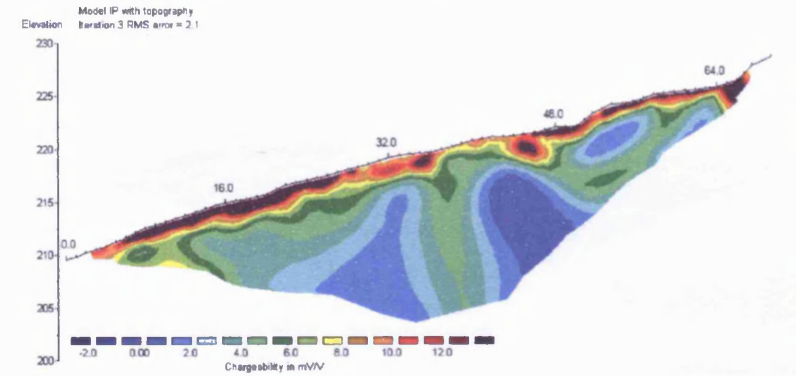
program RES2DINV (Geotomo Software), choosing a refined model with a cell equal to half electrode spacing. The software has the option to invert combined resistivity and IP datasets concurrently for each iteration or to invert IP data after (or 'sequentially') the completed inversion of resistivity data. Both options were tested, but without any noticeable differences in the IP final sections. Therefore only the results of concurrent inversion will be shown in the thesis.

Figures 2.60 and 2.61 show the chargeability sections obtained for IP test line A and IP line Y, acquired with different types of electrodes, with both Dipole-Dipole and Wenner-Schlumberger electrode configurations. Already during editing in Prosys, the datasets appeared of good quality and a very limited number of points were edited out. This is confirmed by the low RMS values of the chargeability sections (ranging from 0.33 to 2.1 %). Also the values of chargeability are very similar and for the same electrode configuration, the difference in chargeability measured with different kind of electrodes is minimal (of the order of 1-2 mV/V). The slight difference in the shape of the green contours in the central area of the test line A could be due to one or more faulty jelly pot electrodes. There is a clear difference due to a change in electrode configuration. The Dipole-Dipole one was considered more reliable only after comparing the IP results with the ones obtained from other geophysical techniques.

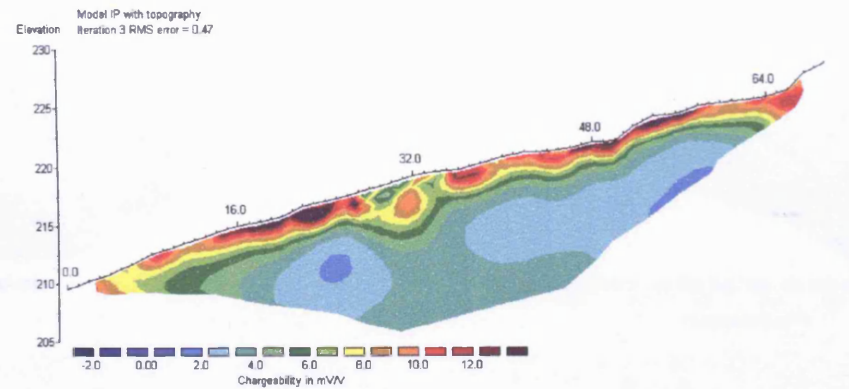
Copper Rods, Dipole-Dipole configuration



Jelly Pots, Dipole-Dipole configuration

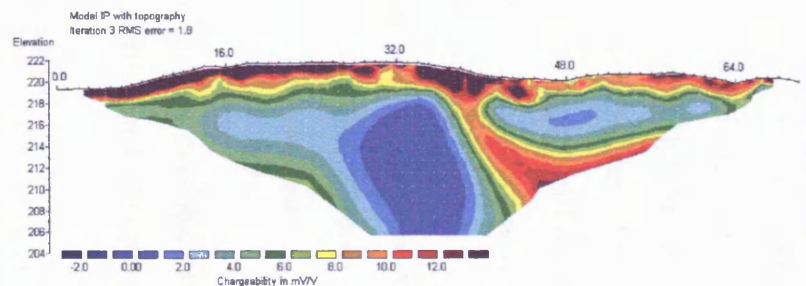


Jelly Pots, Wenner-Schlumberger configuration

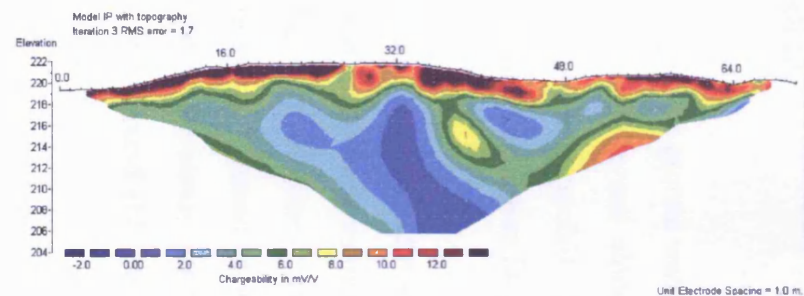


189 *Figure 2.60 Chargeability sections for IP test Line A, acquired with copper rods and jelly pots in Dipole-Dipole configuration and with jelly pots in Wenner-Schlumberger electrode configuration*

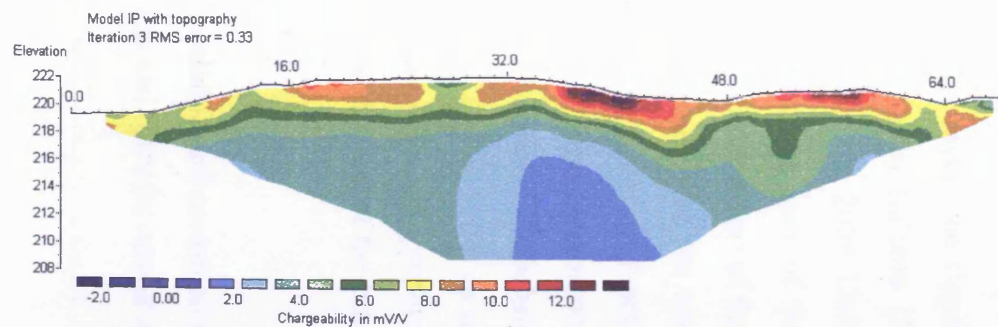
Copper Rods, Dipole-Dipole configuration



Tent pegs, Dipole-Dipole configuration



Copper Rods, Wenner-Schlumberger configuration



Tent Pegs, Wenner-Schlumberger configuration

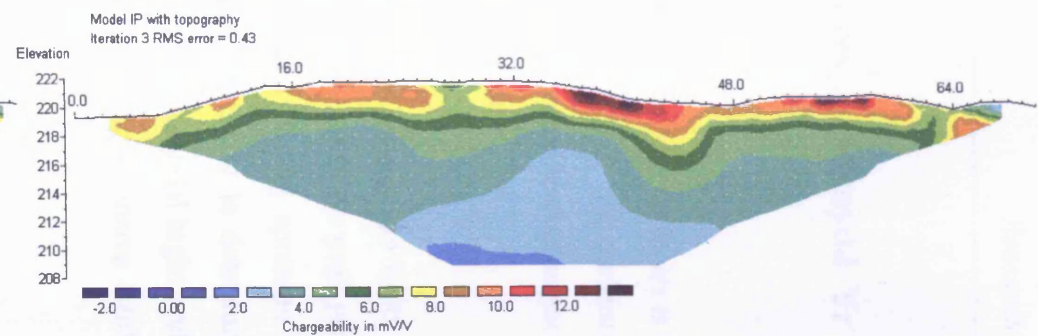


Figure 2.61 Chargeability sections for IP Line Y, acquired with copper rods and tent pegs, in both Dipole-Dipole and Wenner-Schlumberger electrode configurations

2.11 Monitoring of groundwater pressures at Mynydd Yr Eglwys landslide

The monitoring of the ground water pressures acting on the slip surface/s is necessary for landslide modelling and slope stability analyses and for the understanding of groundwater response to rainfall. Moreover, monitoring water level changes inside the slope could provide calibration for geophysical survey data.

Water levels can be measured manually with dip meters during site visits or can be recorded continuously using automatic data acquisition systems. As peak groundwater levels can be very transitory, they are often missed during sporadic (typically monthly) site visits. Continuous measurements are important to determine the lag between rainfall and groundwater response, to determine seasonal highs and lows and the intensity of the rapid changes in water levels following intensive rainfall events (Cornforth, 2005).

Halcrow UK provided some information on water levels inside the slopes of MYE landslide. Manual readings of water levels were carried out by Halcrow UK at eight standpipes located at the toe of MYE landslide from December 2000. Unfortunately, the readings were discontinued in October 2004, before the start of this project. Moreover, Halcrow installed two data loggers on the south-west part of the landslide in December 2000. Unfortunately, these loggers are remote from the main area of interest, their datasets present several data gaps due to instrument malfunctioning and one of the two stopped working in May 2006. At MYE Landslide, vibrating wireline and standpipe piezometers were also installed in 11 boreholes on behalf of Earth Science Partnership (2004). The water levels provided (up to 2004) in their report were considered for the desk study and for the calibration of geophysical data, although the lack of consistency in the lithological descriptions of the borehole logs raised some serious concern.

It was noted that the available rainfall data were unreliable and contained many data gaps. Incomplete or not fully reliable rainfall datasets and sporadic manual dipping of

boreholes were just not providing the necessary information to calibrate geophysical monitoring data and slope movement against rainfall. It was therefore decided to install two automatic data loggers before starting the last phase of resistivity monitoring using permanent electrodes at MYE landslide. A third logger became available from another project later in time and was also added to the network. No new boreholes were drilled for this purpose and there was only a limited choice of available undamaged boreholes that were known to contain water.

A Mini-Diver and a Baro-Diver (manufactured by Schlumberger Water Services) were installed in borehole 6 and another Mini-Diver was installed in borehole 3 on the 30th of May 2008. A CTD-Diver (manufactured by Van Essen Instruments, a Schlumberger Company) was installed in borehole 11 on the 27th August 2008 (when it became available from another project). At the moment of writing, the loggers are still on site, but readings are considered up to 20th May 2009, the date of the last data download.

The instruments

Both the Mini-Diver and CTD-Diver measure and monitor water level and groundwater temperature. The CTD-Diver measures also electrical conductivity. The sensors are housed inside their strong cylindrical casing together with battery and internal memory.

The water level is measured with a built-in pressure sensor. When the Diver is above the water table, it measures atmospheric pressure (as a barometer or as a Baro-Diver). When below the water surface, it measures the atmospheric pressure plus the pressure of the column of water above the pressure sensor. A Baro-Diver (at least one in an area of 15 km of radius, according to site conditions) is used to measure the atmospheric pressure variations necessary to compensate water pressure readings.

Pressure is provided in cmH₂O. The relationship between pressure in mbar and pressure in cmH₂O is:

$$1 \text{ cmH}_2\text{O} = 0.980665 \text{ mbar or } 1 \text{ mbar} = 1.01972 \text{ cmH}_2\text{O}$$

Temperature is measured with a semi-conductor sensor. Temperature can be helpful

to determine groundwater flow and is also used to eliminate the effects of temperature variations on pressure readings.

Electrical conductivity (only for CTD-Diver) is measured using a four-electrode measuring cell.

Divers are available for several ranges of water pressure. The technical specifications of the ones used for this project are reported in Table 2.19.

Table 2.19 Technical specifications for the Mini-Divers (20 m water range) and the CTD-Diver (30 m water range) used to monitor water levels at Mynydd yr Eglwys landslide (Instruments manuals)

Technical specifications		Mini-Diver (DI 502)	CTD-Diver (DI 263)
Dimensions		Ø22 mm x 90 mm	Ø22 mm x 183 mm
Memory		24,000 measurements	16,000 measurements
Sample rate		0.5 sec to 99 hours	0.5 sec to 99 hours
Housing material		Stainless steel 316L	Ceramic (ZrO ₂)
Pressure sensor material		Aluminium oxide (Al ₂ O ₃)	Aluminium oxide (Al ₂ O ₃)
Temperature	Range	-20 °C to 80 °C	-20 °C to 80 °C
	Accuracy	±0.1 °C	±0.1 °C
	Resolution	0.01 °C	0.01 °C
Conductivity	Range	Not applicable	0 to 80 mS/m
	Accuracy	Not applicable	±1% of reading
	Resolution	Not applicable	0.1% of reading
Pressure	Range	20 m H ₂ O	30 m H ₂ O
	Accuracy	1 cm H ₂ O	3 cm H ₂ O
	Resolution	0.4 cm H ₂ O	0.6 cm H ₂ O
Battery life		10 years (depending on use)	10 years (depending on use)
Weight		Approx. 70 grams	Approx. 150 grams

Data acquisition

The software package Logger Data Manager, running on Windows XP and provided with the loggers, was used to start the Divers, to change their settings (i.e. sampling interval), to download data on site, to check downloaded data and to quickly compensate for air pressure variations. The Divers have a suspension eye that can be unscrewed to reveal an optical connector. This connector is inserted into a reading unit to allow interfacing between the logger and the computer and data download

(Figures 2.63 and 2.64). Sampling interval was set to one reading per hour.

The Baro-Diver was suspended above water surface in borehole 6, the Mini- and CTD-Divers below water surface in boreholes 6, 3 and 11, using ropes. The length of the rope was measured before installation, but was also checked for eventual stretching in several occasions by comparing the logger readings with manual readings (carried out with dip metres when on site for data download). The length of the rope (L_{rope}) is equal to the height of the water column measured above the Diver sensor (L_{water}) plus the water level measured with the dip meter from the reference level (Figure 2.62). All the measurements were referred to the same point: the top of the plastic pipe inside the boreholes.

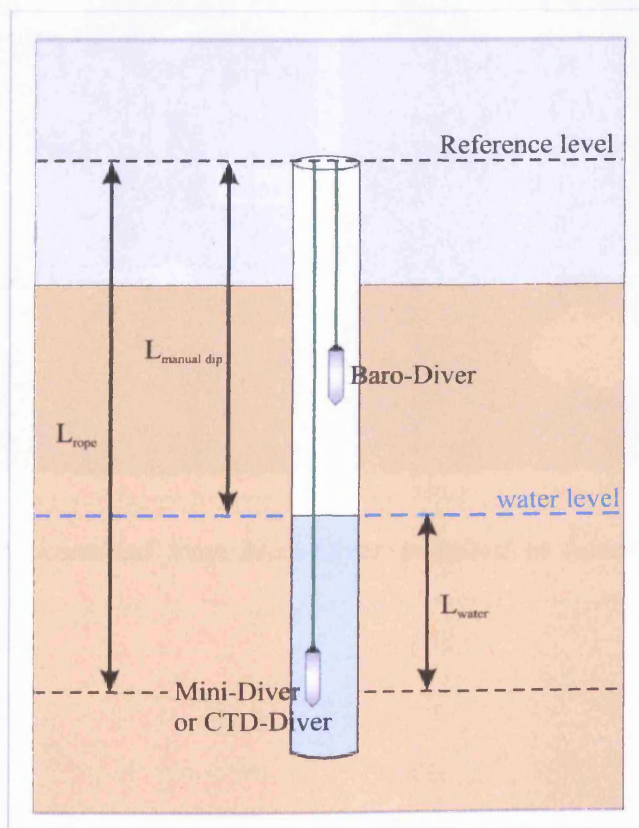


Figure 2.62 Schematic diagram showing installation of Divers inside a borehole and the values necessary to correct the water level readings to a reference point (modified from instrument manual)

Elevations of the top of casing or of the ground level at boreholes were surveyed with the dual-frequency Topcon HiPer Pro GPS+ in RTK mode. Corrections were after

applied to obtain the elevation of the reference point (the top of the internal pipe). The value of water level AOD could then be calculated using the following equation:

$$\text{Water level (AOD)} = \text{Elevation}_{\text{reference point}} - L_{\text{rope}} + L_{\text{water}}$$

Figure 2.63 and 2.64 show data downloading from Mini- and CTD-Divers on site.

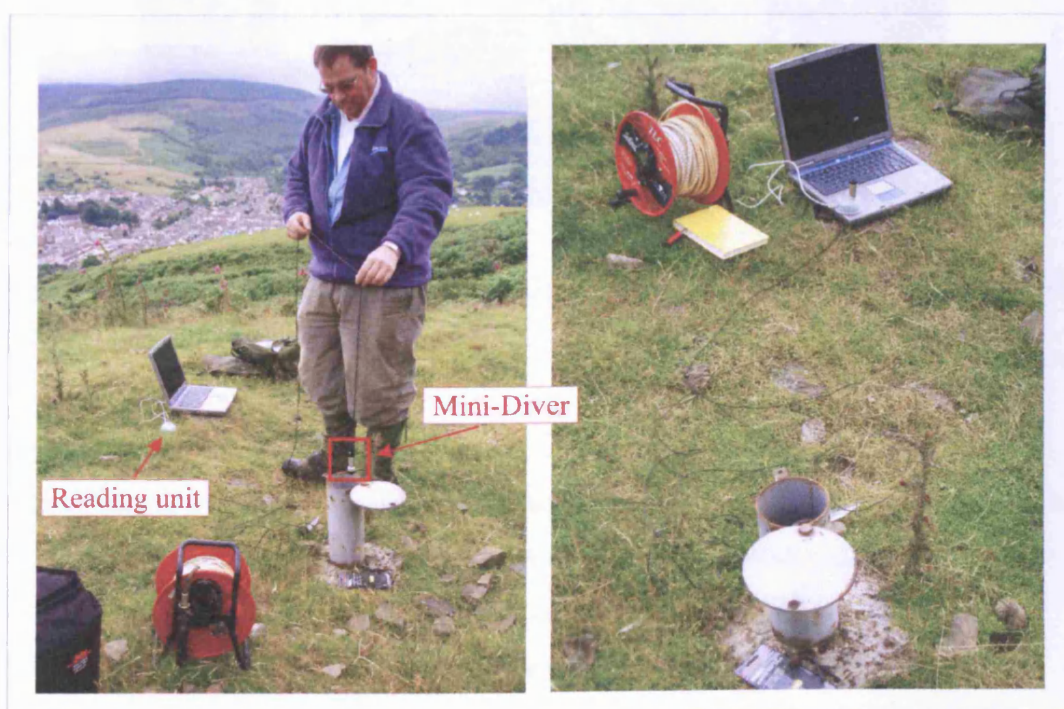


Figure 2.63 Data download from Mini-Diver installed in borehole 3 at Mynydd yr Eglwys landslide

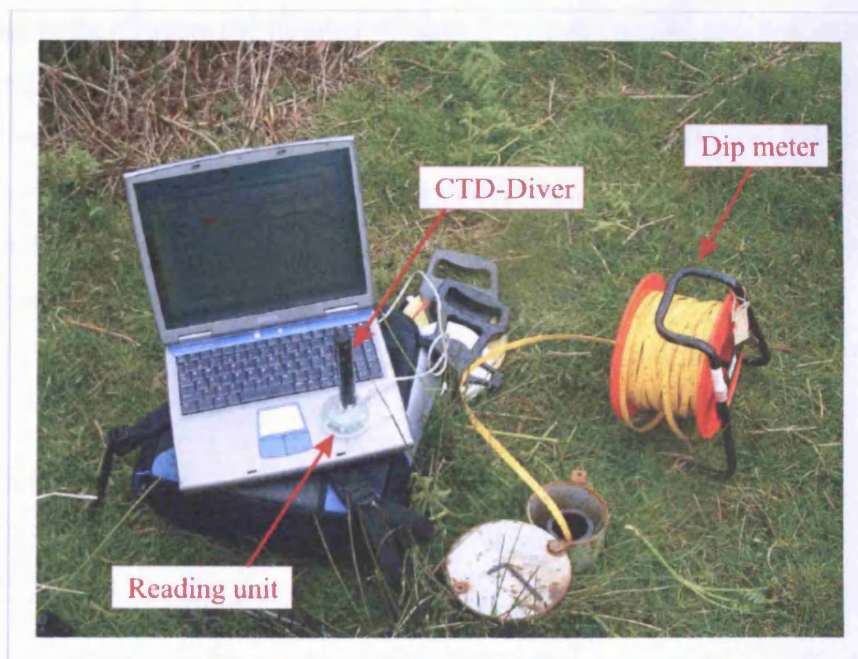


Figure 2.64 Data download from CTD-Diver installed in borehole 11 at Mynydd yr Eglwys landslide (photo by A. Gray)

Data analysis

After applying a compensation for atmospheric pressure in the software Logger Data Manager and corrections to obtain the water level in metres AOD, the data were plotted, analysed and compared to rainfall in order to:

- determine seasonality of data and water level highs and lows;
- establish the intensity of rapid changes in water levels following heavy rainfall;
- determine the lag between rainfall and water response;
- establish the time required for the water level to return to its “normal” value after heavy rainfall.

Most of the analysis was carried out in Excel (Microsoft Office) and by visual interpretation of graphs of hourly water levels versus daily rainfall.

Data were further analysed with the SPSS v 16.0 statistical analysis program by A. Gray (Cardiff University). In particular, Spearman’s correlation was carried out on the data to investigate the existence of correlations at a statistical significant level between the water levels measured at the three boreholes and between the water level of each borehole and the rainfall. Moreover, cross-correlations between the water levels at each borehole and rainfall were calculated to investigate from a statistically

significant point of view the number of days between rainfall and rise in water level (response interval, or lag in the cross-correlogram). Before the data were analysed, consecutive values of water levels were differentiated to eliminate any daily trend. Successively, data were correlated applying different shifts in time (lags). An example of this kind of analysis is provided in Lee et al. (2006). The results of these analyses are described in Chapter 3.

2.12 Rainfall Data

Halcrow (Cardiff office) provided rainfall data from rain gauges at Dan I Deri (Parc Colliery), at the top of Blaencwm Landslide and at Ty'n-y-waun (Treherbert, Gauge No 490261), all in the North Rhondda Fawr Valley. The rain gauge at Parc Colliery was maintained by the Rhondda Cynon Taff County Borough Council (RCTCBC) from September 1998 (Halcrow, 1999) until November 2007. The rain gauge at Treherbert is monitored by the Environmental Agency. Records from this gauge are available since 1892, but daily records were maintained only till 1996 (Halcrow, 1999). After that, readings have been taken monthly and are affected by small gaps and errors (Halcrow, 1999). Halcrow (1999) reported that there were inconsistencies between records at Parc Colliery and Treherbert between January and March 1999. Moreover, when records were compared for the period September to December 1998 the monthly total at Parc Colliery was unexpectedly 17% higher than at Treherbert.

The RCTCBC landfill company provided rainfall data from the two weather stations located at Nant y Gwyddon landfill (on the slope opposite to Mynydd yr Eglwys landslide) and Bryn Pica landfill.

Unfortunately all the datasets are characterised by minor and major data gaps. Sometimes the rainfall values looked unreliable, especially the Nant y Gwyddon weather station. Rainfall values are often zero or very low for several consecutive days, in contrast with other rain gauges or to the field notes of the author reporting very wet site conditions.

A best estimate daily rainfall dataset was then compiled from January 2005 until the end of May 2009, evaluating all the available data. When judged reliable, datasets were selected in this order of importance: Dan I Deri, Blaencwm, Treherbert, Nant y Gwyddon and finally Brin Pica. Dan I Deri was indeed considered the most reliable, but unfortunately it ceased working in 2007. Values from Blaencwm were available for summer 2008, but rainfall readings appeared low when compared with Treherbert and the author's field notes. For this reason, an additional version of rainfall values (relying firstly on Treherbert values when available) is always considered for summer 2008.

The final rainfall data compilation is considered a worst case rainfall scenario based on all available datasets. Daily rainfall data were used for comparisons with water levels, movements at monitoring markers and geophysical results.

Table 2.20 Details on weather stations or rain gauges used for the determination of daily rainfall

Weather station or rain gauge	Approximate distance from Mynydd yr Eglwys landslide (Direction)	Notes
Dan I Deri (Parc Colliery)	3500 m (W)	No data after November 2007
Nant y Gwyddon	1700 m (SSE)	Major data gap between June 2008 and March 2009
Blaencwm	6250 m (NW)	Major data gaps between June and December 2006 and between July and November 2007
Brin Pica	10250 m (NNE)	No data considered for 2005
Ty'n-y-waun (Treherbert)	6500 m (NW)	No major gaps

2.13 Summary and technical discussion

This chapter provided a theoretical background of the geophysical methods used in this research project. It also described the data acquisition, processing and quality assessment of all field data acquired from the Mynydd yr Eglwys landslide.

The main points of the data acquisition and processing procedures are summarised in the following paragraphs, together with a discussion of the optimal field procedures

employed, data quality, resolution and limitations plus realistic commercial costs for each technique on the basis of the field and processing experience gained by the author during this project. Many of these factors are often not taken into consideration in research papers or in geophysical reports, but are fundamental for promoting the use of these surveying and geophysical methods on landslides or potentially unstable slopes.

Airborne LIDAR

The LIDAR data acquired on Mynydd yr Eglwys landslide were processed and supplied by the UK Environmental Agency (Geomatics Group section). These data were captured in April/May 2005 using an Optech ALTM2033 instrument. The vertical accuracy of the data points was ± 8 cm RMSE, while the horizontal accuracy was approximately ± 40 cm, although it was subsequently reduced by 2 m gridding (Mike Plant, pers.com.).

For this project, LIDAR shaded-relief maps and LIDAR surface plots were created in Surfer 8 (Golden Software) and then used to identify landslide features for geomorphological mapping and to produce other terrain modelling images (i.e. slope angle and 3D geological plots) for the desk study (see Chapter 3).

LIDAR shaded-relief maps with geomorphological annotations proved to be very useful for planning the locations of geophysical profiles/grids and GPS monitoring points. These locations had to be accessible and interesting for the characterisation/monitoring of the landslide. Moreover, the possibility of plotting geophysical data locations or results on LIDAR-derived maps (with or without geomorphological annotations) improved data visualisation and, most importantly, data interpretation, as in this way geophysical anomalies could be more easily compared against land features (see Chapter 4 and 5).

Digital Photogrammetry

Imagery of the central part of Mynydd yr Eglwys landslide was acquired with a fixed focal length Ricoh GR Digital II (10 MPixels) camera mounted on a helium balloon, in February 2008. 35 white paper dishes spread across the slope were used as ground control targets and their positions were surveyed with a Topcon HiPer Pro GPS+ in RTK mode. Camera calibration parameters were obtained through Topcon's PI-calib

software, while the landslide imagery was processed with Topcon's PI-3000v3 software. During data processing, automatic surface measurements (as TINs) with a mesh of 0.25 m were carried out in the overlapping areas of the stereo-pairs. More than a quarter of a million terrain points were extracted from the results, allowing for the generation of a very dense DEM.

The quality of the DEM derived with this acquisition procedure and software has not been reported in the literature before. Therefore, these factors were assessed for this project, in terms of precision, accuracy and internal reliability (as defined by Butler et al., 1998; Chandler, 1999):

- Data precision could be evaluated from the results of the bundle adjustment obtained for the eight successful stereo-pairs. The standard deviation of the residual errors between the coordinates of the ground control points computed by bundle adjustment and the ones surveyed with GPS was: 0.0060 m in X, 0.0063 m in Y and 0.0128 m in Z. Imagery ground resolution ranged between 0.0210 and 0.0274 m and imagery depth resolution between 0.0423 and 0.0838 m.

- Accuracy was estimated by comparing heights extracted from the photogrammetry-derived DEM with heights surveyed with GPS at independent check-points. The overall mean of the height differences was 0.103 m and the standard deviation was 0.140 m. However, only a few check-points were located close to the edges of the surveyed area and none were located on the steep back scarp where accuracy could be less. Therefore, more check-points in these areas should have been included for a more thorough accuracy evaluation. The height errors greater than 0.20 m were all located in the part of the DEM extracted from a stereo-pair not containing ground control points (only pass points), underlining the importance of distributing targets evenly across all the area that need to be captured.

- Internal reliability was estimated by comparing elevations provided by adjacent DEMs in their overlapping areas. The overall mean of the height differences was 0.001 m and the standard deviation was 0.024 m and 0.010 m for the main scarp and hummocky areas respectively. These results underlined the validity of the technique and its independence from stereo camera position. As could be anticipated, the points

with greater elevation discrepancies were located at the break of slope on top of the main scarp and at data edges. However, the influence of terrain characteristics (i.e. hummocky terrain or steep slope) on internal reliability appeared minimal.

A rapid way to test accuracy and internal reliability and to analyse the spatial distribution of height differences using Surfer 8 (Golden Software) was proposed and described in section 2.3.3.2.

The influence of the TIN mesh density was not taken into consideration, and, contrary to other software described in the literature (i.e. in Gooch et al., 1999; Lane et al., 2000; Baily et al., 2003), Topcon's PI-3000v3 does not offer the possibility to choose different algorithms or strategy parameters for automatic TIN extraction. This software has also the disadvantage of not including options for camera self-calibration, therefore historical imagery could be used for DEM extraction only if full details of camera calibration parameters have been provided.

Data were acquired only for a small test site in the central area of MyE landslide, covering approximately 14300 m². However, results showed how the 3D platform of Topcon's PI-3000v3 can be used to measure distances and cross-sections, to create contours and to analyse landforms for geomorphological mapping (for the desk study in Chapter 3). Moreover, the software could rapidly produce high-resolution good quality DEMs and orthophotographs of landslides or potentially unstable slopes. There are well discussed practical problems with using terrestrial LIDAR on complex landslide slopes due to line-of-sight problems and expensive airborne LIDAR is not often an option. These photogrammetric products would be ideal as substitutes of LIDAR-derived maps not only for topography and geomorphological mapping but also for location maps of geophysical profiles/grids or GPS movement markers, and, more importantly, for visualisation and interpretation of geophysical data. The spatial resolution and the elevation accuracy of the photogrammetry-derived DEM in areas of such severe topography may not be good enough to provide the precision in elevation required for the processing of ERT, IP and seismic datasets and ground surveying (i.e. with GPS or EDM) would still be necessary along these geophysical profiles.

The results of data quality assessment show a potential for this technique to be repeated in time, to quantify changes of landforms and to monitor long-term landslide movements with spatial resolution higher than the one achieved with GPS monitoring. However, it has to be remembered that most of the landslides in the South Wales Coalfield are translational and complex (Chapter 1). A simple analysis of elevation differences between DEMs from different epochs (as described for example in Mora et al., 2003; Chen et al., 2006; Demoulin, 2006; Baldo et al., 2009; Corsini et al., 2009) would not be very useful in terms of evaluation of real displacements. Time-series of orthophotographs could be compared to define the horizontal movement of homologous points. More importantly, the 3D platform of TopconPI-3000 could be used to identify homologous points or features in TINs with photo-texturing obtained from different epochs, measure them and successively calculate the 3D vectors of displacement. The practical and cost advantages of the availability of stereo photogrammetry, compared to DEMs derived from airborne LIDAR or dGPS surveying, would then be self evident.

Photogrammetric data acquisition at Mynydd yr Eglwys required only two-three hours, and, after familiarizing with the software, data processing was relatively rapid. Optimal field conditions can be chosen with no wind, good sunlight and in the winter when the fern vegetation is minimal. Processing time could be reduced using larger ground targets which are easier to distinguish (for example with different shapes or colours). The software costs only £2500, while data acquisition (including processing and reporting) costs £1500 per day (prices from TerraDat UK Ltd - personal communication, June 2011). These prices are very competitive when compared with airborne/heliborne LIDAR or aerial photography surveys, if the site does not cover a very wide area. Given no financial limitations, LIDAR or RADAR techniques would still be the better choice in cases of smooth ground texture or in areas covered by dense vegetation. Moreover, logistical problems would be encountered during photogrammetric acquisition using a helium balloon in windy weather conditions.

GPS monitoring

A dual-frequency Topcon HiPer Pro GPS+ instrument (described in section 2.4.4.1) was used in RTK surveying mode for the monitoring of surface displacements and for

most of the surveying at Mynydd yr Eglwys landslide.

Nine GPS monitoring campaigns were carried out from November 2007 to December 2008. The network comprised of 13 movement monitoring points and three control (or 'fixed') points located outside the landslide area, on Meadow Walk. The shortest time taken between surveying campaigns was 14 days and the longest was 73 days.

The base antenna was set up on an area of the slope considered to be stable. The rover antenna was set up over each marker using a tripod (plus tribrach) with optical plummet and its height was measured with a tape measure. The rover antenna was programmed to sample GPS data at 1 second interval, with a 10 degree mask angle, and to record only fixed positions when reaching a precision of at least 0.002 m in both horizontal and vertical directions. As a consequence, the time of observations varied, ranging between 26 seconds and 4 minutes c. GPS data recorded at the base station were post-processed with the software Topcon Tools v7.1 (details were provided in section 2.4.4.2). Cumulative horizontal, vertical and total movements were calculated for each marker and then compared with rainfall and water pressure information (results are reported in Chapter 3).

Discrepancies in the GPS results may arise from the use of different types of instruments, antenna set ups, processing algorithms and software packages (Gili et al., 2000 and references therein). As the performance of the Topcon HiPer Pro GPS+ instrument (and post-processing with Topcon Tools) for landslide monitoring has not been reported in the literature before, a data quality assessment was carried out. After the coordinates of base station were compared to confirm its stability, the practical precision of GPS measurements achieved at MyE was evaluated from:

- Analysis of apparent movement of 'fixed' points during different campaigns: the standard deviation at RCBCTC point SB81 was 0.0030 m in Eastings, 0.0063 m in Northings and 0.0143 m in elevation. This point can be considered the worse one on site, because very close to obstacles which reduce sky visibility and may create multipath effects. However, precision was still within instrument specifications.
- Analysis of redundant observations (comparisons between measurements taken at each marker for 3-6 times without moving the tripod during the same campaign): the

range of standard deviations was: 0-0.006 m in Eastings, 0-0.005 in Northings and 0.001-0.015 m in elevation. These readings are not influenced by possible errors in antenna centering or antenna height measurements and confirm the instrument accuracy specifications provided by manufacturers.

- Analysis of re-occupied points (coordinate differences between re-occupied and original points, during the same campaign): differences ranged between -0.005 and 0.010 in Eastings, -0.007 and 0.004 in Northings and -0.011 and 0.011 in elevation. These values of precision take into consideration the influence of re-setting the antenna on the same marker (possible errors in antenna centring and antenna height measurements) and changes in satellite geometry.

Apart from the well known advantages in using a GPS instead of an EDM (Chapter 1), the precision achieved with the GPS at MyE is significantly better than the limit of movement detection of 0.050 m reported by Halcrow (2000) for the EDM surveys carried out by RCTCBC. For a survey using a Trimble GPS in RTK mode and a telescopic pole with auxiliary tripod for rover set-ups, Gili et al. (2000) reported a practical precision of 16 mm in horizontal plane and 24 mm in elevation. The precision achieved with the Topcon GPS at MyE is higher (12 mm in horizontal and 15 mm in elevation) which proves the applicability of using this technique for monitoring even very slow moving landslides, providing that there is adequate sky visibility.

Each campaign was carried out in one day. Redundant measurements are not necessary and therefore can be avoided to increase on site productivity, but measurements at a few control points and re-occupation of 1-3 markers for each campaign should be recommended for data quality assessments. Although it improves with experience, the setting up of the rover antenna on a tripod at each marker is a relatively slow procedure. The alternative, less precise but more rapid use of a simple telescopic pole instead of a static tripod could be considered according to the measuring precision required at the site. Productivity will obviously depend also on site conditions and accessibility to marker locations. The cost of GPS monitoring (including processing) is approximately £1500 per day (prices from TerraDat UK Ltd, personal communication, June 2011).

The results of GPS monitoring have been compared to rainfall, borehole water levels and geophysical monitoring results (in Chapters 3 and 5) for a better understanding of landslide dynamics. However, sporadic GPS measurements can provide only a general (seasonal) trend of landslide movements. The total cost and cost-effectiveness of GPS monitoring for defining the nature and magnitude of surface movements in response to short- or long-term rainfall will depend on the site-visit frequency required at the site. Other monitoring instrumentation, such as inclinometers or extensimeters, may be necessary and much more effective in complex landslides (as discussed for MyE in Chapter 3 and 5).

Mora et al. (2003) described the use of continuous monitoring between two GPS antennas left on site. This would be ideal for research purposes and for high-risk landslides where site security and project funding are high. However, a permanent GPS monitoring system would be prone to vandalism in urban slopes as MyE and would be financially excessive if a receiver has to be positioned at each monitoring location.

At MyE, movement markers consisted of steel ground anchor bars 0.30-0.60 long and two of them with yellow raised heads, located closest to the houses, were dug out and stolen after April 2008, underlining the problem of vandalism in these urban areas. Therefore, even less evident marker heads should be selected for the measuring locations more accessible to the public. According to site conditions, rock engraving would probably be a better option where bedrock is exposed.

A combination of digital photogrammetry and GPS monitoring could be applied to obtain high-precision short-term measurements at a few selected points and long-term measurements at cm-precision over a wider area.

Electromagnetics with the Geophex GEM-2 Instrument

Electromagnetic data at Mynydd yr Eglwys landslide were acquired using the broadband multi-frequency hand-held digital sensor GEM-2, developed by Geophex (described in section 2.5.2). The instrument was used in horizontal coplanar coil

configuration while operating at five transmitter simultaneous frequencies: 47025 Hz, 30025 Hz, 15025 Hz, 5125 Hz and 975 Hz. Data were acquired in January 2008 and May 2009 over three grids, along lines of approximately 2-3 m spacing and at a sampling rate of 120 ms. Data point positioning was provided by a Trimble Pathfinder ProXT GPS connected to the GEM-2 instrument during the survey.

The raw data stored by the instrument were converted into values of apparent conductivity and magnetic susceptibility at Ordnance Survey locations. These data were gridded and plotted as a series of colour contour maps, one for each frequency, using Surfer 8 (Golden Software). These contour maps were then overlaid onto the geomorphological base map to investigate any variations in apparent conductivity and/or magnetic susceptibility across the site and their possible relationship with land features. Moreover, as investigation depth depends on the operating frequency of the instrument, with lower frequencies penetrating deeper into the ground, a qualitative visual comparison between the plots of apparent conductivity or magnetic susceptibility at different frequencies was carried out. Such data should provide information about variations of these geophysical properties with depth (see results in Chapter 4).

Authors describing the use of electromagnetics on landslides generally report only one to five profiles acquired with Geonics EM-31 and/or EM-34 (i.e. Caris and Van Asch, 1991; Bruno and Marillier, 2000; Meric et al., 2005). The Geophex GEM-2 instrument is much more portable and lightweight than the cumbersome EM-31 and compared to EM-34, it does only require one operator instead of two and also does not suffer from the difficulties of keeping a constant and accurate distance between the separated coils. Therefore, GEM-2 offers the possibility to acquire very rapidly many profiles at high data density whilst walking over rough landslide terrain. Indeed, at Mynydd yr Eglwys, an area of approximately 15000 m² at 2-3 m spaced lines could be covered in approximately 3 hours and half on foot. The terrain was in areas hummocky, very wet, and affected by deep cracks. Better site conditions would allow for even a higher productivity. The cost of a GEM-2 survey, including processing and reporting, is £ 1850 per day (price from TerraDat UK Ltd, personal communication, June 2011). Although lateral and depth resolution of conductivity are anticipated to be much lower than in ERT profiles, the GEM-2 is ideal for reconnaissance surveys, due

to the rapidity, facility and data density with which a wide area can be covered on a landslide or a potentially unstable slope. Obviously EM readings would be negatively affected by the presence of near surface metallic objects, which would mask the targeted anomalies, but metallic debris are not commonly found on landslides.

The GEM-2 instrument can be connected to the rover antenna of the Topcon HiPer Pro GPS+ for more precise positioning. However, this antenna has to be kept at a distance greater than 2 m from the GEM-2 instrument to avoid interference (Terradat UK Ltd, personal communication). At Mynydd yr Eglwys landslide this set up was not feasible on rough ground and therefore a Trimble Pathfinder ProXT GPS was connected to the instrument, as it has a receiver made of plastic which is mounted on a belt. To obtain sub-metre accuracy with this Trimble GPS however, the availability and reliability of EGNOS signal is necessary. If there is a lack of EGNOS signal, a precise reference grid must be set up in advance (with Topcon GPS or an EDM) and a time-consuming editing of positional errors during GEM-2 data processing may become necessary, as it happened at MyE for the surveys carried out in 2008. Better quality EGNOS data is obtained if the landslide is south facing, which is the case at MYE.

Compared to the fixed-frequency Geonics EM-31 (constant nominal depth of 6 m), the multi-frequency GEM-2 has also the potential to provide changes of apparent conductivity with depth. Imaging algorithms and inversion techniques for broadband data acquired with GEM-2 are still under research (i.e. Witten et al., 1997; Huang, 2005) and were not applied during this project. However, all the case study papers (i.e. at [WWW 2.10]) report only simple visual comparisons between contour plots obtained at different frequencies without really discussing the precise depth of the anomalies and the real applicability of the GEM-2 for depth sounding has been criticised (i.e. in McNeill, 1996). Therefore, the GEM-2 results obtained at MyE will be compared against other geophysical datasets in Chapter 4 also to evaluate the reliability of the instrument for depth sounding.

Self-Potential (SP)

Self-potential measurements at Mynydd yr Eglwys landslide were carried out with two non-polarizing electrodes (two porous pots with a mesh of copper immersed in a

saturated solution of copper sulphate) in a fixed-base electrode configuration. SP data were acquired in December 2006 and March 2007 in three grids covering almost all the central area of the landslide and along 3 crossing profiles, at a station spacing of 5-10 m. In 2008, SP monitoring data were acquired within two small grids with a 5-m station spacing: one located in the most active area of the landslide (where ERT monitoring with permanent electrodes was also carried out) and one located in the toe area (where SP measurements were undertaken before and after the instalment of a drainage system). SP data were successively corrected for drift, gridded and plotted as contour maps overlaid onto a geomorphological map or a 3D LIDAR terrain model, whereas a few profiles were plotted separately as line graphs. Results are reported in Chapters 5 and 6.

SP anomalies generated by targets of environmental and engineering applications, such as water movements, are generally small (of the order of a few mV). Therefore great care has to be taken on site to be able to recognise and minimise unwanted effects (i.e. electrode polarization and drift) and to improve data reproducibility for SP monitoring purposes. At MyE, data were acquired following the procedures and forms of data quality control reported in Corwin (1990; details were provided in section 2.6.3).

Sub metre station positioning was achieved using two GPS instruments: a Trimble Backpack for the surveys of December 2006 and the Topcon HiPer Pro GPS+ in RTK for all the following surveys. In particular, the Topcon GPS allowed to rapidly set up precise grids and profiles and to rapidly find the location of all SP stations that needed to be reoccupied for monitoring purposes. Furthermore, on site, it appeared very useful to annotate each value of mV directly on its approximate location on a LIDAR-derived geomorphological basemap. Although these mV values were only raw (not yet corrected for drifts or possible errors), the real-time manual plotting helped to identify the areas where it was advisable to add extra SP readings to investigate rapid and complex lateral voltage variations.

The biggest problem was the practical handling of the long connecting cable in relatively difficult site conditions (severe topography, dense/high vegetation in summer, presence of sheep). By using slow, careful data acquisition procedures, the

use of GPS for position fixing, re-positioning of each station, the manual plotting of mV raw values and note taking of moisture conditions for each station were all factors that contributed to reduce productivity on site. An average of approximately 50-60 measurements were undertaken in four hours. The cost of an SP survey, including processing and reporting, is £ 1850 per day (TerraDat UK Ltd, personal communication, June 2011). Therefore, a part from the quality of results (Chapter 4), the cost-effectiveness of SP mapping at reconnaissance stage will strongly depend on the size of the site, site conditions and the spatial resolution required. As a consequence, if not for research purposes, a one-day trial should be recommended before embarking on a more time consuming SP reconnaissance survey.

Lapenna et al. (2003) and Perrone et al. (2004) report examples of SP mapping, but from data acquired with an electrode spacing of 50 m. Indeed, although described with enthusiasm by the authors, the resulting maps in reality provide only very generic information on the water flow within the investigated landslides. For slopes with suspected complex hydrogeology as the ones found in the South Wales Coalfield, the station spacing will have to be at least of the order of 5-10 m or less, as confirmed by field surveys at MyE.

Colangelo et al. (2006) describe time-continuous SP tomography profiles acquired with a permanent remotely-controlled automatic multi-electrode system. This permanent set up would be ideal, but costly and obviously prone to vandalism. At MyE, SP monitoring profiles were acquired without leaving any equipment, returning on site and re-locating the precise station positions with the Topcon GPS. The cost-effectiveness of this approach will obviously depend on the quality of the results (i.e. if changes in water flow are detectable) but also on the required time frequency of such repeated measurements (discussed in Chapter 5).

Seismic methods: Seismic refraction tomography and Multichannel Analysis of Surface Waves (MASW)

Seismic data were acquired simultaneously for both refraction tomography (P-waves) and MASW along four profiles across Mynydd yr Eglwys landslide in May-June 2008. The surveys were carried out using a high-precision 48-channel GEODE

seismic system, 10-Hz vertical geophones at 1 m spacing (and also 0.5 m spacing only for one line) and a source consisting of a 10-kg sledgehammer and metal plate. The simultaneous acquisition of data for both refraction tomography and MASW was achieved by extending the recording time to 1 s and increasing the number of shot locations (see section 2.8.3 for details). Geophone positioning and elevation were surveyed with the Topcon HiPer Pro GPS+ instrument in RTK mode.

Another profile was acquired only for seismic refraction (with a lower number of shot locations, but with a higher number of stacks) in October 2006 and line topography was surveyed with an EDM.

Seismic refraction data were processed with PICKWIN and PLOTREFA software (modules of SeisImager/2D of OYO Corporation; details were provided in section 2.8.4). Data quality was negatively affected by type of source, lateral subsurface heterogeneities, high rock fracturing degree and the limited number of stacks (1-3) selected for the intra-spread shots for MASW purposes. Moreover, processing for one of the profiles was complicated by crossing of a fault zone, severe topography and the presence of shallow and wet material in far off-end shots, which was difficult to model in the inversion software. However, a part for this last line (RMSE=2.54), the resultant inverted velocity sections were still characterised by a low misfit between calculated and measured velocity values (RMSE less than 1.52; see results in Chapter 4). Due to the supposed lack of strong velocity contrasts between the layers of mudstones/siltstones of the Middle Coal Measures and the expected gradual horizontal and/or vertical velocity changes caused by variations in rock fracturing degree or weathering, contour models are presented instead of layer models for the final velocity profiles. Sections with layers of constant velocity could be misleading for an engineer or developer with poor or no geophysical background and would not exploit the benefits of using the more time-consuming tomography instead of simple refraction planar layers, which are not able to depict gradual velocity changes.

MASW data were processed by M. Bottomley (2008) as part of his MSc dissertation, using the software SurfSeis 2.05 (Kansas Geological Survey). Bottomley chose as optimal parameters: 6 or 7 m for the source-to-first receiver offset and 24 m for the spread length. The quality of the dispersion curves was not coherent, probably due to

lateral heterogeneities in the near-surface material and to topography. Furthermore, data quality was considered too poor for one of the lines to be processed.

The cost of simultaneous acquisition of seismic refraction tomography and MASW (including processing and interpretation) is £2300 per day (TerraDat UK Ltd, personal communication, June 2011). At Mynydd yr Eglwys, three lines of 47 m were acquired in approximately 6 hours (with a crew of 4 people).

The MASW technique has some known advantages over seismic refraction (it can work in areas of elevated cultural noise; it does not require a contrast or an increase in velocity with depth). However, it assumes no lateral changes in elastic properties in the near surface and it is severely affected by a surface relief greater than 10% of the geophone spread. Therefore, its effectiveness at MyE and other landslides or potentially unstable slopes is not certain. Results are reported and discussed in Chapter 4, where MASW profiles have been calibrated with borehole information and compared with data from the other geophysical techniques.

In general, the applicability of both seismic methods will depend also on the investigation depth and resolution required at the site (i.e. suspected depth of surface of rupture; thickness of layers of interest). The depth of investigation of the active MASW method is usually 10-30 m and is mainly governed by the kind of seismic source selected. The shallowest resolvable depth of investigation ranges between 0.3 and 1 times the receiver spacing, while vertical resolution is approximately 20% of investigation depth. In theory, greater depths of investigation can be reached with the passive MASW technique, which was not tested during this project. Survey design is fundamental and can be based on the optimum acquisition parameters reported and continuously updated in the website operated by Park Seismic LLC [WWW 2.11].

At MyE the investigation depth of seismic refraction tomography was limited to approximately 15-20 m. The profiles were all located, along ground contour lines in the area of the slope characterised by sequences of mudstones and siltstones with different degrees of fracturing/weathering and possible no bands of sandstone, which would have acted as strong refractors. It has to be remembered that this type of geology may imply the presence of layers of decreasing velocity with depth or too

thin to be detected.

Electrical resistivity tomography (ERT)

From January 2006 to December 2008, ERT data were acquired along 15 profiles on Mynydd yr Eglwys slope, using a 72-channel IRIS SYSCAL resistivity system and a maximum of 72 electrodes, with a minimum electrode spacing of 2 or 5 m. The length of the ERT lines ranged between 70 and 355 m. The surveys were generally carried out with a Wenner-Schlumberger array configuration and stainless steel electrodes. Dipole-dipole configuration and copper-rods were used when data were acquired simultaneously for both resistivity and IP measurements. Electrode topography and positioning were surveyed initially with an EDM and then with the Topcon HiPer Pro GPS+ in RTK mode.

Some profiles were acquired more than once during the duration of the project. Four profiles were repeated between 2 to 6 times at intervals of several months (i.e. one time in summer and one in winter) with repositioning of electrodes based on wooden pegs, which were left on site as markers along the profiles. Steel tent pegs driven almost completely into the ground at 2 m spacing were instead installed in June 2008 and used as permanent electrodes for the monitoring of other three profiles (X, Y, Z). In particular, profile X, located along the slope in the most active area of the landslide, was repeated 6 times between June and August 2008 (plus once again in December 2008), while simultaneous continuous monitoring of water levels in two on-site boreholes was also undertaken.

ERT pseudo-sections were inverted to obtain true 2D resistivity sections using the software RESDINV (Geotomo Software), with good results. Apart for one of the sections (line 1L of 17 July 2006, with 9.9% RMS), the difference between calculated and measured values of apparent resistivity described in terms of root-mean-squared error (RMS), after three inversions, comprised between 1.7 and 4.9%. For the monitoring profiles, similarly to Jomard et al. (2007), resistivity changes in time were calculated subtracting the reference resistivity value from the repeated resistivity value at each measuring point. The plots of resistivity variations were then compared to rainfall and water level data. Results of ERT surveying and monitoring are reported in Chapter 4 and 5 respectively.

As resistivity data alone are not good indicators of lithology (Figures 2.40 and 2.41) and low resistivity zones can be associated to zones of high water or clay content, both important targets in slope stability investigations, ERT sections need to be calibrated with borehole information or interpreted in combination with data from other geophysical techniques. The effectiveness of ERT method for the investigation of MyE landslide and the ideal geophysical techniques in support of ERT interpretation are discussed in Chapter 4.

The applicability of ERT will obviously depend on the exploration depth and the resolution requested at the site (i.e. depth of surface of rupture, thickness of displaced material). The investigation depth of ERT depends on the maximum value of electrode spacing (a possible constrain on site), with greater depths achieved at the expenses of resolution, which is determined by the minimum electrode spacing. The practical exploration depth will be also a function of layering and resistivity contrast. The 72-electrode profiles at MyE comprised of 683 measurements (collected in approximately 45 minutes on site), denser at shallower depths. For the 2m-spacing profiles, the pseudo-sections were characterised by a maximum depth of penetration of approximately 20 m (for the central part), a horizontal resolution of 2 m, and a vertical resolution ranging from 0.8 m in the first 5.2 m of depth to 2.3 m from 13.6-20.6 m of depth. For the 5m-spacing profiles, the pseudo-sections were characterised by a maximum depth of penetration of approximately 50 m (for the central part), a horizontal resolution of 5 m, and a vertical resolution ranging from 1.9 m in the first 10.5 m of depth to 5.8 m from 34.1-51.5 m of depth.

Productivity will depend on site conditions and access. At MyE, a maximum of three profiles of 355 m were acquired in one day. The Topcon GPS was fundamental for surveying as the initial use of an EDM was very time-consuming because of the numerous set ups required to obtain line of sight in such rugged topography. The price of an ERT survey, including processing and reporting, is £1850 per day (TerraDat UK Ltd, personal communication, June 2011).

ERT monitoring was based on full re-deployment of lines along wooden markers left on site or on the use of permanent cheap electrodes (steel tent pegs), overcoming the

problems of vandalism or expensive equipment. However, if ERT monitoring results effective in depicting changes in water flow/content, questions arise on the frequency with which the profiles need to be repeated to establish a relationship between these changes and rainfall, borehole water levels and surface displacements (see results and discussion in Chapter 5). The South Wales Coalfield is characterised by complex hydrogeology and unpredictable wet weather throughout the year (Chapter 1), a permanent automated system that can be operated remotely and on demand as the ALERT system of BGS [WWW 2.12] may be required, but would be not applicable due to vandalism and limited financial budgets for low-risk urban landslides.

Induced Polarization (IP)

Seven IP profiles were acquired on Mynydd yr Eglwys landslide in 2008 with the aim to resolve the ambiguity between a clay-rich body (e.g. fault zone) and a water-saturated porous sandstone unit, as both may be the source of the low resistivity (or high conductivity) zones observed in both ERT and GEM-2 results. IP data were collected with an IRIS SYSCAL resistivity system, using a maximum of 72 electrodes and a minimum electrode spacing of 2 m. The IP lines were acquired with copper rods in Dipole-Dipole electrode configuration. However, IP tests were also carried out along two profiles using three types of electrodes (Copper Sulphate jelly pots, copper rods and steel tent pegs) and using the Wenner-Schlumberger configuration.

IP pseudo-sections were inverted to obtain true 2D chargeability sections using the software RES2DINV (Geotomo Software), with RMS values ranging between 0.33 and 5.8 %. All the datasets, regardless of the electrode type and electrode array configuration used, appear to exhibit good data quality. No evident differences in chargeability values or noise level were found during data processing, neither in PROSYS or RES2DINV. The greater reliability of the Dipole-Dipole array could be established only by comparison with the results provided by other geophysical techniques (in particular ERT and GEM-2). After the initial trials, the copper rods were preferred to the jelly pots for IP surveying, because of the more complex logistics of handling the jelly pots on a landside, plus the potential environmental issues of leaving any Copper Sulphate solution behind on the landslide.

The considerations on data resolution, applicability, limitations and costs of the IP

technique are the same as the ones made for ERT surveying. Indeed, the same equipment can be used for the simultaneous acquisition of both resistivity and chargeability data. However, the electrical current injection time must be at least doubled for IP surveying. Therefore, significantly more time is required for each survey line. For example, a single IP profile with 72 electrodes, using a Dipole-Dipole protocol file of 803 measurements, took over 3 hours to acquire.

Rainfall data and monitoring of water levels

Halcrow UK Ltd (Cardiff Office) provided rainfall data from three rain gauges located in the North Rhondda Fawr Valley (Dan I Deri, Treherbert and Blaencwm). Furthermore, the company Amgen Cymru provided information from weather stations located at Nant y Gwyddon and Bryn Pica landfills. Unfortunately, Dan I Deri rain gauge (the closest to the site) ceased working in November 2007 and all the other rainfall datasets were characterised by inconsistencies, minor and major data gaps, and probable errors (no rain while the field notes of the author described very wet site conditions). Therefore, a very time consuming generic regional daily rainfall dataset had to be compiled for this project (see section 2.12). This data were successively compared with water level variations, GPS surface displacements and geophysical monitoring profiles with the aim of investigating landslide dynamics (see results in Chapter 3 and 5).

Some historical water level data were supplied by Halcrow UK or could also be found in Earth Science Partnership reports and were also used for the desk study of MyE (Chapter 3). However, these measurements stopped in 2004 or May 2006, before the start of this project. Unfortunately, the only continuous logger still functioning on site is located far from the area of interest.

As rainfall datasets were found to be unreliable and sporadic borehole dipping was not providing sufficient data for calibration of geophysical monitoring data and for interpretation of GPS displacement measurements in terms of landslide dynamics, two automatic data loggers (Mini-Divers manufactured by Schlumberger Water Services) were installed on site in borehole 3 and 6 on the 30th May 2008, before the last phase of ERT monitoring using permanent electrodes. A third logger (CTD-Diver

manufactured by Van Essen Instruments, a Schlumberger Company) was installed in borehole 11 on the 27th August 2008, when it became available (see section 2.11 for instruments details). The loggers were programmed to measure water level once every hour.

These water level data were compensated for atmospheric pressures (measured with a Baro-Diver in borehole 6) and corrected in terms of elevation AOD. They were then visually and statistically analysed and compared to rainfall information in order to determine: the lag between rainfall and groundwater level response, the intensity of rapid water level changes following heavy rain, the time required for the water level to return to 'normal' values, and the seasonal water level highs and lows (see results in Chapter 3). Unfortunately, the integrity of the boreholes selected for monitoring is unknown. It is believed that borehole 3 has been damaged due to ground displacements, but the choice of available boreholes at MyE was very limited.

This research project was negatively affected by the unpredicted unreliability of all five rainfall datasets. If ERT and SP monitoring are effective in detecting water movements within the South Wales Coalfield slopes (see Chapter 5), and a complete geophysical monitoring procedure will be undertaken in the future for research or commercial purposes, a locally secure and fully functioning reliable rainfall rain gauge or weather station will have to be installed at/near the site. If there are undamaged boreholes containing water on site, the use of the Mini-Divers would be highly recommended. They were very reliable in terms of battery and memory storage and relatively inexpensive (approximately £400 each in 2008). Moreover, being inside the borehole casings, they were less prone to vandalism. Continuous water level data provide useful information for the understanding of groundwater response to rainfall within the slope that, if available in advance, could help designing geophysical monitoring procedures in terms of frequency and time lag after heavy or prolonged rainfall events.

Chapter 3 Mynydd yr Eglwys Landslide

3.1 Introduction

In the Autumn of 1998, a new deep-seated landslide developed on Mynydd yr Eglwys (MYE), the hillside above the village of Ystrad in the Rhondda Fawr valley. The new failure reactivated ancient debris slides which then moved downslope and created a potential risk to the properties of a modern housing estate. The uppermost street of the housing estate (Meadow Walk), which was built in the 1970s and 80s, is located close to the toe of the debris slides. The MYE landslide was first reported to Rhondda Cynon Taff County Borough Council (RCTCBC) by local residents in February 1999, when cracking in the main scarp area was clearly visible. The precise date of initiation of ground movement activity is not actually known, however it is believed that the new landslide was triggered by the exceptional heavy rainfall of October 1998 (Halcrow, 1999; 2000).

The new deep-seated landslide is believed to be of compound type (following definition of Hutchinson, 1988; section 1.2.1) and several factors may have contributed to its development (Halcrow, 1999; 2000).

This chapter describes the site and its historical land use. It provides information on geology, mining, geomorphology, hydrology and hydrogeology, landslide failure mechanisms, landslide possible causes and landslide kinematics.

The desk study was based on: available reports by Halcrow UK (1999; 2000), factual and interpretative descriptions of site investigations reported by Earth Science Partnership (2004) and C. J. Associates (2003), aerial and terrestrial photography, LIDAR data (provided by Environmental Agency UK), Historical Ordnance Survey maps, published British Geological Survey maps and map memoirs (Woodland and Evans, 1964), rainfall and EDM movement monitoring data provided by Halcrow and RCTCBC.

The chapter includes also results of walk-over surveys, geomorphological mapping, digital photogrammetry processing, water levels monitoring and GPS movement monitoring carried out by the author. It concludes with a summary highlighting the potential targets identified for geophysical investigations and monitoring.

3.2 Site location and general site description

MYE Landslide is located on the south facing side of Mynydd yr Eglwys hillslope, above Ystrad (NGR: SS 977956; Figure 1.21). The landslide lies upslope of the modern houses of Meadow Walk and Oaklands Drive (Figures 3.1 and 3.2). Mynydd yr Eglwys hillslope rises up from a valley floor at 150 m AOD to a plateau at 400-430 m AOD (Figure 3.4). The area affected by landsliding is situated between 190 m and 290 m AOD and extends to the east of the derelict Church Sandstone Quarry, extending over a footprint width of 400-450 m (Figures 3.2 and 3.4).

The main scarp of the landslide, with a slope angle greater than 40°, displaces an escarpment (slope angle between 30° and 40°) that is located between the 240 and 270 m land contours. The new landslide has developed between the outcrop workings of the Rhondda No 3 and Tormynydd coal seams (Figures 3.2 and 3.3). The main backscarp has a width of 150-200 m and it has a maximum height of approximately 20 m at its centre, which decreases laterally. Upslope of the main scarp there are a few old fissures, above which the slope becomes gentler, before steepening again towards the plateau. Immediately at the base of the main scarp there is a dry area with scree, ridges, displaced blocks of strata and fallen boulders.

Further downhill, the site is covered by ancient landslide deposits and colliery spoil material that form several hummocky lobes. The central area, to the south of the main scarp and a minor scarp, is characterised by numerous tension cracks. The slope angle of the ancient landslide deposits is generally between 15° and 20°, but increases at their toes and in zones of ridges, cracks and scarps (Figure 3.3). The lobes are covered by dense fern vegetation during the summer which makes fieldwork hazardous. The lobes are poorly drained and several ponds, streams, issues and wet areas can be

found within this area. During summer 2008, a simple ground drainage system was installed at the toe of the landslide with the aim to drain around the landslide toe.

The landslide is separated from the modern houses by an old tramway which once accessed Church sandstone quarry but is now used as a public footpath. The footpath has a drainage ditch running alongside which takes water off site. The area of the main backscarp has been fenced off by the landowner who uses the hillside for sheep rearing.



Figure 3.1 View of Mynydd yr Eglwys Landslide from Nant y Gwyddon landfill site on the opposite side of the valley (photo P. J. Brabham)

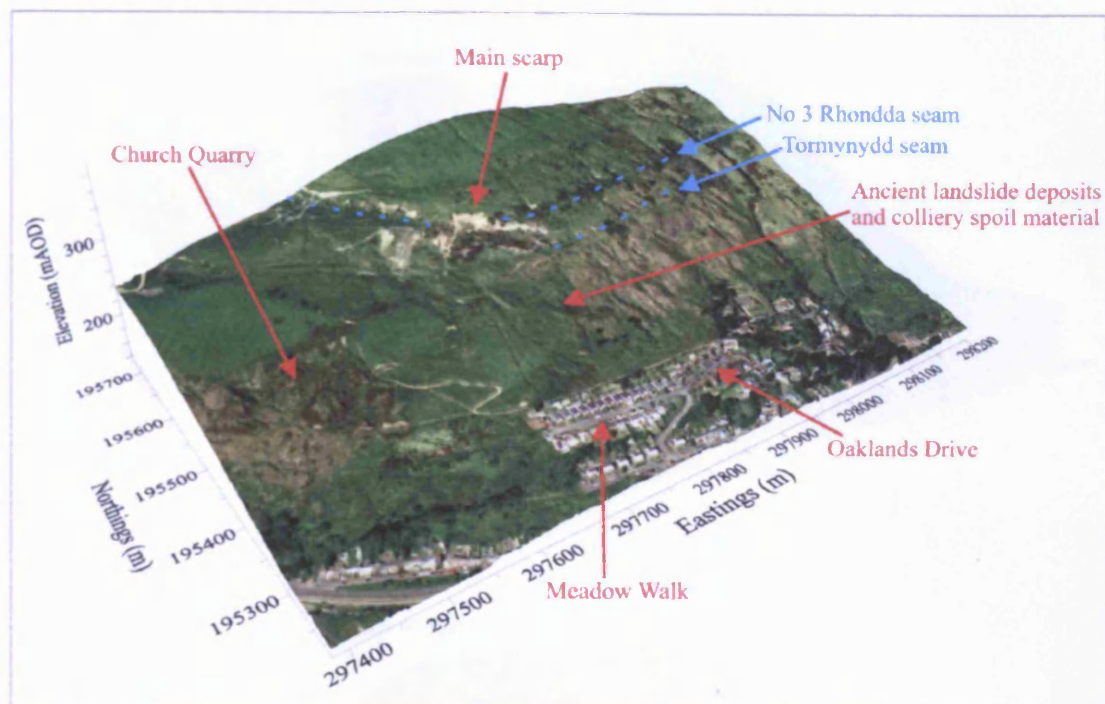


Figure 3.2 Terrain model of Mynydd yr Eglwys Landslide obtained by overlaying 2000 air photography (Getmapping website [WWW3.1]) onto LIDAR data (Environmental Agency UK)

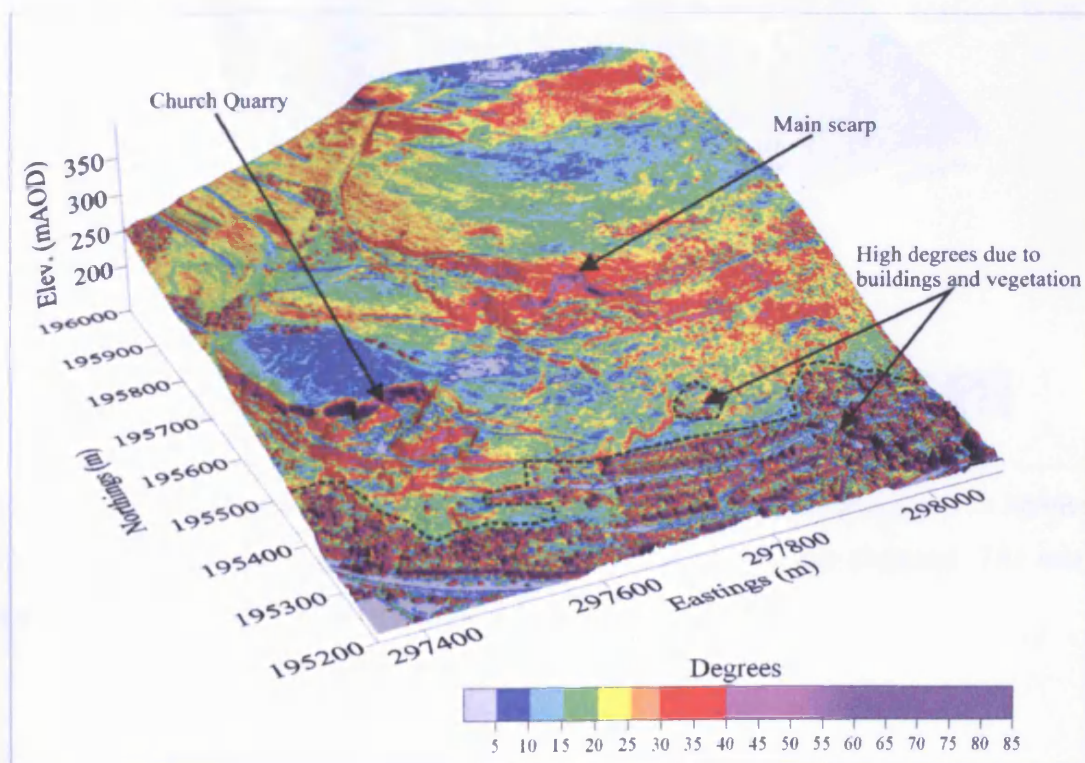


Figure 3.3 Slope angle map for part of Mynydd yr Eglwys hillslope, derived from LIDAR data

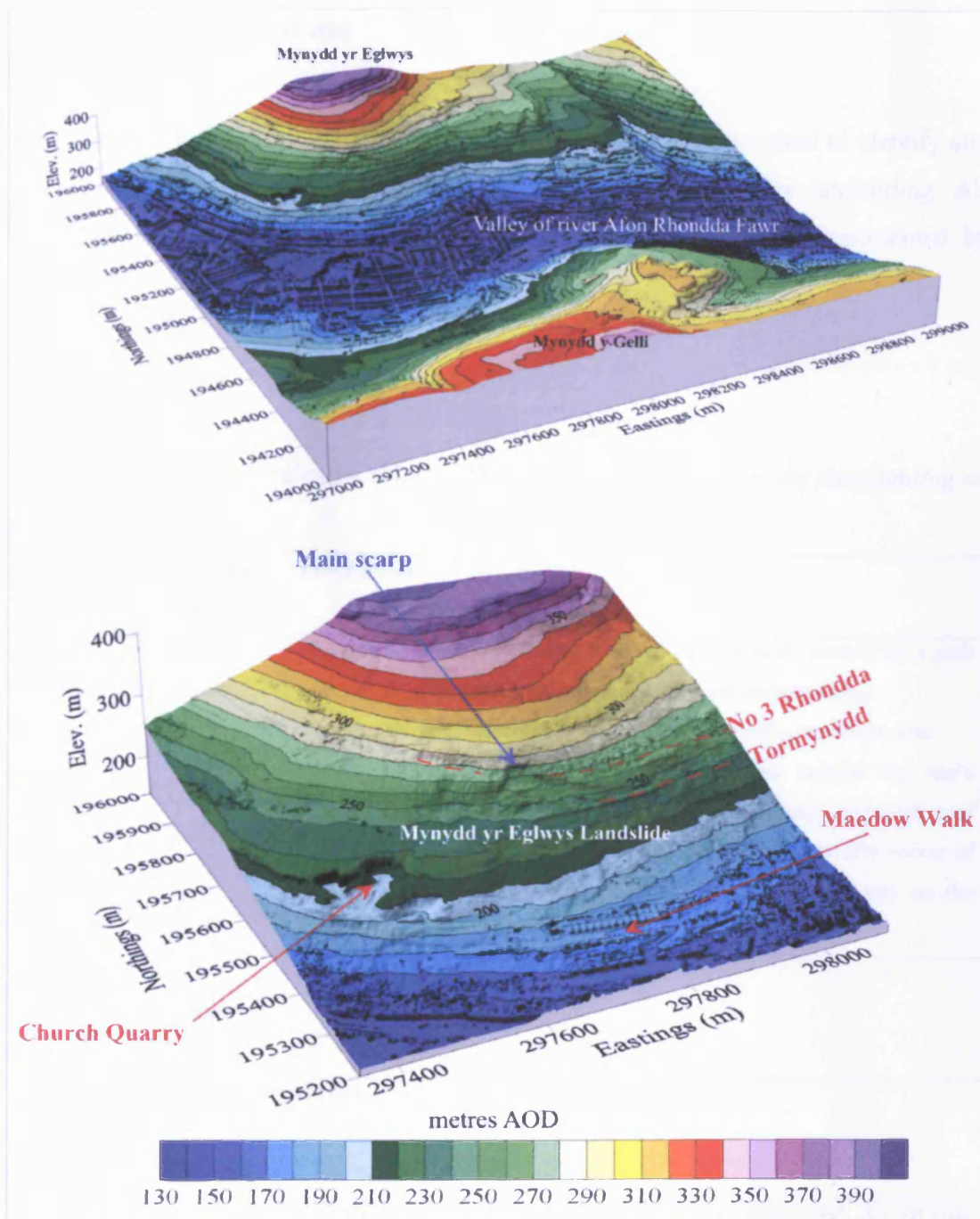


Figure 3.4 Topography across the Rhondda Fawr from Mynydd yr Eglwys to Mynydd y Gelli (top) and in the area of Mynydd yr Eglwys Landslide only (bottom). The images were obtained from EA LIDAR data using Surfer 8

3.3 Historical land use

All available historical maps and air photographs have been consulted to identify any ground changes that have occurred in the area now affected by landsliding. All identified ground changes are summarised in Table 3.1 and are documented by Figures 3.5-3.9.

Table 3.1 Summary of relevant changes that occurred on site or in the surrounding area from 1875 to 1962

Published date and scale (Reference and Figure)	Description
1875 (Ordnance Survey Map) (Figure 3.5)	The area of the site is shown as open pasture land, crossed by a path running SW-NE, similar in position to the one present today. Church Quarry represents the main man-made influence in the area. A trial coal level is located in the NE area, outside the site's boundaries. There is no sign of other crop workings, although coal mining was taking place at "Ty Fry Levels", beyond the NW corner of the site (also in Halcrow, 1999). Buildings are located only on the valley floor.
1877, 1:2500 (Ordnance Survey Map, County Series, 1 st edition)	No relevant changes have been noticed.
1884-85, 1:10560 (Ordnance Survey Map, County Series, 1 st edition)	No relevant changes have been noticed.
1900, 1:10560 (Ordnance Survey Map, County Series, 1 st revision of 1884-85 map) (Figure 3.6)	The trial level to the east of the site had been abandoned. An old coal level and an old air shaft are shown outside the North-West boundary of the site. Ty-fry Levels are marked as disused. A water spring is shown close to the SW-NE path. As noticed in Halcrow (1999), a tramway connects a level in Church Quarry with Bodringallt Colliery to the East and this corresponds to today's footpath upslope of the house gardens of Meadow Walk.

Table 3.1 (Continue)

Published date and scale (Reference and Figure)	Description
1919, 1:2500 (Ordnance Survey Map, County Series, 2 nd revision of 1887 map) (Figure 3.6)	<p>Allotment gardens are shown in the area today occupied by the houses and gardens of Meadow Walk. An old trial coal level is located to the West of the allotments.</p> <p>Abandoned coal levels and spoil heaps are shown in the upper part of the slope, now affected by landsliding (to the East of today's main scarp). According to Halcrow (1999), the coal workings belonged to the Cymric Rhondda Colliery.</p> <p>An old coal level and an old quarry are located at the west boundary of today's main scarp.</p>
1921, 1:10560 (Ordnance Survey Map, County Series, 2 nd revision of 1884-85 map)	No relevant changes have been noticed.
1948 Air Photography (Figure 3.7)	<p>The air photograph shows many crop workings along No 3 Rhondda and Tormynydd seams with some clear drainage channels carrying water out of the mine adits. According to Halcrow (1999), the crop workings were probably carried out during the miner's strike of 1926.</p> <p>There is evidence of fissuring upslope of the area of today's main scarp. Lobes of ancient landslide deposits can also be identified.</p> <p>There are allotments immediately downhill of the toe of the lobes.</p> <p>Church sandstone quarry has been abandoned.</p>
1962, 1:2500 (Ordnance Survey Map, National Grid) (Figure 3.8)	<p>The crop coal workings along No 3 Rhondda and Tormynydd seams are marked on the map. A wide spoil heap is shown in the area today affected by the main scarp.</p> <p>An allotment/enclosure is shown close to the SW-NE path.</p> <p>Two issues are marked at the toe, close to the main track.</p> <p>A water collecting point is located to the south of the central spoil tip of Tormynydd coal seam and water runs from there through an area with trees towards an allotment/enclosure.</p> <p>Allotments/enclosures with one building are located immediately downhill of the toe of the lobes only in the east part of the site.</p>

Since the late 1970s, new housing developments have been built downhill of the landslide toe (The Uplands, Oaklands Drive and in Meadow Walk). The westernmost house of Meadow Walk was only completed in 1992 (Halcrow, 1999).

Figure 3.9 shows an air photograph of the site before (1993) and after the new landslide event (2000). In 1993 the line of crop workings of No 3 Rhondda appeared almost continuous, while in 2000 it has been clearly displaced by the MYE landslide event.

In the MYE area, no signs of instability were recognised or reported in the 1980 South Wales Coalfield landslip survey of Conway et al. The area was described as a “shallow translational debris slide in superficial deposits” and evaluated as “recently active” in the report “Rhondda landslip potential assessment” carried out by Halcrow (1988; see section 3.8).

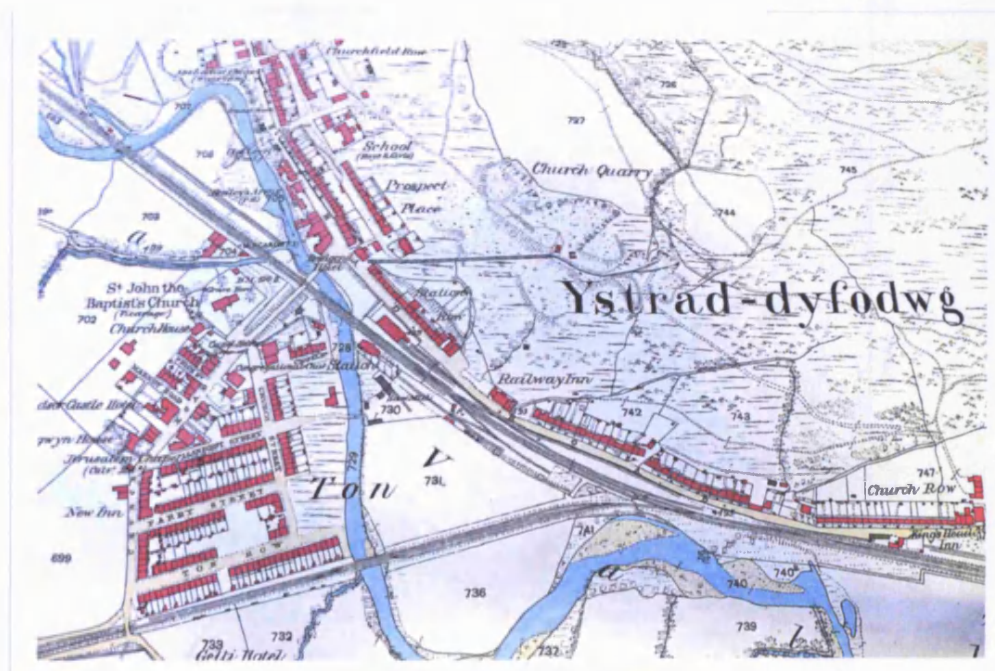


Figure 3.5 Part of the 1875 Ordnance Survey Map 6" to 1 Mile coloured

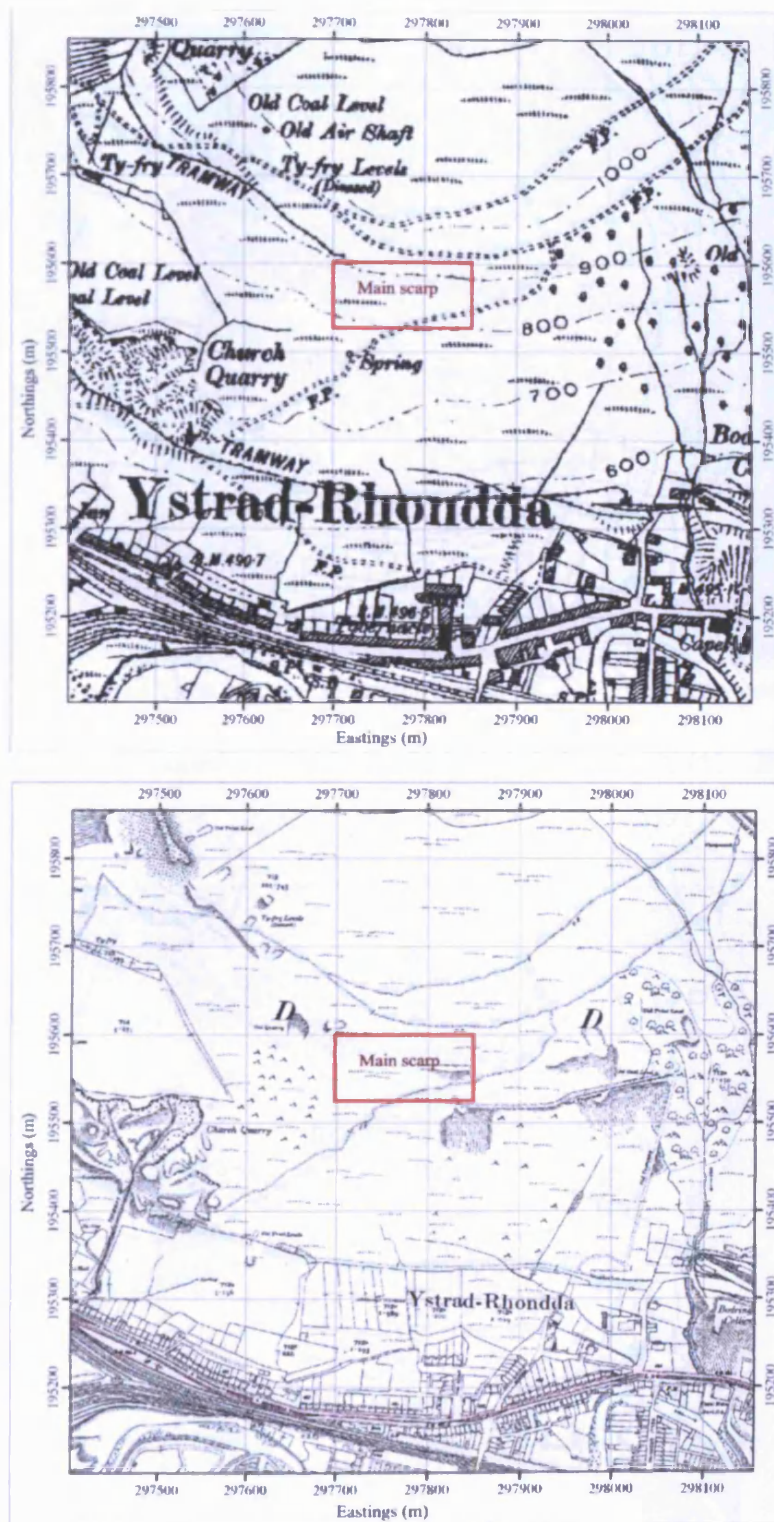


Figure 3.6 Reproduced from 1900 (top) and 1919 (bottom) Ordnance Survey Maps, (©Crown copyright 2009. An Ordnance Survey/EDINA supplied service; [WWW 3.2]). The red box shows the approximate location of the main scarp visible today. See Appendix D for legend

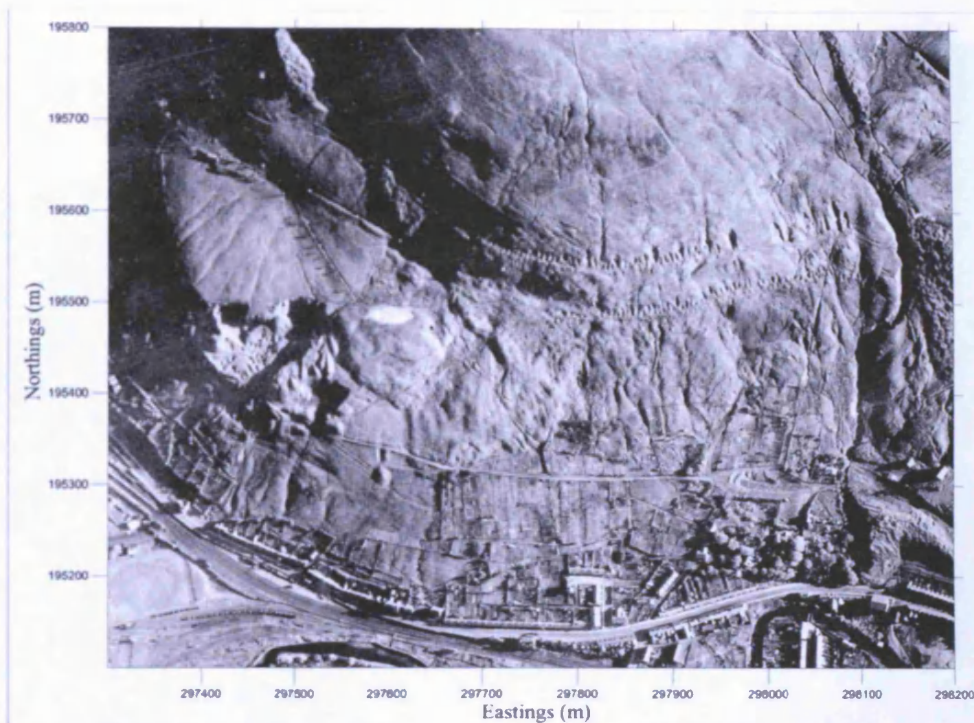


Figure 3.7 Geo-referenced air photograph of 1948 (RAF: Welsh Assembly Government archive)



Figure 3.8 Reproduced from 1962 Ordnance Survey Map, 1:2500 (with 1:25000 OSM in transparency) (©Crown Copyright/database right 2009. An Ordnance Survey/EDINA supplied service; [WWW 3.2]). The red box shows the approximate location of the main scarp. See Appendix D for legend



Figure 3.9 Air photography of 5 May 1993 (Ordnance Survey) and air photography of 2000 (Bottom; Getmapping [WWW 3.1]). The two photographs show Mynydd yr Eglwys slope before (top) and after (bottom) the new deep-seated landslide event

3.4 Geology

3.4.1 Solid geology

Mynydd yr Eglwys slope is composed of Carboniferous Middle Coal Measures overlain by the Llynfi Beds of the Upper Coal Measures (Figures 3.10-3.14). The geological map and the geological cross section produced by Halcrow (1999; 2000) for MYE Landslide are shown in Figures 3.12 and 3.13. The map and the section were drawn before any invasive investigations were carried out at the MYE site and were based on 6 inch British Geological Survey maps, previous site investigations at Pentre Landslide and the shaft section of Pentre Colliery.

The NW-SE trending Cymmer Fault crosses the site and downthrows strata to the SW. Following site investigations at Pentre site, H. J. Siddle of Halcrow (Halcrow, 1979) proposed a splitting of the Cymmer Fault at the plateau above Church Quarry (Figure 3.11). According to Halcrow (1999) the area of the fault is likely to be characterised by clay gouge, due to the mainly argillaceous soft nature of the strata.

In June, July and August 2003 ground investigations were carried out by C. J. Associates Geotechnical Ltd on behalf of Earth Science Partnership (C.J. Associates, 2003; Earth Science Partnership, 2004). The location of boreholes, trial pits/trench is shown in Figure 3.11. The results of the site investigations generally confirm the geology conjectured by Halcrow. However, borehole logs and their interpretation appear unreliable, with lithological descriptions being incoherent, with clear discrepancies between closely adjacent boreholes.

Middle Coal Measures (from Abergorky Seam to Upper Cwmgorse Marine Band)

The Middle Coal Measures between the Cefn Coed Marine Band and the Upper Cwmgorse Band in the Northern Rhondda Fawr area are composed mainly of mudstone and siltstone, with subordinate sandstones and common ironstone nodules and ribs (Woodland and Evans, 1964). The Abergorky Seam is overlain mainly by mudstones, with sandstones in places, of generally 10.7-12.2 m thickness and then by a thin rider coal. This coal is followed by a mainly argillaceous sequence (24 -33 m thickness) of mudstones with ironstone bands. Above this sequence, there is the

Hafod Seam with an almost white thick seatearth beneath it. The Hafod Seam is overlain by other two thin coal seams (Woodland and Evans, 1964).

Llynfi Beds (lower part of Upper Coal Measures)

The Llynfi Beds are between 122 and 137 m thick in the northern Rhondda Fawr area (Woodland and Evans, 1964). Woodland and Evans (1964) describe a sequence from the Upper Cwmgorse Marine Band to the Tormynydd Seam in detail. The sequence comprises of mudstone, seatearth, coal, siltstone and sandstone. Halcrow (1999) underlines that the mainly argillaceous strata between the Upper Cwmgorse Marine Band and the Tormynydd Seam were approximately 25 m thick at Pentre site. Moreover, they contained “three seatearths associated with two thin coals and the Tormynydd Seam itself”. The Tormynydd Seam is overlain by persistent sandstones known as the Llynfi Rock (Woodland and Evans, 1964), which is overlain by 5 m of argillaceous rocks and the No 3 Rhondda Seam (Halcrow, 1999). The sandstone is approximately 14 m thick at Church Quarry and also forms the escarpment above 250 m AOD (Halcrow, 1999). The sequence between No 3 and No 2 Rhondda is 61-72m thick and is composed of mudstone, striped beds, sandstone, coal and associated seatearths (Woodland and Evans, 1964).

Detailed geology gained from ground investigations by C. J. Associates

The logs of the boreholes drilled in the area above the main scarp are characterised mainly by sandstone (Figure 3.14). In these boreholes (2A, 2B, 6 and 6A) layers comprise of weathered/broken sandstone, mudstone and coal with voids which has been interpreted by Earth Science Partnership (ESP) as the No 3 Rhondda Seam and the mine workings within it. Below the No 3 Rhondda Seam and associated workings, weathered sandstone was found to a depth of 73 m b.g.l. in borehole 2A. Some strata of siltstone were reported for borehole 2B, whereas in borehole 6, the No. 3 Rhondda Seam was underlain by 1.3 m thick sandstone and 7.3 m of mudstone.

In borehole 1 (0-25 m depth), located to the west of the main scarp, possibly between the two branches of the Cymmer Fault (Figure 3.11), strata are mainly argillaceous, with coal (1.7 m thick) at 23 m depth that ESP interpret as the No 3 Rhondda coal seam.

In the 36 m deep boreholes immediately below the displaced block, strata are mainly argillaceous (boreholes 3, 3A, 4 and 4A; Figure 3.14). The strata are composed of sometimes iron stained weathered siltstones and mudstones and two coal seams. ESP interprets the shallower coal in borehole 3A as the Tormynydd seam and the deeper seam in borehole 3 as the Hafod seam.

Borehole 8 shows that strata in the central area of the MYE site comprise of weathered and iron stained siltstone, with a 0.3 m coal horizon at 17 m b.g.l. This coal horizon was interpreted by ESP as being the Tormynydd Seam (Figure 3.14).

3.4.2 Superficial deposits

Before any site investigations took place, Halcrow (1999; 2000) suggested the presence of Periglacial Head deposits over the upper part of the hillslope and glacial till over its lower part. They report that the ancient landslide deposits contain a gravel of mudstone in the western part of the site, but consist mainly of Periglacial Head over the eastern section. Colliery spoil material found on site consists of “loose gravel of mudstone and carbonaceous shale” (Halcrow, 1999).

Detailed information gained from ground investigations by C. J. Associates and Halcrow

Above the main scarp (boreholes 2A, 2B, 6, 6A) superficial sediments consist of 0.6-1 m of clay overlying highly weathered sandstone. These sediments were interpreted by ESP (2004) as being Periglacial Head.

In the area downhill of the main scarp (borehole 4), 1.7 m thick gravelly clay overlies 4 m of mudstone. The clay deposits are considered as being of glacial meltout origin by ESP (2004). Mudstone gravel makes up the first 5.4 m of borehole 3. Superficial deposits in the central area of the site (boreholes 8, 7, 9, trial pit 1) consist generally of 4-6 m of alternating layers of clay and gravel. These sediments were considered glacial melt out deposits and possible landslide materials by ESP (2004). Alternating layers of clay, gravel and sand were found in the first 6 m of borehole 5.

From an engineering point of view the highly weathered bedrock found below the

superficial deposits would be difficult to differentiate and the “engineering rockhead” lies at the base of bedrock weathering.

3.4.3 Structure

The large NW-SE trending Cymmer Fault crosses the central part of the MYE site and downthrows strata 41m to the SW (Figures 3.10-3.12; Halcrow, 1999). According to the Coal Authority mine plans for the Lower Six Feet and Tormynydd seams, strata dip 4 degrees to the south-east on the upthrow side of the Cymmer Fault (Halcrow, 1999; 2000). However, according to Halcrow (1999; 2000) dips are likely to be complex around the zone of the Cymmer Fault. ESP (2004) analysed the results obtained from optical and acoustic imaging investigations carried out down boreholes. Contrary to Halcrow suggestions, they concluded that the general dip of strata is 6 degrees to the south-west, with exception of Borehole 1 which is in the vicinity of the Cymmer Fault.

Table 3.2 Summary of dip and dip direction of strata provided by Earth Science Partnership (2004)

Borehole	Average fabric dip (degrees)	Average azimuth or dip direction (degrees)
Bh1	23.25	185
Bh3	4.68	157
Bh4	3.61	200
Bh6	6.73	217
Bh7	7.11	233
Bh8	5.33	113

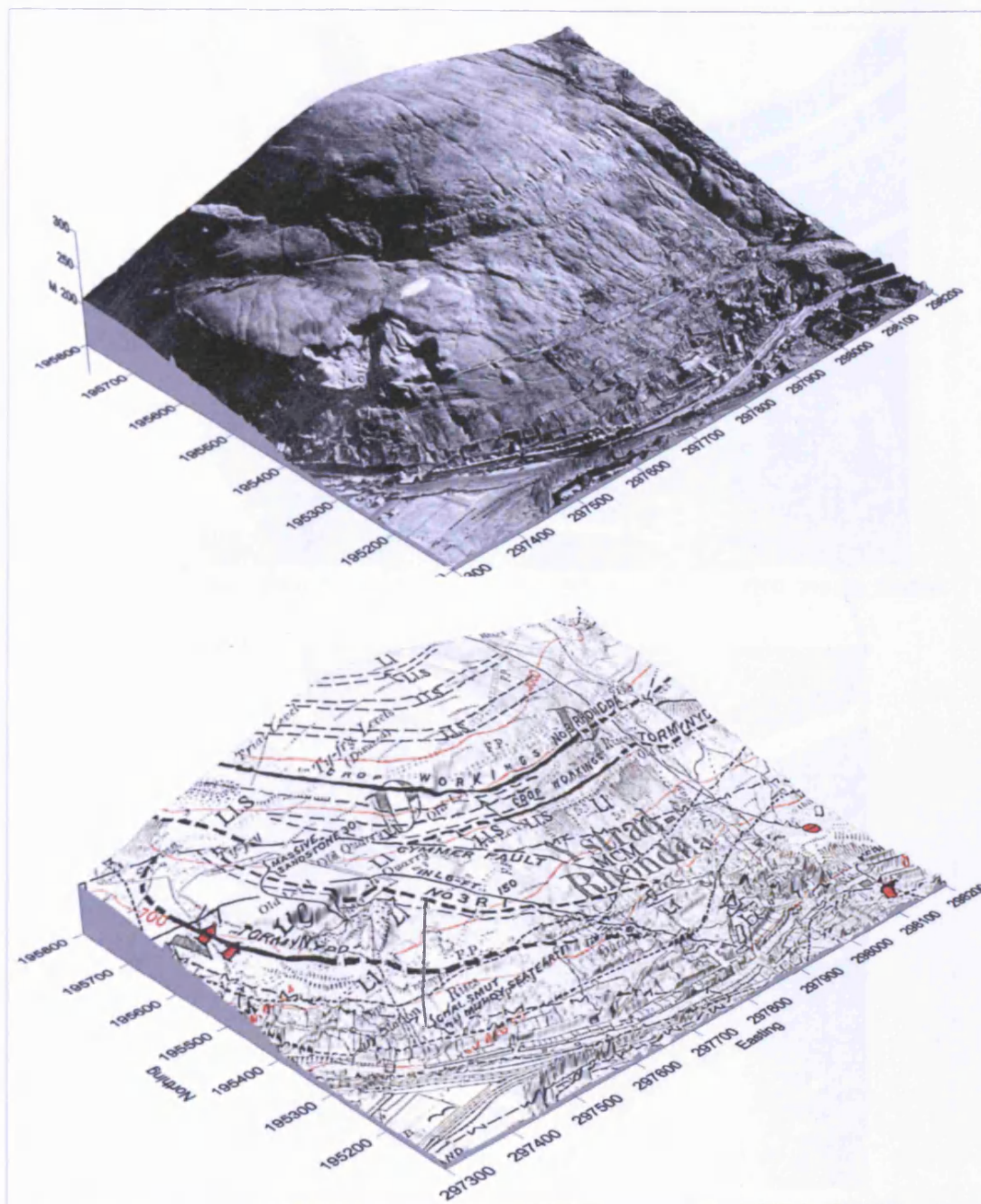


Figure 3.10 1948 air photography (top) and geological map (bottom) overlaid on LIDAR DTM data. The geological map is reproduced from Glamorgan Sheet XVIII S.W., published in 1960, from an original geological survey by W. Gibson in 1896, resurveyed by W. B. Evans in 1953 and A. W. Woodland in 1946. Red circles and red arrows indicate mine shafts and mine adits respectively

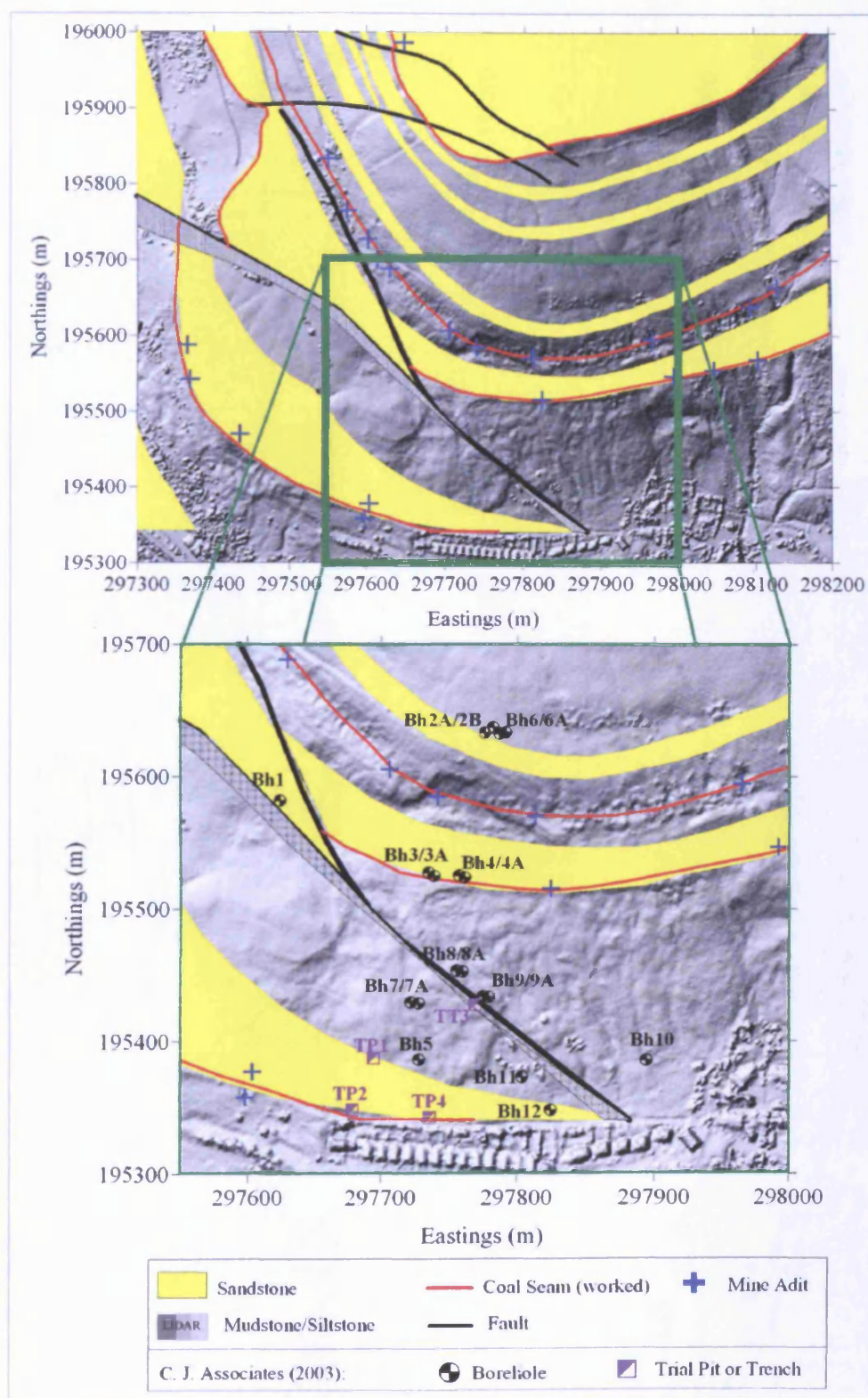


Figure 3.11 Solid geology map digitized from Halcrow report on Pentre Landslide (Halcrow, 1979) and overlaid on LIDAR data (top). Zoom on the area of Mynydd yr Eglwys Landslide showing the location of boreholes driven into the ground in 2003 by C.J. Associates (bottom)

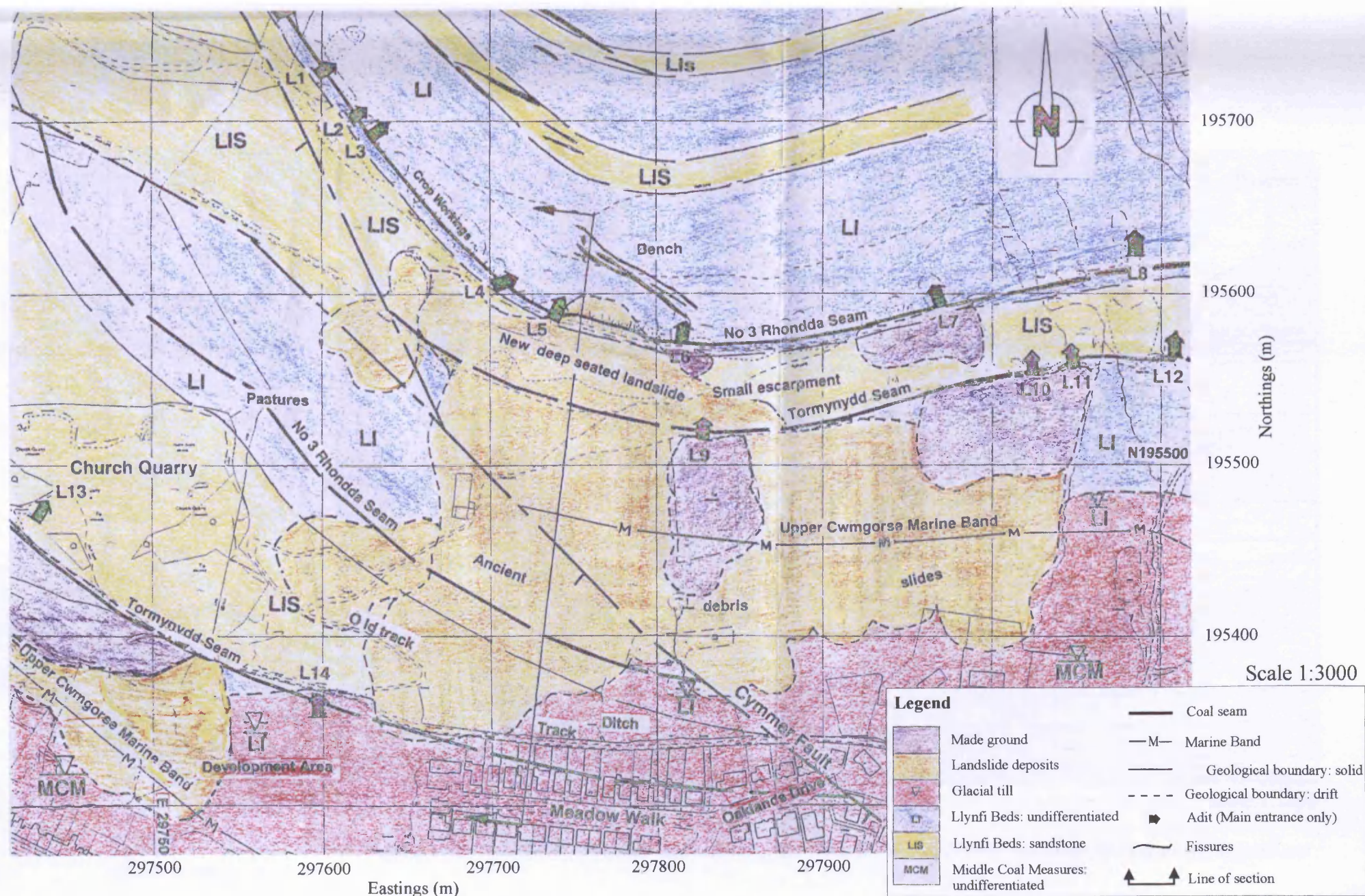


Figure 3.12 Geological plan for Mynydd yr Eglwys landslide reproduced from Halcrow report (1999) (the geological cross section is shown in Figure 3.13)

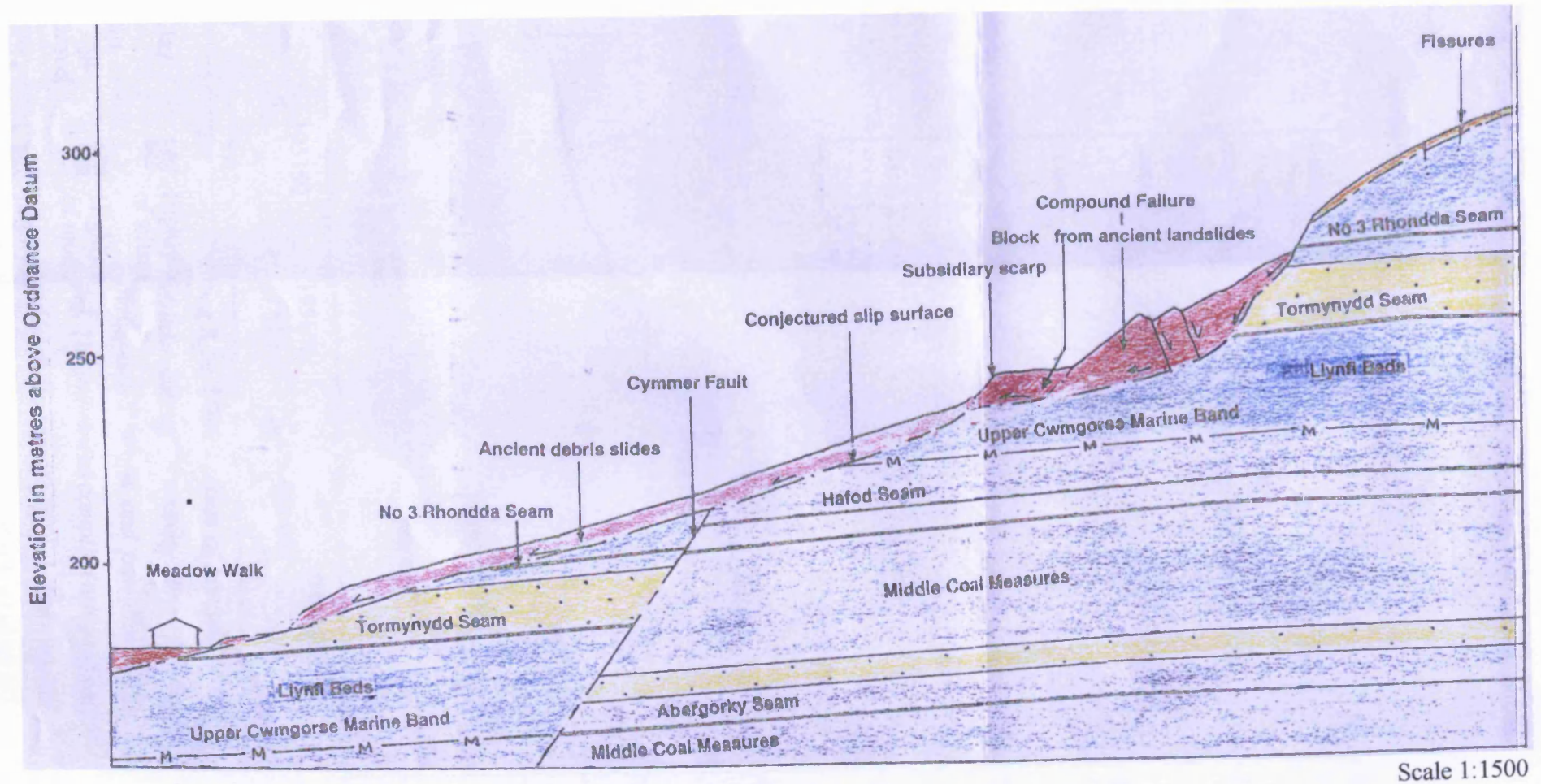


Figure 3.13 Geological section of Mynydd yr Eglwys Landslide reproduced from Halcrow report (1999) (location of section and legend are shown in Figure 3.12)

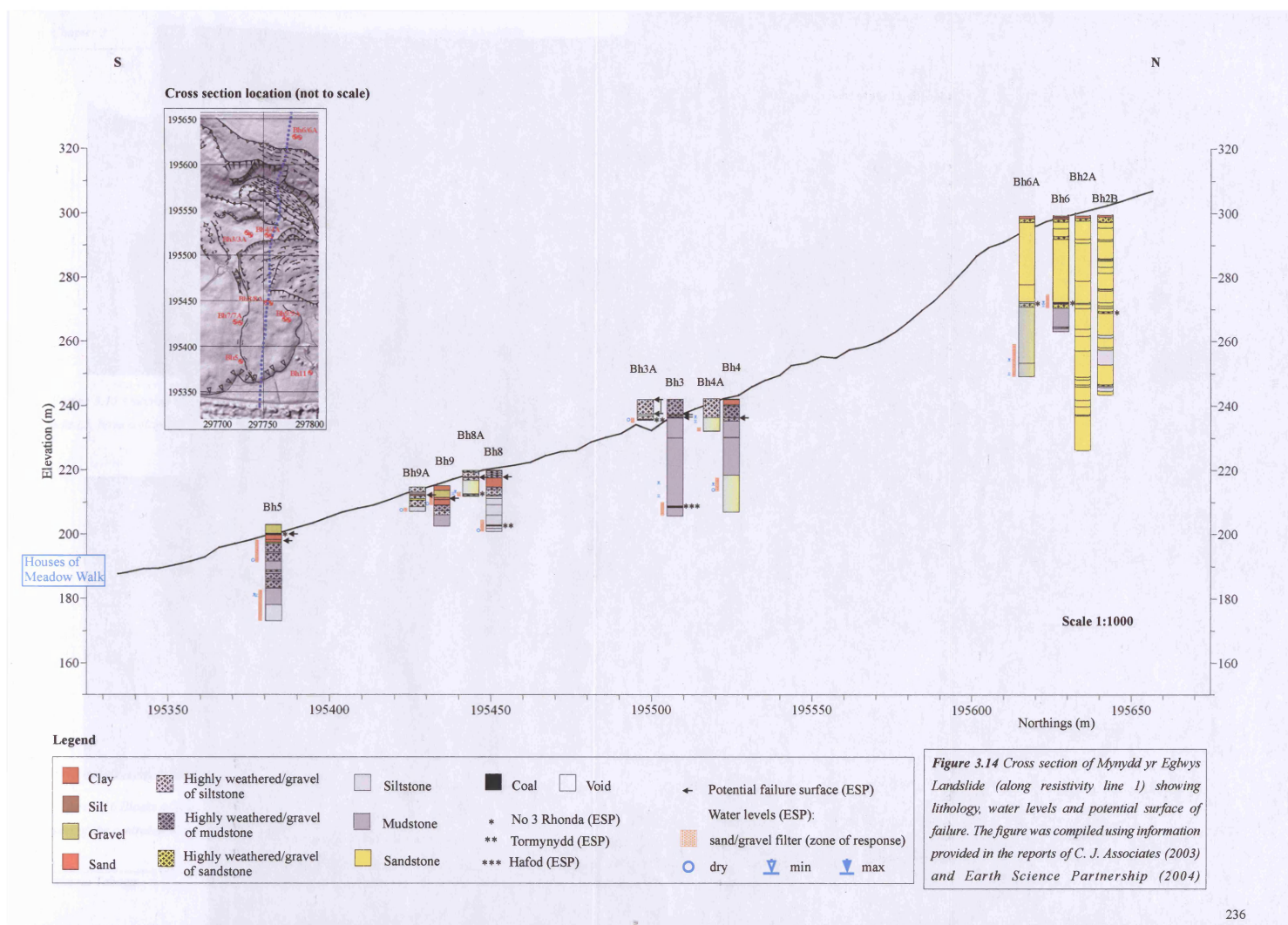




Figure 3.15 Outcrop of No 3 Rhondda Seam. The strata above it, in the area of mine adit L5, have collapsed



Figure 3.16 Blocks of argillaceous shale with iron staining can be found in the northern part of the central debris slides



Figure 3.17 View of the minor scarp immediately downslope of boreholes 3, 3A, 4 and 4A. As evident from borehole logs and outcrops at cracks and scarps, landslide superficial deposits are characterised in this area by gravel of mudstone/siltstone and highly weathered argillaceous rocks

3.5 Mining

Coal mining in the study area commenced around 1857 with the opening of the Pentre and Church Levels (Lewis, 1959; Halcrow, 1999). Information gathered from Coal Authority mining records were compiled by Halcrow (1999) and are summarised below.

Shallow workings

Coal mining from horizontal outcrop levels was carried out at both the No 3 Rhondda and Tormynydd seams. These outcrop workings were probably only of limited extent into the hillslope.

The 0.6 m thick No 3 Rhondda Seam was mined between 1857 and 1906 from the levels numbered L1 to L8 of Ystrad Rhondda Colliery (Halcrow, 1999; Figure 3.12). The coal seam was worked by pillar and stall methods and according to Halcrow (1999), voids may possibly still be present but are unlikely due to their age. Figure 3.18 shows the abandonment mine plan of No 3 Rhondda workings overlaid onto a LIDAR DTM model and 1948 air photograph. The figure suggests that these workings extended upslope of the main scarp of the landslide and that a triangular unworked area was left between levels L4/L5 and L6. This unworked area is now characterised by old subsidence fissures and lies immediately north of the main scarp of MYE landslide.

The 0.6 m thick Tormynydd coal seam was worked up to 1906 from levels L9, L10 and L11 of Cymric Rhondda Colliery (Halcrow, 1999; Figure 3.12). The spoil tips associated to these two levels are evident on site. Coal was probably mined by longwall methods and only the main roadways may still be open (Halcrow, 2000). Figure 3.19 shows the abandonment mine plan of Tormynydd workings overlaid onto LIDAR data and 1948 air photograph. From the figure, it is evident that these coal workings extended beneath the MYE landslide area.

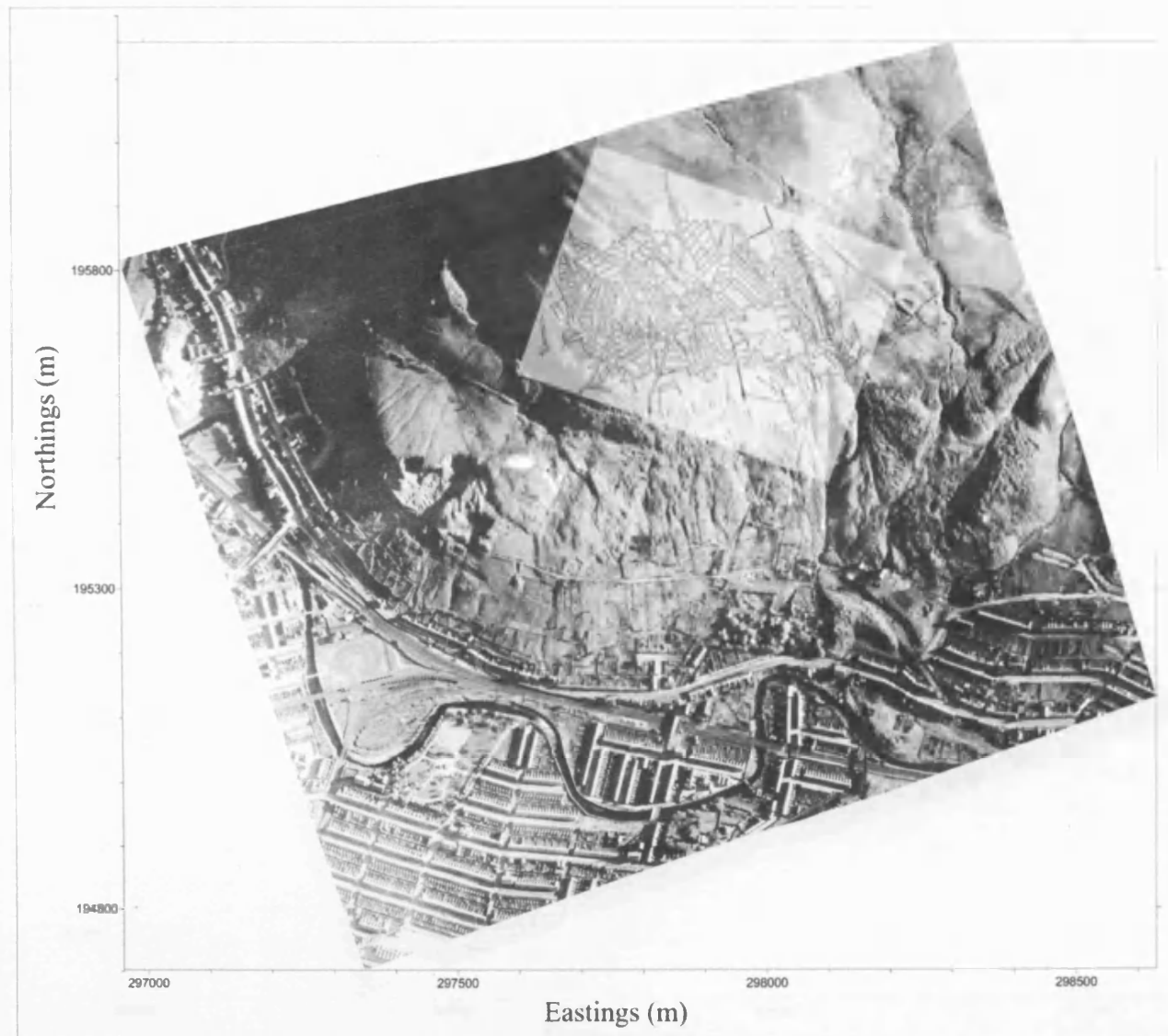


Figure 3.18 Abandonment mine plan of No 3 Rhondda Seam (Coal Authority) overlaid onto LIDAR data and 1948 air photograph

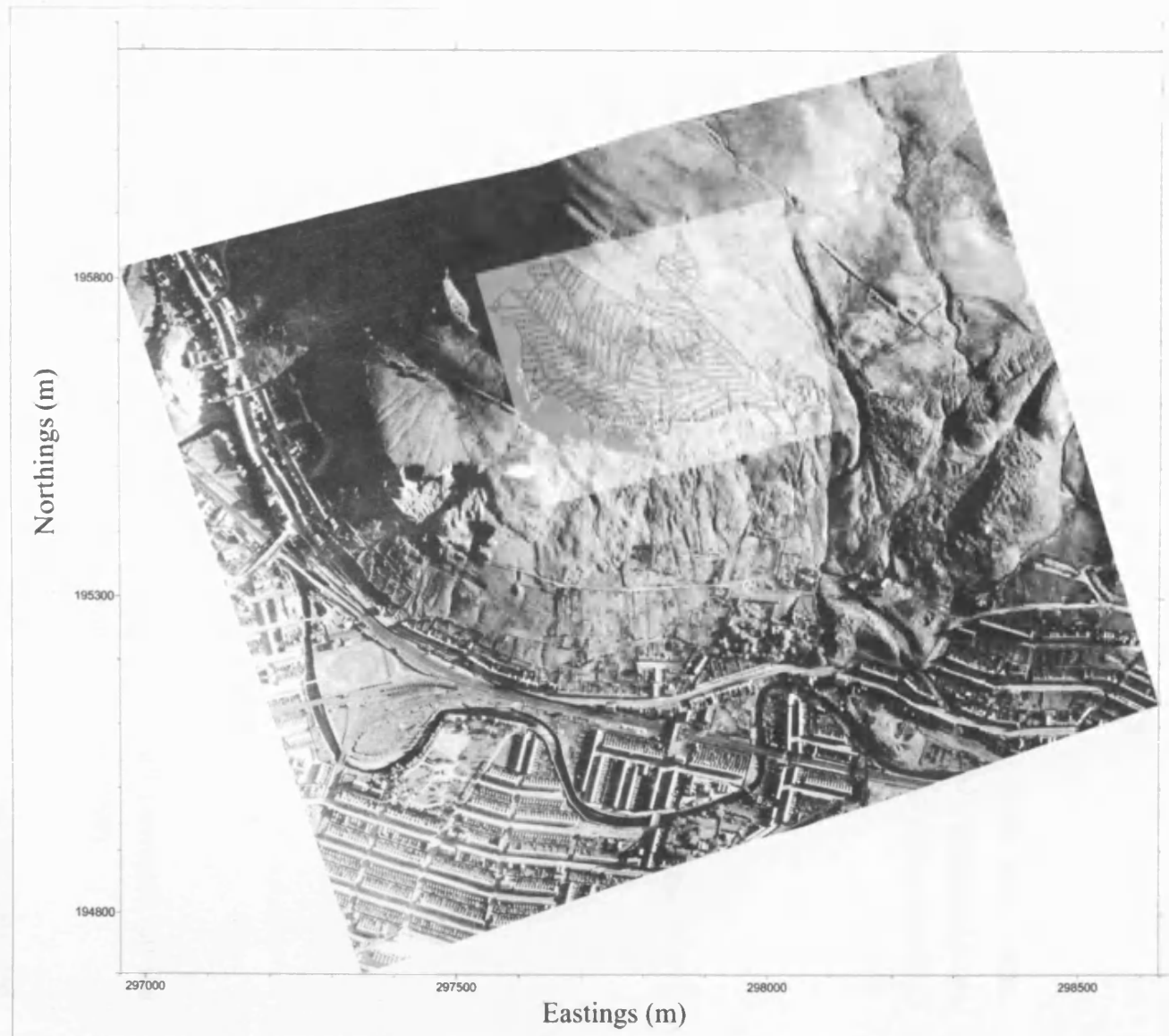


Figure 3.19 Abandonment mine plan of Tormynydd Seam (Coal Authority) overlaid onto LIDAR data and 1948 air photograph

The Tormynydd Seam was also mined in the area of Church Quarry from level L13 of Morgan and Ramsay Colliery (Figure 3.12), where it was however erroneously called the Hafod Seam (Halcrow, 1999). As shown on historical maps (i.e. Figure 3.6), another abandoned coal level into the Tormynydd Seam is located to the west of Meadow Walk (Halcrow, 1999).

Deep workings

Twelve coal seams were mined from shafts and associated drifts from Pentre, Bodringallt, Church and Gelli Collieries beneath the site or within its influencing area (Halcrow, 1999 and 2000, plus information taken from Coal Authority seam records):

- Abergorky (0.9 m thick; worked probably in the 1860s)
- Pentre (0.8 m thick; worked till 1931)
- Lower Pentre (0.9 m thick; worked till 1941)
- Two Feet Nine (1.5 m thick; worked till 1889 from Pentre Colliery and till 1925 from Bodringallt Colliery)
- Four Feet (2.1 m thick; worked till 1932)
- Six Feet (1.7 m thick)
- Nine Feet (1.4 m thick; worked till 1933)
- Bute (1.2 m thick; worked till 1928)
- Yard (1.4 m thick; worked till 1914)
- Seven Feet (2.5 m thick; worked till 1903)
- Five Feet (1.5 m thick; worked till 1908)
- Lower Five Feet (1.3 m thick; worked till 1919).

The Pentre and Lower Pentre seams were mined with longwall conveyors, all the other seams were exploited using hand-mined longwall (Halcrow, 1999).

Calculations on the probable maximum total thickness of coal that had been extracted beneath the site were carried out by Halcrow (1999). Their results show that up to 10 m of thickness of coal were extracted in the upper part of the slope, whereas the amount of coal mined in the lower part of the slope was very limited. Moreover, results highlight that these extractions followed a NW-SE trend (125 degrees).

Differential mining subsidence has likely caused the opening of natural joints parallel to this trend, creating the subsidence fissures that can be found upslope of main scarp and visible on the 1948 air photograph (Figure 3.7; Halcrow, 1999).

In addition to coal, it is possible that seatearth material was mined for local brick manufacture (Halcrow, 1999).

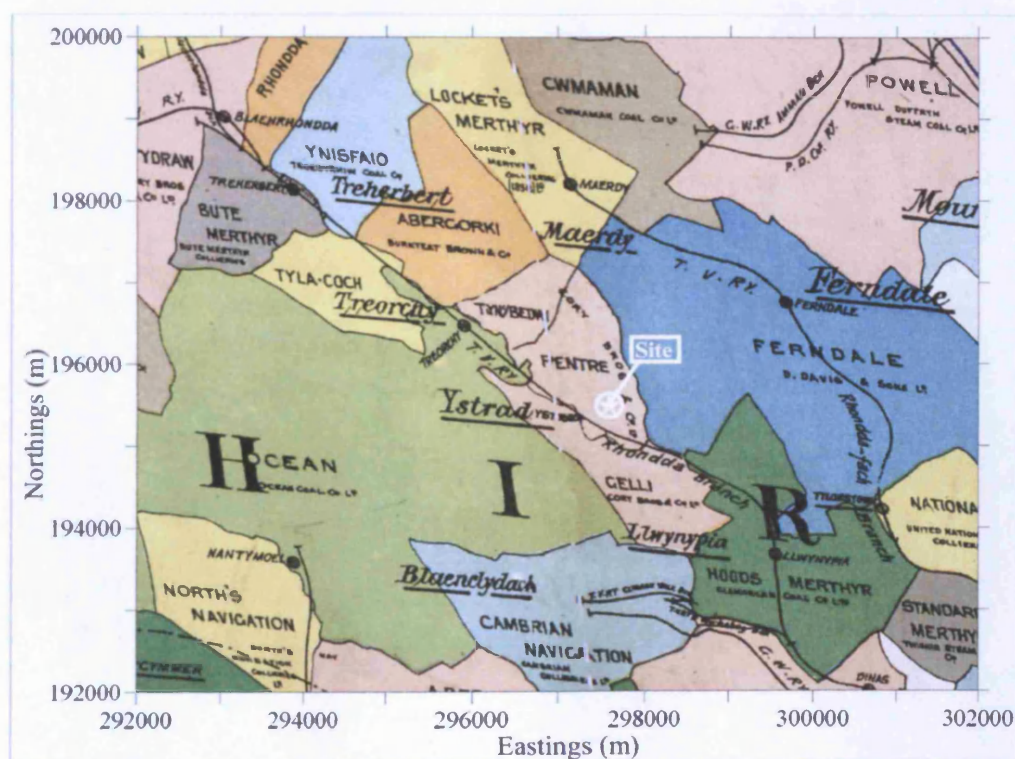


Figure 3.20 - 1927 Gordon's map of the South Wales coalfield (mineral takings)

3.6 Geomorphology

Figure 3.21 shows the geomorphological map that was prepared for this project, following walkover surveys at the end of March and beginning of April 2007. Mapping was carried out only in the eastern and central (the more active) parts of the landslide. The debris slide systems found in the eastern area, above Oakland Drive, were not covered by geomorphological mapping or for subsequent geophysical investigation/monitoring.

Some of the landforms/features marked on the geomorphological map are better visualised using the results of digital photogrammetry. Therefore, the orthophotograph and a perspective 3D view obtained from photogrammetry processing are included as Figure 3.22 and Figure 3.23 respectively. Some annotations were added to the images to help the reader visualise the landforms described in the following paragraphs. Other landforms are illustrated by the photographs shown in Figures 3.24-3.26.

For ease of reference, two different geomorphological zones have been marked on the map (Figure 3.21): zone 1 comprises the elements characterising the new deep-seated landslide, whereas zone 2 is the most active area of the ancient landslide deposits.

New deep-seated landslide (zone 1)

A main scarp of approximately 150-200 m width is located in the escarpment above the line of workings of Tormynydd Seam. While in 1999 it was reported to have a maximum height of 6 m (in Halcrow, 1999), the scarp is currently in excess of 20 m of height in its central area. The No 3 Rhondda Seam outcrops in the top part of the back scarp. The zone is generally dry except for water seeping from the base of the collapsed mine workings of the Rhondda No.3 coal seam (Figure 3.24).

Above the main scarp (at the crown of the landslide) there are some old fissures trending NW-SE (Figure 3.25) that were already visible in 1948 air photography (Figure 3.7).

Immediately downslope of the main scarp there are three-four linear ridges trending NW-SE and with upslope facing (“obsequent”; Halcrow, 1999) scarps (Figure 3.23 and 3.26). To the East, towards the spoil tip of L9 of Tormynydd Seam, the ridges are covered in boulders of mudstone/siltstone. Moreover, the southern ridge, immediately North of boreholes 4 and 4A, is partly formed by displaced blocks of strata tilted downhill (Figures 3.26).

In their geomorphological map, Halcrow (1999; 2000) highlighted the presence of two blocks of displaced strata associated to ancient deep-seated landslides. The blocks were described as abutting against the escarpment in the western part of the area. Moreover, one of the blocks was starting to be affected by a subsidiary line of fissuring. Comparing Halcrow geomorphological map with Figure 3.21, these two blocks should be located in the relatively flat area with boreholes 3, 3A, 4 and 4A. Halcrow’s hypothesis of ancient deep-seated landsliding was supported by the presence of corresponding hollows in the escarpment in aerial photographs.

Ancient debris slides (comprising zone 2)

From Church Quarry to the houses above Oaklands Drive, Halcrow (1999 and 2000) identified a total of eight ancient debris slide systems, separated by gullies with streams or reedy ground. However, as previously mentioned, the geomorphological mapping carried out for this project focused only on part of the landslide. Therefore, only three of the eight debris slide systems were considered and they have been called A, B and C (Figure 3.21). They are associated with debris slide systems 3, 4 and 5 of the Halcrow reports.

Debris slide A develops from the ridge and wet area to the west of boreholes 3 and 3A. This is the debris slide that extends the furthest downhill. In fact at the toe it approaches the main access track, just reaching the garden of the western house of Meadow Walk. Due to the proximity of its toe to the houses, this debris slide was initially the part of the landslide causing more concern. However, today it does not appear to show any signs of fresh activity (which is also confirmed by movement monitoring data in section 3.11.2).

Debris slides B and C develop from the minor scarp. Both slides are cut by linear

shear zones (Figure 3.25) that extend from the edges of the minor scarp to the debris toes. The eastern linear tear cuts through the spoil tip material associated with mine adit L9 of Tormynydd Seam. These tears were first observed by ESP in 2004, but over the period of this project the cracking has become more obvious.

Zone 2 is the most active, with very hummocky terrain. Outside zone 2, in debris slide B, the topography becomes smoother and cracking less severe, but signs of fresh cracking can be noticed at the toe. Outside zone 2, debris slide C is characterised by the presence of spoil tip to the north and a very wet area, with streams, reedy ground and a pond at its toe.

Several springs and ponds were mapped across the site, from the plateau above Church Quarry to the wet land around debris slide C. Their location appears to follow the NW-SE trend of the Cymmer Fault.

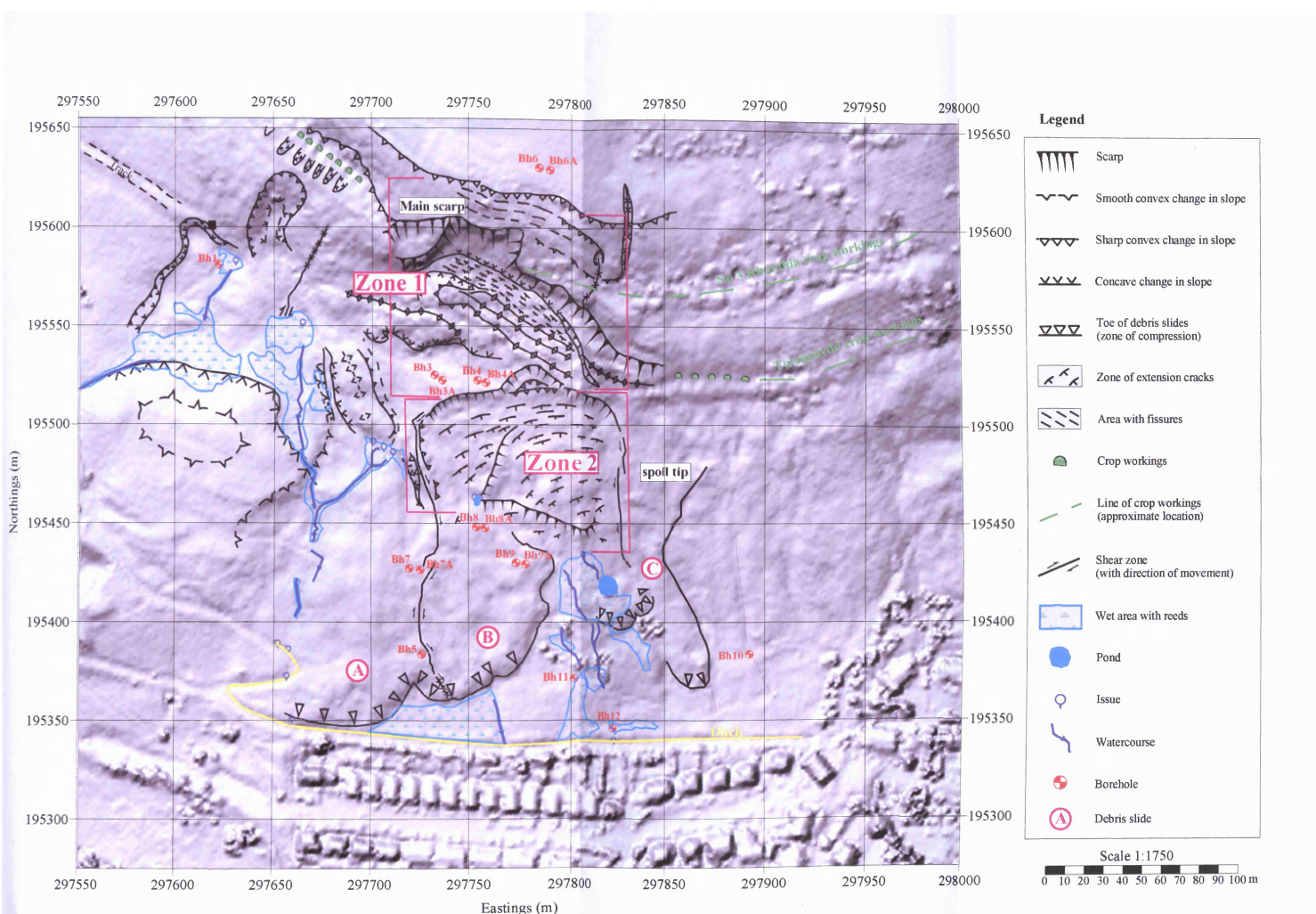


Figure 3.21 Geomorphological map of the area of Mynydd yr Eglwys Landslide investigated for this project, based on walkover surveys and GPS surveying carried out at the end of March and beginning of April 2007

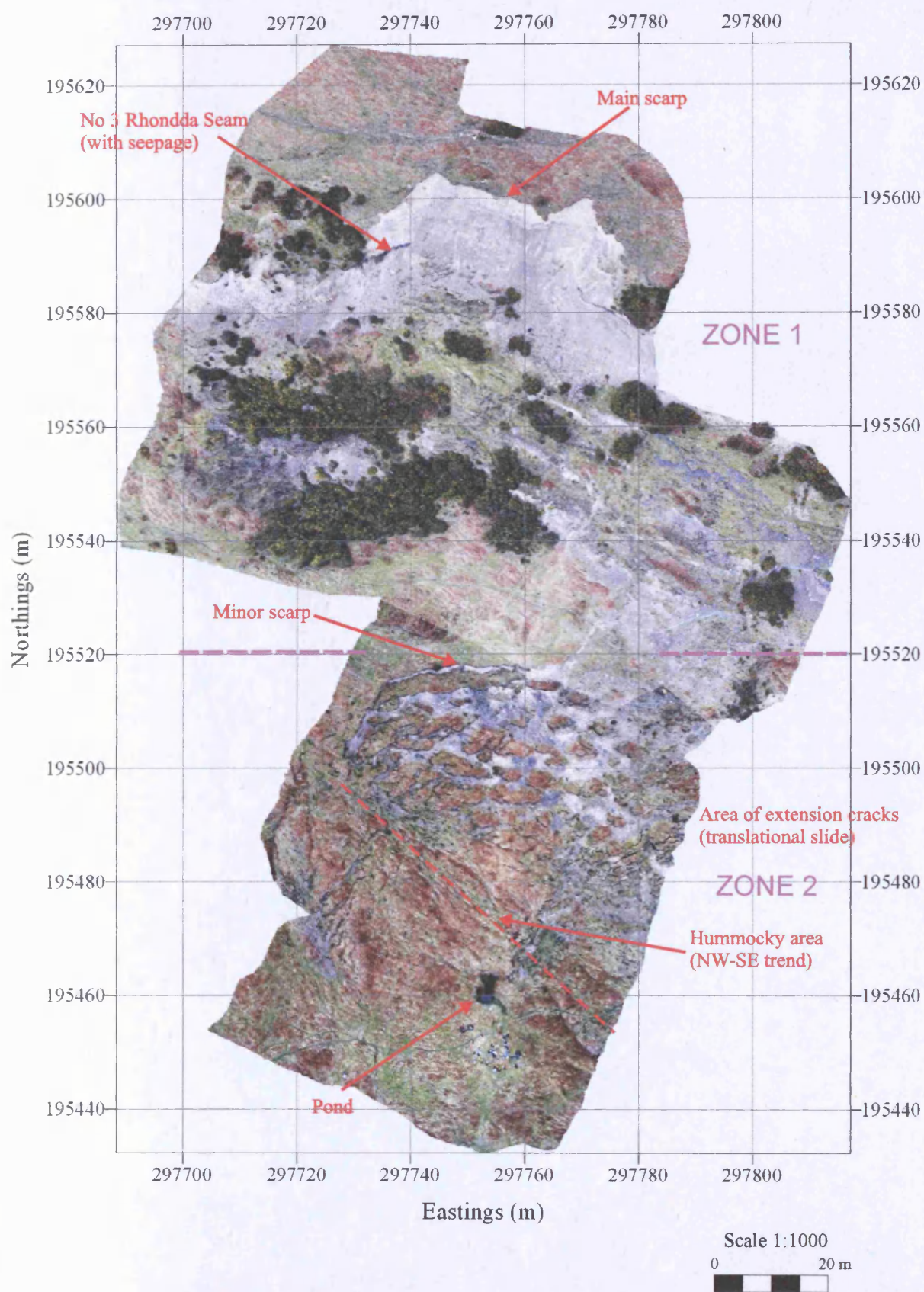


Figure 3.22 Orthophotograph of the northern central part of Mynydd yr Eglwys Landslide obtained from processing of digital photogrammetry. Annotations highlight some of the landforms described in the text

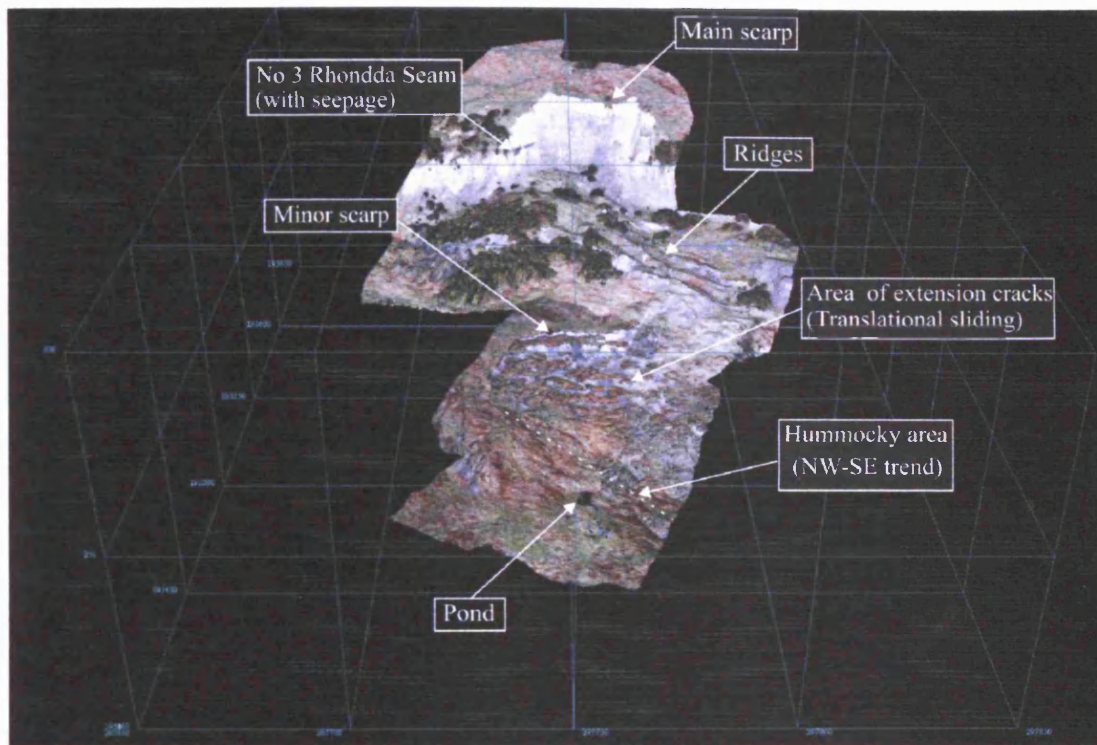


Figure 3.23 Perspective view of the northern central part of Mynydd yr Eglwys Landslide from Topcon's PI-3000v3 photogrammetry software. Annotations highlight some of the landform described in the text



Figure 3.24 View of the western part of the main scarp showing the outcrop of No 3 Rhondda Seam with clear evidence of seepage from its base



Figure 3.25 View of one of the fissures above the main scarp (left; photo by N. Ross) and of the shear zone that crosses debris slide B from the area North of borehole 5 towards the minor scarp (right; photo by P. J. Brabham)



Figure 3.26 View of ridges with upslope facing scarps located at the base of the main scarp. The southern ridge, immediately upslope of boreholes 4 and 4A, consists of a detached block of strata tilted downslope (photo by P. J. Brabham)

3.7 Hydrology and hydrogeology

The site is located in one of the wettest regions of the South Wales Coalfield. The estimated long-term annual average rainfall for the period 1941-1970 is 2398 mm for the rain gauge located at Treherbert (Gauge No 490261, at Ty'n-y-waun) and 2400 mm for the one at Parc Colliery (Halcrow, 1999).

High levels of rainfall are possible throughout the year (Figures 3.27 and 3.28). However, during the summer some of the rainfall is lost to evapotranspiration (Figure 3.28).

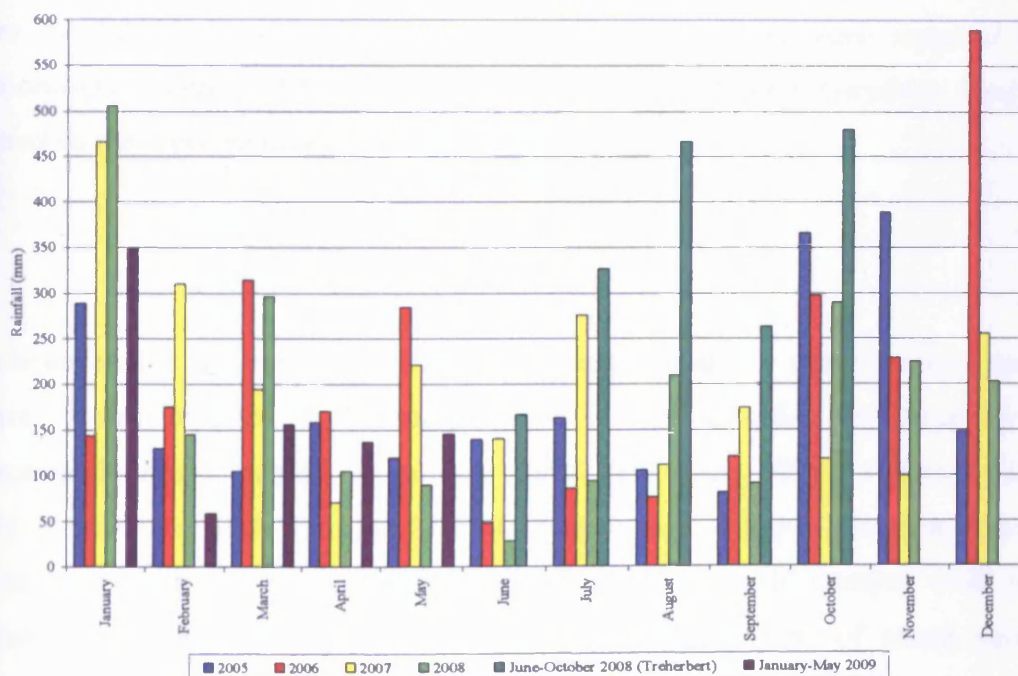


Figure 3.27 Monthly rainfall for the years 2005-2008 and for January-May 2009. A best estimate was obtained from the records of rain gauges and weather stations close to the site (as explained in section 2.12). Estimate may still suffer from errors due to gaps and uncertainties in the data provided. For the period June-October 2008 data from Treherbert rain gauge are shown in addition to the estimate based mainly on Blaencwm rain gauge because probably more reliable (see section 2.12)

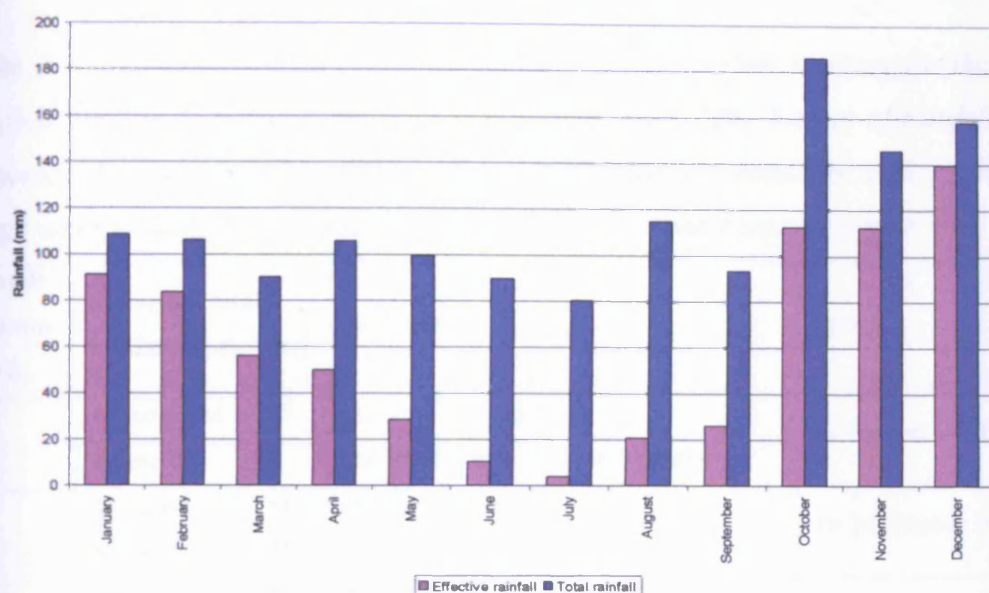


Figure 3.28 Mean monthly effective rainfall and mean monthly total rainfall for the years 1997-2006 for the 40 by 40 km square 155. Data were supplied by the Meteorological Office MORECS for a phd project on Nant y Gwyddon landfill site located on the opposite valley side (Ling, 2007)

It is believed that movement of the new-deep seated landslide started several months before it was reported in February 1999. It was probably triggered by the exceptionally heavy rainfall of autumn 1998 (Halcrow, 1999). Halcrow (1999) analysed rainfall records from the RCTCBC rain gauge at Parc Colliery to establish the severity of rainfall in the area during the period from 10 October 1998 to 26 February 1999. The severity of rainfall was judged in terms of return periods. Halcrow concluded that although rainfall was not particularly unusual for the area on a daily basis, it was notable/severe when considering longer periods of time. In particular, it was very severe, with a return period between or rarer than 1 in 100 or 1 in 1000 years, when considering rainfall durations of 8 and 25 days up to 28 October and 7 November 1998 respectively (Table 3.3).

Table 3.3 Severity of rainfall events for the rain gauge at Parc Colliery for the period (October 1998 to February 1999 from Halcrow report (1999). Values of rainfall where reported also as reduced by 17% (adjusted) because the readings at RCTCBC rain gauge were found to be 17% higher than the ones at Treherbert rain gauge

Rainfall duration (days)	Maximum total rainfall depth (mm)		Severity	Period
1	As measured	115	About 1 in 10 years	28 October 1998
	Adjusted	98	Between 1 in 2 and 1 in 10 years	
2	As measured	181	About 1 in 50 years	To 24 October 1998
	Adjusted	155	About 1 in 20 years	
3	As measured	222	Between 1 in 50 and 1 in 100 years	To 24 October 1998
	Adjusted	190	About 1 in 20 years	
4	As measured	247	Between 1 in 50 and 1 in 100 years	To 27 December 1998
	Adjusted	211	Between 1 in 10 and 1 in 20 years	
8	As measured	432	Between 1 in 100 and 1 in 1000 years	To 28 October 1998
	Adjusted	369	Slightly rarer than 1 in 100 years	
25	As measured	793	Rarer than 1 in 1000 years	To 7 November 1998
	Adjusted	677	Rarer than 1 in 100 years	

Geomorphological mapping shows that the area of the active landslide scarp is visibly dry, with the exception of seepage from the base of No 3 Rhondda Seam located in the backscarp. The area of ancient landslide deposits outside zone 2 is poorly drained and is characterised by several issues, streams, ponds and wet areas. These water features follow a NW-SE trend, likely associated with the Cymmer Fault. Due to the low permeability of the glacial till (Halcrow, 1999), wet areas, issues and streams are common also at the toe of the debris slides.

As typical for the South Wales Coalfield, the site geology is characterised by a cyclic alternation of permeable and impermeable layers, which leads to the probable presence of multiple perched water tables. Coal mining activities and faulting have probably caused the enlargement of pre-existing fissures and the creation of new fissures increasing the secondary permeability of sandstones and modifying the capability of the argillaceous layers of acting as aquicludes.

According to Halcrow (1999; 2000), rainwater is likely to percolate into the sandstone of the Llynfi Beds above the No 3 Rhondda Seam through the old fissures above the main scarp until it reaches an underlying impermeable layer, such as the seatearth below the No 3 Rhondda Seam. Groundwater will then move laterally along that impermeable layer, following the dip of strata to outcrop. The Llynfi Rock above the Tormynydd Seam and the mine workings of No 3 Rhondda and Tormynydd seams are probably the principal reservoirs of groundwater. Furthermore, these mine workings may have created preferential water paths within the slope (Halcrow, 1999; 2000).

The Cymmer Fault could act as a groundwater barrier or as a preferential pathway for water. However, Halcrow (1999) suggested that, due to the probable presence of a clay rich gouge within it and the high water pressures measured on its upthrow side at Pentre Landslide, this fault is more likely to act as a groundwater barrier, forcing groundwater up to the surface.

At the toe, the presence of low permeability glacial till creates a potential for artesian water pressures (Halcrow, 1999; 2000).

During the site investigations of 2003, standpipe or vibrating wireline piezometers were installed in seventeen boreholes. Water readings (1 or 2 per month) for the period between 19 September 2003 and 27 January 2004 were summarised in the ESP report (2004). These values and the instrument installation details provided by C. J. Associates (2003) were included in the cross section in Figure 3.14. For the area of the main scarp, these data confirm the presence of water in the No 3 Rhondda Seam and its workings and in the rock unit between No 3 Rhondda and Tormynydd Seam. The high water pressure in borehole 3 located on the upthrow side of the Cymmer Fault could indicate that the fault acts as a barrier for water flow, in accordance with Halcrow suggestions. However, due to the unreliability of borehole information in this area, this high water pressure cannot be considered conclusive. Moreover, as shown for example from water levels for borehole 5, some of the mudstones and siltstones do not act as aquicludes but are indeed able to transmit water, probably due to discontinuities or fractures.

3.7.1 Results from continuous monitoring of ground water levels

As explained in section 2.11, due to unreliability and data gaps in available rainfall information, two Mini-Divers and a CTD-Diver were installed at Mynydd yr Eglwys landslide for the continuous monitoring of water levels during the last phase of this project. The data provided by these automatic loggers were analysed to establish: the lag between water level rise and rainfall, the intensity of rapid water level changes following heavy/prolonged rainfall events, the time required for the water level to return to its 'normal' value, and the seasonal water level highs and lows.

The Mini-Divers were installed in boreholes 3 and 6 on the 30th of May 2008, while the CTD-Diver was installed in borehole 11 on the 27th of August 2008. Data were last downloaded on the 20th of May 2009.

The location of the boreholes in relation to geomorphological elements is shown in Figure 3.21, whereas schematic diagrams and lithological descriptions for the boreholes are reported in Figures 3.29-3.31. These last figures illustrate also at which depth the Divers were installed and the minimum and maximum water levels recorded by the loggers during the monitoring period. Unfortunately, there is no available information regarding the integrity of the boreholes and in particular of the standpipes and the original sand/gravel filters.

In summary, it can be seen (Figure 3.29) that the Diver in borehole 6 was installed in the area of the original sand/gravel filter, in the highly weathered sandstone beneath a coal seam (interpreted as No 3 Rhondda by ESP, 2004) and that minimum and maximum water levels are similar to the ones reported by ESP (2004). Borehole 3 has probably been partly damaged by ground movements as its depth has been truncated (see also Table 3.7). The Diver was installed close to its new depth, just below the highly weathered/gravel of mudstone (Figure 3.30). In borehole 11, the CTD-Diver was installed in siltstone/coal, in an area originally with a sand/gravel filter (Figure 3.31). As for borehole 6, also here there is a good correspondence with the minimum and maximum levels reported by ESP (2004).

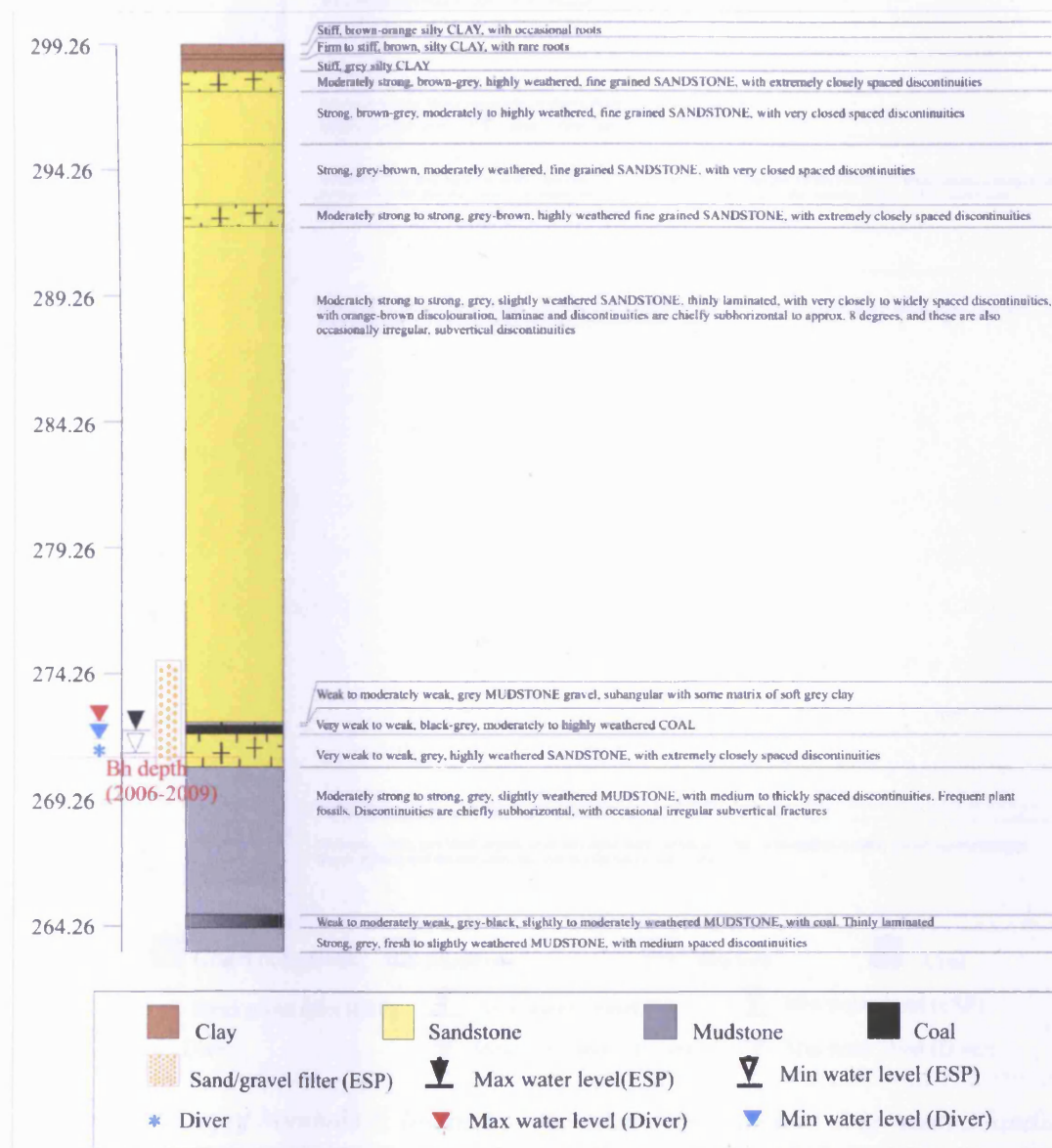


Figure 3.29 Log of borehole 6, located above the main scarp of the landslide. The figure shows the depth at which the Diver was installed and the minimum and maximum water levels measured by the logger between the 30th of May 2008 and the 20th of May 2009. The elevation of the ground level is the one measured with the dual-frequency Topcon HiPer Pro GPS+ for the project

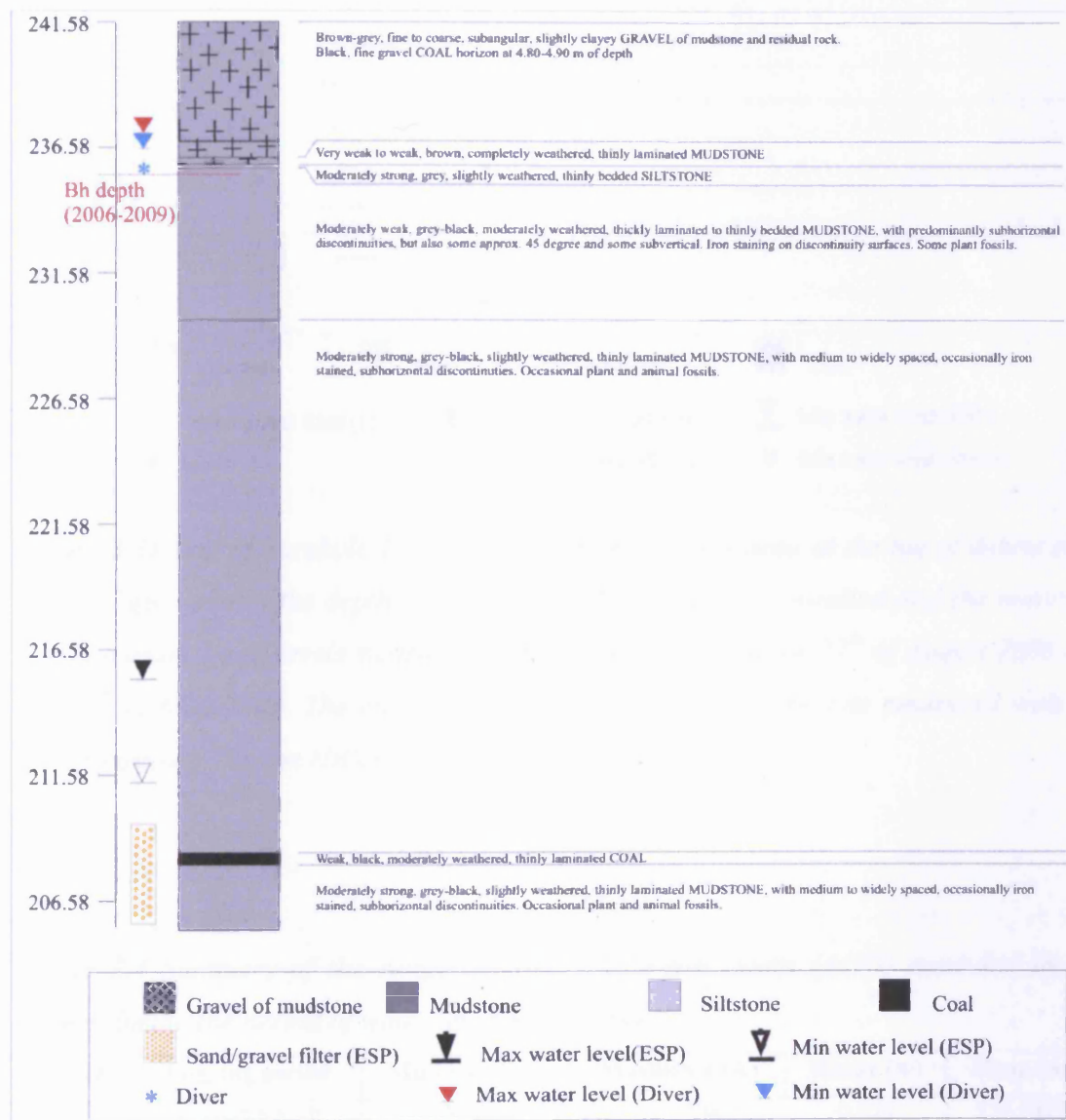


Figure 3.30 Log of borehole 3, located in the area of the ancient deep-seated landslide blocks. The figure shows the depth at which the Diver was installed and the minimum and maximum water levels measured by the logger between the 30th of May 2008 and the 20th of May 2009. During the years of the project the depth of the borehole was found to be much reduced with respect to the original, possibly because of damage caused by ground movements. The elevation of the ground level is the one measured with the dual-frequency Topcon HiPer Pro GPS+ for the project

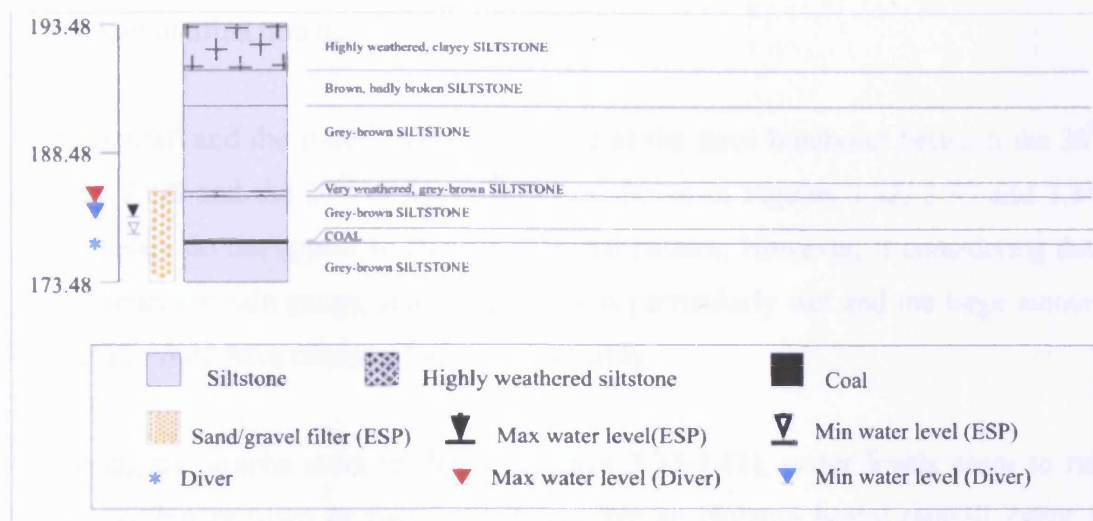


Figure 3.31 Log of borehole 11, located South of the wet area at the toe of debris slide C. The figure shows the depth at which the CTD Diver was installed and the minimum and maximum water levels measured by the logger between the 27th of August 2008 and the 20th of May 2009. The elevation of the ground level is the one measured with the dual-frequency Topcon HiPer Pro GPS+ for the project

Table 3.4 Summary of the range of values of water levels (AOD) recorded by the Divers during the period of water level monitoring

Borehole	Logging period	Minimum (m)	Maximum (m)	Range (m)	Mean (m)
3	30/05/2008 till	236.521	237.148	0.627	236.7123
	20/05/2009	(on 18/06/2008)	(on 05/09/2008)		
6*	30/05/2008 till	271.642	272.390	0.748	271.9348
	20/05/2009*	(on 06/06/2008)	(on 10/07/2008)		
11	27/08/2008 till	185.935	186.573	0.638	186.2384
	20/05/2009	(on 27/09/2008)	(on 05/12/2008)		

* Data for Diver in borehole 6 are not available for the period 13:00 of 18/07/08 to 13:00 of 27/08/2008 and for the period 16:00 of 19/11/2008 to 15:00 of 21/11/2008

The range of values recorded by the loggers during the monitoring period (almost one year for Divers in borehole 3 and 6) is reported in Table 3.4. Unfortunately, data from the Diver in borehole 6 are not available for the period between 18 July 2008 and 27 August 2008 and between 19th November 2008 and 21 November 2008 due to the

instrument malfunctioning.

Daily rainfall and the water levels monitored at the three boreholes between the 30th of May 2008 and the 20th of May 2009 are shown in Figures 3.32, 3.33 and 3.34. Water levels do not appear to show a seasonal pattern. However, if considering data from Treherbert rain gauge, summer 2008 was particularly wet and the large amount of rainfall could have caused a lack in seasonality.

Analysing the graphs more in detail (Figures 3.35-3.41), water levels seem to rise rapidly within one-two or two-three days after an isolated heavy rainfall event in borehole 3 and 6 respectively. After that, water levels decrease asymptotically for several days (even for more than two weeks), but with the major decrease during the first 6-8 days. In the case of more than one heavy rainfall event close in time, the response of the water levels becomes more complicated and the effects appear to super-impose.

Regarding the intensity of these rapid changes in water levels, they obviously vary according to the amount of rainfall. For example, after the isolated heavy rainfall of the 4th of October 2008, water levels rose of 0.42 m in both borehole 3 (Figure 3.36) and borehole 6 (Figure 3.37). If more heavy rainfall events are close in time, the total intensity of the change in water level increases. In fact the maximum water levels recorded at the two boreholes (Table 3.4) follow a period of several days of rainfall.

Water level response at borehole 11 appears to be more complicated. For example, contrary to the other two boreholes, there is no obvious response to the heavy rainfall of the 4th of October 2008 (Figure 3.38). In contrast, there is a rapid change in water level within one-two days following heavy rainfalls for the period December – February (Figure 3.41), such as following rainfalls of 4th and 13th December 2008. The more complicated response at borehole 11 could be related to its location. This borehole is in the lower part of the slope and the debris slides are covered in dense vegetation (high ferns) during summer-beginning of autumn. Moreover the borehole is just to the South of a very wet area with reedy ground, springs, streams and a pond (Figure 3.21).

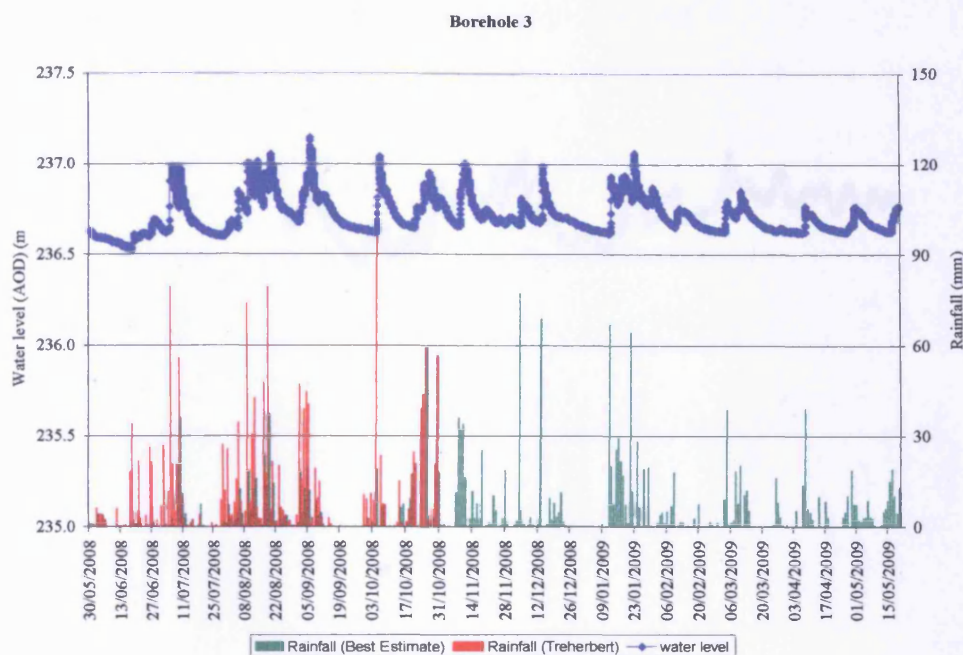


Figure 3.32 Daily rainfall and water levels recorded at borehole 3 during all the monitoring period. The maximum value of water level was recorded on the 5th of September 2008, following a wet period. There appears to be a clear correspondence between heavy rainfall events and picks in the water level values

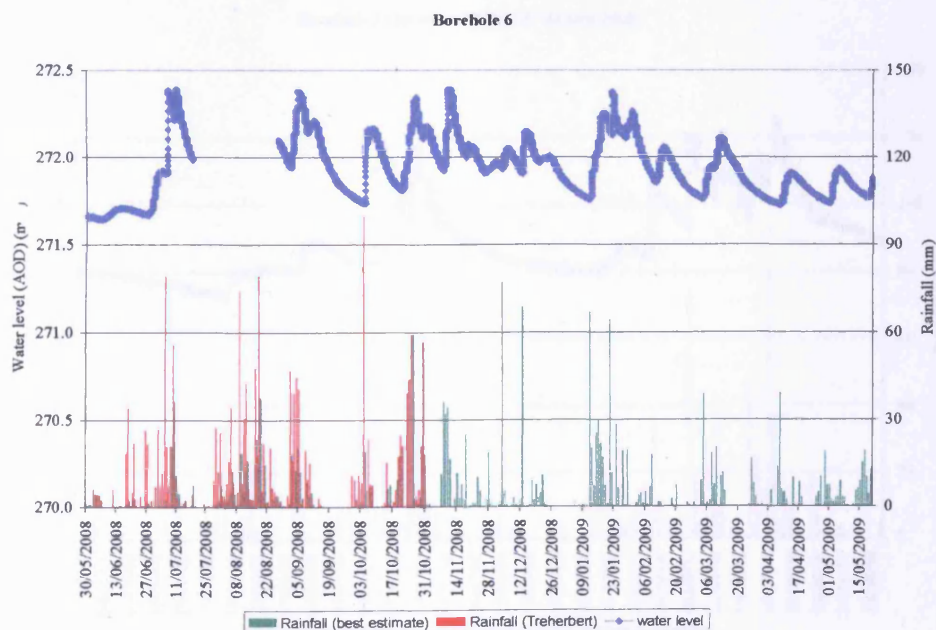


Figure 3.33 Daily rainfall and water levels recorded at borehole 6 during all the monitoring period. The maximum value of water level was recorded on the 6th of July 2008, following a wet period. There appears to be a clear correspondence between heavy rainfall events and picks in the water level values

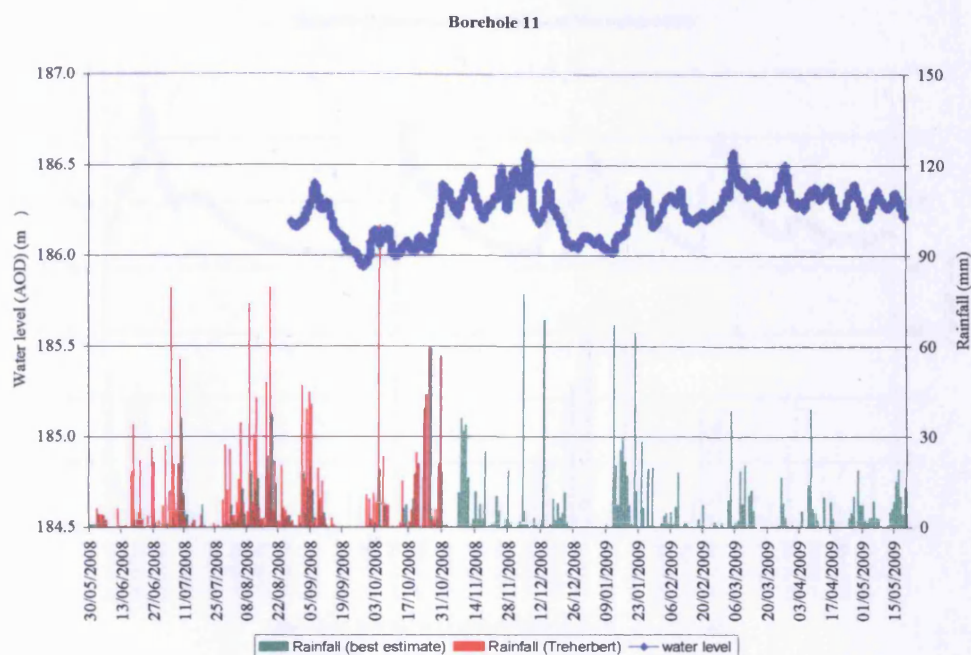


Figure 3.34 Daily rainfall and water levels recorded at borehole 11 during all the monitoring period. The relationship between water levels and rainfall is not clear from the graph

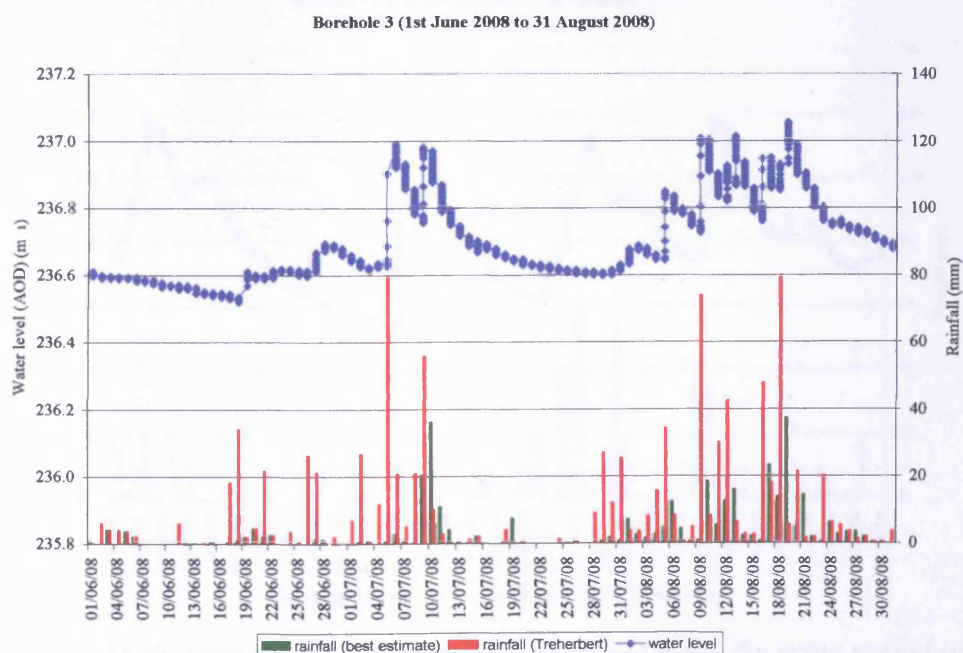


Figure 3.35 Daily rainfall and water level at borehole 3 for the period 1st of June to 31st of August 2008. Picks in water level are evident in correspondence of the intensive rainfall of 5th and 9 July and the wet period of 5-19 August

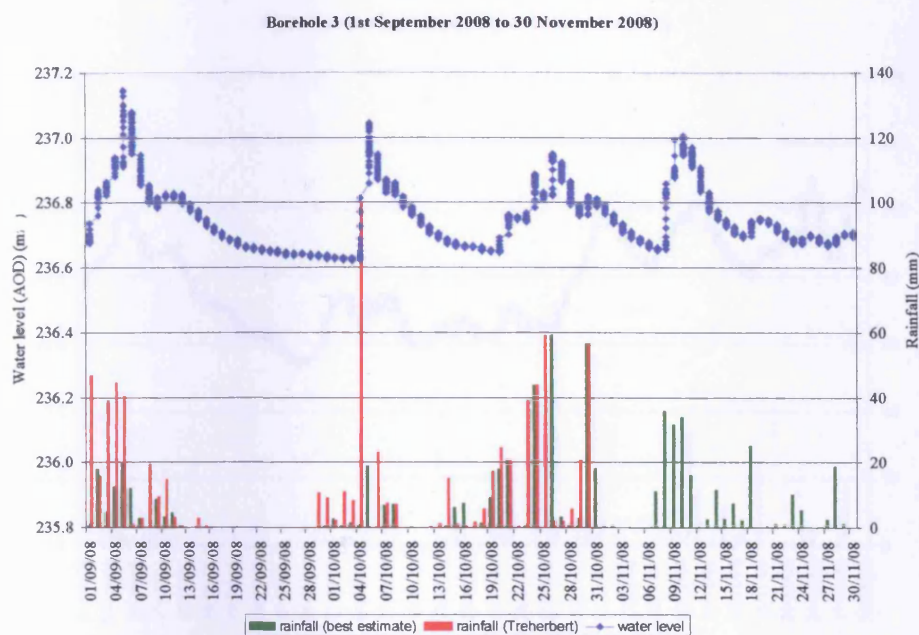


Figure 3.36 Daily rainfall and water level at borehole 3 for the period from 1st of September to 30th of November 2008. The highest water level in borehole 3 for the entire logging period was recorded on the 5th of September 2008. Other picks are evident in the graph, such as the one following the intensive rainfall of 4th October 2008

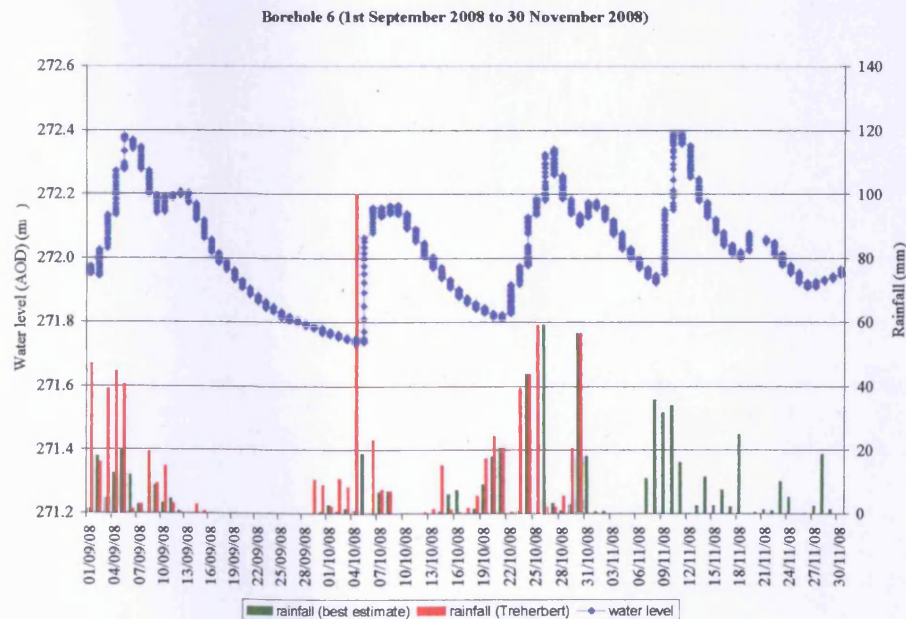


Figure 3.37 Daily rainfall and water level at borehole 6 for the same period of Figure 3.36. While in borehole 3 the response to the heavy rainfall of 4th October 2008 seems to start on the same day and carry on the following, in borehole 6 water level appears to rise over the two days following the rainfall event

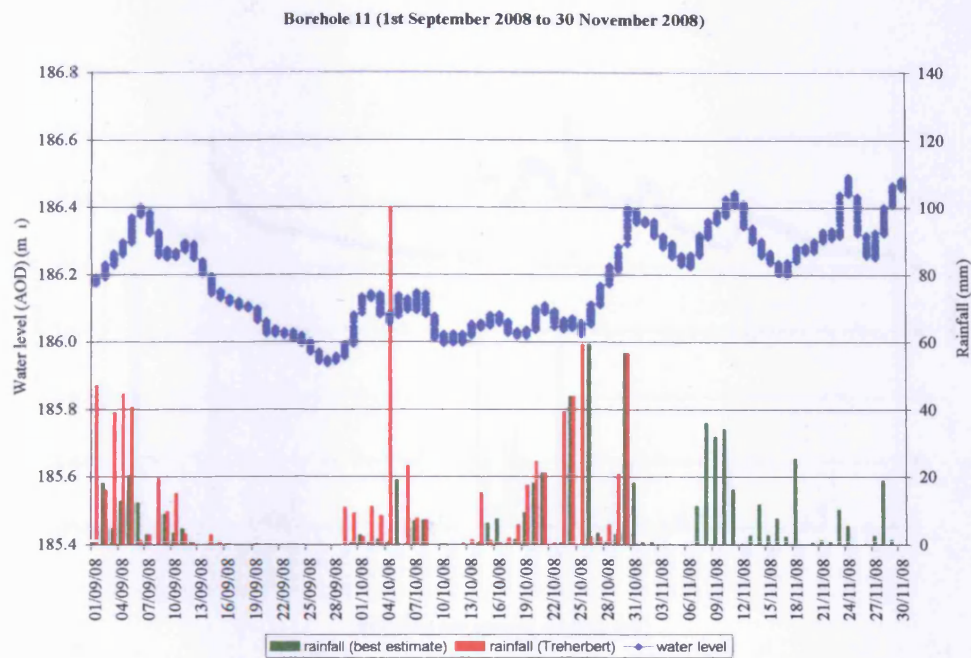


Figure 3.38 Contrary to what noticed in boreholes 3 and 6, water level at borehole 11 does not have an immediate and simple response to the rainfall (see for example rainfall of the 4th of October)

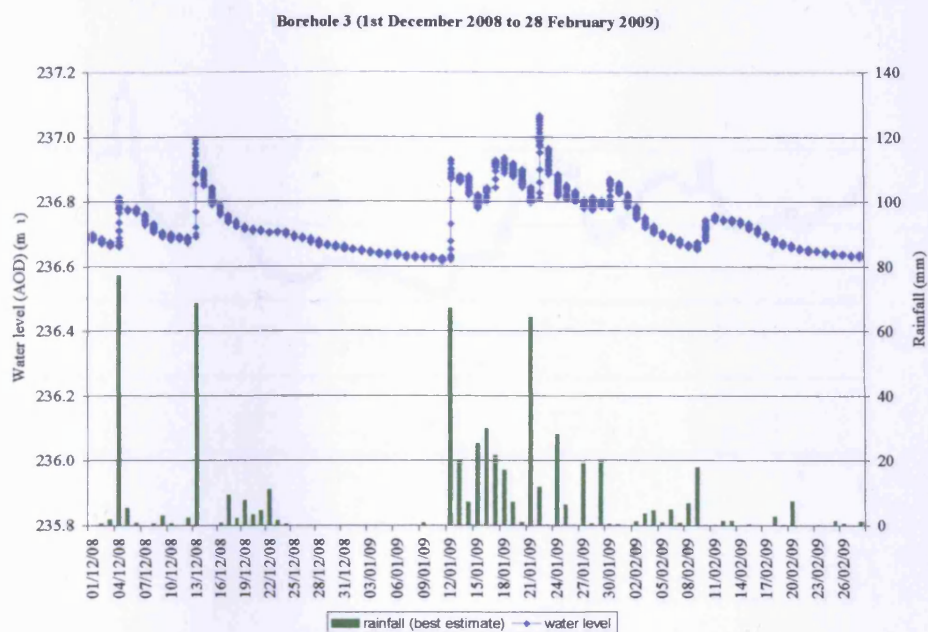


Figure 3.39 Daily rainfall and water level at borehole 3 for the period 1st of December 2008 to 28th of February 2009. The rise in water levels is again clearly evident in correspondence of heavy rainfall events. After the rainfall of the 13th of December the weather was relatively dry for the following 29 days. During this time the water level continues to decrease asymptotically. However, it decreases mainly during the first 6 days

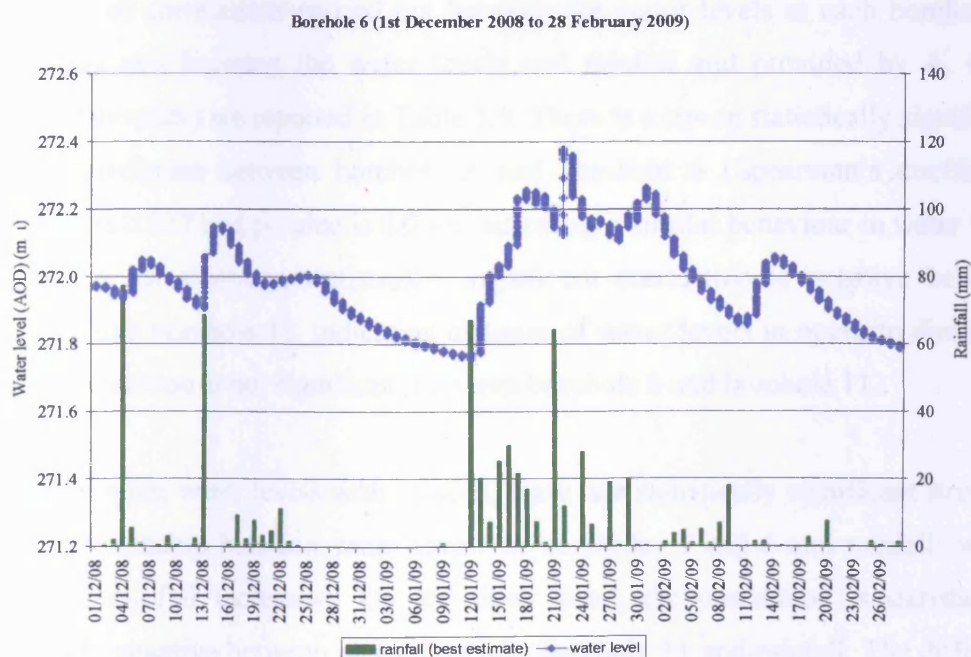


Figure 3.40 Daily rainfall and water level at borehole 6 for the same period

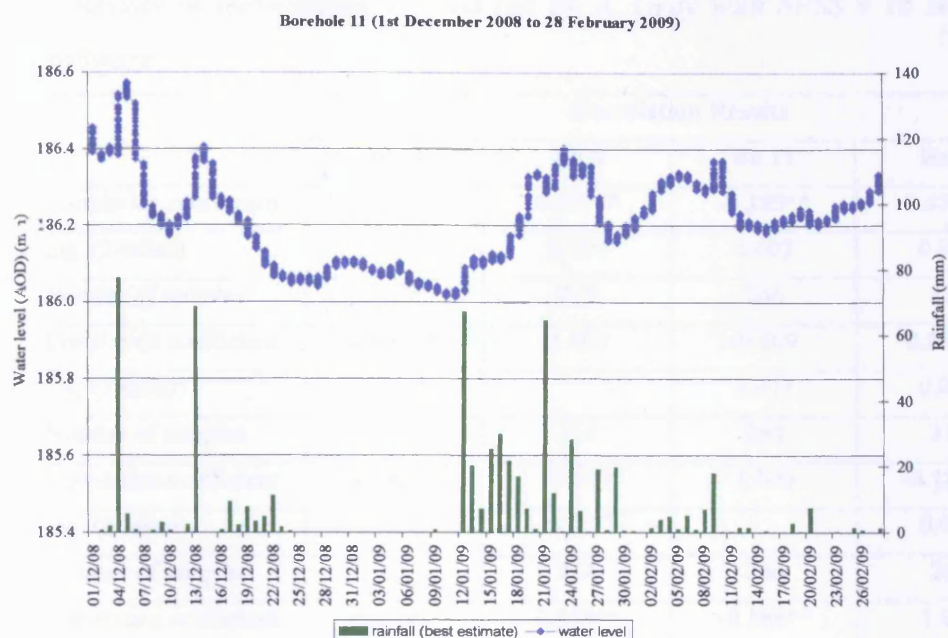


Figure 3.41 Daily rainfall and water level at borehole 11 for the same period. During this period there seems to be a correspondence between rainfall and water level increase also in this borehole.

Results from statistical analyses

The results of correlations carried out between the water levels at each borehole at 23:00 hours and between the water levels and rainfall and provided by A. Gray (Cardiff University) are reported in Table 3.5. There is a strong statistically significant positive correlation between borehole 3 and borehole 6 (Spearman's coefficient correlation is 0.837 and p-value is 0.000) indicating a similar behaviour in water level changes. On the contrary, statistically significant correlation is negative between borehole 3 and borehole 11, indicating changes of water levels in opposite direction, whereas correlation is not significant between borehole 6 and borehole 11.

When comparing water levels with rainfall, there is a statistically significant strongly positive relationship between water levels in boreholes 3 and 6 and rainfall (water rises when rainfall increases). On the other hand, the correlation is statistically significantly negative between water levels in borehole 11 and rainfall. The different behaviour of water levels in this borehole was already noticed in the visual analysis of the graphs.

Table 3.5 Results of correlations carried out by A. Gray with SPSS v 16 statistical analysis software

		Correlation Results			
		Bh 3	Bh 6	Bh 11	Rain
Bh 3	Correlation coefficient	1.000	0.837**	-0.185**	0.475**
	Sig. (2-tailed)		0.000	0.002	0.000
	Number of samples	355	313	266	355
Bh 6	Correlation coefficient	0.837**	1.000	-0.109	0.253**
	Sig. (2-tailed)	0.000		0.077	0.000
	Number of samples	313	313	264	313
Bh 11	Correlation coefficient	-0.185**	-0.109	1.000	-0.188**
	Sig. (2-tailed)	0.002	0.077		0.002
	Number of samples	266	264	266	266
Rain	Correlation coefficient	0.475**	0.253**	-0.188**	1.000
	Sig. (2-tailed)	0.000	0.000	0.002	
	Number of samples	355	313	266	355
** Correlation is significant at the 0.01 level (2-tailed)					

Figures 3.42-3.44 show the cross-correlograms obtained from the analysis of water levels at the three boreholes at 23:00 hours versus daily rainfall.

Figure 3.42 shows that water levels in borehole 3 rise within the same day and the day after the rainfall, but there is also a delayed response after 4 days from rainfall (and after 5 at the limit of statistical significance).

Water levels at borehole 6 rise within the same day (to limit of statistical significance) and mainly 3 and 4 days after the rainfall event (Figure 3.43).

There is no significant positive cross-correlation between water levels at borehole 11 and rainfall (Figure 3.44).

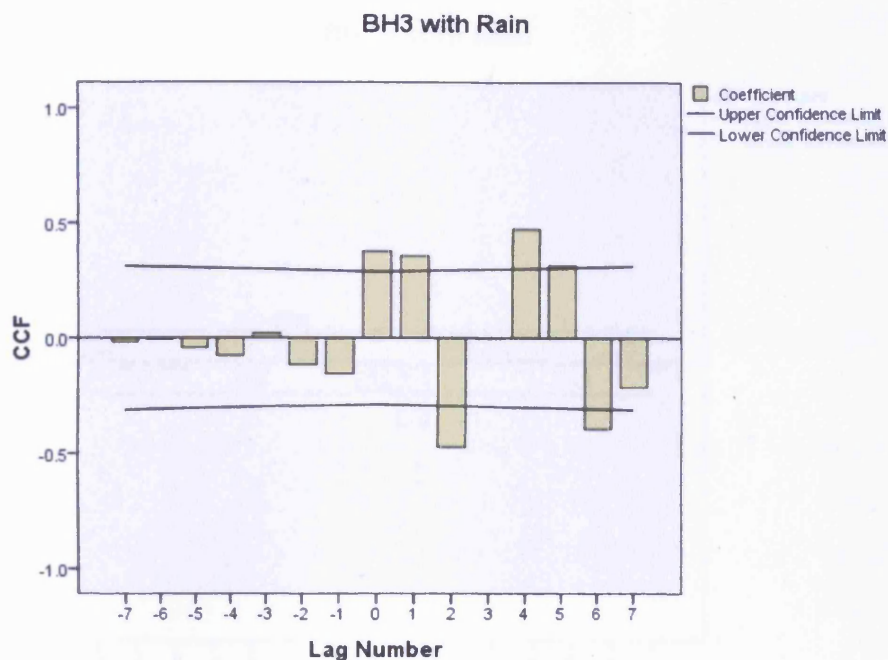


Figure 3.42 Cross-correlogram for water level in borehole 3 and rainfall provided by A. Gray. The correlation coefficient is above the upper limit of confidence for lags of 0, 1 and 4 days.

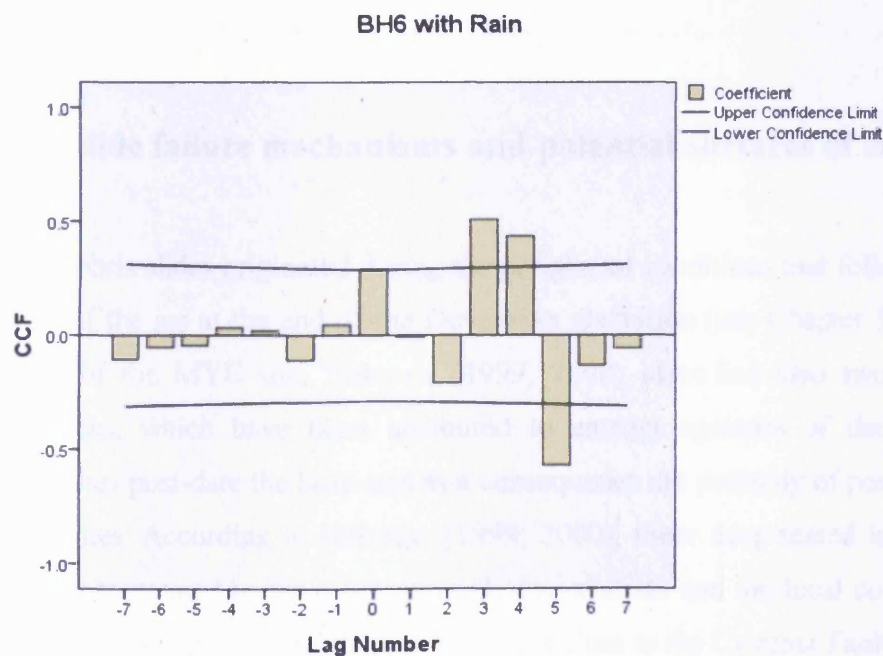


Figure 3.43 Cross-correlogram for water level in borehole 6 and rainfall provided by A. Gray. The correlation coefficient is above the upper limit of confidence for lags of 3 and 4 days.

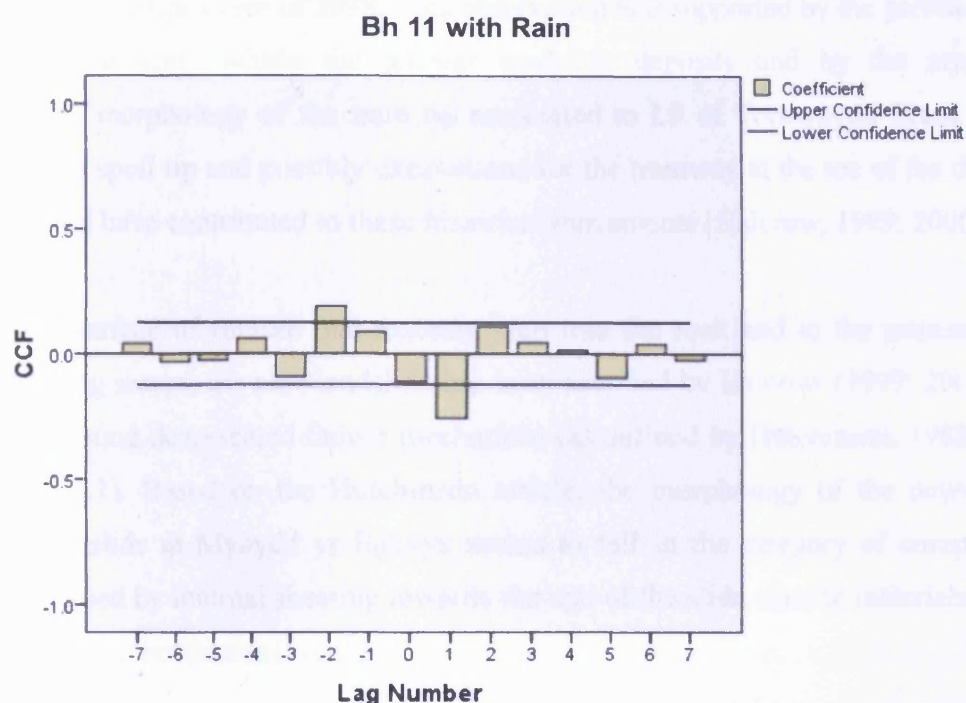


Figure 3.44 Cross-correlogram for water level in borehole 11 and rainfall provided by A. Gray. There are no positive correlation coefficients above the upper limit of confidence.

3.8 Landslide failure mechanisms and potential surfaces of rupture

The ancient debris slides originated during the periglacial conditions that followed the rapid retreat of the ice at the end of the Devensian glaciation (see Chapter 1). In the western part of the MYE site, Halcrow (1999; 2000) identified also two ancient landslide blocks, which have been attributed to ancient episodes of deep-seated landsliding. They post-date the head and as a consequence are probably of post-glacial (Holocene) times. According to Halcrow (1999; 2000), these deep-seated landslides were probably associated to the inherent weakness of strata and the local component of dip out of the slope in the area of the escarpment close to the Cymmer Fault.

In the “Rhonddda landslip potential assessment” (Halcrow, 1988), the ancient debris slides were described as “recently active”. In fact, Halcrow (1999; 2000) underlines that the debris slides had experienced small displacements in historical time before the

new MYE landslide event of 1998. This observation was supported by the presence of old landslide scars within the ancient landslide deposits and by the atypical hummocky morphology of the tram tip associated to L9 of Tormynydd Seam. The load of this spoil tip and possibly excavations for the tramway at the toe of the debris slides could have contributed to these historical movements (Halcrow, 1999; 2000).

Due to a surface of rupture that extends deep into the rock and to the presence of uphill facing scarps, the new landslide has been ascribed by Halcrow (1999; 2000) to be a compound deep-seated failure mechanism (as defined by Hutchinson, 1988; see section 1.2.1). Based on the Hutchinson article, the morphology of the new-deep seated landslide at Mynydd yr Eglwys seems to fall in the category of compound slides released by internal shearing towards the rear of the slide mass in materials with low to medium brittleness (Figure 1.5-D3a).

On the basis of his experience, H. J. Siddle (Halcrow, 1999; 2000) believes that the surface of rupture of this new compound deep-seated landslide is steeply concave at the rear where it has probably developed following pre-existing joints. In the flatter sole area instead, the surface of rupture has probably developed following the dip of weak horizons (seatearths) in the strata beneath the Tormynydd Seam.

According to Halcrow (1999), the toe of the new compound deep-seated landslide seems to correspond with the ancient deep-seated blocks. Therefore, Halcrow (1999) interpreted the new failure as a possible retrogression of the ancient landslide which has probably partly made use of the same surface of failure. However, as underlined by Hutchinson (1988), compound failures require displacement also in previously unsheared material.

The new compound deep-seated landslide has reactivated the movement of the ancient debris slides immediately downhill. This is evident from the ground cracking at the head of the debris slides (Halcrow, 1999). Since the reports of Halcrow (1999; 2000), this ground cracking has become more severe and extends for a wider area. Moreover, two linear shears (already described in section 3.2.5) have developed from the area of the minor scarp till the toe of debris slides B and C (Figure 3.21) and fresh cracking is also clearly evident at the toe of debris slide B.

Halcrow (1999; 2000) suggested that the ancient debris slides have a thickness of 5-8 m because of their morphology and that they are probably “underlain by a shear surface or zone of weak material”.

ESP (2004) identified potentially low shear horizons and materials with slip planes found within them. Their results are reported in Table 3.6 and are also shown in the boreholes of the cross section in Figure 3.14 (as a black arrow). In these boreholes and trial pits, the slip planes seem to develop at shallow depth, between 0 and 5.80 m. At the time of reporting, ESP (2004) underlined that no movement had been detected from the ground instrumentation installed in boreholes 3, 4 and in the boreholes located in the ancient debris slides.

In several occasions during this project, the depth of the boreholes and their internal water levels were measured using a dip-meter. A summary of the measured depths is provided in Table 3.7. Depth data could indicate shearing at a shallow depth comprised between 3.3 and 6.4 m for boreholes 3, 4, 5 and 9, but slip rods should be used for a correct measurement of the depth of the surface of rupture.

Table 3.6 Materials with potentially low shear horizons or with observed slip planes within according to Earth Science Partnership (2004)

Borehole or Trial pit ID	Depth (m)		Thickness (m)	Material description
	From	To		
Bh3	4.80	4.90	0.10	Black, fine Coal GRAVEL horizon
	5.40	5.70	0.30	Very weak to weak, brown, completely weathered, thinly laminated MUDSTONE
Bh3A	0.00	4.50	4.50	Dark brown, highly weathered SILTSTONE
Bh4	5.75	5.80	0.05	Black Coal Gravel-sized fragments
Bh5	2.90	3.20	0.30	Black slightly sandy, slightly gravelly SILT of coal and claystone
	4.80	5.55	0.75	Brown grey rarely orange brown slightly sandy gravelly CLAY
Bh7A	1.80	2.30	0.50	Light brown SILT
Bh8	1.60	2.30	0.70	Brown grey fine to coarse angular GRAVEL of mudstone with a damp very soft clayey matrix
Bh8A	2.00	2.30	0.30	Light brown SILT
Bh9	3.65	4.35	0.70	Soft brown orange grey mottled silty CLAY
Bh9A	2.30	2.70	0.40	Light brown SILT
Bh10	0.00	3.00	3.00	Soft brown CLAY with grey mudstone and coal stringers
TP1	1.80	2.30	0.50	Soft grey silty CLAY with much fine to coarse gravel and cobbles
TP2	2.40	2.70	0.30	Soft grey SILT with occasional medium to coarse weathered ironstone gravel
TT3	0.30	0.50	0.20	Very weak sheared black COAL, recovered as fine to medium gravel sized fragments
	1.00	1.10	0.10	Very weak sheared black COAL, recovered as fine to medium gravel sized fragments
TP4	0.70	0.90	0.20	Soft to firm friable grey black silty CLAY with some roots (relic Topsoil)

Table 3.7 Depths of some of the boreholes at Mynydd yr Eglwys measured with a dip-metre by a member of the crew during field work

Date	Depth of borehole from top of casing (m)								
	Bh 3	Bh 4	Bh 5		Bh 6	Bh 7	Bh 9	Bh 11	Bh 12
			ø 19 mm	ø 50 mm					
2003*	35.20*	28.00*	24.00*	11.50*	28.50*	25.00*	6.00*	10.00*	8.50*
20/12/06**	6.07**			11.55**			4.02**		
25/01/08	6.40	6.7		3.40		24.80	4.34		
01/02/08	6.40	9.6				25			
30/04/08	6.35	6.35		3.40	28.56	24.60	4.25		
14/05/08	6.35	6.32							
29/05/08	6.38	6.37				24.40	4.22		
30/05/08	6.36				28.50	24.43			
13/06/08									
18/07/08	6.26	6.32						10.20	8.25
27/08/08		6.30	3.38	3.36	28.57	24.40	4.24	10.15	8.20
24/10/08	6.37								
10/12/08		3.36	3.28	3.35			4.24		
19/05/09	6.44	3.49	3.38	3.40		24.9	5.27		

* Original depth of the tip of standpipe from C. J. Associates (2003)

** This day measurements were taken from ground level

3.9 Causes of new deep-seated failure

The new MYE landslide was probably triggered by the exceptionally heavy rainfall of autumn 1998 (section 3.2.6; Halcrow, 1999). The slope at Mynydd yr Eglwys may have been susceptible to failure for several reasons, all contributing to the progressive weakening of strata which is necessary for compound failures to develop. These reasons (or preparatory factors) have been identified and discussed by Halcrow (1999). They are summarised in Table 3.8.

Table 3.8 Summary of the possible preparatory factors that may have contributed to the initiation of the compound deep-seated landslide in 1998-99 at Mynydd yr Eglwys identified and discussed by Halcrow (1999)

Preparatory factor	Details (from Halcrow, 1999)
Geological and topographic setting	Layers of sandstone aquifers and weak argillaceous strata
	Seatearts of low strength underlying Tormynydd Seam
	Fracturing and weakening of strata due to Cymmer Fault
	Local dips out of strata in the vicinity of Cymmer Fault
	Possible weak layers due to shearing on bedding caused by Cymmer Fault
	Convex nature of the slope, and as a consequence without lateral support
Geomorphological history	Ancient deep-seated failures left the escarpment over-steepened with less support and susceptible to retrogression
	Slow but intermittent and persistent movements of the ancient debris slides reduced the support of the escarpment area
Modifications to the slope due to human activities	Excavations at the toe of the debris slides for enclosures and track (but effects are considered to be of small degree)
	Possible deforestation of deciduous woodland to provide wood for collieries (but limited effect on the change in the amount of effective rainfall in winter)
	Tipping of spoil from L9 of Tormynydd Seam caused increased displacement of debris slide C with consequent reduction in support to the slope
Climatic change	Analysis of winter rainfall (October-February) at Ty'n-y-waun gauge for the period 1892-1999 show an increase of 20 mm/decade. The 9-year moving average rainfall shows a cyclical trend but with a considerable increase in the late 1980s and 1990s
	Magnitude and incidence of significant rainstorms within the Coalfield has increased (in Halcrow, 1999 but citing Walsh et al., 1982; Perry and Howells, 1982)

(continue in the next page)

Preparatory factor	Details
Mining (deep workings)	Differential subsidence caused extension of strata and widening of NW-SE trending joints. These fissures increase water infiltration and alter water flows. (However, these fissures were already developed in 1948, date of air photography)
	The effects of mining strains with the associated changes in stress regime within the slope can generally cause/contribute to failure. From research carried out by Halcrow (1989), failures associated with deep longwall mining occur shortly after mining (i.e. Ffaldau Landslide, while slope was undermined), whereas failures associated to partial extraction methods may develop after a few years (i.e. East Pentwyn Landslide, five years after abandonment of workings). However, deep longwall mining underneath the slope at Mynydd yr Eglwys ended many years ago and as a consequence also subsidence effects. Therefore, deep workings alone are probably not responsible for the new failure
Mining (shallow workings)	Workings in the No 3 Rhondda and Tormynydd seams may have remained open causing delayed subsidence. The edge of workings of the Tormynydd Seam appears to correspond to the rear scarp and to follow a NW-SE trend. Therefore they may have influenced the position of the scarp and introduced water into its area. The collapse of these workings could have caused subsidence and development of internal displacements and shears. The working of No 3 Rhondda Seam are upslope of the scarp and may not have influenced the new failure

After considering all the possible preparatory factors listed in Table 3.8, Halcrow (1999) concluded that the most relevant were the ancient episodes of landsliding. In particular, they suggested that the new landslide has developed as a retrogression of the previous deep-seated failures and the continuous intermittent movements of the ancient debris slides have reduced the support of the slope at their head. In addition, internal shears could have been developed due to the collapse of the shallow workings of Tormynydd seam.

3.10 Remediation works

In summer 2008, two horizontal drains were installed between the toe of debris slide B and the public footpath. Plastic drainage pipes were laid within the drainage trenches and then backfilled with gravel (Figures 3.45 and 3.46)



Figure 3.45 Instalment of drainage in the area between the toe of debris slide B and the ditch (photos by the author)



Figure 3.46 Drainage after completion of works (photo by the author)

3.11 Landslide kinematics

3.11.1 Landslide movements determined by EDM measurements (by RCTCBC)

MyE landslide has been monitored since 1999 by conventional topographic surveying techniques. In May 1999, 29 movement markers were installed by RCTCBC on Mynydd yr Eglwys hillside at locations suggested by Halcrow UK. Ten other markers were installed by June 2000 and others have been added to the EDM network over the years, up to a total of 70 monitoring locations.

The results of the first year of monitoring (May 1999 - May 2000) reported by Halcrow (2000) showed that ground movements, greater than the surveying precision, were occurring in the areas of new and relict deep-seated landslides and in the ancient debris slides A, B and C. The maximum rate of displacement was measured at marker P7, originally located immediately downslope of the zone where the

secondary scarp successively developed, and at marker P3, located in the area of the new deep-seated landslide. Furthermore, by comparison with monthly rainfall, Halcrow underlined that rates of displacements were observed to be greater during the winter/wet months than in the summer/dry periods. For example, the average rate of displacement at P3 was 10 mm/day in the summer 1999, but increased to 35 mm/day in the winter 1999-2000. At P7 the rate of displacement was approximately 20 mm/day in summer 1999, but exceeded 100 mm/day in September and December 1999, due to heavy/prolonged rainfall events.

Figure 3.47 shows the approximate location of a few selected RCTCBC markers (as in December 2007), which have been considered as representative of different geomorphological areas and have been successively compared with GPS results in section 3.11.2.

Table 3.9 summarises the data that were reported in Halcrow (2000) for the first year of monitoring of these markers in reference to the geomorphological elements identified in Figure 3.21, whereas Figure 3.48 shows the cumulative inclined (or total) movement of the same markers up to January 2009 as provided by Halcrow office in Cardiff. The rates of movement have decreased with time and generally show accelerations during autumn-winter.

Table 3.9 Summary of EDM monitoring results for the period May 1999-May 2000 (modified from Halcrow, 2000)

Location	Marker	Total displacement (m)	Maximum rate of displacement (mm/day)	Vector of displacement (degrees)*
New deep-seated landslide	P3	4.71	36	-28
Ancient deep-seated landslide blocks	P6	3.61	29	-8
Debris slide B (in Zone 2)	P7	12.94	120	-17
Debris slide B (outside Zone 2, closer to toe)	P17	No significant movement		
Debris slide C	P18	0.88	12	-16

* negative values represent vectors below the horizontal

** Data for P60 are missing because this marker was installed in 2004

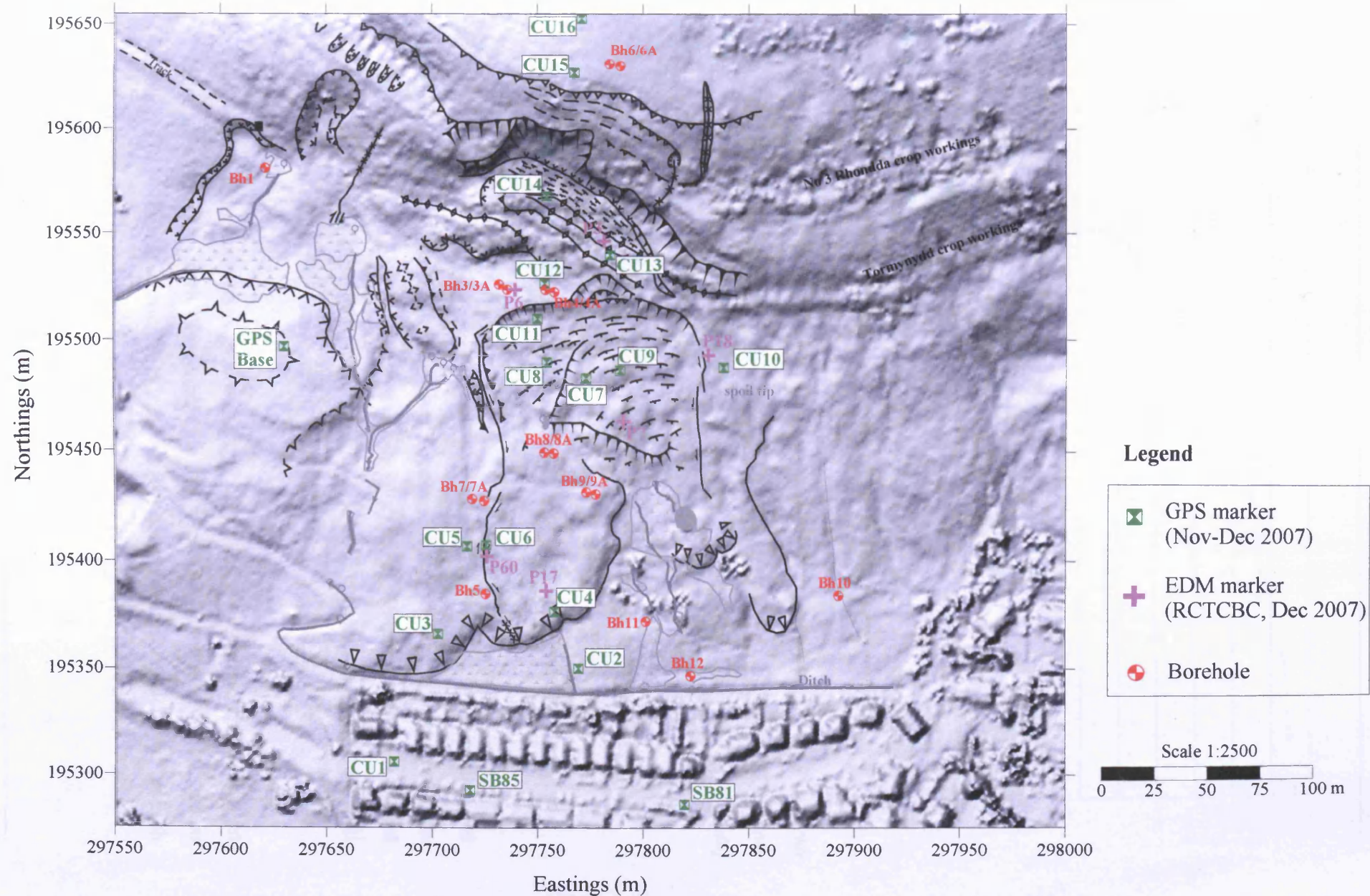


Figure 3.47 Location of GPS movement markers (installed and surveyed for this project) and approximate location (in December 2007) of six of the markers surveyed with EDM on behalf of Rhondda Cynon Taff County Borough Council (D. P. Jones, personal communication). CU1, SB81 and SB85 are control points, whereas CU15 and CU16 were surveyed only once (not monitored)

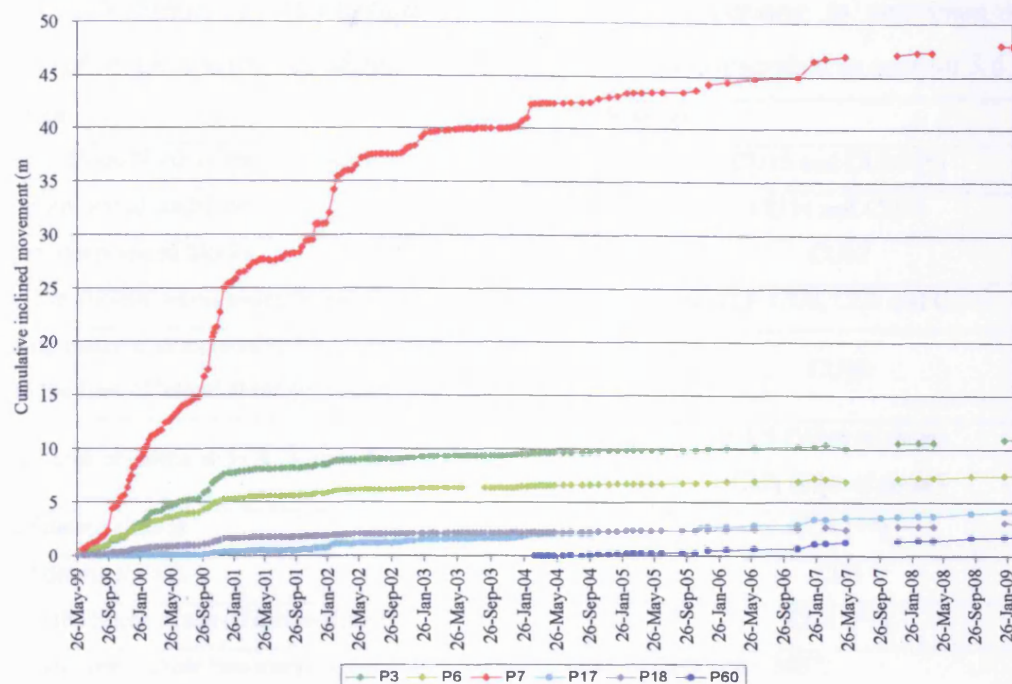


Figure 3.48 Cumulative inclined movement for markers P3, P6, P7, P17, P18 and P60 surveyed with EDM instrument by surveyors on behalf of Rhondda Cynon Taff County Borough Council. The results of their movement were provided by Halcrow (Cardiff office). Marker locations were shown in Figure 3.47

3.11.2 Landslide movements determined by GPS observations

As explained previously in section 2.4.4, 13 markers (CU2-CU14) were installed and then monitored with a dual-frequency Topcon HiPer Pro GPS+ instrument from November 2007 to December 2008 as part of this project. The monitoring was carried out to evaluate the surveying technique, but also to investigate the rate and spatial distribution of surface displacements at MyE landslide.

The location of the markers is shown in Figure 3.47 and is described in Table 3.10 in terms of relationship with the geomorphological elements previously discussed in section 3.6. Horizontal, vertical and inclined (or total) movements calculated for each marker in relation to their previous coordinates are reported in Table 3.11.

Table 3.10 Summary description of GPS marker locations in reference to the geomorphological elements identified in Figure 3.21 and described in section 3.6

Location	Marker
Crown – Slope North of the main scarp	CU15 and CU16 (*)
New deep-seated landslide	CU14 and CU13
Ancient deep-seated blocks	CU12
Zone 2 in ancient debris slides B and C	CU11, CU9, CU8 and CU7
Spoil tip material associated to L9 of Tormynydd Seam and to the East of lateral shear (in debris slide C)	CU10
Central area of debris slide B close to lateral shear	CU5 (West of shear) CU6 (East of shear)
Toe of debris slide B	CU4 (**)
Toe of debris slide A	CU3
Area to the South of toe of debris slide B	CU2 (**)

* not monitored (these two markers were surveyed only once in December 2007)

** stolen sometime after April 2008

Table 3.11 Horizontal (H), vertical (V) and inclined (I) movement for each marker in relation to its coordinates from the previous survey

Marker		Movement from previous survey								
		27-11-07	11-12-07	13-02-08	26-04-08	24-06-08	15-08-08	03-10-08	14-11-08	16-12-08
CU2	H	0	0.003	0.006	0.004	(stolen)				
	V	0	-0.012	-0.010	0.010					
	I	0	0.012	0.012	0.011					
CU3	H	0		0.053	0.013	0.012	0.012	0.021	0.006	0.001
	V	0		-0.038	0.008	-0.001	-0.002	-0.003	0.006	-0.011
	I	0		0.065	0.015	0.012	0.012	0.021	0.008	0.011
CU4	H	0	0.125	0.108	0.004	(stolen)				
	V	0	-0.029	-0.006	-0.003					
	I	0	0.129	0.108	0.005					
CU5	H	0		0.060	0.006	0.005	0.014	0.018	0.004	0.007
	V	0		-0.044	0.010	-0.005	0.005	-0.017	0.007	-0.004
	I	0		0.074	0.012	0.007	0.015	0.025	0.008	0.008
CU6	H	0		0.197	0.010	0.004	0.058	0.096	0.041	0.008
	V	0		-0.075	0.000	-0.006	-0.014	-0.035	-0.018	-0.009
	I	0		0.210	0.010	0.007	0.060	0.102	0.045	0.012
CU7	H	0	0.202	0.337	0.068	0.009	0.110	0.327	0.170	0.054
	V	0	-0.098	-0.143	-0.019	-0.008	-0.044	-0.135	-0.056	-0.032
	I	0	0.225	0.366	0.070	0.012	0.119	0.354	0.179	0.063
CU8	H	-	0	0.224	0.051	0.011	0.099	0.219	0.116	0.045
	V	-	0	-0.095	-0.004	-0.009	-0.021	-0.079	-0.027	-0.021
	I	-	0	0.243	0.052	0.015	0.101	0.233	0.119	0.050
CU9	H	0	0.217	0.341	0.057	0.010	0.107	0.352	0.177	0.057
	V	0	-0.088	-0.117	-0.016	-0.010	-0.023	-0.121	-0.048	-0.027
	I	0	0.234	0.360	0.059	0.014	0.110	0.372	0.183	0.063
CU10	H	0		0.062	0.018	0.006	0.020	0.041	0.036	0.012
	V	0		-0.053	0.001	-0.009	0.000	-0.021	0.003	-0.016
	I	0		0.081	0.018	0.011	0.020	0.046	0.036	0.020
CU11	H	-	0	0.237	0.064	0.013	0.090	0.202	0.108	0.045
	V	-	0	-0.084	-0.020	-0.004	-0.030	-0.087	-0.034	-0.027
	I	-	0	0.252	0.067	0.014	0.095	0.220	0.114	0.053
CU12	H	-	0	0.087	0.022	0.005	0.034	0.048	0.034	0.015
	V	-	0	-0.008	-0.001	-0.001	-0.005	-0.014	0.007	-0.009
	I	-	0	0.088	0.022	0.005	0.034	0.050	0.035	0.018
CU13	H	-	0	0.066	0.021	0.006	0.023	0.033	0.025	0.011
	V	-	0	-0.053	-0.007	-0.014	-0.006	-0.035	-0.015	-0.011
	I	-	0	0.084	0.022	0.015	0.024	0.048	0.029	0.016
CU14	H	-	0	0.062	0.016	0.007	0.019	0.034	0.018	0.014
	V	-	0	-0.045	-0.015	-0.006	-0.012	-0.018	-0.025	-0.012
	I	-	0	0.076	0.022	0.009	0.022	0.039	0.031	0.018

The surveying results obtained from GPS observations for each monitoring marker are presented on graphs of Eastings and Northings (Figure 3.49) and on graphs of vertical versus horizontal displacement (Figure 3.50). Vectors of total horizontal displacement (for period 27 November 2007 – 16 December 2008) have also been drawn on the geomorphological map of MyE landslide (Figure 3.51). Figures 3.52 and 3.53 instead show cumulative horizontal, vertical and inclined (or total) movements.

The highest rates of displacement appear to be concentrated in debris slides B and C, in the area between the two N-S lateral shears, particularly in Zone 2. Maximum movements were observed at markers CU9, CU7, CU11 and CU8. More specifically, the highest values of displacement were measured at CU9, which moved a total of 1.397 m (1.319 m horizontal, -0.450 m vertical), and at CU7, which moved a total of 1.387 m (1.277m horizontal, -0.535 m vertical). These values correspond to an average rate of displacement of 3.6 mm/day and MyE landslide can be classified as very slow (section 1.2.2.4). Movement in this area is approximately towards South (between 171° and 186° from North) and downslope (decrease in elevation or negative vertical values), at an inclination of 20° circa, which is approximately the same as the slope angle.

The movement decreases towards the central (CU6) and toe area (CU4) of debris slide B, although, unfortunately, there is no full record for marker CU4 (stolen after April 2008). The direction of movement is still towards South (between 172° and 177° from North) and downslope, at an inclination of approximately 20° and 9° for CU6 and CU4 respectively.

Markers CU13 and CU14, located in the area of the new deep-seated landslide, moved a total of 0.238 and 0.218 m respectively (i.e. 0.6 mm/day), in a direction of 190° from North and at an inclination of 36-38°. The total movement and its direction are approximately the same (0.250 m and 197°) at marker CU12, located in the area interpreted by Halcrow as belonging to old deep-seated landslide blocks. However, the inclination is much smaller and the decrease in elevation is close to limits of survey precision.

Ground movement extends to the spoil tip material associated with L9 of Tormynydd

Seam (CU10), whereas is very limited in debris slide A. Although the toe of this debris slide was initially considered the main threat for the property of Meadow Walk, a total movement of only 0.145-0.149 m was measured at CU3 and CU5. These are the lowest displacements measured at the site and correspond to an average rate of displacement of 0.4 mm/day. These markers appear to move in direction 174° from North and downslope, but coordinate changes were at times at the limit of survey precision.

Although physically very close to each other, it is remarkable to notice the difference in ground movement between markers CU5 and CU6. The two markers are separated by the tension gash/lateral shear crossing debris slide B, with CU6 being on the East and more active side of it.

A comparison between horizontal and vertical components shows that, a part for CU13 and CU14, total movement is largely dominated by the horizontal component. Moreover, graphs of cumulative movement (Figures 3.52 and 3.53) underline the temporal variability of rates of displacement. The velocities varied with the season, being lower during spring-early summer. For example, for marker CU9, the daily rate of movement ranged between a maximum average value of 16.7 mm/day, calculated from 27 November 2007 to 11 December 2007, to a minimum average value of 0.07 mm/day, calculated from 26 April 2007 to 24 June 2007.

GPS data display a seasonal variation in ground movement velocities, with greater accelerations during wetter periods. These velocity variations suggest a possible link between surface movements and rainfall (and possible water pressure increase; Figure 3.53). However, higher frequency movement data (i.e. from extensimeters, inclinometers or continuous GPS monitoring) would be necessary to confirm this observation and fully describe the complex relationship between rainfall, water level rises and accelerations in surface displacements.

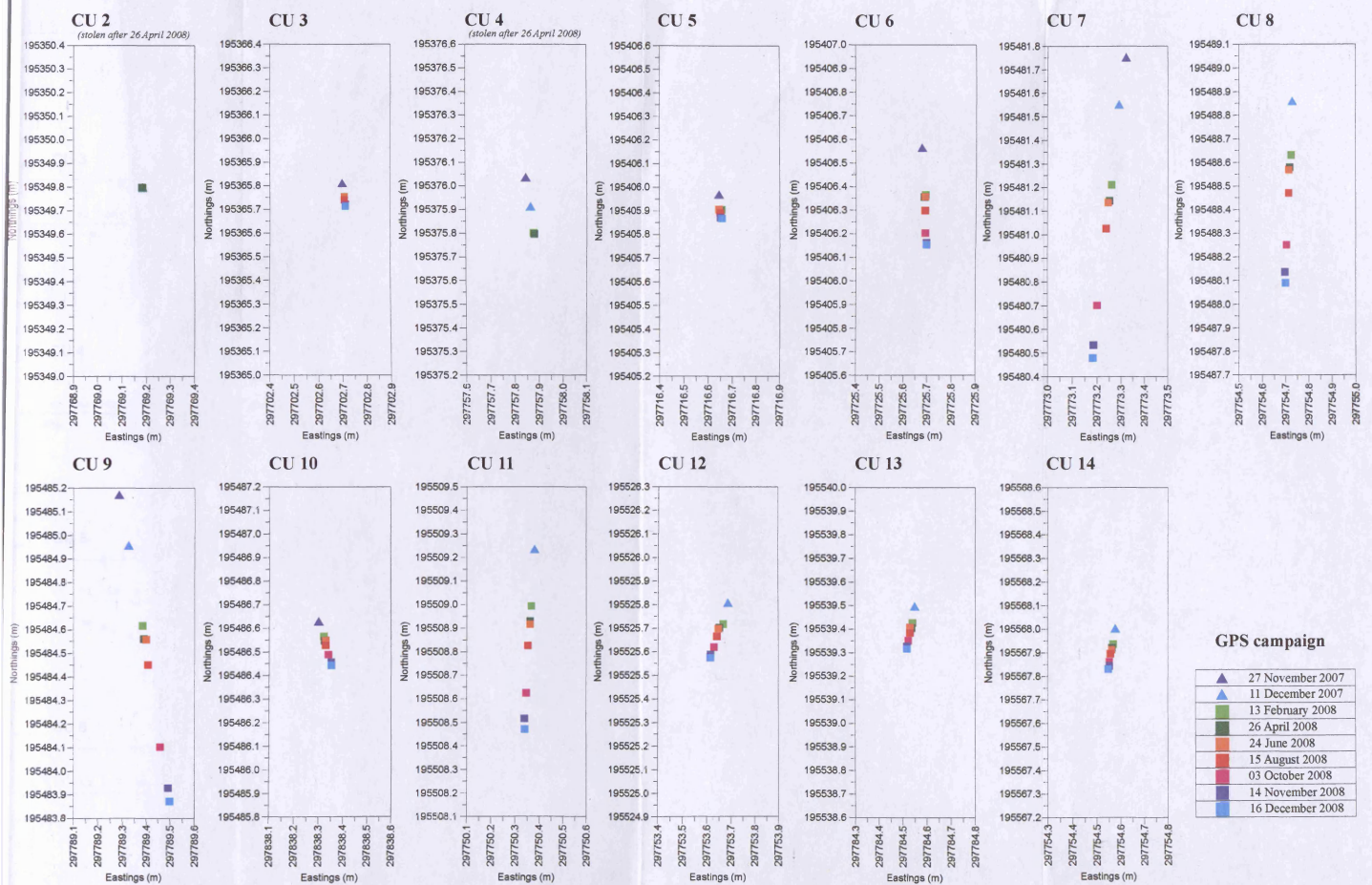
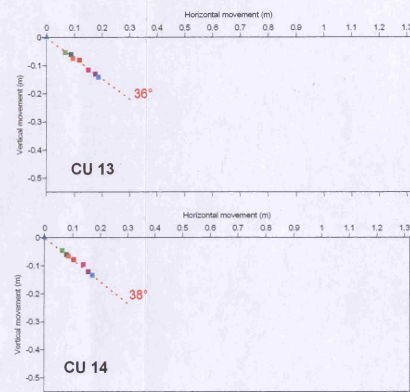
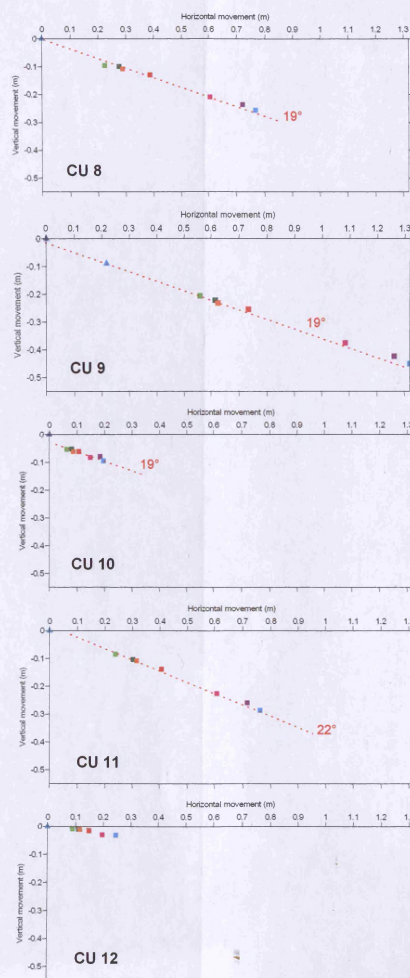
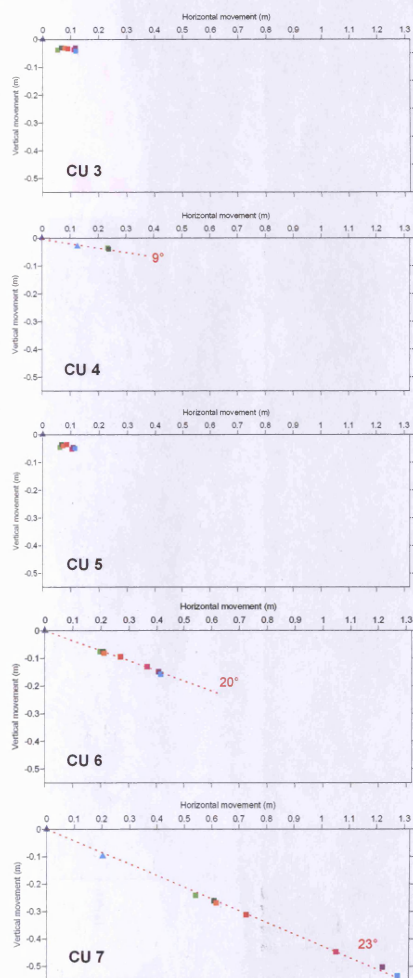


Figure 3.49 Change in Eastings and Northings coordinates for markers CU2-CU14 during all the GPS monitoring campaigns. For ease of comparison, all the boxes have the same dimensions: 0.50 m in Eastings and 1.4 m in Northings



GPS campaign

▲	27 November 2007
▲	11 December 2007
■	13 February 2008
■	26 April 2008
■	24 June 2008
■	15 August 2008
■	03 October 2008
■	14 November 2008
■	16 December 2008

Figure 3.50 Vertical movement versus horizontal movement for markers CU3-CU14. For ease of comparison, all the boxes have the same dimensions. The approximate value of the inclination of the vector of movement (in degrees) is indicated in red.

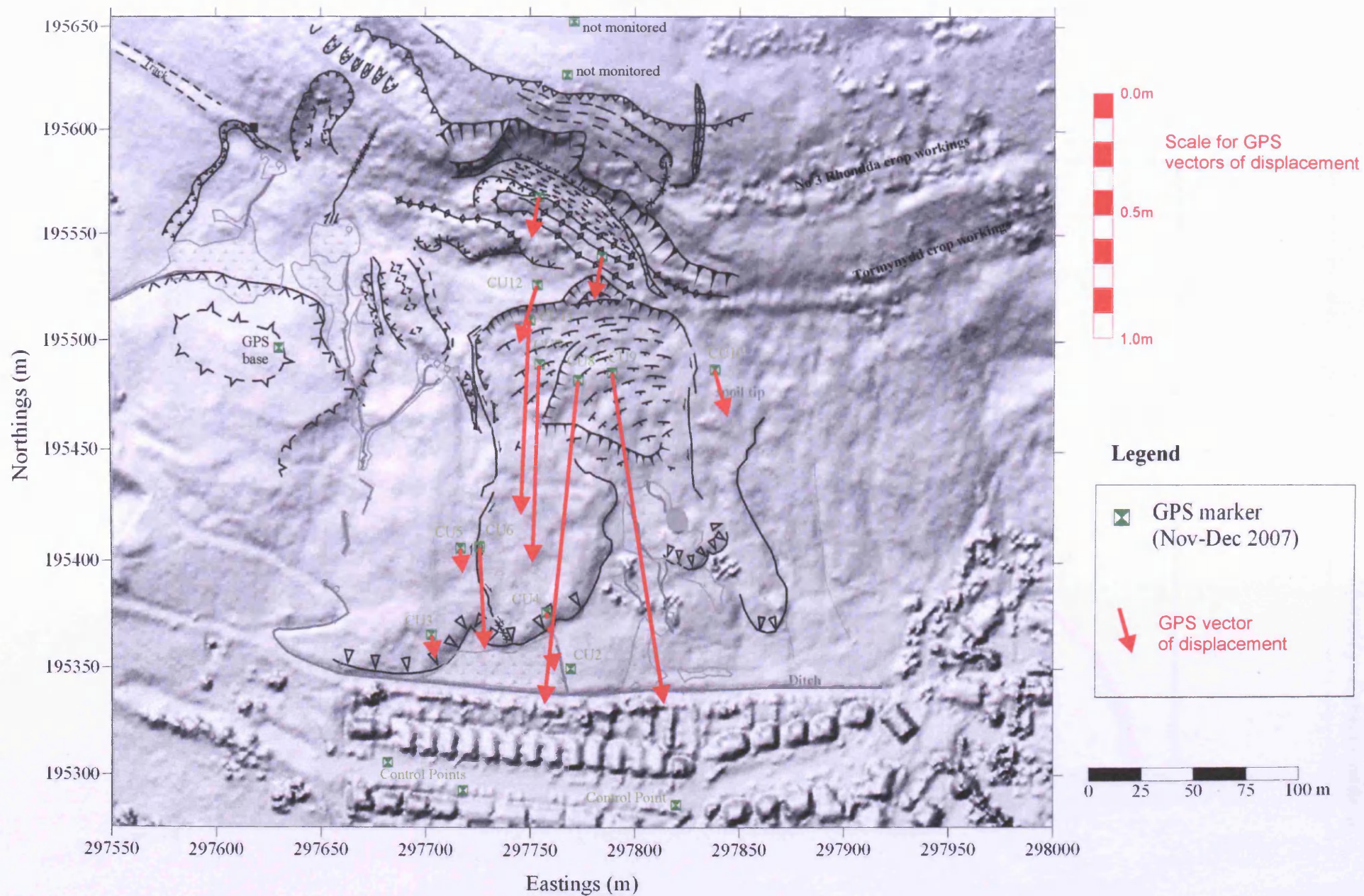


Figure 3.51 Total horizontal displacement vectors obtained with GPS surveying over the period 27 November 2007 (or 11 December 2007) and 16 December 2008. Markers CU2 and CU4 were stolen after April 2008

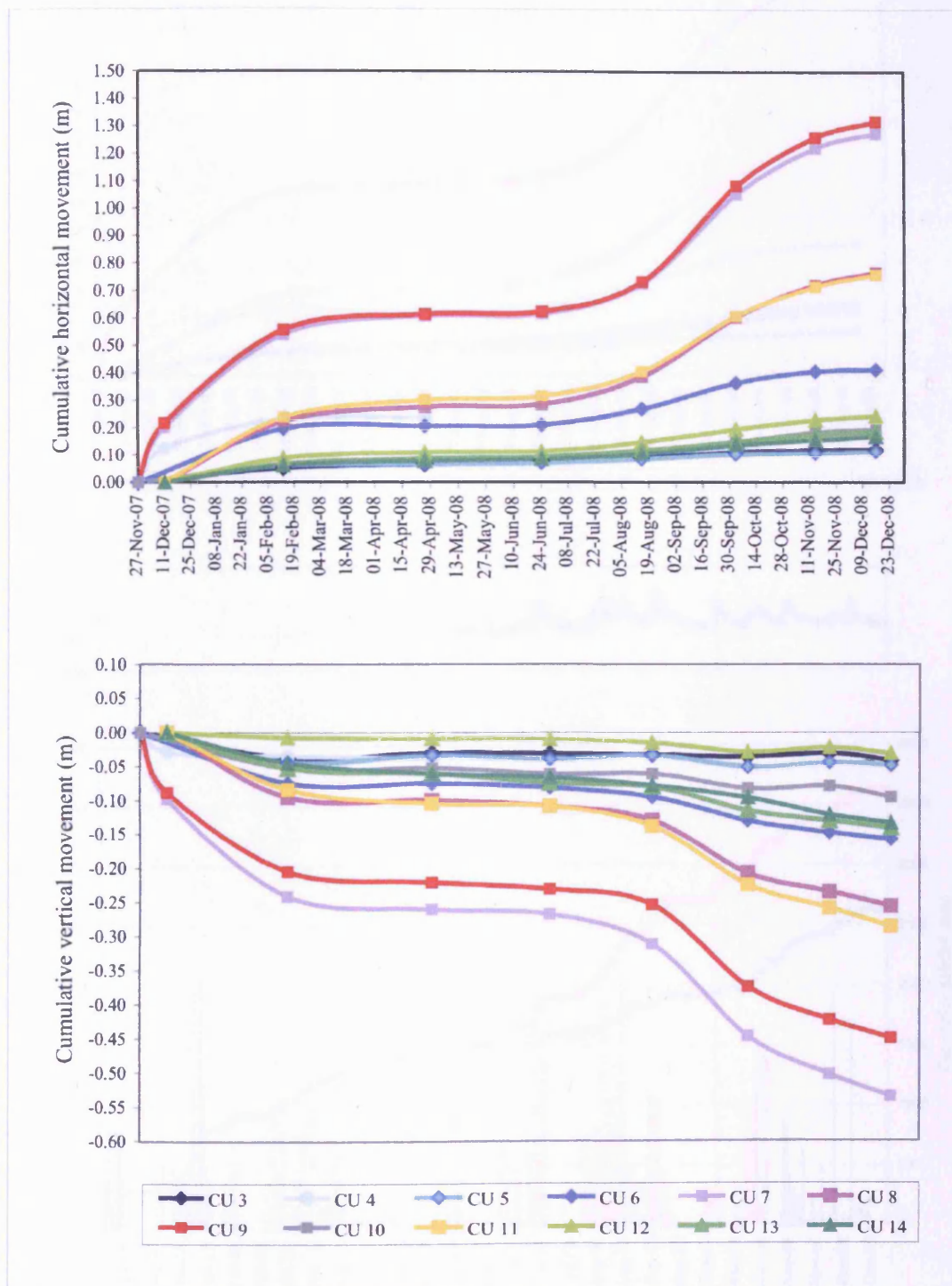


Figure 3.52 Cumulative horizontal (top) and vertical (bottom) movement for markers CU3-CU14 over the monitoring period (27 November 2007 – 16 December 2008). The two graphs have a different vertical scale

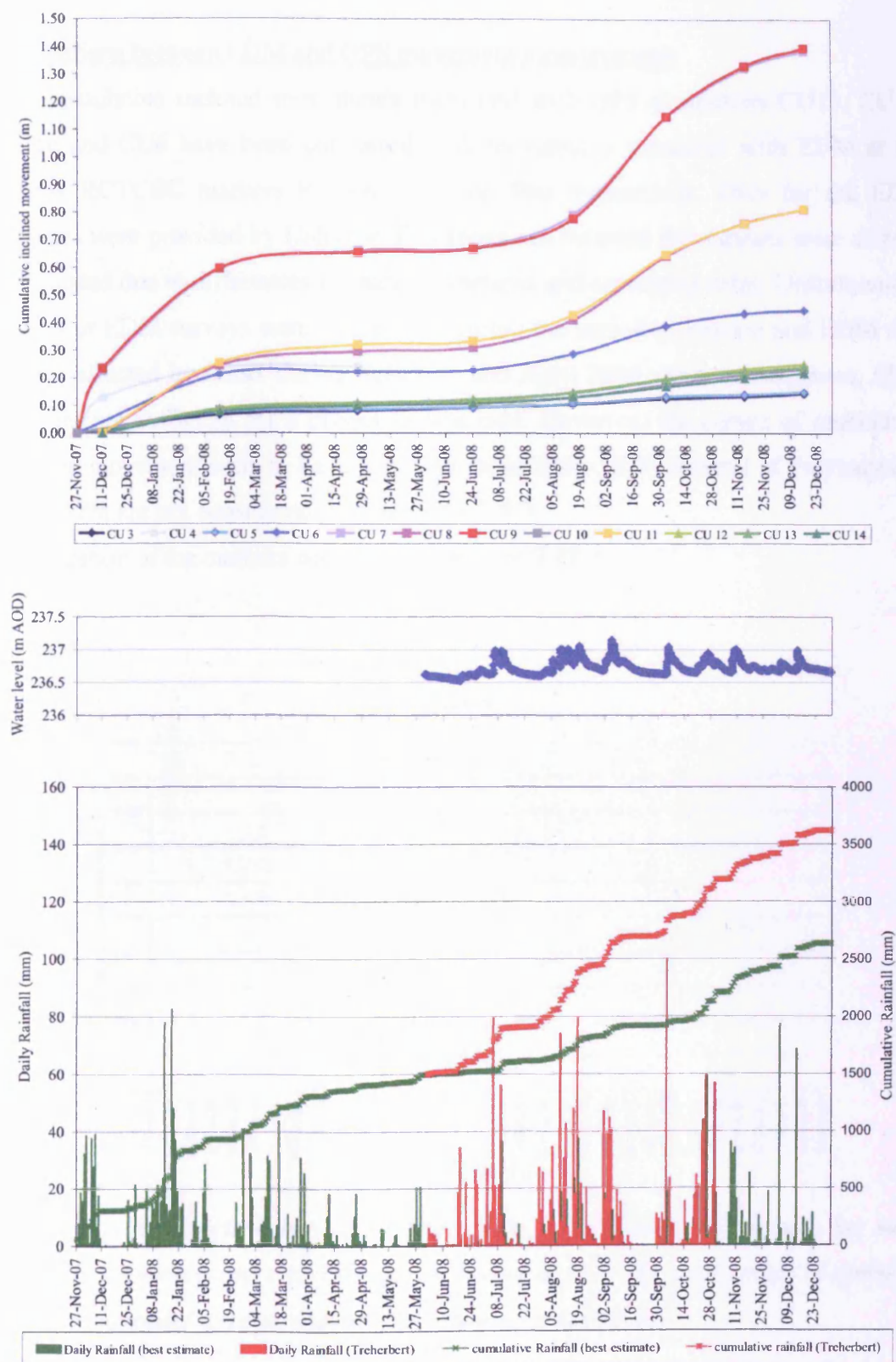


Figure 3.53 Cumulative inclined movement for markers CU3-CU14 (top), water level measured at Borehole 3 (centre – available only from 30 May 2008) and daily/cumulative rainfall for the period of GPS monitoring

Comparison between EDM and GPS movement measurements

The cumulative inclined movements measured with GPS at markers CU13, CU12, CU10 and CU6 have been compared with movements measured with EDM at the nearby RCTCBC markers P3, P6, P18 and P60 respectively. Data for the EDM markers were provided by Halcrow. Discrepancies between the datasets were already anticipated due to differences in marker positions and surveying dates. Unfortunately, only four EDM surveys were carried out during the period of interest and EDM data appear affected by errors during February and April 2008. As a consequence, EDM data are not sufficient for a proper comparison. However, the curves of cumulative inclined movement seem to have a similar trend if the EDM surveys of February and April 2008 are not considered (Figures 3.54-3.57).

The location of the markers was shown in Figure 3.47.

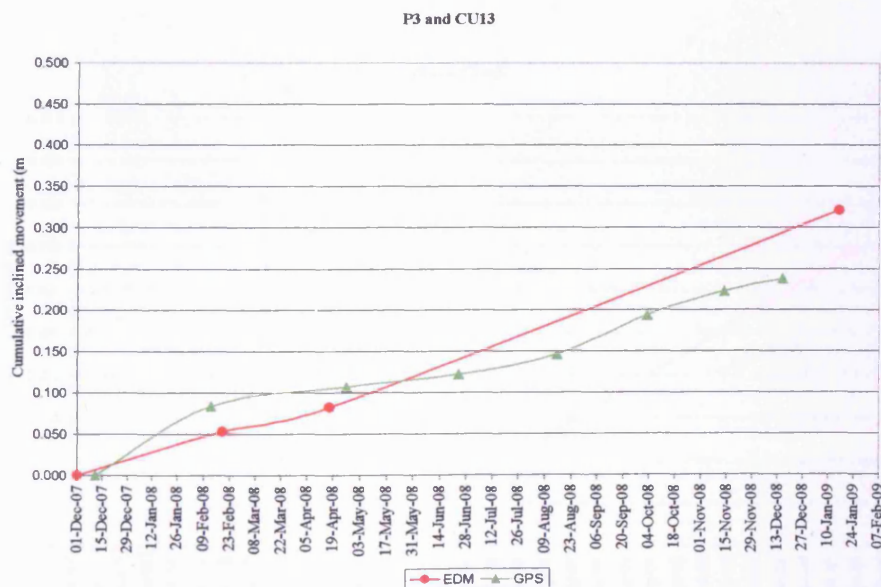


Figure 3.54 Comparison between EDM results for P3 and GPS results for marker CU13. EDM surveys were carried out on behalf of RCTCBC and values of cumulative inclined movement were provided by Halcrow (Cardiff office).



Figure 3.55 Comparison between EDM results for P6 and GPS results for marker CU12. EDM surveys were carried out on behalf of RCTCBC and values of cumulative inclined movement were provided by Halcrow (Cardiff office)

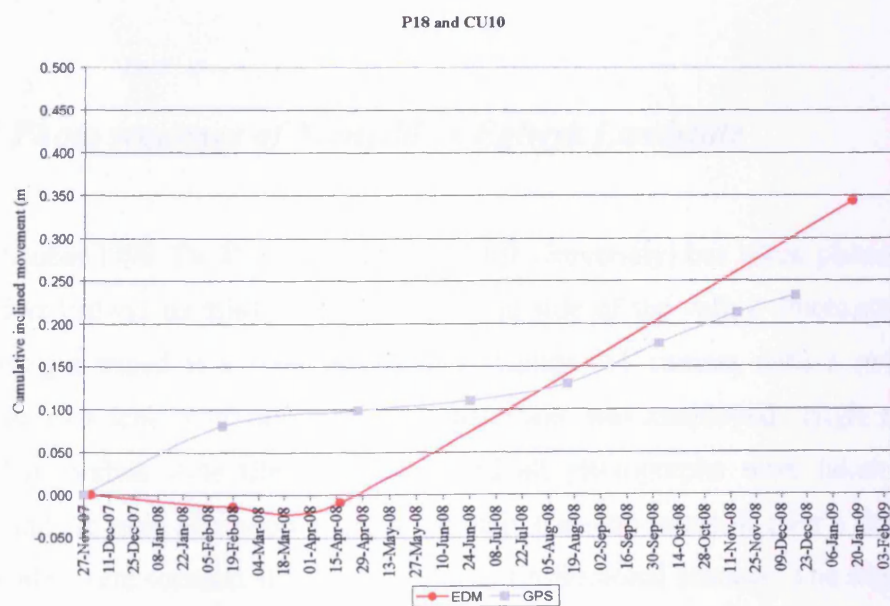


Figure 3.56 Comparison between EDM results for P18 and GPS results for marker CU10. EDM surveys were carried out on behalf of RCTCBC and values of cumulative inclined movement were provided by Halcrow (Cardiff office)

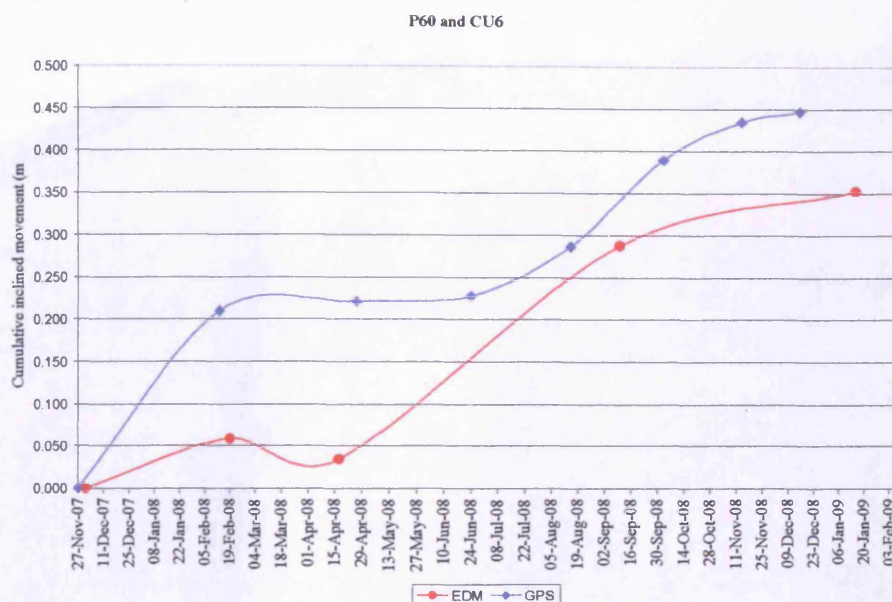


Figure 3.57 Comparison between EDM results for P60 and GPS results for marker CU6. EDM surveys were carried out on behalf of RCTCBC and values of cumulative inclined movement were provided by Halcrow (Cardiff office)

3.11.3 Photo sequence of Mynydd yr Eglwys Landslide

Since October 1999, Dr. P. J. Brabham (Cardiff University) has taken photographs of Mynydd yr Eglwys landslide from the opposite side of the valley. Photographs were taken using a tripod at a fixed location. A Canon A1 camera with a professional 80mm portrait lens with minimal lens distortion was employed. High resolution 35mm Fuji Velvia slide film was used and all photographs were taken between midday and the early afternoon at approximately 6 month intervals over a decade. The 35mm slides were scanned at 3200dpi using a professional scanner. The digital scans were sharpened and contrast enhanced. Four common ground points were identified on each photograph and all images were commonly rectified using these four points. From the photographs (Figures 3.58-3.66), the gradual movement of the landslide is easily observed.



Figure 3.58 Photograph of Mynydd yr Eglwys Landslide taken in October 1999 by P. J. Brabham



Figure 3.59 Photograph of Mynydd yr Eglwys Landslide taken in January 2000 by P.J. Brabham



Figure 3.60 Photograph of Mynydd yr Eglwys Landslide taken in September 2000 by P.J. Brabham



Figure 3.61 Photograph of Mynydd yr Eglwys Landslide taken in November 2000 by P.J. Brabham



Figure 3.62 Photograph of Mynydd yr Eglwys Landslide taken in June 2002 by P.J. Brabham

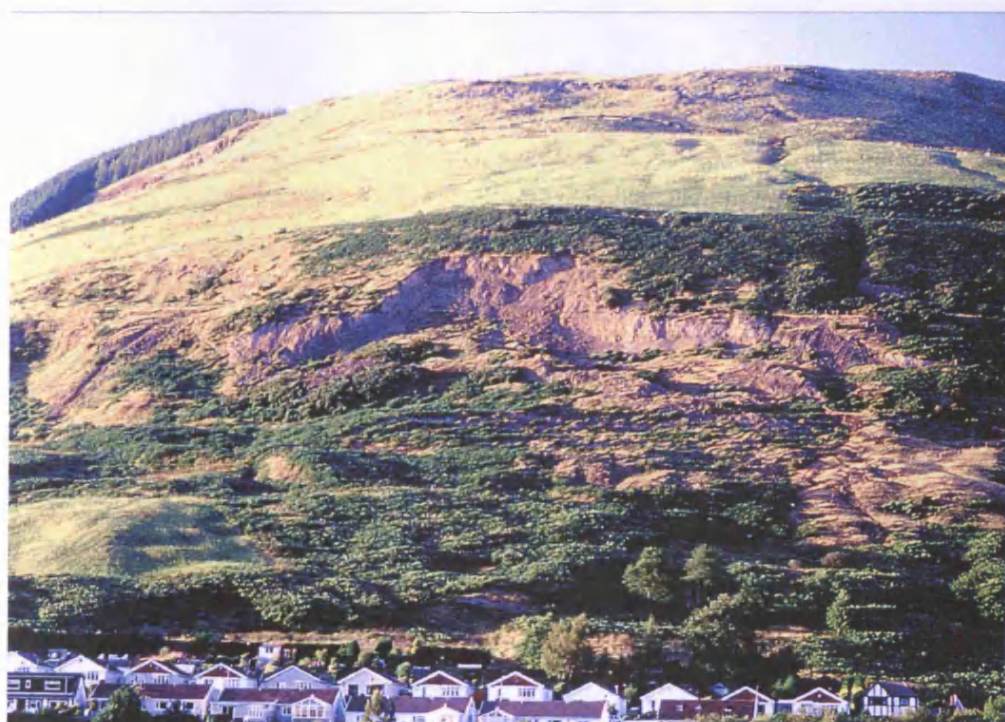


Figure 3.63 Photograph of Mynydd yr Eglwys Landslide taken in August 2002 by P.J. Brabham



Figure 3.64 Photograph of Mynydd yr Eglwys Landslide taken in March 2003 by P.J. Brabham



Figure 3.65 Photograph of Mynydd yr Eglwys Landslide taken in September 2004 by P.J. Brabham



Figure 3.66 Photograph of Mynydd yr Eglwys Landslide taken in May 2009 by P.J. Brabham

3.12 Summary

This chapter described the results of desk study and preliminary investigations carried out for MyE landslide. Following is a summary list of the main observations:

- A new compound deep-seated landslide developed in the mid slope of MYE in 1998-1999, probably triggered by the exceptional prolonged rainfall of October-November 1998. The loads imposed by this new landslide reactivated ancient debris slides downslope. Halcrow (1999; 2000) identified also two blocks of ancient episodes of deep-seated landsliding which approximately coincide with the toe of the new deep-seated landslide.
- The MyE slope is composed of mudstones, siltstones, coal seams, seatearths and bands of sandstones of Middle Coal Measures, overlaid by Lynfi Beds of Upper Coal

Measures. Two coal seams, Rhondda No.3 and Tormynydd, outcrop at the main scarp. The strata below Tormynydd seam are probably mainly argillaceous, while strata between Tormynydd and Rhondda No.3 are mainly sandstones (Lynfi Rock). In general, the strata dip gently out of the slope.

- The geology was mined for coal using both C19th outcrop adit and C20th deeper coal workings until the 1930s. Rhondda No. 3 seam was mined by pillar and stall method and the workings were located upslope of today's main scarp. Tormynydd seam was instead mined by longwall method and the NW-SE trending edge of the workings appears to coincide with today's main scarp. Voids associated with these shallow workings could still be present, but are unlikely. Deep mining has caused differential regional subsidence, possible fault reactivation and the opening of NW-SE fissures located at the crown of the landslide.

- The large NW-SE Cymmer fault crosses the mid part of the landslide and downthrows strata to the SW. It has caused fracturing of strata and probably local changes of dip of strata. There may also be a possibility of fault re-activation from deep workings of the Gelli colliery that closed in the mid 1960s, as the fault would form a limit of coal workings.

- The surface of rupture in the new compound landslide is probably steep at the rear, where it developed following pre-existing joints. The surface of rupture is flatter at the sole, where probably follows weaker strata (i.e. seatearths) found beneath the Tormynydd coal seam.

- The surface of rupture of the debris slides was originally estimated by Halcrow to be at a depth of 5-8 m (1999; 2000), whereas it was detected in borehole samples at depths of 0-5.80 m by ESP. The deformation of boreholes measured during this project, indicates that possible shearing occurs at 3.3-6.4 m depth.

- Water seepage was observed at the base of Rhondda No. 3 in the main scarp area. Many wet areas and issues can be found along a NW-SE trend across the slope probably in association with the Cymmer fault. Other wet areas can be observed at the toe of the debris slides, due to the low permeability of the glacial till.

- The slope is probably characterised by several perched water tables and mining is likely to have altered the groundwater paths. Rain water is likely to percolate through the enlarged fissures in the crown area till it reaches the impermeable seatearth below Rhondda No.3 and then moves laterally along dip of strata to the outcrop. The more likely sources of water at the site are the workings/voids in Rhondda No.3 and Tormynydd seams and the Lynfi Rock. The Cymmer Fault could act as a preferential conduit for water or as a barrier (due to clay gouge). The impermeable glacial till creates potential for artesian water pressures at the Southern part of the slope.

- Only a few ground investigations have been carried out on site and most of the information above listed is conjectured. The borehole logs suffer from a great degree of incoherency/unreliability, however borehole data were taken into consideration and successively used for geophysical calibration.

- The results of continuous monitoring of water levels (30 May 2008 - 20 May 2009) show that there is a strongly significant positive correlation between boreholes 3, 6 and rainfall. In particular, water level rises within 1-2 days of heavy rainfall in borehole 3 and correlograms have revealed also a second delayed pick after 4 days. Water level rises within the same day and mainly after 4-6 days after heavy rainfall in borehole 6. In both boreholes the water level rises of approximately 0.4 m after an isolated rainfall event, and then it decreases asymptotically mainly in the first 6-8 days. The effects of water rising appear to super-impose reaching higher water level values after numerous and close heavy rainfall events. These boreholes did not show a seasonal pattern, but summer 2008 was exceptionally wet.

The water level response in borehole 6 is more complex, probably because of its proximity to different wet areas/sources and its location at the toe of debris slides which are covered in dense vegetation during the summer.

- Geomorphological mapping and in particular the results of GPS monitoring helped identifying areas of heterogeneity (i.e. different level of activity) within the slope. In general, the landslide is moving at very slow rates (maximum of 3.5 mm/day in CU9) approximately towards South (i.e. towards the house in Meadow Walk). Surface rate of displacements are higher in the area between the two N-S lateral shears and in

particular in Zone 2 of debris slides B and C. Here the vectors of movement are inclined of approximately 20° downslope, similarly to slope angle (i.e. parallel to topography). Movements, at slower rates, were observed also in the new and old deep-seated landslide areas and in the spoil tip in debris slide C, while they were close to survey detectability for debris slide A.

- GPS results show a temporal variability in rate of displacements, which is probably associated with rainfall and water pressures. However, the low frequency of GPS campaigns allowed only depicting a general seasonal trend of rate of displacements (acceleration occurs in wetter periods). Data were not sufficient to establish and describe the link between rainfall – water level rise – acceleration in surface displacements.

- Many preparatory factors which are typical of the South Wales Coalfield may have contributed to the development of the new deep-seated landslide (Chapter 1; Table 3.8). Compound failures require a progressive weakening of strata to develop. Halcrow (1999; 2000) suggests that the new landslide is a retrogression of the ancient deep-seated landslides and was also influenced by the removal of support of previous downslope movements of the ancient debris slides. Mining may have caused fracturing and weakening of strata and may have introduced water into the area. However, it ceased in the 1930s and no other examples are known in which mine workings have caused landsliding with such long temporal delay.

This information was fundamental for an effective design of geophysical investigations/monitoring and for a successive realistic geological and hydrogeological interpretation of geophysical results.

Several targets for MyE landslide could be identified for geophysical investigations:

- lithology and structure;
- surface of rupture in deep-seated landslides and in debris slides;
- precise location of Cymmer Fault and its role as barrier or preferential water path;
- rock fracturing degree;
- water sources and water paths;

- differences between areas of ancient debris slides characterised by different rates of displacement (i.e. is there a change in geophysical data when crossing the N-S lateral shears or zone 2?).

Moreover, as GPS monitoring data suggest that heavy/prolonged rainfall and water pressures can be responsible for accelerations in rate of displacement, geophysical monitoring could be effective in detecting water paths or water level variations within the slope following heavy/prolonged rainfall.

Chapter 4 - Geophysical characterisation of Mynydd yr Eglwys Landslide

4.1 Introduction

This chapter describes the geophysical results obtained at Mynydd yr Eglwys (MYE) landslide for each of the survey techniques employed in the site investigations: electromagnetics (Geophex GEM-2), self-potential (SP), seismic refraction tomography (P-waves), multichannel analysis of surface waves (MASW), electrical resistivity tomography (ERT) and induced polarization (IP).

The geophysical results are jointly interpreted to develop a conceptual model of the landslide and discussed in terms of effectiveness of the methods in detecting the specific targets, which were introduced in the aims of this research project (section 1.8).

Details of the acquisition and processing methodologies employed on the geophysical data were provided in Chapter 2, whereas the MYE landslide features/properties (i.e. geomorphology, geology and kinematics), which the geophysical interpretation refers to, were previously explained in Chapter 3.

4.2 Results and interpretation of electromagnetic data acquired with Geophex GEM-2 instrument

Figure 4.1 shows the location of all the GEM-2 profiles acquired on MYE landslide essentially as three grids. The contour plots of the apparent electrical conductivity for the three GEM-2 frequencies 47025, 30025 and 15025 Hz are presented in Figure 4.2. Table 4.1 provides an approximate investigation depth for different values of ground conductivity (or resistivity) for the three frequencies, for a simplified model of a half-space below a single layer, based on equation 2.16 and assuming a detection threshold

of 30%.

The values of apparent conductivity at 47025 Hz range between 0.1 and 26 mS/m. The contour plot is characterised by three main high conductivity (or low resistivity) anomalies, which are coloured in green-blue:

- X) an area immediately to the South of the toe of debris slides A and B, bounded to the north by an abrupt decrease in conductivity;
- Y) a linear feature with a NW-SE trend located in the central part of the landslide leading into the wet area of debris slide C;
- Z) a broad area located in the NW part of the site which is separated from a resistive in the SW by a clear linear boundary.

Unfortunately (due to logistical problems and high cost) none of the boreholes are located in these three anomaly zones to provide data calibration. However, the broad conductive anomaly Z has a sharp southern boundary which runs along strike with the central anomaly Y. The NW-SE trend and its location suggest a probable association with an increase in water and/or clay content within the large Cymmer Fault. The conductive area found immediately south of the debris slides toe (X) could be due to water draining from beneath the dry landslide lobes and/or to the high clay content of the glacial till.

In general, the most active area of the landslide (Zone 2 of geomorphological map in Figure 3.21) is characterised by numerous relatively strong but irregular lateral variations in conductivity, ranging between 1 and 7 mS/m. The highest values (6-7 mS/m) can for example be found immediately downslope of the minor scarp. Again there are no boreholes located in this area. Therefore the anomalies could be related to variations in water and/or clay content.

Outside Zone 2, debris slides A and B are generally more electrically resistive, with conductivity values mainly between 0.1 and 4 mS/m.

There is no evident geophysical difference between the areas of the debris slides to the west and to the east of the N-S lateral shear, that is between the less active debris slide A and the more active debris slide B. On the contrary, there is an abrupt change

in conductivity at the toe of the debris slides, which coincides with the conductivity contour of 3 mS/m.

The ground located around boreholes 7 and 8 is characterised by higher conductivity than the ground around the other boreholes (even if very close, such as boreholes 7A and 8A). The logs of borehole 7 and 8 indeed report a clay layer of 1.3 to 2.85 m thickness, at depth between 2.3 and 5.15 m from the surface which can justify this observed higher conductivity (as the water table was recorded at depth greater than 15 m). All the other boreholes located within the GEM-2 dataset, with the exception of borehole 9, are generally characterised by gravel or mudstone/siltstone also in the first 5-6 m of depth, which expresses itself geophysically in lower conductivity values. The log of borehole 9 reports clay between 3.65 and 6.05 m depth, but this does not seem to show geophysically in any of the GEM-2 plots.

In GEM-2 surveying, the depth of investigation increases with the decrease in the electromagnetic frequency employed. The values of apparent conductivity measured at 30025 Hz range between 0.1 and 32 mS/m. All the three main high conductivity anomalies X, Y and Z are still evident. However, both high conductivity areas at the toe (X) and in the NW part of the site (Z) are slightly narrower. The most active area of the landslide (Zone 2) is still characterised by numerous and irregular lateral conductivity variations, but is generally more resistive when compared with the 47025 Hz dataset. This observation suggests perhaps a greater influence from deeper, dry weathered rock. Also the area of the debris slides outside Zone 2 appears generally more resistive, whereas the observed abrupt change in conductivity coinciding with the debris toe is still very evident.

The values of apparent conductivity at 15025 Hz range between 0.1 and 54 mS/m. At this frequency the high conductivity zone X narrows further and zone Z is difficult to identify, as it is only present at the edges of the dataset. The most obvious geophysical feature is the lineation trending NW-SE in the centre of the study area (Y). Apart from this anomaly, the landslide is characterised by low conductivity values, in the range of 0.1 to 2 mS/m (or resistivity higher than 500 Ohm.m). These low values, found also in the area surrounding boreholes 7 and 8, suggest that the signal has indeed penetrated deeper and is mainly influenced by the weathered/fractured rock.

Considering Table 4.1 and anomaly Y, which appears clearly in all the three plots, a conductivity of 10 mS/m corresponds to approximate depths of investigation of 5.0, 5.5 and 6.6 m for frequencies 47025, 30025 and 15025 Hz respectively. The differences in the GEM-2 penetration depths are in reality quite limited, mostly in the conductive areas. As previously mentioned, the logs of boreholes 7 and 8 seem to suggest that the 47025 Hz dataset is mostly influenced by the first 5 m of the subsurface. Considerations on the validity of GEM-2 datasets in terms of detecting changes in conductivity with depth will be made later in this chapter, when GEM-2 results will be compared to data obtained using other geophysical techniques.

Figure 4.3 shows the contour plot of observed apparent magnetic susceptibility using the 15025 Hz frequency. This plot generally confirms the suspected absence of metal debris on this green field site. There are only a limited number of small anomalies, which can be attributed to observed metal borehole casings and RCTCBC steel surveying pegs. Therefore, metallic debris sources can be excluded as being responsible for any variations in the apparent conductivity values observed in the datasets.

Table 4.1 Approximate depths of investigation for each of the GEM-2 frequencies over a range of material conductivities (calculated from equation 2.16)

Conductivity (mS/m)	Resistivity (Ohm.m)	Investigation depth (m)		
		47025 Hz	30025 Hz	15025 Hz
0.1	10000	15.7	17.5	20.8
1	1000	8.8	9.8	11.7
2	500	7.4	8.3	9.8
5	200	5.9	6.6	7.8
8	125	5.2	5.9	7.0
10	100	5.0	5.5	6.6
20	50	4.2	4.7	5.5
100	10	2.8	3.1	3.7
1000	1	1.6	1.8	2.1

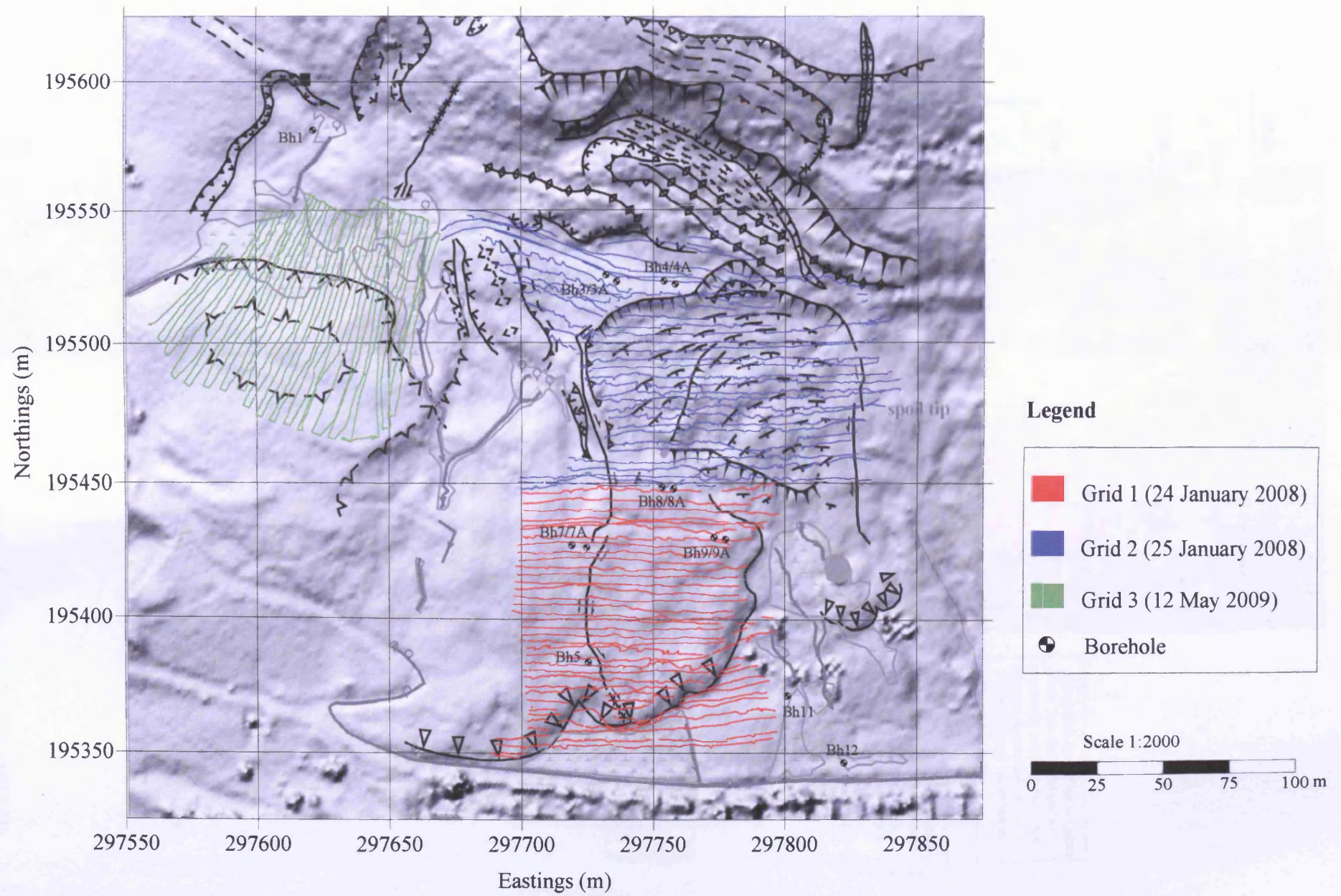


Figure 4.1 Location of lines acquired with the instrument GEM-2 (Geophex) at Mynydd yr Eglwys Landslide

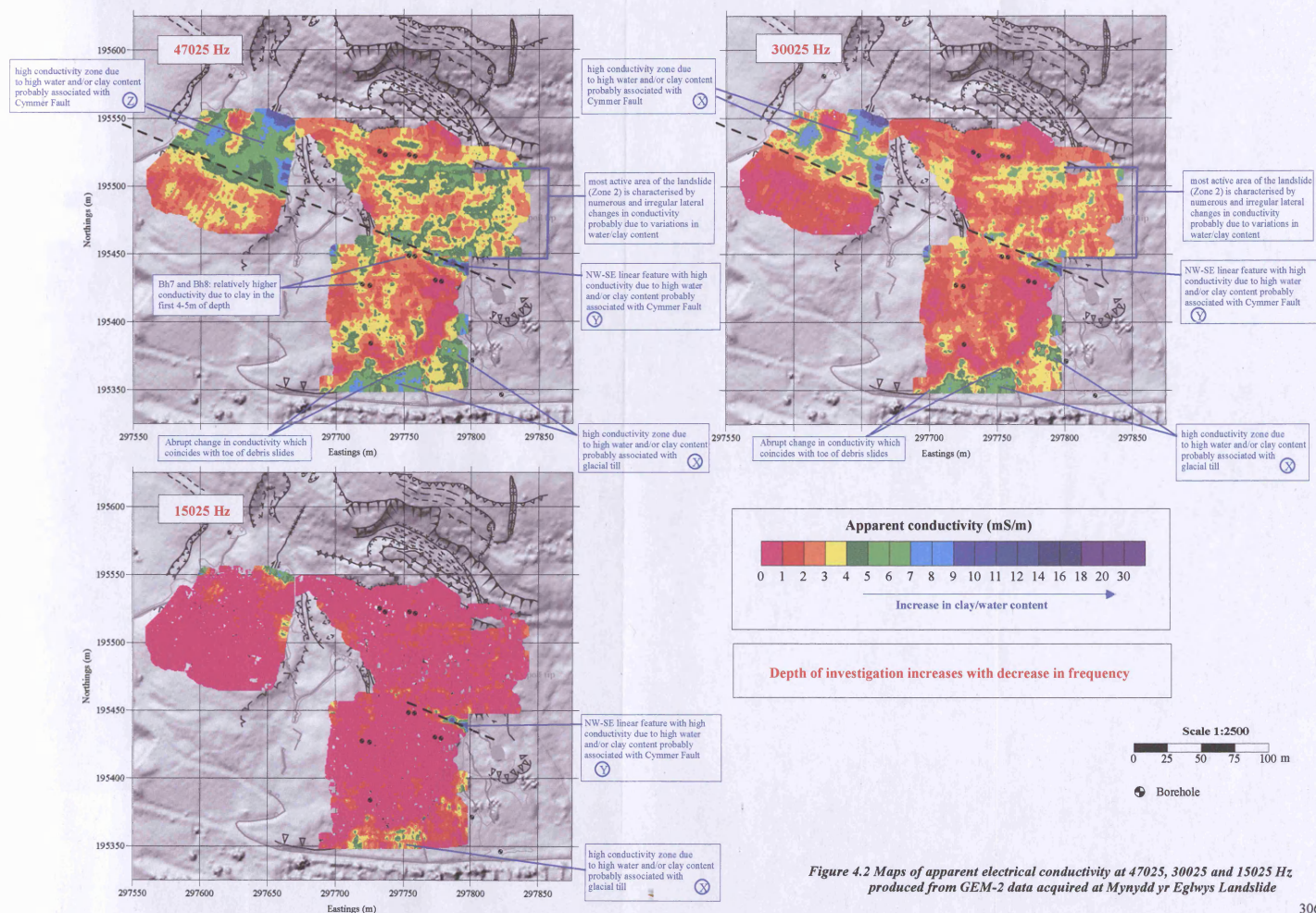


Figure 4.2 Maps of apparent electrical conductivity at 47025, 30025 and 15025 Hz produced from GEM-2 data acquired at Mynydd yr Eglwys Landslide

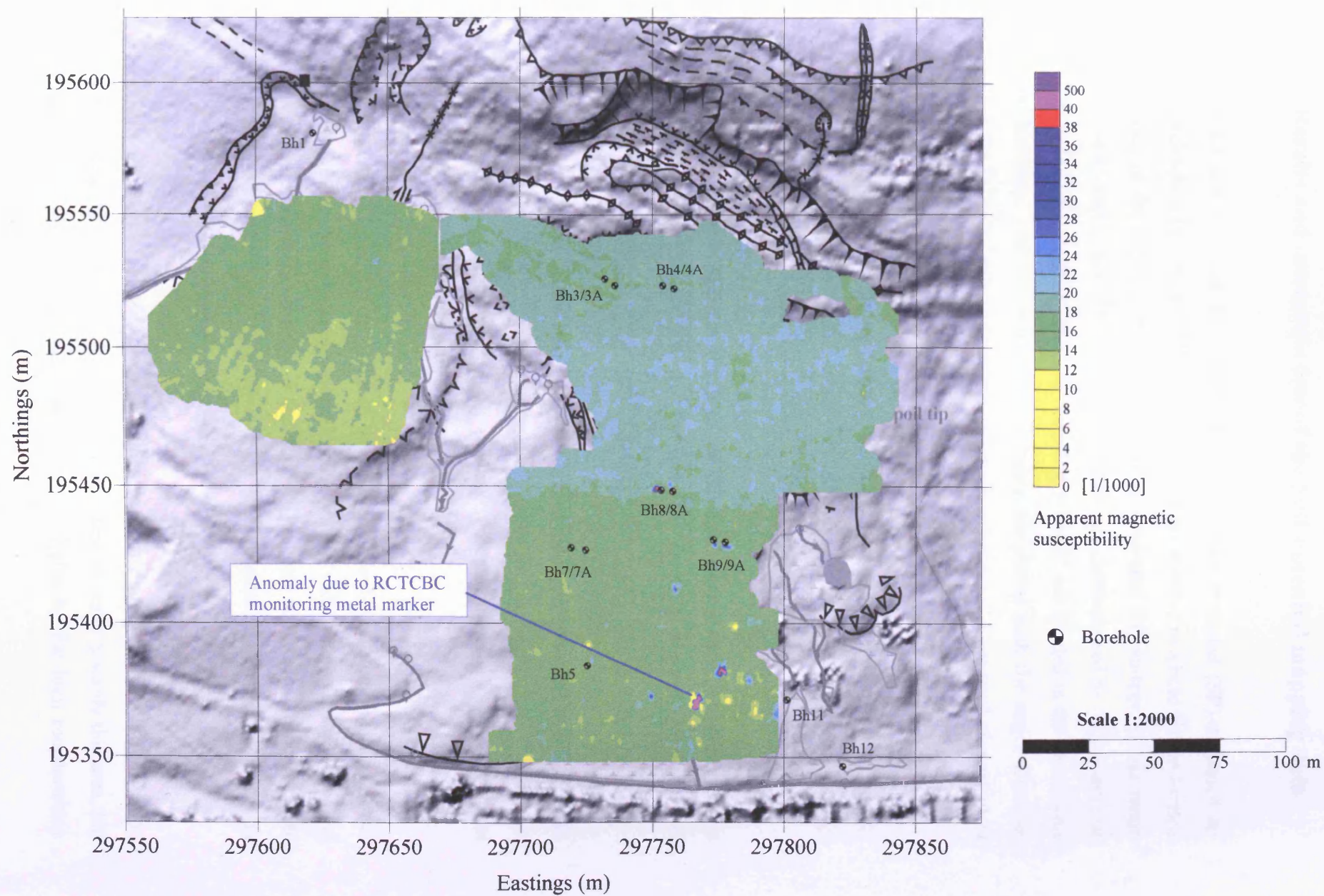


Figure 4.3 Map of apparent magnetic susceptibility at 15025 Hz produced from GEM-2 data acquired at Mynydd yr Eglwys Landslide

4.3 Results and interpretation of the Self Potential mapping data

Figures 4.4 and 4.5 show the values of electrical Self Potential (SP) measured on MYE landslide in December 2006. The SP values are relative to a base station located in bedrock in the exposed main scarp. These measured SP voltage values range between -19.5 and 31 mV. The self potential plots are characterised by the presence of a 30 m wide linear negative anomaly, trending NW-SE and located in the central part of the landslide. This SP anomaly is probably associated with the major Cymmer Fault in the bedrock, and its negative character indicates a downward movement of water through the fault zone.

A localised but relatively strong positive SP anomaly is present at the western edge of the landslide main scarp. This anomaly coincides with an observed water seepage from collapsed mine workings in the base of Rhondda No.3 coal seam.

The positive SP anomalies in the area of the new deep-seated landslide suggest movement of water towards this area, whereas the localised negative SP anomalies could also indicate water infiltrating through fractures.

The most active part of the landslide (Zone 2 of geomorphological map in Figure 3.21), outside the NW-SE negative anomalous linear feature as previously described, is characterised by short wavelength, positive voltage anomalies, which suggest localised upward movements of groundwater.

Figures 4.6 and 4.7 are contour plots of the voltage values measured on site in March 2007 (relative to a different base station). These voltage values range between -19 and 20 mV, but are generally between -6 and 6 mV. The most active area of the landslide is characterised by stronger, short wavelength lateral anomalies. The relatively strong positive anomalies could indicate localised upward movement of water.

Another area of positive SP anomalies is located immediately to the south of the toe of the debris slide B. This could indicate movement of water towards this area, but the positive SP values could have been influenced also by the high moisture/clay

content of the soil. Here the abrupt increase in voltage (more than 10 mV) seems to coincide with the toe of the debris slide.

SP data acquired along the three cross profiles at 195480 N, 195490 N and 195500 N are shown as contour plots (in Figures 4.6 and 4.7) but also as line graphs (in Figure 4.8), with annotations of observed geomorphological features. The voltage values measured on the more stable part of the slope, in the plateau above Church Quarry, show limited variations between -6 and 0 mV. Stronger positive and negative anomalies, with rapid lateral variations, can be observed in the rest of the profiles, especially in the most active area of the landslide. Moreover, a relatively strong negative anomaly seems to coincide with the lateral shear to the east (in the spoil tip), but the number of SP measurements is too few to conclude that an abrupt change in voltage delineates the eastern limit of the most active area of the slope. To the west, due probably to the strong effect of the Cymmer Fault crossing the slope between the plateau and the most active area of the landslide, a clear change in voltage at the geomorphological limit of the most active area of the landslide can not be identified.

Both December and March SP datasets were acquired in dry conditions, although different amounts of rainfall had occurred during the days previous to the surveys and may have influenced the results (Figures 4.9 and 4.10).

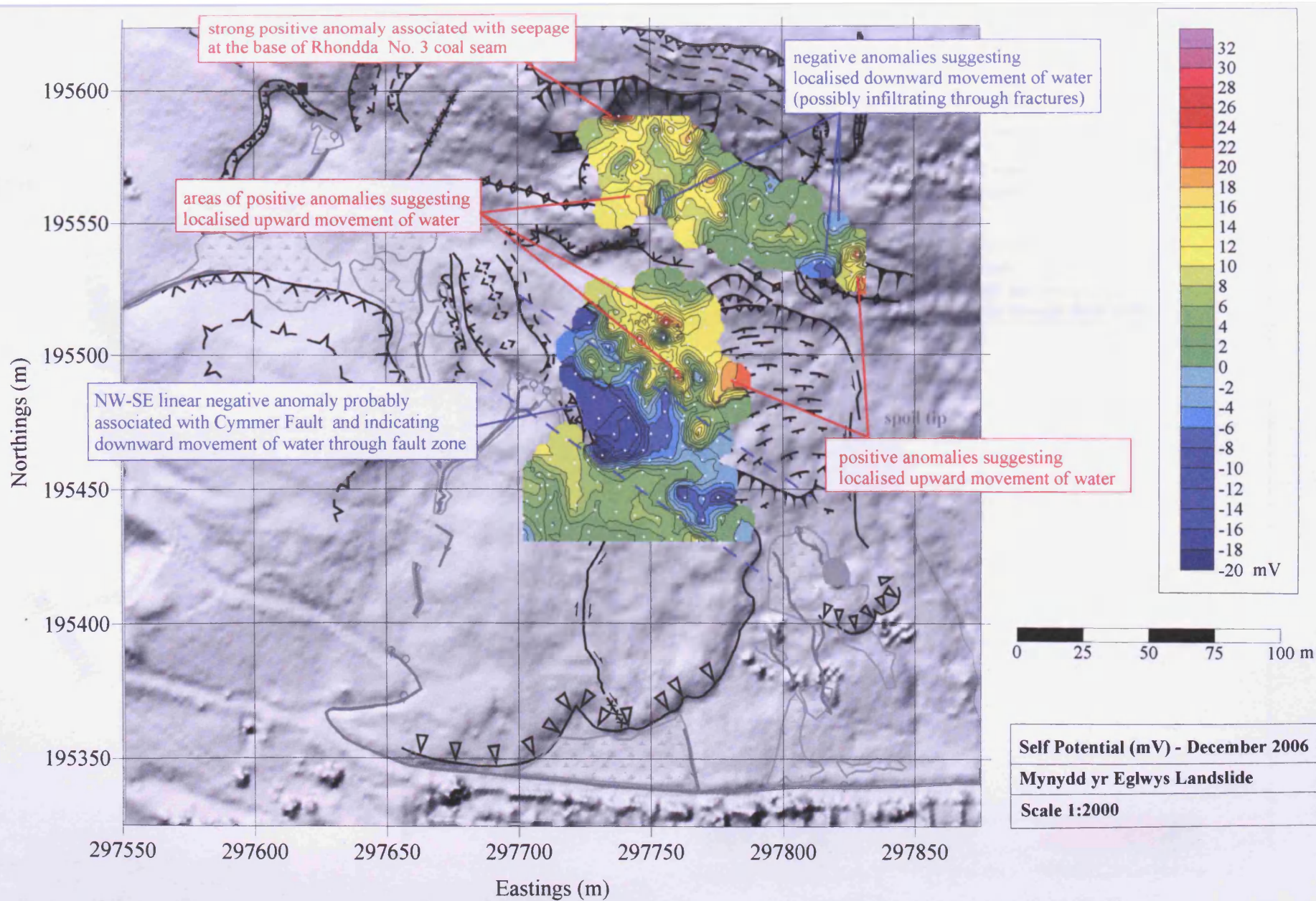


Figure 4.4 Self potential map derived from data acquired in December 2006 (on the 15th for the area of the main scarp and on the 19th and 21st for the central area). Location of SP stations is indicated with a white circle

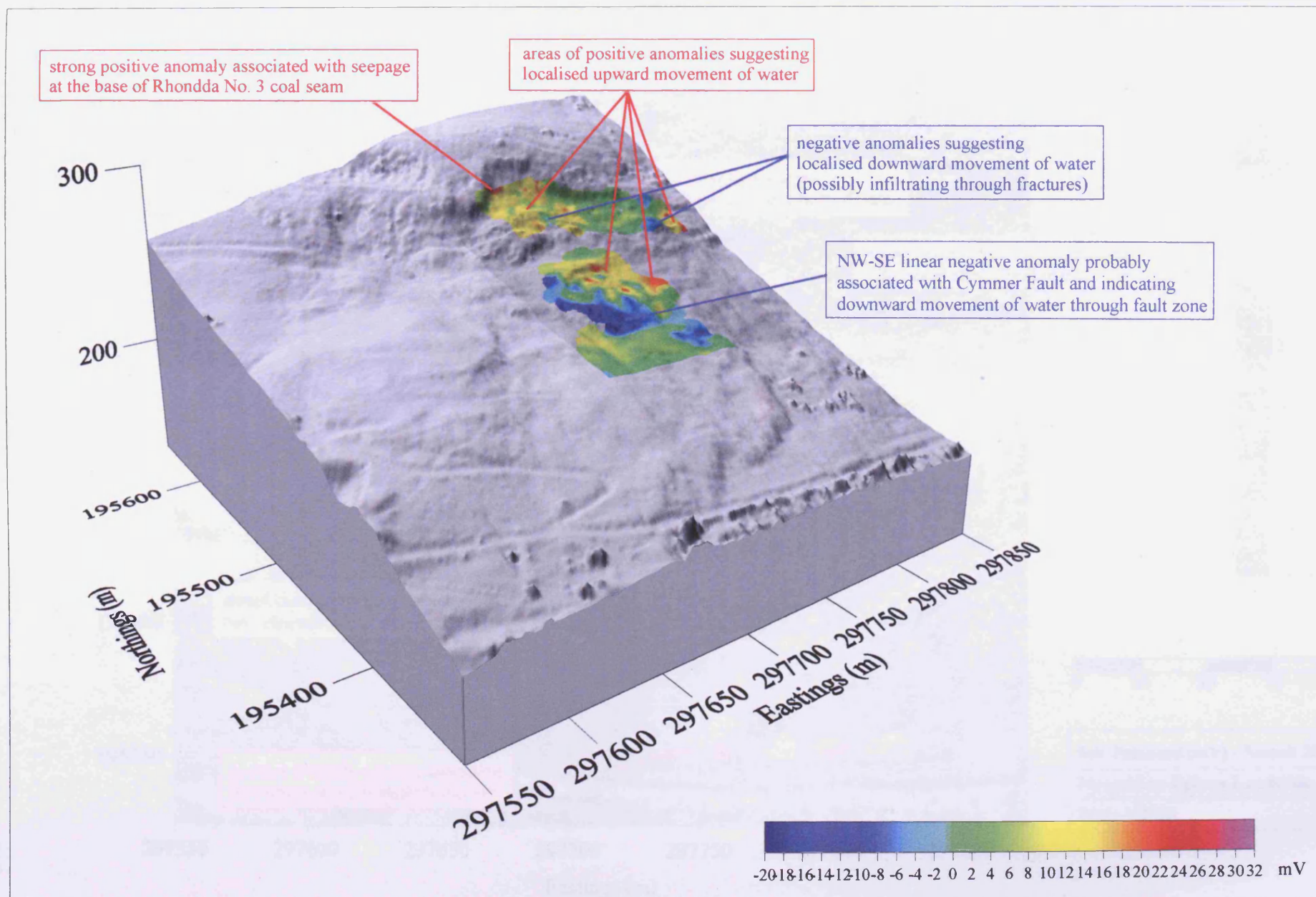


Figure 4.5 Self Potential map derived from data acquired in December 2006 draped onto a 3D LIDAR surface

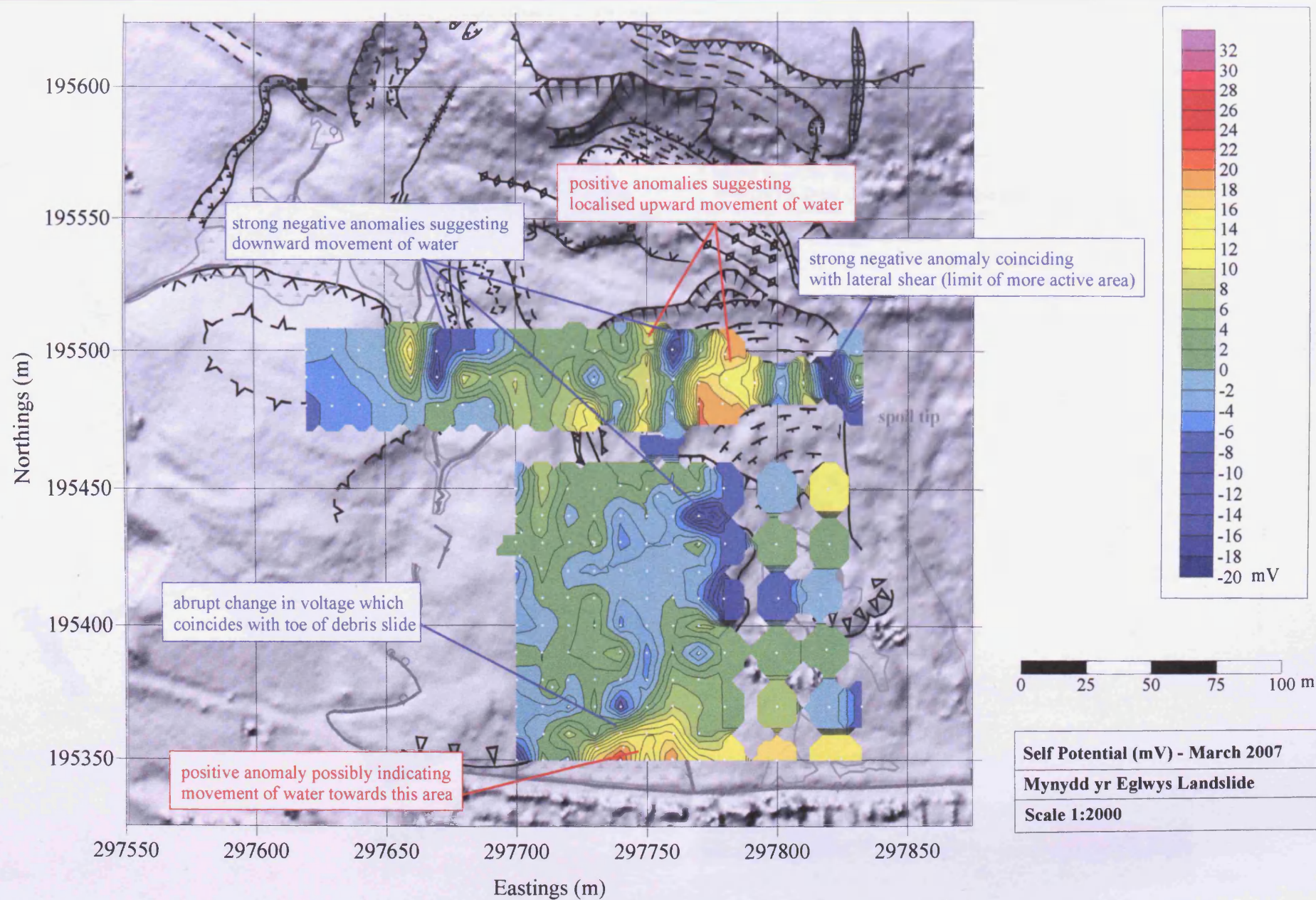


Figure 4.6 Self Potential map derived from data acquired in March 2007. Data in the central and toe areas were acquired on the 8th and 12th of March. Data along the three crossing profiles at 195480N, 195490N and 195500N were acquired on the 14th of March. Location of SP stations is indicated with a white circle

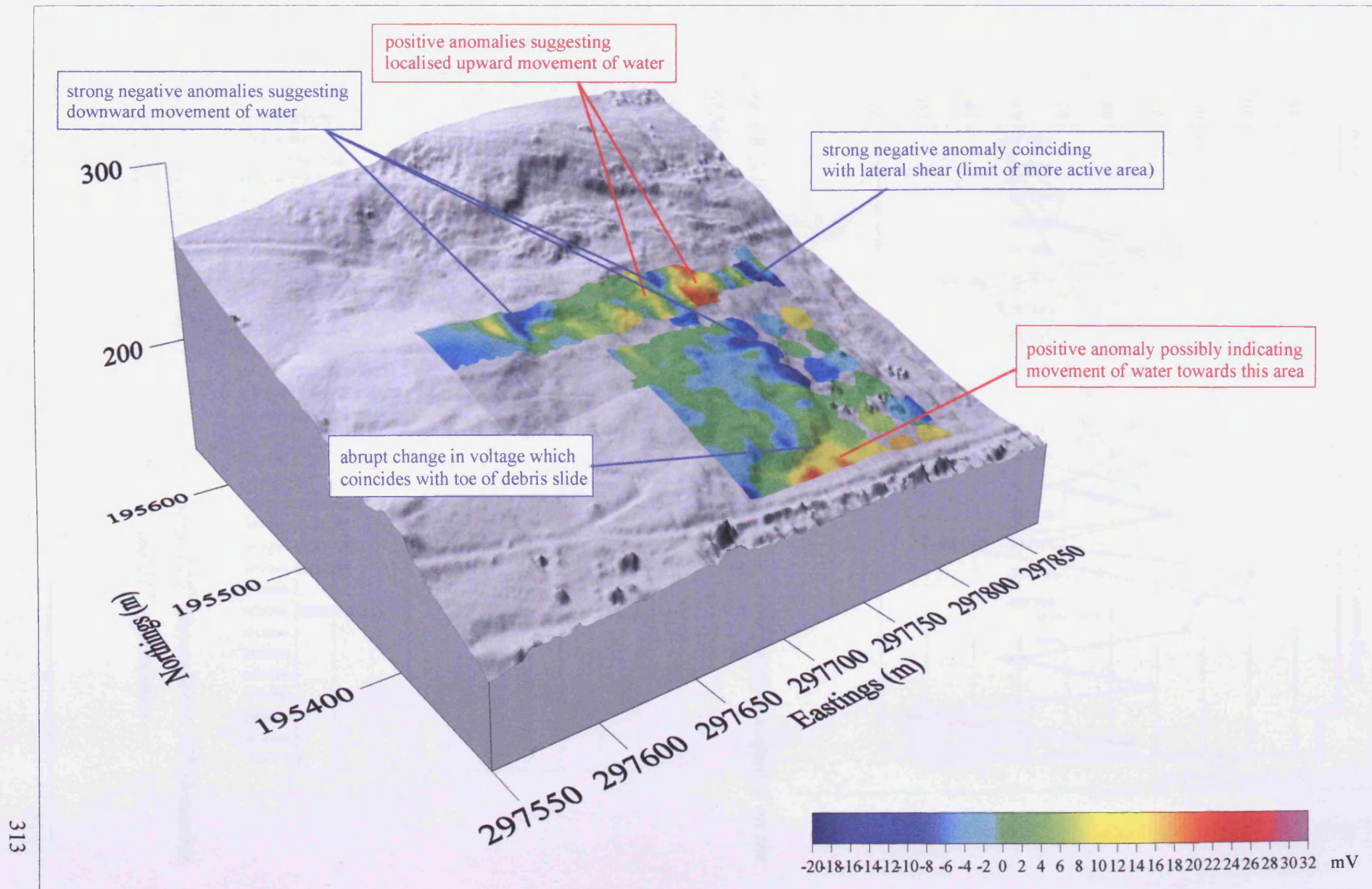


Figure 4.7 Self Potential map of data acquired in March 2007 draped onto a 3D LIDAR surface

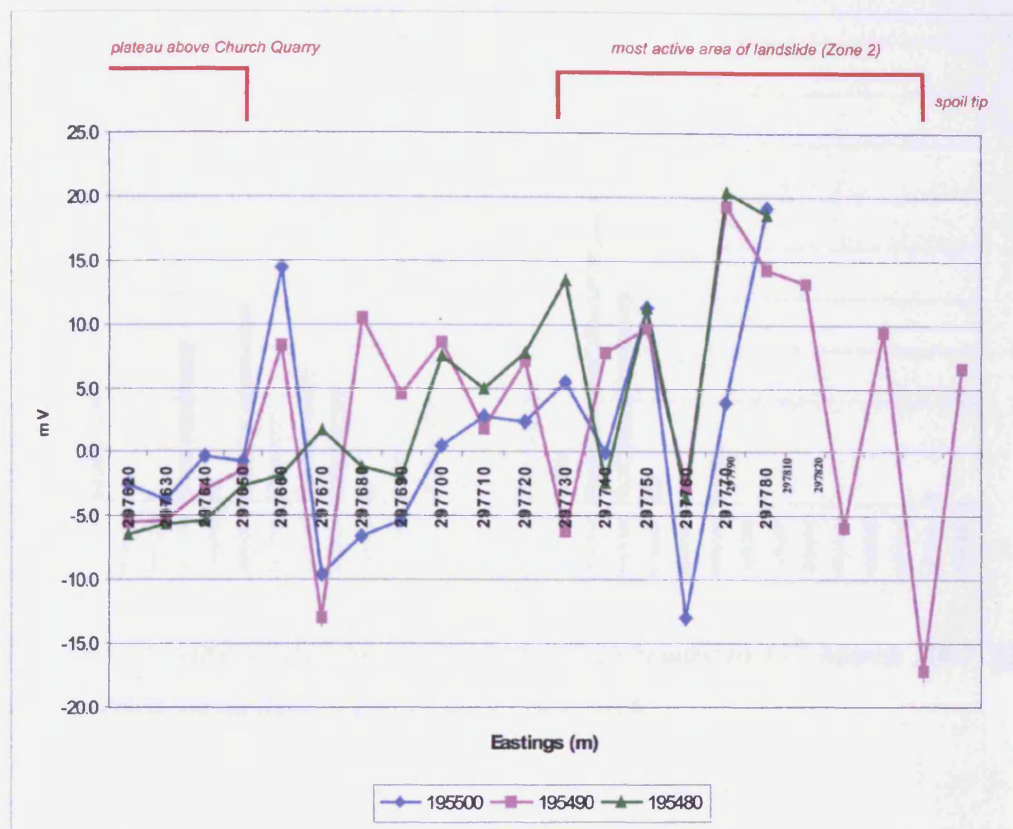


Figure 4.8 Self Potential measurements along the three cross profiles acquired on the 14th of March along 195480 N, 195490 N and 195500 N

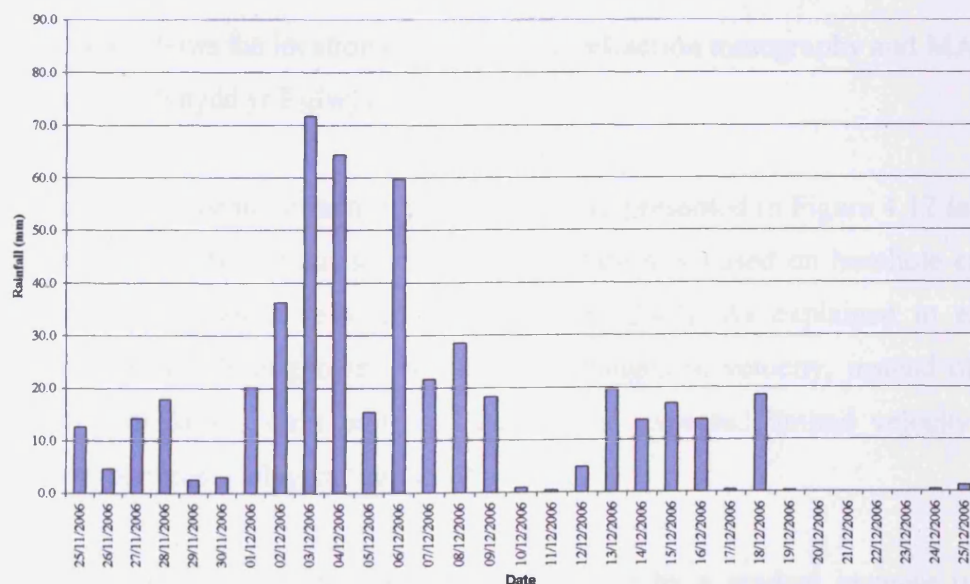


Figure 4.9 Daily rainfall (best estimate) for the period 25th November to 25th December 2006. SP surveys were carried out on the 15th, 19th and 21st of December

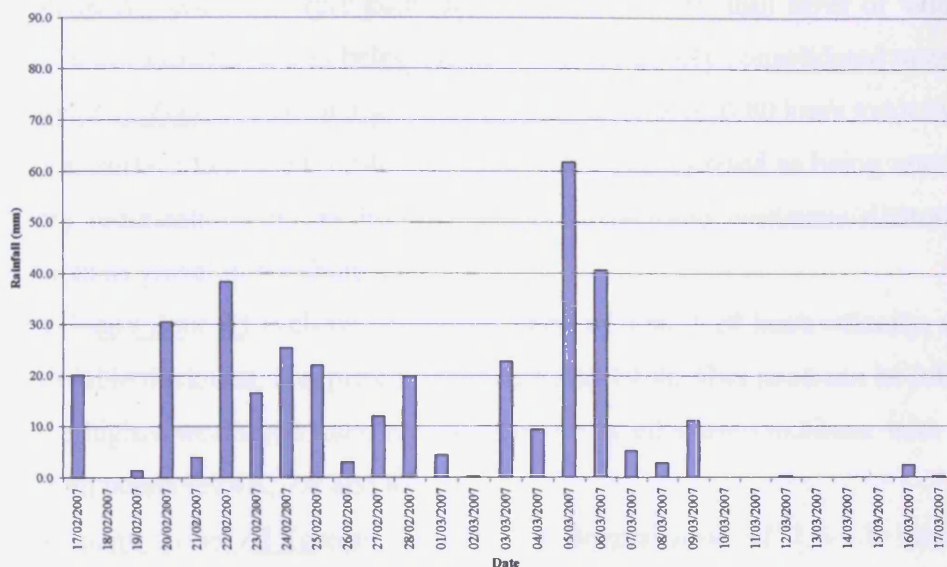


Figure 4.10 Daily rainfall for the period 17th February to 17th March 2007. SP surveys were carried out on the 8th, 12th and 14th of March

4.4 Results and interpretation of seismic refraction tomography and MASW data

Figure 4.11 shows the location of the seismic refraction tomography and MASW lines acquired at Mynydd yr Eglwys landslide.

The results of seismic refraction tomography are presented in Figure 4.12 in the form of seismic velocity contour sections. Interpretation is based on borehole calibration and published seismic velocity tables (Figure 2.47). As explained in chapter 2, geophysical models employing transitional changes in velocity, instead of discrete velocity boundaries, were preferred due to the expected limited velocity contrast observed between geological units.

In general, the seismic profiles are characterised by a gradual increase in P-wave velocity from surface to depth. From the surface, four discrete zones of velocity can be identified in the seismic sections:

Velocity Zone X (purple contours): superficial very thin layer of velocity 0.10-0.20 km/s interpreted as being the near-surface poorly consolidated material;

Velocity Zone Y (red-orange contours): zone of 0.40-0.80 km/s velocity from the near surface to a depth of 4-6 m. This can be interpreted as being unconsolidated dry sediments or as dry highly weathered/fractured mudstone/siltstone (defined often as gravel in borehole logs);

Velocity Zone Z1 (yellow contours): zone of 0.90-1.20 km/s velocity, with a very variable thickness, comprised between 1 and 10 m. This zone can be interpreted as the highly weathered/fractured bedrock or as siltstone/sandstone with water (i.e. from boreholes 4A, 7A and 8A);

Velocity Zone Z2 (green contours): a deeper zone of 1.6-1.8 km/s velocity, interpreted as less weathered/fractured bedrock.

Seismic line A is located in the blocks of ancient deep-seated landsliding described by Halcrow (1999; 2000) and which should also be at the toe of the new compound deep-seated landslide. In this line, there appears to be a good correlation between the base of velocity Zone Y and the surface of rupture identified by ESP. Moreover, this contour of 0.80-0.90 km/s velocity coincides with the depths of Boreholes 3 and 4 recorded on site during field work (possible shear depth). Therefore, Zone Y could correspond to the displaced material.

The base of velocity Zone Y is very close to the ESP surface of rupture also in line D at borehole 9. However, as indicated more clearly in borehole 9A, the surface of rupture could be within Zone Y at shallower depths and therefore the contour 0.80-0.90 km/s could correspond simply to a different degree of rock weathering/fracturing.

Unfortunately there is no data calibration available for line B, located in the most active area of the debris slides (Zone 2 of the geomorphological map in Figure 3.21). The interpretation provided in Figure 4.12 is based mainly on the observations made for line A, but the surface of rupture could be much shallower, as in line C (at boreholes 8 and 8A).

As previously mentioned, Zone Z1 has been interpreted as being the moderately-

highly weathered/fractured rock, possibly containing water. This zone is particularly thick (up to approximately 10 m) and with sharp lateral boundaries in both lines C and D. These two profiles are located close to or within the Cymmer Fault zone, which would likely be responsible for this increase in the degree of bedrock fracturing and possibly also an increase in water content.

Line E is located partly in the more stable area of the ancient debris slide A. The N-S lateral shear (previously described in MYE geomorphological section), which separates the less active area of the site from the more active one, passes just to the East of borehole 7A. However, there is no obvious lateral change in velocity in the section and this velocity profile could not be distinguished from line A and B without knowledge of the geomorphology and the activity of the landslide.

To summarise, all the seismic refraction tomography sections are characterised by a decrease in rock weathering/fracturing degree with depth. There is no obvious strong geophysical contrast observed between the displaced material and the weathered/fractured bedrock. The velocity contour 0.80-0.90 km/s seems to perfectly coincide with the observed surface of rupture in line A, but not in the other lines. Moreover, there are no obvious significant velocity changes observed when crossing from the less, to the more active parts of the ancient debris slides. The Cymmer Fault zone appears to be characterised by a high degree of fracturing, with a possible associated increase in water content.

MASW data acquired along lines A, B and E were processed by M. Bottomley (2008), who provided the coloured contoured plots of V_s shown in Figures 4.13, 4.14 and 4.15. As explained in chapter 2, processing of MASW data for line C was unsuccessful, probably due to the severity of topographic changes along the geophone spread or to strong lateral heterogeneities.

In general, all the three MASW lines are characterised by the presence of a low V_s zone (V_s between 200 and 275 m/s) located between 1 and 5 m of depth and then by an increase in velocity with depth, which can be associated with an increase in material stiffness. In profile A (Figure 4.13) this low velocity zone is between 2 and 5 m depth and, as indicated in borehole 4, could be associated to highly weathered

(gravel of) mudstone. This low velocity zone of V_S is within the Zone Y of V_P of the seismic refraction profile. The surface of rupture identified by ESP (and the depth shear recorded on site) appears to correspond to the contour line of 350 m/s below this V_S low velocity zone. Taking into consideration the V_P/V_S velocity ratios, a Poisson's ratio of approximately 0.42 can be obtained for a depth of 4 m ($V_P=600$ m/s, $V_S=225$ m/s, $V_P/V_S=2.6$), and of 0.40 for depths of 7 and 12 m ($V_P=1100$ m/s, $V_S=450$ m/s, $V_P/V_S=2.4$ and $V_P=1400$ m/s, $V_S=550$ m/s, $V_P/V_S=2.5$ respectively).

There is no calibration for MASW line B. The low V_S zone is here located between 1 and 5 m of depth and is again within V_P velocity Zone Y.

In MASW line E the low V_S zone is approximately between 1 and 4.5 m depth and could be associated with clay and very weathered mudstone (in borehole 7). It corresponds to the base of velocity Zone Y of seismic refraction results. In contrast, the low V_S zone is not present in the area of borehole 7A, which is located close to the lateral shear, which separates the more stable (west) from the more active (east) parts of the ancient debris slides.

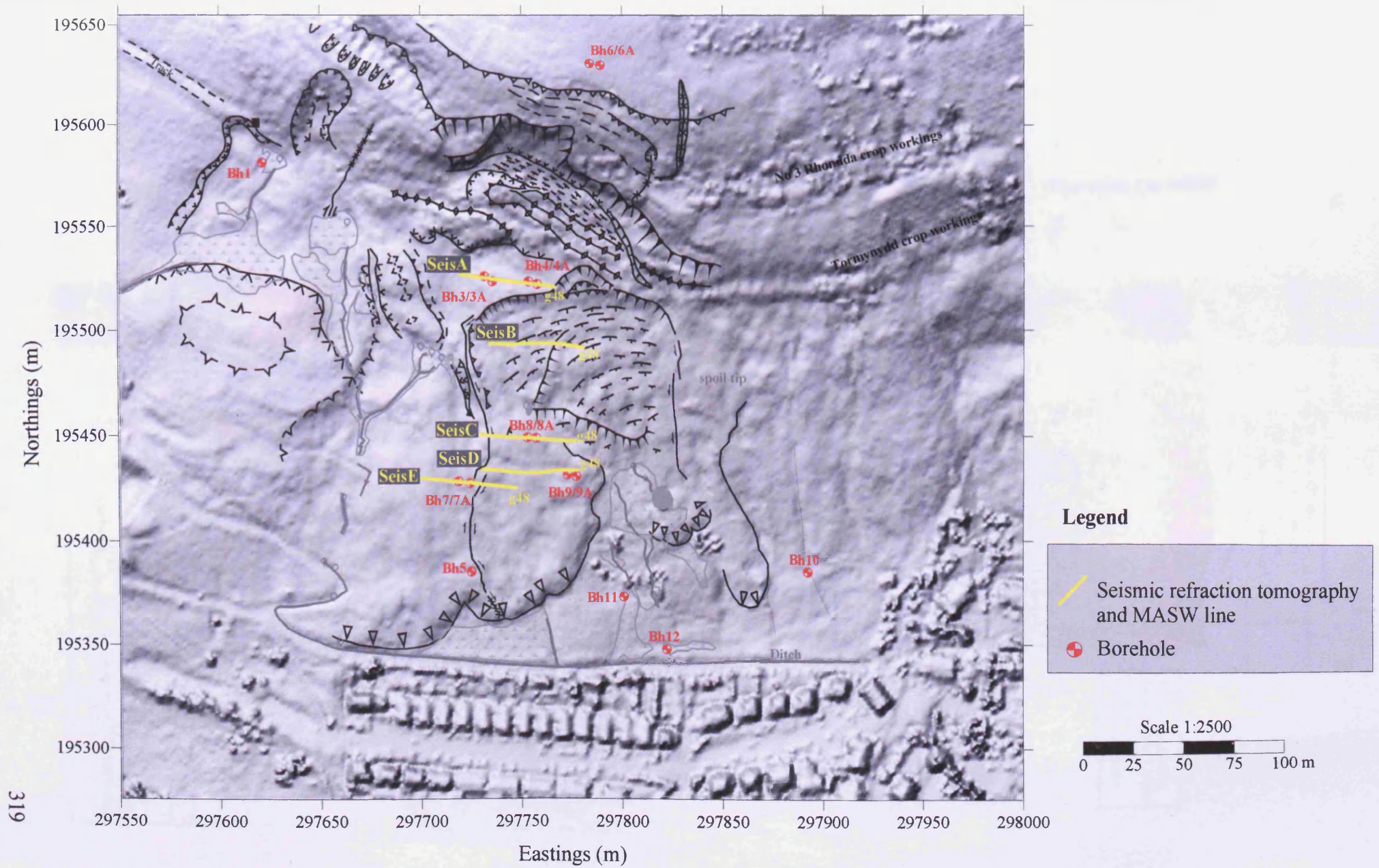


Figure 4.11 Location of seismic refraction tomography and MASW lines acquired at Mynydd yr Eglwys Landslide

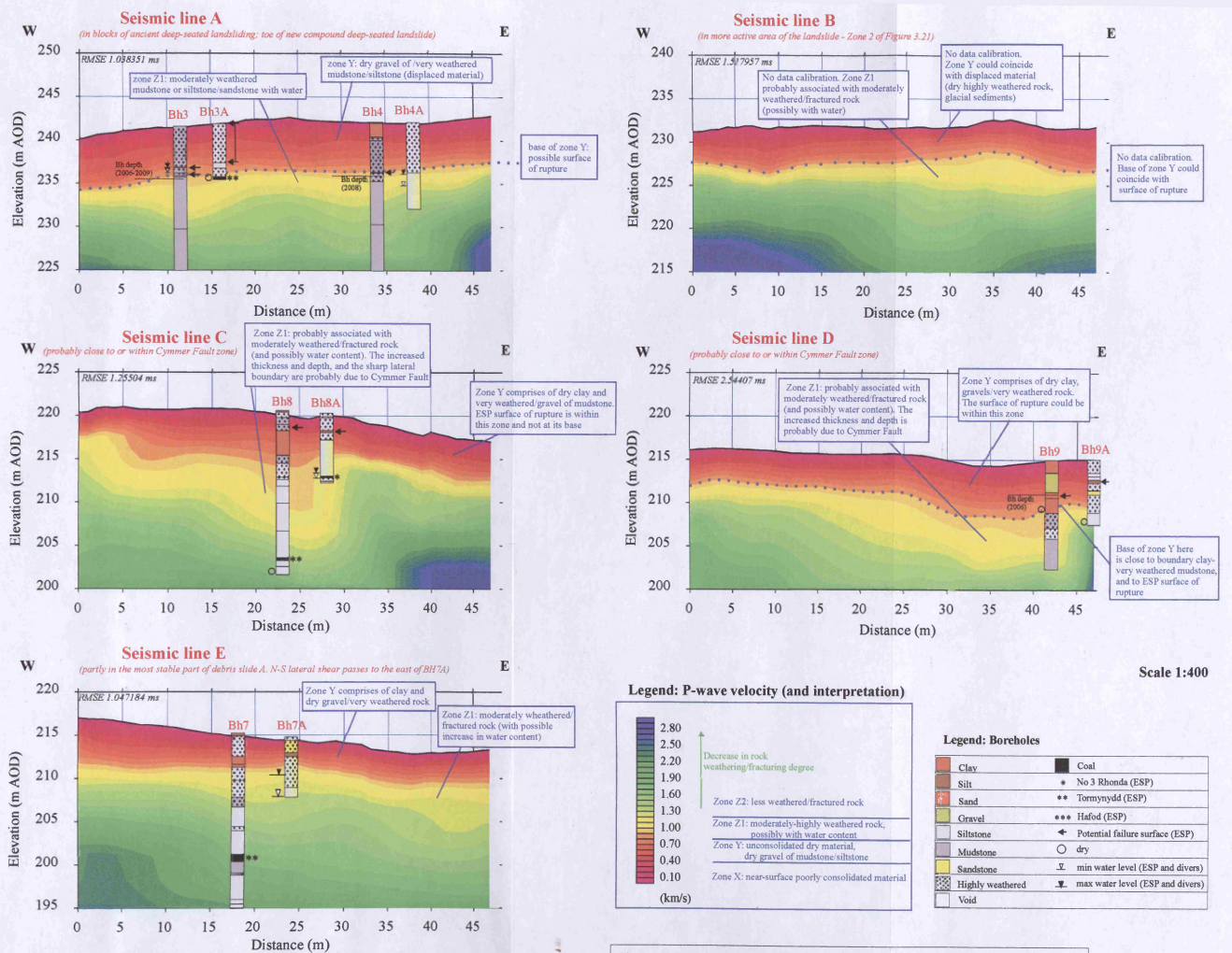


Figure 4.12 Seismic refraction tomography lines, Mynydd yr Eghwys Landslide

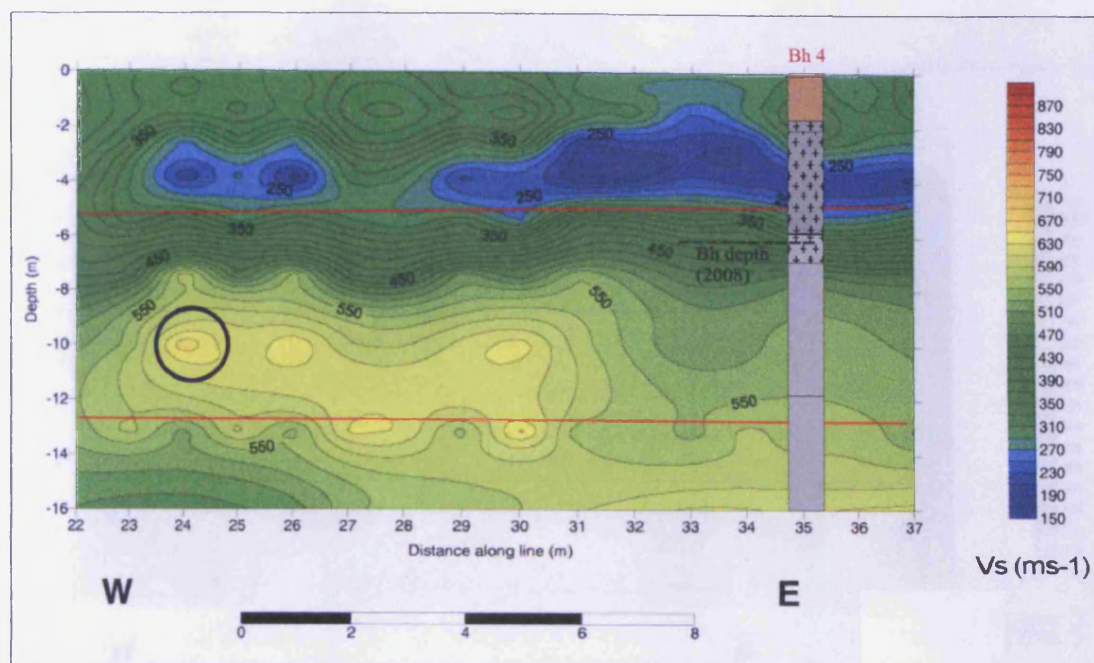


Figure 4.13 MASW line A processed by M. Bottomley (2008); H:V exaggeration 1:2. The figure has been here modified only by plotting Borehole 4 using the same legend of Figure 4.12. The blue circle indicates an anomaly possibly due to processing, whereas red lines indicate boundaries of velocity contrast identified by M. Bottomley in its processing of seismic refraction data

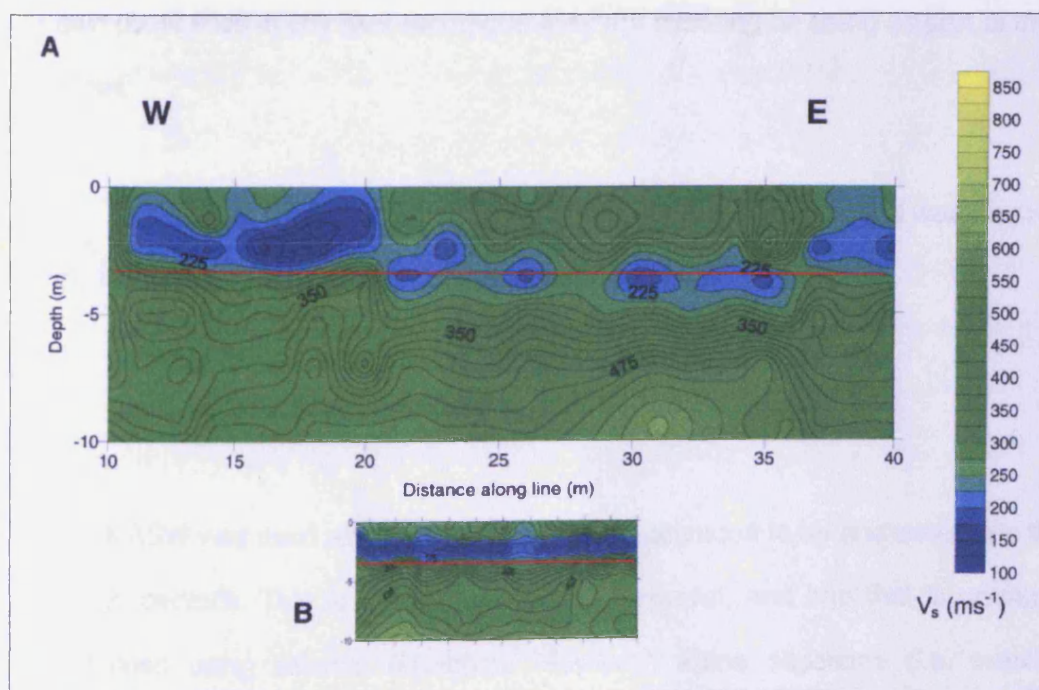


Figure 4.14 MASW line B processed by M. Bottomley (2008); H:V exaggeration 1:2. For Bottomley, red line indicates a seismic refraction boundary

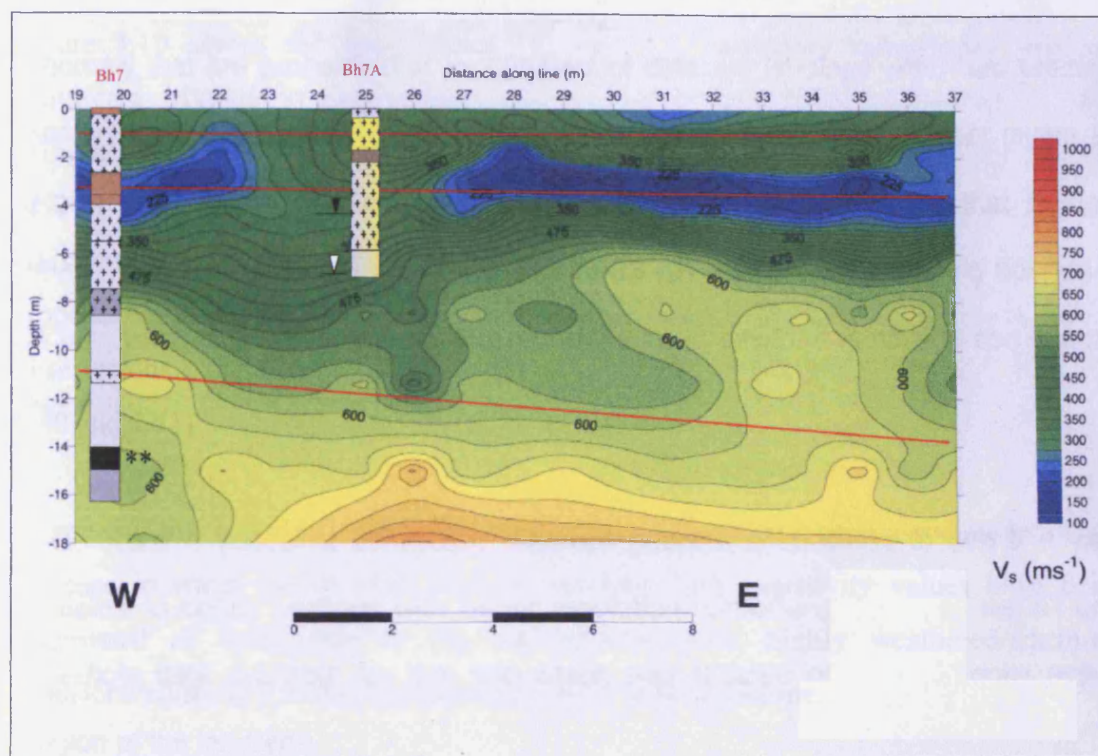


Figure 4.15 MASW line E processed by M. Bottomley (2008); H:V exaggeration 1:2. The figure has been here modified only by plotting Boreholes 7 and 7A using the same legend of Figure 4.12. Red lines indicate boundaries of velocity contrast identified by M. Bottomley in its processing of seismic refraction data

4.5 Results and interpretation of ERT profiles

Figure 4.16 shows the location of the electrical resistivity tomography profiles acquired at Mynydd yr Eglwys landslide between January 2006 and December 2008, using a Wenner-Schlumberger array configuration and a minimum electrode spacing of 2 or 5 m. The results of a few representative selected profiles are presented as resistivity contoured sections in Figures 4.17 and 4.18 (others can be found in Appendix E). Interpretation is based on borehole calibration, geomorphological observations and published tables of resistivity values for earth materials (Figures 2.40 and 2.41).

In general, low resistivity (or high conductivity) values have been associated with an increase in water and/or clay content, whereas high resistivity values have been interpreted as being due to dry and clay-deficient highly weathered/fractured mudstone/siltstone (i.e. the displaced material) or to sandstone.

ERT line 1L (Figure 4.17) was acquired along the axis of the slope, from the access track to the area above the main scarp. The area of the main scarp is generally characterised by high resistivity values (yellow/red/purple contours) which can be associated with the sandstones of the Llynfi Beds. A relatively low resistivity zone (green/cyan contours), which is found approximately at depth greater than 23 m, could be due to presence of water in the workings of Rhondda No 3 coal seam and in the Llynfi Rock. This water could enter the area of the new landslide and then percolate through the fractures/cracks in the graben area immediately downslope. High resistivity values are found also in correspondence of the displaced blocks and in the displaced material at the toe of the new compound deep-seated landslide (or possible blocks of ancient landsliding). As indicated by boreholes 4/4A, the surface of rupture could correspond to the yellow contour (279-340 Ohm.m), or, more probably, to the second green contour below that (194-232 Ohm.m). The distinction is not easy to make because the contours are very close to each others in all available borehole locations.

In the area of borehole 4A, below the high resistive layer (or displaced material), there is a zone of low resistivity, which is probably due to water content in the

sandstone/siltstone. This water is in the area of the secondary scarp and could enter the more active zone of the landslide (Zone 2 of geomorphological map, Figure 3.21).

The area of ancient debris slide is characterised by a near-surface high resistive layer of approximately 4 m thickness. This layer appears to correlate well with the dry and highly fractured mudstone/siltstone and therefore to the displaced material (see boreholes 8/8A). Again the surface of rupture could correspond to the yellow contour or to the two green contours just below this. However, looking at the toe of the debris slide, the surface of rupture is more likely to coincide with the base of the green contour of 194 Ohm.m. Therefore, the displaced material could have some areas of localised increase in thickness, reaching 8 m at the toe of the debris slide.

Below the near-surface resistive layer, there is a zone of low resistivity located in the area of boreholes 8 and 8A which extends upslope, below the NW-SE hummocky area (identified for example in Figure 3.22), and downslope in an inclined direction. This low resistivity zone is probably due to high water and/or clay content within the Cymmer Fault zone.

The 2 m spacing lines (ERT 1s and ERT X) along the same profile, confirm these observations, with major resolution at shallow depth and providing more information on possible localised small wet/clay areas below the displaced material.

However, it has to be underlined that the sections shown in this and the following Figure (4.18) were acquired during different days/seasons and therefore are probably influenced by differences due to changes in site conditions in response to rainfall (as discussed in next chapter).

Figure 4.18 shows three cross profiles. ERT 8L and 9L were deployed across the slope starting from the stable area above Church Quarry (that is beyond the landslide lateral limits) in order to explore also the differences in resistivity values between stable and unstable parts of the slope. The two profiles are characterised mainly by a nearly linear, wide, low resistivity zone which extends at depth and is inclined towards the more active area of the slope. In plan, this anomalous zone follows a NW-SE trend (see annotations 'a' and 'b' in Figure 4.16 and 4.18) and comes to surface at

the wet areas with reeds mapped near the plateau. It is therefore probably associated with the Cymmer Fault and it is due to high water and/or clay content within the fault zone. The area of the plateau is characterised by higher resistivity values, probably associated with sandstones of the Llynfi Beds with low water content.

ERT 8L crosses the toe of the new deep-seated landslide (or the blocks of ancient deep-seated landsliding described by Halcrow 1999, 2000). As observed in ERT 1L, this area is characterised by a near-surface high resistivity layer, which corresponds to dry highly weathered mudstone/siltstone (boreholes 3, 3A, 4, 4A). The surface of rupture identified by ESP appears to correspond to the base of this resistive layer (approximately yellow contour, as explained before). Below the interpreted displaced material, there are two low resistivity zones (one at Borehole 4 and one to the east boundary of the section), which are probably associated with increase in water content. More detail at shallow depth is provided by the 2 m spacing profile in Appendix D.

ERT 9L crosses the most active area of the debris slides, for which there is no local borehole calibration. The displaced material could correspond to the very thin (2-6 m) near-surface high resistivity layer (yellow to purple contours). However, it could also extend deeper into the first or second green contours below. In the 2 m spacing line (line 9s in Appendix D) the high resistivity layer, probably associated with the displaced material, is characterised by localised thickening of up to 10 m. Moreover, a moderately low resistivity zone (more evident in the 2 m spacing line), associated with higher water/clay content, is located at the eastern margin of the profile.

ERT 4L crosses the southern part of the slope and is generally characterised by lower resistivity values, which can be due to clay (glacial till), but mainly to water draining towards this area. The profile crosses the toe of debris slide A, which appears on the line as the near-surface resistive material at chainage 25-60 m. There is a very low “wedge”-shaped resistivity anomalous zone in the eastern part of the line, which in plan (see annotation ‘c’ in Figures 4.16 and 4.18 for reference) follows the NW-SE of the Cymmer Fault and the main wet areas identified during geomorphological mapping. This low resistivity is therefore probably due to high water and/or clay content within the fault zone.

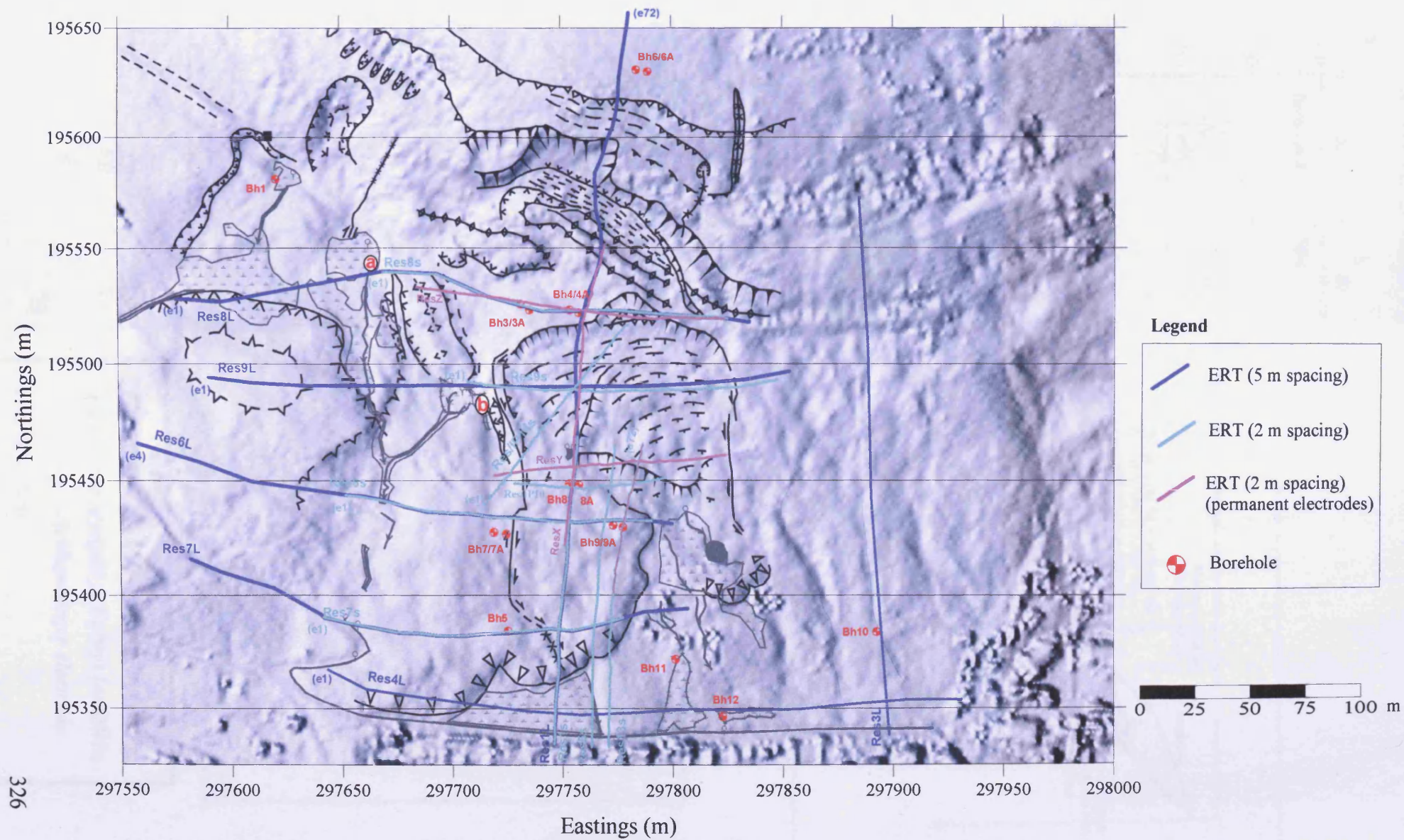
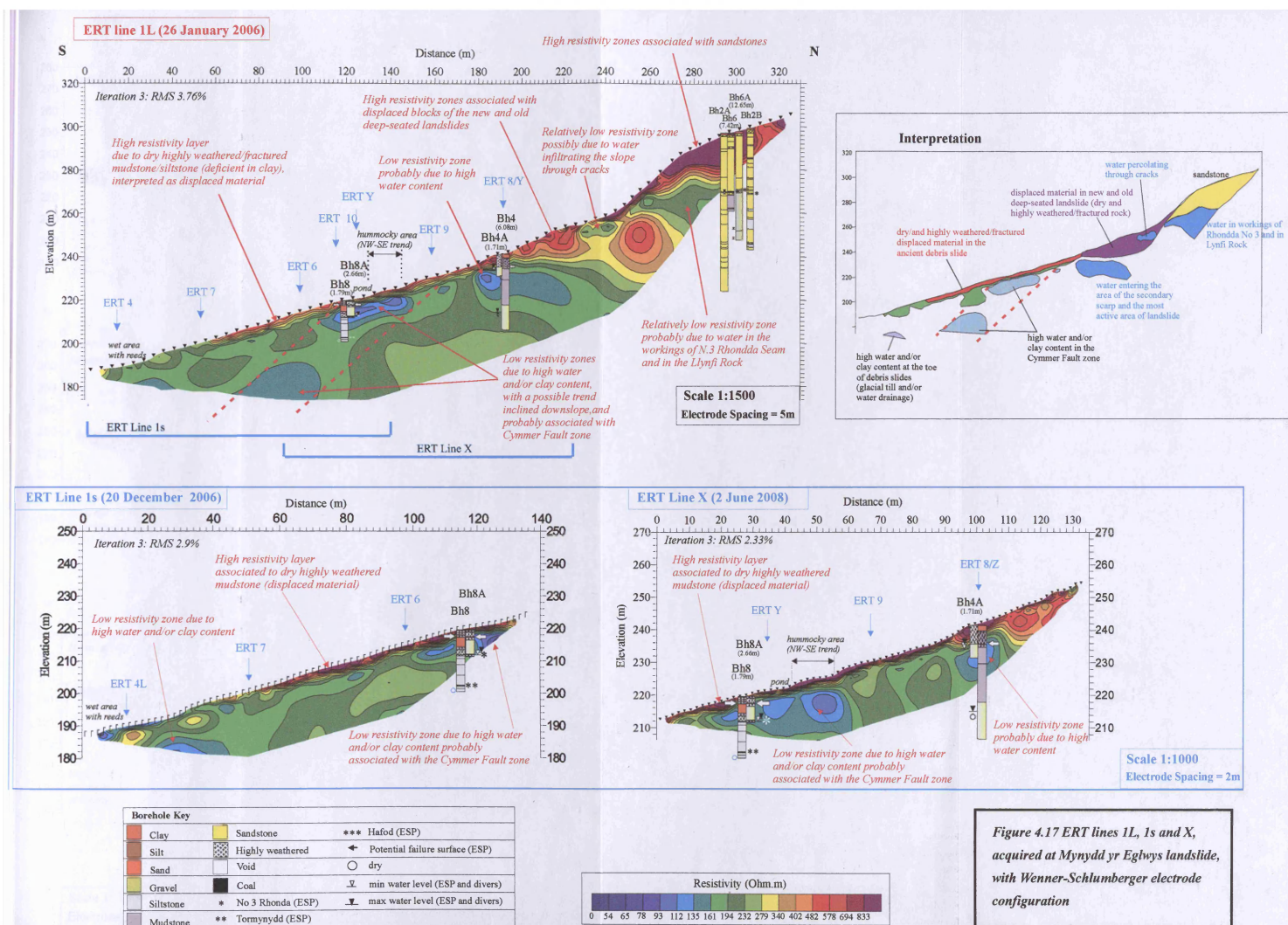
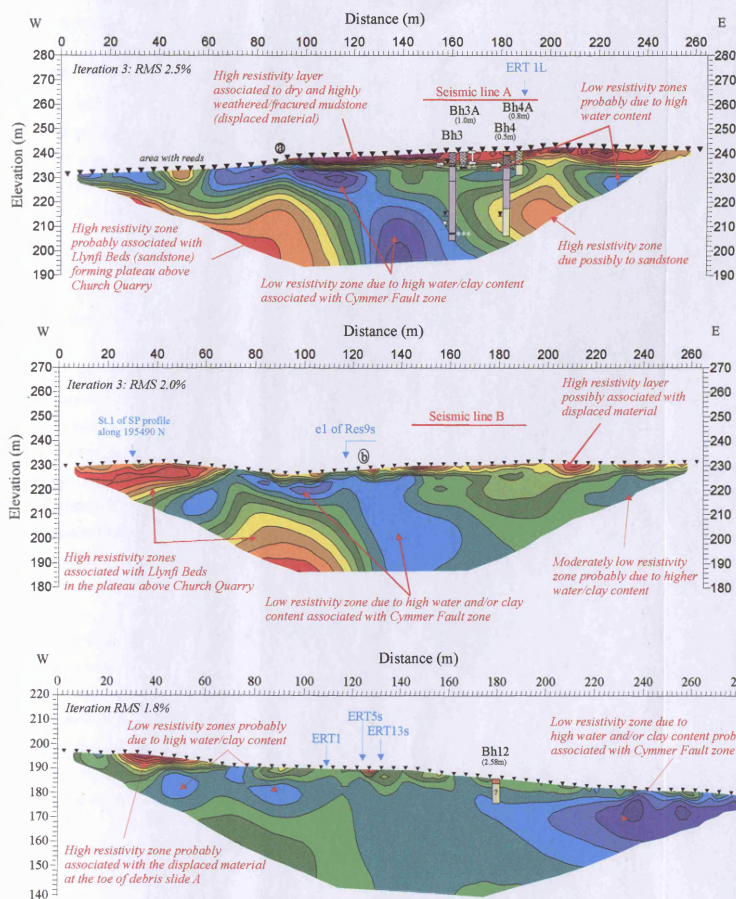


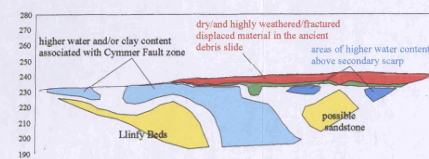
Figure 4.16 Location of ERT profiles acquired at Mynydd yr Eglwys Landslide





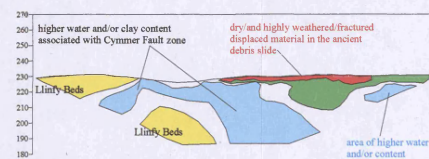
ERT Line 8L (18 December 2006)

(crossing area with blocks of ancient deep-seated landslide or toe of new deep-seated landslide)



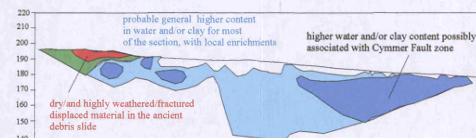
ERT Line 9L (20 March 2007)

(crossing the most active area of the landslide - Zone 2 of Figure 3.21)



ERT Line 4L (18 July 2006)

(crossing the toe area of the landslide)



Borehole Key			
Clay	Sandstone	*** Hafod (ESP)	
Silt	Highly weathered	◆ Potential failure surface (ESP)	
Sand	Void	○ dry	
Gravel	Coal	△ min water level (ESP and divers)	
Siltstone	No 3 Rhonda (ESP)	▽ max water level (ESP and divers)	
Mudstone	** Tormynydd (ESP)		

Figure 4.18 ERT lines 8L, 9L and 4L acquired at Mynydd yr Eglwys landslide with Wenner-Schlumberger electrode configuration

4.6 Results and interpretation of IP data

Figure 4.19 shows the location of the IP tomography profiles acquired at Mynydd yr Eglwys landslide in 2008, using Dipole-Dipole array configuration and a minimum electrode spacing of 2 m. The results of three selected profiles are presented as chargeability contours sections in Figure 4.20. Interpretation is based on borehole calibration and geomorphological observations.

The profiles were deployed mainly along and across the area of boreholes 8 and 8A and possibly within the Cymmer Fault to investigate the low resistivity (or high conductivity) anomalous zones observed in both ERT and GEM-2 datasets.

All the three IP profiles are characterised by a near-surface layer of higher chargeability (above 6 or 8 mV/V, the yellow/red/purple contours) of approximately 4 m thickness. The base of this layer seems to correspond with the surface of rupture indicated by ESP. However, the chargeability contours are very narrow in the areas with local borehole calibration. Therefore it is not possible to precisely associate the surface of rupture with the base of the yellow or the dark green contour. Some localised high chargeability zones are found just below the near-surface layer above described. These zones are probably areas of higher clay content, but could also still represent the displaced material, leading to a deeper surface of rupture.

In the deeper part of the sections there are wide anomalies of low chargeability (blue-cyan contours) which correspond to highly weathered/fractured mudstone/siltstone (in boreholes 8, 8A, 9). These low chargeability values can be associated with presence of water in the fractured bedrock within the Cymmer Fault zone. However, in the area upslope of borehole 9 (line 13top) and to the east of boreholes 8/8A, there is a zone of high chargeability, which could indicate localised areas of increase clay content within the fault zone.

IP line Y crosses the N-S lateral shear at around 14 m chainage. Although the shear is not so developed as in the southern and northern areas of the debris slide, it seems to correspond to the western limit of the low chargeability zone at depth (previously associated with water content within the Cymmer Fault).

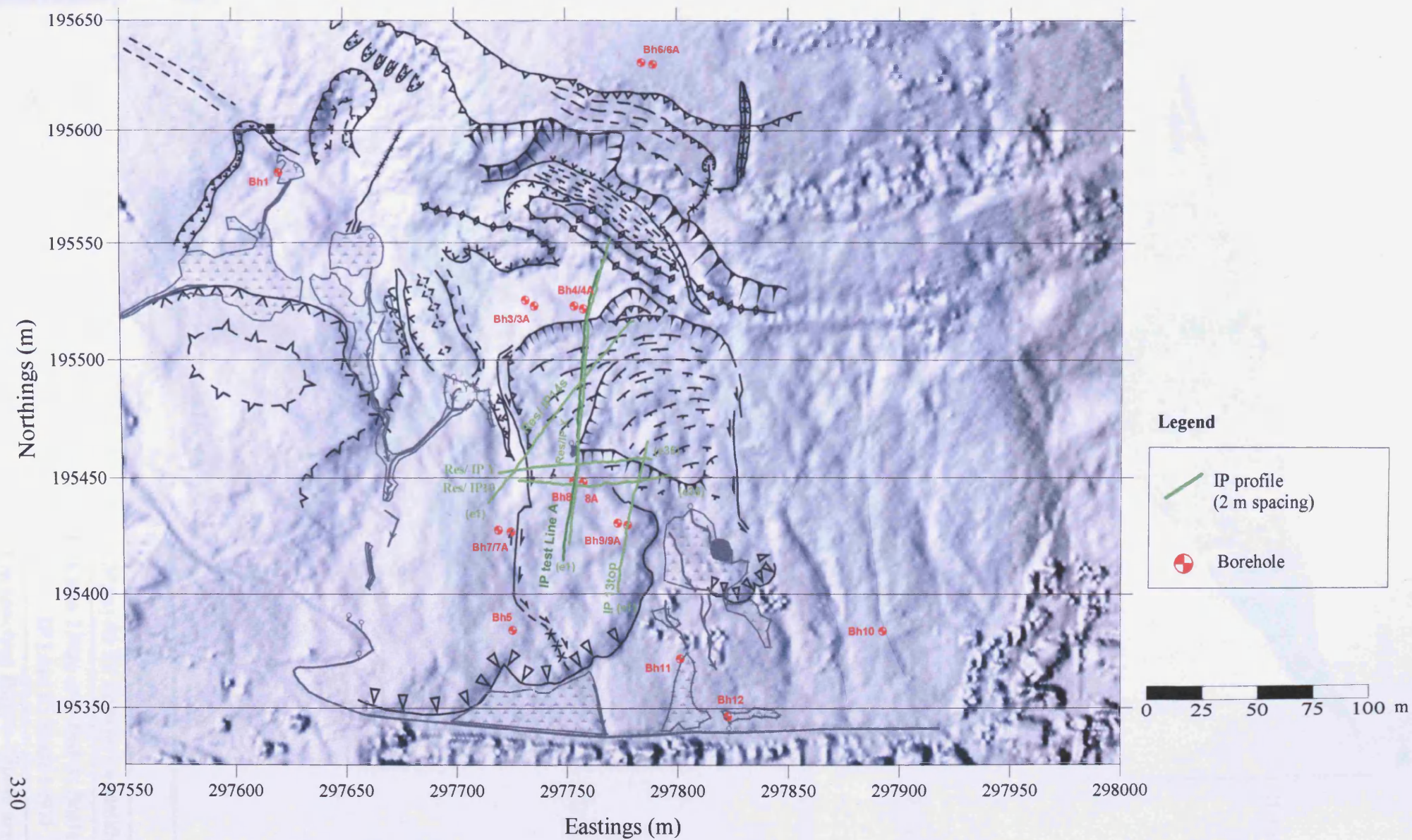
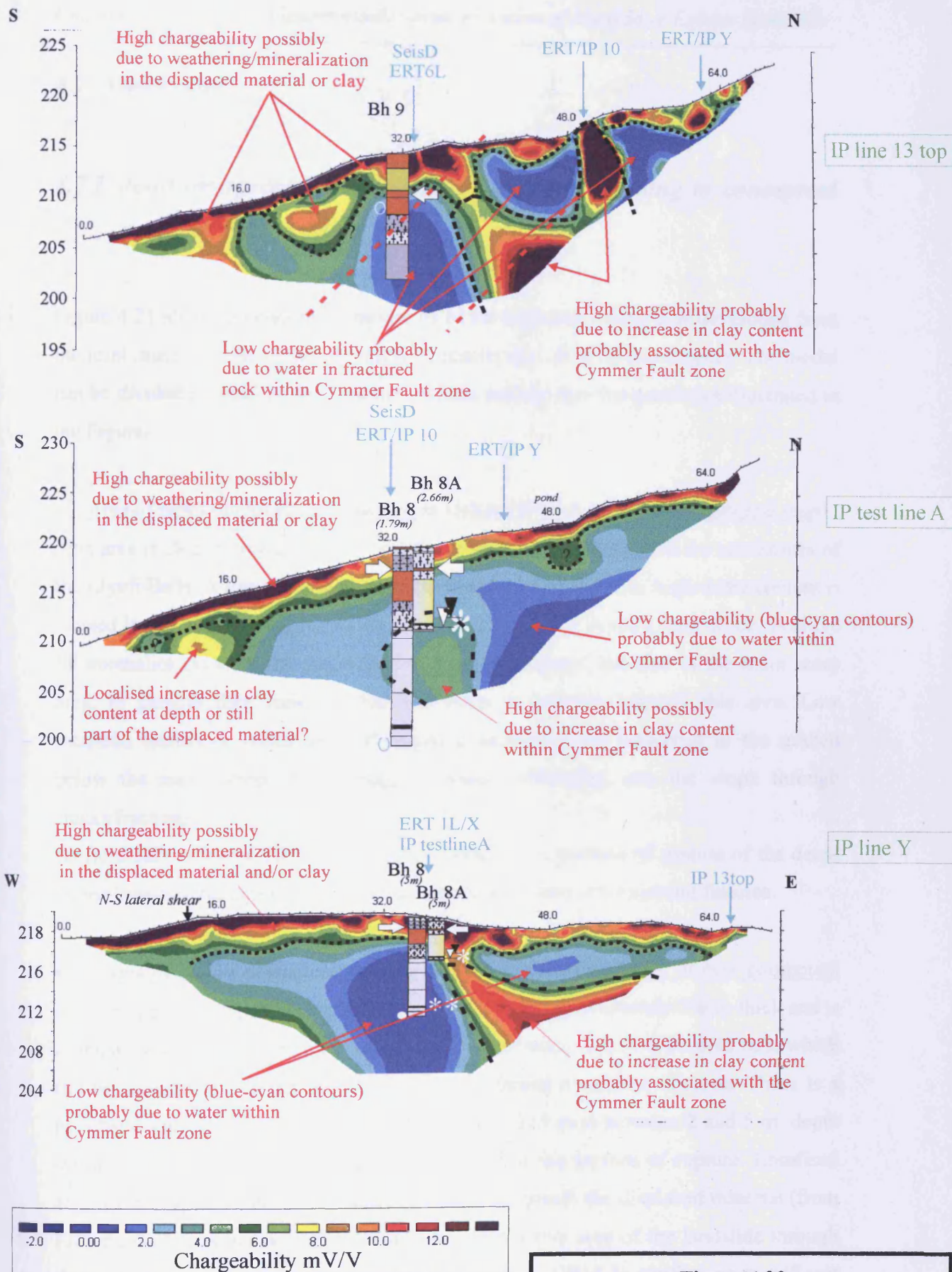


Figure 4.19 Location of IP tomography profiles acquired at Mynydd yr Eglwys Landslide



Borehole Key		
Clay	Sandstone	*** Hafod (ESP)
Silt	Highly weathered	◀ Potential failure surface (ESP)
Sand	Void	○ dry
Gravel	Coal	∇ min water level (ESP and divers)
Siltstone	* No 3 Rhonda (ESP)	⬇ max water level (ESP and divers)
Mudstone	** Tormynydd (ESP)	

Figure 4.20

Mynydd Yr Eglwys Landslide

IP Lines 13top and Test A; Scale 1:1000

IP Line Y; Scale 1:500

2 m spacing; Dipole-Dipole array

4.7 Discussion

4.7.1 Joint interpretation of geophysical results leading to conceptual model of the landslide

Figure 4.21 shows a conceptual model of MYE landslide which was developed from the joint interpretation of the geophysical results described in this chapter. The model can be divided in areas of the landslide which include the characteristics illustrated in the Figure:

- Area of new compound deep-seated landslide (Zone 1 of geomorphological map)

This area is characterised by high resistivity values associated with the sandstones of the Llynfi Beds. A low resistivity zone (detected by ERT) due to high water content is located in the workings of Rhondda No 3 coal seam and in the Llynfi Rock. Positive SP anomalies occur at the Rhondda No 3 water seepage, but also in the main scarp area. In general they indicate that the water is moving towards this area. Low localised resistivity zones and SP negative anomalies are observed in the graben below the main scarp, which suggest water infiltrating into the slope through cracks/fractures.

As from calibration of ERT line 1L at borehole 4, the surface of rupture of the deep-seated landslide flattens towards the toe area as expected in compound failures.

- Area of blocks of ancient deep-seated landsliding and/or toe of new compound deep-seated landslide. The displaced material is here approximately 5-6 m thick and is characterised by high resistivity values and V_P velocities below 0.80-0.90 m/s, which can be associated with dry, clay-deficient weathered mudstone/siltstone. There is a possible decrease in material stiffness (V_S of 200-275 m/s) between 2 and 5 m depth and an observed V_S value of 350 m/s measured at the surface of rupture. Localised areas of increased water content can be found underneath the displaced material (from ERT data). This water is likely to enter the most active area of the landslide through the secondary scarp. Electromagnetic mapping data (GEM-2) confirm no significant lateral variation in water/clay content within the displaced material.

- Most active area of the debris slides (Zone 2 of geomorphological map). Data interpretation suffered from lack of local borehole calibration. However, the displaced material has still been associated with high resistivity values (dry, clay deficient unconsolidated material) and low seismic velocities (high fracturing degree). In this area the displaced material appears to have lateral variations in thickness, which can vary from 2 to 10 m. This is confirmed by both ERT and GEM-2 datasets. Indeed the numerous relatively strong but irregular variations in electrical conductivity observed using the highest GEM-2 frequencies can be associated with these thickness variations which bring the lower resistive material underneath the surface of rupture closer to the surface. This area is also characterised by localised increase in water/clay content underneath the slip surface (ERT) and by a localised upward movement of water (observed from the SP dataset). The lower frequency GEM-2 dataset is characterised by high resistivity (low conductivity) values, suggesting therefore by method comparison, that the signal does not penetrate deeper than the displaced material.

- Cymmer Fault zone. The fault zone is well defined in all datasets. It appears as a wide N-W trending zone of low resistivity (high conductivity) values in both ERT and GEM-2 datasets. These values could be associated with high clay and/ or water content within the fault zone. This ambiguity has been solved using the IP profiles, which show that the fault area is high in water content at depth, but may also have some localised areas of clay enrichment. When these local clay enrichments are closer to the surface (approximately in the first 5 m of depth) they are depicted also by the GEM-2 (anomaly Y, at intersection with anomaly in IP 13 top). In this area in particular, Seismic lines (C and D) show that there is an increase in fracturing degree at depth of up to 15 m within the fault zone and which can have sharp lateral boundaries. The strong SP negative anomaly suggests that the fault acts mainly as a preferential pathway for water, which moves downwards into the slope and probably in a SE direction.

- Lateral boundaries of landslide

The geophysical signal in the area of the slope between the plateau above Church Quarry and the most active area of the landslide is dominated by the presence of the

Cymmer Fault zone. This strong anomalous area probably coincides with the north-western lateral limit of the landslide. It masks a possible SP difference in signal when crossing from the more to the less stable part of the slope, which was instead observed to the east, in the area of the spoil tip material. The lateral limit is instead very well defined in the ERT line crossing the ancient deep-seated blocks of landsliding (ERT 8L). On the contrary, there is no evidence of the N-S lateral shear which separates debris slides A and B (that is less active from more active parts of the slope) neither in GEM-2, SP or seismic refraction (line E) datasets. Only MASW profile E shows a lateral variation (a lack of the low V_s velocity zone) mostly in correspondence with the lateral shear. When looking at ERT profiles in this area, the more active part of the slope shows generally lower resistivity values at depth, possibly due to higher water content (line 6L in appendix). In the western part of the site (close to Church Quarry and on the plateau) there are stronger resistivity values (sandstones of the Llynfi Beds). The displaced material seems to show also high chargeability values, which were evident in the IP sections. However, no IP profiles were acquired across the lateral shear.

- Toe of ancient debris slides. An abrupt increase in electrical SP voltage and in conductivity (contour of 3 mS/m) in GEM-2 dataset coincides with the toe of the debris slides. The 2 m spacing ERT profiles (ex. Line 5s in appendix) show the high resistive displaced material reaching the toe area with a thickness of approximately 8 m.
- Area to the South of toe of debris slides. This area is characterised by low resistivity (or high conductivity) values in both ERT and GEM-2 datasets, probably due to the wetter ground conditions and to the clay content of the glacial till. The positive SP values suggest movement of water towards this area, although they could have been influenced by the high moisture/clay content of the soil. The Cymmer Fault crosses the SE toe area of the slope, with the associated high clay/water content (ERT 4L).

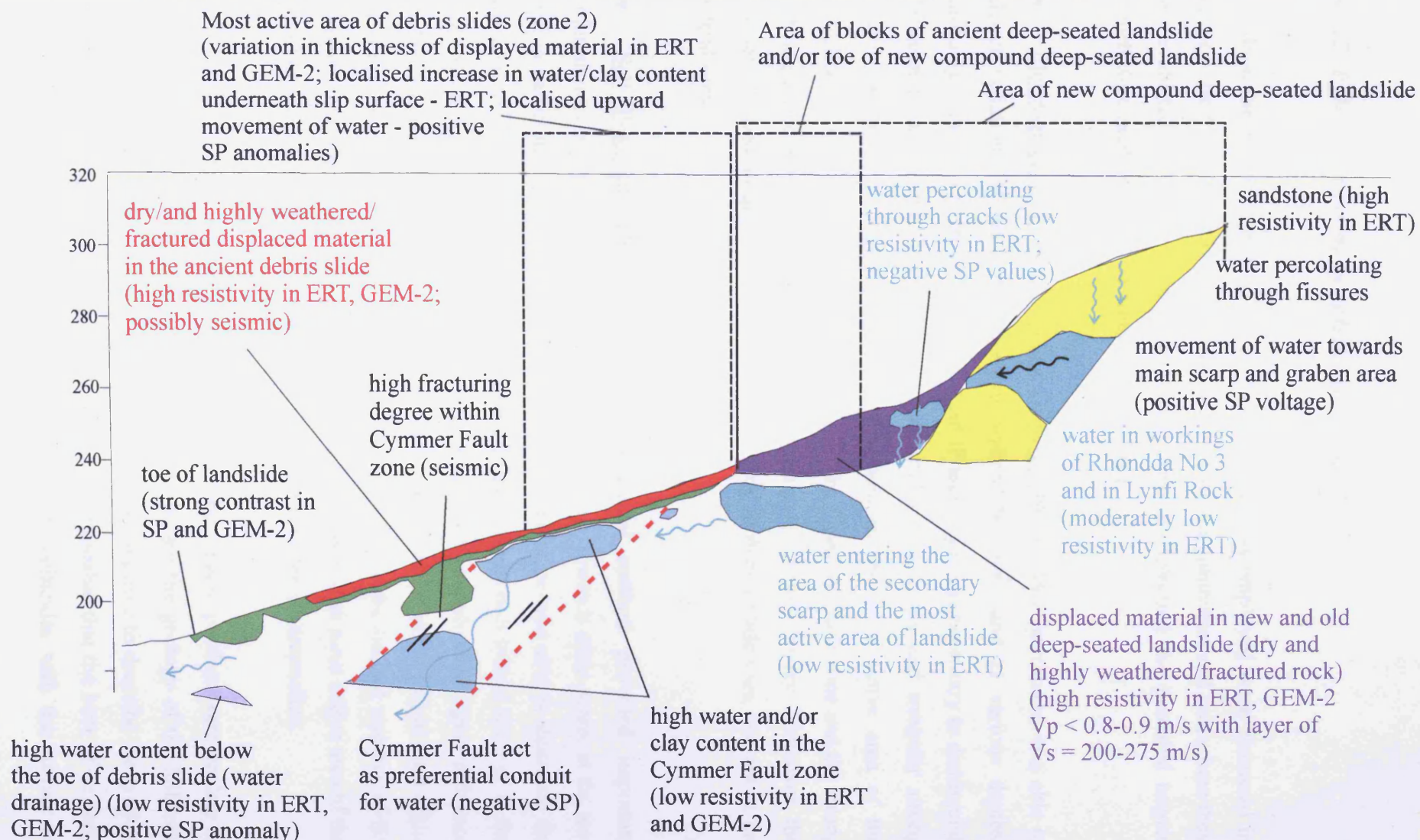


Figure 4.21 Conceptual model of Mynydd yr Eglwys landslide obtained from joint interpretation of all geophysical techniques employed on site

4.7.2 Effectiveness of geophysical methods

While at the end of chapter 2 the geophysical methods employed were discussed in terms of best field procedures, data quality, resolution, limitation and costs, here they are evaluated on the basis of their effectiveness in detecting the potential targets which were established in the aims of this project.

- Electromagnetics (with Geophex GEM-2). The GEM-2 instrument was able to detect variations of water/clay content within the slope and at various depths, probably within 5-6 m from the surface (but IP technique was necessary to distinguish between these possible two sources of anomaly). Numerous and irregular strong lateral variations in conductivity were observed in the most active area of the landslide. GEM-2 in particular depicted part of the Cymmer Fault zone and the strong lithological contrast in the area of the plateau above Church Quarry. Moreover, the datasets showed an abrupt change in conductivity at debris slide toes, but not at the lateral shears.
- Self Potential. The electrical Self Potential method provided important information on groundwater flow within the slope (i.e. towards main scarp, at the toe) and in particular within the Cymmer Fault. The technique was able to delineate the limits of the debris slides at the toe, but not in the western N-S lateral shear or in the north-western part of the site due probably to the strong geophysical signal influence of the Cymmer Fault. An SP negative anomaly was identified at the lateral limit of the most active area to the east, in the spoil tip, but due to the limited number of SP measurements this result cannot be considered conclusive. The most active area of the landslide was characterised by numerous and short wavelength anomalies.
- Seismic refraction tomography (P-waves). The seismic profiles were unclear as a result of the limited velocity contrast observed within the geology of the hillslope (i.e. the displaced and stable ground). The technique was able to describe the gradual decrease in rock fracturing degree with depth. It is probable that the base of velocity Zone Y (contour 0.80-0.90 km/s), at 4-5 m depth, coincides with the surface of

rupture at the toe of the new deep-seated landslide. However, borehole data in other profiles seem to suggest that the surface of rupture could be shallower, with the base of velocity Zone Y reflecting perhaps simply changes in the degree of fracturing. No evident difference within a seismic velocity section was observed when moving from more to less stable areas of the landslide. On the contrary, the seismic refraction method was useful in depicting the increase in the degree of fracturing up to depth of 15 m associated with the Cymmer Fault (possibly with water).

- MASW. The data provided by M. Bottomley were characterised by a zone of low V_s velocity (200-275 m/s) from 1 to 5 m of depth which corresponds to highly weathered material or clay. From borehole data calibration, it appears that the surface of rupture could be just below this low velocity zone (contour of 350 m/s). This anomalous low velocity zone is present also in the less active debris slide. However it is discontinuous and it is not present in the area of the N-S lateral shear (line E).

- ERT. This technique was probably the most efficient on site. It was able to map the displaced material, although with a certain degree of ambiguity as a result of determining the precise resistivity contour to define the surface of rupture. This leads to possible variations in the predicted thickness of displaced material. The ERT method was able to provide information on lithology (sandstones) and on areas of increase water/clay content. However, IP data were necessary to distinguish between clay/water as possible sources of low resistivity zones, while SP datasets could provide information on the direction of water flow. ERT datasets clearly show the wide area of the NW-SE trending Cymmer Fault, which extends deep into the bedrock. The lateral limits of displaced material interpreted from ERT data coincide with the ones from geomorphological mapping in the area of the blocks of ancient landsliding and the toe of the debris slides. However, the less active debris slide A is still characterised by a thin shallow high-resistive layer.

- IP. The IP datasets allowed distinguishing between clay and water rich areas within the Cymmer Fault zone, as both were characterised by low resistivity values in the ERT and GEM-2 datasets. IP profiles revealed also other areas of possible enrichment in clay content. Moreover, the displaced material seemed associated with

relatively high values of chargeability, possibly caused by weathering.

Chapter 5 Results of geophysical monitoring at Mynydd yr Eglwys Landslide

5.1 Introduction

Over the period of this research project, six ERT profiles and two SP grids were repeated in time. The aim was to investigate temporal changes in the groundwater table, in the moisture content and in the possible preferential groundwater paths within Mynydd yr Eglwys hillslope. This may then lead to a relationship being determined between resistivity changes, local rainfall, an increase in groundwater levels and an acceleration in the rate of ground surface displacements.

The six ERT profiles were repeated in time (2 to 6 times each) during the project. However, the complex hydrogeology of the site and the lack of obvious periods of definitely dry or very wet conditions (due to South Wales' variable weather conditions) show that infrequent measurements throughout the year are not sufficient to fully understand the response of the slope to rainfall. Therefore, only the results of the profiles ERT 1L and X are reported here and discussed in detail, as they were the lines repeated most frequently. Two SP profiles acquired twice along ERT line X are also shown in support of ERT monitoring data interpretation.

As previously described in chapters 2 and 3, the information on local rainfall, groundwater levels and EDM defined rates of ground displacement (Halcrow and RCTCBC) were all affected by errors and data gaps. Therefore there were limited data available for detailed correlation of the variations in observed resistivity values along profile 1L and other climatic factors. Profile X was acquired six times between June and August 2008, while GPS movement monitoring and borehole continuous monitoring of groundwater levels were also undertaken.

5.2 Results and interpretation of monitoring measurements along ERT 1L

Figure 5.1 shows the location of the ERT line 1L, which was acquired with a minimum electrode spacing of 5 m and with the Wenner-Schlumberger array configuration. The line was first acquired on the 26th of January 2006 and then again on the 17th of July, 13th of December, 20th February 2007 and lastly on the 3rd of May 2007.

Figure 5.2 displays the results of the profiles which are presented as separate coloured and contoured resistivity sections. Each section was finalised after 3 inversion iterations and the RMS values (representing the misfit between theoretical and original data), are less than 4.2%, except for profile of 17th of July 2006, which has an RMS value of 9.9%. The profile acquired in January 2006 was previously described in section 4.5 (Figure 4.17). Here it is reported again to facilitate visual comparison with the repeated sections; the January 2006 resistivity section will subsequently be called the reference section. As changes in resistivity between the repeated profiles can be masked by the chosen colour scale and therefore be difficult to identify, plots of calculated resistivity differences between each section and the reference section are also shown (Figure 5.3).

The profile of 26 January 2006 was acquired in a dry period: only one significant rainfall event (>30 mm of rainfall) was recorded in the previous 10 days. The resistivity profile acquired on the 20 February 2007 is virtually identical to the reference section, which is also apparent in the lack of variations shown on the plot of resistivity differences (Figure 5.3).

The profile showing the greatest changes from the reference section is that of July 2006. The profile was acquired in summer after a very dry period. It is evident that the low resistivity zone in the area of the secondary scarp extends throughout the section depth. This low resistivity block is clearly defined by an adjacent downslope high resistivity zone, which could be due to a sandstone horizon. The zone of the Cymmer Fault is characterised by a significant decrease in resistivity, which is interpreted as

being due to an increase in groundwater content. This increase in groundwater may be due to an isolated local heavy rainfall event which has not been picked up in the rainfall dataset. Such an event could result in groundwater rapidly percolating through the fractures within the Cymmer Fault from the NW area of the site towards the SE.

The resistivity profile of 13th of December 2006 was surveyed after a wet period. The low resistivity zone in the area of the secondary scarp now appears to extend deeper into the slope. In the centre of the profile at >15m depth, a high resistivity zone (yellow contour) is observed, which could also be associated with a sandstone horizon. Due to the wetter conditions, it is difficult to understand why this zone is apparently more resistive than in the reference profile, which was acquired during a period of less rainfall.

The resistivity section acquired on 3 May 2007 also shows a relatively high resistivity zone in the same location at a depth >30 m. The plot of resistivity difference with the reference profile shows higher resistivity values for the top half of the profile, associated with the relatively dryer conditions.

To summarise, the temporal monitoring performed with ERT line 1L has confirmed the applicability of the methodology in detecting changes in the groundwater content and defining preferential groundwater pathways within the hillslope. The main changes in resistivity values were observed in the areas of the secondary scarp, at depth in Zone 2 (the most active part of the landslide) and also within the Cymmer Fault zone. However, due to the lack of reliable local rainfall and groundwater data, it is difficult to interpret such resistivity changes in great detail. Moreover, the long interval of time between the repetitions of the resistivity measurements renders interpretation difficult in terms of understanding the phase of the groundwater response to rainfall on the slope. The profiles are ‘snapshots’ of a particular ‘hydrogeological stage’ which is not properly documented by other datasets or by continuous geophysical monitoring.

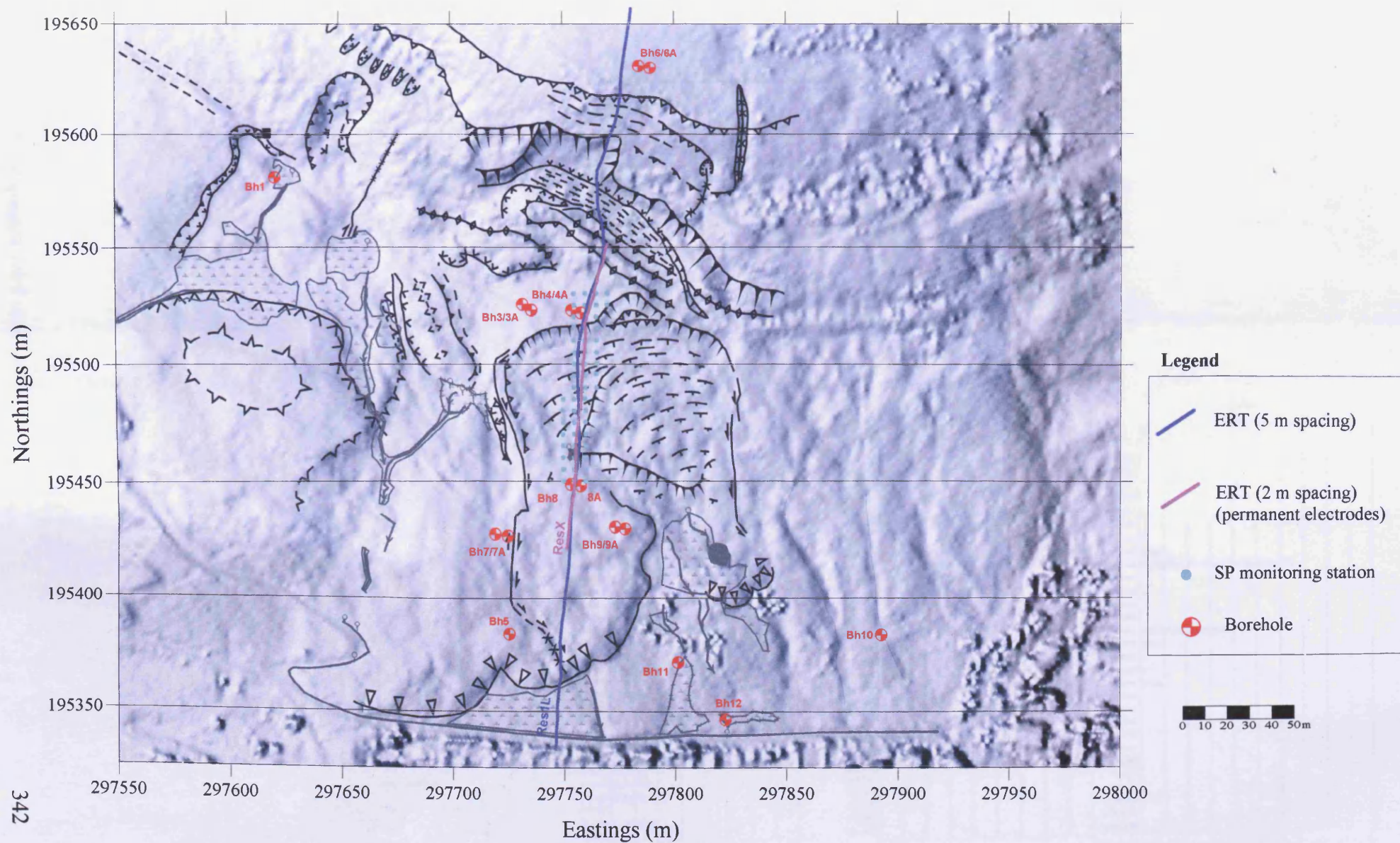


Figure 5.1 Location of ERT and SP monitoring profiles acquired at Mynydd yr Eglwys Landslide

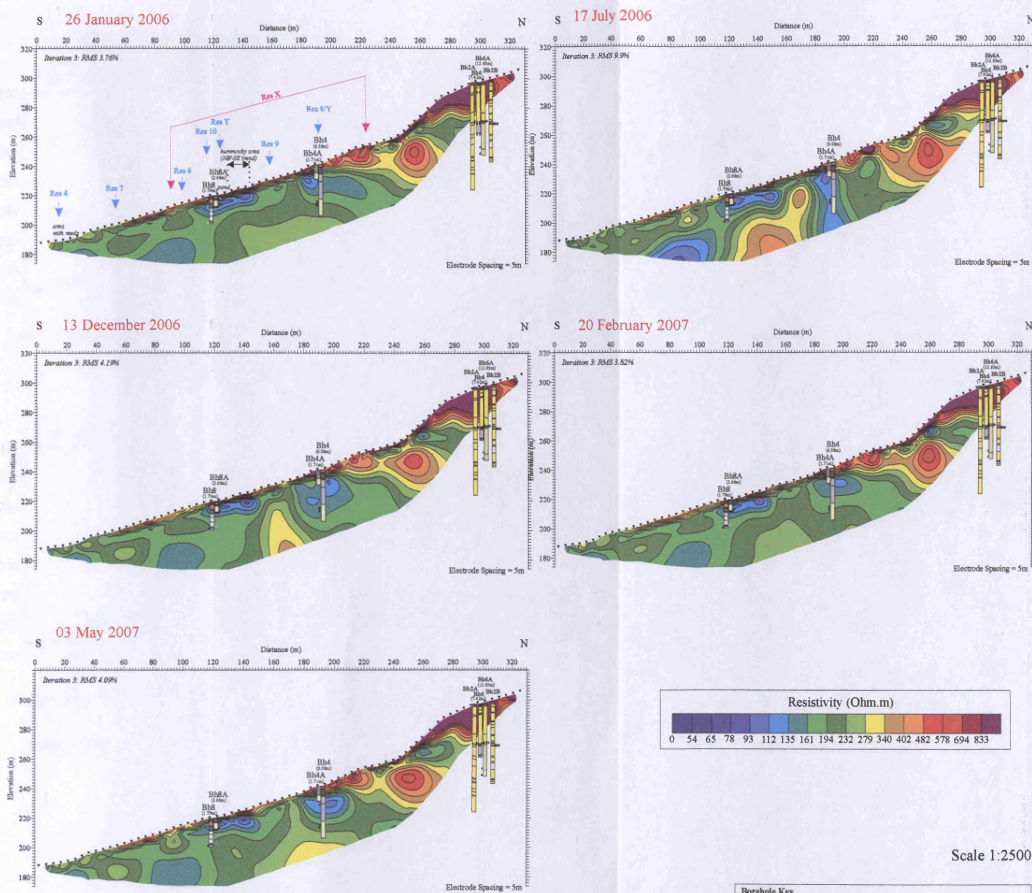


Figure 5.2 Repeated ERT line 1L shown as resistivity colour contour plots

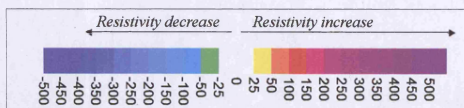
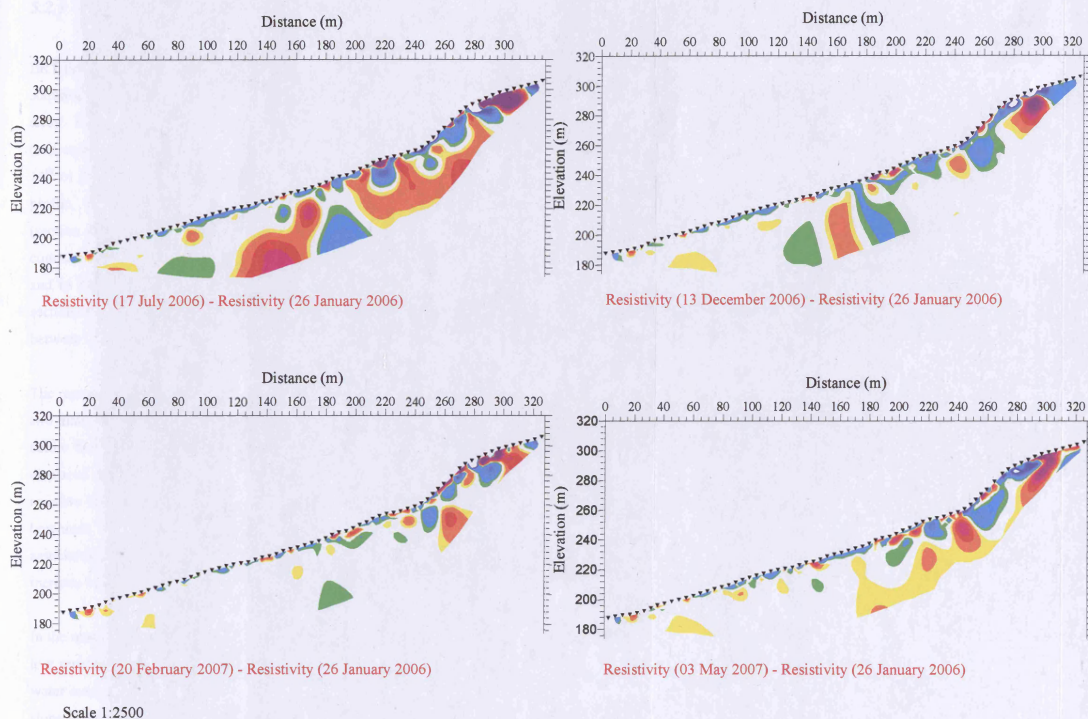
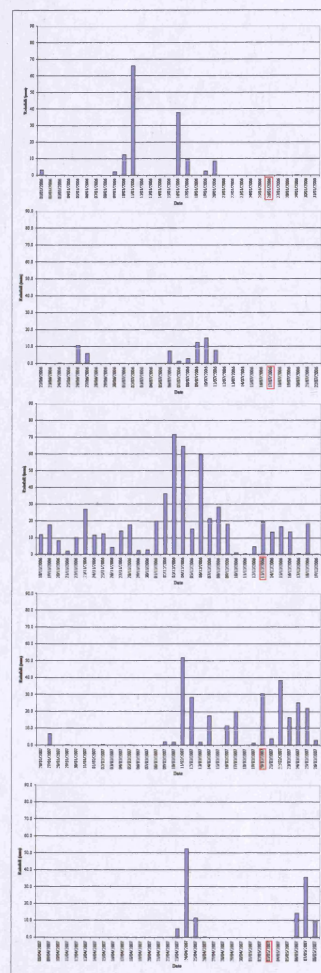


Figure 5.3 Monitoring results for line 1L (shown as plots of resistivity differences calculated from reference profile of 26 January 2006) and rainfall



5.2.1 Monitoring along ERT line X (also with SP profiles)

ERT line X is located in the most active area of the landslide (Figure 5.1). Data were acquired using permanent electrodes at 2 m spacing using the Wenner-Schlumberger array. Resistivity measurements were first carried out on the 2nd of June 2008 (subsequently called the reference profile) and then repeated again on the 13th of June, 14th of July, 17th of July, 22nd of August and 27th of August 2008. The reference profile, line X of 2nd of June 2008, has been previously interpreted in chapter 4 (section 4.5; Figure 4.17). It has been reported again in Figure 5.4 for ease of result comparisons. The results are shown in Figure 5.4 as resistivity colour contour sections and in Figure 5.5 as plots of resistivity differences. All the resistivity tomography sections were calculated with 3 inversion iterations and the final RMS values range between 2.4 and 3.5%.

The repeated sections appear to be very similar to each other and are characterised by two main low resistivity zones. One zone is located in the area of the minor scarp, just below the near-surface high resistive layer previously interpreted as the shallow displaced material. The other zone is located in the area underneath the same shallow resistive layer and extends downslope from the NW-SE hummocky terrain towards boreholes 8/8A. These two anomalies, already described in chapter 4, are probably associated to an increase in water content in the area of the minor scarp and to an increase in water and/or clay content within the Cymmer Fault zone.

In the most active area of the landslide (58-92m along the profile), there is a 2m thick low resistivity layer below the surface displaced material which displays a changing water content and which likely represents water entering the most active area of the slope from the minor scarp.

The greatest change in resistivity can be seen in the profile acquired on the 14th of July. The colour contoured resistivity section (Figure 5.4) is characterised by two adjacent 10m-wide vertical linear anomalies (60-80m along the profile) of contrasting high and low resistivity values. These features are located in the most active area of the landslide and extend from approximately 5 m of depth to the maximum depth of

the section. Rainfall information and data from the continuous monitoring of water levels at borehole 3 show that just 9 days prior to the survey there had been 3 days of heavy rainfall events which have caused groundwater level to rise. On the day of the survey, the groundwater level was dropping asymptotically after a peak value was reached 5 days earlier. The groundwater levels were continuing to drop three days later when the profile was repeated. Interestingly, the two contrasting linear anomalies noted in the profile of 14th of July are no longer present on the 17th of July. These observations suggest that a vertical 10-m wide zone of a preferential water pathway exists in the most active area of the landslide. This zone appears to be bounded downslope by a high resistivity anomaly (possibly a sandstone), which may function as a temporary barrier for groundwater flow. As this high resistive zone was no longer visible after 3 days after the previous survey, the water may have percolated through this area. Due to its relatively narrow linear vertical shape, the negative anomalous feature could be associated with water moving through deep vertical fractures, which are likely to be present due to the proximity of the Cymmer Fault zone, or to water forced to move vertically upwards by a less permeable barrier formed by the resistive material located downslope. This may be confirmed by the fact that SP profiles carried out in the area of ERT line X on the 14th of July suggest an upward movement of water through this zone.

However, it is important to remember that the data of the GPS monitoring campaigns showed a seasonal trend in the rate of surface displacements characterised by very slow velocities during April-July 2008. Therefore, although an increase in water levels and a localised decrease in resistivity values have been observed in response to isolated heavy rainfall events during summer 2008, these did not cause significant accelerations in measured surface displacements.

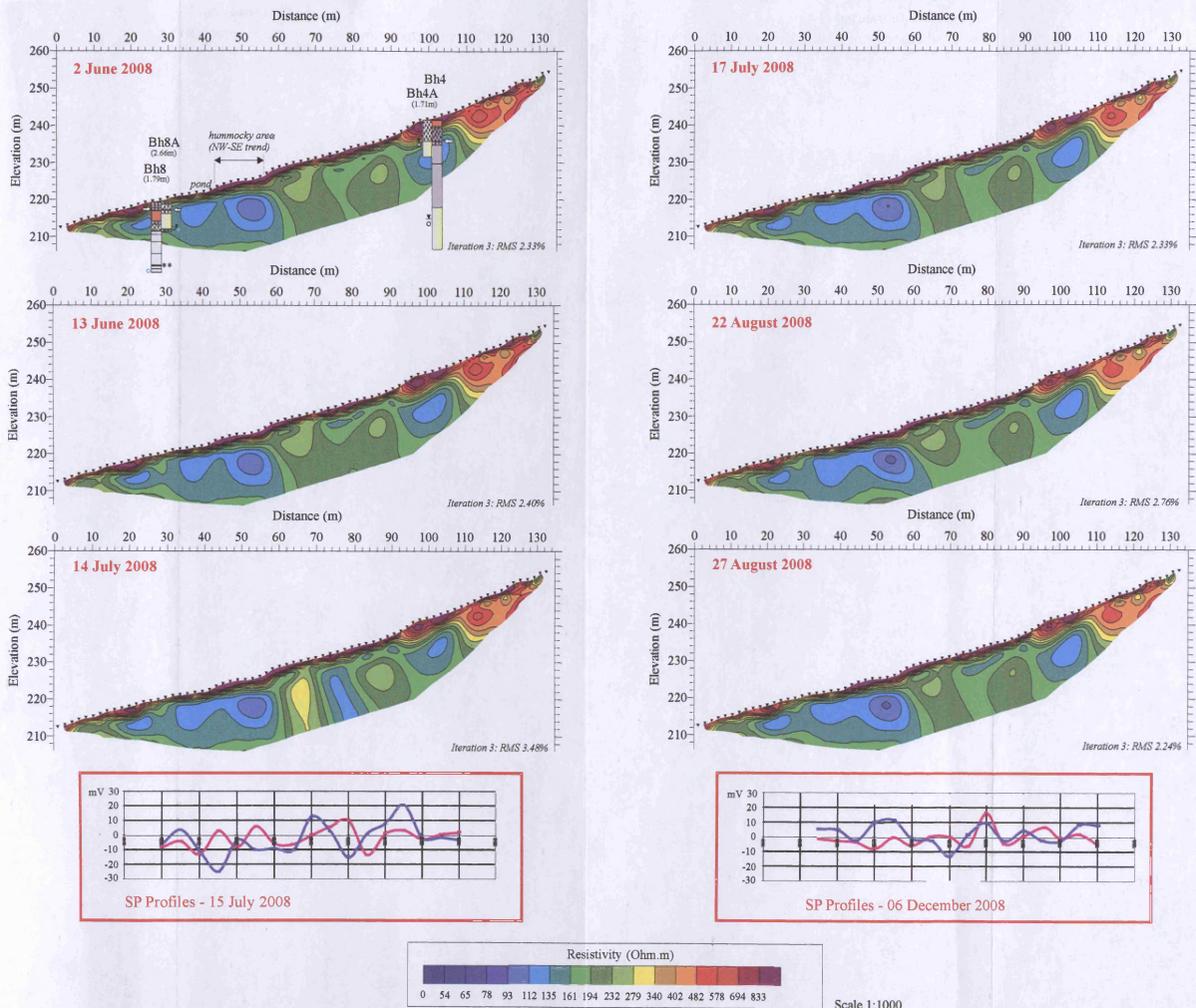


Figure 5.4 Results of ERT monitoring line X presented as resistivity contour colour plots and of two SP profiles acquired along the same line (in purple along 297755E and in blue along 297760E)

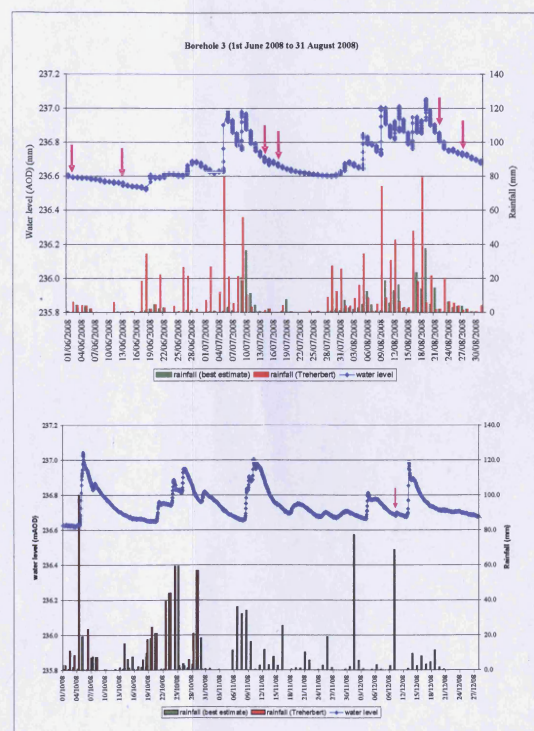
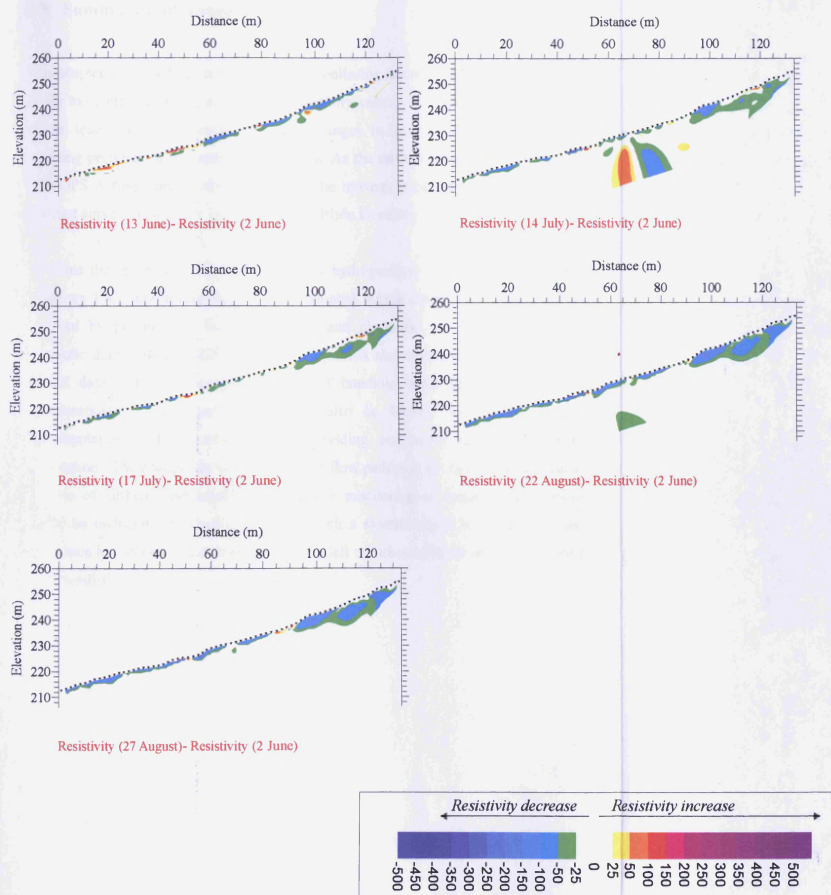


Figure 5.5 Monitoring results for Line X (shown as plots of resistivity differences calculated from reference profile of 2 June 2008), rainfall and water levels recorded by Diver in borehole 3

5.3 Summary and discussion

This chapter presented the results of ERT monitoring carried out along lines 1L and X. By monitoring changes in observed resistivity values, the data show the potential of the technique in detecting temporal changes in groundwater content and in detecting preferential groundwater pathways. As the rates of displacement measured with GPS during summer are very small, the movement of water above described does not appear to have any influence on landslide kinematics.

To refine the technique in areas of complex hydrogeology, it would require higher frequency ERT monitoring than the one adopted during the project. This could be achieved by permanently burying a cable and electrodes into the landslide and automatic data logging (BGS, [WWW 2.12]). It is also essential that reliable local rainfall data and continuous monitoring of borehole water levels are recorded simultaneously. GPS surveying should also be backed up with down-hole instrumentation such as inclinometers providing continuous ground movement information. The changes in water content or flow path may not cause acceleration in the rate of surface displacements. Therefore monitoring of surface displacement should be included. Practically, however, such a system would be expensive, plus experience has shown that automatic systems left on urban hillsides are prone to theft and vandalism.



Chapter 6 Conclusions and Future Research

6.1 Conclusions

The primary aim of this research project is to develop an integrated and cost-effective approach (based on surveying and geophysical techniques) for the characterisation and monitoring of slow moving active landslides and other potentially unstable slopes which can be found within the South Wales Coalfield, an area of complex geology, coal mining and hydrogeology.

This study focused on the complex slow-moving Mynydd yr Eglwys landslide, which can be considered representative of many landslides which are found in this region. The landslide was investigated and monitored with a wide range of techniques: digital photogrammetry (from an helium balloon), GPS surveying/monitoring, self-potential mapping, electromagnetic ground conductivity mapping (with Geophex GEM-2), seismic refraction tomography, multichannel analysis of surface waves, electrical resistivity tomography and induced polarization tomography. Such comprehensive integrated surveying-geophysical study has never been undertaken previously. To our knowledge, the broadband multi-frequency Geophex GEM-2 instrument, and the MASW and IP techniques have very rarely been used on landslides or potentially unstable slopes. Moreover, apart from Rouse et al. (1991), no previous research has been published on geophysical investigations of the hillslopes of South Wales.

All methods were assessed in terms of their effectiveness in determining specific targets established from desk study and literature review, such as: ground surface model, rates and spatial distribution of surface displacements, depth and shape of surface of rupture, thickness and lateral limits of displaced material, geology and hydrogeology of the slope. The precision, resolution, quality of data provided were also evaluated together, along with the commercial costs, the optimal field procedures and the technical/logistical limitations of each technique.

Data were interpreted first separately for each technique and then jointly, leading to a conceptual model of the landslide. Furthermore, a few ERT and SP profiles were repeated in time to investigate the temporal changes in water content and water paths within the slope and eventually establish a relationship between such changes and changes in rainfall, borehole water levels and rates in surface displacements.

Digital photogrammetry, acquired with a 10MPixel camera mounted on a helium balloon, allowed the rapid generation of a high-resolution good quality DEM. Data precision was 0.0060 m in X, 0.0063 m in Y and 0.0128 m in Z. The difference between GPS heights and the ones derived from the photogrammetry DEM had a mean value of 0.103 m and a standard deviation of 0.140 m. A rapid way to test accuracy and reliability of the photogrammetry-derived DEM in Surfer was here proposed. The 2D and 3D plots that can be produced and the 3D platform of the photogrammetry software would have been ideal for visualisation and interpretation of geophysical data against landforms.

The performance of the dual-frequency Topcon HiPer Pro GPS+, used in RTK mode, for landslide monitoring has not been previously reported in the literature. A data quality assessment on monitoring observations for MYE landslide was carried out and revealed that the surveying precision achieved on site at MYE was 12 mm in horizontal and 15 mm in elevation.

Geomorphological mapping and in particular the results of GPS monitoring helped identifying areas of heterogeneity (i.e. different levels of activity) within the slope. Moreover, GPS results showed a temporal variability in rate of displacements, which is probably associated with rainfall and water pressures. However, the low frequency of GPS campaigns allowed only the depiction of a general seasonal trend of the rate of displacements (acceleration occurs in wetter periods) and was not able to establish a precise relationship with rainfall and borehole water levels.

A combination of digital photogrammetry and GPS monitoring could be applied to slow-moving landslides to obtain high-precision short-term measurements at a few selected locations and long-term measurements at cm-precision over a wider area. However, other instrumentation (i.e. inclinometers or extensimeters) which provide

continuous movement data is necessary to define the dynamic response of the slope to rainfall in areas of such complex hydrogeology.

The broad-band multi-frequency GEM-2 instrument allowed the rapid acquisition of numerous profiles at high data density whilst walking over rough landslide terrain, which makes it very practical for reconnaissance surveys. This technique was able to detect variations in water/clay content within the slope and at various depths, within the first 5-6 m from the surface, but the IP method was necessary to distinguish between these two possible sources of anomaly. The technique was also able to delineate the landslide boundaries at the toe. Only a visual comparison between plots from different frequencies was here carried out. Inversion algorithms for GEM-2 data are still under research.

The Self Potential method provided very useful information on the direction of groundwater flow (i.e. towards the main scarp area, along the Cymmer Fault or at the toe). The SP technique was able to detect the lateral limits of the landslide with certainty only at the toe. The most active area of the landslide was characterised by strong, short-length numerous lateral voltage anomalies, suggesting localised upward water flows.

Seismic refraction tomography data suffered from the lack of strong velocity contrast between the displaced material and the weathered bedrock and the surface of rupture could not be defined in all the profiles. However, the refraction data were useful in detecting vertical and lateral variations in degree of fracturing and in particular within the Cymmer Fault. No difference among the seismic profiles was noticed between the data acquired on more stable or more active debris slides.

MASW data were negatively influenced by strong lateral ground heterogeneities and severe topography at the site. However, the profiles were characterised by a low V_s zone at depth between 1 and 5 m, which correspond to highly weathered mudstone/siltstone and/or clay. Borehole data calibration show that the surface of rupture is just below that zone. The low S-wave_velocity zone is present also in the less active ancient debris slides.

ERT was probably the most effective technique, as it was able to detect the lateral limits and the thickness of the displaced material, the depth and shape of the surface of rupture (in both deep-seated and debris slide areas), lithology (sandstones), zones of increase water and/or clay content. However, an IP survey was necessary to distinguish between clay/water sources of low resistivity anomalies and SP mapping to determine the direction of water flow. Repeated ERT surveys showed the potential of ERT monitoring in detecting temporal changes in groundwater content and in detecting preferential water paths. However, the frequency of such surveys would have to be very high in slow moving landslides with complex hydrogeology in order to determine the relationship between water changes within the slope, rainfall and acceleration in rates of displacement. Moreover, ERT monitoring needs to be calibrated by reliable rainfall data, continuous monitoring of water levels and inclinometer/extensiometer information on ground displacement.

The IP technique was able to solve the ambiguity between clay-rich or water-saturated silica units (both characterised by low resistivity values). Moreover, tests on electrode types and array configurations revealed that copper electrodes can be used instead of non-polarizable electrodes and that the Dipole-Dipole array configuration provides better results when compared with datasets obtained from other techniques.

6.2 Future research

- The results on rates and spatial distribution of surface displacements provided by the combination of digital photogrammetry (long-term) and GPS (short-term) monitoring, plus the 3D information on landslide geology and hydrogeology provided by geophysical investigation/monitoring could be used as input and calibration for the more sophisticated hydro-mechanical models of large slow-moving landslides based on 3D finite element mesh and described in François et al. (2007) and Ferrari and Laloui (2011). These models allow prediction of rates/distribution of displacements in response to different conditions, such as in rainfall events (climate change).

- Geophysical techniques were able to detect the increase in degree of fracturing,

water/clay content and the direction of water movement within the Cymmer Fault. Therefore they could be used to investigate the features of lateral spreading described by Donnelly et al. (2000) and Donnelly (2005), which are typical of the South Wales Coalfield and are located close to major deep-seated landslides.

- Halcrow identified several common factors in the most ‘recent’ first time deep-seated landslides which occurred in the South Wales Coalfield (in terms of geology, structure, topography) and were triggered following different raining conditions (Chapter 1). Moreover deep-seated landslides show some signs of instability before the main episode. Geophysical and surveying methodologies could be used to investigate potentially unstable slopes characterised by the above factors to study conditions before failure and/or, if possible, slopes during the formation of the surface of rupture.

-The results of the methods were combined at interpretation level, but further research could be carried out to combine geophysical results at processing level with fuzzy fusion techniques.

- GEM-2 data were not inverted and further research should be carried out in this field. The datasets provided by all the other techniques could be used then to evaluate the GEM-2 inversion results.

References:

Agnesi, V., Camarda, M., Conoscenti, C., Di Maggio, C., Di Liberto, I. S., Madonna, P., and Rotigliano, E., 2005. A multidisciplinary approach to the evaluation of the mechanism that triggered the Cerda landslide (Sicily, Italy). *Geomorphology* 65, pp. 101-116.

Ahokas, E., Kaartinen, H., and Hyyppä, J., 2003. A quality assessment of airborne laser scanner data. *Proceedings WG III/3 Workshop '3-D reconstruction from airborne laser scanner and InSAR data'*, Dresden, Germany 8-10 October 2003. In: *International Archives of the Photogrammetry, Remote Sensing and Spatial Information Sciences*, volume 34, part 3/W13, pp. 1-7.

Amitrano, D., Gaffet, S., Malet, J-P., and Maquaire, O., 2007. Understanding mudslides thorough micro-seismic monitoring: the Super-Sauze (South-East French Alps) case study. *Bulletin de la Societe Géologique de France* 178, pp. 149-158.

Anderson, M. G., and Richards, K. S., 1987. *Slope stability: geotechnical engineering and geomorphology*. Chichester: John Wiley and Sons, 648 pp.

Ashkenazi, V. and Yau, J., 1986. Significance of discrepancies in the processing of GPS data with different algorithms. *Journal of Geodesy* 60(3), pp. 229-239.

Babuska, V. and Cara, M., 1991. *Seismic anisotropy in the earth*. Dordrecht: Kluwer Academic Publishers, p. 217.

Baily, B., Collier, P., Farres, P., Inkpen, R., and Pearson, A., 2003. Comparative assessment of analytical and digital photogrammetric methods in the construction of DEMs of geomorphological forms. *Earth Surface Processes and Landforms* 28, pp. 307-320.

Baldi, P., Cenni, N., Fabris, M., and Zanutta, A., 2008. Kinematics of a landslide derived from archival photogrammetry and GPS data. *Geomorphology* 102, pp. 435-444.

Baldo, M., Bicocche, C., Chiocchino, U., Giordan, D., and Lollino, G., 2009. LIDAR monitoring of mass wasting processes: The Radicofani landslide, Province of Siena, Central Italy. *Geomorphology* 105, pp. 193-201.

Baltsavias, E. P., 1999a. Airborne laser scanning: basic relations and formulas. *ISPRS Journal of Photogrammetry & Remote Sensing* 54, pp. 199-214.

Baltsavias, E. P., 1999b. Airborne laser scanning: existing systems and firms and other resources. *ISPRS Journal of Photogrammetry & Remote Sensing* 54, pp. 164-198.

Baltsavias, E. P., 1999c. A comparison between photogrammetry and laser scanning. *ISPRS Journal of Photogrammetry & Remote Sensing* 54, pp. 83-94.

References

- Bentley, S. P., and Siddle, H. J., 1996. Landslide research in the South Wales coalfield. *Engineering Geology* 43(1), pp. 65-80.
- Bentley, S. P., Cooper, L. M., and Geddes, J. D., 1980. Slope instability in the upper coal measures: South Wales. In: Perkins, J.W. ed. *Cliff and slope stability*. South Wales. Cardiff: Department of Extra-Mural Studies, University College, Cardiff, pp. 111-134.
- Bichler, A., Bobrowsky, P., Best, M., Douma, M., Hunter, J., Calvert, T., and Burns, R., 2004. Three-dimensional mapping of a landslide using a multi-geophysical approach: the Quesnel Forks landslide. *Landslides* 1, pp. 29-40.
- Bogoslovsky, V. A. and Ogilvy, A. A., 1970. Application of geophysical methods for studying the technical status of earth dams. *Geophysical Prospecting* 18, pp. 759-773.
- Bogoslovsky, V. A. and Ogilvy, A. A., 1970b. Natural potential anomalies as a quantitative index of the rate of seepage from water reservoirs. *Geophysical Prospecting* 18(2), pp. 261-268.
- Bogoslovsky, V. A. and Ogilvy, A. A., 1972. The study of streaming potentials on fissured media models. *Geophysical Prospecting* 20, pp. 109-117.
- Bogoslovsky, V. A. and Ogilvy, A. A., 1977. Geophysical methods for the investigation of landslides. *Geophysics* 42(3), pp. 562-571.
- Bottomley, M., 2008. MASW on unstable ground: Case studies from around UK. Msc thesis, University of Leeds.
- Brabham, P. J., 1986. The application of seismic surveys to the evaluation of shallow coal deposits. PhD. Durham University.
- Brabham, P. J., 2004. The Rhondda Valleys: using GIS to visualise a variety of geological issues in an intensely mined area. In: Nichol, D. et al. eds. *Urban Geology in Wales*. Cardiff: National Museums & Galleries of Wales, pp. 222-233.
- Brabham, P. J., 2005. The Rhondda Valleys: using GIS to visualise the rise and fall of coal mining and its industrial legacy. In: Bassett, M.G. et al. eds. *Urban Geology in Wales*. Vol. 2. Cardiff: National Museum of Wales Geological Series No. 24, pp. 193-204.
- Brabham, P. J., Thomas, J., and McDonald, R. J., 2005. The terrestrial shallow seismic reflection technique applied to the characterization and assessment of shallow sedimentary environments. *Quarterly Journal of Engineering Geology and Hydrogeology* 38, pp. 23-38.
- Bromhead, E. N., 1992. *The Stability of slopes*. 2nd ed. London: Blackie Academic & Professional, 411 pp.

Brown, K., Duncan, A., O' Dwyer, C. Davison, B., Hogarth, P., Butler, D., and Sampson, E., eds. 2003. Integrated airborne data collection by the Environmental Agency. RSPSOc 2003: Scales and Dynamics in Observing the Environment. Nottingham, 10-12 September.

Brückl, E. and Brückl, J., 2006. Geophysical models of the Lesachriegel and Gradenbach deep-seated mass-movements (Schober range, Austria). *Engineering Geology* 83, pp. 254-272.

Brückl, E., Brunner, F. K., and Kraus, K., 2006. Kinematics of a deep-seated landslide derived from photogrammetric, GPS and geophysical data. *Engineering Geology* 88, pp. 149-159.

Brueckl, E. and Paroditis, M., 2001. Estimation of large-scale mechanical properties of a large landslide on the basis of seismic results. *International Journal of rock Mechanics and Mining Sciences* 38, pp. 877-883.

Bruno, F. and Marillier, F., 2000. Test of high-resolution seismic reflection and other geophysical techniques on the Boup landslide in the Swiss Alps. *Surveys in Geophysics* 21(4), pp. 333-348.

Brunsden, D., and Prior, D. B., 1984. *Slope instability*. Chirchester: John Wiley and Sons, 620 pp.

Butler, J. B., Lane, S. N., Chandler, J. H., 1998. Assessment of Dem quality for characterizing surface roughness using close range digital photogrammetry. *The Photogrammetric Record* 16, (92), pp. 271-291.

Cadman, J. D. and Goodman, R. E., 1967. Landslide noise. *Science* 158(3805), pp. 1182-1184.

Cardarelli, E., Marrone, C., and Orlando, L., 2003. Evaluation of tunnel stability using integrated geophysical methods. *Journal of Applied Geophysics* 52, pp. 93-102.

Caris, J. P. T. and Van Asch, T. W. J., 1991. Geophysical, geotechnical and hydrological investigations of a small landslide in the French Alps. *Engineering Geology* 31, pp. 249-276.

Carrara, E., Rapolla, A., and Roberti, N., 1992. *Le indagini geofisiche per lo studio del sottosuolo: metodi geolettici e sismici*. Napoli: Liguori Editore, 291 pp.

Cassinis, R., Tabacco, I., Bruzzi, G. F., Corno, C., Brandolini, A., and Cardarelli, E., 1984/85. The contribution of geophysical methods to the study of the great Ancona landslide (December 13, 1982). *Geoexploration* 23, pp. 363-386.

Casson, B., Delacourt, C., Baratoux, D., and Allemand, P., 2003. Seventeen years of the "La Clapière" landslide evolution analysed from ortho-rectified aerial photographs. *Engineering Geology* 68, pp. 123-139.

- Challis, K., 2006. Airborne laser altimetry in alluviated landscapes. *Archeological Prospection* 13, pp. 103-127.
- Chambers, J. E., Wilkinson, P. B., Kuras, O., Ford, J. R., Gunn, D. A., Meldrum, P. I., Pennington, C. V. L., Weller, A. L., Hobbs, P. R. N., Ogilvy, R. D., 2011. Three-dimensional geophysical anatomy of an active landslide in Lias Group mudrocks, Cleveland Basin, UK. *Geomorphology*, 125, pp. 472-484.
- Chandler, J. H., 1999. Effective application of automated digital photogrammetry for geomorphological research. *Earth Surface Processes and Landforms* 24, pp. 61-63.
- Chandler, J. H., 2001. Terrain measurement using automated digital photogrammetry. In: Griffith, J.S. ed. *Land surface evaluation for engineering practice*. London: The Geological Society, Engineering Geology Special Publications Vol. 18, pp. 13-18.
- Chen, R.-F., Chang, K.-J., Angelier, J., Chan, Y.-C., Deffontaines, B., Lee, C.-T., and Lin, M.-L., 2006. Topographical changes revealed by high-resolution airborne LiDAR data: The 1999 Tsaoiling landslide induced by the Chi-Chi earthquake. *Engineering Geology* 88, pp. 160-172.
- C. J. Associates 2003. Site investigation No. P0426. Factual report. Mynydd yr Eglwys. November 2003 (Draft Copy).
- Coe, J. A., Ellis, W. L., Godt, J. W., Savane, W. Z., Savane, J. E., Michael, J. A., Kibler, J. D., Powers, P. S., Lidke, D. J., and Debray, S., 2003. Seasonal movement of the Slumgullion landslide determined from Global Positioning System surveys and field instrumentation, July 1998-March 2002. *Engineering Geology* 68, pp. 67-101.
- Colangelo, G., Lapenna, V., Perrone, A., Piscitelli, S., and Tedesca, L., 2006. 2D Self-Potential tomographies for studying groundwater flows in the Varco d'Izzo landslide (Basilicata, southern Italy). *Engineering Geology* 88, pp. 274-286.
- Conway, B. W., Forster, A., Northmore, K. J., and Barclay, W. J., 1980. South Wales Coalfield landslip survey. London: Institute of Geological Sciences. Special Surveys Division. Engineering Geology Unit, Report No EG 80/4. Volume 1 (text), 218 pp.; Volume 2 (catalogue), 131 pp.
- Cooper, R. G., 2007. Mass movements in Great Britain. Peterborough: Geological Conservation Review Series, No. 33, Joint Nature Conservation Committee, 348 pp.
- Cornforth, D. H., 2005. *Landslides in practice: Investigation, analysis and remedial/preventative options in soils*. New Jersey: John Wiley & Sons, Inc., 596 pp.
- Corsini, A., Borgatti, L., Cervi, F., Dahne, A., Ronchetti, F., and Sterzai, P., 2009. Estimating mass-wasting processes in active earth slides – earth flows with time-series of High-Resolution DEMs from photogrammetry and airborne LiDAR. *Nat. Hazards Earth Syst. Sci.*, 9, pp. 433–439.
- Corry, C. E., 1985. Spontaneous polarization associated with porphyry sulfide mineralization. *Geophysics* 50(6), pp. 1020-1034.

- Corwin, R. F., 1990. The self-potential method for environmental and engineering applications. In: Ward, S.H. ed. *Geotechnical and environmental geophysics*. Vol. 1. Tulsa: Society of Exploration Geophysicists, pp. 127-145.
- Corwin, R. F. and Hoover, D. B., 1979. The self-potential method in geothermal exploration. *Geophysics* 44(2), pp. 226-245.
- Crozier, M. J., 1986. *Landslides: causes, consequences and environment*. London: Croom Helm, 252 pp.
- Cruden, D. M., 1991. A simple definition of a landslide. *Bulletin International Association for Engineering Geology* 43, pp.27-29.
- Cruden, D. M. and Varnes, D. J., 1996. Landslide types and processes. In: Turner, A.K. and Schuster, R.L. eds. *Landslides: Investigation and mitigation*. Special Report 247 - Transportation Research Board, National Research Council. Washington DC: National Academy press, pp. 36-75.
- Daughton, G., Noake, J. S. and Siddle H. J., 1997. Some hydrogeological aspects of hillsides in South Wales. *Proc. Conference on Rock Engineering*, Newcastle-Upon-Tyne, pp. 423-439.
- Demoulin, A., 2006. Monitoring and mapping landslide displacements: a combined DGPS-stereophotogrammetric approach for detailed short- and long-term rate estimates. *Terra Nova* 18(4), pp. 290-298.
- Denness, B., Conway, B. W., McCann, D. M. and Grainger, P., 1975. Investigation of a coastal landslip at Charmouth, Dorset. *The Quarterly Journal of Engineering Geology* 8, pp. 119-140.
- Department of the environment, 1996. *Planning policy evidence Note 14: Development on unstable land, Annex 1: Landslides and planning*, HMSO, London.
- De Vita, P., Agrello, D., and Ambrosino, F., 2006. Landslide susceptibility assessment in ash-fall pyroclastic deposits surrounding Mount Somma-Vesuvius: Application of geophysical surveys for soil thickness mapping. *Journal of Applied Geophysics* 59, pp. 126-139.
- Dewitte, O., Jasselette, J. - C., Cornet, Y., Van Den Eeckhaut, M., Collignon, A., Poesen, J., and Demoulin, A., 2008. Tracking landslide displacements by multi-temporal DTMs: A combined aerial stereophotogrammetric and LIDAR approach in western Belgium. *Engineering Geology* 99, pp. 11-22.
- Dijkstra, T. A. and Dixon, N., 2010. Climate change and slope stability in the UK: challenges and approaches. *Quarterly Journal of Engineering Geology and Hydrogeology* 43, pp. 371-385.
- Dikau, R., Brunsden, D., Schrott, L., and Ibsen, M.-L., 1996. *Landslide recognition: Identification, movement and causes*. Chichester: John Wiley & Sons, 251 pp.

- Donnelly, L., 2005. Fault reactivation in South Wales and the effects on ground stability. In: Bassett, M.G. et al. eds. *Urban Geology in Wales: 2*. Cardiff: National Museum of Wales Geological Series no 24, pp. 99-117.
- Donnelly, L. J., Northmore, K. J., and Siddle, H. J., 2000. Lateral spreading of moorland plateaux in south Wales. In: Siddle, H. J. et al. eds. *Landslides and Landslide Management in South Wales*. Cardiff: National Museums & Galleries of Wales, pp. 43-48.
- Duncan J. M., 1996. State of the art : Limit equilibrium and finite-element analysis of slopes. *Journal of geotechnical engineering* 122(7), pp. 577-596.
- Earth Science Partnership, 2004. Feasibility study for the assessment and remediation of Mynydd yr Eglwys Landslip. January 2004 (Draft for discussion). Report prepared for Environmental Services Department of Rhondda Cynon Taff County Borough Council.
- Ferrari, A. and Laloui, L., 2011. Coupled Hydrogeological and Geomechanical Modelling for the Analysis of Slowly Moving Landslides. ASCE Conference Proceedings Geo-Frontiers 2011: Advances in Geotechnical Engineering, doi:10.1061/41165(397)172
- Ferrucci, F., Amelio, M., Sorriso-Valvo, M., and Tansi, C., 2000. Seismic prospecting of a slope affected by deep-seated gravitational slope deformation: the lago Sackung, Calabria, Italy. *Engineering Geology* 57(1-2), pp. 53-64.
- Fitterman, D. V. and Labson, V. F., 2005. Electromagnetic induction methods for environmental problems. In: Butler, D.K. ed. *Near-surface geophysics*. Tulsa, Oklahoma: Society of exploration geophysicists, pp. 301-355.
- Forster, A., Northmore, K. J., and Hobbs, P. R. N., 2000. Landslide survey and research in the South Wales Coalfield by the British Geological Survey. In: Siddle, H. J. et al. eds. *Landslides and landslide management in South Wales*. Cardiff: National Museums & Galleries of Wales, pp. 15-21.
- Fraseri, A., Kapllani, L., and Dhima, F., 1998. Geophysical landslide investigation and prediction in the hydrotechnical works. *Journal of the Balkan Geophysical Society* 1(3), pp. 38-43.
- François, B., Tacher, L., Bonnard, Ch., Laloui, L., Triguero, V., 2007. Numerical modelling of the hydrogeological and geomechanical behaviour of a large slope movement: the Triesenberg landslide (Liechtenstein). *Canadian Geotechnical Journal*, 44(7), pp. 840-857.
- Fredlund, D. G., Morgenstern, N. R., Widger, R. A., 1987. The shear strength of unsaturated soils. *Canadian Geotechnical Journal*, 15(3), pp.313-321.
- Friedel, S., Thielen, A., and Springman, S. M., 2006. Investigation of a slope endangered by rainfall-induced landslides using 3D resistivity tomography and geotechnical testing. *Journal of Applied Geophysics* 60 (2), pp. 100-114.

- Geomorphological Services Ltd., 1987. Review of research into landsliding in Great Britain. Volume IV Wales. Report for Department of the Environment.
- Geophex Ltd, 2004. GEM-2 Manual.
- George, A., 2006. Development of geoelectrical techniques for investigation and monitoring of landfills. PhD thesis. Cardiff University.
- Geotomo Software, 2002. RES2DINV and RES3DINV manual. Malaysia.
- Gili, J. A., Corominas, J., and Rius, J., 2000. Using Global Positioning System techniques in landslide monitoring. *Engineering Geology* 55, pp. 167-192.
- Giraud, A., Desvarreux, P., Antoine, P., and Villain, J., 1995. Landslides in the coal-bearing series of the Arc Valley, France. *Engineering Geology* 39(1-2), pp. 95-102.
- Gochioco, L. M. and Ruev, F., 2006. Detecting and imaging hard-to-find abandoned wells and pipelines. *The Leading Edge* 25(3), pp. 358-361.
- Godio, A. and Bottino, G., 2001. Electrical and electromagnetic investigation for landslide characterisation. *Physics and Chemistry of the Earth* 26(9), pp. 705-710.
- Godio, A., Strobbia, C., and De Bacco, G., 2006. Geophysical characterisation of a rockslide in an alpine region. *Engineering Geology* 83, pp. 273-286.
- Gooch, M. J., Chandler J. H., and Stojic, M., 1999. Accuracy assessment of digital elevation models generated using the Erdas Imagine OrthoMAX digital photogrammetric system. *Photogrammetric Record* 16(93), pp. 519-531.
- Graham, J., 1984. Methods of stability analysis. In: Brunsden, D., and Prior, D.B. eds., *Slope Instability*. Chichester: John Wiley and Sons, pp. 171– 215.
- Griffiths, D. V., and Lane, P. A., 1999. Slope stability analysis by finite elements. *Géotechnique* 49(3), pp. 387-403.
- Hack, R., 2000. Geophysics for slope stability. *Surveys in Geophysics* 21(4), pp. 423-448.
- Hagerdoon, J. G., 1959. The plus-minus method of interpreting seismic refraction sections. *Geophysical Prospecting* 7, pp. 158-182.
- Halcrow UK, 1988. Rhondda landslip potential assessment. Report for the Welsh Office and Department of the Environment (3 Volumes).
- Halcrow UK, 1979. Pentre Landslip. Report on a landslip. November 1979. Report prepared for Rhondda Borough Council, Mid Glamorgan County Council and National Coal Board.
- Halcrow UK ,1989. Landslides and undermining research project final report. Report for the Department of the Environment and Welsh Office.

- Halcrow UK, 1993. Rhondda landslip potential assessment. Planning Guideline. Report for the Department of the Environment and Welsh Office.
- Halcrow UK, 1993b. Rhondda landslip potential assessment. Summary report for the Department of the Environment and Welsh Office.
- Halcrow UK, 1998. Landslides and Mining Research Project (3 volumes). Report for Welsh Office and Department of the Environment.
- Halcrow UK, 1999. Mynydd yr Eglwys Landslide. Preliminary interpretative report. June 1999. Report prepared for Rhondda Cynon Taff County Borough Council.
- Halcrow UK, 2000. Land at Mynydd yr Eglwys, Ystrad. Abatement notice. Expert report by H J Siddle, June 2000. Report prepared for Rhondda Cynon Taff County Borough Council.
- Heincke, B., Green, A. G., van der Kruk, J., and Hortstmeier, H., 2005. Acquisition and processing strategies for 3D georadar surveying a region characterized by rugged topography. *Geophysics* 70, pp. K53-K61.
- Heincke, B., Maurer, H., Green, A. G., Willenberg, H., Spillmann, T. and Burlini, L., 2006. Characterizing an unstable mountain slope using shallow 2D and 3D seismic tomography. *Geophysics* 71, pp. B241-B256.
- Hofmann-Wellenhof, B., Lichtenegger, H., and Collins, J., 2001. GPS. Theory and Practice. 5th ed. Wien: Springer, 382 pp.
- Huang, H., 2005. Depth of investigation for small broadband electromagnetic sensors. *Geophysics* 70(6), pp. G135-G142.
- Huang, H. and Won, I. J., 2000. Conductivity and susceptibility mapping using broadband electromagnetic sensors. *Journal of Environmental and Engineering Geophysics* 5(4), pp. 31-41.
- Huising, E. J. and Pereira, L. M., 1998. Errors and accuracy estimates of laser data acquired by various laser scanning systems for topographic applications. *ISPRS Journal of Photogrammetry & Remote Sensing* 53, pp. 245-261.
- Hungr, O., Evans, S. G., Bovis, M. J. and Hutchinson J. N., 2001. A review of the classification of landslides of the flow type. *Environmental & Engineering Geoscience* 7 (3), pp. 221-238.
- Hutchinson, J. N., 1988. General report: Morphological and geotechnical parameters of landslides in relation to geology and hydrogeology. In: Bonnard, C. ed., *Proceedings of the 5th International Symposium on Landslides, Lausanne* 1(3), pp. 3-35.
- Israil, M. and Pachauri, A. K., 2003. Geophysical characterization of a landslide site in the Himalayan foothill region. *Journal of Asian Earth Sciences* 22, pp. 253-263.

- Jomard, H., Lebourg, T., Binet, S., Tric, E. and Hernandez, M., 2007. Characterization of an internal slope movement structure by hydrogeophysical surveying. *Terra Nova* 19, pp. 48-57.
- Jones, D. B. and Siddle, H. J., 2000. Effect of mining on hillslope stability. In: Siddle, H. J. et al. eds., *Landslide and landslide management in South Wales*. Cardiff: National Museums & Galleries of Wales, pp. 40-43.
- Jones, D. K. C. and Lee, E. M., 1994. *Landsliding in Great Britain*. Department of the Environment, HSMO, London.
- Jongmans, D. and Garambois, S., 2007. Geophysical investigation of landslides: a review. *Bulletin de la Societe Geologique de France* 178(2), pp. 101-112.
- Kasser, M. and Polidori, L., 2002. From the aerial image to orthography: different levels of rectification. In: Kasser, M. and Egels, Y. eds., *Digital photogrammetry*. London: Taylor and Francis, pp. 282-287.
- Kearey, P., Brooks, M., and Hill, I., 2002. *An introduction to geophysical exploration*. 3rd ed. Oxford: Blackwell Publishing, 262 pp.
- Knight, R. J. and Endres, A. L., 2005. An introduction to rock physics principles for near-surface geophysics. In: Butler, D.K. ed., *Near-surface geophysics*. Tulsa: Society of Exploration Geophysicists, pp. 31-70.
- Konecny, G., 2003. *Geoinformation: remote sensing, photogrammetry and geographic information systems*. London: Taylor and Francis, p. 248.
- Lane, S. N., James, T. D., and Crowell, M. D., 2000. Application of digital photogrammetry to complex topography for geomorphological research. *Photogrammetric Record* 16(95), pp. 793-821.
- Lankston, R. W., 1990. High-resolution refraction seismic data acquisition and interpretation. In: Ward, S.H. ed., *Geotechnical and environmental geophysics*. Vol. 1. Tulsa: Society of Exploration Geophysicists, pp. 45-73.
- Lapenna, V., Lorenzo, P., Perrone, A., and Piscitelli, S., 2003. High-resolution geoelectrical tomographies in the study of Giarossa landslide (southern Italy). *Bulletin of Engineering Geology and the Environment* 62, pp. 259-268.
- Lapenna, V., Lorenzo, P., Perrone, A., Piscitelli, S., Rizzo, E. and Sdao, F., 2005. 2D electrical resistivity imaging of some complex landslides in the Lucanian Apennine chain, southern Italy. *Geophysics* 70, pp. B11-B18.
- Lebourg, T., Binet, S., Tric, E., Jomard, H. and El Bedoui, S., 2005. Geophysical survey to estimate the 3D sliding surface and the 4D evolution of the water pressure on part of a deep seated landslide. *Terra Nova* 17, pp. 399-406.

- Lee, E. M., Jones, D. K. C., and Brunsten, D., 2000. The landslide environment of Great Britain. In: Bromhead, E. et al. eds., *Proceedings of the 8th International Symposium on Landslides*, Cardiff, 26-30 June: Landslides in research, theory and practice. Vol. 2. London: Thomas Thelford, pp. 911-916.
- Lee, L. J. E., Lawrence, D. S. L., and Price, M., 2006. Analysis of water-level response to rainfall and implications for recharge pathways in the Chalk aquifer, SE England. *Journal of Hydrogeology* 330, pp. 604-620.
- Lee, C.-C., Yang, C.-H., Liu, H.-S., Wen, K.-L., Wang, Z.-B., Chen, Y.-J., 2008. A study of the hydrogeological environment of the Lishan landslide area using resistivity image profiling and borehole data. *Engineering Geology* 98, pp. 115-125.
- Leick, A., 2004. *GPS satellite surveying*. 3rd ed. Hoboken, New Jersey: John Wiley & Sons., 435 pp.
- Lewis, E. D., 1959. *The Rhondda Valleys*. Phoenix House.
- Lillesand, T. M., Kiefer, R. W., and Chipman, J. W., 2004. *Remote sensing and image interpretation*. New York: Wiley, 763 pp.
- Ling, S. R. A., 2007. *Assessing the effectiveness of landfill restoration and remediation at a closed landfill site*. PhD, Cardiff University.
- Malet, J.-P., Maquaire, O., and Calais, E., 2002. The use of Global Positioning System techniques for the continuous monitoring of landslides: application to the Super-Sauze earthflow (Alpes-de-Haute-Provence, France). *Geomorphology* 43, pp. 33-54.
- Malet, J.-P., van Asch, Th. W. J., van Beek, R., and Maquaire, O., 2005. Forecasting the behaviour of complex landslides with a spatially distributed hydrological model. *Natural Hazards and Earth System Sciences* 5, pp 71-85.
- Mallet, C. and Bretar, F. 2009. Full-waveform topographic Lidar: State-of-the-art. *ISPRS Journal of Photogrammetry & Remote Sensing* 64, pp. 1-16.
- Marescot, L., Monnet, R., and Chappelier, D., 2008. Resistivity and induced polarization surveys for slope instability studies in the Swiss Alps. *Engineering Geology* 98, pp. 18-28.
- Mather, J. D., 2000. The influence of mining subsidence on the hydrogeology of Carboniferous sandstones at Aberfan. In: Siddle, H. J., et al. eds., *Landslide and landslide management in South Wales*. Cardiff: National Museums & Galleries of Wales, pp. 9-14.
- Mauritsch, H. J., Seiberl, W., Arndt, R., Römer, A., Schneiderbauer, K., and Sendlhofer, G. P., 2000. Geophysical investigations of large landslides in the Carnic Region of southern Austria. *Engineering Geology* 56(3-4), pp. 373-388.

- McCann, D. M. and Forster, A., 1990. Reconnaissance geophysical methods in landslide investigations. *Engineering Geology* 29, pp. 59-78.
- McNeill, J. D., 1980. Electrical conductivity of soils and rocks. Mississauga, Ontario, Canada: Geonics Limited. Technical Note TN-5, 22 pp.
- McNeill, J. D., 1980b. Electromagnetic terrain conductivity measurement at low induction numbers. Mississauga, Ontario, Canada: Geonics Limited. Technical Note TN-6, 15 pp.
- McNeill, J. D., 1990. Use of electromagnetic methods for groundwater studies. In: Ward, S.H. ed., *Geotechnical and environmental geophysics*, Vol. 1. Tulsa, Oklahoma: Society of Exploration Geophysicists, pp. 191-218.
- McNeill, J. D., 1996. Why doesn't Geonics Limited build a multi-frequency EM31 or EM38? Mississauga, Ontario, Canada: Geonics Limited. Technical Note TN-30.
- Meric, O., Garambois, S., Jongmans, D., Wathélet, M., Chatelain, J. L. and Vengeon, J. M., 2005. Application of geophysical methods for the investigation of the large gravitational mass movement of Séchilienne, France. *Canadian Geotechnical Journal* 42, pp. 1105-1115.
- Meric, O., Garambois, S., Malet, J.-P., Cadet, H., Guéguen, P. and Jongmans, D., 2007. Seismic noise-based methods for soft-rock landslide characterization. *Bulletin de la Société Géologique de France* 178(2), pp. 137-148.
- Miller, R. D., Xia, J., Park, C. B., and Ivanov, J., 1999. Multichannel analysis of surface waves to map bedrock. *The Leading Edge* 18(12), pp. 1392-1396.
- Miller, R. D., Xia, J., Park, C. B., and Ivanov, J., 2000. Shear wave velocity field from surface waves to detect anomalies in the subsurface. *Proceedings of the 1st International Conference on the Application of Geophysical Methodologies to Transportation Facilities and Infrastructure*, Paper 4-8, St. Luis, December 11-15.
- Mondal, S. K., Sastry, R. G., Pachauri, A. K. and Gautam, P. K., 2008. High resolution 2D electrical resistivity tomography to characterize active Naitwar Bazar landslide, Garhwal Himalay, India. *Current Science* 94(7), pp. 871-875.
- Mora, P., Baldi, P., Casula, G., Fabris, M., Ghiotti, M., Mazzini, E., and Pesci, A., 2003. Global Positioning Systems and digital photogrammetry for the monitoring of mass movements: application to the Ca' di Malta landslide (northern Apennines, Italy). *Engineering Geology* 68, pp. 103-121.
- Müller, K., 1977. Geophysical methods in the investigation of slope failures. *Bulletin of the International Association of Engineering Geology* 16, pp. 227-229.
- Nadim, F., Kjekstad, O., Peduzzi, P., Herold, C. and Jaedicke, C., 2006. Global landslide and avalanche hotspots. *Landslides* 3, pp. 159-173.

- Nash, D., 1987. Comparative Review of Limit Equilibrium Methods of Stability Analysis. In: Anderson, M. G., and Richards, K. G. eds., *Slope Stability: Geotechnical Engineering and Geomorphology*, John Wiley and Sons, New York. pp. 11-75.
- Novosad, S., Blaha, P., and Kneijzlik, J., 1977. Geoacoustic methods in the slope stability investigation. *Bulletin of the International Association of Engineering Geology* 16, pp. 229-231.
- Ogilvy, A. A., Ayed, M. A., and Bogoslovsky, V. A., 1969. Geophysical studies of water leakages from reservoirs. *Geophysical Prospecting* 17(1), pp. 36-62.
- Oka, N., 1998. Application of photogrammetry to the field observation of failed slopes. *Engineering Geology* 50, pp. 85-100.
- Palmer, D., 1980. *The generalized reciprocal method of seismic refraction interpretation*. Tulsa: Society of Exploration Geophysicists.
- Parasnis, D. S., 1997. *Principles of applied geophysics*. 5th ed. London: Chapman & Hall, 429 pp.
- Park, C. B., Miller, R. D., and Xia, J., 1999. Multichannel analysis of surface waves. *Geophysics* 64(3), pp. 800-808.
- Park, C. B., Miller, R. D., and Xia, J., and Ivanov, J., 2007. Multichannel analysis of surface waves (MASW) - active and passive methods. *The Leading Edge* 26(1), pp. 60-64.
- Paroditis, N. and Polidori, L., 2002. Overview of digital surface models. In: Kasser, M. and Egels, Y. eds., *Digital photogrammetry*. London: Taylor and Francis, pp. 159-163.
- Pelton, J. R., 2005. Near-surface seismology: Surface-based methods. In: Butler, D.K. ed., *Near-surface geophysics*. Tulsa: Society of Exploration Geophysicists, pp. 219-263.
- Pelton, J. R., 2005b. Near-surface seismology: Wave propagation. In: Butler, D.K. ed., *Near-surface geophysics*. Tulsa: Society of Exploration Geophysicists, pp. 177-217.
- Penman, A. D. M., 2000. The Aberfan flow slide, Taff Valley. In: Siddle, H. J. et al. eds., *Landslide and landslide management in South Wales*. Cardiff: National Museums & Galleries of Wales, pp. 62-67.
- Perrone, A., Iannuzzi, A., Lapenna, V., Lorenzo, P., Piscitelli, S., Rizzo, E., and Sdao, F., 2004. High-resolution electrical imaging of the Varco d'Izzo earthflow (southern Italy). *Journal of Applied Geophysics* 56(1), pp. 17-29.
- Perry, A. H. and Howells, K. A., 1982. Are large falls of rain in Wales becoming more frequent? *Weather* 37, pp. 240-243.

- Peyret, M., Djamour, Y., Rizza, M., Ritz, J.-F., Hurtrez, J.-E., Gourdazi, M. A., Nankali, H., Chéry, J., Le Dortz, K. and Uri, F., 2008. Monitoring of the large slow Kahrod landslide in Alborz mountain range (Iran) by GPS and SAR interferometry. *Engineering Geology* 100, pp. 131-141.
- Rizzo, V., 2002. GPS monitoring and new data on slope movements in the Maratea Valley (Potenza, Basilicata). *Physics and Chemistry of the Earth* 27, pp. 1535-1544.
- Rouse, C., Styles, P. and Wilson, S. A., 1991. Microseismic emission from flowslide-type movements in South Wales. *Engineering Geology* 31, pp. 91-110.
- Sass, O., Bell, R., and Glade, T., 2008. Comparison of GPR, 2D-resistivity and traditional techniques for the subsurface exploration of the Öschingen landslide, Swabian Alb (Germany). *Geomorphology* 93, pp. 89-103.
- Sato, M. and Mooney, H. M., 1960. The electrochemical mechanism of sulfide self-potentials. *Geophysics* 25(1), pp. 226-249.
- Schmutz, M., Albouy, Y., Guérin, R., Maquaire, O., Vassal, J., Schott, J.-J. and Descloîtres, M., 2000. Joint electrical and time domain electromagnetism (TDEM) data inversion applied to the Super Sauze earthflow (France). *Surveys in Geophysics* 21, pp. 371-390.
- Sharma, P. V., 1997. *Environmental and engineering geophysics*. Cambridge: Cambridge University Press, pp. 475.
- Schenck, T., 1994. Concepts and algorithms in digital photogrammetry. *ISPRS Journal of Photogrammetry and Remote Sensing* 49, pp. 2-8.
- Schenk, T., 1997. Towards automatic aerial triangulation. *ISPRS Journal of Photogrammetry and Remote Sensing* 52(3), pp. 110-121.
- SeisImager/2D manual, Version 3.3, OYO Corporation (2009).
- Sheriff, R. E. and Geldart, L. P., 1985. *Exploration seismology I: History, theory and data acquisition*. Cambridge University Press.
- Shroder, 1971: *Landslides of Utah*. Utah Geological and Mineral Survey Bulletin 90, 51 pp.
- Siddle, H. J., 2000. Craig yr Amos and Ffaldau landslides, Meardy. In: Siddle, H. J., et al. eds., *Landslide and landslide management in South Wales*. Cardiff: National Museums & Galleries of Wales, pp. 60-62.
- Siddle, H. J., 2000. Blaencwm landslide, Rhondda Fawr. In: Siddle, H. J. et al. eds., *Landslide and landslide management in South Wales*. Cardiff: National Museums & Galleries of Wales, pp. 55-59.

- Siddle, H. J. and Bentley, S. P., 2000. A brief history of landslide research in South Wales. In: Siddle, H. J. et al. eds., *Landslide and landslide management in South Wales*. Cardiff: National Museums & Galleries of Wales, pp. 9-14.
- Siddle, H. J., Bromhead, E. N., and Bassett, M. G., 2000. *Landslides and landslide management in South Wales*. Cardiff: National Museum & Galleries of Wales, 116 pp.
- Siddle, H. J., Wright, M. D., and Hutchinson, J. N., 1996. Rapid failures of colliery spoil heaps in the South Wales Coalfield. *Quarterly Journal of Engineering Geology* 29, pp. 103-132.
- Siddle, H. J., Wright, M. D., and Hutchinson, J. N., 2000. Rapid failures of spoil heaps in the South Wales Coalfield. In: Siddle, H. J. et al. eds., *Landslide and landslide management in South Wales*. Cardiff: National Museums & Galleries of Wales, pp. 32-35.
- Smith, M. J., Smith, D. G., Tragheim, D. G., and Holt, M., 1997. DEMs and ortho-images from aerial photographs. *Photogrammetric Record* 15(90), pp. 945-950.
- Spillmann, T., Maurer, H., Willenberg, H., Evans, K. F., Heincke, B., and Green, A. G., 2007. Characterization of an unstable rock mass based on borehole logs and diverse borehole radar data. *Journal of Applied Geophysics* 61, pp. 16-38.
- Squarzon, C., Delacourt, C., and Allemand, P., 2005. Differential single-frequency GPS monitoring of the La Valette landslide (French Alps). *Engineering Geology* 79, pp. 215-229.
- Statham, I., 2004. Abandoned shallow mineworkings and subsidence risk: a case history from South Wales Coalfield. In: Nichol, D. et al. eds., *Urban Geology in Wales*. Cardiff: National Museums & Galleries of Wales, pp. 117-122.
- Stokoe, K. H., Wright, G. W., Bay, J. A., and Roesset, J. M., 1994. Characterization of geotechnical sites by SASW method. In: Woods, R. D., ed., *Geophysical characterization of sites*: Oxford Publishers.
- Suzuki, K. and Higashi, S., 2001. Groundwater flow after heavy rain in landslide-slope area from 2-D inversion of resistivity monitoring data. *Geophysics* 66(3), pp. 733-743.
- Tanzini, M., 2001. *Fenomeni franosi e opere di stabilizzazione*. Palermo: Dario Flaccovio Editore, 292 pp.
- Telford, W. M., Geldart, L. P., and Sheriff, R. E., 1990. *Applied geophysics*. 2nd ed. Cambridge: Cambridge University Press, 770 pp.
- Thiel, K.-H. and Wehr, A., 2004. Performance capabilities of laser scanners - An overview and measurement principle analysis. *Proceedings of the ISPRS working group 3(2)*, pp. 1-18.

- Tingey, B. E., McBride, J. H., Thompson, T. J., Stephenson, W. J., South, J. V., and Bushman, M., 2007. Study of a prehistoric landslide using seismic reflection methods integrated with geological data in the Wasatch Mountains, Utah, USA. *Engineering Geology* 95, pp. 1-29.
- Topcon 2006. HiPer® Pro operators's manual. Topcon Positioning Systems.
- Tullen, P., Turberg, P., and Parriaux, A., 2006. Radiomagnetotelluric mapping, groundwater numerical modelling and 18-Oxygen isotopic data as combined tools to determine the hydrogeological system of a landslide prone area. *Engineering Geology* 87, pp. 195-204.
- Uren, J. and Price, W. F., 2006. *Surveying for engineers*. 4th ed. Basingstoke: Palgrave Macmillan, 824 pp.
- Varnes, D. J., 1978. Slope movement types and processes. In: Schuster, R. L., and Krizek, R. J., eds., *Landslides: Analysis Control, Transportation Research Board Special Report 176*, pp. 11-33.
- Walsh, R. P. D., Hudson, R. N., and Howells, K. A., 1982. Changes in the magnitude-frequency of flooding and heavy rainfalls in the Swansea Valley since 1875. *Cambria* 9, pp. 36-60.
- Walstra, J., Dixon, N., and Chandler, J. H., 2007. Historical aerial phographs for landslide assessment: two case histories. *Quarterly Journal of Engineering Geology and Hydrogeology* 40, pp. 315-332.
- Wangensteen, B., Guðmundsson, Á., Eiken, T., Kääb, A., Farbrot, H., and Etzelmüller, B., 2006. Surface displacements and surface age estimates for creeping slope landforms in Northern and Eastern Iceland using digital photogrammetry. *Geomorphology* 80, pp. 59-79.
- Watt, P. J., Donoghue, D. N. M., McManus, K. B., and Dunford, R. W., 2004. Predicting forest height from Ikonos, Landsat and LiDAR imagery. *Proceedings of ISPRS working group VIII/2 "Laser scanner for Forest and Landscape assessment"*. Fierburg, Germany , October 3-6.
- Wehr, A. and Lohr, U., 1999. Airborne laser scanning - an introduction and overview. *ISPRS Journal of Photogrammetry & Remote Sensing* 54, pp. 68-82.
- Witten, A., Calvert, G., Witten, B., and Levy, T., 2003. Magnetic and electromagnetic induction studies at archaeological sites in Southwestern Jordan. *Journal of Environmental and Engineering Geophysics* 8(3), pp. 209-215.
- Witten, A., Won, I. J., Norton, S., 1997. Imaging underground structures using broadband electromagnetic induction. *Journal of Environmental and Engineering Geophysics* 2(2), pp. 105-114.
- Wolf, P. R. and Ghilani, C. D., 2002. *Elementary Surveying. An introduction to geomatics*. 10th ed. Upper Saddle River, New Jersey: Prentice Hall, 900 pp.

- Won, I. J., 1980. A wide-band electromagnetic exploration method - Some theoretical and experimental results. *Geophysics* 45(5), pp. 928-940.
- Won, I. J., 2003. Small frequency-domain electromagnetic induction sensors. How in the world does a small broadband EMI sensor with little or no source-receiver separation work? *The Leading Edge* 22(4), pp. 320-322.
- Won, I. J. and Huang, H. 2004. Magnetometers and electro-magnetometers. *The Leading Edge* 23(5), pp. 448-451.
- Won, I. J., Keiswetter, D. A., Fields, G. R. A., and Sutton, L. C., 1996. GEM-2: A new multifrequency electromagnetic sensor. *Journal of Environmental and Engineering Geophysics* 1(2), pp. 129-137.
- Woodland, A. W. and Evans, W. B., 1964. The geology of the South Wales Coalfield. Part IV: The country around Potypridd and Maesteg. 3rd ed. London: The Stationary Office, p. 391.
- WP/WLI, 1993. The multilingual landslide glossary. The International Geotechnical Societies' UNESCO Working Party for World Landslide Inventory. BiTech Pubs, Canada.
- Wright, M. D., 2000. Glacial and periglacial superficial deposits of the South Wales Coalfield. In: Siddle, H. J. et al. eds., *Landslide and landslide management in South Wales*. Cardiff: National Museum & Galleries of Wales, pp. 26-29.
- Wright, M. D. and Harris, C. 1980. Superficial deposits in the South Wales Coalfield. In: Perkins, J.W., ed., *Cliff and slope stability*. South Wales. Cardiff: Department of Extra-Mural Studies, University College, Cardiff, pp. 193-205.
- Xia, J., Miller, R. D., and Park, C. B., 1999. Estimation of near-surface shear-wave velocity by inversion of Rayleigh waves. *Geophysics* 64(3), pp. 691-700.
- Yamaguchi, S., 1977. Determination of the location of drains and assessment of the effect of the work by repeated electric resistivity survey. *Bulletin of the International Association of Engineering Geology* 16, pp. 183-184.
- Yilmaz, S., 2007. Investigations of Gürbulak Landslide using 2D electrical resistivity image profiling method (Trabzon, Northeastern Turkey). *Journal of Environmental and Engineering Geophysics* 12(2), pp. 199-205.
- Zonge, K., Wynn, J., and Urquhart, S., 2005. Resistivity, induced polarization and complex resistivity. In: Butler, D.K., eds. *Near-surface geophysics*. Tulsa: Society of exploration geophysicists, pp. 265-300.

Website references

[WWW 1.1] <http://www.emdat.be>

[WWW 1.2] <http://unisdr.org>

[WWW 1.3] <http://preventionweb.net>

[WWW 1.4]

http://www.bgs.ac.uk/landslides/How_does_BGS_classify_landslides.html

[WWW 2.1] <http://gulfsi.usgs.gov/tampabay/data/1mapping/lidar/images/Eaar11.gif>

[WWW 2.2] <http://www.getmapping.com>

[WWW 2.3] <http://www.terrageomatics.com>

[WWW 2.4] <http://intarch.ac.uk/journal/issue25/reviews/masinton.html>

[WWW 2.5] <http://www.navcen.uscg.gov>

[WWW 2.6]

http://www.trinityhouse.co.uk/aids_to_navigation/the_task/satellite_navigation.html

[WWW 2.7] <http://www.gps.gov.uk>

[WWW 2.8] <http://www.glonass-ianc.rsa.ru>

[WWW 2.9] <http://www.topcon.com>

[WWW 2.10] <http://www.geophex.com>

[WWW 2.11] <http://www.masw.com>

[WWW 2.12] <http://www.bgs.ac.uk/research/tomography/ALERT.html>

[WWW 3.1] <http://www.getmapping.com>

[WWW 3.2] <http://www.edina.ac.uk/digimap>

Appendix A Classification of slope movements by Hutchinson (1988)

Classification of sub-aerial slope movements proposed by Hutchinson (1988)

A) Rebound	Movements associated with: 1. Man-made excavations 2. Naturally eroded valleys
B) Creep	1. Superficial, predominantly seasonal creep; mantle creep: a) Soil creep, talus creep (non-periglacial) b) Frost creep and gelifluction of granular debris (periglacial) 2. Deep-seated, continuous creep; mass creep 3. Pre-failure creep; progressive creep 4. Post-failure creep
C) Sagging of mountain slopes	1. Single-sided sagging associated with the initial stages of landsliding: a) of rotational (essentially circular) type (R-sagging) b) of compound (markedly non-circular) type (C-sagging); i) listric (CL); ii) bi-planar (CB) 2. Double-sided sagging associated with the initial stages of double landsliding, leading to ridge spreading: a) of rotational (essentially circular) type (DR-sagging) b) of compound (markedly non-circular) type (DC-sagging); i) listric (DCL), ii) biplanar (DCB) 3. Sagging associated with multiple toppling (T-sagging)
D) Landslides	1. Confined failures: a) in natural slopes b) in man-made slopes 2. Rotational slips: a) single rotational slips b) successive rotational slips c) multiple rotational slips 3. Compound slides (markedly non-circular, with listric or bi-planar slip surfaces): a) released by internal shearing towards rear i) in slide mass of low to moderate brittleness ii) in slide mass of high brittleness b) progressive compound slides, involving rotational slip at rear and fronted by subsequent translational slide 4. Translational slides a) Sheet slides b) Slab slides; flake slides c) Peat slides d) Rock slides: i) Planar slides; block slides ii) Stepped slides iii) Wedge failures e) Slides of debris: i) Debris-slides; debris avalanches (non-periglacial) ii) Active layer slides (periglacial) f) Sudden spreading failures

E) Debris movements of flow-like form	<ol style="list-style-type: none"> 1. Mudslides <ol style="list-style-type: none"> a) Sheets b) Lobes (lobate or elongate) 2. Periglacial mudslides (gelifluction of clays): <ol style="list-style-type: none"> a) Sheets b) Lobes (lobate or elongate, active and relict) 3. Flow slides: <ol style="list-style-type: none"> a) in loose, cohesionless materials b) in lightly cemented, high porosity silts c) in high porosity, weak rocks 4. Debris flows, very to extremely rapid flows of wet debris: <ol style="list-style-type: none"> a) involving weathered rock debris (except on volcanoes): <ol style="list-style-type: none"> i) Hillslope debris flows ii) Channalized debris flows; mud flows; mud-rock flows b) involving peat; bog flows, bog bursts c) associated with volcanoes; lahars: <ol style="list-style-type: none"> i) Hot lahars ii) Cold lahars 5. Sturzstroms, extremely rapid flows of dry debris
F) Topples	<ol style="list-style-type: none"> 1. Topple bounded by pre-existing discontinuities: <ol style="list-style-type: none"> a) Single topple b) Multiple topples 2. Topples released by tension failure at rear of mass
G) Falls	<ol style="list-style-type: none"> 1. Primary, involving fresh detachment of material; rock and soil falls 2. Secondary, involving loose material, detached earlier; stone falls
H) Complex slope movements	<ol style="list-style-type: none"> 1. cambering and valley bulging 2. Block-type slope movements 3. Abandoned clay cliffs 4. Landslides breaking down into mudslides or flows at the toe: <ol style="list-style-type: none"> a) Slump-earthflows b) Multiple rotational quick-clay slides c) Thaw slumps 5. Slides caused by seepage erosion 6. Multi-tiered slides 7. Multi-storied slides

Appendix B Classification of landslides of flow type by Hungr et al. (2001)

Classification of landslides of flow type (Hungr et al., 2001):

Material	Water Content ¹	Special Condition	Velocity	Name
Silt, Sand, Gravel, Debris (talus)	Dry, moist or saturated	-no excess pore-pressure, -limited volume	Various	Non-liquefied sand (silt, gravel, debris) flow
Silt, Sand, Debris, Weak rock ²	Saturated at rupture surface content	-liquefiable material ³ , -constant water	Ex. Rapid	Sand (silt, debris, rock) flow slide
Sensitive Clay	At or above liquid limit	-liquefaction <i>in situ</i> ³ , -constant water content ⁴	Ex. Rapid	Clay flow slide
Peat	Saturated	-excess pore-pressure	Slow to very rapid	Peat flow
Clay or Earth	Near plastic limit	-slow movements, -plug flow (sliding)	< Rapid	Earth flow
Debris	Saturated	-established channel ⁵ , -increased water content ⁴	Ex. Rapid	Debris flow
Mud	At or above liquid limit	-fine-grained debris flow	> Very rapid	Mud flow
Debris	Free water present	-flood ⁶	Ex. Rapid	Debris flood
Debris	Partly or fully saturated	-no established channel, -relatively shallow, steep source	Ex. Rapid	Debris avalanche
Fragmented Rock	Various, mainly dry	-intact rock at source, -large volume	Ex. Rapid	Rock avalanche

¹ Water content of material in the vicinity of the rupture surface at the time of failure.

² Highly porous, weak rock (examples: weak chalk, weathered tuff, pumice).

³ The presence of full or partial *in situ* liquefaction of the source material of the flow slide may be observed or implied.

⁴ Relative to *in situ* source material.

⁵ Presence or absence of a defined channel over a large part of the path, and an established deposition landform (fan). Debris flow is a recurrent phenomenon within its path, while debris avalanche is not.

⁶ Peak discharge of the same order as that of a major flood or an accidental flood. Significant tractive forces of free flowing water. Presence of floating debris.

⁷ Volume greater than 10,000 m³ approximately. Mass flow, contrasting with fragmental rock fall.

Classification of materials for landslide of flow-type, based on genetic and morphological aspects (Hung et al., 2001):

Origin	Character	Condition ¹	Name
SORTED (marine, lacustrine, fluvial, eolian, volcanic, anthropogenic)	Non-cohesive (Plastic Limit < 5%)	Dry or saturated	-Gravel -Sand -Silt
	Cohesive (Plastic Limit > 5%)	-Plastic ($I_L < 0.5$) -Liquid ($I_L > 0.5$)	-Clay -Sensitive Clay
UNSORTED (residual, colluvial, glacial, volcanic, anthropogenic)	Non-cohesive (Plastic Limit < 5%)	Dry or saturated	-Debris ²
	Cohesive (Plastic Limit < 5%)	-Plastic ($I_L < 0.5$) -Liquid ($I_L > 0.5$)	-Earth -Mud
PEAT	Organic	Saturated	-Peat
ROCK	Fragmented	Dry or saturated	-Rock

¹ Related to the material found in the vicinity of the rupture surface at the time of failure, if it can be determined. In many cases, the material condition must be deduced from the behaviour of the landslide, especially velocity.

² Debris may contain a considerable portion of organic material.

Appendix C Literature review of published papers on the application of geophysics to landslide research

Author/s	Year	Site Location	Landslide Type and Geological Setting	Geophysical methods employed	Results of geophysical surveys (<i>with some personal notes</i>)
Cadman and Goodman	1967	Laboratory experiments and fieldwork (not specified)	Lab tests: on moist sand Fieldwork: Not specified	Micro-seismics (from geophones at surface or in boreholes)	Geophysical Location of slip surface
Denness et al.	1975	Coastal landslip at Higher Sea Lane (Black Ven Complex, Charmouth, Dorset, UK)	Reactivated fossil mudflow. Clays, mudstones and limestones (Lower Lias) overlain by clays and sands (Gault and Upper Greensand) and head	Electrical resistivity mapping (grid repeated two times: Dec 1970 and July 1972); Electrical resistivity sounding ; Acoustic velocity scanning ; (between boreholes)	Variations in moisture content and lithology within the slope; Relationship between resistivity values and moisture content; Evaluation of changes in moisture content due to heavy rainfall
Bogoslovsky and Ogilvy	1977	<i>General review supported by case studies:</i> a) Landslide in Volga River Valley; b) Landslide on Black Sea coast of Caucasus; c) Other landslides on the Black Sea coast of Caucasus and Crimea (near town of Adler, near town of Gagra)	Types not specified; a) landslide deposits underlain by undisturbed clayey rocks; b) loamy rocks underlain by weathered argillites on top of undisturbed argillites; c) not specified	Vertical electrical soundings (along profiles); Electrical resistivity mapping (repeated in winter/summer); Seismic Refraction (P- and S-waves); SP mapping ; Magnetics	Determination of sliding material thickness and bedrock depth (VES and seismics); Determination of slip zone thickness and depth (VES); Determination of water table and its changes in time (seismic P-waves); Determination of groundwater flow and landslide lateral limits (SP mapping); Determination of water saturation degree (resistivity mapping in areas of homogeneous geology) Identification of differences in resistivity, seismic wave velocities and attenuations between rocks occurring in landslide bodies and same rocks in bedrock; Identification of changes in moisture content occurring mostly in the upper layer during winter and summer (repeated VES); <i>Determination of landslide displacements (magnetics and magnets in boreholes)</i>

Author/s	Year	Site Location	Landslide Type and Geology	Geophysical Methods	Results from geophysical methods
Müller	1977	<i>General Review supported by experiences in CSSR (not specified)</i>	Not specified	Electrical resistivity profiling; Electrical resistivity sounding; Self Potential; Thermal methods; Seismic refraction; Borehole seismo-acoustic; Seismic or ultrasonic logging; Magnetics	Delineation of landslide lateral limits and cracks between slide blocks (electrical resistivity profiling; SP; thermal methods; seismic refraction); Determination of sliding material base and sliding surface/zone (electrical resistivity sounding; seismic refraction; borehole seismo - acoustic; seismic and ultrasonic logging); Determination and quantification of movement (repeated surveys; magnetic surveys with magnets in boreholes)
Novosad et al.	1977	<i>Several landslides (not specified, a part for one landslide - at Turany, Slovakia)</i>	Very slow mass movement of creep-like type; For landslide at Turany: loams, sandstone and clayey shales	Geoacoustic	Determination of depth of sliding surface (14-16 m for landslide at Turany); Investigation of landslide activity; Possibility of providing prompt information about landslide activity
Yamaguchi	1977	<i>Kushibayashi landslide, near Otsu city (Japan)</i>	Type not specified; Silty clay interbedded in places with sand layers	Electrical resistivity mapping with several electrode spacings (survey repeated three times; before and during remediation phases)	Identification of areas of groundwater accumulation; Identification of best location for water drainage; Evaluation of effectiveness of remedial works
Cassinis et al.	1984/5	<i>Site on the coast of Ancona (Italy)</i>	Shallow local earthslide plus deep rotational (?); Clays overlain in places by Quaternary sands	Seismic refraction (P-waves); Down-hole borehole seismics; Vertical electrical sounding; Sonic log	Determination of depth (up to 100m below surface) and shape of slip surface; Physical model of earthslide

Author/s	Year	Site Location	Landslide Type and Geology	Geophysical Methods	Results from geophysical methods
McCann and Forster	1990	<i>General review</i> and two case studies: a) toe of Black Ven landslide complex at Charmouth (Dorset, UK); b) Conon Valley landslide at Glen Uig (Skye, UK)	a) Complex landslide with mudflows at the toe; Shales, limestones and marls (Lower Lias) overlain by Gault and Upper Greensand; b) Multiple retrogressive, rotational degrading to debris flow down slope; Shales overlain by basalt lavas	Seismic refraction (for a); Electromagnetics (EM-31 mapping) (for b); <i>(microseismic monitoring, electrical resistivity, magnetics and borehole geophysics just as review of previous works)</i>	Determination of thickness of toe fan material and determination of bedrock depth (seismic for case a) Determination of drainage patterns within the slope and landslide extent in the toe area (EM mapping for b) <i>Monitoring of landslide activity and location of failure area (microseismic monitoring);</i> <i>Determination of structural geology (VES with calibration or seismics);</i> <i>Determination of hydrogeological regime and moisture content (resistivity mapping)</i> <i>Monitoring of movement and distinction between in-situ and displaced dolerite (magnetics)</i>
Caris and Van Asch	1991	Small landslide in the Riou-Bourdouy Valley (French Alps)	Type not specified (stationary since 1980); Weathered clayey black marls (Terres Noires) underlain by bedrock of clayey black marls and chalky Flysch	Electromagnetic profiling (EM34-3); Vertical electrical sounding; Resistivity borehole logging; Seismic refraction (P-waves)	Identification of differences in water content between stable and unstable areas and within the landslide body (resistivity and electromagnetics); Determination of bedrock depth (= slip surface) (4-9m below surface) (all methods except EM); Geophysical methods provide (together with geotechnical information) input parameters for stability analysis
Rouse et al.	1991	Valley slope at a) Pant-teg and b) Glynrhigos (South Wales Coalfield)	Complex, in part flowslides; a) Lower Pennant Measures (Brithdir Sandstones overlain by Brithdir Shales) overlain by glacial till b) Middle Coal Measures overlain by Lynfi Beds	Acoustic emission / microseismic monitoring	Identification of acoustic emission signals with specific frequency picks; Identification of a changes in seismic emission with localised soil saturation and of increase in activity due to loading

Author/s	Year	Site Location	Landslide Type and Geology	Geophysical Methods	Results from geophysical methods
Giraud et al.	1995	Poucet, Francoz and Bonvillard landslides (Arc Valley, France)	Large scale landslides with planar geometry; Coal-bearing series ('Briançonnais facies belt'); schists and sandstones alternating with conglomerate horizons and coal seams	Seismic refraction (P-waves) (only results: no data or acquisition parameters provided)	Determination of thickness of slipping material (weathered rock) and determination of bedrock depth (80-160m for Poucet landslide, 60-70m for central part of Francoz landslide, 50-250m for Bonvillard landslide); Seismic results are in agreement with borehole and inclinometer information;
Fraseri et al.	1998	Sites in Albania: a) Porava landslide (shores of Fierza hydropower plant lake); b) Ragami landslide (shores of Lake Vau Dejes); c) Banja landslide (Banja hydropower plant)	a) deluvial-eluvial deposits overlying volcano-sedimentary rocks; b) Deluvions overlying serpentized rocks; c) Slipping material overlying Flysch	Vertical electrical sounding; Seismic refraction (P- and S-waves); Seismological activity monitoring	Identification of main and secondary sliding planes; Determination of depth and geometry of bedrock; Determination of slipping body structure (made of several blocks); Determination of differences in activity between parts of the slope (for Porava landslide)
Bruno and Marillier	2000	Boup landslide (Canton Wallis, western Swiss Alps);	Complex: rotational movement in the upper part, flow in the lower one; Triassic series of mainly gypsum underlain by shales	High-resolution seismic reflection; Ground penetrating radar; Electromagnetic profiling (EM-34 and EM-31); Self potential profiling	Determination of subsurface geometry (seismics); Determination of depth of sliding surface (50m below surface at survey location) (seismic and EM34); Definition of landslide lateral boundaries at surface (SP and EM-31) and at depth (EM34); Location of areas of upward flow of mineralized water (SP); GPR provided poor results; Determination of schematic cross-section (geophysics and other information)
Ferrucci et al.	2000	Sackung of Lago, Catena Costiera mountain range (Calabria, Italy)	Deep-seated gravitational deformation (sackung type); Phyllitic rocks overlain by gneiss and porphyroids and alluvial deposits	Seismic reflection; (Seismic refraction only to define velocity of weathered material)	Determination of structure and geology of the slope but with no definition in the upper weathered layer (seismic reflection); Method failed partly in detecting slip surface (lack of migrated data)

Author/s	Year	Site Location	Landslide Type and Geology	Geophysical Methods	Results from geophysical methods
Hack	2000	General review only from theoretical point of view (no case studies)		Seismics (refraction, reflection and tomography); Electrical resistivity (profiling, sounding and imaging); Electromagnetics; Ground penetrating radar; Self potential; Gravity	Determination of internal structure .Calculation of of Young's modulus, Poisson ratio and of rock quality using seismics; (only general/theoretical descriptions are provided for the other methods)
Mauritsch et al.	2000	Schlanitzen sliding mass, Carnic region (southern Austria)	Dominant deep-seated creep (with 3 landslide domains: 2 rockfall-debris slides and 1 rock topple-debris slide); Limestone, shales and graphitic shales overlain by limestone and limestone with interbedded schists	Seismic refraction (P-waves); Electromagnetics (EM-34); Electrical resistivity tests	Determination of overburden thickness and bedrock depth (very variable, 4-30m); Determination of bedrock relief; Location of saturated areas within the slope; Identification of extremely large rock blocks within debris material and in contact with the basement; Velocity changes in a the basement were associated with differences in lithology or with areas affected by failure surfaces; Identification of a possible landslide model that requires further investigation; Methods failed in detecting a distinct slip surface
Schmutz et al.	2000	Super Sauze earthflow (southern French Alps)	Earthflow; Black marls	Vertical electrical soundings; Time domain electromagnetics (TDEM)	Stratification in earthflow material, with possible slip surface (at 3-8m depth) and wet layers; Identification of unstable material base; Determination of substratum depth; Importance of joint inversion of datasets for accurate structure definition
Brueckl and Paroditis	2001	Koefels landslide (Ötztal, Tirol, Austria)	Giant ancient deep creep	Seismic reflection; Seismic refraction	Definition of depth of sliding surface (300m); Estimation of landslide mass porosities; Determination of geomechanical parameters from fitting of geochemical model to seismic.
Godio and Bottino	2001	Landslide in Paroldo, Langhe (Piedmont, Italy)	Large, slow moving planar landslide; Alternating marls, silts ,arenaceous layers and stiff marl sequences	Vertical electrical sounding; Electrical resistivity tomography; Electromagnetic sounding (TDEM)	Determination of geometry and depth (20m and 35m) of potential slip surfaces; Determination of bedrock depth; Determination of geology (with borehole calibration) and possible water paths

Author/s	Year	Site Location	Landslide Type and Geology	Geophysical Methods	Results from geophysical methods
Suzuki and Higashi	2001	a) Laboratory experiment; b) Field study in mountainous area of Kyushu region (Japan)	a) two tanks: one filled with sand and one with bricks; b) bedrock of sandstone and alternating beds of sandstone and shales overlaid by volcanic ash and lacustrine deposits	Electrical resistivity tomography monitoring	Laboratory proof of the possibility of monitoring water level changes using ERT in unconsolidated sediments, highly porous and permeable rocks or heavily weathered, altered or fractured rocks (sand tank model); Monitoring of resistivity changes associated to rainfall, leading to cross-section conceptual model of groundwater flow within the slope
Cardarelli et al.	2003	Catchment tunnel of potable water (Central Apennines, Italy)	Highly tectonised limestone	Ground penetrating radar (200, 225, 450 MHz); Seismic refraction; Seismic transmission tomography	Location of rock discontinuities; Determination of rock elastic properties; Evaluation of quality of contact between concrete lining and rock
Israil and Pachauri	2003	Landslide in the Mohand area, foothill of Garhwal Himalaya	Rotational possibly followed by quasi-translational failure; Boulders and gravels in sandy or silty clayey matrix overlain by coarse clayey sands and by fine sands and interbedded clay layers	Vertical electrical sounding; Seismic refraction (P-waves); Spectral analysis of surface waves (SASW)	Determination of thickness and geometry of landslide body; Determination of shape and depth (up to 16-17m) of slip surface; Determination of water table position and saturated/unsaturated soil distribution (not from SASW)
Lapenna et al.	2003	Giarossa landslide, Potenza (Southern Italy)	Transrotational earthflow slide (inactive, local reactivations in accumulation zones); Clayey-marly terrains (Varicoloured Clays) overlain by conglomerates with sandy intercalations	Electrical resistivity tomography; SP mapping (repeated: April and September); SP tomography	Determination of thickness of slipping material and determination of depth of slip surface (25-35m below surface); Identification of intercalations within slipping material; Identification of water concentration areas and changes in time (SP mapping); Determination of landslide lateral limits (ERT and SP tomographies)

Author/s	Year	Site Location	Landslide Type and Geology	Geophysical Methods	Results from geophysical methods
Bichler et al.	2004	Quesnel Forks landslide (British Columbia, Canada)	Retrogressive dry earth slide – debris flow; Glacial sediments (sand and clay, sand, gravel, clay)	Ground penetrating radar (50MHz) (reflection profiling and CMP); Electrical resistivity tomography (profiles and fence diagram); Seismic refraction (P- and S-waves); Seismic reflection (P- and S-waves)	Identification of 7 radar facies, 6 resistivity units and 8 seismic units that correlate within geophysical methods and with stratigraphy; Determination of rupture surface geometry (GPR and ERT); Determination of 3D model of landslide (with correlation with other information); Calculation of landslide volume (best estimation compared to DTMs and field observations); Evaluation of methods: ERT is the most useful; GPR resolves shallow structures (max 25 m depth) while seismics the deep ones (more than 80 m depth)
Perrone et al.	2004	Varco d'Izzo landslide, Potenza (southern Italy)	Rototranslational movement followed by earthflow; Clayey-marly terrains with local intrusions of blocks and layers of lapideous rocks (Argille Varicolori)	Electrical resistivity tomography; SP mapping; SP tomography	Determination of landslide material thickness (10-50m); Identification of areas with high water content (SP mapping) and groundwater circulation system; Determination of landslide lateral limits (SP tomography).
Agnesi et al.	2005	Cerda landslide (Sicily, Italy)	New debris block slide triggered by earthquake and affecting ancient landslide bodies (main is multiple rotational slide); Clayey-arenitic slope	Vertical electrical sounding	Identification of discontinuity, possible slip surface (100m depth)

Author/s	Year	Site Location	Landslide Type and Geology	Geophysical Methods	Results from geophysical methods
Heincke et al.	2005	Randa rockslide (Swiss Alps)	Rockslide; Crystalline rocks (gneisses, schists, amphibolites and granitic intrusions)	Ground penetrating radar	Determination of GPR acquisition and processing procedures for area of rugged topography; Identification of overburden/rock boundary, possible changes in lithology and some of the fracture zones
Lapenna et al.	2005	a) Giarossa earthflow b) Varco Izzo earthflow c) Latronico landslide (Lucanian Apennine chain, southern Italy)	Rototranslational slides a) and b) Clayey-marly terrains (Varicolori Clays and Flysch Galestrino) overlain by conglomerates; b) shales, calcareous marls, calcarenites and quartzites	Electrical resistivity tomography	Determination of sliding material thickness (15-35m for Giarossa, 25-35m for Varco Izzo, 10-40m for Latronico); Determination of landslides lateral limits
Lebourg et al.	2005	Part of La Capière landslide (Alpes Maritimes, France)	Rotational landslide (part of the toe of the large active deep-seated La Capière landslide); Gneissic bedrock overlain by fluvio-glacial deposits	Electrical resistivity tomography 2D, 3D (from parallel profiles) and 4D (one profile repeated three times in April-July 2003)	Determination of depth and geometry of perched water table and/or sliding surface (between 2 and 15m depth); Identification of two vertical draining discontinuities; Determination of changes in drainage system due to different hydrogeological stages (repeated profile)
Meric et al.	2005	Séchillienne movement, near Grenoble (French Alps)	Large complex probably deep-seated rockslide; Micaschists with interbedded quartz-feldspar-rich layers	Electromagnetic profiling (EM-34); Electrical resistivity tomography; Seismic refraction tomography (P-waves); SP profile (repeated 3 times); Seismic noise measurements	Determination of landslide lateral limits; Characterization of rock mass (fracturing degree); Determination of bedrock depth (more than 30-100m); Agreement between geophysical techniques and displacement movements

Author/s	Year	Site Location	Landslide Type and Geology	Geophysical Methods	Results from geophysical methods
Brückl and Brückl	2006	Two rock masses in the Schober range, Austria: a) Lesachriegel b) Gradenbach,	Deep-seated gravitational creep or sagging of rock mass; a) mica-schists, schistose gneisses and amphibolites; b) phyllites, quartzites, calcareous and chlorite schists	Seismic refraction tomography ???(P-waves only or both P- and S-waves)	Determination of basal sliding plane (used also as input for landslide volume calculation); Determination of Poisson's ratio; Estimation of average porosity of creeping masses (from P-wave velocity versus depth graphs)
Colangelo et al.	2006	Varco d'Izzo landslide (Basilicata, Italy)	Rotational-translational slide evolving into earthflow; Clayey-marly terrains (Argille Varicolori)	SP mapping; Static SP tomography; Time-continuous SP	Determination of superficial landslide lateral limits (SP mapping); Determination of groundwater system within the landslide (SP mapping); Identification of distribution of electrical charges and groundwater at depth (SP tomography); Potential application for the study of groundwater regime after rainfall events (time-continuous SP)
De Vita et al.	2006	Sample area of Monte Pizzo d'Alvano (Sarno, Italy)	Site representative of initiation area of debris slides; Carbonate bedrock (limestone and dolomitic limestone) overlain by unconsolidated ash-fall pyroclastic deposits	Vertical electrical sounding; Seismic refraction soundings; (resistivity measurements on outcrops)	Determination of pyroclastic deposits thickness (5.5 m) and bedrock depth; Characterization and differentiation within pyroclastic series (only VES); Location of possible perched water table (VES)
Friedel et al.	2006	50 x 20 m test site on a slope near Toessegg (Rhine Valley, North Switzerland)	Rainfall induced landslide; Sandstone bedrock overlain by loose weathered or residual sands and silty sands of glacial and fluvial origin	2D and 3D electrical resistivity tomography; Repetition of one ERT profile in dry and wet conditions; (GPR survey only mentioned)	Identification of units and spatial changes in moisture content; Determination of bedrock depth; Comparison and evaluation of several electrode arrays and their combinations; Identification of changes in water content after wet period (from repeated profile); (GPR results were unsatisfactory)

Author/s	Year	Site Location	Landslide Type and Geology	Geophysical Methods	Results from geophysical methods
Godio et al.	2006	Rockslide in the valley of Soana torrent, Graie Alps (Piedmont, Italy)	Rockslide; Gneissic bedrock overlain by overburden	Electrical resistivity tomography; Seismic refraction tomography; Surface waves method (SWM); Borehole horizontal seismic profiling; Sonic log; Laboratory measurements of P-waves	Determination of overburden thickness (ERT, SRT, SWM); Determination of depth to bedrock; Determination of fracturing degree and rock mass quality; Determination of seismic Poisson ratio and Young's modulus (Sonic Log); Determination of useful information for tunnel feasibility assessment, in good agreement with geotechnical measurements
Heincke et al.	2006	Mountain slope close to Rhanda village (Matter Valley, Swiss Alps)	Rockfall; Gneissic rock mass with cracks, fracture zones and faults	2D and 3D seismic refraction tomography (P-waves) (and P-wave velocity measurements on samples)	Determination (in 2D and 3D) of ultralow and low velocity areas associated with low rock quality; Evaluation of seismic tomography sensitivity to heterogeneities and data reliability; The 3D tomographic technique provides better results than 2D tomograms
Tullen et al.	2006	Hohberg landslide, canton of Fribourg (Switzerland)	Translational landslide with associated debris flow; Flysch substratum overlain by moraines and slope debris	Radiomagnetotelluric	Determination of resistivity distribution within the slope used after for a permeability model
Amitrano et al.	2007	Super-Sauze mudslide (South-East French Alps)	Mudslide; Black marls	Broadband micro-seismic monitoring (13 days)	Finding a correlation between displacement acceleration and seismic noise (0.1-10 Hz) due to shearing of moving mass; Determination of highest sensitivity of 0.1-1 Hz range




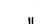

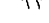

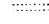



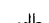



Author/s	Year	Site Location	Landslide Type and Geology	Geophysical Methods	Results from geophysical methods
Jomard et al.	2007	Secondary landslide at the foot of La Capière landslide (Alpes Maritimes, France)	Rotational landside with toppling affecting substratum; Fluvio-glacial deposits overlain gneiss	Time-lapse electrical resistivity tomography (following injection experiment) (laboratory resistivity measurements on samples)	Determination of geometry, depth (maximum of 10m) and draining function of slip surface; Identification of two drainage systems (one shallow and one deep); Determination of slope geometry and hydrogeology along cross-section and understanding of landslide dynamics (from combination of geophysical, geological, hydrological and geodetic information)
Jongmans and Garambois	2007	<i>General literature review (no original case studies)</i>		<i>Seismics reflection; Seismic refraction; Seismic tomography; Seismic noise measurements; Seismic surface waves; Electrical resistivity methods (VES, profiling and tomography); Self Potential; Electromagnetics; Ground Penetrating Radar</i>	<i>Review from other authors</i>
Meric et al.	2007	Sites in the South French Alps: a) 'Sauper Sauze' mudslide; b) 'Saint Guillaume' landslide	a) mudslide; Black marls; b) translational landslide; Marly limestone bedrock overlain by varved clays	Electrical resistivity tomography; Seismic profiles (for surface-waves inversion); Seismic noise measurements (H/V and seismic noise network)	Determination of slip surface/landslide thickness (from 0 to 50 m); Determination of bedrock depth (not from H/V for 'Sauper Sauze' mudslide)
Spillmann et al.	2007	Randa rockslide (Swiss Alps)	Rockslide; Crystalline rocks (heterogeneous gneisses)	Borehole radar (single-hole, vertical profiling and crosshole)	Identification of geometry and location of several fracture zones (single-hole radar); Crosshole and vertical radar profiling provided unsatisfactory results

Author/s	Year	Site Location	Landslide Type and Geology	Geophysical Methods	Results from geophysical methods
Tingey et al.	2007	Little Valley landslide (Wasatch Mountains, Utah, USA)	Prehistoric landslide with debris mapped as deposited by rotational and translational movements; Volcanic bedrock overlain by landslide mass (weathered volcanic rock) overlain by alluvial and colluvial deposits	Seismic reflection	Determination of basal plane depth (approx 55m below surface) and geometry; Determination of slope structure (not near surface)
Yilmaz	2007	Gürbulak landslide, Trabzon (Northeastern Turkey)	Type not specified; Weathered marl and clay overlaying marl	Electrical resistivity tomography (profiles and depth slices)	Determination of thickness (7.5 m) and depth (between 2.5 and 10 m bgl) of mobilized material; Determination of sliding surface depth (10 m bgl); Location of areas of high saturation degree; Identification of clay lenses that can influence water path
Lee et al.	2008	Lishan landslide (central Taiwan)	Landslide mitigated with drainage works; Slate bedrock overlain by colluvium (slaty fragments and clayey soils)	Electrical resistivity tomography (resistivity measurement on outcrops)	Determination of depth and shape of shear zones; Information about moisture content
Marescot et al.	2008	Site near Dent the Nendaz, Rhone Valley (Swiss Alps)	Probably translational; Sandstone-like metapelites, quartzitic conglomerates and metapelites (Sivie-Mischabel nappe) and quartzites, corneules, marbles and corneules (Pontis nappe) overlain by Quaternary sediments	Electrical resistivity mapping; Electrical resistivity tomography; Induced polarization	Determination of groundwater circulation within the slope (resistivity mapping and ERT); Distinction between permeable water-bearing and low permeable clay/graphite rich features (combination of ERT and IP) Impossibility of distinguish between clay rich fractures/fault zones and areas of local graphite enrichment inside bedrock; Determination of unstable material thickness (0 to 20 m) (ERT)

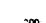




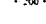
Author/s	Year	Site Location	Landslide Type and Geology	Geophysical Methods	Results from geophysical methods
Mondal et al.	2008	Naitwar Bazar landslide (Garhwal Himalaya, India)	Type not specified; Schists	Electrical resistivity tomography;	Identification of slip zones (range 10-20m depth bgl); Identification of possible groundwater pockets
Sass et al.	2008	Öschingen landslide (Swabian Alb, South-West Germany)	Type not certain: Single rotational slide or successive rotational slides or multiple rotational slide; Marls and clays overlain by limestone	Electrical resistivity tomography; Ground penetrating radar	Identification of near surface structures (rotated blocks ; GPR); Identification of landslide base (10-16 m bgl) (GPR and ERT); Determination of landslide lateral limits (ERT); Insufficient data to determine landslide type; Due to lack of penetration and noise, GPR method provided limited results
Chambers et al.	2011	Northeastern edge of Sheriff Hutton Carr (Cleveland Basin, UK)	Very slow to slow moving composite multiple earth slide-earth flow; Lias Group mudrocks: Redcar Mudstone overlain by Staithes Sandstone and Cleveland Ironstone and by Whitby Mudstone Formations (WMF)	Resistivity mapping; 2D and 3D ERT; SP mapping, profiling and tomography	Determination of drainage patterns and preferential flows (3D SPT model); Delineation of lateral limits of displaced material and of zones of depletion and accumulation; determination of thickness of each lobe; determination of geological boundaries and dip of strata; determination of variations in moisture content (2D and 3D ERT); Due to lack of sufficient resistivity contrast within WMF, 3D ERT failed to image surface of rupture, subsurface continuations of fault scarps and slip planes between multiple earth flows lobes.

Appendix D Generical legend for historical maps

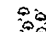
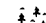
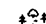



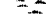
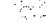
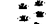
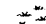




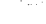

Road and Railway Features

	Railway dual track
	Railway single track and Tramways
	Railway over road
	Level crossing
	Railway over river
	Main road (fenced)
	Main road (unfenced)
	Minor road (fenced)
	Minor road (unfenced)
	Road over railway
	Road over river
	Road over stream
	Sunken road
	Raised road
	Mile Stone

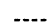






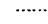
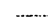




Height (in Feet)

	Contour (pre 1895)
	Contour (Instrumental)
	Contour (Instrumental)
	Contour (Sketched)
	Contour (Sketched)
	Surface level







Landscape Features

	Deciduous Woods
	Fir Woods
	Mixed Woods
	Brushwood
	Orchard
	Rough Pasture
	Furze
	Marsh
	Reeds
	Osiers
	Parks
	Gravel Pit
	Sand Pit
	Other Pit
	Shingle
	Quarry

Boundaries

	Counties
	County and Civil Parish
	Administrative County and Civil Parish
	County Borough
	Parliamentary County Divisions
	Poor Law Union (obsolete since 1930)
	Parliamentary Boroughs
	Divisions of Parliamentary Boroughs
	Municipal Boroughs
	Urban Districts
	Police Burghs (Scotland)
	Rural Districts
	Civil Parish

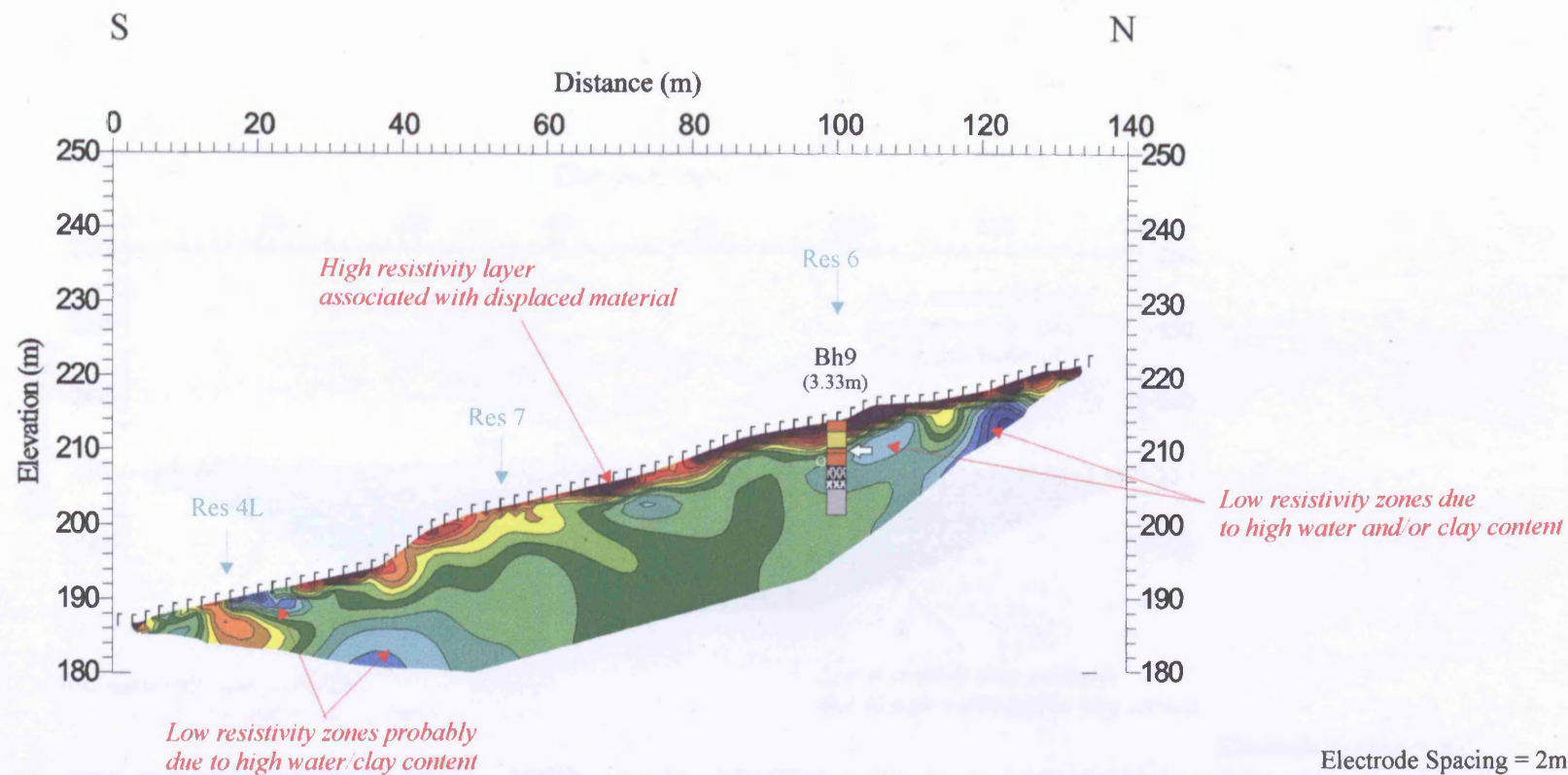
Point Features

	Flow Arrow
	Site of Antiquities
	Trigonometrical Station
	Benchmark (BM)
	Pump, Guide Post or Signal Post
	Well, Spring or Boundary Post

Text

C	County Boroughs
P	Parliamentary Boroughs
D	Divisions of Parliamentary Boroughs
M	Municipal Boroughs
U	Urban Districts or Police Burghs (Scotland)
P	Civil Parishes
T	Towns (other than above)
D	Districts (Close) in Towns and Suburbs
D	Districts (Open) in Towns and Suburbs

(from [WWW 3.2])

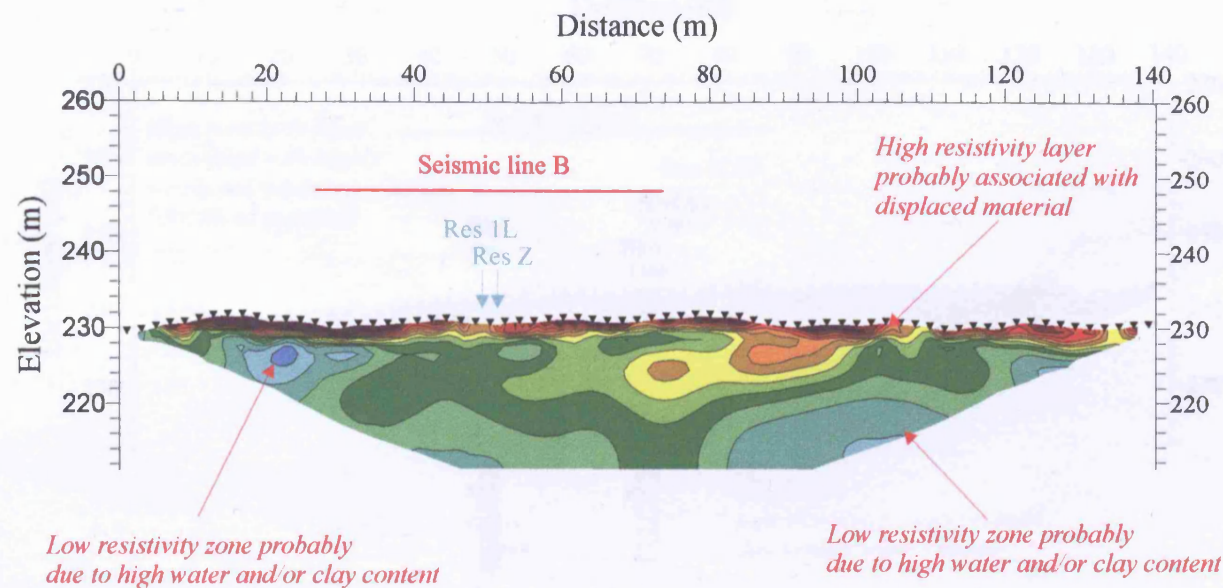


Borehole Key		
Clay	Sandstone	*** Hafod (ESP)
Silt	Highly weathered	← Potential failure surface (ESP)
Sand	Void	○ dry
Gravel	Coal	∇ min water level (ESP and divers)
Siltstone	* No 3 Rhonda (ESP)	▴ max water level (ESP and divers)
Mudstone	** Tormynydd (ESP)	

Appendix E-I
Mynydd Yr Eglwys Landslide (Ystrad)
Line 5s - Wenner Schlumberger
Scale 1:1000 Date: 20 December 2006

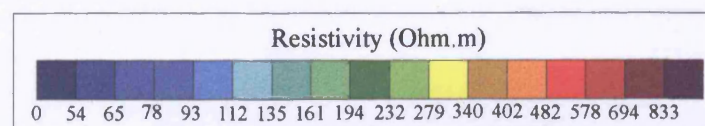
W

E



Iteration 3: RMS 2.1%

Electrode Spacing = 2m

**Borehole Key**

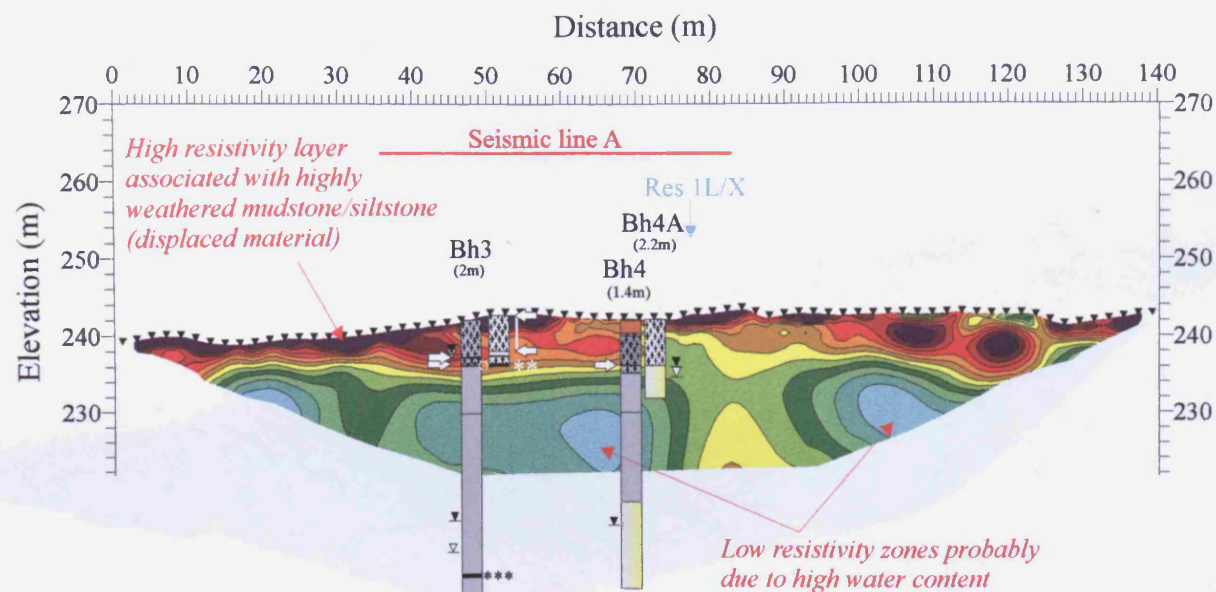
Clay	Sandstone	*** Hafod (ESP)
Silt	Highly weathered	← Potential failure surface (ESP)
Sand	Void	○ dry
Gravel	Coal	∇ min water level (ESP and divers)
Siltstone	* No 3 Rhonda (ESP)	▴ max water level (ESP and divers)
Mudstone	** Tormynydd (ESP)	

Appendix E-2**Mynydd Yr Eglwys Landslide (Ystrad)****Line 9s - Wenner Schlumberger**

Scale 1:1000 Date: 29 May 2008

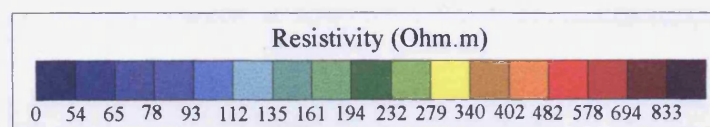
W

E



Iteration 3: RMS 2.8%

Electrode Spacing = 2m



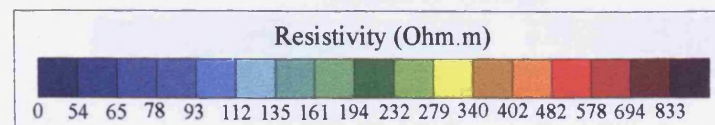
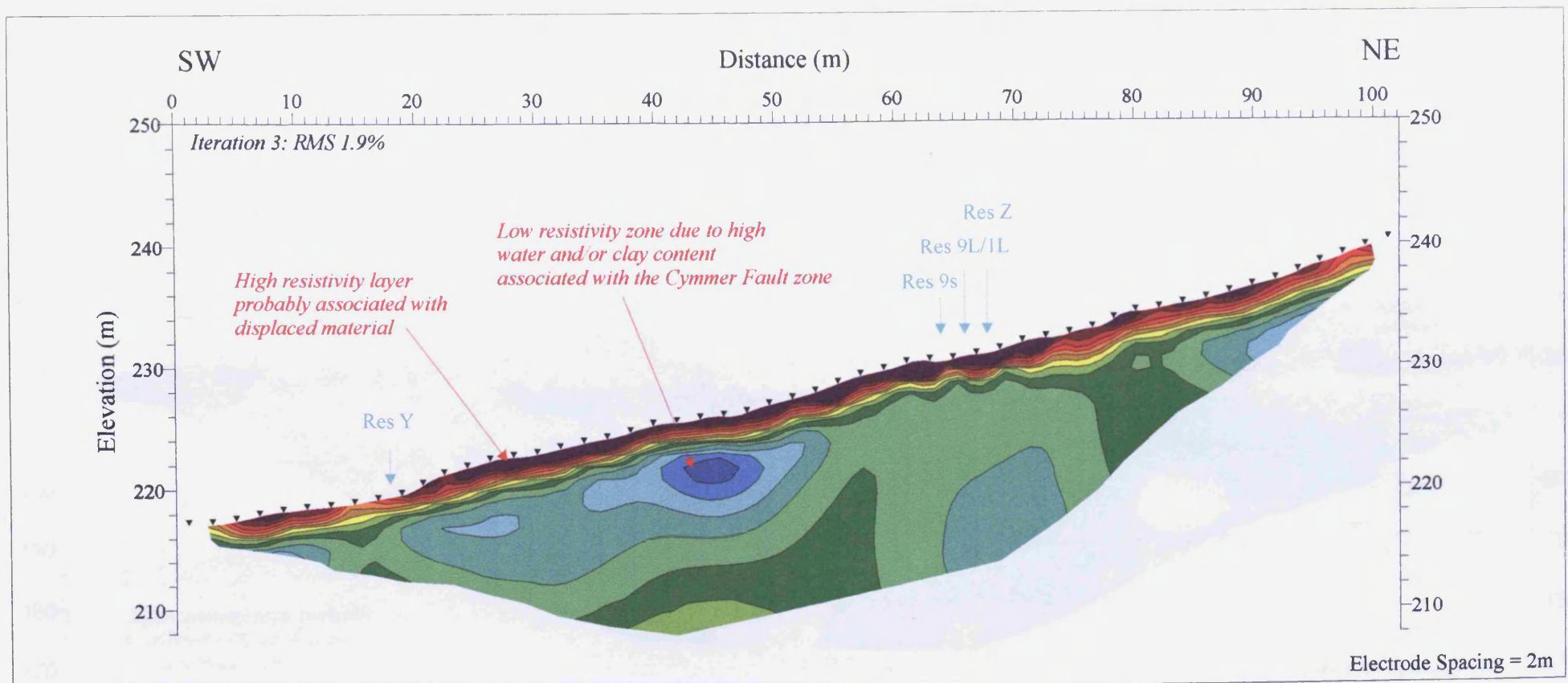
Borehole Key		
Clay	Sandstone	*** Hafod (ESP)
Silt	Highly weathered	← Potential failure surface (ESP)
Sand	Void	○ dry
Gravel	Coal	▽ min water level (ESP and divers)
Siltstone	* No 3 Rhonda (ESP)	▼ max water level (ESP and divers)
Mudstone	** Tormynydd (ESP)	

Appendix E-3

Mynydd Yr Eglwys Landslide (Ystrad)

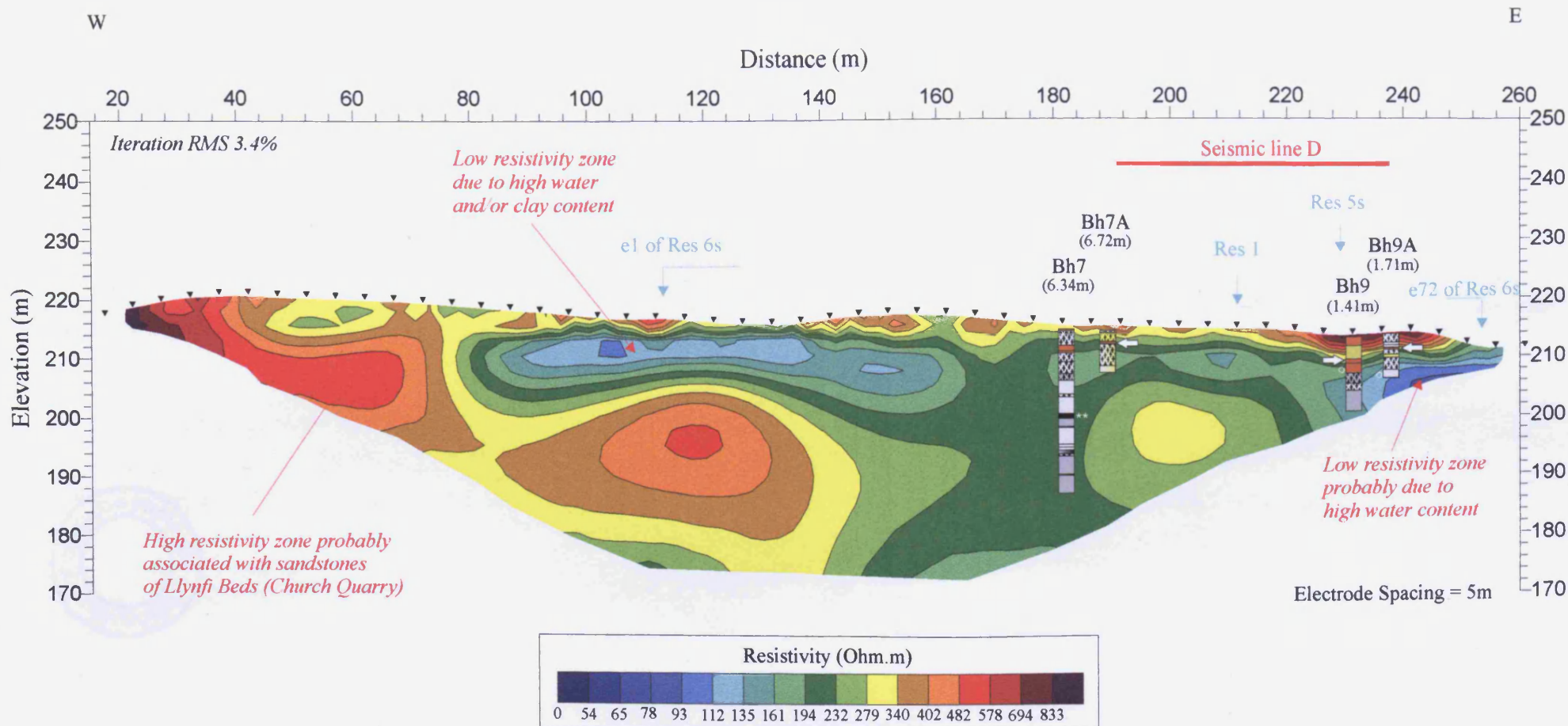
Line Z - Wenner Schlumberger

Scale 1:1000 Date: 13 June 2008



Borehole Key		
Clay	Sandstone	*** Hafod (ESP)
Silt	Highly weathered	← Potential failure surface (ESP)
Sand	Void	○ dry
Gravel	Coal	∇ min water level (ESP and divers)
Siltstone	* No 3 Rhonda (ESP)	▼ max water level (ESP and divers)
Mudstone	** Tormynydd (ESP)	

<i>Appendix E-4</i>
Mynydd Yr Eglwys Landslide (Ystrad)
Line 14s - Wenner Schlumberger
Scale 1:500 Date: 28 November 2008



Borehole Key		
Clay	Sandstone	*** Hafod (ESP)
Silt	Highly weathered	← Potential failure surface (ESP)
Sand	Void	○ dry
Gravel	Coal	∇ min water level (ESP and divers)
Siltstone	* No 3 Rhonda (ESP)	▼ max water level (ESP and divers)
Mudstone	** Tormynydd (ESP)	

Appendix E-5

Mynydd Yr Eglwys Landslide (Ystrad)

Line 6L - Wenner Schlumberger

Scale 1:1000 Date: 13 December 2006